



8-2001

## **Development of a subsonic free-jet nozzle for inlet-engine integration ground test facilities**

David K. Beale

Follow this and additional works at: [https://trace.tennessee.edu/utk\\_gradthes](https://trace.tennessee.edu/utk_gradthes)

---

### **Recommended Citation**

Beale, David K., "Development of a subsonic free-jet nozzle for inlet-engine integration ground test facilities. " Master's Thesis, University of Tennessee, 2001.  
[https://trace.tennessee.edu/utk\\_gradthes/9564](https://trace.tennessee.edu/utk_gradthes/9564)

This Thesis is brought to you for free and open access by the Graduate School at TRACE: Tennessee Research and Creative Exchange. It has been accepted for inclusion in Masters Theses by an authorized administrator of TRACE: Tennessee Research and Creative Exchange. For more information, please contact [trace@utk.edu](mailto:trace@utk.edu).

To the Graduate Council:

I am submitting herewith a thesis written by David K. Beale entitled "Development of a subsonic free-jet nozzle for inlet-engine integration ground test facilities." I have examined the final electronic copy of this thesis for form and content and recommend that it be accepted in partial fulfillment of the requirements for the degree of Master of Science, with a major in Mechanical Engineering.

Frank Collins, Major Professor

We have read this thesis and recommend its acceptance:

Ahmad Vikili, Roy Schulz

Accepted for the Council:

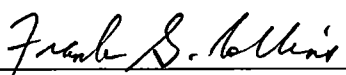
Carolyn R. Hodges

Vice Provost and Dean of the Graduate School

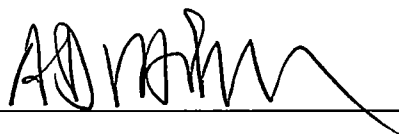
(Original signatures are on file with official student records.)

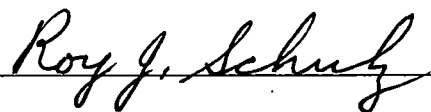
To the Graduate Council:

I am submitting herewith a thesis written by David K. Beale entitled "Development of a Subsonic Free-jet Nozzle for Inlet-Engine Integration Ground Test Facilities". I have examined the final copy of this thesis for form and content and recommend that it be accepted in partial fulfillment of the requirements for the degree of Master of Science, with a major in Mechanical Engineering.


  
\_\_\_\_\_  
Dr. Frank Collins, Major Professor

We have read this thesis  
and recommend its acceptance:

  
\_\_\_\_\_

  
\_\_\_\_\_

Accepted for the Council:

  
\_\_\_\_\_  
Associate Interim Vice Provost  
and Dean of the Graduate School

**DEVELOPMENT OF A SUBSONIC FREE-JET NOZZLE  
FOR INLET-ENGINE INTEGRATION  
GROUND TEST FACILITIES**

A Thesis  
Presented for the  
Master of Science  
Degree  
The University of Tennessee, Knoxville

David K. Beale  
August 2001



## ACKNOWLEDGMENTS

I would like to thank my committee members; Dr. Frank Collins, Dr. Roy Schulz, and Dr. Ahmad Vakili; for their support and patience during the preparation of this thesis. I would also like to thank Ms. Brenda Bush for her help in the preparation of the final document.

## ABSTRACT

The Arnold Engineering Development Center (AEDC) offers a unique test capability for the evaluation of inlet-engine compatibility. The capability features a variable-attitude and variable-Mach number free-jet nozzle that subjects an aircraft propulsion system to a flow field approximating the flight environment. The free-jet nozzle provides a flow quality commensurate with inlet-engine compatibility test requirements over a wide range of pitch angles, yaw angles, and Mach numbers. The development of the nozzle centered on achievement of the required flow quality.

Initial flow quality experiments revealed a tendency for large, secondary vortical flows to develop in the free-jet nozzle flow field. These vortical flows severely degraded the flow quality delivered by the nozzle. The failure of the initial nozzle to achieve flow quality goals motivated research focused on preventing the formation of vortices in subsonic free-jet nozzles.

This thesis describes a comprehensive investigation that coupled water flow and airflow experiments to improve the understanding of the mechanisms leading to the formation of nozzle vortices, and to develop vortex suppression methods. Providing a unique flow visualization capability, the water tunnel revealed features of the complex flow field associated with the vortex formation and facilitated the identification of vortex suppression techniques. The airflow tests provided detailed flow-field measurements for validating water tunnel findings and verifying achievement of flow requirements.

The water flow and airflow experiments provided information that enabled the development of specifications for a subsonic free-jet nozzle to be applied in the AEDC

Aeropropulsion Systems Test Facility (ASTF) free-jet test system. The experiments used two sub-scale models of the ASTF Test Cell C-2. The airflow model quantified nozzle exit flow quality through measurements of Mach number and flow angle distributions. The measurements were obtained at nominal Mach numbers ranging from 0.3 to 0.9 and nozzle pitch angles ranging from 0 to 50 deg. The water flow model, installed in the University of Tennessee Space Institute water tunnel, used dye injection to delineate streaklines of the flow entering and exiting free-jet nozzle configurations.

The development of the free-jet nozzle employed multiple entries in both the air flow and water flow facilities. The work progressed through the process of identifying flow anomalies, determining the critical parameters that dominate the secondary flow formation, identifying candidate flow quality improvement methods, selecting a method for application in the ASTF free-jet nozzle, and validating nozzle configurations prior to full-scale implementation.

This thesis provides both visual and measured free-jet nozzle flow characteristics obtained during the investigation. Comparisons of airflow and water flow simulations illustrate the validation of the water tunnel as a tool for studying secondary internal flows. Parametric results reveal the nozzle and installation features that influence the secondary flow formation. Finally, results show the numerous methods investigated for preventing the formation of vortices.

The research yielded two successful vortex suppression methods. Each method modified the flow field in the vicinity of the vortex attachment point, near the nozzle inlet, to prevent vortex formation. The thesis describes the selection and application of

one method in a nozzle configuration that meets the requirements for the ASTF free-jet test system.

## CONTENTS

	PAGE
1.0 INTRODUCTION.....	1
1.1 Background .....	1
1.2 Subsonic Free-Jet Nozzle .....	6
1.3 Scope of Investigation .....	11
2.0 APPARATUS.....	17
2.1 Test Facilities .....	17
2.2 Test Articles .....	22
2.3 Instrumentation .....	36
3.0 TEST DESCRIPTION .....	44
3.1 General .....	44
3.2 Test Procedure.....	45
3.3 Data Reduction.....	58
3.4 Uncertainty of Results.....	59
4.0 RESULTS AND DISCUSSION .....	61
4.1 R2A2 Phase I.....	61
4.2 Water Tunnel Phase I.....	65
4.3 R2A2 Phase II .....	81
4.4 Water Tunnel Phase II.....	85
4.5 R2A2 Phase III.....	97
4.6 Water Tunnel Phase III.....	105
5.0 SUMMARY AND CONCLUSIONS .....	110
REFERENCES .....	117
APPENDIXES .....	127
APPENDIX A. FIGURES.....	128
APPENDIX B. TABLES.....	343
APPENDIX C. FLOW ANGLE DEFINITIONS.....	355
APPENDIX D. ASTF FREE-JET NOZZLE CONCEPT DEVELOPMENT .....	363
VITA .....	388

## LIST OF FIGURES

FIGURE	PAGE
1. Free-Jet Test Concept .....	129
2. ASTF C-2 Test Cell in Free-Jet Configuration.....	130
3. Chronology of Experimental Approach.....	131
4. Research Test Cell R2A2 in Free-Jet Configuration .....	132
5. Research Test Cell R2A2 Performance with Atmospheric Inlet .....	134
6. University of Tennessee Space Institute Water Tunnel.....	135
7. Water Tunnel Model of Research Test Cell R2A2.....	136
8. Variable-Area Free-Jet Nozzle Airflow Model .....	137
9. Variable-Area Free-Jet Nozzle Airflow Model Wall Contours.....	139
10. Variable-Area Nozzle Airflow Nozzle Model Installation in R2A2 .....	140
11. Modified Variable-Area Nozzle Airflow Model .....	141
12. Variable-Area Nozzle Airflow Model Ramp Configurations.....	142
13. ASTF Subsonic Free-Jet Nozzle Airflow Model.....	148
14. Nozzle Attitude Positioning Mechanism for ASTF Free-Jet Nozzle Model Airflow Tests .....	150
15. Nozzle Attitude Positioning Mechanism Pitch Actuator and Position Indicator.....	151
16. Photograph of ASTF Subsonic Freejet Nozzle Airflow Model.....	152
17. Variable-Area Free-Jet Nozzle Water Flow Model.....	153
18. Variable-Area Free-Jet Nozzle Water Tunnel Installation .....	155

FIGURE	PAGE
19. Photograph of Variable-Area Nozzle Water Flow Model .....	156
20. Variable-Area Nozzle Water Tunnel Model Flow Straightener Configurations .....	158
21. Variable-Area Nozzle Water Flow Model Ramp Configurations .....	162
22. Locations of Suction Regions on Variable-Area Nozzle Water Flow Model .....	170
23. Piccolo Tube Assembly for Variable-Area Nozzle Model Blowing Experiments in Water Tunnel .....	171
24. Generic 2-D Free-Jet Nozzle Water Flow Models .....	172
25. Generic Axisymmetric Nozzle Water Flow Models .....	177
26. Water Flow Model Slotted Bulkhead and Nozzle Position Parameter Definitions .....	179
27. Water Flow Model Nozzle Exit Cavity Installation .....	181
28. Water Flow Model Artificial Bulkhead Installation .....	183
29. Water Flow Model Artificial Floor Installation .....	184
30. Water Flow Model Horizontal Baffle Installation .....	185
31. Water Flow Model Vertical Baffle Installation .....	186
32. Ramp 1 Configuration for Short Axisymmetric Nozzle Water Flow Model .....	187
33. Ramp 2 Configuration for Short Axisymmetric Nozzle Water Flow Model .....	188
34. ASTF Nozzle Water Flow Model .....	191
35. Mounting Fixture for ASTF Nozzle Water Flow Model .....	194
36. ASTF Nozzle Water Flow Model Ramp B Planform .....	195

FIGURE	PAGE
37. Water Flow Model of ASTF Free-Jet Nozzle Attitude Positioning Mechanism.....	196
38. R2A2 Test Cell Parameter Measurement Locations.....	198
39. Mach/Flow Angularity Rake for Flow-Field Surveys in R2A2.....	200
40. Mach/Flow Angularity Rake Installation in R2A2.....	201
41. ASTF Nozzle Airflow Model Pressure Measurement Locations .....	203
42. Water Flow Test Dye Injection Probe System.....	204
43. Water Flow Test Dye Injection Locations .....	205
44. Water Flow Model Exit Dye Injection Zone Designations .....	206
45. Variable-Area Nozzle Exit Mach Number Measurements with HN = 11.25 in. and DIV = 0 deg .....	207
46. Variable-Area Nozzle Exit Flow Angularity Measurements with MACH = 0.6, HN = 11.25 in., and DIV = 0 deg .....	212
47. Variable-Area Nozzle Exit Flow Angularity Measurements with $\theta = 30$ DEG, HN = 11.25 in., and DIV = 0 deg.....	216
48. Variable-Area Nozzle Exit Mach Number Measurements with HN = 5.63 in. and DIV = 0 deg .....	218
49. Variable-Area Nozzle Exit Flow Angularity Measurements with MACH = 0.6, HN = 5.63 in., and DIV = 0 deg.....	223
50. Variable-Area Nozzle Exit Flow Angularity Measurements with MACH = 0.8, $\theta = 30$ deg, HN = 5.63 in. and DIV = 0 deg.....	225
51. Variable-Area Nozzle Exit Flow Angularity Measurements with MACH = 0.6, $\theta = 20$ deg, HN = 11.25 in., and DIV = 4 deg.....	226
52. Water Flow Visualization of Variable-Area Nozzle Vortices.....	227



FIGURE	PAGE
53. Water Flow Visualization of Variable-Area Nozzle Streaklines in Zones without Vortices.....	229
54. Water Flow Streaklines for 2-D ASY Nozzle Set at $\theta = 30$ deg .....	233
55. Water Flow Streaklines Inside Nozzle Exit Cavity with 2-D SYM Nozzle Set at $\theta = 30$ deg and ZI = 0.6 in. ....	235
56. Water Flow Streaklines for 2-D ASY Nozzle Set at $\theta = 45$ deg and ZI = 2 in. ....	236
57. Water Flow Streaklines for 2-D SYM Nozzle Set at $\theta = 30$ deg.....	237
58. Water Flow Streaklines for 2-D SYM Nozzle Set at $\theta = 30$ deg with Artificial Floor Installed .....	239
59. Water Flow Streaklines for 2-D SYM Nozzle Set at $\theta = 30$ deg and ZI = 3.3 in. with Artificial Bulkhead Installed.....	240
60. Water Flow Streaklines in Short Axisymmetric Nozzle Set at $\theta = 30$ deg .....	241
61. Water Flow Streaklines in Long Axisymmetric Nozzle Set at $\theta = 30$ deg and ZI = 0.85 in. ....	244
62. Water Flow Streaklines in Zone 3 of Variable-Area Nozzle Set at $\theta = 30$ deg with Inlet Screen Installed .....	245
63. Water Flow Streaklines in Zone 3 of Variable-Area Nozzle Set at $\theta = 30$ deg with Vertical Vanes Installed.....	246
64. Water Flow Streaklines in Zone 3 of Variable-Area Nozzle Set at $\theta = 30$ deg with Honeycomb Installed.....	247
65. Water Flow Streaklines in Zone 3 of Variable-Area Nozzle Set at $\theta = 30$ deg with Horizontal Turning Vanes Installed.....	248
66. Water Flow Streaklines in Zone 3 of Variable-Area Nozzle Set at $\theta = 30$ deg with Inlet Ramps Installed .....	249

FIGURE	PAGE
67. Water Flow Streaklines in 2-D SYM nozzle at $\theta = 30$ deg and ZI = 1.4 in. with Ramps Installed.....	252
68. Water Flow Streaklines in Short Axisymmetric Nozzle at $\theta = 30$ deg and ZI = 1.4 in. with AXI Ramp 1 installed .....	254
69. Water Flow Streaklines in Short Axisymmetric Nozzle at $\theta = 30$ deg and ZI = 1.4 in. with AXI Ramp 2 Installed.....	255
70. Water Flow Streaklines in 2-D High- $\alpha$ Nozzle Set at $\theta = 30$ deg and ZI = 0.6 in. ....	260
71. Water Flow Streaklines in 2-D High- $\alpha$ Nozzle Set at $\theta = 45$ deg and ZI = 0.6 in. ....	263
72. Variable-Area Nozzle Exit Mach Number Measurements at MACH = 0.6 with Ramp Installed.....	265
73. Variable-Area Nozzle Exit Flow Angularity Measurements at $\theta = 30$ deg with 30-deg Contoured Ramp Installed .....	267
74. Variable-Area Nozzle Exit Flow Angularity Measurements at MACH = 0.6 and $\theta = 30$ deg with 30-deg Straight Ramp Installed .....	269
75. Variable-Area Nozzle Exit Flow Angularity Measurements at $\theta = 50$ deg with 50-deg Contoured Ramp Installed .....	270
76. Variable-Area Nozzle Exit Flow Angularity Measurements at MACH = 0.6 and $\theta = 50$ deg with 50-deg Straight Ramp Installed.....	272
77. Water Flow Streaklines in Variable-Area Nozzle at $\theta = 30$ deg with Piccolo Tube Set at ZT = 0.75 in. and YBL = 2.375 in. ....	273
78. Water Flow Streaklines in Variable-Area Nozzle at $\theta = 30$ deg with Piccolo Tube Set at ZT = 0.75 in. and YBL = 0.9 in. ....	274
79. Water Flow Streaklines in Variable-Area Nozzle at $\theta = 30$ deg with Piccolo Tube Set at ZT = 0.75 in., W = 1.5 gph, and Variable YBL .....	276

FIGURE	PAGE
80. Water Flow Streaklines in Variable-Area Nozzle at $\theta = 30$ deg with Piccolo Tube Set at ZT = 1.19 in., W = 1.5 gph, and Variable YBL.....	277
81. Water Flow Streaklines in Variable-Area Nozzle at $\theta = 30$ deg with Region 1 Suction.....	278
82. Water Flow Streaklines in Variable-Area Nozzle at $\theta = 30$ deg with Region 2 Suction.....	279
83. Water Flow Streaklines in Variable-Area Nozzle at $\theta = 30$ deg with Region 3 Suction.....	282
84. Water Flow Streaklines in Variable-Area Nozzle at $\theta = 30$ deg with Region 4 Suction.....	283
85. Water Flow Streaklines in 2-D SYM Nozzle at $\theta = 30$ .deg and ZI = 0.6 in. with Baffles Installed.....	284
86. Water Flow Streaklines in Variable-Area Nozzle at $\theta = 30$ deg with Ramp 21 Installed.....	285
87. Water Flow Streaklines in Variable-Area Nozzle at $\theta = 30$ deg with Ramp 22 Installed.....	287
88. Water Flow Streaklines in ASTF Nozzle Model Installed Inverted and Set to $\theta = 30$ deg and ZI = 1.6 in. ....	288
89. Water Flow Streaklines in ASTF Nozzle Model Set at $\theta = 45$ deg and ZI = 1.2 in. with RMP = 20 deg.....	289
90. Water Flow Streaklines in ASTF Nozzle Model Set at $\theta = 45$ deg and ZI = 1.2 in. with Ramp Extension Installed.....	291
91. Water Flow Streaklines in ASTF Nozzle Model Set at $\theta = 30$ deg and ZI = 2.25 in.with RMP = -10 deg.....	293
92. Water Flow Streaklines in ASTF Nozzle Model Set at $\theta = -10$ deg and ZI = 1.05 in. ....	296

FIGURE	PAGE
93. ASTF Nozzle Model Exit Mach Number Measurements with MACH = 0.6 and R2A2 Configuration A.....	297
94. ASTF Nozzle Exit Flow Angularity Measurements with MACH = 0.6, $\theta = 0$ deg, Ramp Configuration A1, RMP = -10 deg, and R2A2 Configuration A.....	301
95. ASTF Nozzle Model Exit Flow Angularity Measurements with MACH = 0.6, $\theta = 30$ deg, Ramp Configuration A1, RMP = -10 deg, and R2A2 Configuration A.....	303
96. ASTF Nozzle Model Exit Flow Angularity Measurements with MACH = 0.6, $\theta = 45$ deg, Ramp Configuration A1, RMP = -10 deg, and R2A2 Configuration A.....	305
97. ASTF Nozzle Model Exit Mach Number Measurements with MACH = 0.6 and R2A2 Configuration B.....	307
98. ASTF Nozzle Model Exit Flow Angularity Measurements with MACH = 0.6, $\theta = 45$ deg, Ramp Configuration A1, RMP = +20 deg, and R2A2 Configuration B.....	311
99. ASTF Nozzle Model Exit Flow Angularity Measurements with MACH = 0.6, $\theta = 45$ deg, Ramp Configuration A2, RMP = +20 deg, and R2A2 Configuration B.....	313
100. ASTF Nozzle Model Exit Flow Angularity Measurements with MACH = 0.6, $\theta = 30$ deg, Ramp Configuration A2, RMP = -10 deg, and R2A2 Configuration B.....	315
101. Water Flow Streaklines in ASTF Nozzle Model with Ramp Configuration B at RMP = 20 deg, $\theta = 45$ deg and $\psi = 0$ deg.....	317
102. Water Flow Streaklines in ASTF Nozzle Model with Ramp Configuration B at RMP = -10 deg, $\theta = 30$ deg and $\psi = 0$ deg.....	323
103. Water Flow Streaklines in ASTF Nozzle Model with Ramp Configuration B at RMP = 20 deg, $\theta = 45$ deg, and Variations in Yaw Angle.....	329

FIGURE	PAGE
104. Water Flow Streaklines in ASTF Nozzle Model with Ramp Configuration B, $\psi = -10$ deg, and Variations in Pitch Angle.....	335
105. Water Flow Streaklines in Zone 8 of ASTF Nozzle Model with Ramp Configuration B, Zero Yaw Angle, and Variations in Pitch Angle.....	339
106. Water Flow Streaklines in ASTF Nozzle Model with Ramp Configuration B, $\theta = 25$ deg, $\Psi = 0$ deg and Variations in RMP .....	340
C-1. Definition of ALPHA and BETA .....	360
C-2. Free-Jet Nozzle Orientation Angle Definitions .....	361
C-3. Flow-Field Probe Aerodynamic Angle Definitions .....	362
D-1. Two-Position Nozzle Operation .....	375
D-2. Nozzle Exit Area Layout .....	376
D-3. Nozzle/Ramp Concept.....	379
D-4. Free-Jet Nozzle Installed in ASTF .....	380
D-5. Ramp Hinge .....	381
D-6. Nozzle Contours .....	383
D-7. Ramp A1 Contour.....	386
D-8. Ramp Inclination Schedule.....	387

## LIST OF TABLES

TABLE	PAGE
1. Airflow Test Phase I Matrix .....	344
2. Airflow Test Phase II Matrix .....	345
3. Airflow Test Phase III Matrix .....	345
4. Water Tunnel Test Phase I Matrix .....	346
5. Water Tunnel Test Phase II Matrix .....	348
6. Water Tunnel Test Phase III Matrix .....	349
7. Measured Parameter Uncertainties .....	351
8. Calculated Parameter Uncertainties .....	352
9. Summary of Water Tunnel Test Phase III Results .....	354

## NOMENCLATURE

ALPHA	Flight or wind tunnel angle of attack, deg (Appendix C)
ALPFJ	Free-jet angle of attack, deg (Appendix C)
ALPL	Local angle of attack measured by probe, deg (Appendix C)
ALPL-AVG	Local angle of attack deviation from nozzle exit average, deg
BETA	Flight or wind tunnel angle of sideslip, deg (Appendix C)
BETFJ	Free-jet angle of sideslip, deg (Appendix C)
BETL	Local angle of sideslip measured by probe, deg (Appendix C)
BETL-AVG	Local angle of sideslip deviation from nozzle exit average, deg
D	Free-jet nozzle diameter, in.
DIV	Inclination angle of upper or lower nozzle wall relative to nozzle longitudinal axis, deg
DP13-j	Probe j differential pressure, pressure orifice 3 - pressure orifice 1, psid
DP24-j	Probe j differential pressure, pressure orifice 4 - pressure orifice 2, psid
H	Height of inlet above ground plane, in.
HN	Spacing between upper nozzle wall and lower nozzle wall, in.
HRN	Nozzle exit fluctuating total pressure, psid
HRP	Plenum chamber fluctuating total pressure, psid
MACH	Free-jet nozzle exit Mach number
ML	Local Mach number measured by probe
ML-AVG	Local Mach number deviation from nozzle exit average

P or PFJ	Free-jet nozzle exit static pressure, psia
PITCH, $\theta$	Free-jet nozzle pitch angle, deg (Appendix C)
PNB1-PNB5	Free-jet nozzle lower wall static pressure, psia
PNT1-PNT5	Free-jet nozzle upper wall static pressure, psia
PR1-PR4	Free-jet ramp static pressure, psia
PT or PTFJ	Free-jet total pressure, psia
PTNB1, PTNB2	Free-jet nozzle exit total pressure measured near lower wall, psia
PTNT1, PTNT2	Free-jet nozzle exit total pressure measured near upper wall, psia
PTPj	Plenum chamber total pressure measured by pitot probe j, psia
P1A1-P1A4	Station 1A plenum chamber static pressure, psia
P1B1-P1B4	Station 1B plenum chamber static pressure, psia
P2C1-P2C4	Station 2 test section static pressure, psia
P3C1-P3C4	Station 3 test section static pressure, psia
P4C1-P4C4	Station 4 test section static pressure, psia
Pi-j	Pressure measured at orifice i on cone probe j, psia
RAKE	Flow-field survey rake vertical position, in nozzle axis system, relative to nozzle centerline, in.
RE	Free-jet nozzle exit unit Reynolds number, $\text{ft}^{-1}$
RMP	Free-jet nozzle ramp inclination angle, deg
ROLL	Free-jet nozzle roll angle, deg (Appendix C)
s	Curvilinear nozzle wall coordinate, in.
T	Free-jet nozzle exit static temperature, $^{\circ}\text{R}$
THETA	Local total flow angle measured by cone probe, deg (Appendix C)



TT or TTFJ	Free-jet nozzle total temperature, °R
u,v,w	Components of the flight, wind tunnel, or free-jet nozzle exit velocity vector in the x, y, and z directions, respectively
u <sub>p</sub> , v <sub>p</sub> , w <sub>p</sub>	Components of the flight, wind tunnel, or free-jet nozzle exit velocity vector in the x <sub>p</sub> , y <sub>p</sub> , and z <sub>p</sub> directions, respectively
V	Flight, wind tunnel, or free-jet nozzle exit velocity, ft/sec
V <sub>i</sub>	Free-jet Nozzle inlet velocity, ft/sec
WN	Width of free-jet nozzle at exit, in.
x,y,z	Test article orthogonal body axis system (Appendix C) or nozzle wall coordinates, in.
XI	Distance from free-jet nozzle inlet to bulkhead, in. (Fig. 26)
x <sub>n</sub> , y <sub>n</sub> , z <sub>n</sub>	Free-jet nozzle orthogonal axis system (Appendix C)
x <sub>p</sub> , y <sub>p</sub> , z <sub>p</sub>	Cone probe orthogonal axis system (appendix C)
x <sub>w</sub> , y <sub>w</sub> , z <sub>w</sub>	Orthogonal wind axis system (appendix C)
YBL	Width of piccolo tube blowing region, in.
W	Piccolo tube blowing rate or boundary layer suction rate, lbm/sec
YAW, ψ	Free-jet nozzle yaw angle, deg (appendix C)
ZI	Distance from plenum chamber floor to lower nozzle wall leading edge, in. (Fig. 26)
ZP	Piccolo tube immersion, vertical distance from plenum floor to piccolo tube blowing orifice, in.

## Abbreviations

APM	Attitude Positioning Mechanism
ASTF	Aeropropulsion Systems Test Facility
DDAL	Dynamic Data Analysis Laboratory
ETF	Engine Test Facility
NBS	National Bureau of Standards
NIST	National Institute of Standards
UTSI	University of Tennessee Space Institute

## Apparatus Configuration Codes

ASTF Nozzle	Designation for ASTF subsonic free-jet nozzle configuration
AXI Ramp 1	Designation for short axisymmetric nozzle ramp configuration (Fig. 32)
AXI Ramp 2	Designation for short axisymmetric nozzle ramp configuration (Fig. 33)
C-2 Config	Designation for water tunnel model of ASTF Test Cell C-2 plenum (Fig. 7)
High- $\alpha$	Designation for 2-D nozzle designed for high pitch operation (Fig. 24)
LONG AXI	Designation for long axisymmetric nozzle (Fig. 25)
Ramp A1	Designation for ASTF nozzle ramp configuration (Fig. 13)
Ramp A2	Designation for ASTF nozzle ramp configuration (Fig. 13)
Ramp B	Designation for ASTF nozzle ramp configuration (Fig. 36)

Ramp n	Designation for variable-area 2-D nozzle ramp n, where n = 1-5 or 21-22 (Fig. 21)
R2A2	Designation for ETF Research Test Cell R2A2
R2A2 Config	Designation for water tunnel model of Test Cell R2A2 plenum (Fig. 7)
R2A2 Config A	Designation for original R2A2 plenum with 63-in. diameter section (Fig. 4)
R2A2 Config B	Designation for modified R2A2 plenum with extension to mask 63-in. diameter section (Fig. 4)
SHORT AXI	Designation for short axisymmetric nozzle (Fig. 25)
VAR AREA	Designation for 2-D variable-area free-jet nozzle (Fig. 8)
2-D ASY	Designation for 2-D free-jet nozzle with asymmetric contraction section (Fig. 24)
2-D SYM	Designation for 2-D free-jet nozzle with symmetrical contraction section (Fig. 24)

## 1.0 INTRODUCTION

### 1.1 BACKGROUND

High-performance aircraft rely extensively on the propulsion system for completing the design missions. Components such as the engine, inlet, diffuser duct, external airframe, and controls, must function in harmony over flight envelopes that may contain harsh conditions. For example, the fighter pilot depends on his aircraft to maneuver at extremes in angle of attack and angle of sideslip with a minimal loss of airspeed and altitude. Such a requirement demands high thrust to offset the drag that accompanies excursions into the high-angle-of-attack regime. At the same time, the combat environment subjects the engine to high levels of adverse flow distortion that can prevent delivery of peak engine performance. Furthermore, the advent of technologies such as thrust vectoring and powered lift have expanded the role of the propulsion system from that of simply a thrust producer to a producer of thrust, lift, and control moments. The expanded role of the propulsion system has, in turn, augmented the extension of the flight envelope into the supermaneuver regime and the addition of V/STOL capabilities.

Airframe-propulsion interactions, and in particular inlet-engine interactions, can lead to unacceptable flight problems ranging from thrust degradation at demanding points in the flight envelope to engine flameout. Inlet-engine compatibility issues group into three areas: (1) operability, (2) performance, and (3) aeromechanics. Operability addresses engine stability and surge margin, performance addresses thrust, and

aeromechanics addresses structural integrity. Through historical experiences with problems encountered in these three areas, designers came to recognize the importance of assessing the compatibility of the airframe, inlet, and engine early in the aircraft development cycle. To help avoid the unacceptable cost of discovering problems after deployment of a system, the turbine engine community developed propulsion system test and evaluation methods employing ground test facilities.

The most widely used ground test method evaluates inlet-engine compatibility using a combination of wind tunnel tests and engine tests. Wind tunnel tests using subscale models of the inlet, duct, and influential sections of the airframe establish the distortion characteristics of the flow delivered to the engine face. Inlet simulators subsequently subject the turbine engine to similarly distorted flow in the direct-connect test facility. The most commonly used inlet simulators include such devices as the distortion screen and the air jet distortion generator. References 1-48 may be consulted for additional information on the test method, inlet simulation devices, distortion descriptors, and inlet distortion analysis processes.

The necessity to employ artificial flow distortion generators and distortion descriptors to correlate subscale inlet wind tunnel tests and full-scale engine tests presents limitations in the methodology. The evaluation captures only the effect of the inlet-airframe on the engine and only to the extent that the inlet simulator can approximate the actual flow field. The effects of the engine on the inlet are generally neglected. Furthermore, current inlet simulators generally provide only steady distortion patterns and neglect the time variation encountered during aircraft maneuvers.

To avoid the above approximations, wind tunnel tests of the coupled propulsion system components have been successfully applied. Existing propulsion wind tunnels have been applied to fully coupled cruise missile and even full-scale fighter-size systems such as the F-15 (Ref. 49). However, for fighter-size systems, physical size limits the pitch angle (PITCH) and yaw angle (YAW) envelopes so that only modest angles of attack and sideslip can be simulated.

The Arnold Engineering Development Center (AEDC) added a free-jet test technique to the resources available for evaluating inlet-engine compatibility. The technique offers the advantage of allowing full-scale testing of fighter-size propulsion systems with the inlet, diffuser duct, engine, and influential sections of the external airframe physically fully coupled. As a result, the various steady-state and dynamic interactions between the propulsion system components can be evaluated and the approximations associated with inlet simulators and distortion descriptors avoided. Furthermore, the capability allows the testing of fighter-size systems at high angles of attack and sideslip as well as the transient conditions encountered during aircraft maneuvers.

The free-jet approach applies two techniques to allow testing large systems over wide range of simulated flight conditions. First, unlike the wind tunnel test method, the free-jet method changes the orientation of the flow velocity vector to vary angle of attack and sideslip. Second, rather than immersing the entire test article as in the wind tunnel, the free-jet flow geometry covers only the minimum portion of the inlet and external airframe necessary to replicate the flow entering the inlet. As a result, the free-jet

requires a much smaller air stream and control of the air stream orientation over a wide range of pitch and yaw angles becomes practical.

Descriptions of the free-jet test method for evaluating inlet-engine compatibility appear in Refs. 50-59. Reference 50 provides a description of the free-jet method used in the Tornado fighter aircraft propulsion system development. References 51-59 provide descriptions of the AEDC free-jet system. A schematic of the technique appears in Fig. 1 (figures appear in Appendix A). The propulsion system is mounted downstream of a variable-attitude and variable Mach number free-jet nozzle. The nozzle provides conditioned air at a temperature, pressure, and Mach number commensurate with a given flight condition. The aircraft external airframe, which influences the flow entering the inlet, is approximated using an aerodynamic body compatible with the free-jet flow field dimensions. Typically, the forward section of the fuselage produces the largest influence. Hence, the aerodynamic body is known as the forebody simulator. Flow-field measurements at a reference plane in front of the inlet provide the basis for establishing the flight inlet flow field (Refs. 53-59).

The Aeropropulsion Systems Test Facility (ASTF) at the Arnold Engineering Development Center (AEDC) provides the facility size, airflow capacity, and altitude simulation capabilities needed for full-scale free-jet testing of fighter size propulsion systems. Therefore, the ASTF facility forms the basis of the AEDC free-jet inlet-engine compatibility test system. The free-jet system development encompassed the apparatus and the methodology for applying the apparatus in propulsion system test and evaluation. The ASTF facility provided the framework for the development in the sense that all

physical and operational constraints were derived from the existing ASTF plant, test cell, and subsystems.

A schematic of the ASTF C-2 test cell in the free-jet configuration appears in Fig. 2. It consists of a 30-ft-diam stilling or plenum chamber and a 28-ft-diam test section. The free-jet nozzle mounts in an attitude positioning mechanism (APM) installed in the bulkhead that adjoins the plenum chamber and test section. A 2.5-ft vertical offset in the plenum chamber centerline provides space for positioning free-jet nozzles at high angles of pitch. More comprehensive descriptions of the ASTF C-2 facility appear in Refs. 51 and 52.

One requirement for the successful implementation of the free-jet test technique is the development of a suitable free-jet nozzle. A number of sometimes conflicting criteria define the suitability of the nozzle. The nozzle must be large enough to enclose the inlet and forebody simulator in the jet test rhombus. However, it must be small enough to provide the needed altitude-Mach number performance with the available plant capacity. The nozzle length and contraction ratio must be small enough to achieve the required pitch angle and yaw angle envelope without mechanical interference with the stilling chamber walls or support hardware. But, the nozzle contraction ratio and length must be sufficient to achieve adequate flow quality.

Criteria for the ASTF free-jet system performance were established early in the concept development. Specifications pertaining to the development of a subsonic free-jet nozzle included the selection of a propulsion system that must be accommodated by the nozzle test rhombus, the required operating envelope, and flow quality. The objective of



the work reported herein was to define a subsonic free-jet nozzle configuration that would satisfy the ASTF free-jet system criteria.

## 1.2 SUBSONIC FREE-JET NOZZLE

The specific requirements for the full-scale ASTF subsonic free-jet nozzle evolved during the early stages of the free-jet technology development work. Flow quality requirements were specified first. Allowable nozzle exit flow non-uniformities included the following:

1.  $\pm 0.05$  variation in local Mach number (ML).
2.  $\pm 1$  deg variation in flow angle (ALPL or BETL) at nozzle pitch angles below 10 deg.
3.  $\pm 10$  percent of nozzle pitch angle variation in flow angle at nozzle pitch angles above 10 deg.

In addition the specifications allowed a total pressure turbulence level, the root-mean-square of the total pressure fluctuations, of 1 percent. As the adequacy of the above flow quality requirements for the free-jet propulsion test application was unknown at the outset, the development of the free-jet test technique included comprehensive experiments to validate the specifications (Refs. 53, 55, 57, 58).

Nozzle size and operating envelope requirements followed the flow quality specifications. The coupling between the free-jet nozzle configuration and the test article necessitated the selection of a particular aircraft for a hypothetical test requirement.

The selection yielded the following requirements:

1. Fixed-geometry nozzle.
2. Nozzle test rhombus compatible with an F-15 aircraft propulsion system including one inlet, a forebody simulator, and the engine.
3. A rectangular PITCH-YAW envelope with a pitch angle range of  $-10$  deg to  $+45$  deg and a yaw angle range of  $\pm 10$  deg.
4. A subsonic Mach number (MACH) range of 0 to 0.9.

The free-jet technology development work employed a subscale pilot free-jet facility, modeling the ASTF C-2 test cell, to provide the experimental information required. The initial nozzle studies, which preceded establishment of the nozzle sizing requirements, considered a variable-area two-dimensional (2-D) nozzle. A model of the variable-area nozzle concept was fabricated and installed in the pilot facility for use in flow quality experiments and initial free-jet test method validation tests. The nozzle was intended to provide uniform test rhombuses, of various sizes, and calibrated non-uniform flow conditions. It would thus provide the means to establish the relationships between nozzle size and test article size as well as the effect of nozzle flow non-uniformities, such as flow angularity, on the simulation of flight at the test article. The latter experiments focused on a goal of validating the flow quality requirements.

The variable-area nozzle flow-field calibrations, conducted in 1982, revealed nozzle exit flow anomalies at high pitch angle conditions. Secondary flows in the form of vortices embedded in the nozzle flow resulted in measured flow angularity far outside

the target limits. The results clearly indicated the need for an experimental investigation to address the flow quality aspect of the ASTF C-2 free-jet nozzle criteria.

The literature provides examples of at least three main mechanisms that can result in the appearance of embedded vortices. The first is the corner vortex that often appears in straight rectangular ducts or open channels. The second are the s-duct vortices that appear in closed curved ducts. The third is the inlet ground vortex that is often observed when an aircraft inlet operates near the ground. A free-jet system, with a 2-D nozzle, contains the elements that could be conducive to the formation of all three types of vortices.

Examples of the corner vortex appear in Ref. 60. The reported studies attribute the phenomenon to viscous effects in corners oriented parallel to the main flow. The vortex diameter is generally on the order of the corner boundary layer thickness. In a duct with fully developed flow, such vortices could, therefore, fill the entire cross-section. However, the 2-D free-jet nozzle does not produce fully-developed flow. The wall boundary layer represents less than 3 percent of the nozzle exit width. Furthermore, the nozzle would be sized to spill the viscous shear layer that bounds the jet around the inlet. As a result, the free-jet nozzle corner vortices were only a concern to the extent to which they influence the core flow.

Descriptions of secondary flows in s-ducts appear in Refs. 61-82. The studies attribute the vortical flows to fluid viscosity and centrifugal forces on the flow through a bend in the duct. Viscous effects produce velocity gradients in the duct. As the higher velocity fluid experiences higher centrifugal forces, the velocity gradients lead to

gradients in centrifugal forces. As the flow moves towards the outside of the bend, the gradients establish secondary flow patterns leading to the formation of counterrotating vortices. The effect occurs both in rectangular and circular ducts.

At high pitch conditions, the free-jet nozzle accelerates and redirects the approaching flow. Thus, the basic requirement for the s-duct type vortices, the change in flow direction, presents itself in the free-jet system regardless of the nozzle cross-section shape. Therefore, the development of such flows became a concern as a threat to achieving the flow quality goals.

The so-called inlet ground vortex presents a particularly interesting vortex phenomenon. During ground operation, the vortices are often observed forming between an aircraft inlet and an adjacent surface such as the ramp or fuselage. They have also been observed during turbine engine ground tests in open air sea level test stands. With respect to aircraft operations, the troublesome vortices can lead to the ingestion of debris from the vicinity of the attachment point on the ground. They have been known to lift pebbles from the runway or ramp. Furthermore, the vortices can produce excessive inlet distortion and engine surges during thrust reverser operation. With respect to engine tests in sea level stands, the inlet distortion produced by the inlet vortex can invalidate engine operability and performance measurements. The inlet vortex has even been detected in altitude turbine engine test facilities attaching to the test facility plenum chamber wall and entering the bellmouth and engine air supply duct. The difficulties presented by the inlet vortex prompted a number of experimental and analytical investigations such as those reported in Refs. 83-93.

Two main mechanisms for the formation of inlet vortices have been identified in the literature. The first, and most generally understood, involves the amplification of ambient vorticity in the flow approaching the inlet (Refs. 84, 90, 93). The ambient vorticity may be produced far upstream of the inlet. The shear flow resulting from the wind across the ground represents a typical source. The study reported in Ref. 93 included an investigation of two ambient vorticity components and the resulting inlet ground vortices. The experimenters introduced transverse ambient vortices and vertical ambient vortices in the far stream. The results showed the vertical component to be of most significance in the formation of inlet vortices.

References 85, 86, and 92 identify a second mechanism for the inlet vortex formation that does not require ambient vorticity in the far stream. The investigators discovered that the inlet vortex may occur in the presence of irrotational upstream flow, if conditions subjected the inlet to a cross wind. The axial variation of circulation along the inlet results in a vortex system consisting of a trailing vortex and an inlet ground vortex. The investigators supposed that the inlet and trailing vortices produced the same circulation. Subsequent results showed this to be the case (Ref. 92).

The key parameters associated with the inlet ground vortex include inlet height above the ground, inlet diameter, inlet shape (rectangular or axisymmetric), inlet velocity, ambient flow velocity, and ambient flow direction. In addition, a stagnation point or region on the ground in front of the inlet appears to be a requirement. Non-dimensional parameters for the inlet velocity ( $V_i/V$ ) and the inlet height ( $H/D$ ) appear in the literature.

In general, an increase in  $V_i/V$  or a decrease in  $H/D$  increases the strength of the inlet ground vortex or the likelihood that it will form.

The free-jet system, shown in Fig. 2, contains the primary ingredients for the formation of inlet ground vortices, an inlet operating near a solid boundary. The parameters  $V_i/V$  and  $H/D$  favor the vortices as well. The confinement of the free-jet nozzle within the stilling chamber further complicates the flow-field in the vicinity of the nozzle inlet. The plenum boundary layer, plenum wall separations, and endwall (bulkhead) effects present numerous opportunities for the production of ambient circulations. The latter includes flow reversal and swirl that occurs when flow bypassing the nozzle inlet encounters the free-jet bulkhead and is redirected.

### 1.3 SCOPE OF INVESTIGATION

The free-jet system contains a complex combination of the features known to produce secondary flows. The scope of the present work did not focus on an in-depth study of the various mechanisms involved in the observed free-jet nozzle vortices. Such a study would be required for the purpose of thoroughly understanding the physics involved or for developing predictive models. Rather, the effort focused on the needs of the ASTF free-jet system development and the empirical identification of design features that would assure achievement of the specific requirements. The specific objectives of

the work included the following:

1. Identify the features and key parameters in the free-jet system pertinent to the formation of nozzle vortices.
2. Develop vortex suppression techniques that can be applied to a free-jet system.
3. Select the optimum technique and verify the performance in a free-jet system.
4. Recommend a subsonic free-jet nozzle configuration for the ASTF C-2 free-jet system that will achieve the target flow quality.
5. Verify modifications to the recommended configuration that evolved during the full-scale development cycle.

The first three objectives center only on flow quality with the development and verification of vortex suppression techniques. The fourth and fifth objectives address the integration of the flow quality considerations into a nozzle concept commensurate with the other ASTF C-2 requirements.

The overall approach to addressing the flow quality issues relied on experiments in two types of test facilities: a water tunnel and a pilot free-jet test facility. The experiments were selected in such a way as to capitalize on the attributes of each type of facility. Water tunnel simulations provided an efficient and cost-effective means to qualitatively investigate a large number of configurations. Although the water tunnel did not provide quantitative measurements such as would be needed for computational model development or validation, it did provide an extremely valuable tool for flow visualization. This tool proved sufficient for identifying key parameters influencing

vortex formation as well as methods of suppressing the vortices. The pilot free-jet facility, considerably more costly to operate than the water tunnel, provided the quantitative measurements, with air at true Mach number conditions as the test medium, for key configurations identified in the water tunnel experiments. It was used to validate water tunnel results and provide data for evaluation with respect to the ASTF requirements. Thus, the approach employed an optimized combination of the two facilities.

Flow visualization in the water tunnel has become a proven and accepted technique for studying vortex phenomenon (Refs. 94-100). Dye introduced into the flow will trace the streaklines, allowing viewing and photographic recording. Streamwise vortices generally produce a helical or corkscrew pattern in the dye traces. For many vortex phenomena, the qualitative aspects of the flow-field are relatively independent of the velocity, Mach number, and the Reynolds number. This permits use of a water tunnel to study vortical flows produced by full-scale airflow apparatus.

The approach to accomplishing objective 1 encompassed a systematic search for factors contributing to vortex development. Construction of a number of water tunnel models allowed parametric variations in the following:

1. Downstream effects such as nozzle exit blockage and test section cavity recirculation.
2. Nozzle cross-section shape such as rectangular or circular.
3. Nozzle contraction section configuration.
4. Nozzle proximity to the plenum chamber wall.



## 5. Nozzle contraction ratio.

In an incompressible flow,  $V_i$  is linearly proportional to  $V$  for a given nozzle cross-sectional area. The proportionality resulted in  $V_i/V$  being independent of water flow rate in the water tunnel simulation.

The approach to objective 2 was to start with the factors identified under objective 1 and investigate vortex suppression methods in water tunnel simulations. The methods proposed fell into two categories: (1) vortex attenuation and (2) vortex prevention. The former approach applied flow straightening devices, such as screens and honeycombs, to reduce existing vortices to acceptable levels. The latter approach focused on modifying the flow approaching and entering the nozzle to prevent the objectionable vortices from forming. Reported techniques in this category often suppressed vortex formation by modifying or eliminating potential vortex attachment points at the surface adjacent to the inlet (Ref. 84). Lacking an attachment point, the vortex becomes unable to sustain itself. The present experiments considered such techniques as well as others. Proposed prevention techniques included nozzle inlet ramps, nozzle boundary layer control, blowing techniques, and stilling chamber recirculation control.

The approach to accomplishing objective 3 applied a choice vortex suppression technique, derived under objective 2, to the existing variable-area free-jet nozzle in the pilot free-jet facility. Flow-field measurements would verify or refute the water findings as well as quantify the flow quality improvements achieved.

The approach to accomplishing objective 4 included the following steps: (1) the determination of a nozzle configuration that would meet the ASTF C-2 size and operating

envelope criteria, (2) the addition of the vortex suppression technique proven under objective 3 to the nozzle configuration, (3) iterations on the resulting configuration using water tunnel simulations, and (4) verification and quantification of the final configuration performance in the pilot free-jet facility.

The approach to objective 5 used qualitative water tunnel simulations and quantitative pilot facility tests, as needed, to investigate potential modifications to the configuration that could impact the flow quality. The potential for such modifications surfaced during the full-scale system conceptual design.

The flow quality investigation, summarized herein, included a number of separate steps that evolved during the free-jet technology development. Various tests were conducted during the period between March, 1982 and August, 1987. The chronology of the work appears in Fig. 3, with each overall step depicted in the center column of the diagram.

The first three steps focused on developing an understanding of the vortex phenomena and the tools that might be brought to bear in a vortex study. Step 1 quantified the anomalies generated by the vortices. Step 2 validated the water tunnel simulation of the vortex formation phenomena. Step 3 consisted of a parametric investigation of the parameters influencing the formation of vortices.

The fourth and fifth steps focused on identifying vortex suppression or prevention methods. Step 4 involved screening a large number of potential remedies in the water tunnel with sufficient detail to enable the selection of techniques for subsequent

development. Step 5 centered on validating the effectiveness of the selected approach prior to implementation.

Finally, steps six and seven focused on applying the selected techniques in the development of a free-jet nozzle for ASTF. They included both refinement studies using water flow simulations and validation tests using airflow.

To avoid repetition, sections 2 and 3 are organized according to test facility, bearing no resemblance to the order presented in Fig. 3. However, subsequent sections of this thesis present the results chronologically to document the logic followed during the multi-phase program.

## 2.0 APPARATUS

### 2.1 TEST FACILITIES

#### 2.1.1 Free-jet Test Cell

The pilot free-jet test facility, designated Research Test Cell R2A2, consists of a 15-percent scale model of the ASTF C-2 test leg. Figure 4 illustrates the R2A2 test cell in the free-jet configuration. The stilling chamber diameter and test section diameter scale to 54 in. and 50.4 in., respectively. The R2A2 stilling chamber deviates from the C-2 geometry with the inclusion of a 63-in.-diam (35-ft diam full scale) section at the junction with the test chamber. The section provides space for the variable-area 2-D free-jet nozzle assembly. During experiments with the ASTF fixed-area nozzle concept, a 54-in.-diam section that extended downstream of the nozzle inlet section more closely modeled the C-2 plenum.

The R2A2 test facility may be configured to receive supply air either through an atmospheric inlet or from the Engine Test Facility (ETF) air supply plant. The atmospheric inlet supply limits total pressure, total temperature, and humidity to the ambient conditions that exist on the day of the test. The air supply plant provides conditioned air over a wide range of pressures and temperatures at substantially higher costs. During the free-jet nozzle flow quality studies, an atmospheric inlet section supplied the R2A2 stilling chamber as shown in Fig. 4. The atmospheric inlet section

included filters to minimize particulate ingestion. A screen located immediately downstream of the atmospheric inlet transition section enhanced the stilling chamber flow quality.

The R2A2 test section exhausts to the ETF exhauster plant. A control valve in the exhaust duct allows establishment of cell pressures corresponding to desired Mach numbers. During the free-jet nozzle experiments, the flow exhausted through a 24-in.-diam schedule 20 pipe as shown in Fig. 4. Subsequently, a 36-in.-diam exhaust duct replaced the 24-in.-diam duct to increase the mass flow capacity. An 8-in.-diam auxiliary exhaust duct provides an additional flow path for simulating engine airflow during aircraft inlet model free-jet tests.

In the atmospheric inlet configuration, R2A2 provides a range of subsonic test conditions ranging from a Mach number of 0 to approximately 0.92. The nozzle size, exhaust duct size, and hardware design limits fix the operating envelope associated with the atmospheric inlet. The lack of plenum chamber inlet air control results in a unique relationship between simulated altitude and Mach number (for a given day). In other words, a unique Reynolds number (RE) accompanies each Mach number condition and the investigator has the ability to control Mach number only. For the atmospheric inlet, the altitude-Mach number envelope becomes an altitude-Mach number curve. The curve for a standard day at the AEDC elevation appears in Fig. 5. The figure also provides the temperature and Reynolds number curves.

## **2.1.2 Water Tunnel**

### **2.1.2.1 Basic Facility**

The University of Tennessee Space Institute (UTSI) water tunnel used in this research is a closed-circuit continuous-flow facility as shown in Fig. 6. The circuit lies in a horizontal plane with the test section contained in a dark room for photographic purposes. An electric motor drives a propeller in the downstream leg of the circuit to induce water flow. A continuously-variable transmission allows adjustment of the water flow velocity.

A stilling chamber located outside the building, immediately upstream of the test section, contains screens and honeycombs to minimize test section turbulence. A smooth transition section with a contraction ratio of 13.5 accelerates the flow from the circular plenum chamber into a 12 in. by 18 in. rectangular duct inside the building.

The standard test section, 59 inches in length, provides a rectangular cross section measuring 18 in. wide by 12 in. deep. Mounted between two flanges, the standard test section may be removed for special test requirements. For the present work, a model of the free-jet test cell replaced the UTSI test section. A more detailed description of the UTSI water tunnel may be found in Ref. 101.

### 2.1.2.2 Free-jet Test Cell Model

The water flow simulations used a 21.4-percent scale model of the R2A2 pilot free-jet facility in place of the removable water tunnel test section as shown in Fig. 7. Thus, the free-jet facility model contained its own stilling chamber, free-jet bulkhead, and test section that mounted as an assembly between existing flanges in the 12-in. by 18-in. duct. A fairing installed upstream of the free-jet facility model provided a smooth transition from the rectangular water tunnel duct to the circular free-jet plenum. Constructed entirely of plexiglass, the model permitted visual access to the flow fields in the free-jet stilling chamber, nozzle, and downstream test chamber. The stilling chamber consisted of an assembly of two sections corresponding to the R2A2 54-in.-diam plenum section and 63-in.-diam plenum section, respectively. Bolted flanges joined the sections and rubber gaskets formed the seals. A 1.0-in. offset in the adjoining flange bolt-hole patterns produced the scaled centerline offset between the plenum and test section. The assembly of sections included provisions for sandwiching a 0.5-in. thick flange between the plenum and the test section flanges. The 0.5-in.-flange served as the free-jet bulkhead model as shown in Fig. 7. An opening in the top of the plenum and test section provided access for configuration changes.

During the Phase III water flow experiments, the plenum section was modified to more closely simulate the ASTF C-2 geometry. A constant 11.5-in.-diam model plenum modeled the 30-ft-diam full-scale C-2 plenum as shown in Fig. 7. An orifice plate installed in the model plenum simulated the C-2 venturi bulkhead. Beveled holes in the

model venturi bulkhead, 0.875 inches in diameter, matched the full-scale venturi bulkhead pattern. A honeycomb-screen assembly simulated the C-2 foreign object damage (FOD) screen. The 1.5-in.-thick honeycomb contained hexagonal cells approximately 0.3 in. corner to corner. The upstream face of the honeycomb supported two layers of screen. The 18 mesh screens with 0.01-in.-diam wires approximated the blockage of the ASTF FOD screen. The basic plenum and the modified plenum will henceforth be referred to as the R2A2 configuration and the C-2 configuration, respectively.

In addition to the internal plenum modifications, the Phase III water tunnel investigation included external modifications to the water tunnel model. A reservoir added in the 9-inch long spool section that houses the nozzle enclosed a portion of the circular model duct. When filled with water, the planar walls of the reservoir eliminated the light refraction effects normally encountered with the curved plenum wall. This improved flow visualization by reducing optical distortion.



## 2.2 TEST ARTICLES

### 2.2.1 R2A2 Models

#### 2.2.1.1 Variable-Area Nozzle

The advantages of tailoring the nozzle exit area and shape according to aircraft propulsion system configurations motivated the initial development of a variable-area free-jet nozzle concept. However, the full-scale ASTF free-jet system ultimately adopted a much simpler and lighter fixed-area nozzle, as will be shown. The change reduced cost and enabled the development of a system capable of delivering rapid transients in pitch and yaw for aircraft maneuver simulation. Although the progression to the full-scale ASTF free-jet test system abandoned the variable-area concept, a model of the variable-area nozzle served the initial flow quality studies as well as the initial free-jet test technique validation experiments.

The variable-area 2-D subsonic free-jet nozzle, intended for free-jet test method validation experiments, consisted of two fixed walls and two movable walls. As shown in Fig. 8, two fixed sidewalls vertically spanned the plenum cross section. The sidewall spacing was fixed at 11.25 in. Independently actuated upper and lower walls, positioned between the sidewalls, provided various combinations of nozzle height and pitch angle. Figure 8a provides an isometric sketch of the assembly with one sidewall removed to show the components. Figure 8b shows three views with one sidewall removed to

provide pertinent dimensions. Figure 9 provides the contours of the upper and lower walls as well as the sidewall contraction section. The figures show that the sidewall contraction occurred upstream of the upper and lower wall contractions. In the elevation view, the figure illustrates that the sidewall contraction section consisted of five segments, each inclined with respect to the test cell axis.

Two seal plates, joined end to end with hinges, connected each movable nozzle wall to the nozzle assembly (Fig. 8). Positioning of each nozzle wall required three hydraulic actuators corresponding to the wall itself, the center seal plate, and the outer seal plate, respectively. Thus, each nozzle configuration required setting and maintaining six actuator positions. The system provided the capability to vary nozzle height from essentially 0 in. to 11.25 in. while varying pitch angle from  $-10$  deg to  $+55$  deg. Combinations of free-jet angle of attack and sideslip could be achieved through an appropriate combination of nozzle roll and pitch angles. Nozzle roll angles could be set manually by rolling the entire assembly in 10-deg increments. The system also permitted the establishment of desired flow gradients by inclining either one or both of the movable walls with respect to the nozzle axis.

A schematic of the variable-area nozzle installed in the Research Test Cell R2A2 appears in Fig. 10. The illustration clearly shows the relative positions of the nozzle assembly, plenum centerline, and test section centerline. It also shows the accommodation of the apparatus in the 63-in.-diam section of the plenum chamber. The nozzle actuators were calibrated to maintain an 8.4-in. spacing between the nozzle exit

plane and the pitch center on the test section centerline. The selection of 8.4 in. satisfied requirements for the free-jet technique validation experiments reported in Ref. 53.

Following the initial flow quality investigation, the nozzle was converted to a fixed-area nozzle and used in a free-jet validation experiment. The modification included the addition of a mechanical link between the upper and lower nozzle walls that fixed the height at 11.25 inches. This corresponded to a full-scale exit area of 126.6 sq in. or 39.06 sq ft (ASTF). The link used space available in the nozzle exit cavity as shown in Fig. 11. With the degrees of freedom reduced to pitch angle only, a single hydraulic actuator provided the only needed drive system. The link geometry preserved the 8.4-in. spacing between the nozzle exit plane and the pitch center. Experiments conducted for the purpose of verifying water tunnel results used the nozzle assembly in the modified configuration. However, it continued to be designated as the variable-area nozzle to distinguish it from the subsequent single-block nozzle configurations.

As will be shown, the water tunnel experiments yielded four leading edge ramp configurations that would improve the variable-area nozzle flow quality (Fig. 12). Models of these ramps, added to the nozzle, permitted measurement of the flow quality improvements and verification of the water tunnel findings. Two ramps were designed for use at a nozzle pitch angle of 30 deg. A contoured ramp intersected the lower nozzle wall in the tangent plane as shown in Fig. 12b. The second ramp consisted of a planar surface that intersected the lower nozzle wall at an oblique angle as shown in Fig. 12c. The two ramps acquired the designations "30-deg contoured" and "30-deg straight," respectively. Two additional ramps, shown in Figs. 12d and 12e, were designed for a

nozzle pitch angle of 50 deg following the same design philosophy. The use of 0.25-in.-thick mild steel plate in the ramp fabrication permitted minor adjustments to the platform during final fitting. Fig. 12f provides a photograph of a typical ramp installation.

#### **2.2.1.2 ASTF C-2 Free-jet Nozzle**

The ASTF C-2 free-jet nozzle concept validation tests in R2A2 used a 12.9-percent scale model of a proposed concept. The scale selection allowed the nozzle model to be mounted in an existing R2A2 attitude positioning mechanism while preserving the scaled nozzle inlet height above the stilling chamber floor. It will be shown that the spacing between the nozzle inlet and the stilling chamber floor influences the flow quality and needed to be scaled for the flow-field measurements.

The nozzle model, illustrated in Fig. 13, was fabricated using 0.5-in. thick aluminum plate bent to the required wall contour and welded. A leading edge flap or ramp attached to the lower nozzle wall improved the flow quality at high pitch angles. The nozzle inlet ramp concept, a product of the water tunnel experiments preceding the development of the ASTF nozzle concept (Fig. 3), evolved during the course of the investigation and will be described in subsequent sections. The ramp inclination angle relative to the nozzle wall varied with nozzle pitch angle according to a schedule. Manual adjustments of the turnbuckles shown in Fig. 13 established the required ramp angles. The investigator set the required ramp angles by manually adjusting the turnbuckles shown in Fig. 13. Versions of the nozzle model fabricated subsequent to this

investigation replaced the turnbuckles with linear actuators for remote positioning capability. The basic schedule varied ramp angle linearly from  $-10$  deg to  $+20$  deg as the nozzle pitch angle increased from  $30$  deg to  $45$  deg. Below  $30$  deg of nozzle pitch, the ramp angle remained constant at  $-10$  deg. The R2A2 tests included experiments with ramp settings on and off the basic schedule. The R2A2 tests also included two ramp planform shapes designated as configuration A1 and configuration A2. Figure 13b illustrates the ramp planform shapes and the nozzle wall contours.

The model ASTF free-jet nozzle deviated from the full-scale design concept proposal, shown in Appendix D, with the omission of the beveled sections on the top corners of the contraction section. The full-scale nozzle concept used the beveled corners to avoid mechanical interference that did not occur in the subscale installation. The deviation simplified model nozzle fabrication without detracting from the region of interest in the lower sections of the nozzle.

A remotely actuated attitude positioning mechanism supported and positioned the ASTF C-2 nozzle model. As shown in Fig. 14, the mechanism consisted of a pair of hemispheres: a fixed outer hemisphere and a movable inner hemisphere. The outer hemisphere bolted to an adapter ring between the stilling chamber and the test section to form the pressure bulkhead. The nozzle assembly attached to the inner hemisphere that rotated to vary pitch angle. The axis of rotation passed through the hemisphere centers so that the space between hemisphere surfaces remained constant through the pitch range. An inflatable seal between the hemispheres minimized leakage. A slot in the outer hemisphere allowed movement of the nozzle from  $-5$  deg to  $+45$  deg in pitch. An

electric jackscrew actuated the mechanism as shown in Fig. 15. A rotary potentiometer provided the nozzle pitch angle measurement. Combined angle of attack and angle of sideslip conditions could be obtained by using an appropriate combination of nozzle roll angle and nozzle pitch angle. The pitch mechanism could be rolled in 10-deg increments as set by the adapter ring bolt pattern. Figure 16 provides a photograph of the nozzle installed in R2A2.

## **2.2.2 Water Tunnel Models**

### **2.2.2.1 General**

The various water tunnel simulations conducted applied a substantial number of nozzle models and devices for improving the flow quality. The nozzle models included a model of the R2A2 variable-area free-jet nozzle, a family of generic nozzles, and the ASTF nozzle concept. The various models were developed during the course of the investigation outlined in Fig. 2. The initial experiments used the variable-area nozzle model to verify the water tunnel simulation of the vortex phenomenon and to identify suppression concepts. Generic nozzles subsequently provided the means to investigate various parameters associated with the vortex formation and the suppression techniques. The ASTF free-jet nozzle model allowed water tunnel evaluations prior to investing in the more expensive R2A2 tests.

### 2.2.2.2 Variable-Area Nozzle

The water tunnel investigation used a 21.4-percent scale plexiglass model of the R2A2 variable-area free-jet nozzle. Shown in Fig. 17, the model assembly scaled the main features of the R2A2 model described in Section 2.2.1.1. A temporarily installed jig block pivoting on a pin located at the pitch center aligned the nozzle walls to facilitate the setting of nozzle pitch angle. Tightening the screw joining the two sidewalls tightly clamped the upper and lower walls allowing removal of the jig block for testing. Pertinent dimensions of the nozzle components appear in Fig. 17a and the contours appear in Fig. 17b.

The variable-area nozzle model mounted on the flange sandwiched between the plenum and test chamber in the same manner as in test cell R2A2. Figure 18 shows the nozzle model installed in the water tunnel. Figure 19 provides a photograph of the variable-area nozzle assembly and water tunnel installation.

The water tunnel investigation of the variable-area nozzle flow field explored a number of candidate vortex attenuation methods. Figure 20 illustrates the various flow straightening devices applied in attempts to reduce the size or strength of the vortices. The devices included vertically-oriented vanes (Fig. 20a), horizontally oriented turning vanes (Fig. 20b), a honeycomb section (Fig. 20c), and screens (Fig. 20d). For installation, each device mounted in the plane defined by the upper and lower nozzle wall leading edges, as shown. This plane was located between the nozzle sidewalls. Screen tests involved both one and two layer installations. A space of 3/16 in. separated the

screen layers in the latter case. Experiments with the honeycomb and the horizontal vane arrangements included installations with the device mounted parallel to the nozzle inlet plane and with the device inclined 20 deg to the inlet plane.

In addition to the vortex attenuation devices, the water tunnel investigation explored potential vortex prevention devices. Rather than attempting to breakup the vortices, these approaches focused on preventing the vortices from forming in the first place. Approaches included devices for eliminating the stagnation region and vortex attachment point near the nozzle inlet, boundary layer suction devices, and blowing devices.

A family of nozzle leading edge ramps provided the means to modify the flow turning into the nozzle. The set of ramps allowed variation of a number of design parameters such as nozzle wall contact point and tangency. Five ramp configurations, with respective designations of Ramp 1 - Ramp 5, appear in Fig. 21. Each installation used a nozzle pitch angle of 30 deg. Each ramp mounted between the lower nozzle wall and the stilling chamber floor. The side edges of the ramps fit snugly between the nozzle sidewalls. The family of ramps intersected the nozzle lower wall at three different locations as shown in Figs. 21a-21e. With the exception of the 2.7-in. intersection point, two ramps addressed each intersection point. The first ramp employed a curved contour in order to intersect the nozzle wall tangentially. The second employed a simpler planar surface and intersected the nozzle wall at an oblique angle. In addition, the experiments included two ramps that did not contact the floor of the stilling chamber (Figs. 21f-21g). Designated as Ramp 21 and Ramp 22, respectively, the two ramps differed in length and



contour. The ramp 21 configuration included two installations as shown in Fig. 21f.

Figure 21h provides a photograph of a typical ramp.

Phase II of the water tunnel flow quality investigation included porous walls on selected sections of the nozzle for boundary layer suction. The location of the porous walls on the left side of the nozzle, looking upstream, minimized the impact on optical access. Figure 22 shows the sections of the nozzle modified for boundary layer suction. To develop the porosity, the wind side of each section was drilled with #60 holes (0.040 in. diam) spaced approximately 3/16 in. center to center. Each porous wall section emptied into a plenum located behind the wall. Each plenum drained outside the test cell using gravity. Separate valves allowed the application of suction to any combination of the porous sections.

A blowing scheme for vortex prevention used a perforated tube referred to as a piccolo tube. Figure 23 illustrates the piccolo tube. The tube contained #76 holes (0.02 in. diam) drilled in 0.1-in. increments along the length as shown. For tailoring of the bleed flow, plastic collars covered sections of the tube. The tube was installed beneath the lower nozzle wall as shown in Fig. 23. The mounting fixture provided variability in axial station, tube height, and tube angle. An external water source supplied bleed flow for the piccolo tube.

### 2.2.2.3 Generic Nozzles

The water tunnel tests used a number of generic fixed-geometry nozzles to provide the capability for independent variation of nozzle pitch angle, nozzle location in plenum, nozzle inlet geometry, nozzle cross-section shape (2-D or axisymmetric), and nozzle contraction ratio. In addition, the experiments used a 2-D nozzle designed around a centerline curved in the vertical plane of symmetry. All nozzles were fabricated using 0.1-in. thick plexiglass to allow viewing of the internal flow characteristics.

Sketches of the generic 2-D nozzles appear in Fig. 24. The nozzle exit cross-section dimensions matched those set on the water tunnel variable-area nozzle model. The nozzle shown in Fig. 24a, featured a symmetrical contraction section. Designated as the 2-D SYM nozzle, the nozzle used four identical wall contours positioned with the leading edges at the same longitudinal station. The contours matched those used on the upper and lower walls of the variable-area nozzle. A nozzle designated as the 2-D ASY nozzle used an asymmetrical contraction section to simulate the variable-area nozzle inlet configuration (Fig. 24b). The contraction in the vertical plane occurred downstream of the lateral contraction. The upper and lower nozzle walls matched the contours of the variable-area nozzle. The side walls remained flat between the plane defined by the upper and lower wall leading edges and the exit plane. Upstream of the upper-lower wall inlet plane, the side-wall contraction section followed the semi-circular shape used in each segment of the variable-area nozzle side walls. The cut on the side-wall inlet,

shown in Fig. 24b, was added during the experiments to allow a nozzle installation at a lower position without mechanical interference.

Figure 24c illustrates the 2-D nozzle with the curved centerline referred to as the 2-D high alpha nozzle. The cross section at the exit plane matched those of the other nozzles in the 2-D generic nozzle family. A centerline curved 20 deg in the pitch plane provided a more gradual turning of the flow relative to the other generic nozzles. During the course of the water tunnel Phase I experiments, an extension was added to the lower wall as shown in Fig. 24c.

An available AEDC bellmouth, compatible with the test cell R2A2 APM, provided the basis for two axisymmetric nozzle models. The choice preserved the option of verifying water tunnel results in the flow-field survey tests. The models, shown in Fig. 25, differed only in contraction ratio. The long nozzle provided a contraction ratio of 4.5. The short nozzle consisted of the long nozzle configuration with the first 0.43 in. of the contraction section removed to provide a contraction ratio of 2.4. The nozzles were designated as the long axi nozzle and the short axi nozzle, respectively.

A slotted bulkhead, installed in place of the variable-area nozzle flange, supported the generic nozzles (Fig. 26a). The slot allowed the nozzles to be installed at various pitch angles and vertical locations. Plexiglass spacers filled the sections of the slot left vacant by each installation. As shown in Fig. 26b, the parameters XI and ZI defined the nozzle location.

The generic nozzle experiments used a number of additional components to allow adjustment of the independent variables or to investigate vortex suppression techniques.

These included a removable nozzle exit cavity section, a movable artificial bulkhead, a movable artificial plenum floor, a pair of horizontal baffles, a pair of vertical baffles, and a set of nozzle inlet ramps. The following contains a description of each.

The variable-area nozzle configuration, shown in Fig. 8, included a cavity between the nozzle exit plane and the facility test section. The cavity presented the potential for recirculating flows and, at high pitch, flow impingement on the cavity wall. Although the possibility that the cavity interference influenced nozzle vortex formation in some fashion was considered to be remote, the experiments investigated cavity effects. To enable an investigation of the cavity influences, the 2-D SYM nozzle and 2-D ASY nozzle installations included provisions for adding or removing a 6-in. diam cavity. Shown in Fig. 27, the cavity attached to the downstream face of the bulkhead. In the case of the 2-D SYM nozzle, the cavity could be mounted in either of two vertical positions (27a).

A movable artificial bulkhead facilitated the variation of the spacing between the free-jet nozzle inlet and the plenum bulkhead (XI) by eliminating the need to remove and reposition the nozzle. Shown in Fig. 28, the artificial bulkhead consisted of a non-structural aluminum panel offset from the true bulkhead. The artificial bulkhead included an opening to accommodate the 2-D SYM nozzle.

In a similar fashion, an artificial plenum floor facilitated the variation of the nozzle vertical position relative to the floor (ZI). Shown in Fig. 29, the artificial floor consisted of an aluminum panel offset from the true plenum floor. A number of experiments varied ZI by shifting nozzle position in the bulkhead. Others varied ZI by

holding nozzle position constant and shifting floor position. The latter preserved nozzle location relative to the plenum centerline. The artificial floor accommodated the 2-D SYM nozzle installation.

The 2-D SYM nozzle installation included provisions for two types of baffles in the vicinity of the nozzle inlet contraction section. A pair of horizontal baffles, shown in Fig. 30, spanned the space between the plenum wall and the nozzle sidewalls. A pair of vertical baffles, shown in Fig. 31, fitted the gap between the plenum floor and the nozzle bottom wall. The baffles were designed to modify the re-circulating flow that developed between the nozzle inlet and the bulkhead.

The short axisymmetric nozzle included provisions for two ramps. Each employed a straight conical section extending from the nozzle inlet to the plenum wall. Sketches of the ramps, designated as axi ramp 1 and axi ramp 2, appear in Figs. 32 and 33, respectively. With the nozzle set at a pitch angle of 30 deg, the investigator could mount axi ramp 2 in any of five configurations. As shown in Fig. 33, the configurations differed in the location of the ramp trailing edge with respect to the nozzle inlet.

#### **2.2.2.4 ASTF Nozzle Concept**

Water tunnel tests of the ASTF C-2 free-jet nozzle concept used a 21.4-percent scale plexiglass model. Illustrated in Fig. 34, the model included the main features of the ASTF concept, including the beveled corners on the top of the contraction section. The model nozzle contours and the final ramp planform, designated ASTF ramp A1, appear in

Fig. 34b. The figure also shows the geometry of a ramp extension that increases the planform dimensions. The apparatus included the extension to allow an evaluation of ramp planform influence on ramp effectiveness as a vortex prevention device. For each experiment, the ramp was manually attached to the lower nozzle wall at the required angle setting. Photographs of the ASTF nozzle model appear in Fig. 34c.

A fixed nozzle support structure bolted to the slotted bulkhead positioned the nozzle during the water tunnel Phase II tests. Shown in Fig. 35, the fixture increased the maximum pitch angle to 45-deg as needed to simulate the ASTF envelope. A slot in the fixture accepted the nozzle model, and spacer blocks filled the vacant spaces as in the generic nozzle installations. Each installation matched pitch angle and geometrically scaled the spacing between the nozzle inlet and the plenum floor.

A requirement to evaluate an alternative ramp planform in Phase III of the water tunnel investigation resulted in ASTF ramp B shown in Fig. 36. Although equal in length at the planform centerline, the two ramps differed considerably in shape. At the lateral stations off the centerline, ramp B was considerably shorter than ramp A. Unlike ramp A, ramp B attached to the nozzle lower wall with a hinge to facilitate ramp angle changes.

The ramp B performance evaluations used a model of the ASTF C-2 free-jet APM to support and position the nozzle. Illustrated in Fig. 37, the model APM included provisions for manual adjustment of nozzle pitch angle, nozzle yaw angle, and nozzle axial distance from the pitch center. It consisted of a pitch frame that rotated inside a yaw frame. The model located the pitch axis 0.48 in. downstream of the yaw axis,

geometrically scaling the ASTF C-2 configuration. The arrangement thus geometrically scaled the nozzle position relative to the plenum walls and the bulkhead. The model APM pitch angle and yaw angle envelope enclosed the ASTF C-2 APM envelope.

## **2.3 INSTRUMENTATION**

### **2.3.1 Test Cell R2A2 Experiments**

#### **2.3.1.1 Test Cell**

Research Test Cell R2A2 contains the instrumentation needed to measure test conditions, measure test article parameters, and monitor test cell systems. The wide variety of test requirements addressed in the research facility generally requires tailoring the specific instrumentation systems selected according to the specific objectives. Although instrumentation systems typically comply with the practices employed in the Engine Test Facility turbine engine test facilities, unique systems may be used to acquire specialized measurements or to reduce the costs of the research experiments.

Currently, Test Cell R2A2 contains state-of-the-art electronically multiplexed pressure transducers, data acquisition systems, and data processing systems that allow on-line data reduction and data analysis. However, the flow quality experiments used a simpler system that pre-dated the current apparatus. With the original system, selected parameter measurements could be reduced on-line for monitoring and directing the test.

However, the bulk of the measurements were recorded on digital tape for off-line reduction on the AEDC central computer. Analog data systems multiplexed and recorded the high-response measurements on tape for off-line analysis in the ETF Dynamic Data Analysis Laboratory (DDAL).

To acquire various pressure measurements, the experiments used a series of dedicated pressure transducers in conjunction with a set of Scanivalve<sup>®</sup> systems. The system contained fifteen Scanivalves<sup>®</sup> each capable of sensing ten pressures. Therefore, 150 pressure measurements required 15 data channels. The use of pneumatic scanning of the pressures dictated careful selection of the dwell time for each valve position to ensure that the pressure sufficiently stabilized prior to recording. A limited number of dedicated pressure transducers permitted monitoring of parameters defining test conditions.

Pressure transducers may be selected and installed in accordance with the specific test requirements. Decisions generally include the type of transducer, i.e. absolute versus differential, and the measurement range. Measurement uncertainty requirements typically dictate the transducers used. The nozzle flow quality experiments used bonded strain-gauge pressure transducers to measure all of the steady-state pressures. A transducer measurement range selection of 0 to 15 psia spanned the pressure levels encountered during the tests while providing the required accuracy. The transducers were calibrated with respect to secondary standards traceable to the National Bureau of Standards (NBS), now called the National Institute of Standards and Technology (NIST).

Thermocouples provided the temperature measurements. The temperature measurement system consisted of a thermocouple time-share system, analogous to the



pressure Scanivalve<sup>®</sup> system. The system allowed multiplexing up to 12 thermocouples on a single data channel. The data acquisition system scanned the Scanivalve<sup>®</sup> ports and the thermocouples simultaneously. However, analogous to the pressure measurement system, dedicated thermocouples could be used to continuously measure selected temperatures. The requirement for only one temperature measurement in the nozzle model tests rendered the time-share system unnecessary. A dedicated copper-constantan thermocouple furnished the required measurement of free-jet total temperature (TTFJ).

Measurements of stilling chamber total pressure, stilling chamber total temperature, and nozzle exit static pressure defined the test conditions. During experiments with the variable-area nozzle, a pitot probe rake sensed total pressure. The rake included twelve steady-state pitot tubes, a total temperature probe, and a high-response pitot probe. The total temperature and high-response pitot pressure probes were mounted near the centerline of the stilling chamber. The twelve steady-state probes spanned the stilling chamber on the vertical plane of symmetry as shown in Fig. 38. The ASTF nozzle model tests required removal of the twelve-probe rake. In lieu of the rake, two pitot tubes located on the vertical symmetry plane provided the needed total pressure measurements (Fig. 38). Additional pressure measurements were obtained on the stilling chamber wall, the test section wall, and the test cell main exhaust duct as shown in Fig. 38. The nozzle models generally included provisions for measuring exit static pressure. However, in the absence of nozzle exit pressure measurements, the test cell static pressure measurements could be used to establish test conditions.

### 2.3.1.2 Test Article

Test article measurements included nozzle exit flow field, surface pressure, and hardware position. The nozzle exit flow-field measurements included local Mach number and local flow angle. The surface pressure measurements were obtained primarily for determining the nozzle exit Mach number.

A flow-field survey rake provided measurements of nozzle exit plane Mach number and flow angle distributions. Shown in Fig. 39, the rake contained five probes spaced on 2.5-in. centers. Each probe tip consisted of a 20-deg half-angle cone with a pitot pressure orifice and four surface pressure orifices. The surface pressure orifices were located in 90-deg increments around the circumference of the probe tip section (Fig. 39). A calibration related the average surface pressure normalized by pitot pressure, the difference between the top and bottom surface pressures (#1 and #3), and the difference between the side surface pressures (#2 and #4) to local Mach number (ML), local angle of attack (ALPL), and local angle of sideslip (BETL). The calibration provided coefficients used in the data reduction algorithm to account for such effects as probe tip manufacturing tolerances, pressure orifice imperfections, probe tip misalignment, and probe tip interference. Tests in the AEDC aerodynamic wind tunnel 4T established the rake calibration constants.

Flow-field measurements derived from cone probe pressure measurements in a subsonic flow require accurate differential pressure measurements. The sensitivity of flow angle to the orifice 1-3 and orifice 2-4 differential pressures decays significantly

with reductions in Mach number. To accommodate this decay in probe sensitivity while managing measurement uncertainty, the experiments used differential pressure transducers for those key measurements. Two differential pressure transducers, Baracell<sup>®</sup> capacitive transducers, connected the specific Scanivalves<sup>®</sup> serving the probe surface pressure orifices. With proper ordering of the probe surface pressure connections to the Scanivalves<sup>®</sup>, the transducers sensed the required pressure differences. The two transducers provided design maximum differential pressures of 10 mm Hg (0.19 psid) and 100 mm Hg (1.9 psid), respectively. The data processing algorithm selected the appropriate transducer according to the level of the particular measurement.

For each nozzle installation, the flow-field rake was installed with the probe tips at the nozzle exit plane. Using a horizontal orientation, the rake spanned the nozzle exit width as shown in Fig. 40. Figure 40a illustrates the variable-area nozzle installation. Similarly, Fig. 40b illustrates the ASTF nozzle model installation. A high-response pitot pressure probe attached to the rake body as shown. The mounting positioned the high-response probe 2.5 in. below the plane of the cone probe tips.

Flow-field surveys consisted of rake traverses between the upper and lower nozzle walls. A hydraulic actuator comprised the rake drive mechanism. A linear potentiometer attached to the actuator provided a rake position measurement. The zero position was located on the nozzle horizontal plane of symmetry with rake position measured positive up. A pitch sector mounted vertically in the test section supported the rake and hydraulic actuator. The 32-in. pitch sector radius positioned the rake pitch center of rotation at the APM pitch center. The arrangement allowed the rake pitch angle

(survey plane angle) to be manually set equal to the nozzle pitch angle. With the rake so oriented, the probes directly measured flow deviations relative to the nozzle centerline. The arrangement provided the added benefit of moderating the magnitude of the flow angle presented to the probe tips, minimizing the uncertainty.

The variable-area nozzle required six position indicators corresponding to the three upper wall and three lower wall actuators. A linear potentiometer mounted in parallel to each hydraulic cylinder, shown in Fig. 8, provided the needed measurements. The conversion to a fixed-area nozzle included the removal of the six potentiometers. A single linear potentiometer, attached to the yoke joining the upper and lower nozzle walls, sensed pitch angle (Fig. 11). The ASTF nozzle positioning mechanism used a rotary potentiometer to sense pitch angle (Fig. 15).

Two surface pressure orifices installed in the variable-area nozzle yielded measurements of exit static pressure. One orifice was located on the upper nozzle wall and the other was located on the lower nozzle wall.

The ASTF nozzle model instrumentation included pitot tubes and surface pressure orifices as shown in Fig. 41. The four static pressure orifices located at the downstream station provided nozzle exit static pressure measurements. Static pressure orifices installed along the upper wall, the lower wall, and the ramp provided data for pressure load determination. Pitot tubes positioned at the exit plane detected upper nozzle wall flow separation.

The majority of nozzle model pressure orifices were connected to the R2A2 Scanivalve<sup>®</sup> system. However, dedicated pressure transducers provided continuous monitoring of a number of key pressures.

### 2.3.2 Water Tunnel Experiments

Dye introduced into the water tunnel free-jet stilling chamber model served as the tracer for viewing flow streaklines. Movable dye injection probes allowed the injection point to be varied. Figure 42 illustrates a typical probe. A pressurized dye reservoir located outside the tunnel forced the dye through the probes. A regulator allowed adjustment of reservoir pressure and therefore dye flow rate. The installation of a number of fittings at different locations on the stilling chamber floor and the fabrication of a family of probes with various lengths enhanced the variability in dye injection point. The fitting locations appear in Fig. 43. The apparatus allowed the dye injection point to be readily varied during a run. Injection point changes were accomplished by manually setting the perpendicular distance between the probe tip and the chamber wall, by exchanging probes, and by moving probes to different fitting locations.

A set of flow meters measured the rates used for the boundary layer suction and the blowing experiments. Two sets of flow meters were plumbed in parallel and mounted on a portable rack. The measurements used various combinations of meter settings as dictated by the magnitudes of the flow rates.

The water tunnel yielded primarily qualitative results in the form of flow visualization. The streaklines revealed by the dye traces were recorded using 35 mm still photographs. Halogen lamps illuminated the desired regions of the flow field for the photographic coverage.

## 3.0 TEST DESCRIPTION

### 3.1 GENERAL

The airflow tests conducted in Research Test Cell R2A2 consisted of three distinct phases. The airflow experiments differed primarily in the nozzle configurations and test matrices used. Phase I focused on the basic variable-area nozzle, Phase II focused on the variable-area nozzle with vortex suppression modifications, and Phase III focused on the ASTF nozzle concept. The purpose of Phase II was to validate the water tunnel findings with respect to vortex suppression prior to development of the ASTF nozzle concept. The purpose of Phase III was to validate the ASTF nozzle concept prior to full-scale design. The basic procedures, data reduction methods, and uncertainties applied to all three of the airflow test phases.

As in the case of the airflow experiments, the water flow tests consisted of three phases differing primarily in the nozzle configuration and test matrices used. Each phase used the same fundamental test procedures. Phase I focused on validating the water tunnel simulation of the vortex formation phenomena. Phase I also enabled screening of candidate vortex suppression methods. Phase II focused on investigations of additional vortex suppression methods as well as refining methods explored in Phase I. Phase III supported the development of the ASTF nozzle concept.

## **3.2 TEST PROCEDURE**

### **3.2.1 R2A2**

#### **3.2.1.1 General**

Prior to each test period, the rake angle was set to the first nozzle pitch angle designated in the test matrix. Various system calibrations were then performed. A template used to space and align the upper and lower nozzle walls facilitated calibration of the variable-area nozzle actuator system. On-line application of the calibrations used a table of the six potentiometer readings versus nozzle pitch angle and height. An inclinometer set on the lower nozzle wall provided the basis for calibrating the modified variable-area nozzle and the ASTF nozzle model in pitch. The inclinometer also served as the basis for alignment of the ASTF nozzle ramp angle. Direct measurement of the flow-field probe tip position relative to the upper and lower nozzle walls yielded the calibration input for the rake position instrumentation. The pressure measurement system calibration used the laboratory scale factors in conjunction with a resistance shunt calibration procedure. The temperature, differential pressure, and the high-response system calibrations applied voltage substitutions based on the transducer laboratory calibrations.

With the atmospheric inlet system used for the R2A2 tests, establishing free-jet nozzle flow conditions required setting the test cell pressure to achieve a nozzle pressure



ratio, PFJ/PTFJ commensurate with the desired Mach number. Based on the unit Reynolds number curves of Fig. 5 and a nozzle height of 11.25 in., the MACH = 0.9 condition yielded the maximum Reynolds number of  $3.97 \times 10^6$ . With flow established, flow-field rake traverses between the lower and upper nozzle walls mapped the distributions in local Mach number and local flow angle. The surveys generally used a 2.5-in. spacing in the traverse direction. Coupled with the lateral 2.5-in. probe tip spacing, the traverses yielded a measurement grid with equally spaced points in each direction. Occasional traverses with a smaller rake position step size satisfied needs for higher spatial resolution. High-response data were acquired only at selected rake positions in the traverse.

### **3.2.1.2 R2A2 Phase I**

Tests of the variable-area nozzle model comprised Phase I of the R2A2 flow quality investigation. Test variables consisted of nozzle height, nozzle wall divergence angle, nozzle exit Mach number, and nozzle pitch angle. The tests included non-zero wall divergence angles to establish calibrations of non-uniform flow conditions for later use in aircraft inlet model free-jet experiments. The non-uniform flow field would, in principle, facilitate experimental investigations of aircraft inlet distortion to free-jet flow quality. Nozzle height settings included 5 5/8 in. and 11 1/4 in. The tests included variations in nozzle height for use in subsequent aircraft inlet model experiments. In this case, the tests would help define nozzle exit cross-sectional area requirements. The flow-

field traverses at  $H = 5 \frac{5}{8}$  in. used a 1-in. increment in rake position (RAKE). The traverses at  $H = 11 \frac{1}{4}$  in. generally used a  $2 \frac{1}{2}$ -in. increment. However, at the latter height setting, a 1-in. increment was occasionally adopted for all or part of the traverse. The tests used Mach numbers of 0.3, 0.6, and 0.8 for the majority of test configurations. Respective Reynolds numbers included  $1.9 \times 10^6 \text{ ft}^{-1}$ ,  $3.4 \times 10^6 \text{ ft}^{-1}$ , and  $4.1 \times 10^6 \text{ ft}^{-1}$ . Nozzle pitch angle settings included 0-deg, 20-deg, 30-deg, and 40-deg. Nozzle roll angle remained at 0 deg for all tests. Table 1 provides the test matrix (tables appear in Appendix B).

### 3.2.1.3 R2A2 Phase II

Tests of the modified variable-area nozzle model, for the purpose of verifying selected vortex suppression techniques under objective 3, comprised Phase II of the air flow experiments. Unlike the Phase I tests, the nozzle height remained fixed at  $H = 11 \frac{1}{4}$  in. with a fixed wall divergence angle of 0 deg. Test apparatus included the four nozzle inlet ramps: (1) 30-deg contoured, (2) 30-deg straight, (3) 50-deg contoured, and (4) 50-deg straight. Nozzle pitch angle settings of 30-deg and 50-deg corresponded to the respective ramp designations. Nozzle exit Mach numbers included 0.3, 0.6, and 0.9. Based on results from Phase I, the traverses used a 1-in. increment in rake position in the bottom half of the nozzle and a 2.5-in. increment in the top half. The test matrix appears in Table 2.

#### 3.2.1.4 R2A2 Phase III

Tests of the proposed ASTF free jet nozzle concept comprised Phase III of the R2A2 free-jet nozzle flow quality investigation. The experiments included nozzle model pitch angles of 0-deg, 30-deg, and 45-deg with a roll angle of 0 deg. Facility exhaust duct choking instigated by the increase in nozzle area and mass flow with respect to the previous configurations, precluded testing at MACH = 0.9. As a result, the majority of tests adopted a Mach number of 0.6 with a unit Reynolds number of  $3.4 \times 10^6 \text{ ft}^{-1}$ . Based on a nozzle height of 16 in., this corresponds to a Reynolds number of  $4.5 \times 10^6$ . On a standard day, ASTF can provide a Reynolds number of  $2.7 \times 10^7$  based on the full-scale nozzle height of 124 in.

The flow-field survey rake positioning mechanism, designed for the variable-area nozzle, was incapable of traversing the full distance between the upper and lower nozzle walls. However, the positioning mechanism would traverse from RAKE = -5.5 in. to RAKE = +5.5 in. The region between RAKE = +/- 4 in. used a 2-in. survey increment. A 1.5-in. survey increment was used to reach each end point.

The initial Phase III test configuration consisted of ramp configuration A1 and R2A2 stilling chamber configuration A. Experiments included ramp angles both on and off the prescribed ramp schedule. During the Phase III program, the R2A2 stilling chamber was converted to configuration B to reduce a suspected influence of corner separations on the nozzle inlet flow. Experiments that followed the modification tested both ramp configuration 1 and ramp configuration 2. Table 3 depicts the test matrix.

## **3.2.2 Water Tunnel**

### **3.2.2.1 General**

The three water tunnel test phases applied the same basic test procedure. First, test articles were installed at the positions and orientations required for the particular experiment. The water level was then raised to just below the access openings so that the hatches could be left off during the test. The open hatches provided access to the test articles during the runs saving configuration change time. The location of the flow-field region of interest near the bottom of the stilling chamber and the considerable time that would have been required to complete minor configuration changes justified the approach. Nevertheless, initial tests comparing results with and without the hatches installed verified the assumption that the open hatches would not adversely affect the results.

The dye injection reservoirs were filled with a dye composed of milk, food color, and alcohol. The addition of alcohol neutralized the dye buoyancy so that the injected dye would closely follow the streaklines. Pretest procedures included verifying dye neutral buoyancy in a water sample taken from the water tunnel test section. To further ensure that the dye traces would delineate the streaklines, the experiments used the absolute minimum reservoir pressure needed to inject a steady dye stream. Clips pinching the flexible plastic tubes that connected the reservoirs to the probe bodies provided a simple means to interrupt dye flow between experiments.

Early experiments verified that precise water velocity measurements would not be required to achieve the test objectives. The secondary flows of concern developed in the flow nearly independent of the flow velocity used. Therefore, the tests used the low end of the tunnel velocity range. Nominal velocities, estimated by timing dye pulses as they pass between grid marks on the nozzle wall and in the stilling chamber, served as the basis for calibrating the water tunnel console readout. Subsequent tests used the console controls for establishing water flow conditions.

The water tunnel results consisted primarily of qualitative flow visualization data, the quantitative flow-field measurements reserved for the detailed airflow experiments in test cell R2A2. Photographing the streakline traces recorded the water tunnel results for subsequent analysis and archiving. The steadiness and persistence of the secondary flows appearing in the flow field allowed recording using still photography. Generally, the photographic procedure used a combination of three viewing positions: (1) side view of the nozzle inlet section, (2) top view of the nozzle inlet section, and (3) view looking upstream into the nozzle exit. The open test section hatch provided the optical access needed for distortion-free views of the nozzle flow. Adjustments of the halogen lamp positions provided optimum lighting for each view. Typically, the camera recorded test configuration information encrypted in markings placed within the field of view.

To facilitate bookkeeping of the photographic results, the nozzle exit area was divided into nine zones as shown in Fig. 44. The zone identifiers indicated the general location of the streaklines. Finer variations of the dye injection points within each zone more completely mapped the flow field.

### 3.2.2.2 Water Tunnel Phase I

Phase I of the water tunnel flow quality investigation included experiments with both the variable-area nozzle and the generic nozzles. The experiments with the variable-area nozzle grouped into two categories focused on the following objectives: (1) verification of the water tunnel simulation and (2) identification of vortex suppression techniques. The verification that the water tunnel simulation would adequately reproduce the vortical flow features of interest formed a critical precursor to vortex suppression technique development. The experiments used a nozzle height of 2.4 in., scaling to the 11.25 in. nozzle setting in R2A2, and a nozzle pitch angle of 30 deg. The tests also used a nozzle water velocity of approximately 4.4 in./sec, with a corresponding unit Reynolds number of  $3.6 \times 10^4 \text{ ft}^{-1}$ . Thus, the Reynolds number based on a 2.4 in. nozzle height was  $7.2 \times 10^3$ .

Streaklines viewed through the nine nozzle measurement zones mapped the flow to verify that the water tunnel adequately simulated the R2A2 flow field including the development of vortices. The streaklines were photographed from the side view.

Prior to the investigation of vortex suppression techniques, a nozzle exit blockage was introduced to verify the supposition that blockage effects on vortex formation could be neglected during the experiments. A wood block, with dimensions of 1.65 x 1.45 x 5.2 in., served to simulate an aerodynamic interference in the nozzle exit flow. The block was mounted vertically 1.1 in. downstream of the nozzle exit plane to provide a 60

percent blockage of the projected nozzle exit area. The nozzle exit remained open for subsequent experiments with the confidence that the results would apply to highly-blocked free-jet tests of aircraft propulsion systems.

Following verification of the water tunnel simulations and the insensitivity to nozzle exit blockage, the test process proceeded to the identification of flow quality improvement techniques. The investigation considered techniques for preventing formation of the large vortices in the variable-area nozzle with the anticipation that some vortical flows would likely remain. The small vortex in each of the viscous-dominated nozzle corner flows represents one example. The diameter would be on the order of the corner boundary layer thickness. Another possibility was the secondary flow induced by the flow direction change incurred as the nozzle bends the flow to the desired pitch angle. As a result, the experiments emphasized preventing the very large vortices that produce the excessive flow non-uniformities measured in R2A2.

Potential vortex attenuation techniques included screens (one and two layers), vertical straightening vanes, horizontal vanes, and honeycombs that might reduce secondary flows in the variable-area nozzle. The horizontal vane assembly angle and the honeycomb angle, with respect to the nozzle inlet plane, were varied. Tests included angles of 0 deg and 20 deg. Each case applied dye injection points upstream of the flow-straightening device.

The test configurations included the family of nozzle inlet ramps. Experiments using ramp configurations 1-5 enabled an evaluation of ramp performance versus geometric size and complexity. The ramp experiments varied the point of intersection

with the lower nozzle wall, the ramp contour (curved versus straight), and the ramp slope at the intersection point. Photographic recording of the results concentrated primarily on zones 1 and 3.

The Phase I water tunnel experiments also included an investigation of the key parameters influencing the vortices. The tests used the generic nozzles to effect a systematic variation in nozzle exit cavity, nozzle vertical position relative to the plenum floor (ZI), nozzle longitudinal position relative to the bulkhead (XI), nozzle pitch angle ( $\theta$ ), nozzle contraction section geometry, nozzle cross-sectional shape, and nozzle contraction ratio. Nozzle pitch angle settings included 30 deg and 45 deg.

In addition to the exit block test, the experiments employed the removable exit cavity to evaluate the effect of nozzle exit flow interference on the nozzle vortices. The cavity provided the means to assess the role that the cavity might assume in forming vortices in the variable-area nozzle. The experiments included the configuration primarily to verify the assumption that the exit cavity did not induce or enhance the vortices.

Tests of the effect of nozzle vertical position on vortex formation included variations of ZI at constant nozzle pitch. Holding nozzle pitch angle at 30 deg, the 2-D SYM nozzle and the 2-D ASY nozzle were each tested at three vertical positions corresponding to ZI = 0.6 in., 1.4 in., and 3.4 in. In addition, the 2-D SYM nozzle tests included a number of experiments with the artificial floor to effect changes in ZI without changing nozzle location with respect to the plenum centerline. The artificial floor



provided ZI settings of 0.6 in. and 0.0 in. Flow visualization focused only on the zones exhibiting anomalous flow, saving considerable test time.

The experiments employed the artificial bulkhead to vary the spacing between the nozzle inlet and the bulkhead. The test enabled an evaluation of the effect of nozzle longitudinal position, XI, on vortex formation. The tests used the 2-D SYM nozzle with the value of XI reduced to 0.1 in.

To evaluate the effect of nozzle pitch angle on vortex formation, the tests included experiments at nozzle pitch angles of 30 deg and 45 deg. with  $ZI = 2$  in. The experiments used both the 2-D SYM nozzle and the 2-D ASY nozzle.

The direct comparison of results from the 2-D SYM and the 2-D ASY at equivalent test conditions provided the means to evaluate the inlet contraction section geometry effects.

Tests of the axisymmetric nozzles addressed two objectives: (1) to investigate the effect of nozzle cross-sectional shape on the secondary flows and (2) to investigate the effect of nozzle contraction ratio on the flow characteristics. Tests of the short axisymmetric nozzle at 30 deg pitch with  $ZI = 0.5$  in. and 1.4 in. provided results for direct comparison with the corresponding 2-D nozzle results. Tests of the long axisymmetric nozzle at 30 deg pitch and  $ZI = 0.85$  provided results for comparison with the short axisymmetric nozzle to evaluate contraction ratio effects.

Tests of the short axisymmetric nozzle supported an evaluation of the ramp vortex prevention technique application to a generic nozzle installation. The tests used two ramp configurations, Axi Ramp 1 and Axi Ramp 2, each installed with the nozzle set at

PITCH = 30 deg and  $ZI = 1.4$ . The Axi Ramp 2 configuration tests included five positions varying ramp trailing edge location with respect to the nozzle inlet.

The curved 2-D high alpha nozzle tests encompassed pitch angles of 30 deg and 45 deg with  $ZI = 0.6$ . The tests included runs with and without the lower wall extension installed.

The test matrix, including all of the nozzle configurations, appears in Table 4.

### **3.2.2.3 Water Tunnel Phase II**

Phase II of the water tunnel studies included experiments with the variable-area nozzle, the generic nozzles, and the ASTF nozzle concept. The variable-area nozzle tests explored vortex suppression techniques posed subsequent to the phase I work. The experiments encompassed blowing with the piccolo tube, boundary layer suction, and additional ramp configurations. The latter provided information needed to design ramps for the ASTF nozzle. The generic nozzle tests focused on alternative vortex suppression methods with the baffle configurations. Phase II concluded with tests to verify the ASTF nozzle concept prior to investing in the R2A2 airflow experiments.

The blowing experiments applied the piccolo tube concept described in Ref. 87. The piccolo tube approach attempts to remove vorticity by creating a velocity gradient in the direction opposite of the vortex rotation. The introduction of blowing near the point where the vortex attaches to the plenum floor establishes the desired gradient. During the water tunnel experiments, covering selected orifices in the tube produced the needed

gradients. Adjustment of the blowing region width varied the lateral location of the gradient center.

The test matrix appearing in Table 5 presents the piccolo tube test parameters. Test variables included blowing rate, tube height above the plenum floor, and tube width. The mass flow varied from 1.5 gph to 4 gph (0.4 percent to 1.0 percent of nozzle flow rate). The tests included height settings of  $ZP = 0.75$  in., 1.13 in., and 1.19 in. with width settings of 0.9 in., 1.75 in., 1.88 in., and 2.38 in.

The boundary layer control experiments encompassed a systematic variation of suction location and rate. The goal was to not only investigate suction as a means of vortex suppression but to explore the boundary layer influence on vortex formation. The tests procedure involved the independent activation of suction regions 1-4 with the nozzle flow velocity set at approximately 4.4 in./sec. This corresponded to a nozzle flow rate of approximately 394.9 gph. In regions demonstrating a strong influence of flow rate on the flow field, the test procedure included increasing suction rate in 2 gph increments starting at 6 gph. The increase was discontinued when observed changes with flow rate ceased or the maximum available rate was reached. The tests also included a limited number of experiments with combined blowing regions activated. The matrix appears in Table 5.

The Phase II experiments also included a number of additional ramp configurations to support development of the ramp concept for the ASTF nozzle. Tests of the ramp configurations 21 and 22 explored ramp performance with the leading edge unsealed from the plenum section floor. The goal was to evaluate a ramp concept that could readily be adapted to the variable-pitch and variable-yaw ASTF nozzle. Position 1

located the ramp 21 leading edge 0.4 in. above the plenum floor (Fig. 21f). Position 2 located the ramp 21 leading edge 1.0 in. above the plenum floor (Fig. 21f). The ramp 22 configuration tests used a single position as shown in Fig. 21g.

The test Phase II configurations included the two nozzle inlet baffle installations. The horizontal baffle installation and the vertical baffle installation each attempted to reduce the flow circulation in the nozzle inlet region.

The results from the water tunnel Phase II experiments supported the final selection of an ASTF nozzle configuration. Water tunnel experiments at pitch angles of 0 deg, 30 deg, and 45 deg explored the ASTF nozzle model flow quality. During the tests, the nozzle model ramp angles varied from -20 deg to +20 deg. Table 5 provides the test matrix.

#### **3.2.2.4 Water Tunnel Phase III**

Phase III of the water tunnel studies focused on an evaluation of the ASTF nozzle model with ramp configuration B installed. The experiments encompassed a nozzle pitch angle range of 10 deg to 45 deg and a nozzle yaw angle range of 0 deg to -10 deg. The nozzle orientation angles generally varied in 5 deg increments. The ramp angle settings generally applied the ramp A schedule. However, the tests incorporated a number of experiments with off-schedule ramp angle settings in order to evaluate the schedule compatibility with the ramp B design.

Streakline traces were observed and photographed primarily in zones 1-6. Photographic coverage used the side view and the view looking upstream into the nozzle. Some experiments investigated the flow along the upper nozzle wall, at high-pitch conditions, by injecting dye into zone 8. Table 6 provides the water tunnel Phase III test matrix.

### **3.3 DATA REDUCTION**

The steady-state data obtained during the R2A2 tests were reduced off-line using two basic data reduction programs. The Engineering Units Data Reduction Program (EUD) converted the raw data to engineering units by applying the instrument calibrations. The performance data reduction program calculated test conditions and local flow-field characteristics from the EUD data. In addition, the performance program grouped, labeled, and printed all measured and calculated parameters in an easy reference format.

The ETF Dynamic Data Analysis Lab reduced high-response pitot pressure data selected from the data set. The analysis provided the root-mean-square turbulence level normalized by the free-jet total pressure (PT). In addition, Power Spectral Density plots displayed frequency content information.

## **3.4 UNCERTAINTY OF RESULTS**

### **3.4.1 R2A2 Measurement Uncertainty**

Repeat calibrations of the instrumentation system with respect to secondary standards traceable to the National Bureau of Standards provided the basis for measurement uncertainty estimates. The measurement uncertainty combined bias and precision errors according to the following:

$$U = +/- (B + t_{95} \times s)$$

where B represents the bias limit, s represents the sample standard deviation, and  $t_{95}$  represents the 95<sup>th</sup> percentile point for the two-tailed Student's t distribution. For degrees of freedom greater than thirty,  $t_{95}$  assumes the value of two. The uncertainties of the measured data appear in Table 7.

To estimate the uncertainties in the calculated parameters, the analysis applied the Taylor series method of error propagation. Reference 102 describes the Taylor series method. The uncertainties in the calculated parameters appear in Table 8.

### **3.4.2 Water Tunnel Result Uncertainty**

A number of approximations inherent in subscale water tunnel simulations of air flow problems might contribute to the uncertainty of results. These include the

following: (1) geometric detail, (2) incompressibility in the simulation, (3) Reynolds number mismatch, and (4) facility interference (including dye injection). The degree to which the approximations impact the results depends on the mechanisms involved in the flow phenomenon under study. Often, water tunnel simulations produce very reliable qualitative results even if quantitatively inaccurate. The vortex shed off a sharp lip might be an example. The water tunnel may faithfully predict the presence of the vortex but incorrectly reproduce the relative size and strength. However, if the mechanisms involved in the development of a flow phenomenon are highly sensitive to Reynolds number, the water tunnel might misrepresent even the qualitative result. A more in depth investigation of the water tunnel simulation issues appears in Ref. 103.

The assessment of the uncertainty associated with applying the water tunnel to a particular air-flow problem requires estimates of the predominate flow phenomena sensitivities to the aforementioned approximations. The sensitivity of the free-jet nozzle vortex formation to the approximations has not been established. Therefore, the multi-phase flow quality investigation included verification of key water tunnel results in R2A2 tests. Phase I of the water tunnel investigation included a qualitative verification of the variable-area nozzle flow simulation. The test series included Phase II of the R2A2 experiments solely for the purpose of verifying vortex suppression techniques identified in the water tunnel. The program used Phase III of the R2A2 experiments to verify a nozzle concept derived with the aid of the water tunnel. Cross checks between the various test phases showed the water tunnel simulation of the free-jet nozzle vortices to be qualitatively reliable.

## 4.0 RESULTS AND DISCUSSION

### 4.1 R2A2 PHASE I

Free-jet nozzle flow quality anomalies induced by undesired secondary flows first appeared during the R2A2 Phase I experiments. This section presents key results acquired during the tests. Throughout the presentation, the variable-area nozzle flow quality measurements appear in plots of local Mach number distribution and local flow angle distribution. Local flow angles were expressed in terms of ALPL and BETL.

Figure 45 displays the Mach number distribution at a nozzle height of 11.25 in. The results appear in plots of probe vertical position versus local Mach number. Each plot includes the measurements from a single probe with a curve for each combination of pitch angle and Mach number. The five plots, therefore, contain the results of the complete set of surveys for the 11.25-in. height. The lateral symmetry of the distributions may be observed by comparing Figs. 45a and 45e as well as Figs. 45b and 45d. The probe 2 and the probe 4 traverses were highly symmetrical. The main features of the probe 5 traverse also appeared in the probe 1 traverse. However, the latter case displayed larger deviations in the Mach number. The most notable feature was a region of accelerated flow near the nozzle wall (probes 1 and 5) in the lower half of the nozzle. With respect to flow quality requirements, the only point in the data set with a Mach number deviation exceeding the allowable limit of  $\pm 0.05$  occurred at PITCH = 30 deg



and MACH = 0.8. This deviation occurred locally at the location occupied by probe 1 when RAKE = 3 in. (Fig. 45a).

The measured flow angle distributions appear in plots of ALPL and BETL versus probe position. Figure 46 presents results obtained at MACH = 0.6 and H = 11.25 in. with pitch angles of 0 deg, 20 deg, 30 deg, and 40 deg. Each plot includes an outline of the nozzle exit cross section with the survey points marked. The arrow drawn from each point represents a vertical component equal to ALPL and a horizontal component equal to BETL. Although not the actual flow vectors, the arrows represent the projections of the velocity vectors onto the exit plane. Therefore, the arrows show the direction of local flow deviations from the axial direction.

At a pitch angle of 20 deg, a pair of counter-rotating vortices appeared in the lower half of the nozzle (Fig. 46b). The flow angle plot clearly displays the vortices by showing the circulation of the flow. Vortices rotating in the clockwise and counterclockwise senses appeared in the nozzle lower left and lower right quadrants, respectively. The diameters of the vortices were on the order of the quadrant size. The cores of the vortices appeared to be located symmetrically about the nozzle exit vertical centerline. As the pitch angle increased to 30 deg, the vortices increased in severity (Fig. 46c). Measured flow angles ranging up to 16 deg in the vicinity of the vortices far exceeded the allowable limit of 3 deg. At a pitch angle of 40 deg, the magnitude of the flow angles decreased to values comparable to those measured in the 20-deg pitch case (Fig. 46d). The 40-deg pitch case did not retain the symmetry in the vortex pair that characterized the 20-deg and 30-deg pitch cases. In fact, a recognizable vortex appeared

on the right side of the nozzle only. A comparison of Fig. 46c with Figs. 45a and 45e showed that the Mach number spike measured on probes 1 and 5 resulted from accelerated flow near the vortex. The largest occurred at MACH = 0.8.

Figure 47 presents the flow angle measurements at  $H = 11.25$  in. and PITCH = 30 deg with MACH = 0.3 and 0.8. When combined with Fig. 46c, a complete presentation of results spanning the Mach number range results. The main features of the flow field, large counter-rotating vortices in the bottom of the nozzle, persisted at all of the Mach numbers.

The nozzle Mach number distributions measured with the nozzle height reduced to 5.62 in. appear in Fig. 48. As in the  $H = 11.25$  in. case, the profiles displayed a symmetry about the nozzle exit plane vertical line of symmetry. As in the previous results, the nozzle contained regions of accelerated flow along the probe 1 and probe 3 traverses in the bottom half of the nozzle. However, the Mach number deviations remained within the allowable limit of 0.05.

Figure 49 presents the measured flow angle distributions at MACH = 0.6 and  $H = 5.62$  with pitch angles of 0 deg, 20 deg, 30 deg, and 40 deg. The results displayed a consistency with those obtained at  $H = 11.25$  in. At PITCH = 20 deg, the symmetrically located counter-rotating vortices appeared with flow angles far in excess of allowable limits. As the pitch angle increased to 30 deg, an increase in flow angle signified the corresponding increase in vortex strength. At the 40-deg pitch condition, the asymmetry in the lower half of the nozzle developed as before. The large flow angles persisted on the right side of the nozzle and decreased on the left. Figure 50 provides the flow angle

measurements at PITCH = 30 deg and MACH = 0.8. Results appearing in Fig. 50 may be compared with those in Fig. 49c to observe the effect of Mach number. Relative to the MACH = 0.6 case, the MACH = 0.8 case displayed slightly less flow angularity near the vortex. However, the MACH = 0.8 retained the basic features that characterized the MACH = 0.6 case.

The variable-area free-jet nozzle flow quality tests included flow field surveys with the upper and lower nozzle walls positioned at the various divergence angles planned for aircraft inlet model experiments. The results displayed a superposition of the vortex circulations and vertical flow components due to the non-parallel walls. A sample result appears in Fig. 51 for the H = 11.25in., PITCH = 20 deg, MACH = 0.6, and DIV = 4 deg.

Phase I of the R2A2 flow quality investigation was completed in June, 1982. The results can be summarized as follows:

1. Large secondary flows consisting of counter-rotating vortices formed in the lower two quadrants of the nozzle resulting in unacceptable flow angularity.
2. The upper half of the nozzle did not contain large secondary flows.
3. The development of the vortices was a function of the nozzle pitch angle. The vortices first appeared at the 20-deg pitch angle condition.
4. The most severe flow anomalies appeared at the 30-deg nozzle pitch angle condition.
5. Vortex formation was relatively insensitive to nozzle Mach number and nozzle height.

The results of the R2A2 Phase I tests yielded the conclusion that additional work would be required to address the vortex problem.

## **4.2 WATER TUNNEL PHASE I**

### **4.2.1 Vortex Parametric Investigation**

The vortex parametric investigation focused on identifying the parameters that influence the formation of the nozzle vortices. The goal was to improve the understanding of the interactions between the nozzle and plenum flows and provide the insights needed to synthesize viable vortex suppression methods.

During preparations for the water tunnel experiments, the mechanisms producing the vortices remained unknown. As a result, it was not possible to assess, a priori, the sensitivity of the phenomenon to the airflow parameters that the water tunnel could not match. Therefore, the water tunnel experiments started, in February 1984, with a verification that the simulation would qualitatively reproduce the results measured in R2A2. Although the water tunnel tests could not match such parameters as velocity, Reynolds number, and Mach number (compressibility), they did closely approximate the geometry since the stilling chamber and variable-area nozzle model faithfully scaled the R2A2 hardware.

The initial experiments used a free-jet nozzle setting of  $PITCH = 30$  deg and  $H = 2.4$  in. The nozzle height modeled the R2A2 nozzle height of 11.25 in. Upon

establishment of the water flow, the pair of counter-rotating vortices appeared immediately, verifying the validity of the simulation. Experiments demonstrated the insensitivity of the vortices to velocity. Subsequent tests generally used a nominal nozzle exit velocity of 4.4 in./sec. Figure 52 shows the vortices. Figure 52a provides side view photographs of the zone 1 and zone 3 vortices. Figure 52b shows a schematic of the vortex characteristics. The dye streakline traces coiled around the vortex core in a helical pattern. The vortex locations, in zones 1 and 3, and the vortex rotation directions qualitatively matched the R2A2 results. An astonishing result was the time invariance of the vortex phenomenon. The streaklines showed the core location to be steady and displayed little wavering in the helical pattern. This result explained the excellent repeatability in the R2A2 flow-field measurements in the vicinity of the vortex core.

The water tunnel flow visualization capability also provided the means to observe the streamwise structure, unlike the R2A2 nozzle exit plane measurements. The results showed that at the nozzle inlet plane, defined by the upper and lower nozzle walls, the vortices were well developed. As expected, the vortices attached to the stilling chamber floor near the nozzle inlet plane and differed from the vortices expected to develop in the nozzle corner boundary layer.

The streakline traces in zones 2 and 4-9 appear in Fig. 53. The straight streaklines revealed the uniform flow conditions that existed in those regions.

The data presented in Figs. 52 and 53 verified that the water tunnel qualitatively reproduced the R2A2 variable-area nozzle flow characteristics. Despite the mismatches in compressibility (Mach number), velocity, and Reynolds number, the water tunnel

adequately simulated the phenomena leading to the vortex formation. The results yielded the critical conclusion that the water tunnel would provide a valid and valuable tool for the subsequent investigations. This conclusion substantiated a decision to proceed with the water tunnel test plans.

Although not expected to factor into the vortex formation, nozzle exit blockage effects deserved a brief experiment. The experiment used the variable-area nozzle model in conjunction with the nozzle exit block. The blockage changed the path of the nozzle exit streaklines. The paths followed by the vortices also changed. However, the experiments verified that the blockage did not affect the formation of the vortices.

Following the blockage tests, the experiments proceeded to the parametric studies using the generic nozzles. The initial generic nozzle tests used the 2-D ASY nozzle configuration (Fig. 24b). The asymmetric inlet simulated the contraction section of the variable-area nozzle. To expedite the tests, flow visualization generally concentrated on zones 1-3. The remaining zones were surveyed only to the extent necessary to verify uniform conditions. Flow-field photographic coverage consisted of views looking upstream into the nozzle exit.

Unsteady vortices appeared during tests of the 2-D ASY nozzle. Figures 54a and 54b include a photograph and a sketch of the observed vortices at  $PITCH = 30$  deg and  $ZI = 1.4$  in. A relatively small unsteady vortex formed near the lower nozzle wall. Difficult to photograph, the vortex appeared to drift back and forth between zones 1 and 2. The time-variance precluded stabilizing the dye on a helical streakline. However, the dye traced the vortex long enough to obtain the photograph shown in Fig. 54a. The traces

suggested the presence of a pair of small counter-rotating vortices. Streaklines along the lower nozzle in the regions adjacent to the vortices displayed sidewash angles on the order of 10 deg.

The results obtained with the 2-D ASY nozzle set at  $PITCH = 30$  deg and  $ZI = 3.1$  appear in Fig. 54c. The observed streakline patterns qualitatively matched the  $ZI = 1.4$  in. case. Unsteady vortices appeared to exit near the zone 1 and zone 2 border. Attempts to stabilize the dye on the varying vortex remained unsuccessful. Sidewash angles at other positions along the lower nozzle wall appeared to be less than at  $ZI = 1.4$  in. suggesting that the increase in  $ZI$  reduced the severity of the flow anomalies.

Reductions in  $ZI$ , below 1.4 in., required removing part of the 2-D ASY nozzle sidewall contraction section. Figure 54d shows results obtained with the modified nozzle set at  $PITCH = 30$  deg and  $ZI = 0.6$  in. Vortices stronger than those observed at the high  $ZI$  settings formed near zone 3. Careful adjustment of the dye injection point allowed brief observations of the time-variant helical streakline patterns produced by the vortex. Streakline traces mapped using small perturbations in the dye injection point location suggested that a pair of counterrotating vortices may have existed. Occasionally, the dye from the probe split to trace the pair of vortices.

The results with the nozzle exit cavity installed appear in Fig. 55. As expected, the presence of the cavity did not affect the formation of the vortex. The vortex still resided near the bottom wall of the nozzle. The lateral location of the vortex filament may have altered slightly with a shift toward the nozzle vertical plane of symmetry.

However, the small position shift may have been a manifestation of the experiment repeatability.

With the 2-D ASY nozzle installed at PITCH = 45 deg, the free-jet bulkhead restricted ZI to a minimum of 2 in. The results, appearing in Fig. 56, compared to the PITCH = 30 deg and ZI = 1.4 in. case. An unsteady vortex, near the bottom of the nozzle, favored the left side looking upstream.

The 2-D SYM nozzle comprised the second generic nozzle configuration. Figure 57 shows the nozzle flow characteristics observed at PITCH = 30 deg with ZI = 0.6 in., 3.4 in. and 1.4 in. At ZI = 0.6 in., a vortex formed in zone 3 favoring the right side looking upstream (Fig. 57a). Dye introduced into the flow readily traced the helical streaklines suggesting a relatively steady vortex position relative to the 2-D ASY case. Furthermore, the vortex appeared to be larger than in the former case. The dye injection point showed the vortex attachment point location, on the plenum floor, approximately  $\frac{3}{4}$  in. upstream of the lower nozzle wall leading edge. Lateral traverses of the lower half of the nozzle revealed the apparent presence of secondary vortices. A smaller vortex adjacent to the main vortex rotated in the opposite direction. The dye traces behaved as if a small unsteady vortex also existed in zone 3. However, attempts to photograph the small time-variant vortices remained unsuccessful.

Figure 57b provides results obtained with the 2-D SYM nozzle set at PITCH = 30 deg and ZI = 3.4 in. An unsteady vortex formed which appeared to be much less pronounced than in the ZI = 0.6 in. case. The results approximated those obtained with the 2-D ASY nozzle in the corresponding position.



The apparent size of the vortices appearing in the 2-D SYM nozzle at PITCH = 30 deg and ZI = 1.4 resided between those observed in the ZI = 0.6 in. and ZI = 3.4 in. cases. Furthermore, the vortex appeared to be larger than the vortex in the corresponding 2-D ASY nozzle experiments. Shown in Fig. 57c, the main vortex formed in the left side of zone 1. The relatively stable position permitted photographing the helical streaklines. As in the ZI = 0.6 in. case, observations included the vortex attachment point located on the plenum floor and upstream of the lower nozzle wall leading edge. As in previous cases, perturbations in the dye injection point location produced results suggesting the presence of a second counter-rotating vortex.

The artificial floor afforded the means to extend the range of ZI. Furthermore, it provided the means to vary ZI without changing the nozzle position with respect to the plenum centerline. The results obtained with the 2-D nozzle set to ZI = 0.6 in. generally agreed to those obtained with the nozzle positioned 0.6 in. above the actual plenum floor (Fig. 58a). A very distinct vortex resided near the bottom center of the nozzle.

Results obtained with the artificial floor repositioned to ZI = 0.0 in. appear in Fig. 58b. Although the results showed the presence of a vortex, the vortex appeared to be smaller and weaker than in the previous cases.

The artificial bulkhead provided a variation in XI while holding all other parameters constant. The experiments used the 2-D SYM nozzle model set at 30 deg pitch and ZI = 3.3 in. Figure 59 contains a sample result. Although a vortex was observed, it was less pronounced than in the previous case with ZI = 0.9 in.

Although lacking photographic coverage, the 2-D SYM nozzle flow field at PITCH = 45 deg and ZI = 2 in. displayed the presence of vortices. At the nozzle exit, the vortex appeared to be smaller than at the PITCH = 30 deg and ZI = 1.4 case.

Observations included the vortex attachment point on the plenum floor. The results were comparable to those obtained with the 2-D ASY nozzle at PITCH = 45 deg.

Following the 2-D SYM nozzle experiments, the parametric investigation proceeded to the axisymmetric nozzles. The axisymmetric nozzle tests addressed the possibility that the observed vortices were manifestations of the nozzle corner vortices. Figure 60 illustrates the short AXI nozzle flow-field characteristics at PITCH = 30 deg. Figures 60a-c include the results at ZI = 1.4 in. Relative large, unsteady vortices formed near the bottom of the nozzle (Fig. 60a and 60b). Apparently, the nozzle flow field contained at least two counterrotating vortices, drifting in position. Observations included the main vortex attachment point located on the plenum floor upstream of the nozzle inlet (Fig. 60c). The vortices appeared larger in size than those observed in either the 2-D ASY or the 2-D SYM nozzles at the corresponding orientation and position. These results immediately distinguished the large nozzle vortices from vortices that form in the corner boundary layers of 2-D nozzles.

Figures 60d and 60e present results obtained with the short AXI nozzle set at PITCH = 30 deg and ZI = 0.5. Unsteady vortices appeared near the bottom center of the nozzle as in the ZI = 1.4 in. case. The results did not reveal the effect of reducing ZI on the vortex.

Following the short AXI nozzle tests, the experiments proceeded to the long AXI nozzle configuration. The free-jet bulkhead limited the ZI positions available in the long AXI nozzle installation. As a result, the experiments used  $ZI = 0.85$  in. for the  $PITCH = 30$  deg case. The results, shown in Fig. 61, included the unsteady vortices near the bottom of the nozzle. The vortex position drifted as in the short AXI nozzle. The clearly visible vortex attachment point on the stilling chamber floor remained approximately 1 in. upstream of the nozzle inlet. The results demonstrated the insensitivity of the vortex formation to nozzle inlet contraction ratio.

The experiments yielded two additional important observations. First, almost any disturbance artificially introduced in the plenum chamber resulted in the formation or amplification of the unsteady generic nozzle vortices. Disturbances induced by gently stirring the plenum chamber flow with a pencil resulted in large vortices in the nozzle. Second, dye could be carefully introduced into the corners of the 2-D nozzles to observe the corner vortices described in the introduction. The corner vortices were smaller and distinct from the larger unsteady vortices observed near zone 3.

#### **4.2.2 Vortex Suppression Investigation**

The vortex suppression concepts investigated under Phase I of the water tunnel tests grouped into two overall approaches. The first approach considered methods of reducing the flow anomalies produced by the vortical flows to acceptable levels. The approach focused on techniques of straightening the flow to remove the swirl. The

second approach considered methods of preventing the vortices from forming in the first place. This approach investigated techniques of modifying the flow field in the vicinity of the nozzle inlet to thwart the mechanisms leading to vortex formation. These techniques focused on the flow field near the vortex attachment point upstream of the nozzle inlet. They proceeded on the supposition that eliminating the vortex attachment point would eliminate the vortex due to the well-known principle that a vortex cannot begin or end in space, but must extend to infinity or to some attachment point on a boundary.

The first approach to addressing the vortex problem applied the various flow straightening devices to reducing the flow anomalies. The experiments used the variable-area nozzle, the nozzle containing the largest and most persistent vortices. The flow straightening devices included the screens, vanes, and honeycombs.

Figure 62a shows the zone 3 results obtained with one layer of the screen installed at the nozzle inlet plane. Figure 52 should be consulted as a baseline for comparison. The screen appeared to reduce the size and intensity of the vortex as evidenced by a reduction in the diameter of the helical streakline pattern and a reduction in the number of turns per unit length in the helix. The injected dye spread and assumed a fan shape that delineated the vortex as shown in the photograph.

The addition of the second layer of screen yielded the result shown in Fig. 62b. The photograph still shows the vortex with the helical pattern and the fanning of the dye. Thus, neither of the screen configurations appeared to hold promise for reducing the swirl to acceptable levels.

Following the screen tests, the experiments proceeded to the vertical turning vane grid, installed at the nozzle inlet. Results obtained with the vertical vane assembly installed appear in Fig. 63. The vanes appeared to reposition the vortex slightly closer to the sidewall. The vortex may also have been slightly smaller in diameter. However, the apparent reduction in size may have reflected the scatter in the water flow results.

Overall, the vertical vane grid offered little evidence of flow quality improvement.

The honeycomb section provided another method of straightening the swirling flow. Results obtained with the honeycomb mounted at the nozzle inlet appear in Fig. 64. Figure 64a shows results obtained with the honeycomb set parallel to the nozzle inlet plane. The honeycomb did little more than shift the vortex upward slightly. A subsequent experiment inclined the honeycomb section to align the cells with the vortex core. As shown in Fig. 64b, the realignment significantly altered the result. The zone 3 vortex was substantially reduced in size and strength. The limited experiments did not explore variations in honeycomb cell size, relative to the vortices, or the cell length to height ratio. The relative dimensions of the honeycomb and the vortices are known to influence the honeycomb effectiveness in removing flow swirl. Overall, the results suggested that the honeycomb offers some potential for reducing the secondary flows. However, additional experiments would be required to enable selection of the honeycomb design parameters.

The grid or cascade of horizontal turning vanes provided a means of exploring the possibility of improving the flow by pre-turning the approaching stream. The experiments included two cascade positions, analogous to the honeycomb grid positions.

Figure 65a presents the results obtained with the grid mounted parallel to the nozzle inlet plane. Although the size of the zone 3 vortex appeared to be slightly reduced, excessive vorticity remained. Moving the grid to the inclined position produced the streaklines shown in Fig. 65b, offering no improvement.

The water tunnel Phase I tests also employed the second approach to suppressing the vortices. In particular, the experiments used a nozzle inlet ramp to modify the flow field in the vicinity of the nozzle inlet and the vortex attachment point. The idea of the nozzle inlet ramp evolved during observation of the vortex attachment to the plenum floor. Varying the dye injection point upstream of the nozzle inlet clearly showed the existence of a stagnation point, reverse flows, and complex interactions between fluid dynamic interactions between the nozzle contraction section and the plenum floor. The flow experienced an abrupt direction change as it encountered the stagnation region. These observations prompted the idea of using a fairing or ramp to modify the flow and achieve two effects: (1) to gradually turn the flow into the nozzle and avoid the stagnation region entirely and (2) to eliminate the vortex attachment point. Without an attachment point, the vortex would be unable to maintain its existence.

The initial results of the ramp experiments appear in Fig. 66 for zone 3. Originally, the test apparatus included only the ramp designated as ramp #1. Figure 66a shows the results obtained with ramp #1 installed. The ramp virtually eliminated the large vortices from zones 1 and 3. The streaklines followed the nozzle wall contour with no evidence of secondary flows. The only remaining swirl consisted of the very small vortices embedded in the viscous corner flows. As described previously, the small corner

vortices existed in the four corner boundary layers and were not considered to be a concern in the present work.

The spectacular flow improvement achieved using the ramp #1 configuration prompted the ramp geometry parametric investigation using configurations #2 - #5. Ramp configuration #2 intersected the lower wall closer to the leading edge and used a contoured shape to match the nozzle wall slope at the intersection point. Figure 66b illustrates the results obtained with ramp #2 installed. Although the ramp resulted in a large reduction in the zone 3 vorticity, it did not completely eliminate the vortex as in the case of ramp #1.

Ramp configuration 3 moved the nozzle wall intersection point downstream of the ramp #1 position. The configuration used contouring to match the nozzle wall slope at the intersection point. The test results appear in Fig. 66c. As in the case of ramp #1, the ramp completely eliminated the zone 1 and zone 3 vortices.

Ramp configuration 4 intersected the lower nozzle wall at the same station as ramp #1. However, unlike ramp 1, ramp 4 used a straight contour and accepted a slope mismatch at the nozzle wall intersection point. The potential for a simple low-cost ramp design motivated the ramp 4 tests. Figure 66d illustrates the flow field produced with ramp 4 installed. The ramp performed essentially the same as ramp 1 in preventing vortex formation. The result lead to the conclusion that, with respect to vortex suppression, ramp effectiveness does not demand a tangency condition at the intersection point. Therefore, a simple straight ramp design may be viable for the free-jet nozzle application. However, more detailed flow-field measurements would be required to

ascertain the effect of the slope mismatch on the flow quality that remains after removal of the vortex.

Ramp configuration 5 provided the final Phase I perturbation in ramp geometry. Ramp 5 intersected the lower nozzle wall at the same station as ramp 2. However, ramp 5 also used a straight contour and permitted a slope mismatch at the tangency point. The test results, shown in Fig. 66e, qualitatively agreed with those obtained for the ramp 2 installation. Specifically, the ramp reduced but did not eliminate the vortex pair. This result reinforced the conclusion that ramp performance, relative to vortex elimination, depended more on the size of the ramp (extent of stagnation zone and nozzle wall coverage) than on the contour or tangency condition.

Subsequent to the variable-area nozzle tests, the ramp concept was applied to the unsteady vortices observed in the generic nozzles. The initial tests used the 2-D SYM nozzle with settings corresponding to  $PITCH = 30$  deg and  $ZI = 0.5$  in. The results demonstrated a flow field devoid of vortices as shown in Fig. 67. Figures 67a-c include photographs of streaklines through zones 1-3, respectively.

The second set of tests applying the ramp to generic nozzles employed the short AXI nozzle. Nozzle settings included  $PITCH = 30$  deg and  $ZI = 1.4$  in. Results with AXI ramp 1 installed appear in Fig. 68. The photographs indicated that the nozzle flow remained mostly free of vortices. However, dye trace behavior suggested that a small unsteady vortex may have intermittently formed near the bottom of the nozzle. In addition, the exposed ramp edges, upstream of the nozzle inlet, produced vortices that closely followed each side of the nozzle.



Figure 69 provides results obtained with AXI ramp 2 installed on the short AXI nozzle. The tests included five variations of the AXI ramp 2 installation. The first AXI ramp 2 installation, designated configuration 1, included a seal between the ramp surface and the nozzle wall. Photographs of several streaklines appear in Fig. 69a. The test results were comparable to the AXI ramp 1 results. Figure 69b illustrates several streaklines observed with the second AXI ramp 2 installation, designated as configuration 2. The results also approximated the AXI ramp 1 findings.

The third AXI ramp 2 installation, designated as configuration 3, involved a shift in ramp position to produce a gap between the ramp trailing edge and the nozzle wall. The large gap permitted small unsteady vortices to form in the nozzle as shown in Fig. 69c. The vortices occupied the same region near the bottom of the nozzle as in the tests with the ramp absent.

Raising the ramp trailing edge developed configuration 4 of the AXI ramp 2 installation. As evident in Fig. 69d, the configuration failed to improve the performance and the vortices persisted.

Setting configuration 5 of the AXI ramp 2 installation entailed reducing the axial gap and raising the ramp trailing edge to the high position. As shown in Figs. 69e, reducing the gap reduced the vortices to the levels experienced with AXI ramps 1 and 2 in configurations 1-3.

The vortex suppression experiments concluded with tests of the 2-D high alpha nozzle. The experiments started with the nozzle set at  $PITCH = 30$  deg and  $ZI = 0.6$  in. Strong reverse flow underneath the nozzle lower wall characterized the flow on the

bottom of the nozzle. As the flow rounded the leading edge to enter the nozzle, unsteady conditions developed in the conditions along the lower nozzle wall. The addition of a 1/16 in. radius lip to the lower wall improved the flow. Photographs of the streaklines appear in Figs. 70a-c for zones 1-3, respectively. The streaklines displayed no evidence of vortices, although some unsteadiness remained. The addition of the lower wall extension, at the nozzle inlet, produced an even more favorable result. Figures 70d-f illustrates the flow characteristics in zones 1-3 with the extension attached. The flow remained steady with evidence of some sidewash along the lower nozzle wall. However, the flow visualization failed to disclose the presence of vortices.

Figure 71 shows results obtained with the 2-D high alpha nozzle set to PITCH = 45 deg and ZI = 0.6 in. Parts a-c furnish photographs of the streaklines through zones 1-3, respectively. Although the tests directly disclosed no vortices, dye behavior during lateral traverses along the lower wall suggested that a small vortex may have formed intermittently in zone 3.

#### **4.2.3 Water Tunnel Phase I Summary**

Phase I of the water tunnel investigation was completed in May 1984. The following points summarize the results:

1. Water flow simulations provided a valid characterization of the free-jet nozzle vortices.

2. The generic nozzle flows contained vortices that were less steady and more centrally located than those in the variable-area nozzle vortices.
3. Nozzle inlet vortices formed in nozzles with square and circular cross sections.
4. The short axisymmetric nozzle contained vortices that were larger than either of the 2-D nozzles.
5. The 2-D SYM nozzle contained larger vortices than the 2-D ASY nozzle at  $ZI = 0.6$  in. and 1.4 in.
6. The vortices generally increased in strength as  $ZI/H$  or  $ZI/D$  decreased. However, the short AXI nozzle did not display this trend for  $ZI = 0.6$  and 1.4 in.
7. The effect of nozzle pitch angle on vortex intensity decreased between  $PITCH = 30$  deg and 45 deg.
8. Nozzle contraction ratio exerted little influence on the formation of vortices in the axisymmetric nozzles.
9. With the exception of the nozzle corner vortices, each vortex attached to the plenum floor in the complex flow field immediately upstream of the nozzle inlet.
10. Properly oriented flow straightening devices, such as honeycombs, reduced the vorticity.
11. Nozzle inlet screens failed to remove the vortices.

12. Nozzle inlet ramps modified the complex nozzle inlet flow field and prevented vortex formation.
13. Straight and contoured ramps effectively prevented vortex formation.
14. Ramp effectiveness decayed as the platform size decreased.
15. Vortex elimination did not require ramp trailing edge tangency with the nozzle wall.
16. Ramp effectiveness did not require a seal between the ramp trailing edge and the nozzle wall. Moderate gaps, on the order of 5 percent nozzle diameter, allowed acceptable ramp performance.
17. At high pitch angles, modified free-jet nozzle wall contours improved flow quality.

The results suggested that a properly designed honeycomb would remove the nozzle vortices. However, solid structures in the flow create nozzle blockage and present the possibility of mechanical failure and a FOD hazard for the test article. As a result, Phase I of the water tunnel experiments culminated in the selection of the ramp as the most attractive flow quality improvement technique of those tested. The ramp approach was selected for verification in the R2A2 Phase II tests.

### **4.3 R2A2 PHASE II**

Although the water tunnel had demonstrated a faithful simulation of the airflow findings, the investment risks involved in adopting the ramp for the ASTF nozzle

prompted a sub-scale validation of the concept. Phase II of the R2A2 experiments focused on verifying the water tunnel findings in tests using airflow as the medium. The experiments encompassed four ramp configurations derived during the water tunnel Phase I experiments. As described in Section 2.2.1.1, the ramps were designated as 30-deg straight, 30-deg contoured, 50-deg straight, and 50-deg contoured.

The presentation of the ramp performance verification results uses the same format as the presentation of the R2A2 Phase I results. Thus, comparisons with results presented in Section 4.1 may be used to examine the net effects of the ramps.

Figure 72 shows the Mach number distributions measured at  $MACH = 0.6$  for each of the ramp configurations. In the bottom half of the nozzle, the Mach number distributions measured by the probe 2-4 traverses displayed little difference between the straight and contoured ramp configurations. However, the probe 1 and 5 traverses, with the straight ramp configurations, revealed regions of low Mach number flow not observed in the contoured ramp tests. Both the  $PITCH = 30$  deg and the  $PITCH = 50$  deg results displayed this characteristic. However, the Mach number variation remained within the  $\pm 0.05$  target. In the upper half of the nozzle, measurements showed regions of low Mach number near the upper wall, presumably the result of nearby upper wall separations. At  $PITCH = 30$  deg, the low-Mach number regions appeared only in the upper corners (probes 1 and 5). At  $PITCH = 50$  deg, the probe 2 measurements also detected low Mach number flow. In each case, the 50-deg pitch yielded the largest deviation in Mach number. Furthermore, at  $PITCH = 50$  deg, the Mach number drop slightly exceeded the target in the probe 1 and probe 5 positions. Although the survey

resolution precluded detailing the extent of the low Mach number region, the results suggest that the nozzle test rhombus, the region delivering the flow quality targets, may be smaller than the design region defined by the nozzle cross section dimensions with boundary layer offsets.

Figure 73 presents the measured flow angle distributions for each of the ramp configurations. Results obtained at PITCH = 30 deg and MACH = 0.6 with the contoured ramp installed appear in Fig. 73a. The plot shows that the presence of the ramp completely eliminated the large vortices described in Section 4.1. In fact, the results displayed a more generalized secondary flow pattern, in the lower half of the nozzle, with rotation in the opposite direction of the original vortices. The secondary flow included downwash at the sidewalls that turned inward near the lower wall and then washed upward in the center. The flow patterns measured along the probe 2 and 4 traverses suggested that a sidewash in the adjoining quadrant supplied the sidewall downwash. Although the flow angles associated with the secondary flow patterns were much smaller than those associated with the original vortices, they exceeded the  $\pm 30$ -deg limit at four points (Fig. 73a).

Flow angle measurements acquired at PITCH = 30 deg and MACH = 0.9 with the 30-deg contoured ramp installed appear in Fig. 73b. At this higher Mach number condition, the basic features measured at MACH = 0.6 persisted. However, the higher Mach number case displayed a small reduction in the flow angle magnitudes. The survey did not include flow angle measurements at the RAKE = -5 in. position.

Figure 74 provides the flow angle measurements obtained at PITCH = 30 deg and MACH = 0.6 with the 30-deg straight ramp installed. As in the previous cases, the flow-field surveys showed the absence of the large vortex pair measured during the R2A2 Phase I tests. However, the condition did not preserve the flow symmetry previously observed between the lower left and lower right quadrants. Large flow angles measured at two positions in the lower left quadrant were not complemented by large angles in the lower right quadrant. The flow angle pattern suggested that a vortex of unknown origin may have resided along the left sidewall. A defect in the ramp installation may have been responsible for the flow anomaly. The right quadrant measurements might lead to the conclusion that the straight ramp would prove incapable of preventing formation of the main vortex pair.

The measured flow angle distribution at PITCH = 50 deg with the 50-deg contoured ramp installed appears in Fig. 75. Figure 75a shows the results acquired at MACH = 0.6. The main flow pattern observed at PITCH = 30 deg with the 30-deg contoured ramp installed also appeared at PITCH = 50 deg. All measured flow angles remained within the allowable variation of  $\pm 5$  deg. Increasing the Mach number to 0.9 yielded only a slight reduction in the magnitudes of the flow angles (Fig. 75b). The secondary flow pattern remained unchanged.

Flow angle measurements obtained at PITCH = 50 deg and MACH = 0.6 with the straight ramp installed appear in Fig. 76. As in the PITCH = 30 deg case, substitution of the straight ramp for the contoured ramp somewhat degraded the flow quality. However,

the PITCH = 50 deg case preserved the symmetry between the two lower nozzle quadrants.

Phase II of the R2A2 flow quality investigation was completed in October 1984.

The results may be summarized in the following observations:

1. Nozzle inlet ramps effectively eliminated the large pair of vortices characteristic of the variable-area nozzle flow field.
2. The contoured ramps furnished flow quality superior to the straight ramps.
3. Secondary flow with rotation in the opposite direction of the original vortices remained after the ramps removed the primary vortex pair. However, the remaining flow angles were much smaller than those that accompanied the original vortices, and generally within the target limits.

The results measured during the R2A2 Phase II tests verified the chosen vortex suppression technique identified during the water tunnel Phase I investigation and provided the impetus to proceed to the water tunnel Phase II tests.

## **4.4 WATER TUNNEL PHASE II**

### **4.4.1 General**

Phase II of the water tunnel investigation evolved during the development of the ASTF free-jet nozzle concept. The experiments were arranged to supply results to the development effort and to culminate in a test of the selected ASTF nozzle configuration.



Thus, the early portion of the test phase used the variable-area nozzle installation to accomplish two tasks: (1) to explore additional vortex prevention techniques, i.e. blowing and boundary layer suction and (2) to refine the nozzle ramp design criteria. The first task explored a number of potential techniques that deserved consideration before a final decision to proceed with the ramp concept. The second task provided information to aid in adapting the ramp concept to the ASTF nozzle concept. The latter portion of this test phase then proceeded to the ASTF nozzle configuration to provide a qualitative checkout prior to investing in the air-flow tests.

#### **4.4.2 Experiments with Blowing**

The blowing experiments focused on the piccolo tube concept. The initial piccolo tube installation used a height defined by  $ZT = 0.75$  in. and a width setting of 2.375 in. The selected width positioned the piccolo tube vortices, induced by the jets, at the nozzle sidewalls. Prior to activating the tube, the nozzle vortices were photographed to record any installation effects. As shown in Fig. 77a, the presence of the tube did not effect the formation of the vortices. Figure 77b provides a sample of the nozzle flow with the blowing activated. The experiment used a flow rate of 1.5 gph, approximately 4 percent of the nozzle flow at the nominal 4.4 in./sec exit velocity. The most notable effect of the blowing was an increase in nozzle flow turbulence. Although the vorticity seemed to be reduced and repositioned, fluctuating streaklines with constantly changing patterns replaced the steady helical streaklines. A series of photographs helped record the time

variation in streakline pattern. The photograph appearing in Fig. 77b typifies the vortex streakline pattern.

A second piccolo tube test used a width setting corresponding to  $WT = 0.9$  in. to move the piccolo tube vortices laterally toward the center of the nozzle. Activated with a blowing rate of 1 gph, 2.5 percent of the nozzle flow rate, the tube slightly reduced but failed to eliminate the nozzle vortices (Fig. 78). Again, the slight flow quality improvement came at the cost of significantly increased flow turbulence. Figure 78b includes two photographs of the contraction section taken through the stilling chamber access hatch. The photographs clearly show the left-hand vortex induced by the jets. The direction of rotation, opposing the nozzle vortex rotation, can be deduced from the photographs. The results indicated that the piccolo tube vortex was improperly positioned to cancel the forming nozzle vortex.

Figures 79a and 79b provide piccolo tube results obtained at  $ZT = 0.75$  in. with  $WT = 1.75$  in. and 1.875 in., respectively. Although the configuration positioned the piccolo tube vortices closer to the sidewalls, the nozzle vortices persisted. As in the previous cases, the blowing produced unsteady flow characteristics. At  $ZT = 0.75$  in., the unsteady streakline patterns masked the effect of  $WT$  variation.

A number of tests also explored the effect of  $ZT$  on piccolo tube effectiveness. These included  $ZT$  settings of 1.1875, 1.75, and 2.375 in. Figures 80a and 80b show the resulting nozzle flow characteristics for  $WT = 1.75$  and 1.875 in., respectively. At a blowing rate of 1.5 gph, the flow appeared to be steadier than in the case of the previous  $ZT$  setting of 0.75 in. However, the piccolo tube failed to eliminate the vortex. Increases

in blowing only elevated the level of turbulence as evidenced by fluctuations in the streakline patterns.

The piccolo tube experiments clearly showed the effectiveness of the piccolo tube to be very sensitive to the relative locations of vortex induced by the blowing and the free-jet nozzle vortex to be cancelled. Furthermore, the introduction of flow turbulence presented an objectionable effect that contributed to the elimination of the piccolo tube from further consideration.

#### **4.4.3 Experiments with Boundary Layer Suction**

The suction experiments entailed activating the various suction regions or combinations of suction regions to investigate the effect of strategically applied boundary layer control on vortex formation. Photographic recording of the nozzle flow characteristics with boundary layer suction concentrated on zone 1 corresponding to the side of the nozzle containing the boundary layer control.

Results acquired with suction applied only to region 1 appear in Figs. 81a and 81b for suction rates of 20 gph (5.1 percent of nozzle flow) and 33 gph (8.4 percent of nozzle flow), respectively. The latter represented the maximum suction rate available in region 1. Although shifted laterally in position, the free-jet nozzle vortex persisted. The shift in position likely represented simply the sidewash induced by effectively adding a sink at the nozzle sidewall.

Unlike region 1, suction in region 2 profoundly affected the formation of the nozzle vortex. Observation of those effects motivated detailed tests of region 2 suction with the suction rate varied from 6 gph to 18 gph in increments of 2 gph. Figure 82 presents selected results obtained over the suction rate range. At suction rates of 6 to 8 gph (1.5 to 2 percent of nozzle flow rate), the vortex migrated closer to the sidewall and reduced in size. The result at 8 gph appears in Figs. 82a and 82b. Figure 82a includes a photograph with dye injected in the position that traced the nozzle vortex with suction off. Increasing the suction to 8 gph caused the vortex to completely disappear from view. Figure 82b includes a photograph taken with the dye injection point shifted laterally toward the sidewall. The photograph shows that a vortex, smaller than the original, remained at a position roughly half way between the original vortex and the nozzle sidewall.

Figures 82c and 82d, analogous to Figs. 82a and 82b, provide results with the suction rate increased to 12 gph (3 percent of nozzle flow rate). The results presented in Fig. 82c displayed no sign of a vortex in the original location. Figure 82d illustrates the presence of a vortex at the sidewall. With respect to the vortex observed at the 8 gph condition, the vortex was smaller and closer to the sidewall.

Results obtained at a suction rate of 16 gph (4.1 percent of the nozzle flow rate) appear in Figs. 82e and 82f for the original and perturbed dye injection points, respectively. Neither view revealed any sign of the vortex.

The dramatic effect of the region 2 suction on the vortex formation naturally motivated some quantification of the suction flow rates needed to provide adequate flow

quality. The minimum required suction rate proved difficult to establish due to the corner vortex. Relatively low suction rates, approximately 1.5 percent of the nozzle flow rate, dramatically improved the core flow despite leaving a remnant of the original vortex near the sidewall. At 10-12 gph (2.5 percent - 3 percent of nozzle flow rate), a small vortex still presented itself very close to the sidewall. However, the adjacent core flow became completely devoid of vortices. Further increases in suction rate simply continued to attenuate the sidewall vortex until reaching 4 percent of nozzle flow rate. At that point, the vortex became indistinguishable from the corner boundary layer vortex. The corner boundary layer vortices have been deemed acceptable on the basis that they are outside the defined nozzle test rhombus (that excludes the wall and corner boundary layers as well as the free shear layers downstream of the nozzle exit) and would bypass the test article by design. At flow rates below 4 percent of nozzle flow, some degree of sidewall vorticity would need to be accepted on the same basis. However, one must remember that although the experiments verified the water tunnel simulations in a qualitative sense, they did not address validation of quantitative results. Thus, a detailed quantification of the required suction rates would demand airflow experiments.

The results obtained with suction applied at region 3 appear in Fig. 83. The system permitted region 3 suction rates ranging up to 30 gph or 10 percent of the nozzle flow rate. Suction rates between 6 gph (1.5 percent of nozzle flow rate) and 16 gph (4.1 percent of nozzle flow rate) produced only a minimal reduction in vorticity. Figure 83a provides representative results at a suction rate of 14 gph. As the suction rate increased

from 16 gph to 39 gph, additional reductions in vortex size occurred. However, the vortex persisted even at the maximum suction rate of 39 gph (Fig. 83b).

Suction applied at region 4 removed some of the vortex flow leaving a smaller vortex in the nozzle flow field. Figures 84a and 84b shows results for suction rates of 20 gph (5.1 percent of nozzle flow) and 35 gph (8.9 percent of nozzle flow), respectively. At 35 gph, the maximum available flow rate, the vortex persisted although reduced in size. The helpful lateral displacement of the vortex location induced in the previous experiments did not occur.

The suction results, in particular the region 2 suction results, demonstrated that strategically applied boundary layer control offered a feasible vortex elimination method. The region 2 experiments were dramatized by the ability to stop or restart the vortices, at will, simply by cracking a valve to activate the suction. However, consideration of the technique for the ASTF free-jet nozzle introduced the prospects of a complex full-scale boundary layer suction system, substantial operational costs for pumping the mass flow required, and significant maintenance costs associated with porous walls. To avoid these issues, the development proceeded with the ramp concept selection.

#### **4.4.4 Experiments with Baffles**

The success of the ramp approach to eliminating nozzle vortex formation, as demonstrated in the water tunnel phase I tests and the R2A2 phase II tests, had clearly shown the effectiveness of modifying the flow in the vicinity of the nozzle inlet plane. In

particular, the flow in the region near the bottom nozzle wall and the vortex attachment point on the plenum floor dominated the vortex formation and sustenance. The baffle experiments explored alternative means to influence the flow in that critical region. The tests included both the horizontal and vertical baffle configurations.

The experiments used the vertical baffles in an attempt to prevent flow from migrating down the side of the plenum and entering the stagnation region beneath the nozzle. The results, shown in Fig. 85a, revealed the presence of intermittent vortices. The vortices clearly attached well upstream of the nozzle inlet plane. Furthermore, they were unsteady suggesting that turbulence or perhaps the cavity beneath the nozzle was a factor. However, the baffle did appear to reduce the size of the vortices. Removal of the baffle verified this fact by yielding larger steady vortices.

The horizontal baffles offered another approach to modifying the flow entering the stagnation region near the nozzle inlet. The result, shown in Fig. 85b, indicated that a vortex persisted near the bottom center of the nozzle.

The baffle experiments led to the conclusion that the devices did not offer a viable means of eliminating the nozzle vortices.

#### **4.4.5 Ramp Criteria Refinement**

The experiments included tests of additional ramp configurations to aid in developing a ramp configuration for the ASTF free-jet nozzle. The experiments used ramp configurations 21 and 22.

Figure 86 illustrates the zone 3 flow characteristics with ramp 21 installed. In position 1, shown in Fig. 86a, the ramp eliminated the large nozzle vortex. However, shifting the dye injection point laterally revealed evidence of a small vortex very close to the side wall (Fig. 86b). Ramp configuration 21 installed in position 2 completely eliminated the vortex as shown in Fig. 86c.

Figure 87 provides the results obtained with ramp configuration 22 installed. Although the ramp appeared to eliminate the nozzle vortex, the configuration induced turbulence in zone 3. The turbulence manifested itself in large fluctuations in the path followed by the dye. Figure 87 contains two photographs illustrating the turbulent nature of the flow. The turbulence was presumed to be a result of separation on the sharp ramp leading edge located in the complex flow field inside the nozzle contraction section.

The ramp refinement experiments provided qualitative information and insights that would be subsequently used to apply the ramp method to an ASTF free-jet nozzle concept.

#### **4.4.6 ASTF Nozzle Concept Evaluation**

The development of a free-jet nozzle configuration to recommend for application in ASTF C-2 integrated results of the nozzle ramp experiments with the specified ASTF free-jet nozzle requirements. The free-jet nozzle requirements with respect to the orientation angle envelope and the nozzle exit cross section had profound effects on the nozzle design. Satisfaction of these requirements with a nozzle that would function under



the ASTF plenum size constraints demanded a number of design tradeoffs between features conducive to high flow quality and features needed to accommodate fighter-size inlet systems and flight envelopes. The former drove parameters such as nozzle length-to-height ratio and contraction ratio upward. The latter drove the same parameters downward. Appendix D describes the evolution of the nozzle design and illustrates the tradeoffs needed to satisfy the various constraints. The results of the tradeoffs yielded a minimum length nozzle configuration with a rectangular exit cross section using dimensions tailored according to typical fighter aircraft configurations. The nozzle configuration shown in the appendix became the subject of the water tunnel ASTF nozzle concept evaluation under Phase II.

The initial ASTF nozzle model experiment investigated the flow characteristics furnished without a ramp. The experiment served as a baseline for the ramp performance evaluation since the nozzle geometry deviated from the previously tested generic nozzles. To facilitate the experiment, the nozzle was mounted inverted, with  $ZI = 1.6$  in., to position the smooth upper wall contraction section at the plenum chamber floor. This mounting allowed an honest assessment of the performance that could be expected with a simple fixed-geometry nozzle. The installation located the flat nozzle wall and ramp hinge at the top, away from the region of interest. The results, presented in Fig. 88, show that a very large nozzle vortex formed in zone 2.

The nozzle was installed in the upright design position for experiments involving the ramp. Nozzle yaw angle, YAW, remained at 0 deg throughout the experiments. Figure 89 shows results obtained at  $PITCH = 45$  deg and  $RMP = 20$  deg. Figures 89a-c

illustrate the streakline traces through zones 1-3, respectively. All three zones appeared to be devoid of vortices. However, during lateral traverses of the dye injection point across zones 1 – 3, the dye occasionally traced streaklines slightly inclined with respect to the lower nozzle wall. The deflection occurred near zone 2. The slightly anomalous flow may have been caused by small fluctuating vortices that eluded direct observation. Figure 89d provides a photograph, in top view, of the flow approaching the ramp. The photograph shows the streaklines to be nearly perpendicular to the ramp leading edge at the intersection points. The perpendicularity likely helped avoid the formation of ramp leading edge vortices.

The next set of experiments consisted of a repeat test with the ramp extension installed. The flow fields observed in zones 1-3 appear in Figs. 90a-c, respectively. The photographs showed the results to be essentially equivalent to the basic ramp results. This equivalence in the qualitative results suggested that the basic ramp provided a sufficient length.

Figure 91 provides results obtained at  $PITCH = 30$  deg and  $ZI = 2.25$  in. for two ramp inclination angles. Views of zones 1-3, with the ramp set to  $RMP = -10$  deg, appear in Figs. 91a-c, respectively. The results showed the absence of vortices in zones 1 and 3. However, as in the  $PITCH = 45$  deg case, the straight streaklines displayed some angularity near zone 2 attributed to the possible existence of small vortices. As before, the presence of such vortices was not directly observed. Changing the ramp angle to  $+20$  deg yielded the same qualitative results as shown in Figs. 91d and 91e for zones 1 and 3, respectively.

The Phase II ASTF nozzle model experiments concluded with a test of the PITCH = -10 deg condition. Since the water-tunnel plenum deviated slightly from the ASTF C-2 configuration primarily at the top, the tests used the nozzle mounted in the inverted position. Pitched downward 10 deg, the nozzle cleared the plenum floor with  $ZI = 1.05$  in. Figure 92 presents the results. Small, unsteady vortices appeared near the upper nozzle wall (now located at the bottom of the plenum). Although smaller than the vortices previously encountered with the nozzle inverted, the vortices were large enough to observe directly.

#### **4.4.7 Summary and Conclusion**

Phase II of the water tunnel investigation concluded in February 1985. The following list summarizes the results:

1. The piccolo tube reduced but failed to eliminate the variable-area free-jet nozzle vortices. Piccolo tube control and nozzle flow turbulence levels presented severe problems.
2. Boundary layer suction in region 2 effectively prevented formation of vortices in the variable-area nozzle.
3. Boundary layer suction in regions 1, 3, and 4 remained ineffective in preventing vortices from forming in the variable-area nozzle.

4. A nozzle inlet ramp with the leading edge positioned above the stilling chamber floor effectively prevented vortex formation in the variable-area nozzle.
5. The ASTF nozzle concept provided adequate flow quality, with respect to vortical flows, at high pitch angles and zero yaw. The ASTF nozzle ramp concept provided an effective means of vortex suppression.
6. The ASTF nozzle concept yielded small vortices in the top region at PITCH = -10 deg.

The results summarized in item 4 substantiated the leading edge ramp concept that evolved during the experiments.

Test Phase II concluded with a decision to proceed with the ASTF nozzle concept in the R2A2 experiments. Flow-field measurements would be required to quantify nozzle performance with respect to flow quality and ensure achievement of the specified requirements.

#### **4.5 R2A2 PHASE III**

The R2A2 Phase III experiments provided quantification to the ASTF nozzle model flow characteristics qualitatively observed in the water tunnel. With respect to ASTF, the R2A2 experiments replicated the geometry and Mach number. Although the measurements included the compressibility effects neglected in the water tunnel, they were subject to mismatches between Reynolds number between R2A2 and ASTF. The

presentation of the air flow results appearing in this section adopts the format used in the R2A2 Phase I and Phase II presentations (Sections 4.1 and 4.3, respectively).

Flow-field measurements obtained with the R2A2 stilling chamber in the unmodified configuration, without extension, appear in Figs. 93-96. Each test used the Ramp A1 configuration. Figure 93 provides the Mach number distributions corresponding to the following three cases: (1) PITCH = 0 deg with RMP = -10 deg, (2) PITCH = 30 deg with RMP = -10 deg, and (3) PITCH = 45 deg with RMP = 20 deg. Figure 93a provides the absolute Mach number measurements. Figure 93b presents plots of local Mach number deviation from nozzle exit average. The plots include tabulations of average Mach number, maximum deviation, and estimated standard deviation. With the biases removed, the plots display the spatial variations in Mach number. The plots show the Mach number to be uniform with the only notable deviations occurring near the sidewall at PITCH = 45 deg. The measurements exceeded the allowable Mach number deviation at one point; the point occupied by probe 5 with the rake in the -2 in. position. However, one must note that two points, those occupied by probe 5 in the -4.0- and -5.5- in. positions encountered flow angles outside the probe calibration range. As a result, the mean and deviation calculations excluded those points and that region of the flow, even though the Mach number measurements met the flow quality criteria.

Measured flow angles at PITCH = 0 deg and ramp A1 inclined at -10 deg appear in Fig. 94. The absolute measurements, shown in Fig. 94a, displayed a downward bias of 1.04 deg. This bias did not represent an ALPL variation and could easily be removed by adjusting nozzle pitch angle. Likewise, any yaw bias could be removed through suitable

adjustments in nozzle yaw angle. Figure 94b shows a plot of flow angle deviations from the mean. Plotting the deviations effectively removed the pitch angle and yaw angle biases. The figure includes the estimated standard and maximum deviations from the mean flow angle. The resulting deviations exceeded target limits in flow angle at five points in ALPL and three points in BETL. The points that violated the limits generally resided across the bottom of the nozzle or along the sidewall.

Figure 95 presents the measured flow angle distribution at PITCH = 30 deg with ramp A1 inclined at -10 deg. The figure provides plots of the measured flow angles (Fig. 95a), a plot of the flow angle deviations (Fig. 95b) as well as tabulations of the maximum measured deviations and the estimated standard deviation. One point near the bottom left corner of the nozzle exceeded the target ALPL deviation limit of  $\pm 3$  deg or 10 percent of the nozzle pitch angle. One point in the lower right quadrant of the nozzle exceeded the BETL deviation limit. The point resided in a region displaying a curious sidewash angle.

Flow angle measurements acquired at PITCH = 45 deg with ramp A1 set at RMP = +20 deg appear in Fig. 96. The lower right nozzle quadrant contained a region displaying very large flow angles suggesting the presence of a strong counterclockwise vortex. Two points along the sidewalls experienced flow angles that exceeded the probe calibration range. As a result of the uncertainty introduced with the over-range measurements, the mean and deviation calculations excluded the two points. With the exception of three points in or adjacent to the lower right quadrant, the flow field achieved the target flow quality.

The flow anomalies measured at PITCH = 45 deg indicated that the nozzle flow quality would fall short of the goals over a substantial portion of the nozzle area. This observation prompted a review of the test installation in search of features that might contribute to the anomalies. The review identified the following three possibilities: (1) inadequate nozzle design, (2) inadequate ramp design, and (3) upstream disturbances in the plenum chamber flow. A thorough reexamination of each preceded any further testing.

As described in Appendix D, the requirement to provide a free-jet test rhombus of sufficient size to enclose the inlet of a typical mixed-compression fighter aircraft while covering a large PITCH/YAW envelope dominated the nozzle design. The size and orientation envelope requirements, urging the design toward larger nozzles, was opposed by the confinement of the C-2 plenum, urging the design toward smaller nozzles. The opposing constraints imposed severe restrictions on nozzle length (and therefore length-to-height ratio) and contraction ratio. The nozzle design reevaluation revealed little opportunity to relax the design for flow quality improvement.

The investigation reexamined the ramp with the same scrutiny applied to the nozzle design. Unlike the nozzle body, the ramp planform offered the opportunity for enlargement. Furthermore, the ramp mechanical design, for the R2A2 experiments, used fabrication methods that could be readily implemented in the field. As a result, ramp configuration A2, with an enlarged planform, was fabricated to explore the possibility of ramp design inadequacies.

The reexamination then focused on the R2A2 stilling chamber configuration and the possibility that upstream disturbances may have induced the flow anomalies. As described in Section 1.2, the intensification of upstream ambient vorticity represents a known cause of vortices observed in inlets operating in the vicinity of a solid surface. Such ambient vorticity might be introduced by plenum chamber disturbances upstream of the free-jet nozzle inlet. The disturbances might result from the plenum wall boundary layer, the plenum pitot rake, and the junction of the 54-in.-diam and the 63-in.-diam plenum sections.

The junction between the two plenum sections requires further explanation. As shown in Fig. 4, the 54-in.-diam and the 63-in.-diam sections intersect at a tangency point on the bottom of the plenum chamber. Therefore, the flow along the bottom of the chamber experiences only a small step as it enters the larger diameter section. However, the step from the small diameter section to the large diameter section increases at the sides and top of the chamber. Flow along the sides encounters an abrupt reverse step and the associated separation. The fixed sidewalls of the variable-area nozzle extended upstream of the junction and fit close to the bottom of the plenum. Apparently, the flow captured by the nozzle excluded the separated flow. However, high pitch angles positioned the inlet section of the ASTF nozzle model downstream of the junction. In the absence of the fixed side walls in the ASTF nozzle configuration, the nozzle appeared to be capable of directly capturing flow from the junction separation. The rotational flow could then develop into nozzle vortices.



The opportunities for the plenum chamber configuration to introduce vorticity into the flow approaching the nozzle prompted the implementation of a number of modifications prior to continuing with the experiments. The first modification entailed the removal of the bulky pitot probe rake located immediately upstream of the nozzle. Probes located at the top of the stilling chamber replaced the rake as the source of the stagnation pressure measurements. The second modification addressed the backward-facing step produced by the junction between the 54-in.-diam plenum section and the 63-in.-diam plenum section. The addition of a 54-in.-diam extension shifted the step downstream of the nozzle inlet and yielded the plenum configuration designated as plenum configuration B (Fig. 4). Testing then resumed using both ramp configuration A1 and ramp configuration A2.

Figure 97 provides plots of the Mach number distributions for the following three cases: (1) PITCH = 30 deg with ramp configuration A2 at RMP = -10 deg, (2) PITCH = 45 deg with ramp configuration A2 at +20 deg, and (3) PITCH = 45 deg with ramp configuration 2 at RMP = +20 deg. Generally, the Mach number distributions displayed uniform flow. However, low Mach number regions existed in each bottom corner as evident in the probe 1 and probe 5 traverses. Despite the regions of depressed Mach number, all measurements remained within the  $\pm 0.05$  allowable Mach number deviation.

Flow angle measurements acquired with the plenum chamber in configuration B appear in Figs. 98-100. Figure 98 contains the results obtained at PITCH = 45 deg with ramp configuration A1 inclined to +20 deg. A relatively small downwash along the

lower right sidewall replaced the very large upwash measured with the plenum in configuration A. The large flow angles previously measured near the center of the corresponding quadrant dropped by a factor of two. However, the region in the lower left quadrant experienced some degradation in flow quality. Three points exceeded the target ALPL variation limit and two points exceeded the target BETL variation limit. These points occupied the lower 25 percent of the nozzle cross-sectional area.

Flow angles measured at PITCH = 45 deg with ramp configuration A2 set at +20 deg appear in Fig. 99. The flow quality experienced a slight improvement with two points exceeding the target  $\pm 4.5$ -deg ALPL deviation and 1 point exceeding the  $\pm 4.5$ -deg BETL deviation limit. Modest decreases in the estimated standard deviations for ALPL and BETL reflected the improved flow quality. The absolute value of the maximum ALPL deviation decreased by 3.65 deg. Similarly, the absolute value of the BETL deviation decreased by 0.91 deg.

Figure 100 contains plots of the flow angle distributions obtained at PITCH = 30 deg with ramp configuration A2 inclined at -10 deg. Although all measured deviations in BETL fell within the  $\pm 3$ -deg limits, six ALPL measurements exceeded the limits. The delinquent points resided primarily in the lower left quadrant. A degradation in flow quality over the previous PITCH = 30 deg result can be observed by comparing Figs. 100 and 95. The ALPL absolute value of the maximum deviation in ALPL and the estimated standard deviation in ALPL increased by 1.99 and 1.13 deg, respectively. The absolute value of the BETL maximum deviation decreased by 1.52 deg and the estimated standard

deviation increased slightly by 0.12 deg. Thus, the flow quality improvements obtained with ramp A2 at PITCH = 45 deg did not occur at PITCH = 30 deg.

The results suggested that the stilling chamber diameter change point influenced the PITCH = 45 deg condition more than the PITCH = 30 deg condition. This might be expected as the nozzle inlet moved upward from the plenum floor and upstream as pitch angle decreased.

The R2A2 Phase III experiments concluded in March 1985. The following items summarize the results:

1. The ASTF nozzle model generally achieved the flow quality goals over most of the exit area. However, each configuration contained some deviations exceeding the target limits.
2. At PITCH = 45 deg with the plenum in configuration 1, excessive flow angularity appeared in the lower right quadrant of the nozzle.
3. The stilling chamber was modified to remove features suspected of inducing the anomalous flow.
4. The modified stilling chamber improved the flow quality at PITCH = 45 deg.
5. Ramp configuration A2 improved the flow quality relative to ramp configuration A1 at PITCH = 45 deg.
6. Ramp configuration A2 appeared to degrade the flow quality relative to ramp configuration A1 at PITCH = 30 deg.

#### 4.6 WATER TUNNEL PHASE III

The ASTF subsonic free-jet nozzle ramp planform design assumed a two-position nozzle mount concept as described in Appendix D. However, the full-scale nozzle development ultimately adopted a single-position nozzle installation. Due to the confines of the ASTF stilling chamber, the single-position concept affected the ramp design. In particular, the concept included the selection of an intermediate spacing between the nozzle exit plane and the nozzle attitude positioning mechanism pitch center. This compromise in the spacing reduced the space available for ramp placement at the high pitch angles. As a result, the program added Phase III of the water tunnel tests to evaluate the implications of truncating the ramp planform commensurate with the available space. The ramp B configuration was used throughout the tests.

In addition to testing ramp configuration B, the water tunnel Phase III experiments explored other issues that had yet to be fully addressed in the investigation. These issues included the following: (1) the R2A2 stilling chamber design and potential influence on vortex formation, (2) the effects of yaw angle on the ASTF nozzle model flow quality, (3) the low Mach number zones near the upper nozzle wall, and (4) the sensitivity of nozzle flow quality to the ramp positioning schedule. This section briefly summarizes the findings in each of these areas.

The start of the experiments explored the suspicion that the 63-in.-diam stilling chamber section might be influencing the R2A2 ASTF nozzle model flow quality. As

described in Section 4.5, the suspicion stemmed from the concern that separated flow from the corner of the aft-facing step, the corner existing at the junction between the 54-in.-diam section and the 63-in.-diam section, could introduce the vorticity needed to form nozzle vortices. Dye injected in the vicinity of the corner did, in fact, suggest that the separation contributed to intermittent vortices in the nozzle. As a result, the water tunnel model plenum chamber was modified to configuration B prior to proceeding with the Phase III tests.

The water tunnel Phase III tests used the variable-pitch and variable-yaw nozzle attitude positioning mechanism model to support the nozzle. Table 9 summarizes results acquired during execution of the 19-point test matrix. Unsteady or intermittent vortices appeared in zones 1 and/or 3 during the majority of the tests. Figure 101 includes photographs of the zone 1-6 streakline traces obtained at PITCH = 45 deg and YAW = 0 deg. Figures 101a-f correspond to zones 1-6, respectively. Generally, each part contains a photograph of the streaklines in side view and a photograph recording the view looking upstream into the nozzle exit. Figures 101a and 101c display the zone 1 and zone 3 vortices, respectively. Straight streakline traces characterized flows in the other dye injection zones. The unsteadiness of the vortices produced difficulties in resolving the effect of nozzle pitch angle on the vortices. However, the severity of the flow anomalies appeared to decrease as the pitch angle decreased.

Figure 102 presents results obtained at a nozzle orientation corresponding to PITCH = 30 deg and YAW = 0 deg. Figure 102a-f contains photographs of streaklines through zones 1-6, respectively. The streaklines through each zone were recorded in side

view and in a view looking upstream into the nozzle exit. The photographs show streaklines generally devoid of vortices, although a small vortex was intermittently observed in zone 3 (Table 9).

The water tunnel allowed the effect of yaw on the nozzle flow characteristics to be easily observed. In terms of sign convention, positive yaw translated the zone 1 section of the nozzle toward the adjacent plenum wall and zone 3 away from the opposing plenum wall. As shown in Table 9, the zone 1 vortices, observed at zero yaw, generally did not appear at the negative yaw angles. However, the zone 3 vortices increased in severity as the region had shifted toward the plenum wall.

Streakline traces photographed at  $PITCH = 45$  deg with  $YAW = -5$  deg and  $-10$  deg appear in Fig. 103. Photographs of streaklines through zones 1-6 appear in Figs. 103a-f, respectively. The fluctuating vortices of zone 3 appeared to extend to zone 6; however, no vortices originated in the latter zone.

Figure 104 illustrates the zone 1 and zone 3 results obtained at  $YAW = -10$  deg with pitch angles of 30 deg and 10 deg. Photographs of streaklines through zones 1 and 3 with  $PITCH = 30$  deg appear in Figs. 104a and 104b, respectively. The figures provide two views of each zone. The results at  $PITCH = 30$  deg with yaw were comparable to those obtained at  $PITCH = 45$  deg. The  $PITCH = -10$  deg case displayed a reduction in the severity of the zone 3 vortices (Figs. 104c and 104d). The reduction likely related to the reduction in the distance between zone 3 and the plenum wall at the reduced pitch.

The airflow experiments discussed in Section 4.3 included the measurement of low Mach number flow near the nozzle upper wall. As a result, the water tunnel Phase

III experiments included observations of the dye paths along the upper nozzle wall to identify any flow separations. Streakline traces through zone 8 appear in Fig. 105 for nozzle orientations corresponding to  $YAW = 0$  deg combined with  $PITCH = 30$  deg and 45 deg. The  $PITCH = 30$  deg results appear in Fig. 105a. The  $PITCH = 45$  deg results appear in Fig. 105b. The traces indicated that the flow managed to follow the upper wall contour at the high pitch angles even though the zone 8 dye traces displayed a slight unsteadiness at  $PITCH = 45$  deg. However, care must be exercised in interpreting these results since the water tunnel Reynolds number did not match the R2A2 or the ASTF facilities.

The next series of experiments investigated the effect of ramp position schedule on the free-jet nozzle flow quality. The approach centered on perturbing the ramp inclination angle to an off-schedule position and observing the resulting streakline paths. Figure 106 shows a comparison of the nozzle flow characteristics at  $PITCH = 25$  deg with ramp angles of  $-10$  deg, according to the ramp schedule (Appendix D), and  $-20$  deg. Photographs of the zone 1-3 streaklines, with  $RMP = -10$  deg, appear in Figs. 106a-c, respectively. Similar photographs for the  $RMP = -20$  deg setting appear in Figs. 106d-f. The comparison showed the nozzle flow quality with ramp B set at  $-20$  deg to be superior to that with the ramp set to  $-10$  deg inclination. The result suggested that below  $PITCH = 30$  deg, the ramp B positioning schedule should be modified.

The assessment of the ramp B effectiveness used comparisons of the water tunnel Phase III and Phase II results. The comparisons indicated that the use of ramp B degraded the flow quality. Although the ramp A1 results obtained in Phase II showed

some flow anomalies that might be attributed to small vortices, they did not directly display the distinct zone 1 and zone 3 vortices. It happens that zones 1 and 3 correspond to the sections of the ramp B planform that was truncated relative to ramp A1.

Streaklines through zone 2, located downstream of ramp center section, did not reveal the presence of any vortices. The ramp B center section remained true to the ramp A1 dimensions, the truncation having been applied near the outside edges of the ramp. In addition, the generic nozzle model experiments conducted in Phase I, the experiments with the ASTF nozzle mounted inverted in Phase II, and experiments with the ramp removed in Phase III all showed the existence of vortices in zone 2. In each case vortices in either zone 1, zone 3, or both accompanied the zone 2 vortex. The results suggested that truncating the ramp A1 planform to evolve the ramp B shape permitted the formation of the zone 1 and zone 3 vortices while preserving uniform flow characteristics in zone 2.

The water tunnel Phase III experiments concluded in August 1987. The following points summarize the results:

1. Substitution of the ramp B configuration for ramp A1 degraded the free-jet nozzle flow quality. Furthermore, the ramp B installation permitted the formation of vortices in zones 1 and 3.
2. Nozzle yaw angle exerted a strong influence on the zone 1 and zone 3 vortices.
3. At pitch angles below 30 deg, modifications to the ramp positioning schedule improved the flow quality associated with ramp B.



## 5.0 SUMMARY AND CONCLUSIONS

The development of a free-jet test method for evaluating inlet-engine compatibility required the development of a variable-attitude and variable-Mach number subsonic free-jet nozzle. In addition to the pitch-yaw angle envelope and Mach number range, the free-jet requirements specified the flow quality needed for the airframe-propulsion integration test application. The flow quality specifications included allowable deviations in flow angle and Mach number over the nozzle test rhombus, the portion of the jet cross section bounded by the viscosity-dominated flow near the nozzle wall. The latter consisted of the nozzle boundary layer that evolved into the free shear layer or mixing layer downstream of the exit plane.

The free-jet nozzle development included a subsonic free-jet nozzle flow quality investigation to provide information during the design process and to verify that the final nozzle aerodynamic design would meet specifications. The flow quality investigation employed two test facilities. A sub-scale model of the ASTF C-2 test cell provided the air-flow environment and true Mach number conditions for quantifying the free-jet nozzle flow characteristics. Second, the UTSI water tunnel furnished the means to qualitatively investigate the nozzle flow characteristics through the use of flow visualization. In addition to providing insights into the flow features through flow visualization, the water tunnel provided a rapid and inexpensive means to investigate a large number of configurations. The multi-phase flow quality investigation alternated test entries between the two facilities using results from one to support subsequent tests in

the other. In general, the investigation used the water tunnel to screen a large number of test configurations and conduct parametric studies. The investigation used the air-flow facility to validate key water tunnel results and quantify flow uniformity for comparison with specifications.

Flow-field survey tests conducted using a sub-scale variable 2-D nozzle model revealed the presence of strong vortices and excessive flow non-uniformity. This result ultimately expanded the flow quality investigation into six separate test phases, three in each facility. The test phases explored vortex suppression techniques applicable to the ASTF free-jet system.

Flow visualization in water flow simulations enabled a qualitative evaluation of a number of prospective flow improvement methods. Techniques evaluated grouped into the following two categories: (1) vortex attenuation and (2) vortex prevention.

The vortex attenuation approach attempted to reduce existing vorticity to acceptable levels using flow straightening devices at the nozzle inlet or inside the nozzle. Water tunnel results indicated that honeycombs and screens at the nozzle inlet could reduce the secondary flows.

The vortex prevention approach entailed modifying the flow approaching and entering the nozzle to prevent large vortices from forming. Techniques investigated included nozzle inlet ramps, baffles, boundary layer suction, and blowing techniques. Although the water tunnel results highlighted the inlet ramp and selective boundary layer suction as effective vortex prevention methods, the ramp appeared to offer the more robust and low-cost approach. Subsequent flow-field measurements in the sub-scale free-

jet facility, using ramps in conjunction with the variable-area nozzle, quantified the results at true Mach number conditions. Verifying the water tunnel results, the measurements substantiated the selection of the ramp technique for implementation in the ASTF nozzle design.

The investigation next proceeded to the development of a subsonic nozzle configuration for the ASTF C-2 free-jet system. The nozzle definition process integrated the flow quality and ASTF facility requirements. The latter included consideration of the test article, pitch-yaw envelope, altitude-Mach number envelope, and physical space constraints. The conflicting constraints of nozzle size requirements, driving the nozzle exit area upward, and facility physical space, driving the nozzle size downward, resulted in a nozzle with a very low contraction ratio and length-to-height ratio. The resulting geometry rendered the flow quality criteria difficult to achieve. Although the sub-scale flow-field surveys included a few measured flow deviations larger than the flow quality limits, the nozzle exit flow generally met the criteria.

During the evolution of the full-scale version of the nozzle design, the design team proposed modifications to the ramp configuration. The modifications would achieve the following: (1) attainment of the entire pitch-yaw envelope with a single nozzle mounting position and (2) alleviation of mechanical interference with the full-scale nozzle attitude positioning mechanism. The former would reduce test costs by eliminating the requirement to interrupt testing for nozzle repositioning. The latter interference surfaced during the tradeoffs that occurred during the detailed design process. The ramp modification consisted of a reduction in the planform area and shape.

The truncation of the ramp occurred near the outside leading edges with the centerline dimensions remaining essentially intact.

During water tunnel investigations of the proposed truncated ramp configuration, flow anomalies of unknown magnitude appeared in the nozzle. The results indicated that the anomalies could be reduced at pitch angles below 30 deg by modifying the ramp schedule. The project did not receive funding for quantifying the severity of the flow anomalies in air-flow tests.

The experimental results yielded the following general conclusions:

1. The complex flow-field involved in a free-jet test system contains the elements conducive to the formation of secondary flows. These include the features needed for the so-called inlet ground vortex, namely a sink operating near a surface in conjunction with ambient vorticity in the approaching flow. They include the features needed for s-duct type vortices, the change in flow direction as the nozzle bends the flow to the desired combination of pitch and yaw. In the case of the 2-D nozzles, the features include the corner boundary layers needed for the development of corner vortices.
2. Although the flow quality standards needed for free-jet inlet-engine compatibility testing are less stringent than wind tunnel standards, vortices can lead to excessive flow non-uniformity.
3. The formation of large secondary flows is a strong function of nozzle geometry, pitch angle, yaw angle, and proximity to the plenum chamber walls.

4. With the exception of the small corner vortices, formation of the secondary flows does not depend on nozzle exit cross section shape. Square, rectangular, and axisymmetric nozzles have a nearly equal affinity for vortex formation.
5. Flow straightening devices such as honeycombs may be employed to reduce the magnitude of anomalies introduced by vortices.
6. Some nozzle configurations may use strategically-place boundary layer suction to prevent vortex formation. In particular, configurations with complex and out of plane contraction sections might effectively employ this technique.
7. Nozzle inlet ramps offer a robust method of preventing vortex formation that may be applied to a wide range of nozzle configurations. The ramp modifies the flow in the stagnation or separation region upstream of the nozzle inlet eliminating the vortex attachment point and preventing the vortex.
8. Simultaneous achievement of the test rhombus size and pitch-yaw envelope requirements within the physical size constraints of the ASTF C-2 facility demands an unconventional nozzle configuration. A low contraction ratio and a low length-to-height ratio characterize this configuration.
9. Deviations from nozzle design conventions and the requirement for large variations in angles of pitch and yaw may significantly degrade flow quality relative to wind tunnel standards. However, the flow quality goals established

for free-jet propulsion system tests can be achieved over most of the nozzle exit area.

10. The water tunnel offers a unique test capability that will provide valid simulations of numerous air flow situations despite issues of scaling and incompressibility. Qualitative flow visualization provided by the water tunnel used in conjunction with measurements in an air-flow facility can furnish an investigator the tools needed to solve complex flow problems. Using these tools he can gain insights into complex flow mechanisms, the ability to rapidly screen large numbers of configurations, the capability for extensive parametric investigations, and the measurements needed to quantify findings.

The investigation reported in this thesis focused on flow quality requirements that originated in the early concept definition phase of the free-jet system development. At the outset, the adequacy of the specified flow quality for the free-jet propulsion test system lacked an experimental justification. Adding to the complexity of the flow quality issue were the various interactions between the nozzle flow, forebody simulator, and the inlet in the close-coupled and high-blockage configurations characteristic of free-jet installations. As a result, the free-jet method development included a comprehensive validation to verify that the system, including the flow quality specifications, would be adequate for inlet-engine compatibility testing.

Comparisons between sub-scale free-jet tests and wind tunnel tests formed the basis of the free-jet validation program. Steady-state and dynamic inlet distortion measurements at the simulated engine face were first obtained using models of fighter

aircraft inlet-forebody combinations in wind tunnel tests. The same measurements were subsequently acquired in R2A2 using the same inlet models in conjunction with the free-jet nozzles developed in the present investigation. During the free-jet tests, forebody simulators replaced the full aircraft forebody to ensure that the experiments would fully represent a full-scale test configuration and address the various interactions between the nozzle and test article. Comparisons between the free-jet and wind tunnel results, based on inlet distortion measures of merit and predetermined validation criteria, proved that the flow quality delivered by the present nozzle system would meet inlet-engine compatibility test requirements (Refs. 53, 55, 57, and 58).

## REFERENCES



## REFERENCES

1. Society of Automotive Engineers, Inc. "Inlet Total-Pressure Considerations for Gas Turbine Engines." Aerospace Information Report 1419, May 1983.
2. Society of Automotive Engineers, Inc. "Gas Turbine Engine Inlet flow Distortion Guidelines." Aerospace Recommended Practice 1420, March 1978.
3. Anderson, R. E. "Aircraft Engine Inlet Pressure Distortion Testing in a Ground Test Facility." AIAA Paper No. 83-1233, AIAA/SAE/ASME 19<sup>th</sup> Joint Propulsion Conference, Seattle, Washington, June 27-29, 1983.
4. Aulehla, F. and Schmitz, D. M. "New Trends in Intake/Engine Compatibility Assessment." AGARD CP-400, 1987.
5. Aulehla, F. "Intake Swirl - A Major Disturbance Parameter in Engine/Intake Compatibility." 13<sup>th</sup> Congress of ICAS/AIAA, ICAS-82-4.8.1, Seattle, Washington, August 1982.
6. Ball, W. H. "Inlet Planar Waves: A Current Perspective." (Publication unknown).
7. Baumbick, R. J. "Device for Producing Dynamic Distortion Patterns at Inlets of Air Breathing Engines." NASA TM-X-2026, June 1970.
8. Biesiadny, T. J., Braithwaite, W. M., Soeder, R. H., Abdelwahab, M. "Summary of Investigations of Engine Response to Distorted Inlet Conditions." NASA TM-87317, 68<sup>th</sup> Meeting of the Propulsion and Energetics Panel (sponsored by AGARD), Munich, Germany, September 8-9, 1986. Also AGARD CP-400, 1987.
9. Bowditch, D. N. and Coltrin, R. E. "A Survey of Inlet/Engine Distortion Compatibility (Invited Paper)." AIAA Paper No. 83-1166, AIAA/SAE/ASME 19<sup>th</sup> Joint Propulsion Conference, Seattle, Washington, June 27-29, 1982.
10. Braithwaite, W. M., Graber, E. J. Jr., Mehalic, C. M. "The Effect of Inlet Temperature and Pressure Distortion on Turbojet Performance." AIAA Paper No. 73-1316, AIAA/SAE 9<sup>th</sup> Propulsion Conference, Las Vegas, Nevada, November 5-7, 1973.
11. Braithwaite, W. M., Soeder R. H. "Combined Pressure and Temperature Distortion Effects on Internal Flow of a Turbofan Engine." AIAA Paper No. 79-1309, AIAA/SAE/ASME 15<sup>th</sup> Joint Propulsion Conference, Las Vegas, Nevada, June 18-20, 1979.

12. Brimelow, B., Collins, T. P., Pfefferkorn, G. A. "Engine Testing in a Dynamic Environment." AIAA Paper No. 74-1198, AIAA/SAE 10<sup>th</sup> Propulsion Conference, San Diego, California, October 21-23, 1974.
13. Calogeras, J. E., Burstadt, P. L., Coltrin, R. E. "Instantaneous and Dynamic Analysis of Supersonic Inlet-Engine Compatibility." AIAA Paper No. 71-667, AIAA/SAE 7<sup>th</sup> Propulsion Joint Specialist Conference, Salt Lake City, Utah, June 14-18, 1971.
14. Carter, E. C. "Experimental Determination of Inlet Characteristics and Inlet and Airframe Interference." AGARD LS-53, AGARD Lecture Series No. 53 on Airframe/Engine Integration, May 1972.
15. Csavina, F. L., Denny, R. K. "A Global Approach in Evaluating Inlet/Engine Compatibility." (Publication unknown).
16. Eggers, W. C. "Pressure Measurements for Establishing Inlet/Engine Compatibility." ISA ASI 73220, 1973.
17. Ellis, S. H. "Inlet-Engine Compatibility Analysis." AGARD CP-91-71, 38<sup>th</sup> Meeting of AGARD Propulsion and Energetics Panel, Sandefjord, Norway, September 13-17, 1971.
18. Farr, A. P. "Evaluation of F-15 Inlet Dynamic Distortion." AIAA Paper No. 73-784, AIAA 5<sup>th</sup> Aircraft Design, Flight Test, and Operations Meeting, St. Louis, Missouri, August 6-8, 1973.
19. Fuhs, A. E. "Engine Integration and Thrust/Drag Definition." AGARD LS-53 AGARD Lecture Series No. 53 on Airframe/Engine Integration, May 1972.
20. Genssler, H. P., Meyer, W., and Fottner, L. "Development of Intake Swirl Generators for Turbojet Engine Testing." AGARD CO-400, 1987.
21. Goldsmith, E. L. and Seddon, J. Practical Intake Aerodynamic Design, AIAA Education Series, 1993.
22. Graber, E. J. Jr., Braithwaite, W. M. "Summary of Recent Investigations of Inlet Flow Distortion Effects on Engine Stability." AIAA Paper No. 74-236, AIAA 12<sup>th</sup> Aerospace Sciences Meeting, Washington D.C., January 30 - February 1, 1974.
23. Hubble, J. D. and Smith R. E. "Evaluation of an Airjet Distortion Generator Used to Produce Steady-State, Total Pressure Distortion at the Inlet of a General Electric F101-GE-100 Turbofan Engine." AEDC-TR-78-73, August, 1979.

24. Kimzey, W. F., Ellis, S. H. "Supersonic Inlet Simulator – A Tool for Simulation of Realistic Engine Entry Flow Conditions." Society of Automotive Engineers National Aerospace Engineering and Manufacturing Meeting, San Diego, California, October 1-3, 1974.
25. Kimzey, /w. F., McIlveen, M. W. "Analysis and Synthesis of Distorted and Unsteady Turbo Engine Inlet Flow Fields." AIAA Paper No. 71-668, AIAA 7<sup>th</sup> Propulsion Joint Specialist Conference, Salt Lake City, Utah, June 14-18, 1971.
26. Koch, K. E. and Rees, R. L. "Analysis of Pressure Distortion Testing." NASA CR-2766, December 1976.
27. Kutschenreuter, P. H. Jr., Collins, T. P., and Vier, W. F. III "The P<sup>3</sup>G – A New Dynamic Distortion Generator." AIAA Paper No. 73-1317, AIAA/SAE 9<sup>th</sup> Propulsion Conference, Las Vegas, Nevada, November 5-7, 1973.
28. Lazalier, G. R. and Tate, J. T. "Development of a Prototype Discrete-Frequency, Total-Pressure Fluctuation Generator for Jet Engine-Inlet Compatibility Investigation." Proceeding of the Air Force Airframe Propulsion Compatibility Symposium, AFAPL-TR-69-102, June 1970.
29. Longley, J. P. and Greitzer. "Inlet Distortion Effects in Aircraft Propulsion System Integration." AGARD LS-183, May 1992.
30. McAulay, J. E. "Effect of Dynamic Variations in Engine-Inlet Pressure on the Compressor System of a Twin-Spool Turbofan Engine." NASA TMX-2081, September, 1970.
31. Mehalic, C. M. "Effect of Spatial Inlet Temperature and Pressure Distortion on Turbofan Engine Stability." AIAA Paper No. 88-3016, AIAA/ASME/SAE 24<sup>th</sup> Joint Propulsion Conference, Boston Massachusetts, July 11-13, 1988. Also NASA TM-100850.
32. Overall, B. W. "Evaluation of an Airjet Distortion Generator Used to Produce Steady-State, Total-Pressure Distortion at the Inlet of Turbine Engines." AEDC-TR-76-141, December 1976.
33. Pazur, W. and Fottner, L. "The Influence of Inlet Swirl Distortions on the Performance of a Jet Propulsion Two-Stage Axial Compressor." Journal of Turbomachinery, Vol 113, pp 233-240, April 1991..
34. Plourde, G. A. "Pressure Fluctuations Cause Compressor Instability." Proceedings of the Air Force Airframe Propulsion Compatibility Symposium, AFAPL-TR-69-103, June 1970.

35. Povolny, J. H. "Stall and Distortion Investigation of a YTF30-P-1 Turbofan Engine." Proceedings of the Air Force Airframe Propulsion Compatibility Symposium, AFAPL-TR-69-103, June 1970.
36. Richey, G. K., Surber, L. E., and Berrier, B. L. "Airframe-Propulsion Integration for Fighter Aircraft." AIAA Paper No. 83-0084, AIAA 21<sup>st</sup> Aerospace Sciences Meeting, Reno, Nevada, January 10-13, 1983.
37. Sherman, D. A. and Motycka, D. C. "Experimental Study of Inlet-Generated Pressure Fluctuations." Proceedings of the Air Force Airframe Propulsion Compatibility Symposium, AFAPL-TR-69-103, June 1970.
38. Soeder, R. H., Bobula, G. A. "Effect of Steady-State Pressure Distortion on Flow Characteristics Entering a Turbofan Engine." NASA TM-79134, April 1979.
39. Stevens, C. H., Spong, E. D., and Hammock, M. S. "F-15 Inlet/Engine Test Techniques and Distortion Methodologies Studies, Vol I - Technical Discussion." NASA CR-144866, June 1987.
40. Surber, L. "Effect of Forebody Shape and Shielding Technique on 2-D. Supersonic Inlet Performance." AIAA Paper No. 75-1183, AIAA/SAE 11<sup>th</sup> Propulsion Conference, Anaheim, California, September 29 - October 1, 1975.
41. Surber L. E. and Fujimura, C. "Inlet-Engine Compatibility." VKI Lecture Course "Intake Aerodynamics", February 22-26, 1988.
42. Surber, L. and Robinson, Lt. C. P. "Survey of Inlet Development for Supersonic Tactical Aircraft (Invited Paper)." AIAA Paper No. 83-1164, AIAA/SAE/ASME 19<sup>th</sup> Joint Propulsion Conference, Seattle Washington, June 27-29, 1983.
43. Surber, L. and Sedlock D. "Effect of Airframe-Inlet Integration on Half-Axisymmetric and Two-Dimensional Supersonic Inlet Performance." AIAA Paper No. 78-960, AIAA/SAE 14<sup>th</sup> Joint Propulsion Conference, Las Vegas, Nevada, July 25-27, 1978.
44. Tate, J. T. "Inlet-Engine Compatibility Testing Techniques in Ground Test Facilities." (Publication unknown).
45. Van Deusen, E. A. and Mardoc, V. R. "Distortion and Turbulence Interaction, A Method for Evaluating Engine/Inlet Compatibility." AIAA Paper No. 70-632, AIAA 6<sup>th</sup> Propulsion Joint Specialist Conference, San Diego, California, June 15-19, 1970.
46. Williams, D. D. "Review of Current Knowledge on Engine Response to Distorted Inflow Conditions." AGARD CF-400.

47. Younghans, J. L., Moore, M. T., Collins, T. P., and Direnzi, J. G. "Inlet Flowfield Simulation Techniques for Engine/Compressor Testing." AIAA Paper No. 70-591, AIAA 5<sup>th</sup> Aerodynamic Testing Conference, Tullahoma, Tennessee, May 18-20, 1970.
48. Zonars, D. "Dynamic Characteristics of Engine Inlets." AGARD LS-53, AGARD Lecture Series No. 53 on Airframe/Engine Integration, May 1972.
49. Stevens, C. H., Spong, E. D., Nugent, J., and Neumann, H. E. "Reynolds Number, Scale, and Frequency Content Effects on F-15 Instantaneous Distortion." AIAA Paper No. 79-0104, AIAA 17<sup>th</sup> Aerospace Sciences Meeting, New Orleans, Louisiana, January 15-17, 1979.
50. Ashwood, P. F. "Free-Jet Tests of a Full-Scale Supersonic Intake/Engine Combination." AGARD-CP-91-71, 38<sup>th</sup> Meeting of AGARD Propulsion and Energetics Panel, Sandefjord, Norway, September 13-17, 1971.
51. Mitchell, J. G. "The Aero-Propulsion Systems Test Facility." AIAA Paper No. 72-1034, 7<sup>th</sup> Aerodynamic Testing conference, Palo Alto, California, Sept. 13-15, 1972.
52. Mitchell, J. G. "New Test Capability for Propulsion System Testing." AIAA Paper No. 73-1283, 9<sup>th</sup> Propulsion Conference, Las Vegas, Nevada, November 5-7, 1973.
53. Beale, D. K. "Evaluation of a Free-Jet Technique for Testing Fighter Aircraft Propulsion Systems." AIAA Paper No. 86-1460, 22<sup>nd</sup> Joint Propulsion Conference, Huntsville, Alabama, June 16-18, 1986.
54. Duesterhaus, D. A. and Maywald, P. V. "Freejet Test Capability for the Aeropropulsion Systems Test Facility." AIAA Paper No. 89-2537, AIAA/ASME/SAE/ASEE 25<sup>th</sup> Joint Propulsion Conference, Monterey, California, July 1989.
55. Beale, D. K. and Collier, M. S. "Validation of a Freejet Technique for Evaluating Inlet-Engine Compatibility." AIAA Paper No. 89-2325, AIAA/ASME/SAE/ASEE 25<sup>th</sup> Joint Propulsion Conference, Monterey, California, July 1989.
56. Maywald, P. V. and Beale, D. K. "Development of a Freejet Capability for Evaluating Inlet-Engine Compatibility." ASME Paper No. 91-GT-401, International Gas Turbine and Aeroengine Congress and Exposition, Orlando, Florida, June, 1991.

57. Beale, D. K. and Zelenak, M. "Development and Validation of a Freejet Technique for Inlet-Engine Compatibility Testing." AIAA Paper No. 92-3921, AIAA 17<sup>th</sup> Ground Testing Conference, Nashville, Tennessee, July 1992.
58. Beale, D. K. and Kelly, P. G., and Lacasse, J. E. P. "Subscale Validation of a Freejet Inlet-Engine Test Capability." AIAA Paper No. 93-2179, AIAA/SAE/ASME/ASEE 29<sup>th</sup> Joint Propulsion Conference and Exhibit, Monterey, California, June 1993.
59. Maywald, P. V. "C-2 Subsonic Freejet Development and Demonstration." AIAA Paper No. 93-2180, AIAA/ASME/SAE/ASAE 29<sup>th</sup> Joint Propulsion Conference, Monterey, California, June 1993.
60. Gessner, F. B. "The Origin of Secondary flow in Turbulent Flow Along a Corner." Journal of Fluid Mechanics, Vol. 58, Part 1 pp 1-25.
61. Anderson, B. H. and Gibb, J. "Application of Computational Fluid Dynamics to the Study of Vortex Flow Control for the Management of Inlet Distortion." AIAA Paper No. 92-3177, AIAA/ASME/SAE 28<sup>th</sup> Joint Propulsion Conference and Exhibit, Nashville, Tennessee, July 6-8, 1992.
62. Anderson, B. H., Huang, P. S., Paschal, W.A., and Cavatorta, E. "Study on Vortex Flow Control of Inlet Distortion." Journal of Propulsion and Power, Vol 8, No. 6, November-December, 1992.
63. Anderson, B. H. and Levy, R. "A Design Strategy for the Use of Vortex Generators to Manage Inlet-Engine Distortion Using Computational Fluid Dynamics." AIAA Paper No. 91-2474, AIAA/SAE/ASME/ASEE 27<sup>th</sup> Joint Propulsion Conference and Exhibit, Sacramento, California, June 24-27, 1991.
64. Anwer, M. and So, R. M. C. "Swirling Turbulent Flow Through a Curved Pipe. Part I: Effect of Swirl and Bend Curvature." Experiments in Fluids, 14, 1993.
65. Guo, R. and Seddon, J. "An Investigation of the Swirl in an S-Duct." The Aeronautical Quarterly, February, 1982.
66. Guo, R. W. and Seddon, J. "Swirl Characteristics of an S-Shaped Air Intake with Both Horizontal and Vertical Offsets." The Aeronautical Quarterly, May 1983.
67. Guo, R. W. and Seddon, J. "The Swirl in an S-Duct of Typical Air Intake Proportions." The Aeronautical Quarterly, May 1983.
68. Harloff, G. J., DeBonis, J. R., Smith, C. F., and Bruns, J. E. "Three-Dimensional Compressible Turbulent Computations for a Nondiffusing S-Duct." NASA Contractor Report 4391, April 1992.

69. Harloff, G. J., Reichert, B. A. and Wellborn, S. R. "Navier Stokes Analysis and Experimental Data Comparison of Compressible Flow in a Diffusing S-Duct." AIAA Paper No. 92-2699-CP, 1992.
70. Harloff, G. J., Smith, C. F., Bruns, J. E., and DeBonis, J. R. "Navier Stokes Analysis of Three-Dimensional S-Ducts." Journal of Aircraft, Vol. 30, No. 4, July-August, 1993, pp 526-533.
71. McConnaughey, P., Cornelison, J., and Barker, L. "The Prediction of Secondary Flow in Curved Ducts of Square Cross-Section." AIAA Paper No. 89-0276, AIAA 27<sup>th</sup> Aerospace Sciences Meeting, Reno, Nevada, January 1989.
72. Reichert, B. A. and Wendt, B. J. "An Experimental Investigation of S-Duct Flow Control Using Arrays of Low Profile Vortex Generators." NASA Technical Memorandum 106030, February 1993.
73. Rowe, M. "Measurements and Computations of Flow in Pipe Bends." Journal of Fluid Mechanics, Vol. 43, Part 4, pp 771-783, 1970.
74. Seddon, J. "Understanding and Countering the Swirl in S-Ducts: Tests on the Sensitivity of Swirl to Fences." Aeronautical Journal, April 1984.
75. So, R. M. and Anwer, M. "Swirling Turbulent Flow Through a Curved Pipe. Part 2: Recovery from Swirl and Bend Curvature." Experiments in Fluids, 14, 1993.
76. Taylor, A. M. K. P., Whitelaw, J. H., Yianneskis, M. "Developing Flow in S-Shaped Ducts I - Square Cross-Section Duct." NASA Contractor Report 3550, May 1982.
77. Taylor, A. M. K. P., Whitelaw, J. H., Yianneskis, M. "Developing Flow in S-Shaped Ducts II - Circular Cross-Section Duct." NASA Contractor Report 3759, February, 1984.
78. Towne, C. E. "Computation of Viscous Flow in Curved Ducts and Comparison with Experimental Data." AIAA Paper No. 84-0531, AIAA 22<sup>nd</sup> Aerospace Sciences Conference, Reno Nevada, January 1984.
79. Vakili, A. and Wu, J. M. "Comparison of Experimental and Computational Compressible Flow in a S-Duct." AIAA Paper No. 84-0033, AIAA 22<sup>nd</sup> Aerospace Sciences Meeting, Reno, Nevada, January 1984.
80. Vakili, A. D., Wu, J. M., Liver, P., and Bhat, M. K. "Flow Control in a Diffusing S-Duct." AIAA Paper No. 85-0524, AIAA Shear Flow Control Conference, Boulder, Colorado, March 12-14, 1985.

81. Welborn, S. R., Reichert, B. A., and Okiishi, T. H. "An Experimental Investigation of the Flow in a Diffusing S-Duct." AIAA Paper No. 92-3622, AIAA/SAE/ASME/ASME 28<sup>th</sup> Joint Propulsion Conference and Exhibit, Nashville, Tennessee, July 6-8, 1992.
82. Weng, P. F., Shanghai, J. T., and Guo, R. W. "On Swirl Control in an S-Shaped Air Intake at High Angle of Attack." AIAA Paper No. 94-0366, 32<sup>nd</sup> Aerospace Sciences Meeting and Exhibit, Reno, Nevada, January 10-13, 1994.
83. Bissinger, N. C. and Braun, G. W. "On the Inlet Vortex System." NASA CR-132536, September 1974.
84. Colehour, J. L. and Farquhar, B. W. "Inlet Vortex." Journal of Aircraft, Vol 8, No. 1, January 1971.
85. De Sievi, F. "A Flow Visualization Study of the Inlet Vortex Phenomenon." GT & PDL Report No. 159, July 1981.
86. De Sievi, F., Viguier, H. C., Greitzer, E. M., and Tan, C. S. "Mechanisms of Inlet-Vortex Formation." Journal of Fluid Mechanics, Vol. 124, 1982.
87. Motycka, D. L. "Ground Vortex - Limit to Engine/Reverser Operation." Transactions of the ASME, April 1976.
88. Motycka, D. L. and Walter, W. A. "An Experimental Investigation of Ground Vortex Formation During Reverse Engine Operation." AIAA Paper No. 75-1322, AIAA/SAE 11<sup>th</sup> Propulsion Conference, Anaheim, California, September 1975.
89. Motycka, D. L., Walter, W. A. and Muller, G. L. "An Analytical and Experimental Study of Inlet Ground Vortices." AIAA Paper No. 73-1313, November 1973.
90. Ridder, S. O. and Samuelsson, I. "An Experimental Study of Strength and Existence Domain of Ground-to-Air Inlet Vortices by Ground Board Static Pressure Measurements." KTH Aero TN 62, 1982.
91. Robert, L. A. and Garrett, F. B. "Ingestion of Foreign Objects into Turbine Engines by Vortices." NASA TN-3330.
92. Shin, H. and Shippee, C. "Quantitative Investigation of Inlet Vortex Flow Field." GT&PDL Report No. 179, March 1984.
93. Viguier, H. C. "A Secondary Flow Approach to the Inlet Vortex Flow Field." GT&PDL Report No. 155, November 1980.

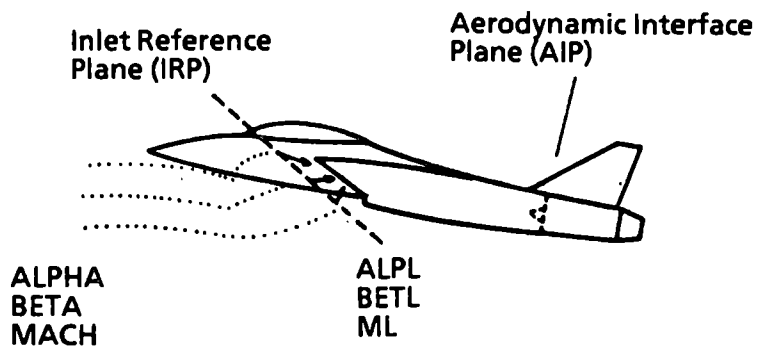


94. Advisory Group for Aerospace Research & Development. Aerodynamics and Related Hydrodynamic Studies Using Water Facilities, AGARD-CP-413, AGARD Conference Proceedings No. 413, October 1986.
95. Lorinez, D. J. "A Water Tunnel Flow Visualization Study of the F-15." NASA CR-144878, December 1978.
96. Malcolm, G. N. "Forebody Vortex Control." AGARD-R-776, Special Course on Aircraft Dynamics at High Angles of Attack: Experiments and Modelling, 1991.
97. Merzkirch, W. "Techniques of Flow Visualization." AGARD-AG-302, 1987.
98. Werle, H. "Application of Hydrodynamic Visualization to the Study of Low Speed Flow Around a Delta Wing Aircraft." Flow Visualization: Proceedings of the International Symposium of Flow Visualization, Tokyo, Japan, October 12-14, 1977.
99. Werle, H. "Flow Visualization Techniques for the Study of High Incidence Aerodynamics." AGARD-VKI Lecture Series 121, 1982.
100. Werle, H. "Hydrodynamic Visualization on Streamlined Bodies of Vortex Flows Particular to High Angles of Attack." Flow Visualization II: Proceedings of the Second International Symposium on Flow Visualization, Bochum, West Germany, September 9-12, 1980.
101. Collins, F. "Description of the University of Tennessee Space Institute Water Tunnel." UTSI 82-1, University of Tennessee Space Institute, Tennessee, 37398.
102. Abernethy, R. B. and Thompson, J. W. "Handbook Uncertainty in Gas Turbine Measurements." AEDC-TR-73-5 (AD755356), February 1973.
103. McDaniels, D. M. "Background and Theoretical Considerations for Utilizing Water Tunnel Flow Visualization." UTSI 86-07, University of Tennessee Space Institute, Tennessee, 37398.

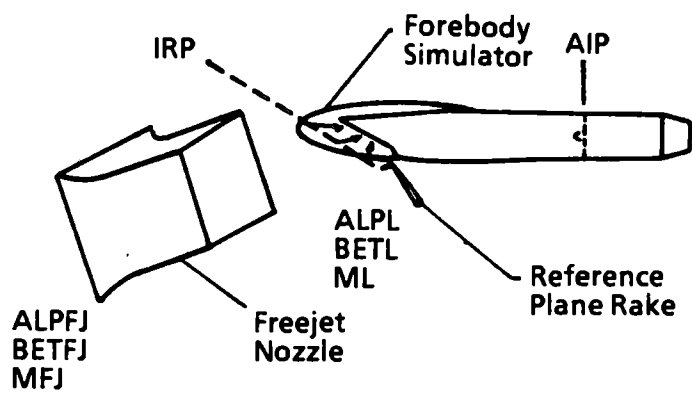
**APPENDIXES**

**APPENDIX A**

**FIGURES**



a. Aircraft in flight



b. Free-Jet Simulation

Figure 1. Free-Jet Test Concept.

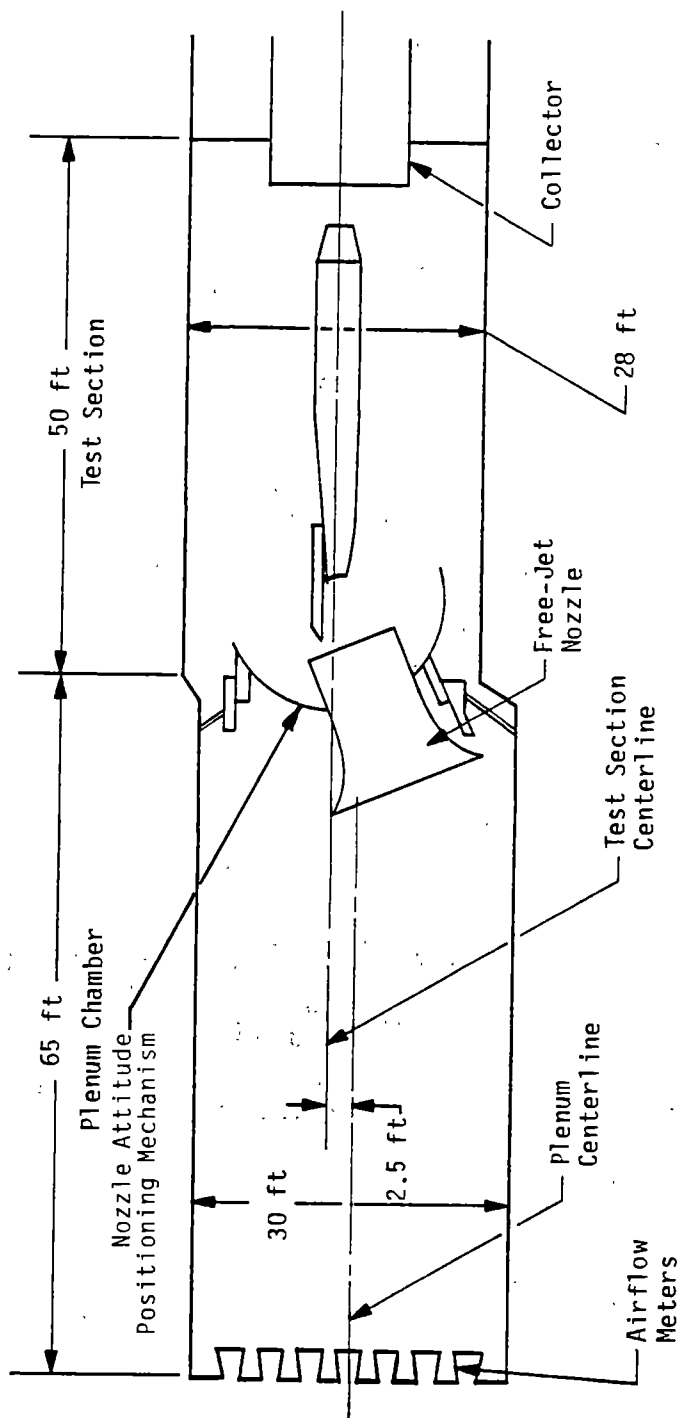


Figure 2. ASTF C-2 Test Cell in Free-Jet Configuration.

**AIRFLOW TESTS**

**WATER FLOW TESTS**

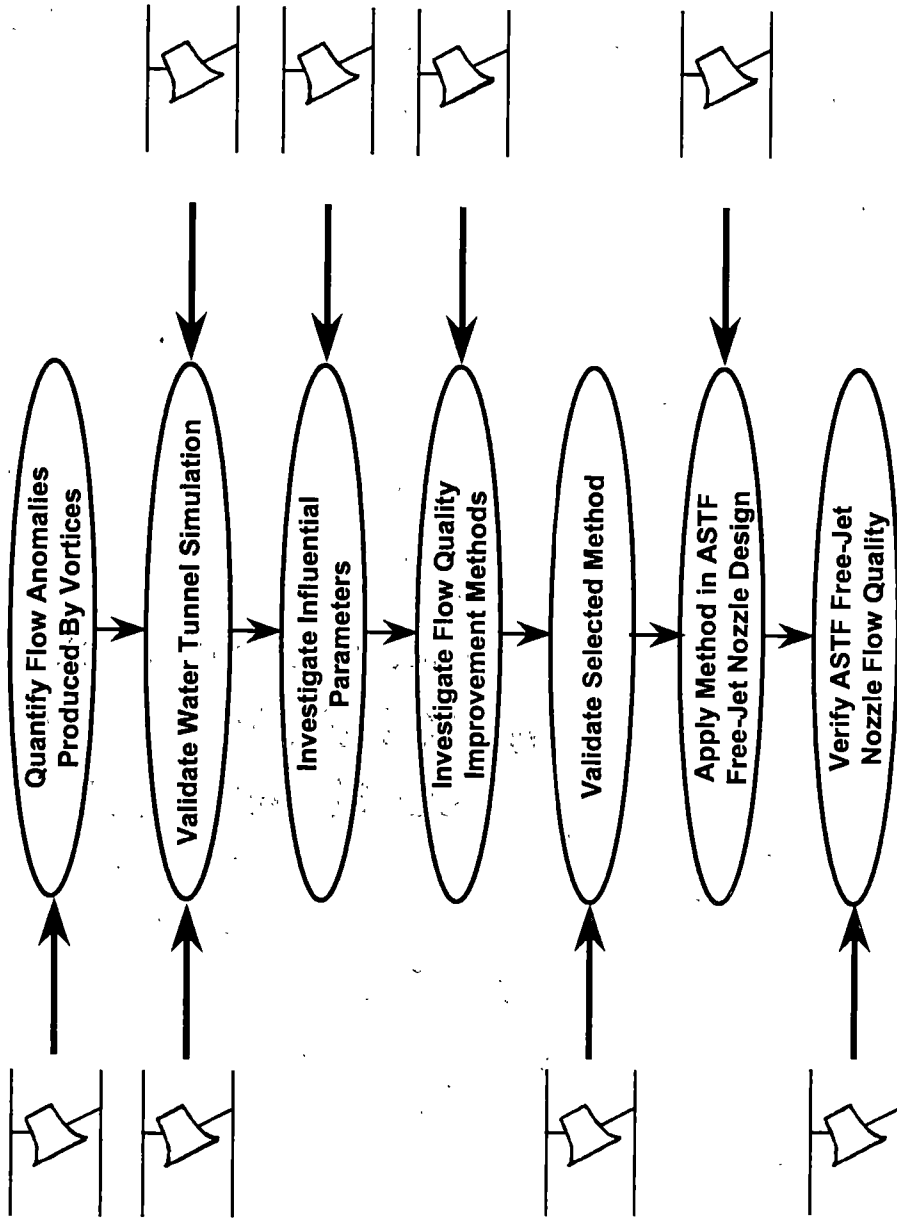
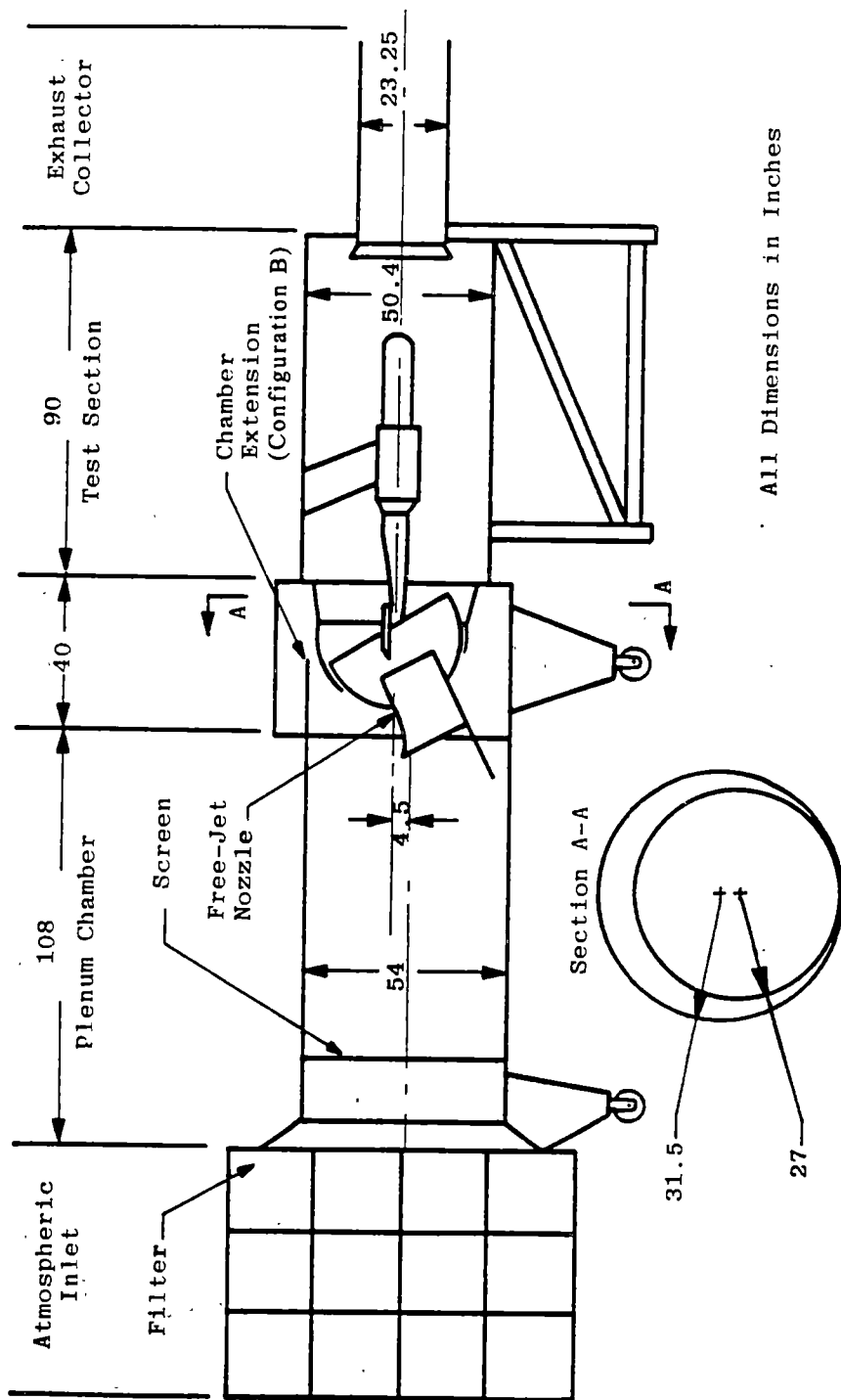
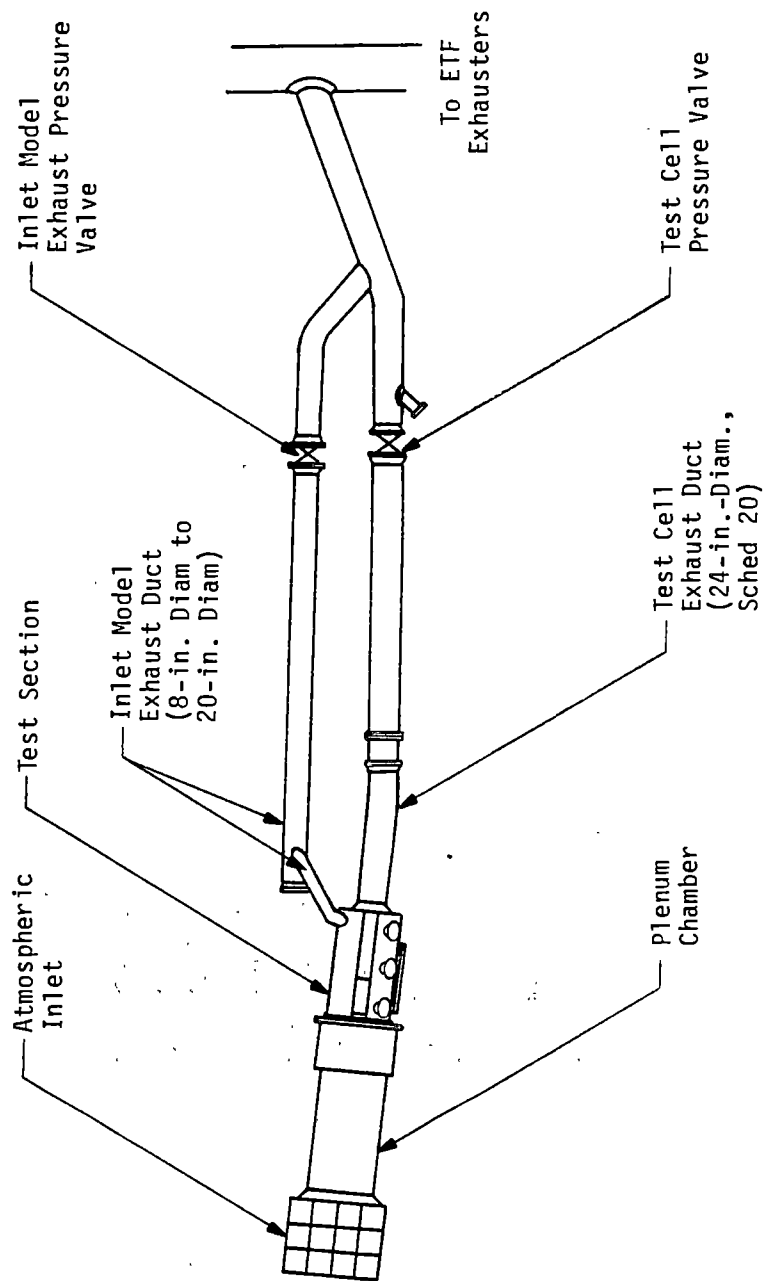


Figure 3. Chronology of Experimental Approach.



a. Elevation View

Figure 4. Research Test Cell R2A2 in Free-Jet Configuration.



b. Top View of Test Cell and Exhaust Ducting

Figure 4. Concluded.



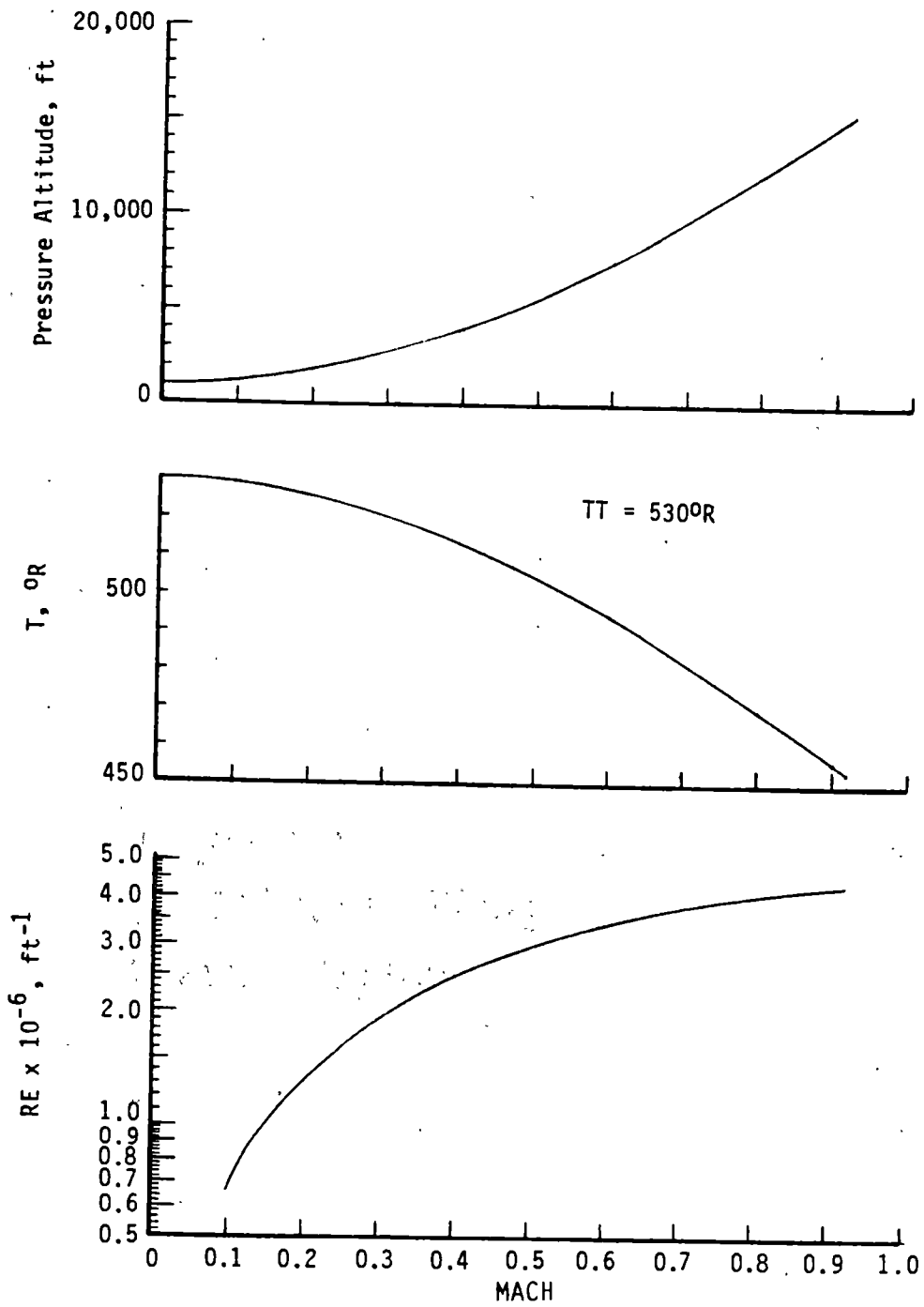


Figure 5. Research Test Cell R2A2 Performance with Atmospheric Inlet.

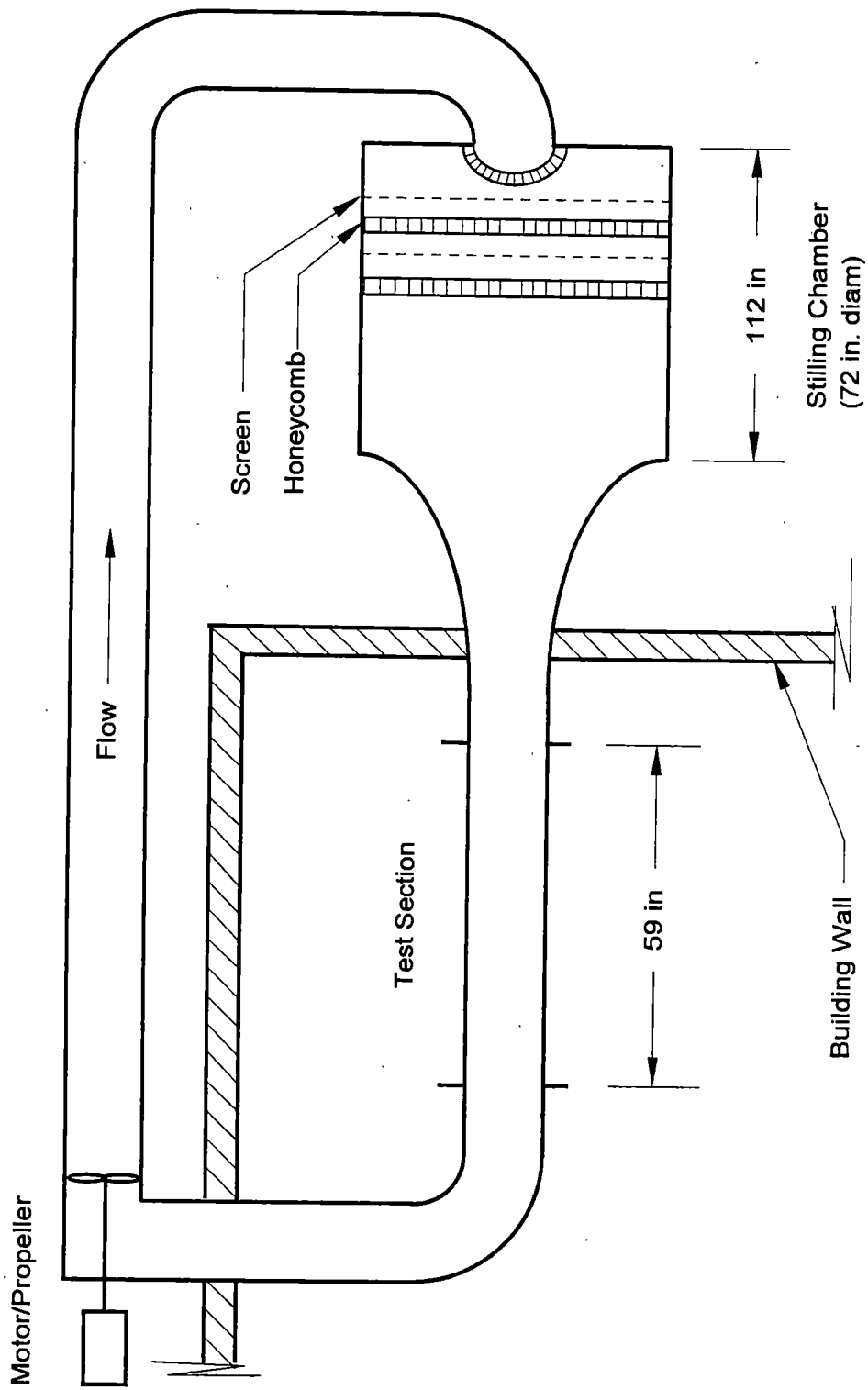


Figure 6. University of Tennessee Space Institute Water Tunnel.

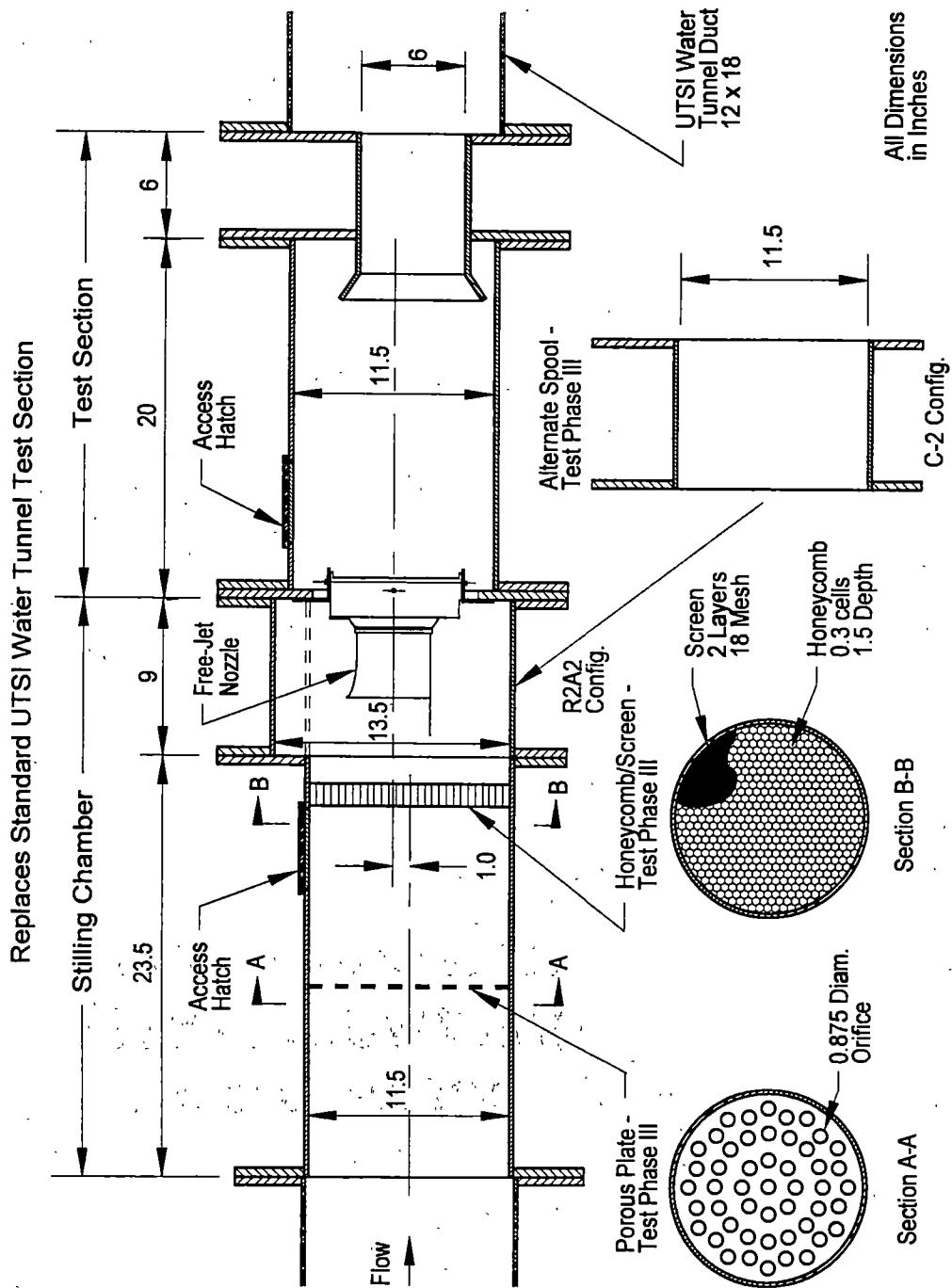
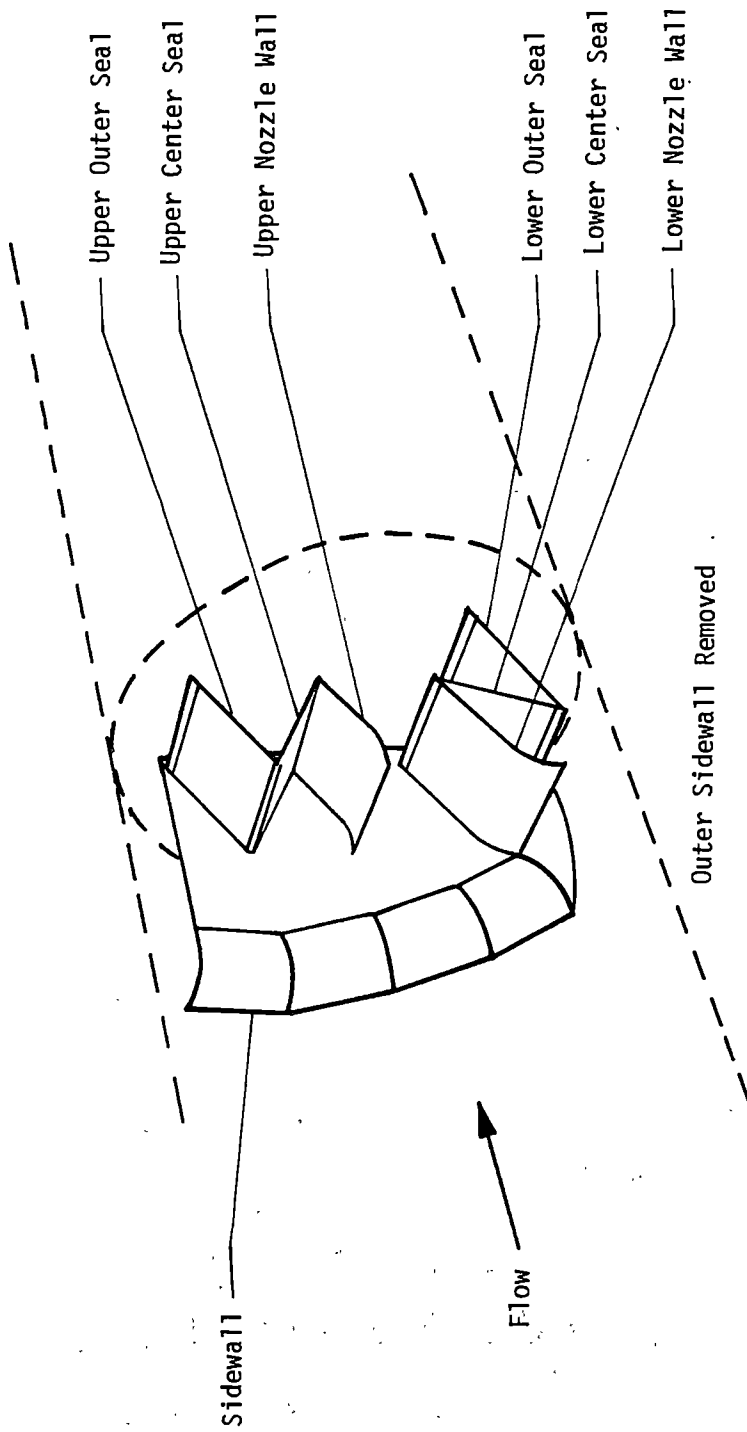
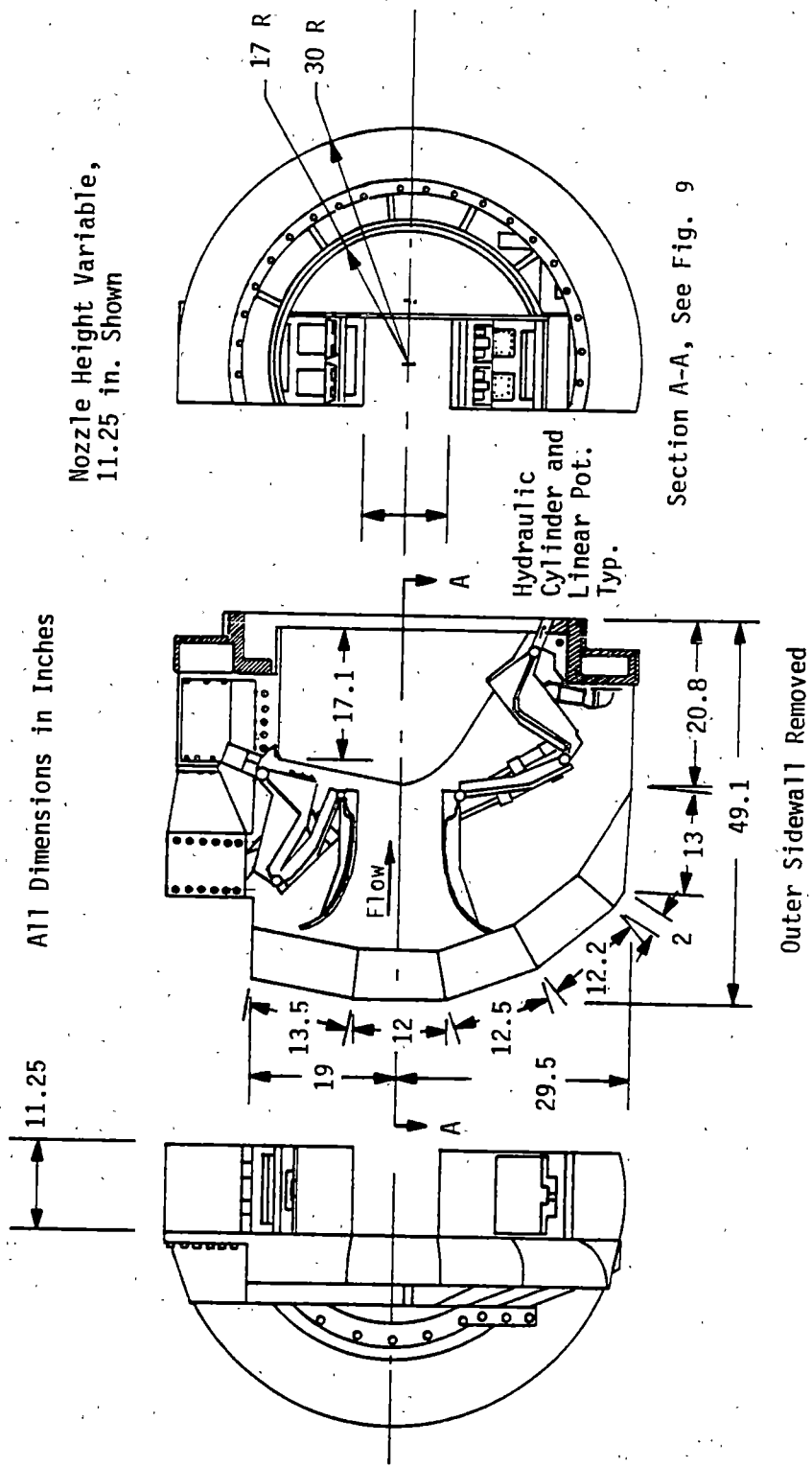


Figure 7. Water Tunnel Model of Research Test Cell R2A2.



a. Isometric View

Figure 8. Variable-Area Free-Jet Nozzle Airflow Model.

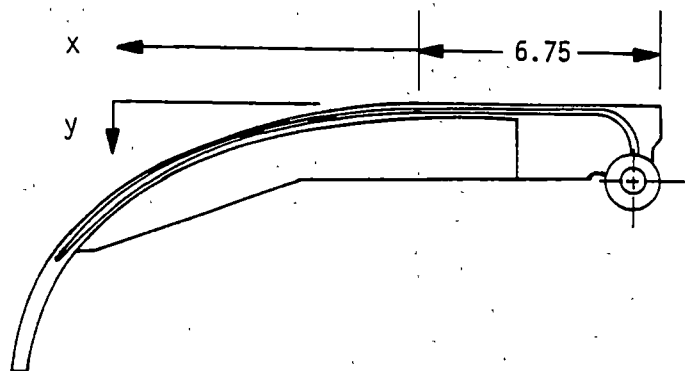


Nozzle Height Variable,  
11.25 in. Shown

All Dimensions in Inches

b. 3-View

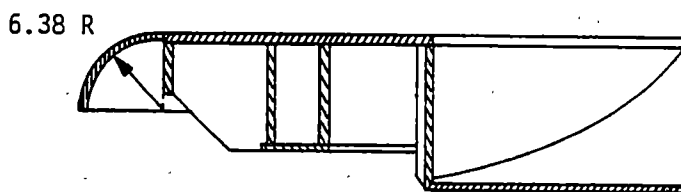
Figure 8. Concluded.



Upper/Lower Nozzle Wall

x	y	x	y
0.000	0.000	6.000	1.156
0.500	0.007	6.500	1.378
1.000	0.030	7.000	1.629
1.500	0.670	7.500	1.909
2.000	0.119	8.000	2.227
2.500	0.188	8.500	2.587
3.000	0.272	9.000	3.000
3.500	0.372	9.500	3.483
4.000	0.490	10.000	4.064
4.500	0.626	10.500	4.807
5.000	0.781	11.000	5.928
5.500	0.957	11.250	7.500

All Dimensions in Inches



Nozzle Sidewall Section A-A (Fig. 6b)

Figure 9. Variable-Area Free-Jet Nozzle Airflow Model Wall Contours.

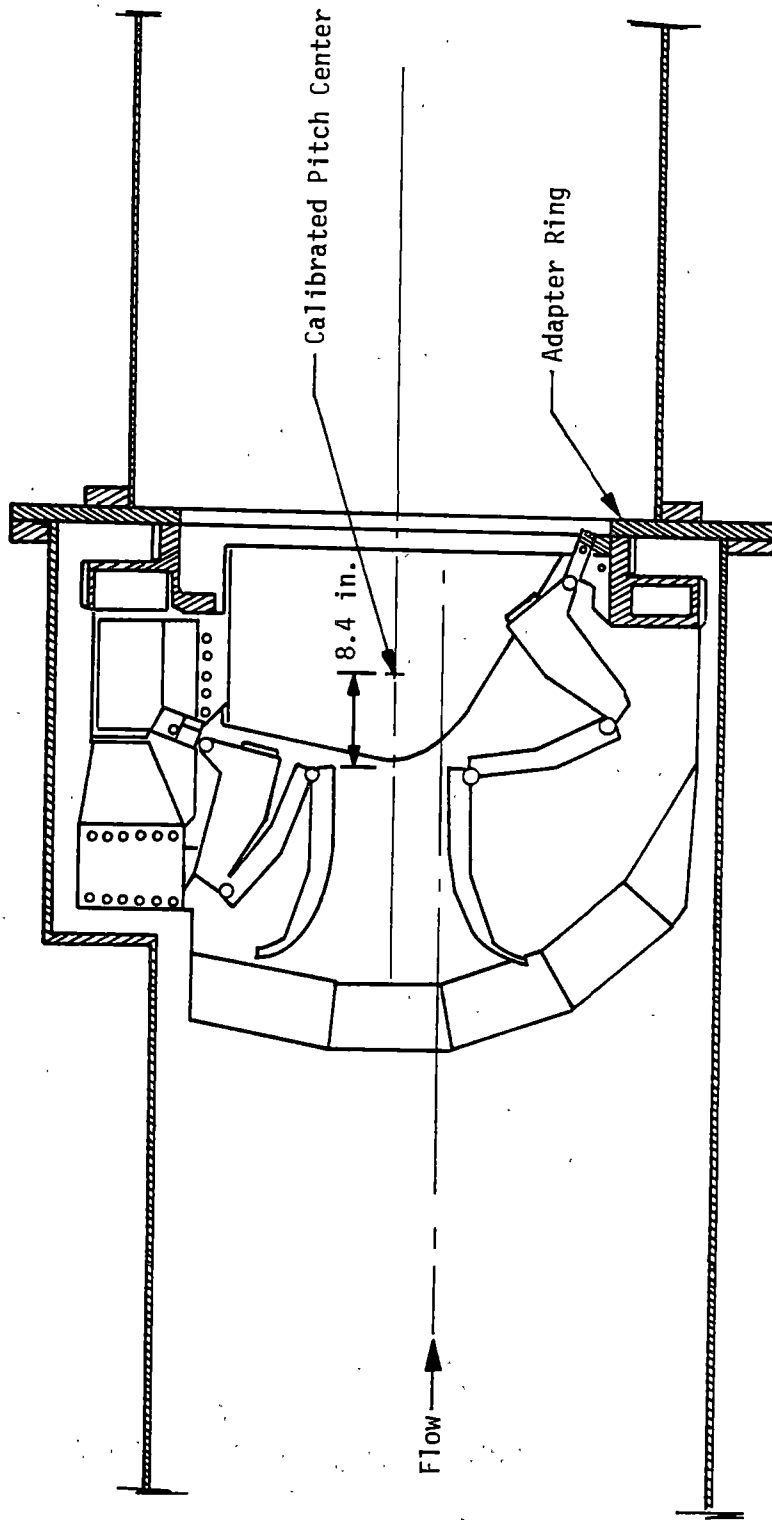


Figure 10. Variable-Area Nozzle Airflow Nozzle Model Installation in R2A2.

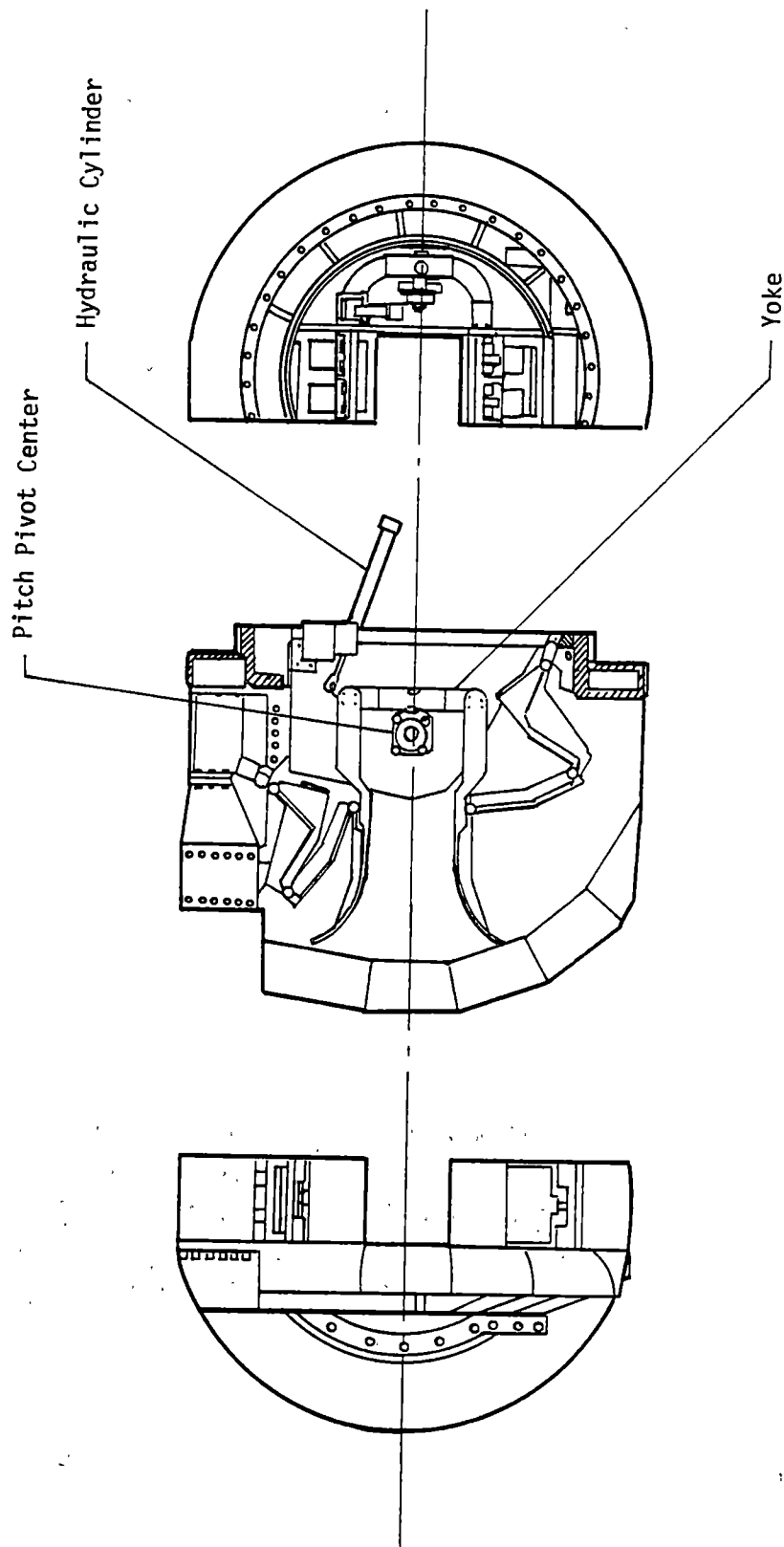
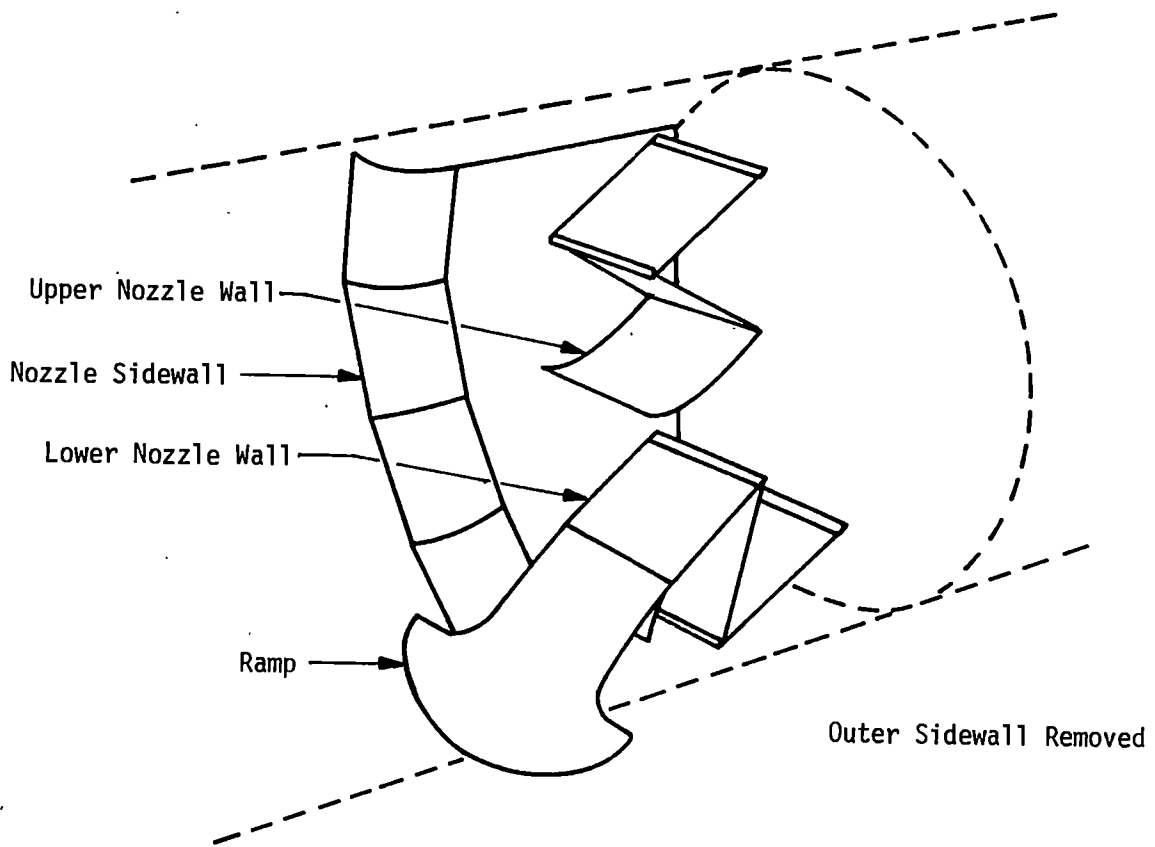


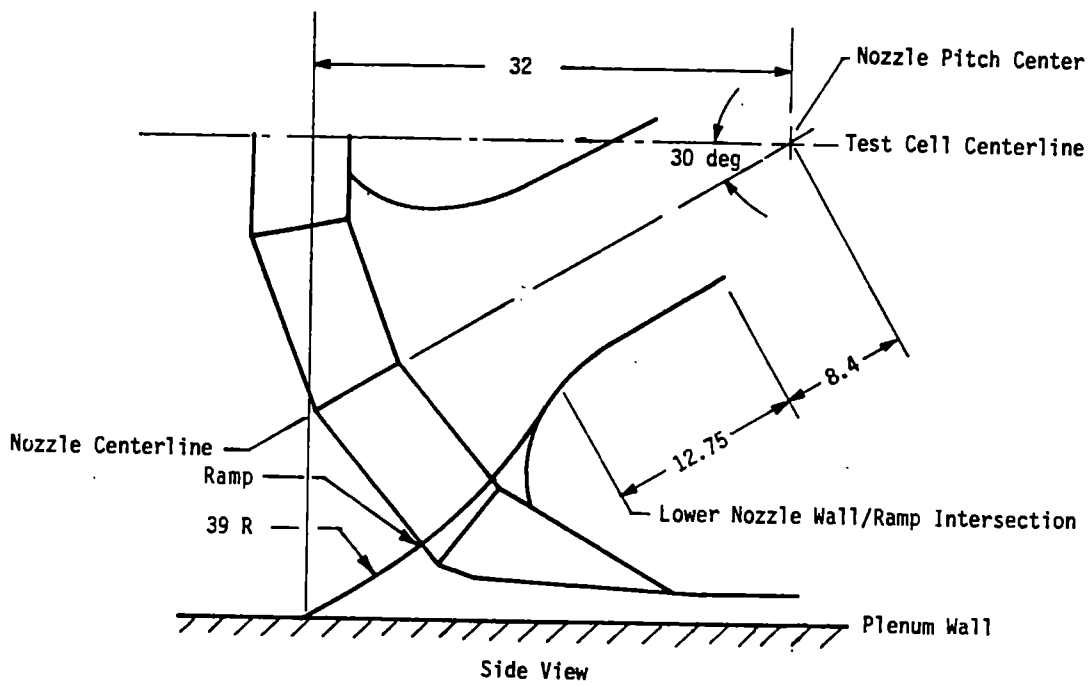
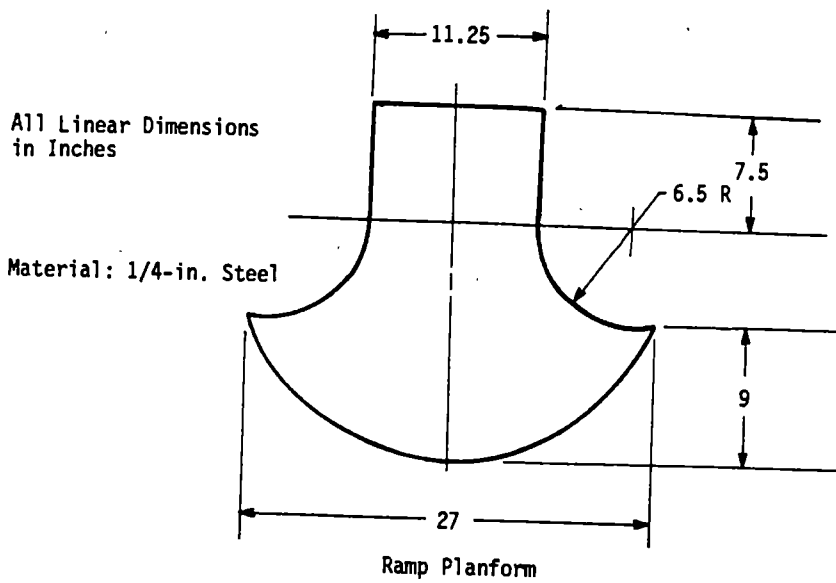
Figure 11. Modified Variable-Area Nozzle Airflow Model.





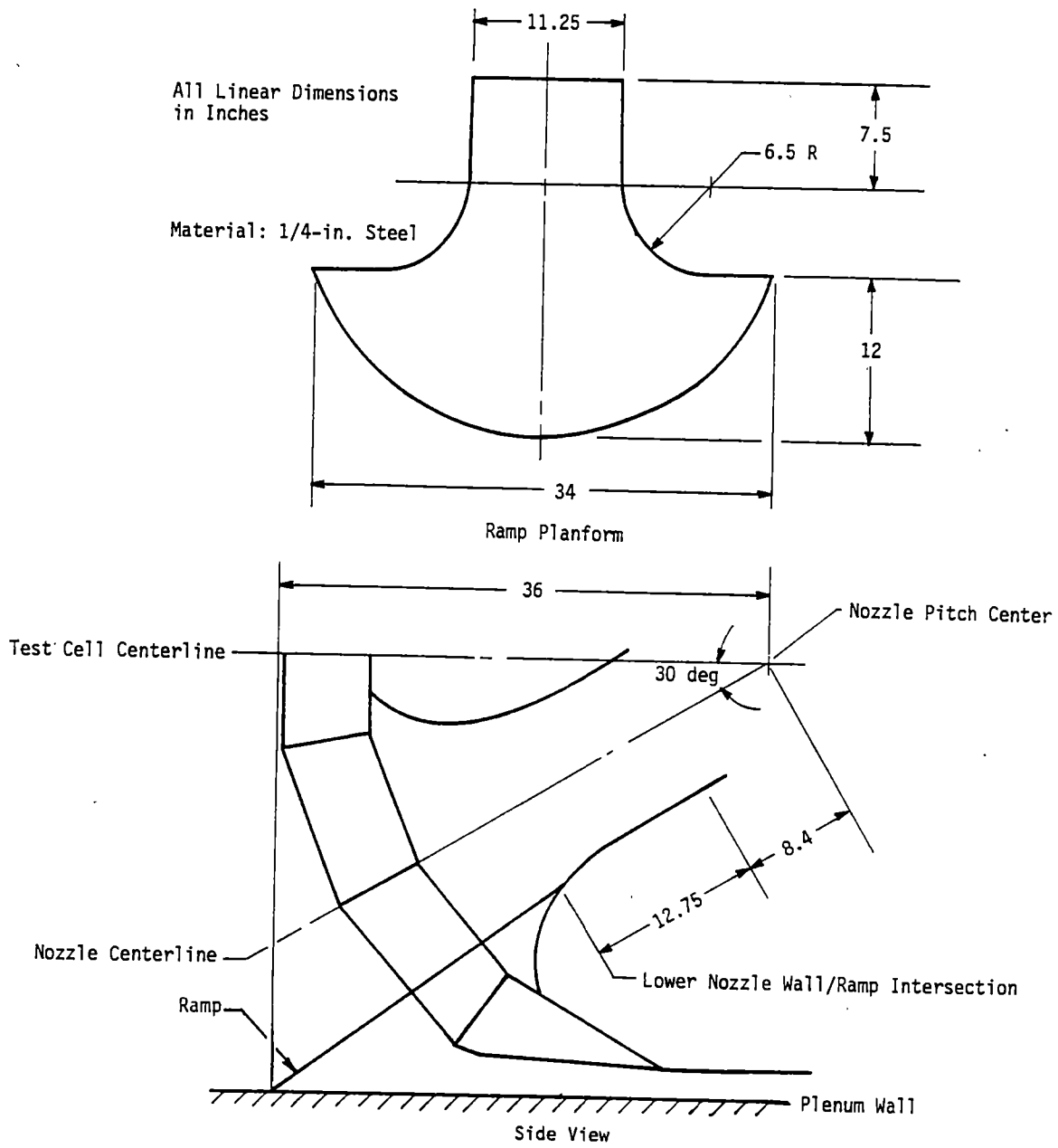
a. Installation

Figure 12. Variable-Area Nozzle Airflow Model Ramp Configurations.



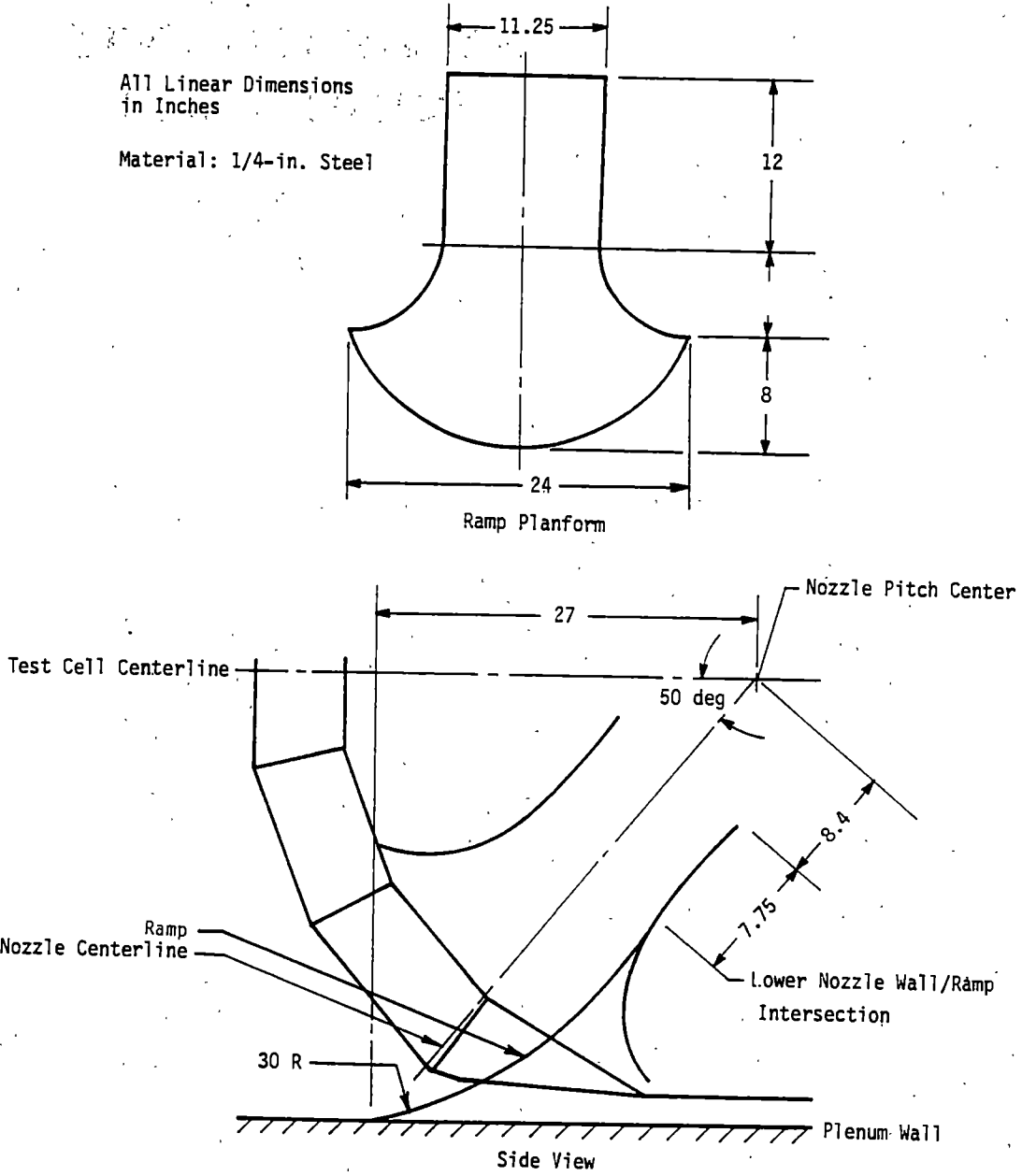
b: 30-Deg Contoured Ramp Configuration

Figure 12. Continued.



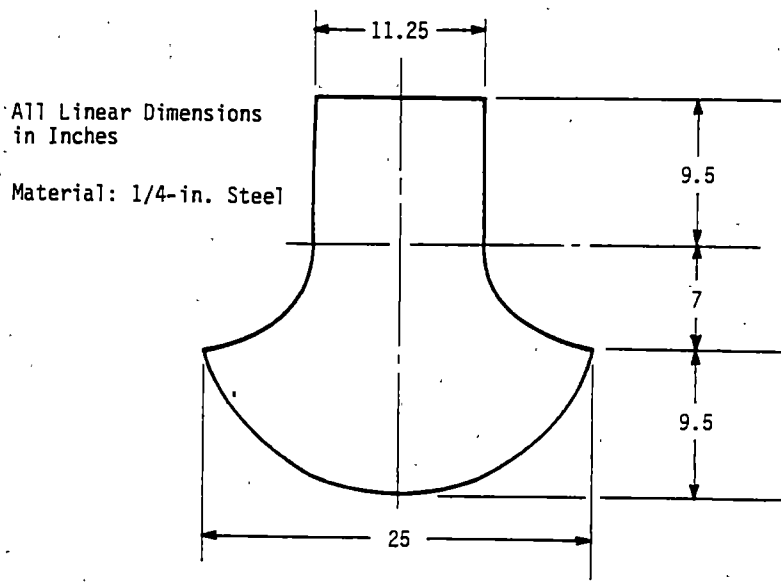
c. 30-Deg Straight Ramp Configuration

Figure 12. Continued.

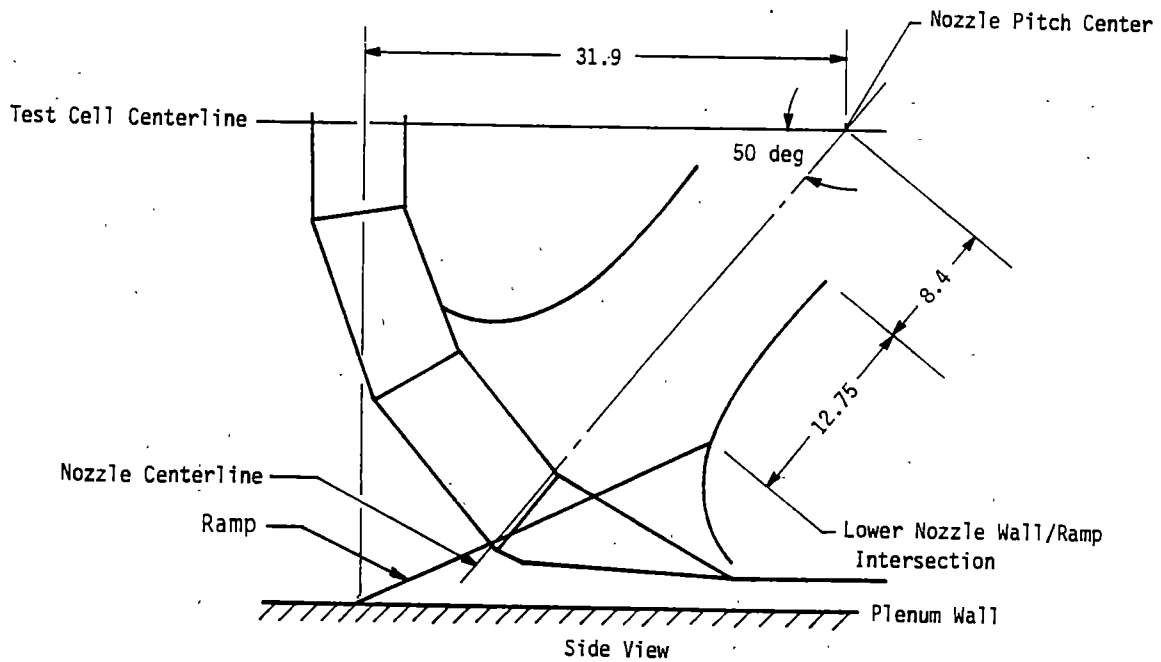


d. 50-Deg Contoured Ramp Configuration

Figure 12. Continued.



Ramp Planform



Side View

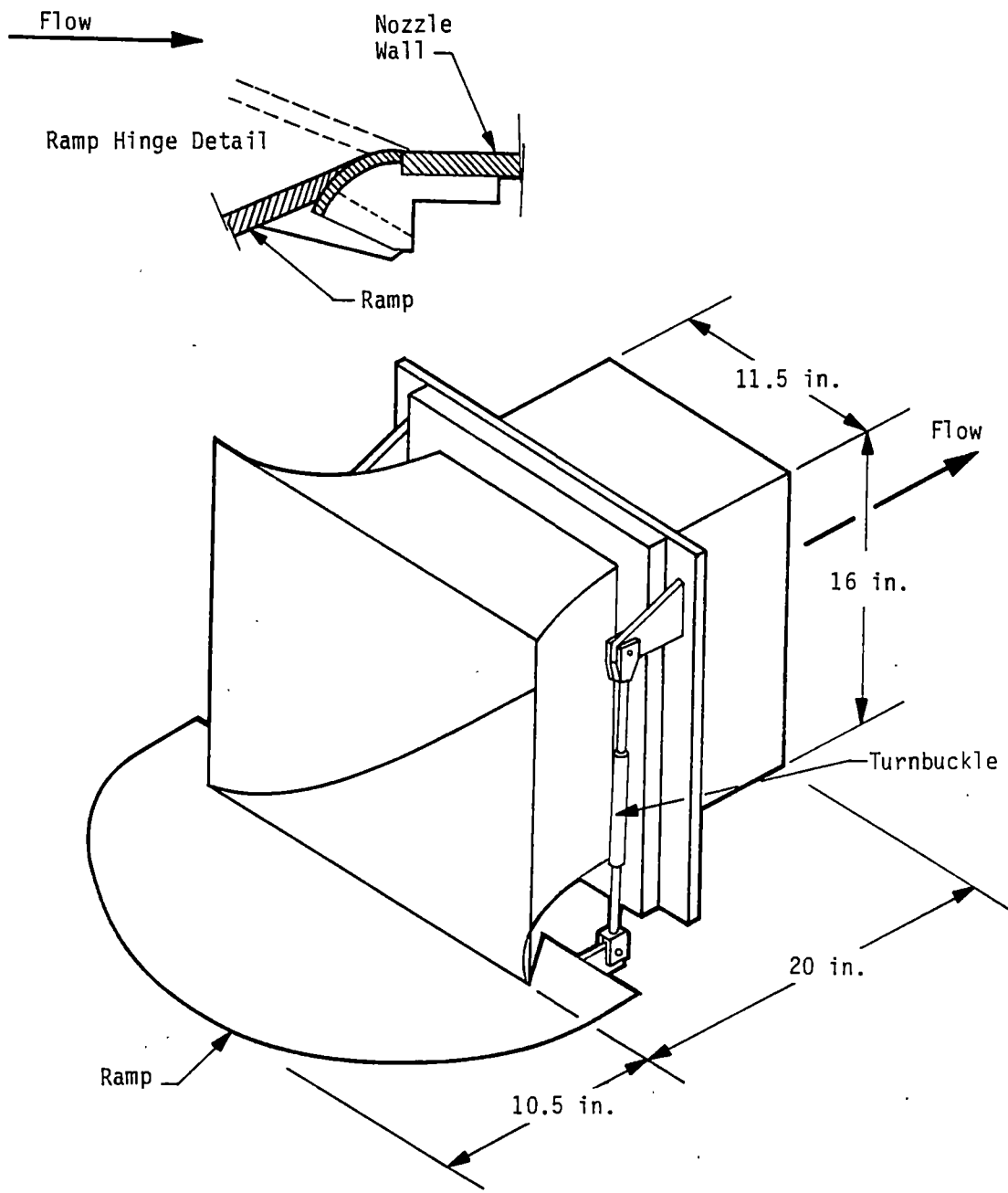
e. 50-Deg Straight Ramp Configuration

Figure 12. Continued.



f. 50-Deg Straight Ramp Installation Photograph

Figure 12. Concluded.

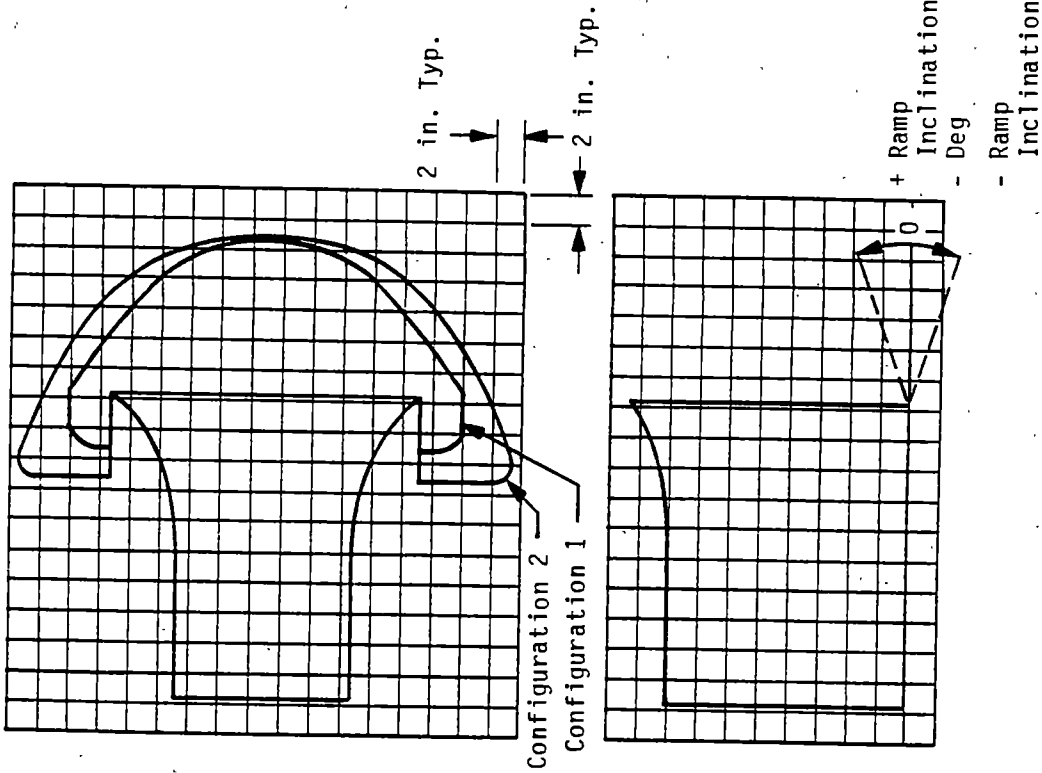


a. Isometric View

Figure 13. ASTF Subsonic Free-Jet Nozzle Airflow Model.

Basic Ramp Inclination Schedule

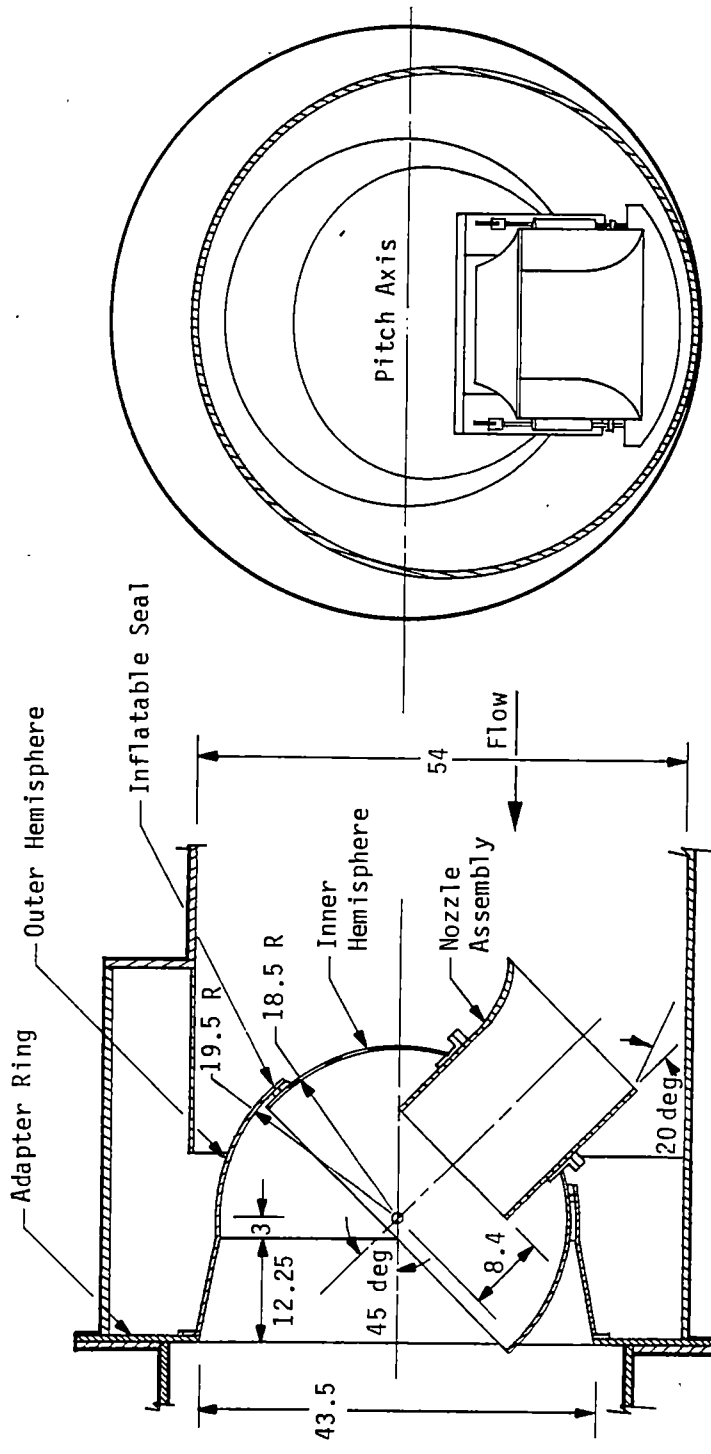
PITCH, deg	Ramp Inclination, deg
0-30	-10
35	0
40	+10
45	+20



b. Ramp Platform and Nozzle Wall Contours

Figure 13. Concluded.





All Linear Dimensions in Inches

Figure 14. Nozzle Attitude Positioning Mechanism for ASTF Free-Jet Nozzle Model Airflow Tests.

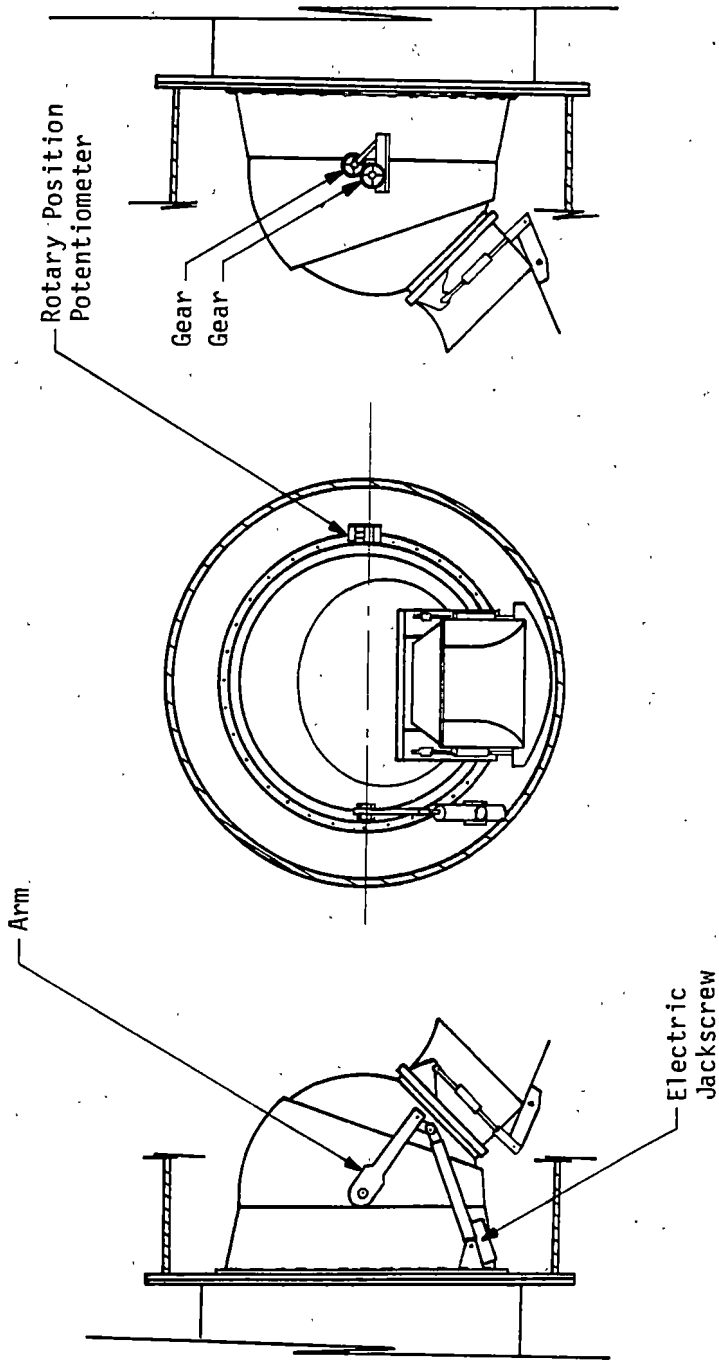
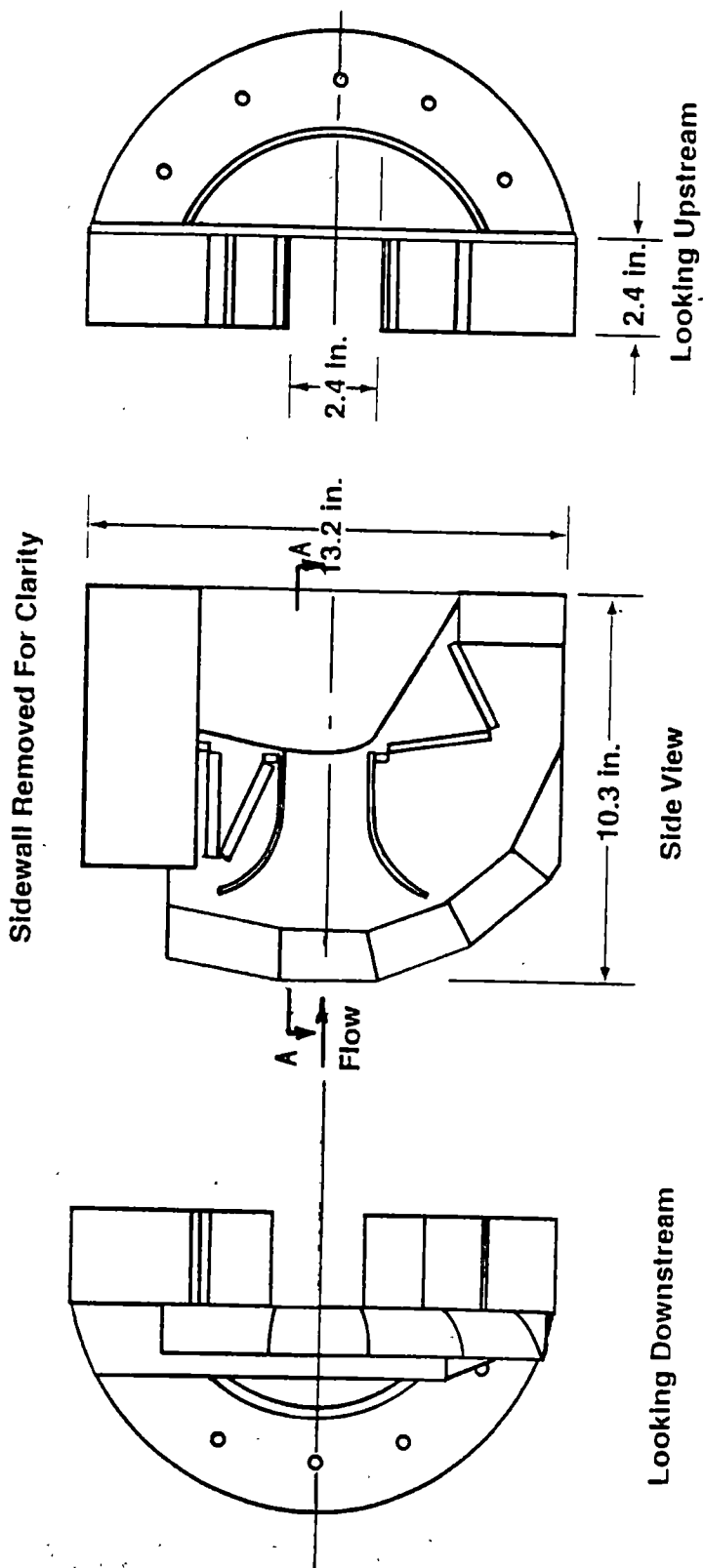


Figure 15. Nozzle Attitude Positioning Mechanism Pitch Actuator and Position Indicator.

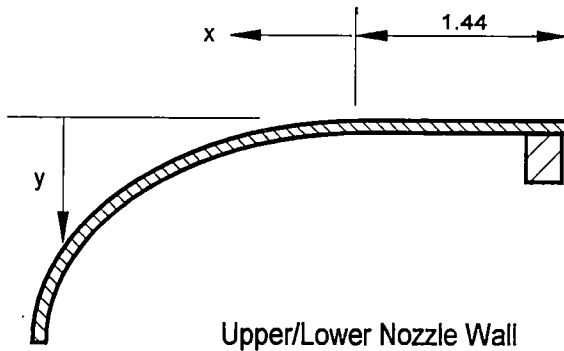


Figure 16. Photograph of ASTF Subsonic Free-Jet Nozzle Airflow Model.



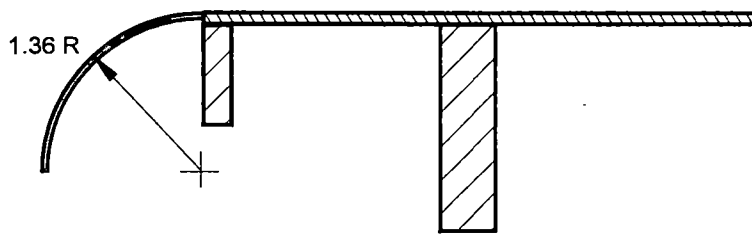
a. 3-View

Figure 17. Variable-Area Free-Jet Nozzle Water Flow Model.



x	y
0.00	0.00
0.11	0.00
0.21	0.01
0.32	0.01
0.43	0.03
0.53	0.04
0.64	0.06
0.75	0.08
0.85	0.10
0.96	0.13
1.07	0.17
1.17	0.20
1.28	0.25
1.39	0.29
1.49	0.35
1.60	0.41
1.71	0.48
1.81	0.55
1.92	0.64
2.03	0.74
2.14	0.87
2.24	1.03
2.35	1.27
2.40	1.60

All Dimensions in Inches



Nozzle Sidewall Section A-A (Fig. 17a)

b. Wall Contours

Figure 17. Concluded.

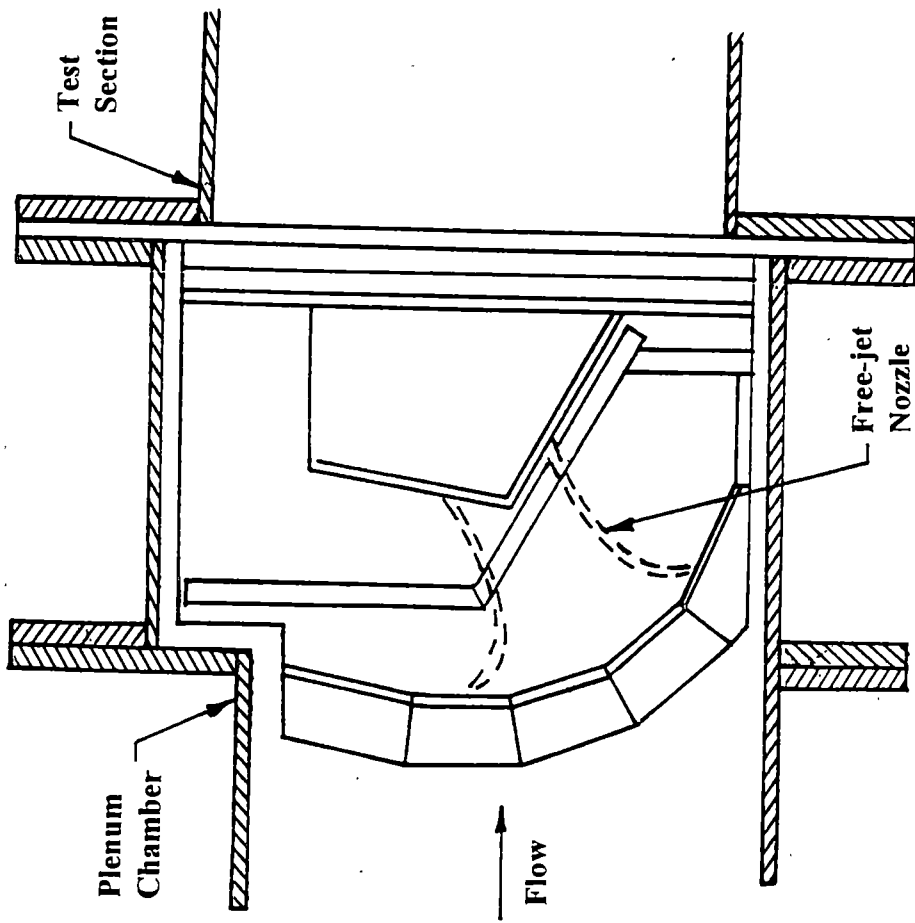
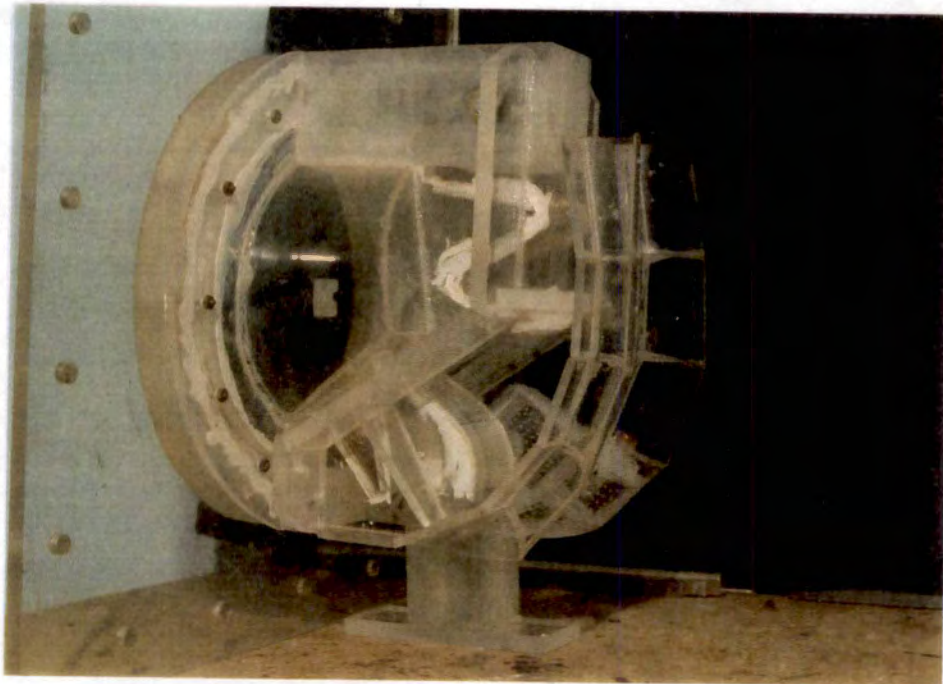
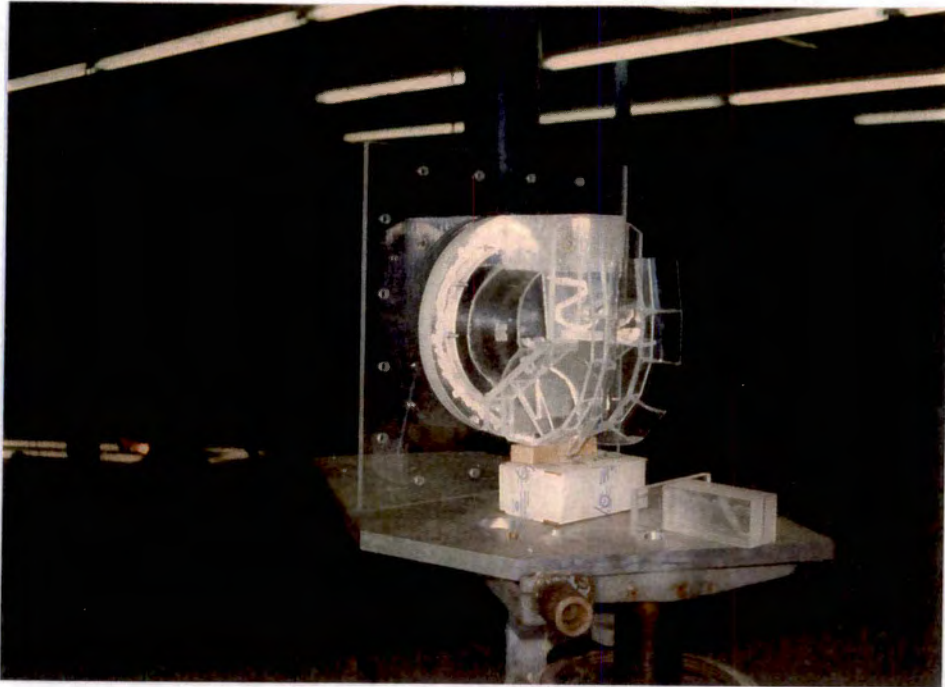


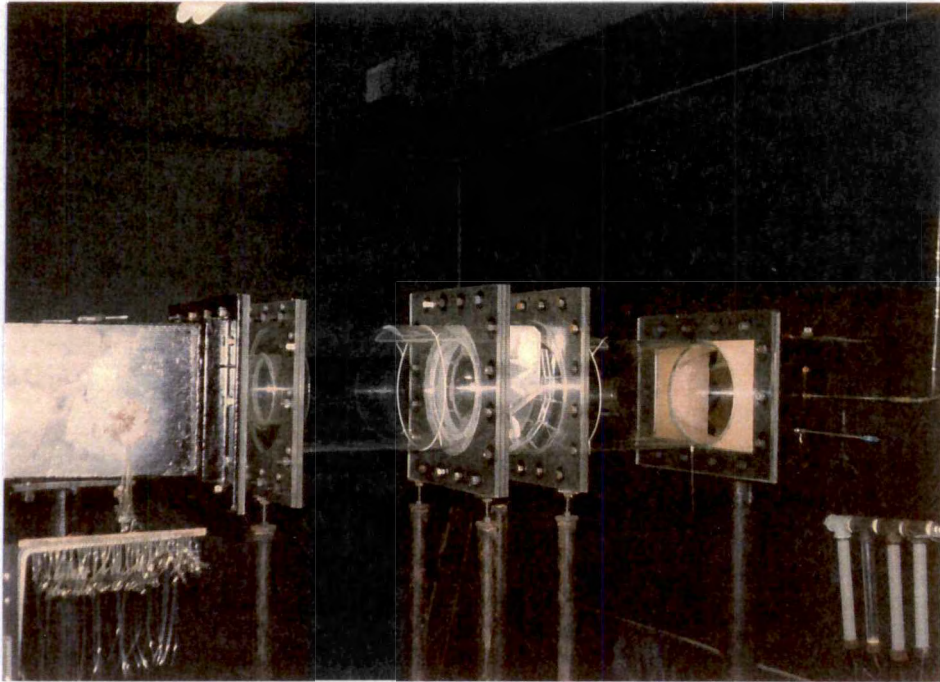
Figure 18. Variable-Area Free-Jet Nozzle Water Tunnel Installation.



a. Nozzle Assembly

Figure 19. Photograph of Variable-Area Nozzle Water Flow Model.

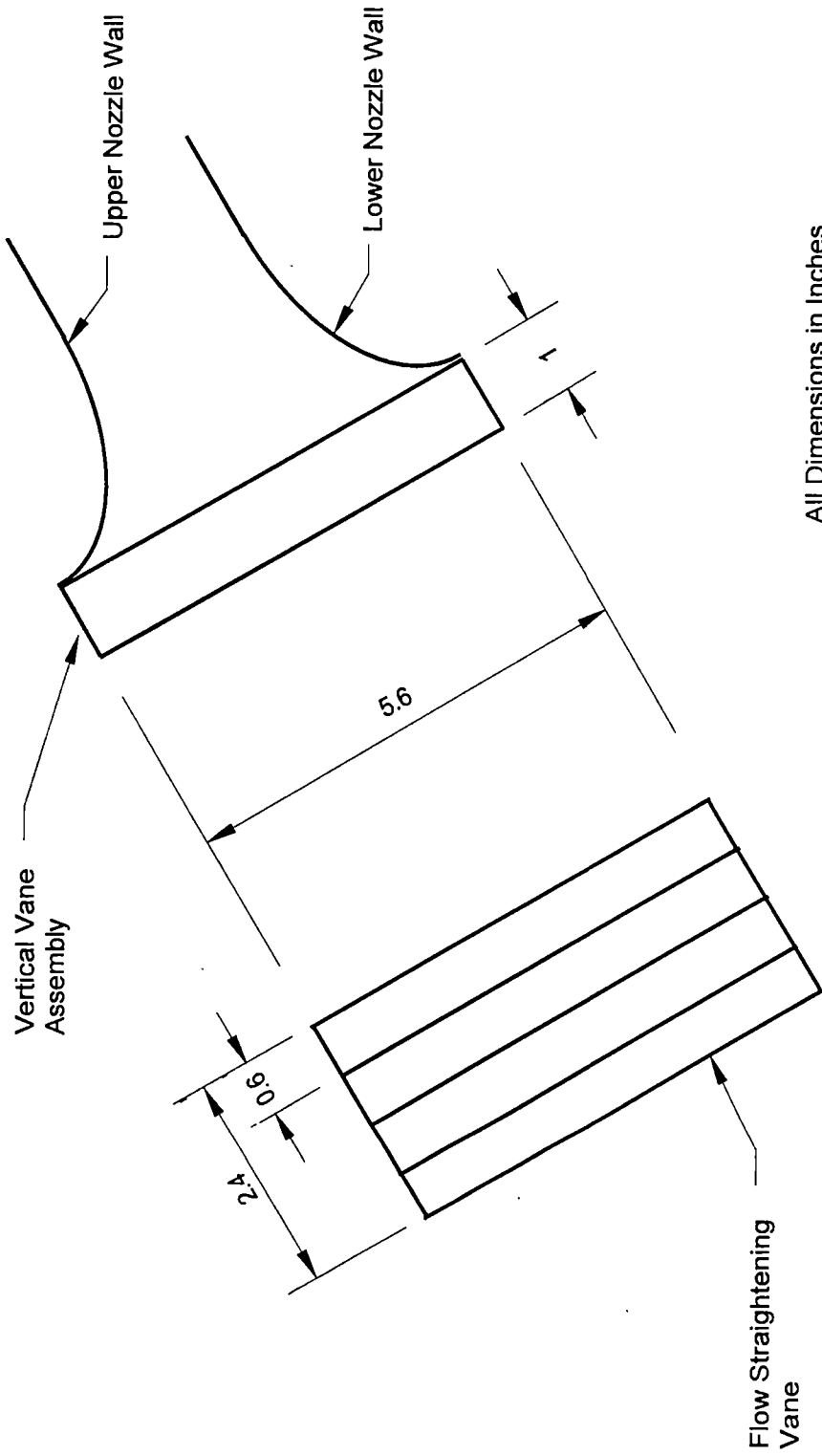




b. Nozzle Installation in Water Tunnel

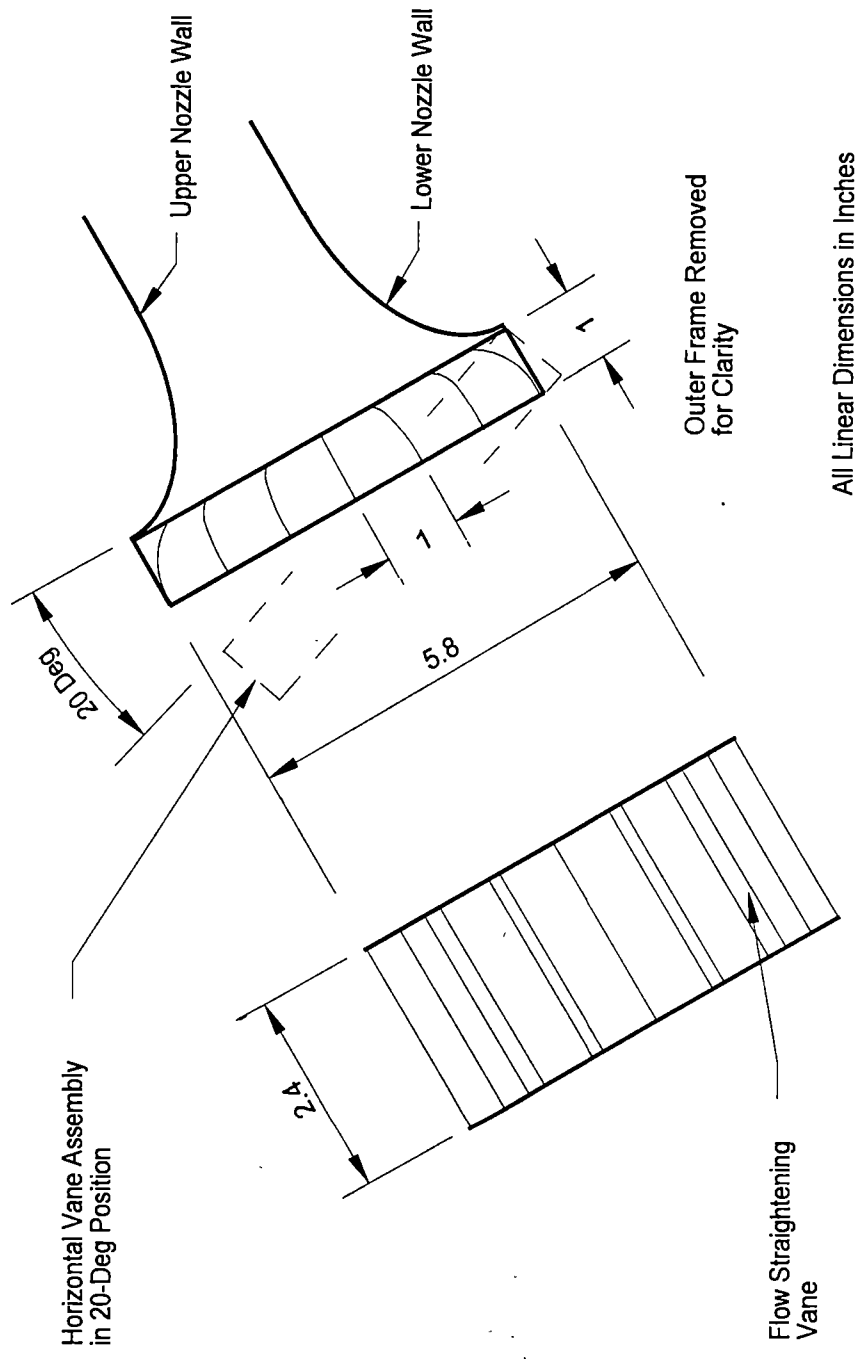
Figure 19. Concluded.





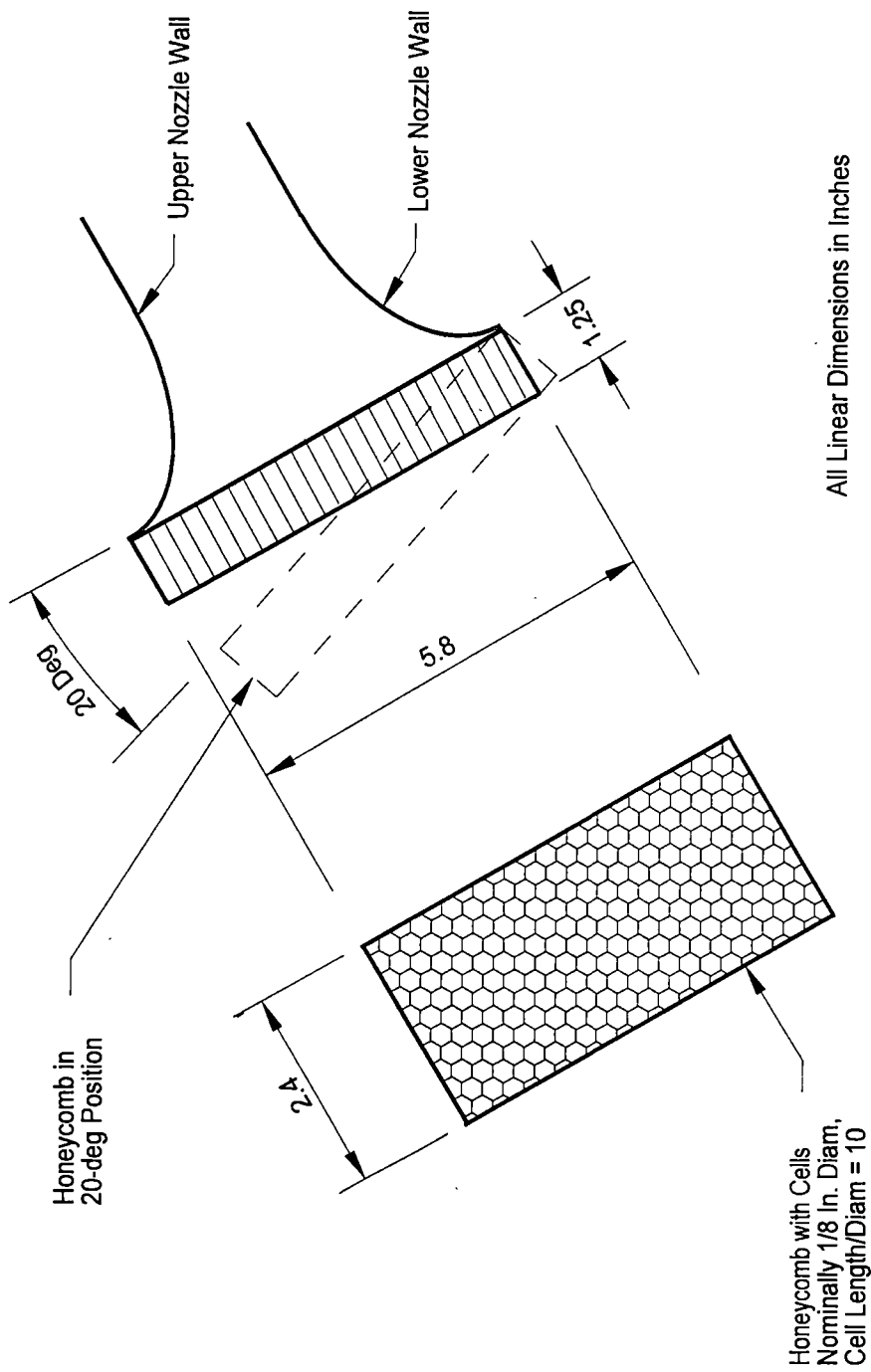
a. Vertical Vane Assembly

Figure 20. Variable-Area Nozzle Water Tunnel Model Flow Straightener Configurations.



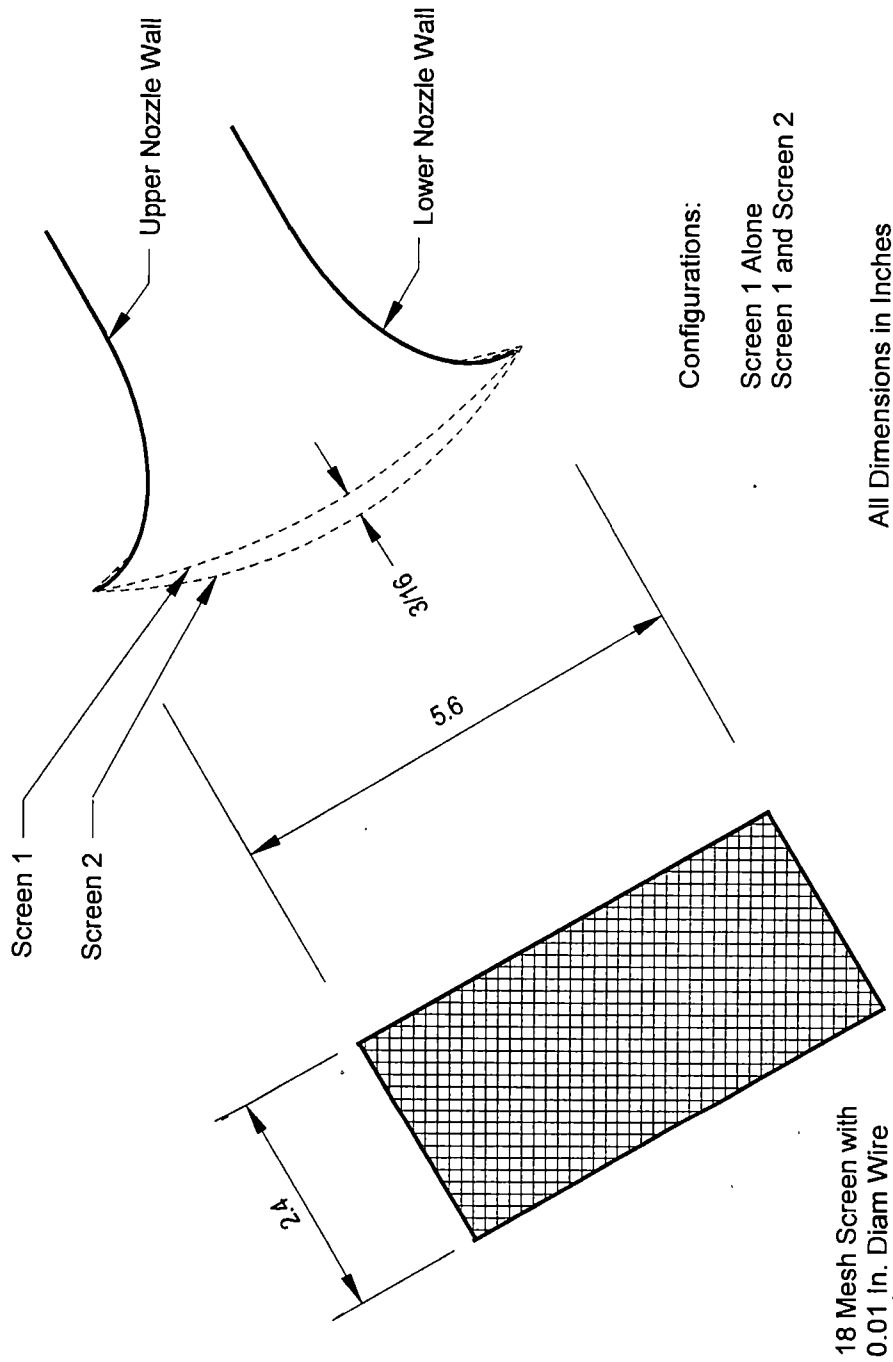
b. Horizontal Vane Assembly

Figure 20. Continued.



c. Honeycomb.

Figure 20. Continued.



d. Flow Screens.

Figure 20. Concluded.

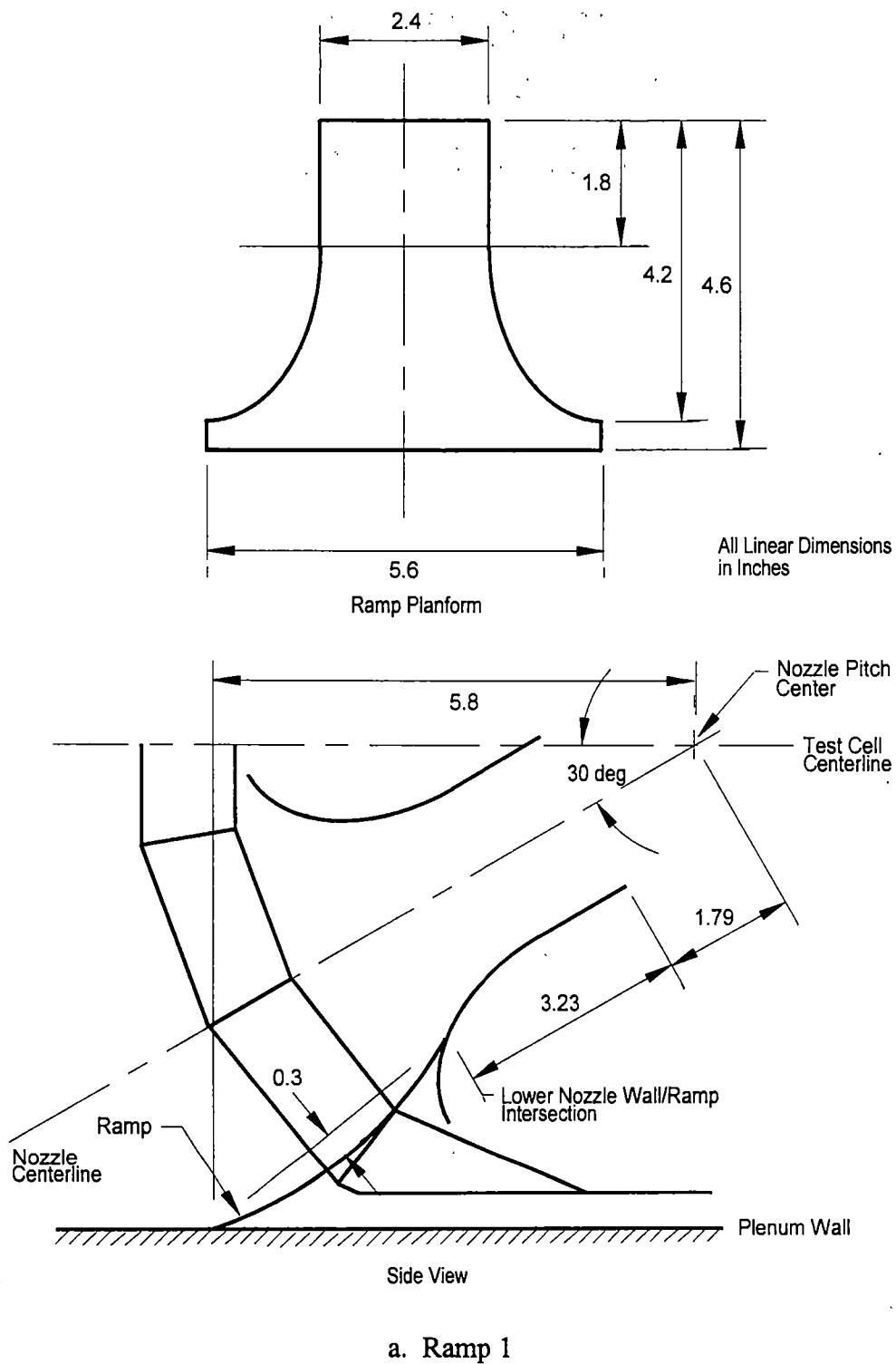
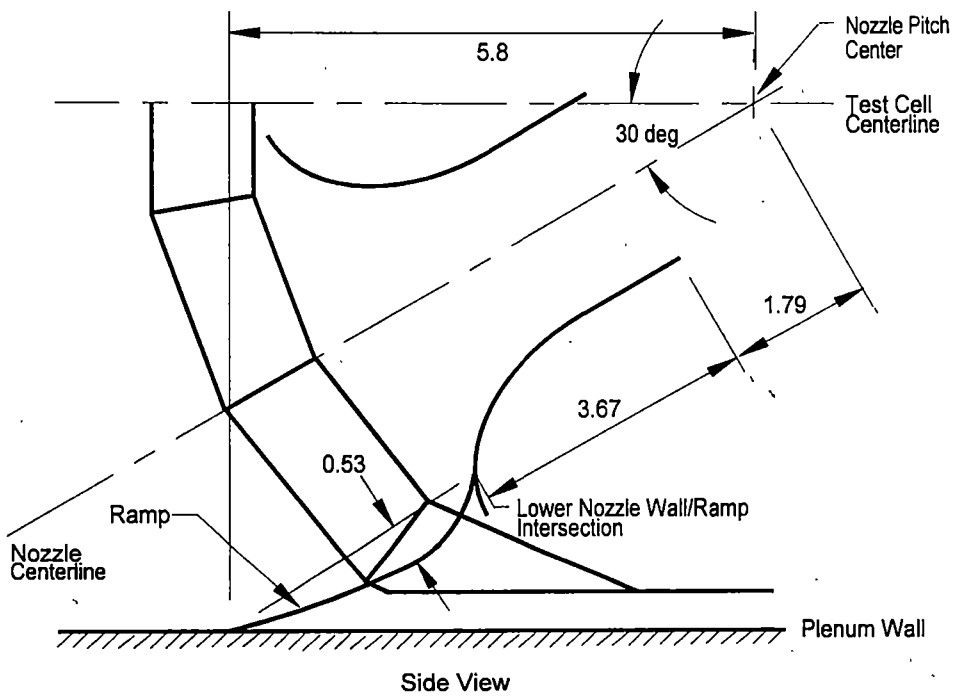
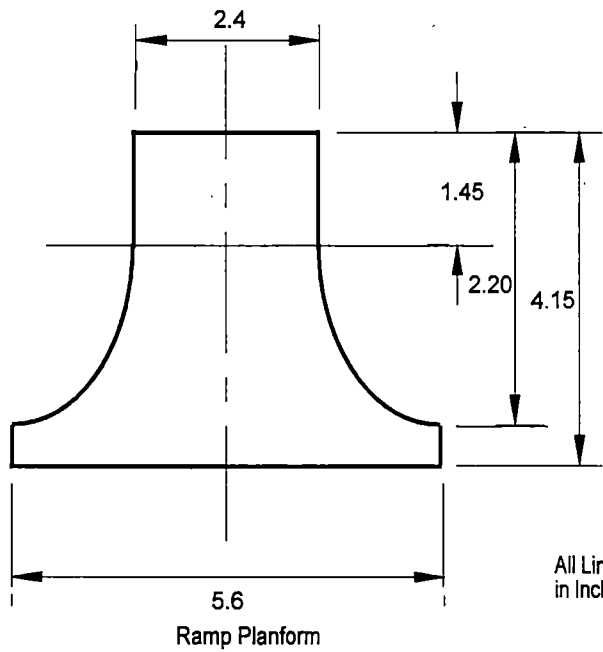
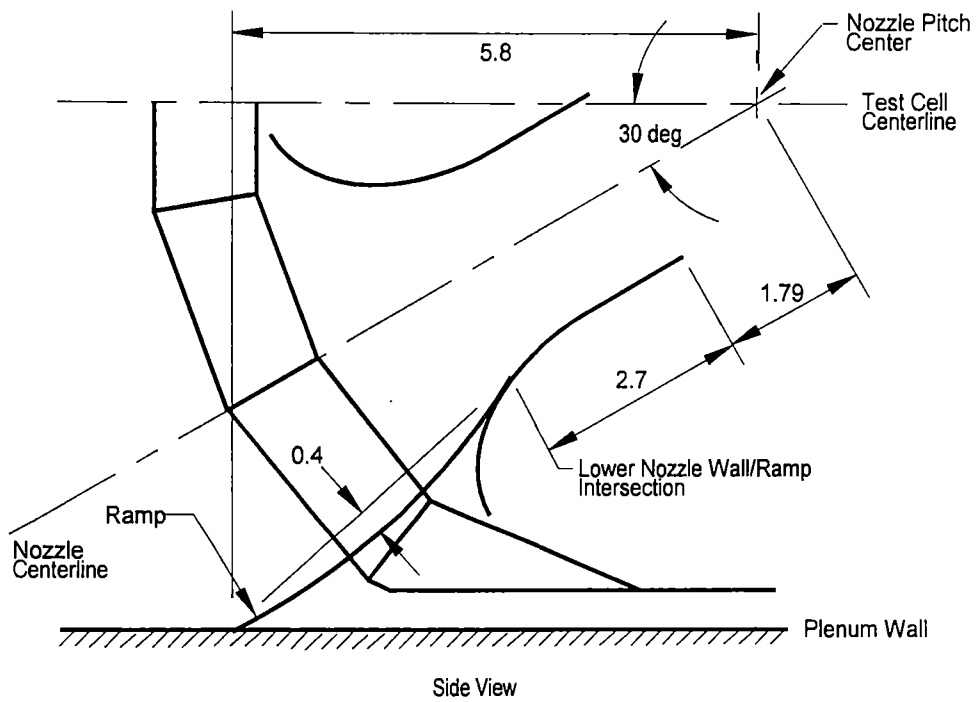
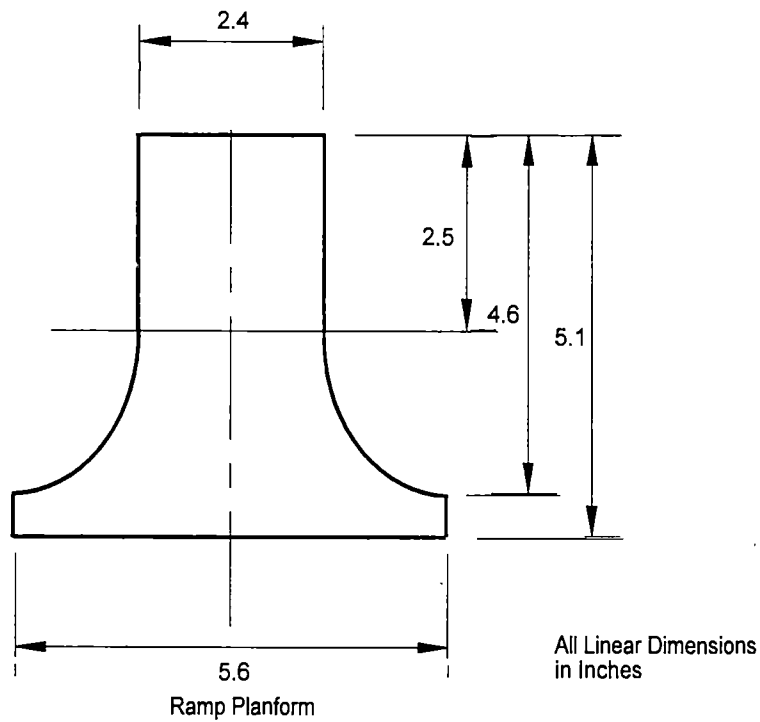


Figure 21. Variable-Area Nozzle Water Flow Model Ramp Configurations.



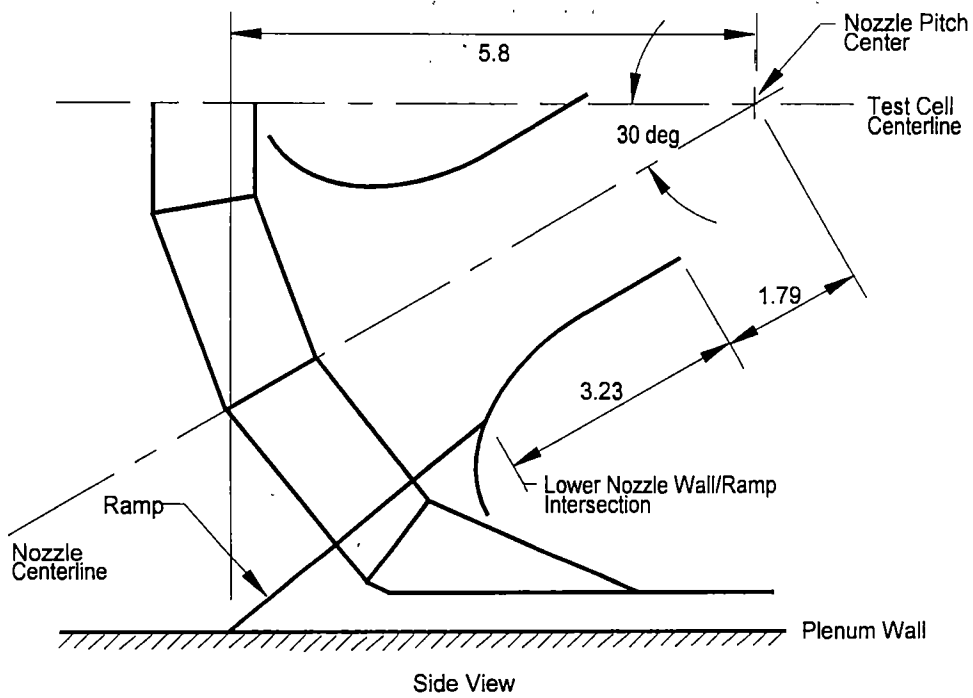
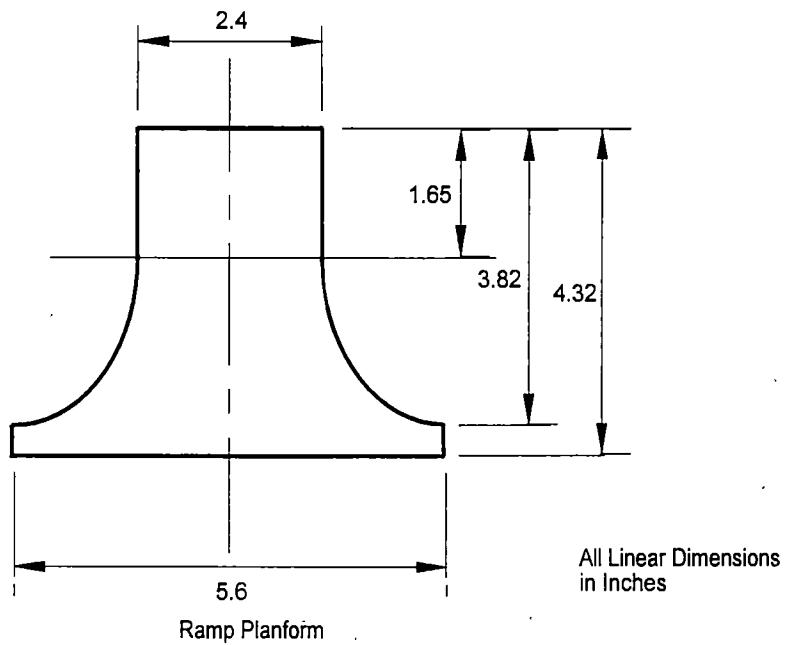
b. Ramp 2

Figure 21. Continued.



c. Ramp 3

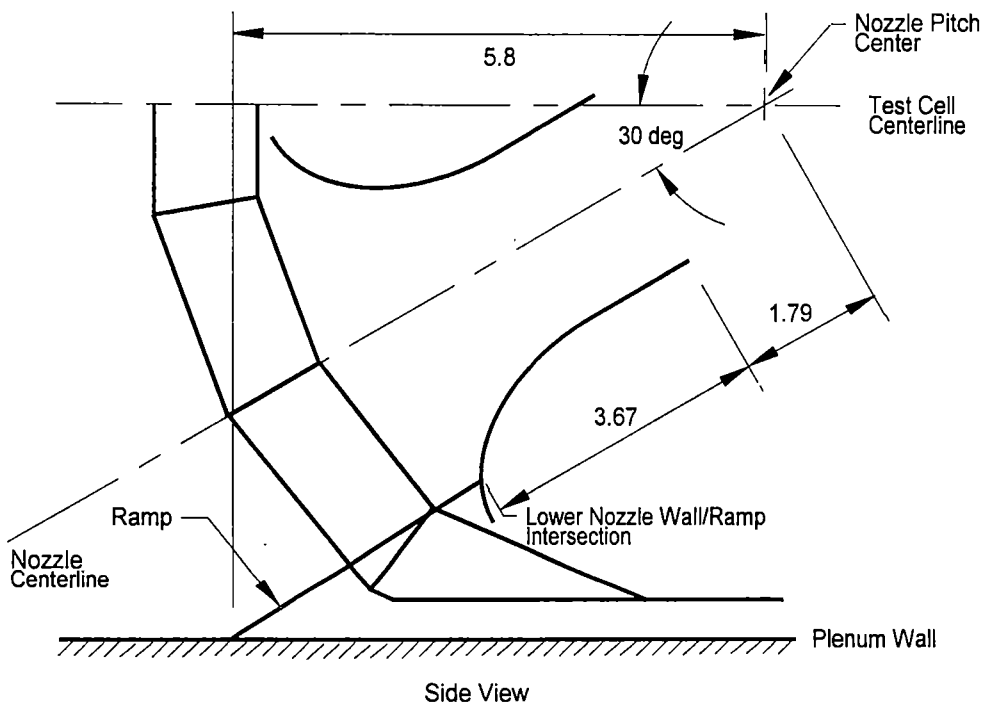
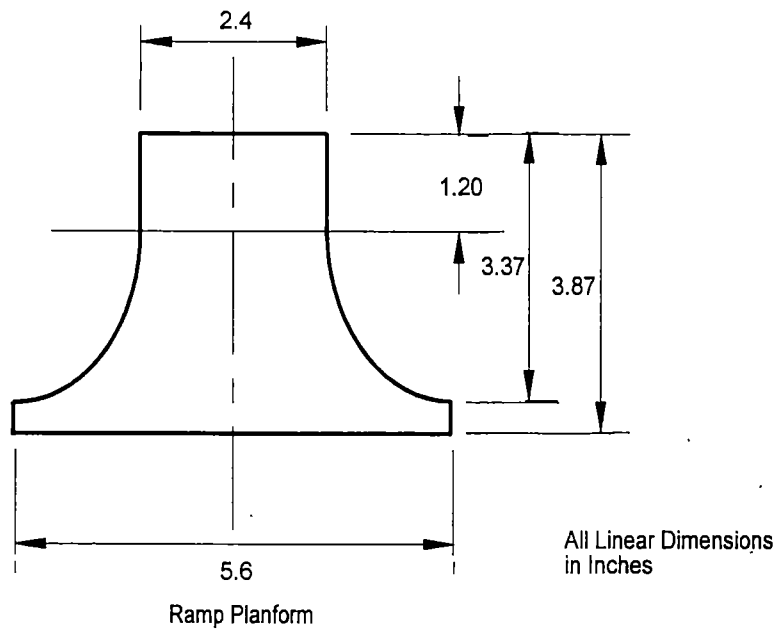
Figure 21. Continued.



d. Ramp 4

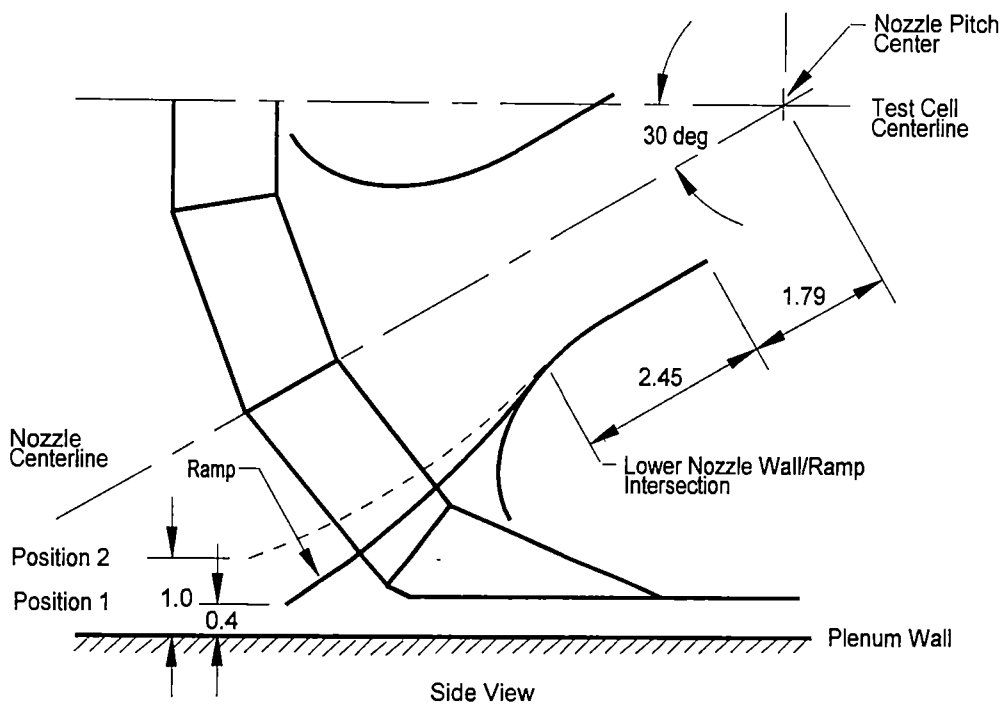
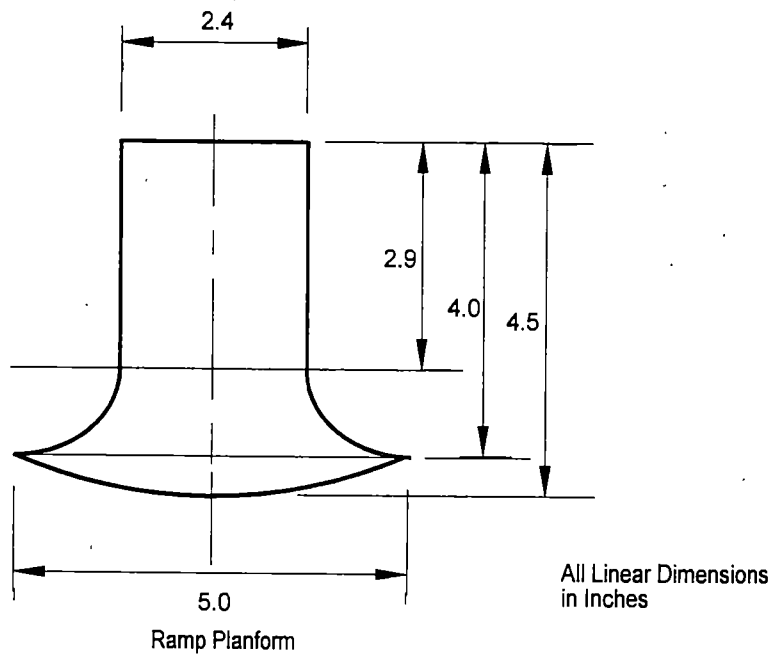
Figure 21. Continued.





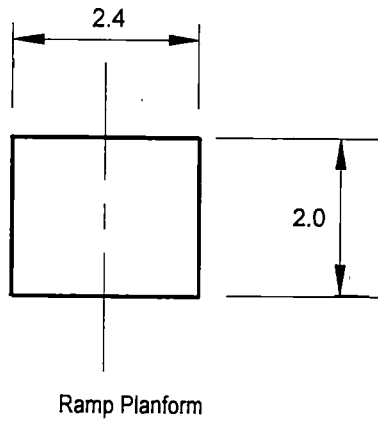
e. Ramp 5

Figure 21. Continued.



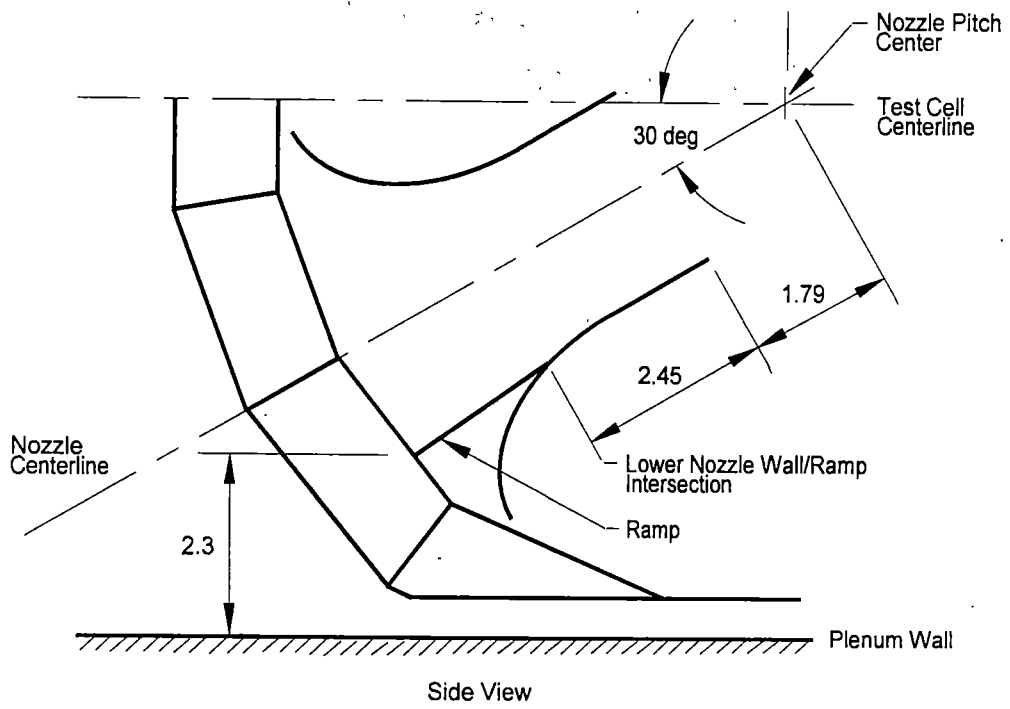
f. Ramp 21

Figure 21. Continued.



Ramp Planform

All Linear Dimensions in Inches



Side View

g. Ramp 22

Figure 21. Continued.



h. Photograph of Typical Ramp

Figure 21. Concluded.

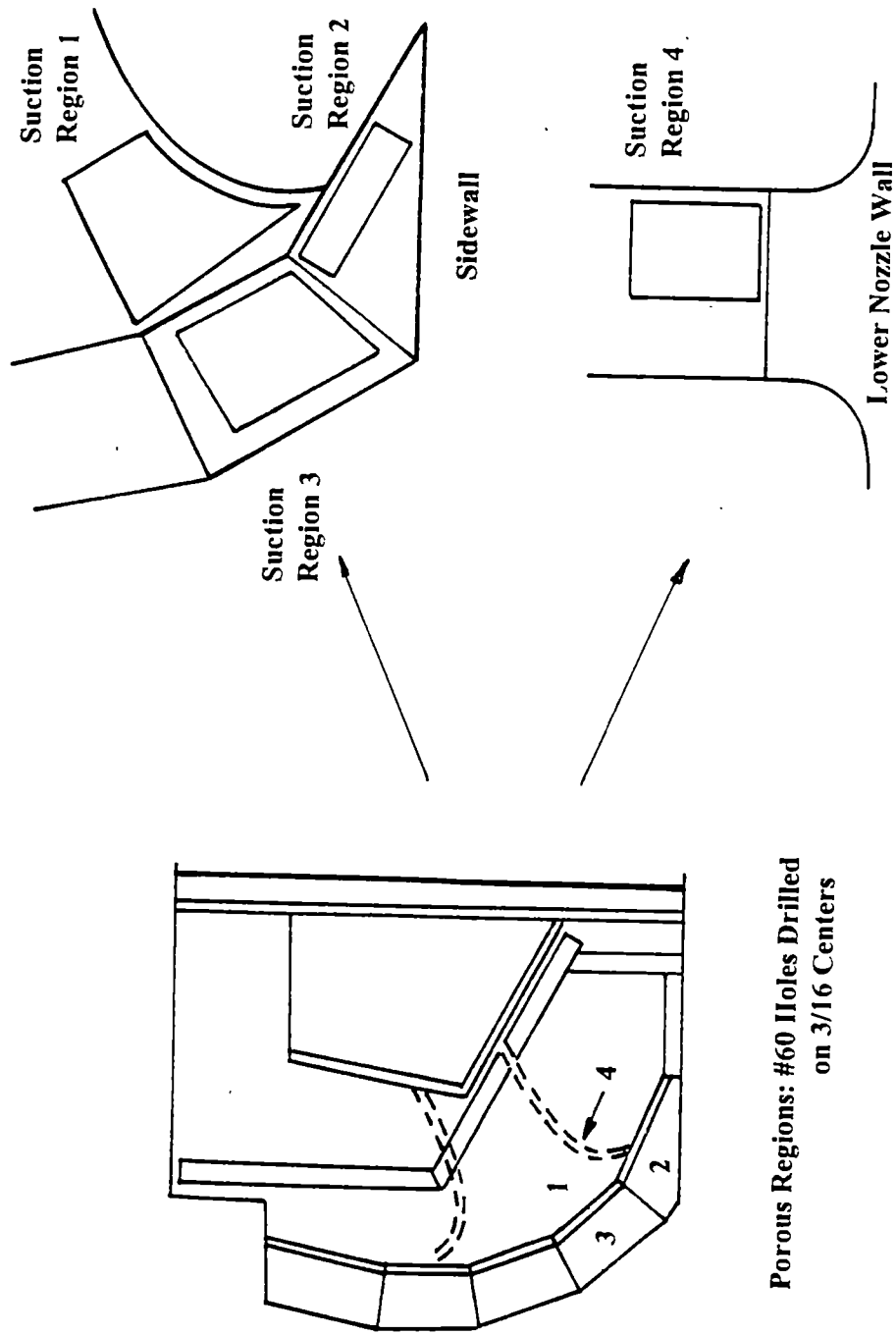


Figure 22. Locations of Suction Regions on Variable-Area Nozzle Water Flow Model.

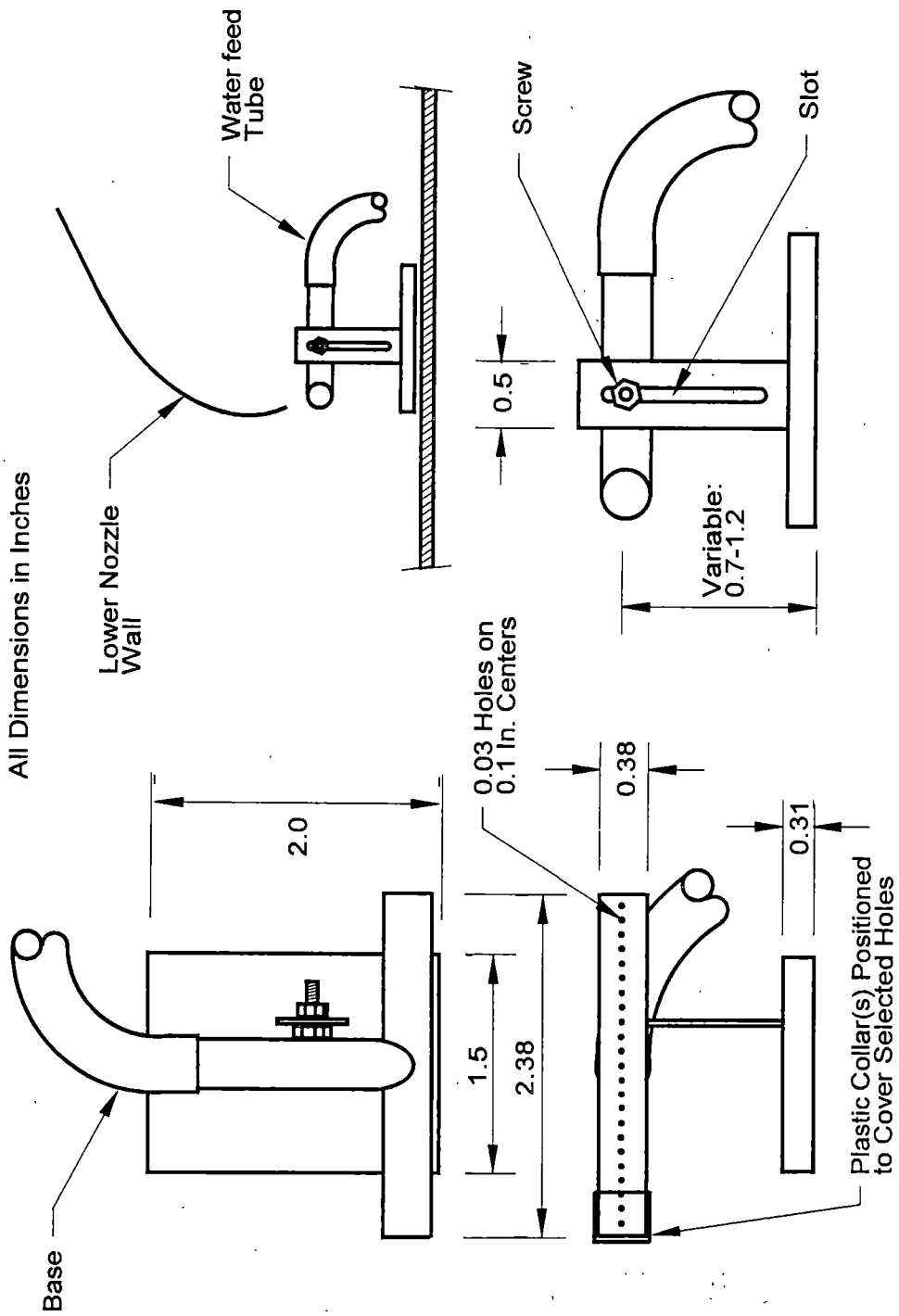
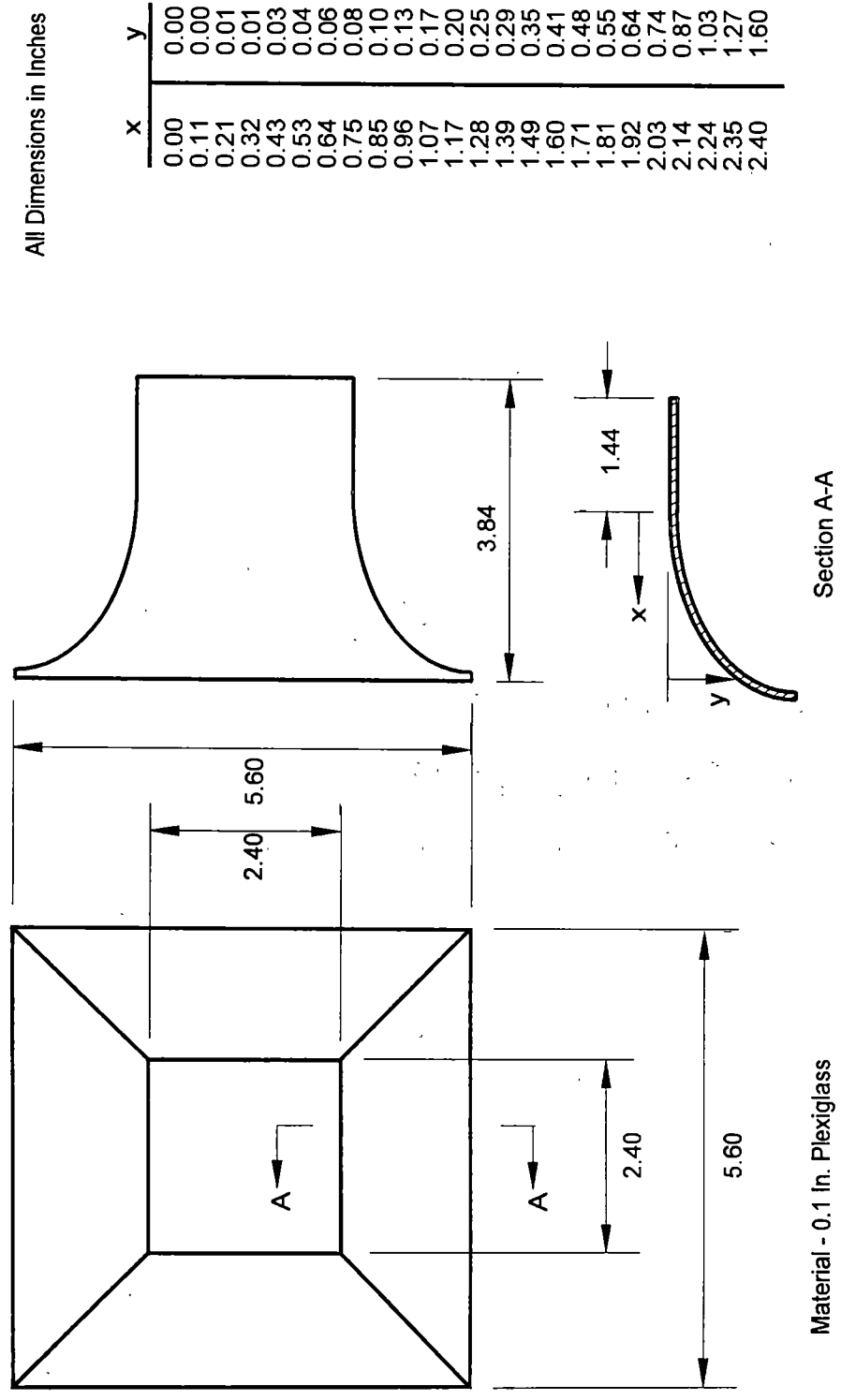


Figure 23. Piccolo Tube Assembly for Variable-Area Nozzle Model Blowing Experiments in Water Tunnel.

All Dimensions in Inches

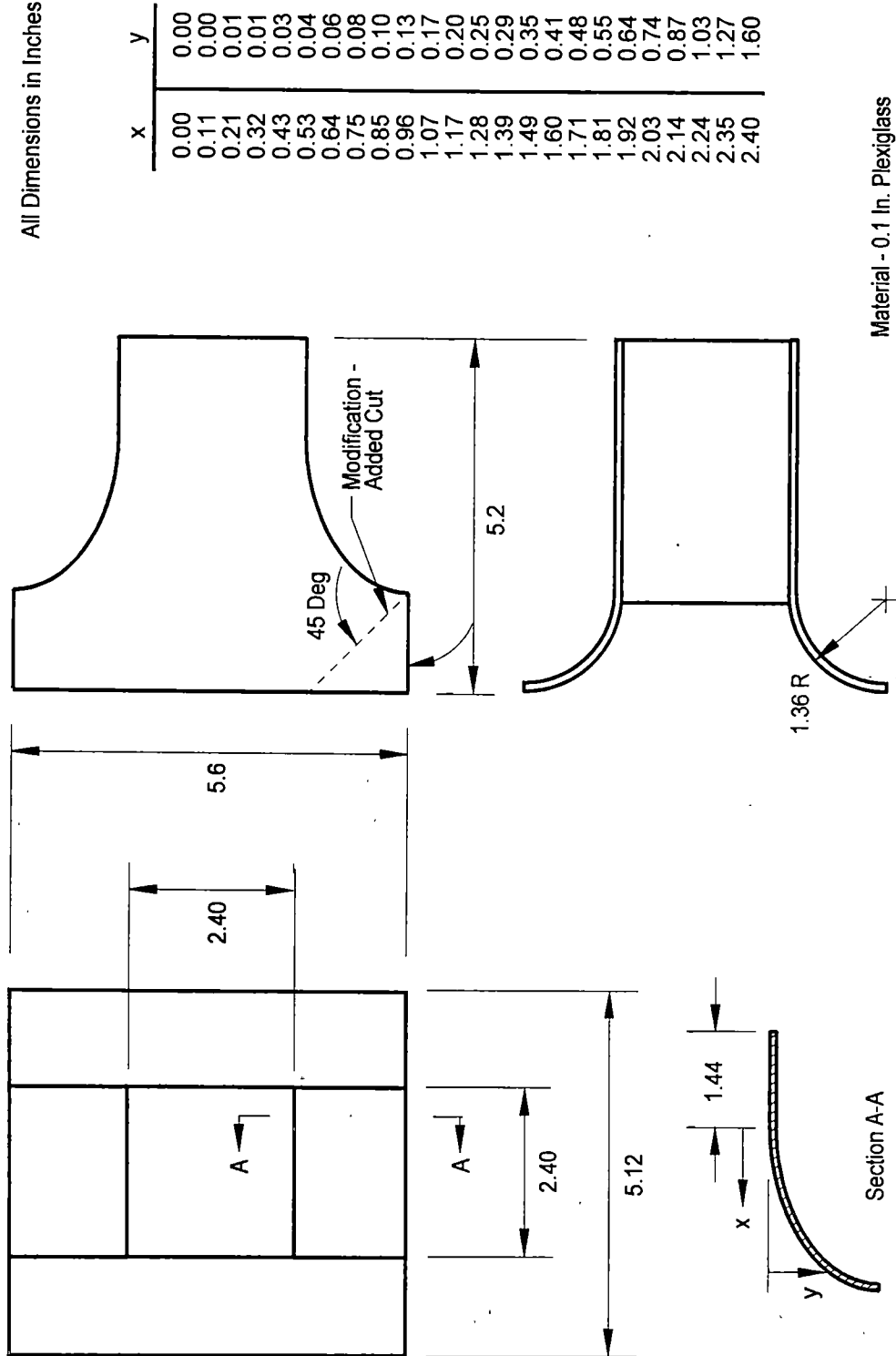


Material - 0.1 In. Plexiglass

a. 2-D Nozzle with Symmetrical Contraction Section (2-D SYM Nozzle)

Figure 24. Generic 2-D Free-Jet Nozzle Water Flow Models.

All Dimensions in Inches

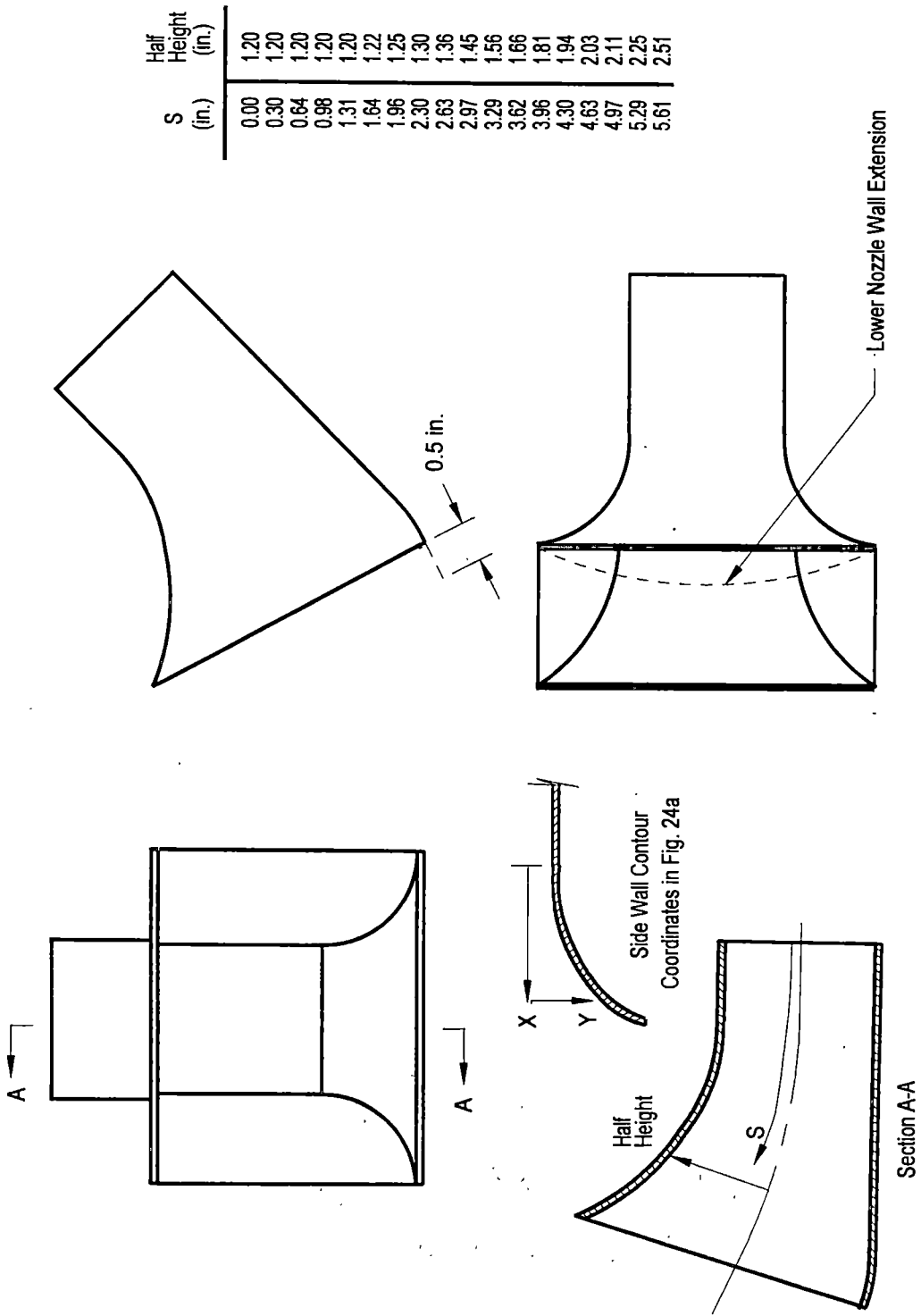


x	y
0.00	0.00
0.11	0.00
0.21	0.01
0.32	0.01
0.43	0.03
0.53	0.04
0.64	0.06
0.75	0.08
0.85	0.10
0.96	0.13
1.07	0.17
1.17	0.20
1.28	0.25
1.39	0.29
1.49	0.35
1.60	0.41
1.71	0.48
1.81	0.55
1.92	0.64
2.03	0.74
2.14	0.87
2.24	1.03
2.35	1.27
2.40	1.60

b. 2-D Nozzle with Asymmetric Contraction Section (2-D ASY Nozzle)

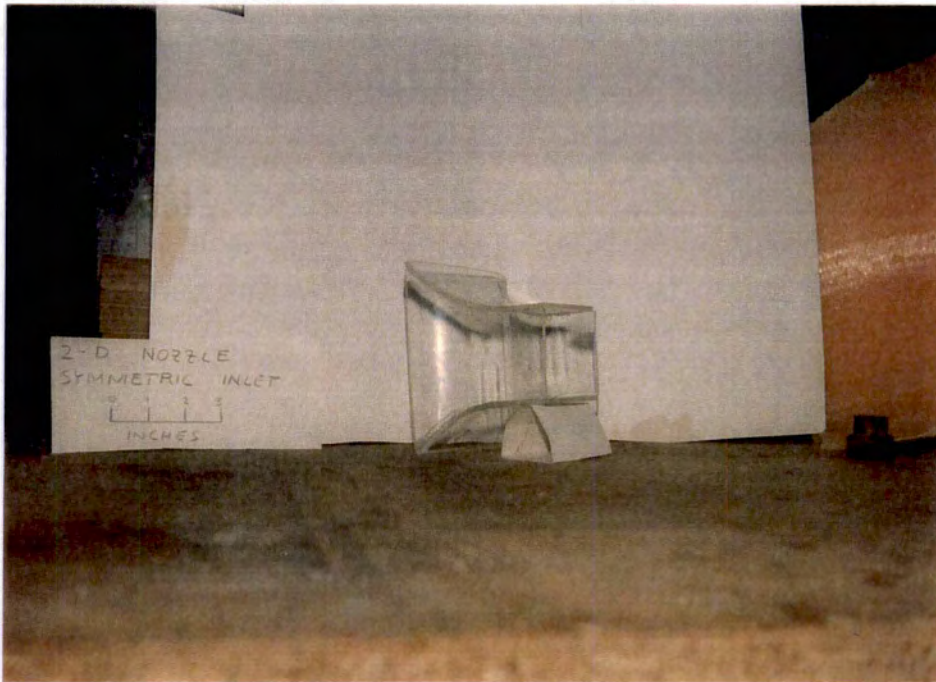
Figure 24. Continued.



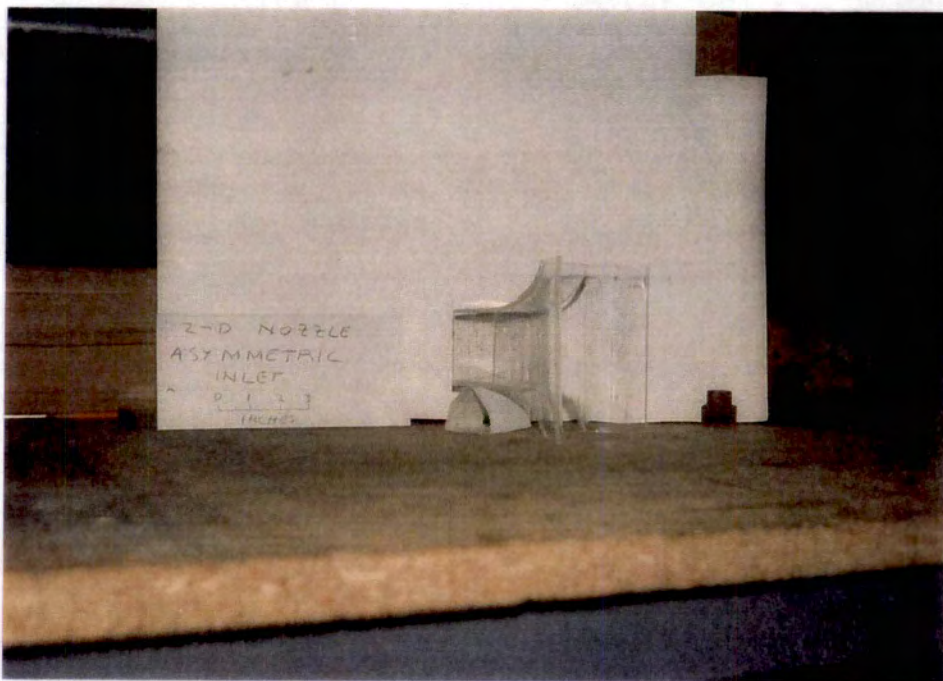


c. 2-D Nozzle with Bend for High Pitch Angles (High- $\alpha$  Nozzle)

Figure 24. Continued.

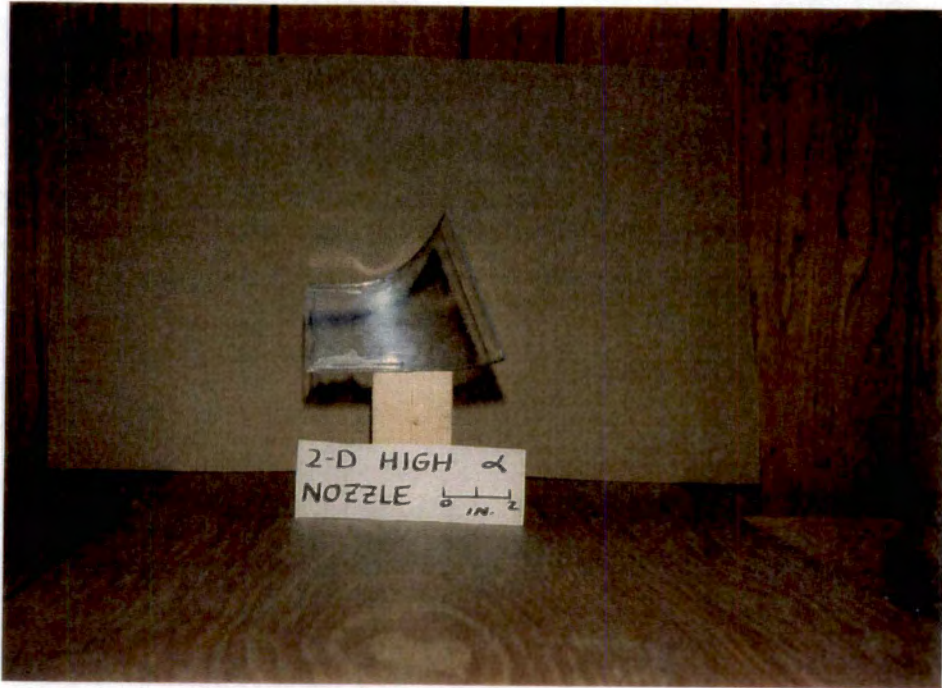


d. Photograph of 2-D SYM Nozzle



e. Photograph of 2-D ASY Nozzle

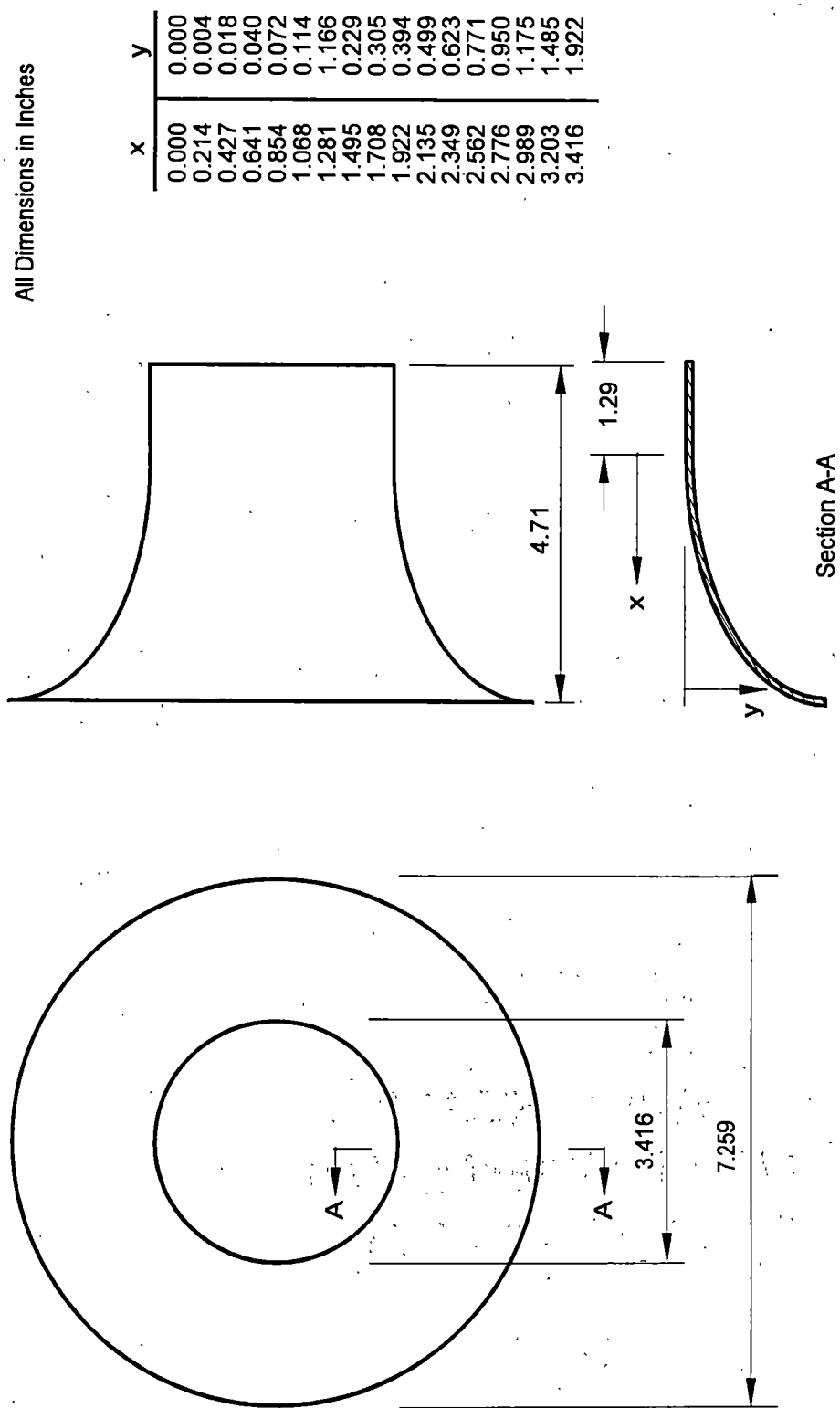
Figure 24. Continued.



f. Photographs of High- $\alpha$  Nozzle

Figure 24. Concluded.

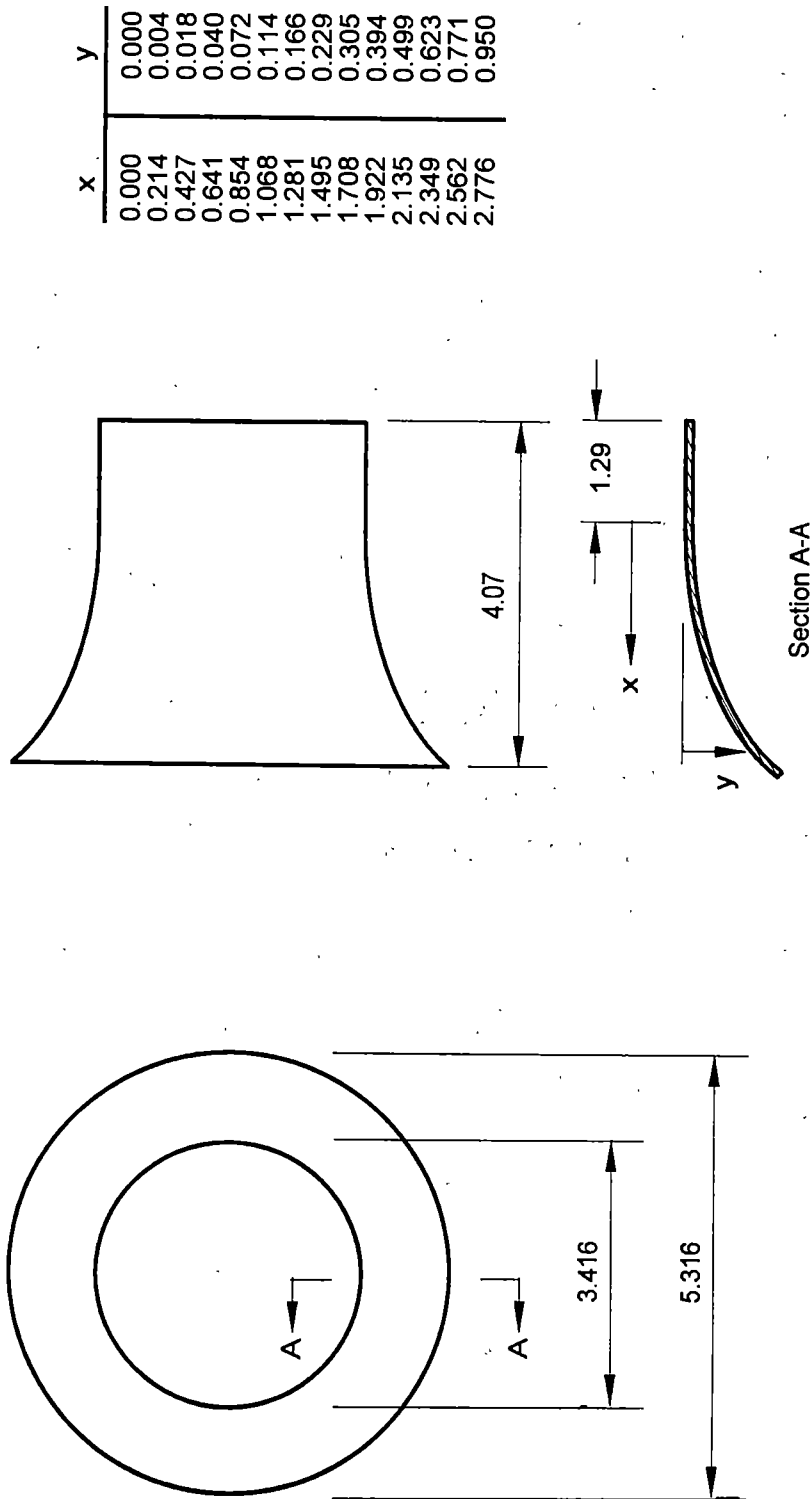
All Dimensions in Inches



a. Long Axisymmetric Nozzle with Contraction Ratio of 4.5 (LONG AXI Nozzle)

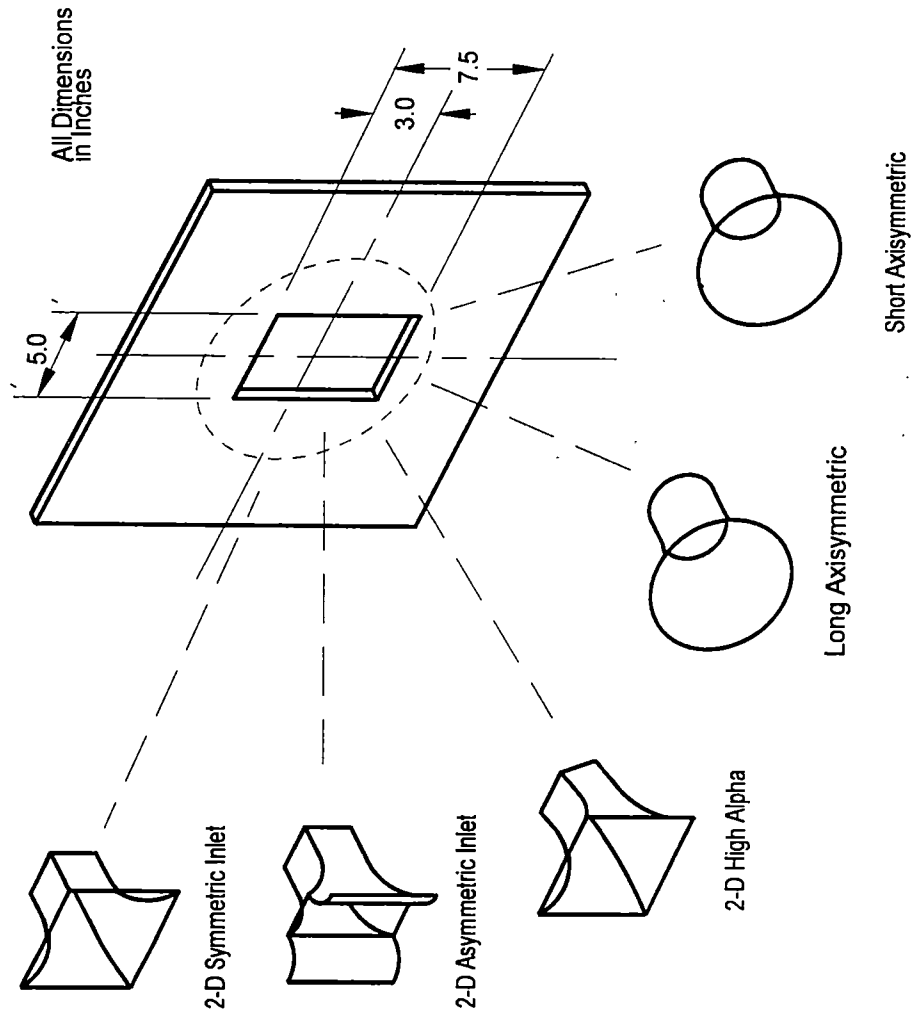
Figure 25. Generic Axisymmetric Nozzle Water Flow Models.

All Dimensions in Inches



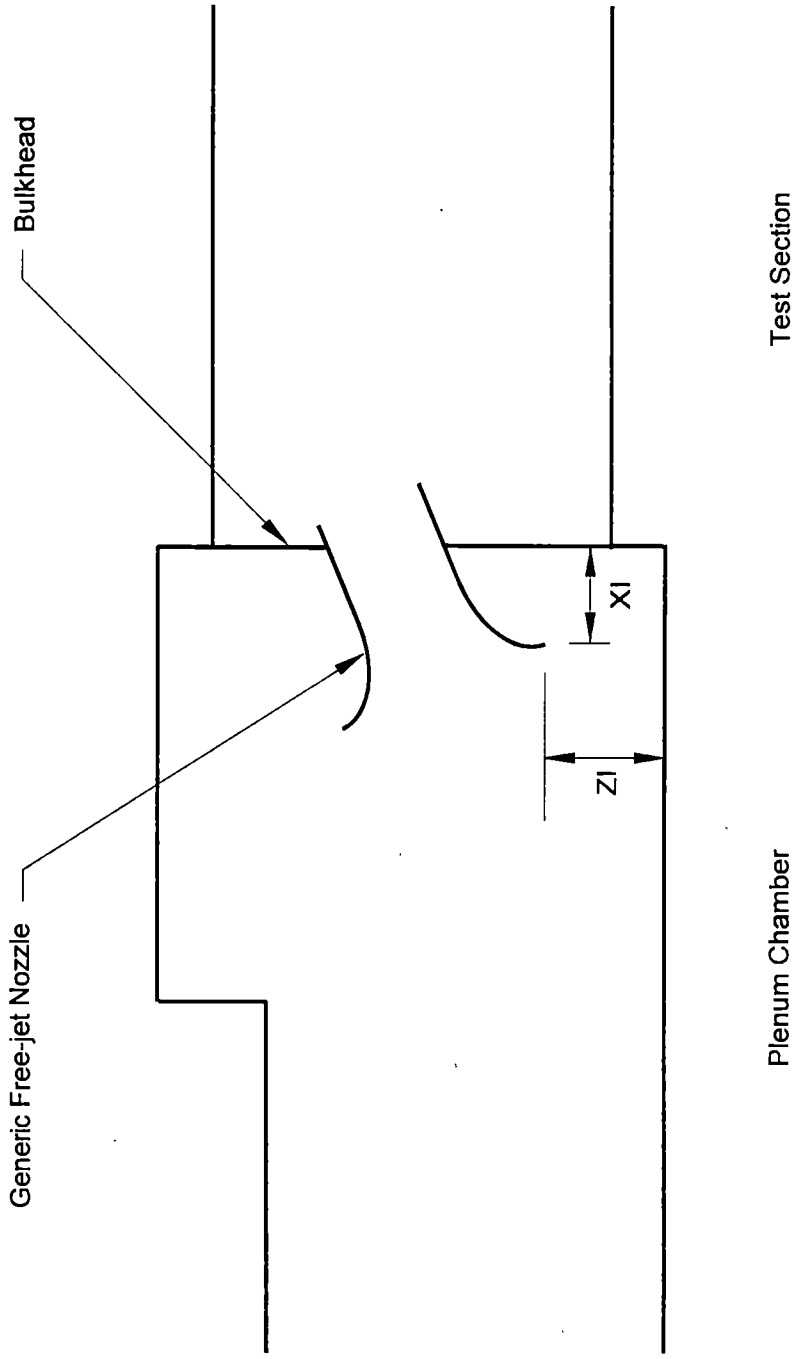
b. Short Axisymmetric Nozzle with Contraction Ratio of 2.4 (SHORT AXI Nozzle)

Figure 25. Concluded.



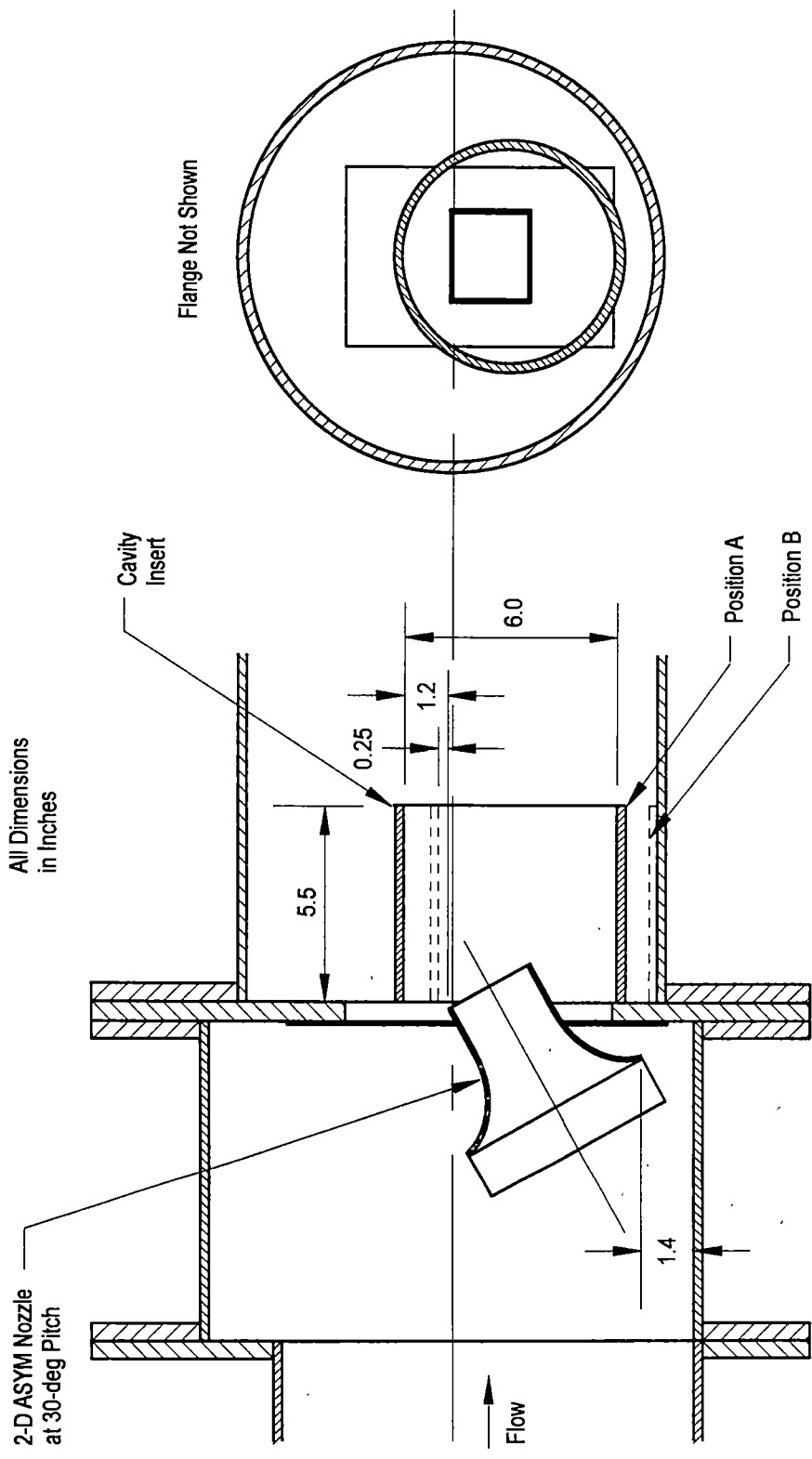
a. Slotted Bulkhead Geometry

Figure 26. Water Flow Model Slotted Bulkhead and Nozzle Position Parameter Definitions.



b. Position Parameter Definitions

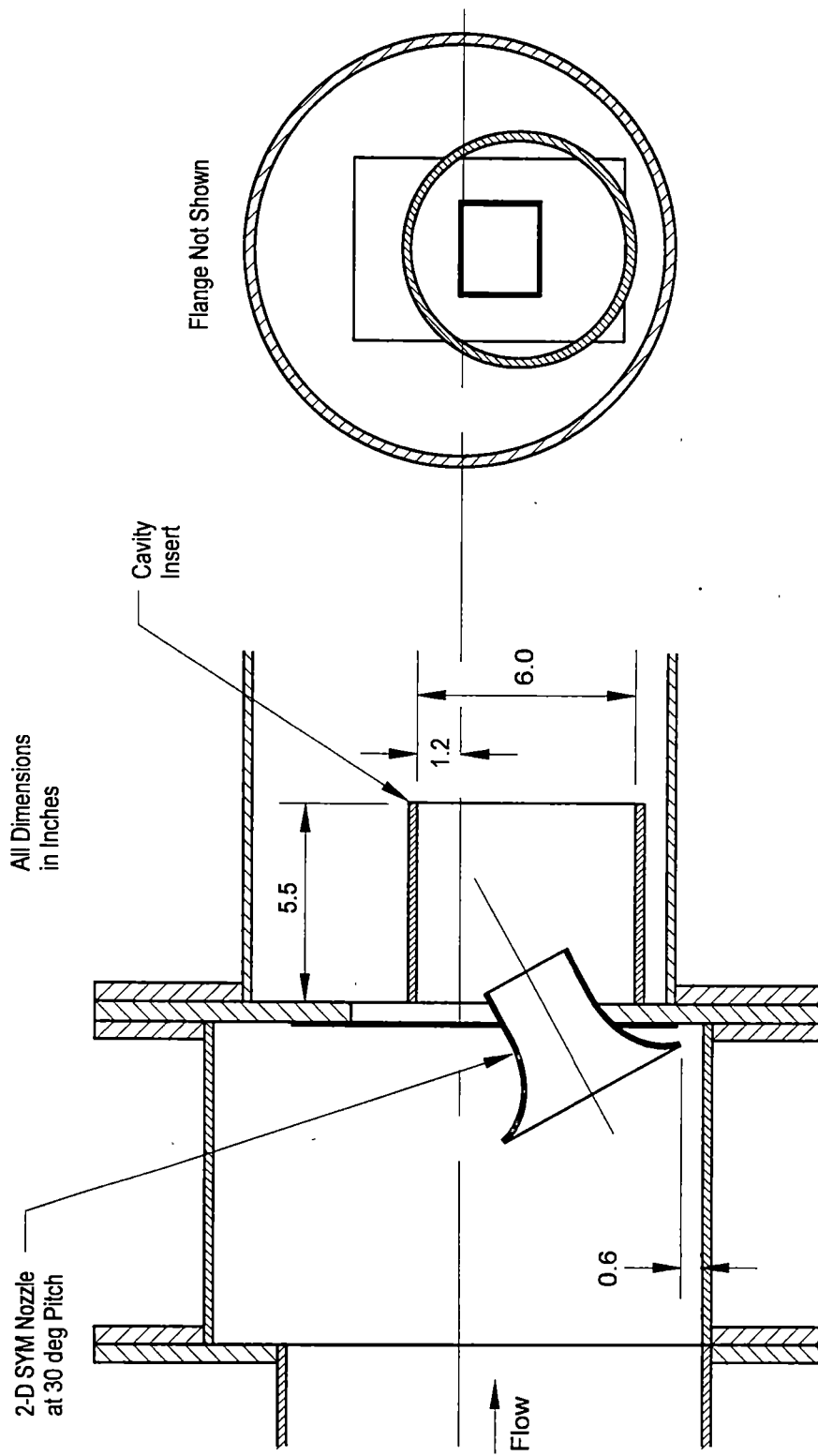
Figure 26. Concluded.



a. 2-D ASYM Nozzle Installation

Figure 27. Water Flow Model Artificial Bulkhead Installation.





All Dimensions  
in Inches

b. 2-D SYM Nozzle Installation

Figure 27. Concluded.

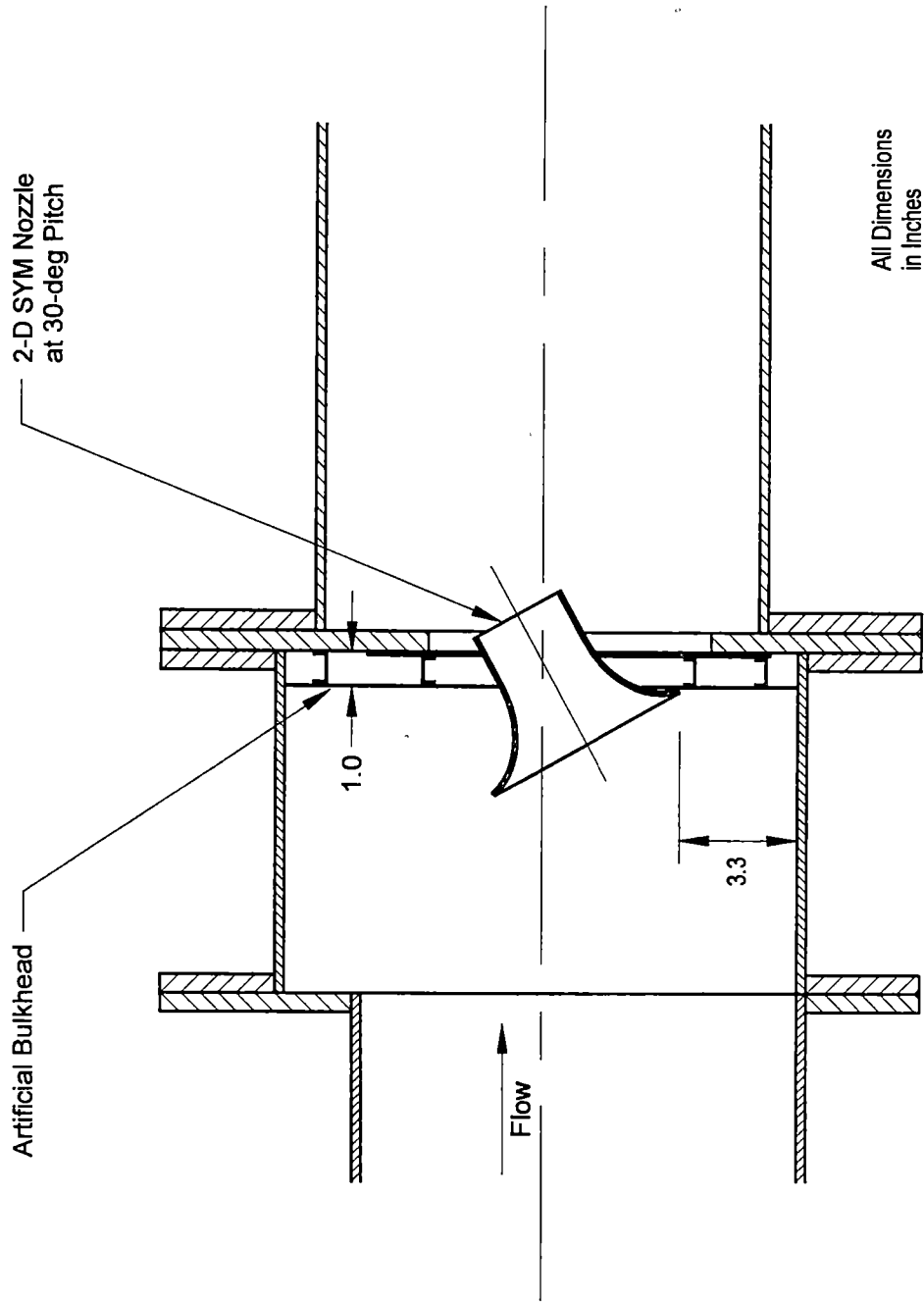


Figure 28. Water Flow Model Artificial Floor Installation.

All Dimensions  
in Inches

Flange Not Shown

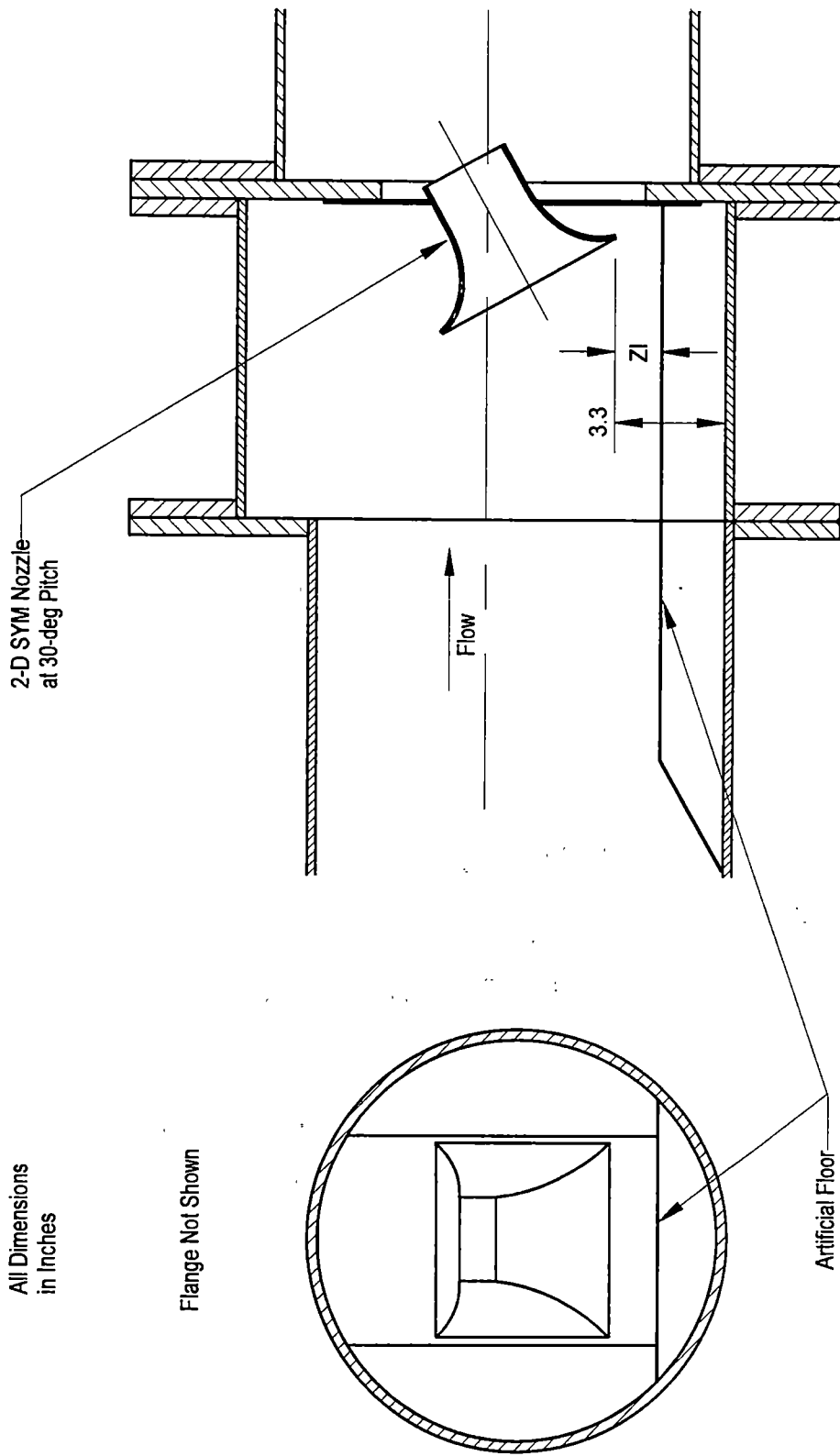


Figure 29. Water Flow Model Nozzle Exit Cavity Installation.

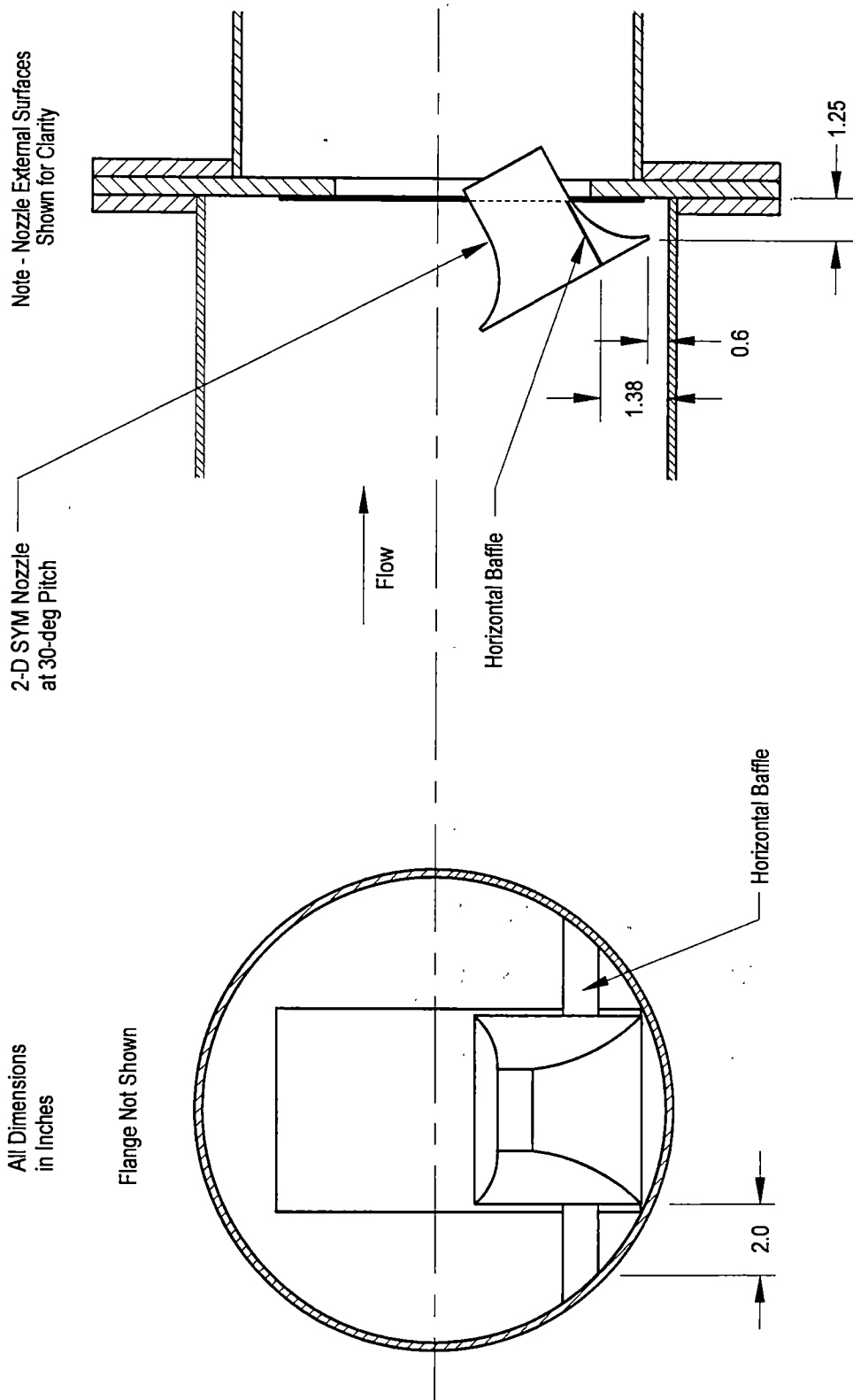
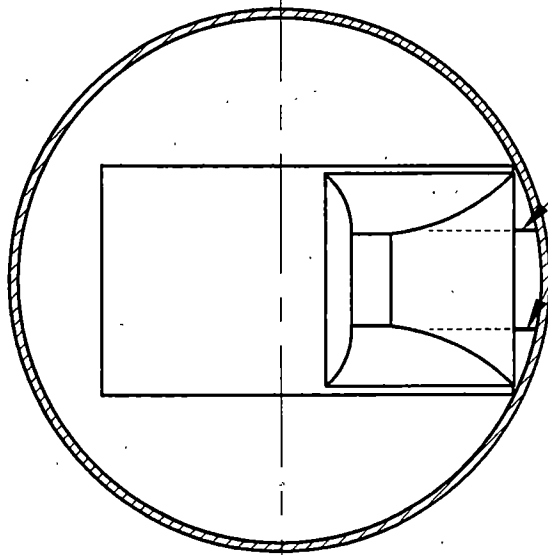


Figure 30. Water Flow Model Horizontal Baffle Installation.

All Dimensions  
in Inches

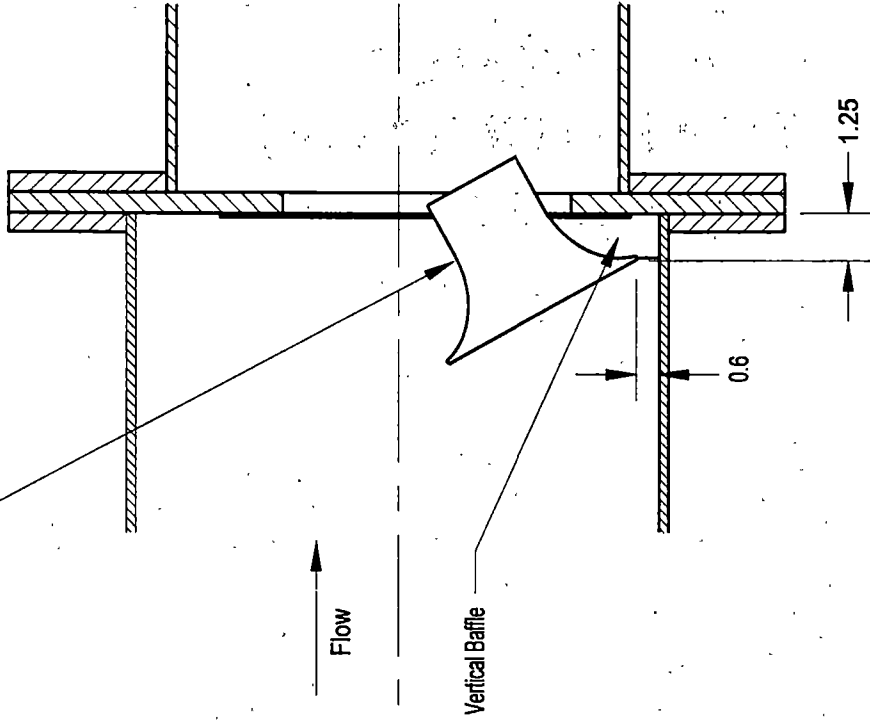
Flange Not Shown



Vertical Baffle

2-D SYM Nozzle  
at 30-deg Pitch

Note - Nozzle External Surfaces  
Shown for Clarity



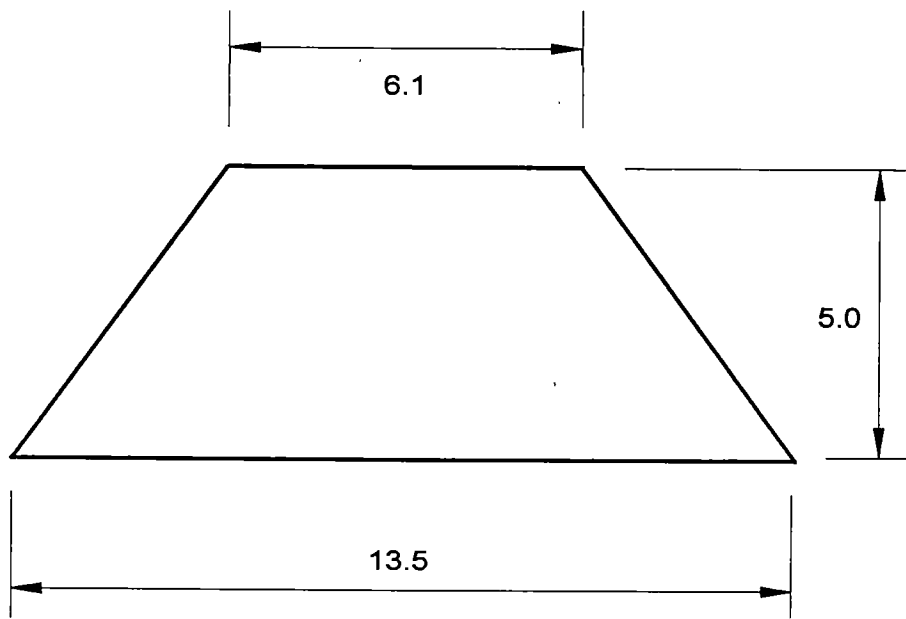
Flow

Vertical Baffle

0.6

1.25

Figure 31. Water Flow Model Vertical Baffle Installation.



Ramp Planform

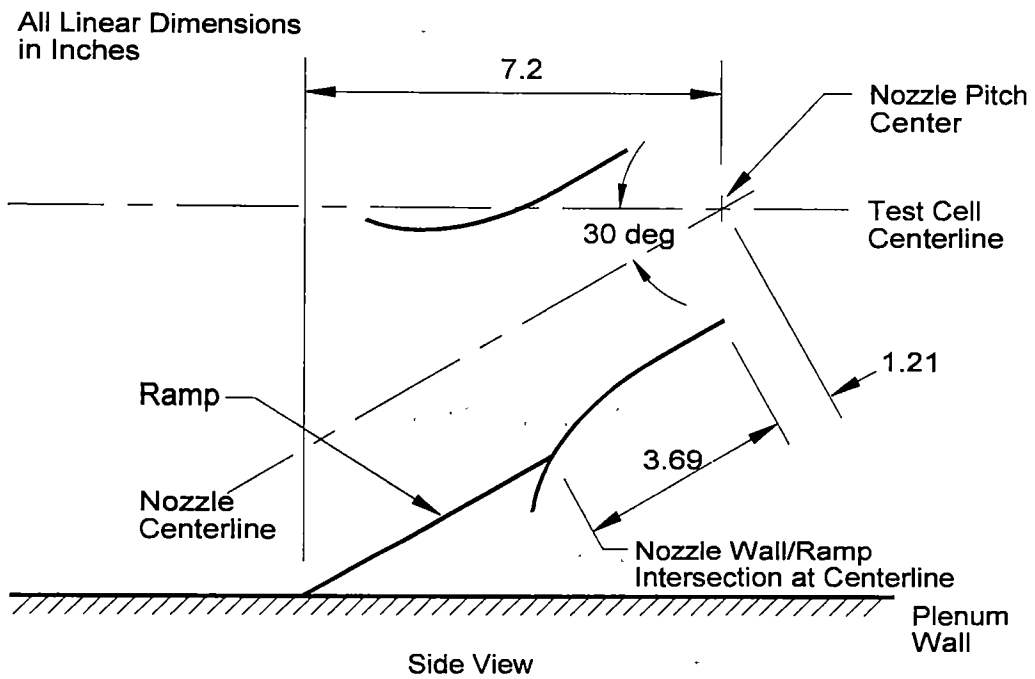
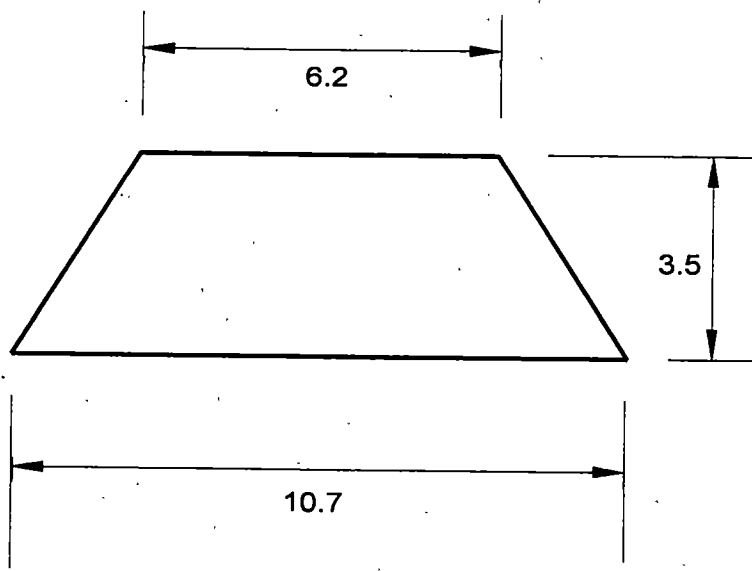
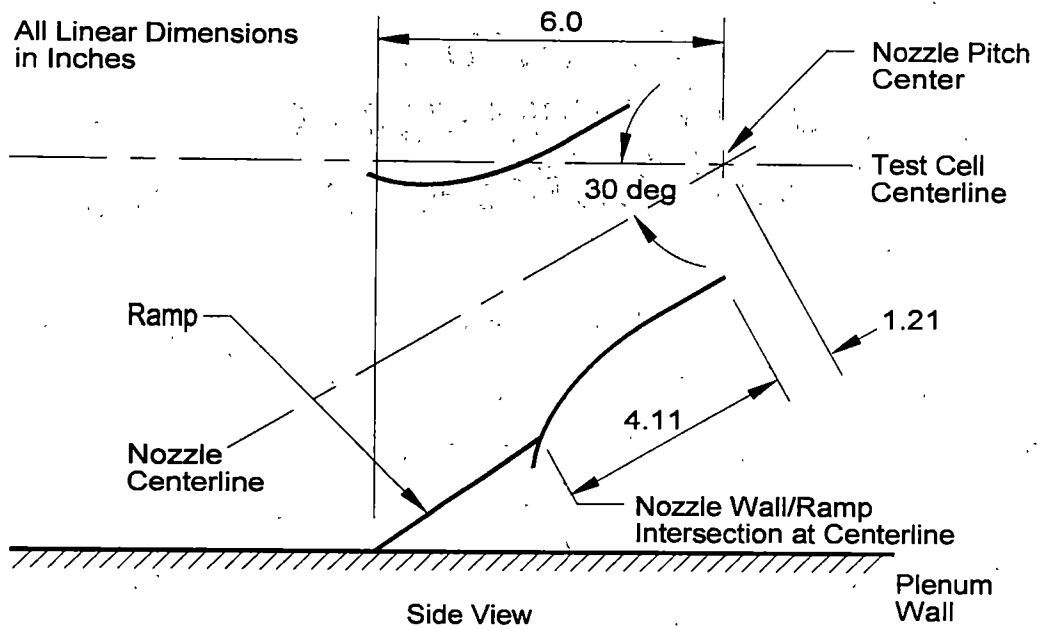


Figure 32. Ramp 1 Configuration for Short Axisymmetric Nozzle Water Flow Model.

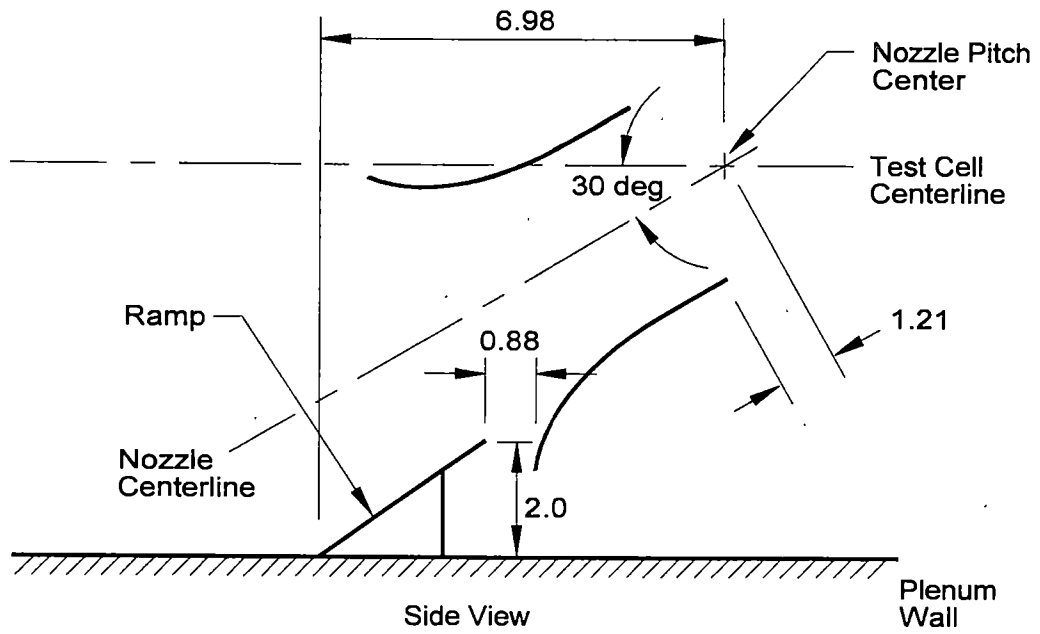


a. Ramp Planform

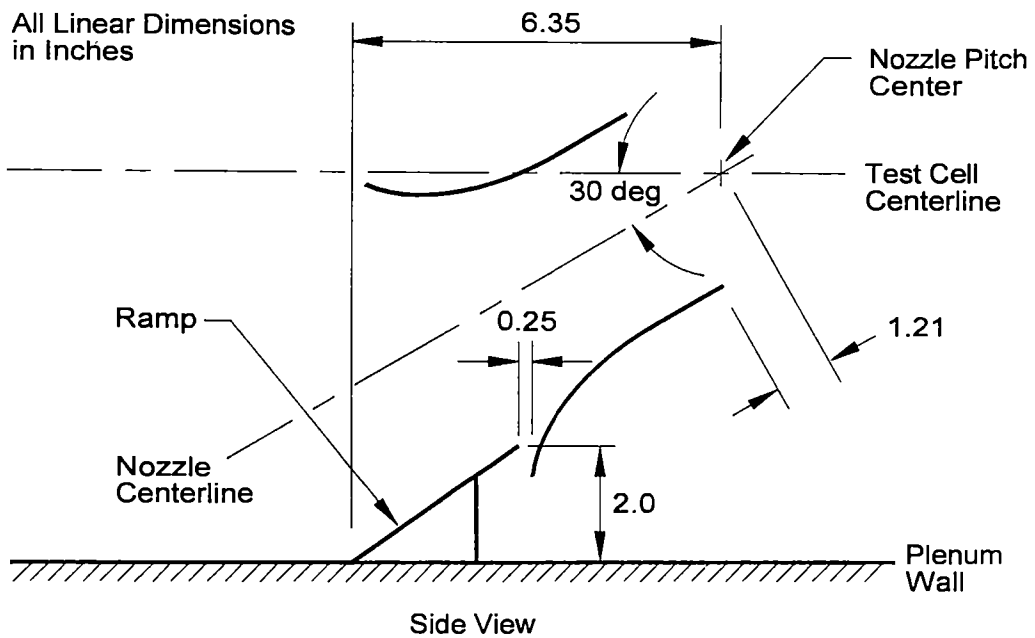


b. Position A

Figure 33. Ramp 2 Configuration for Short Axisymmetric Nozzle Water Flow Model.



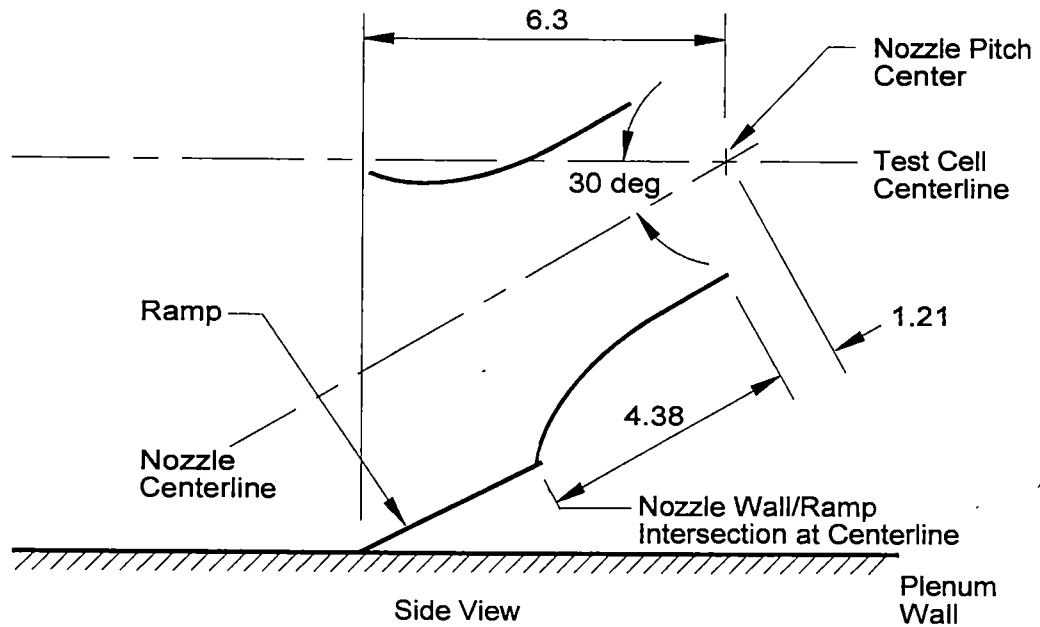
c. Position B



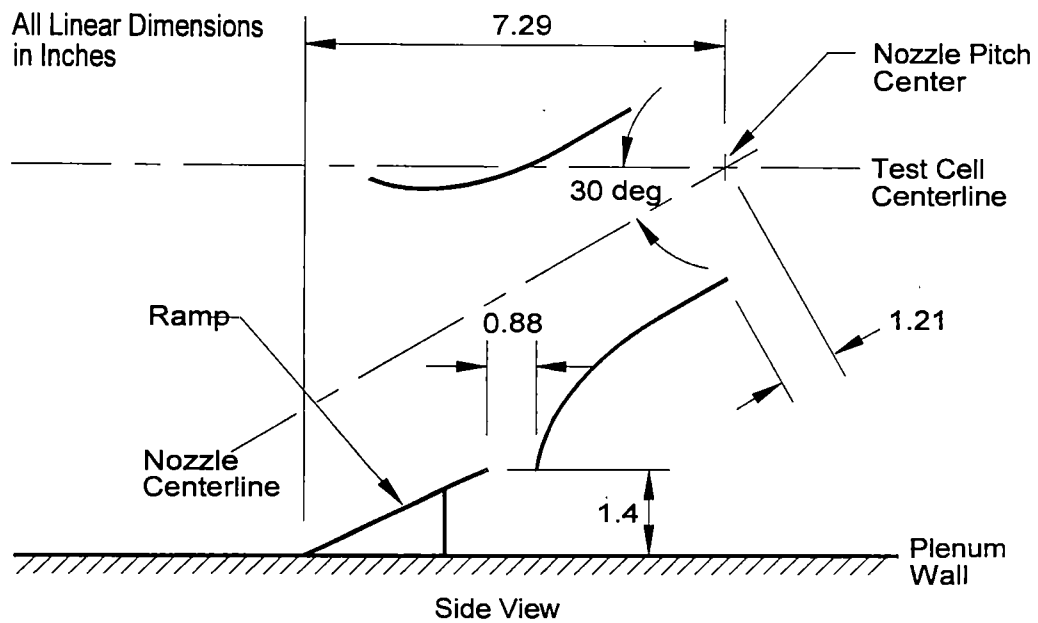
d. Position C

Figure 33. Continued.



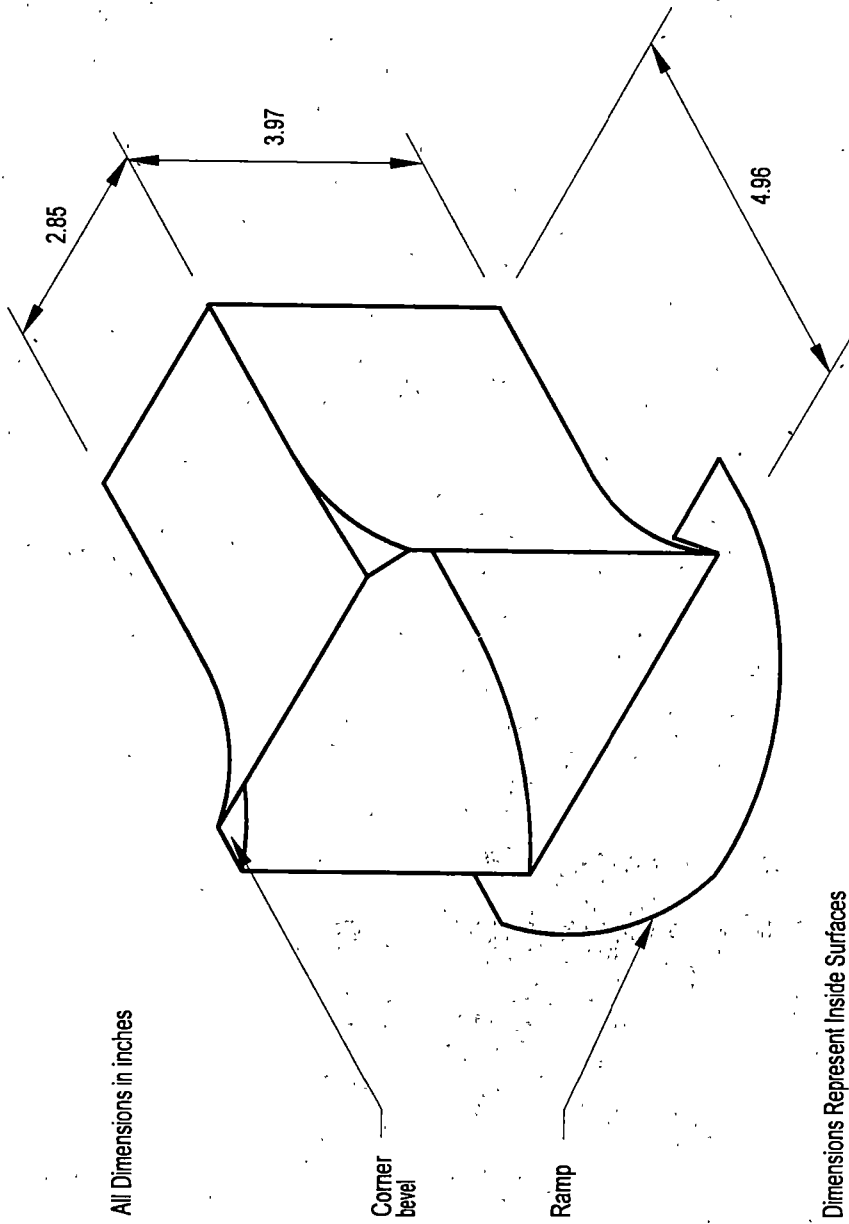


e. Position D



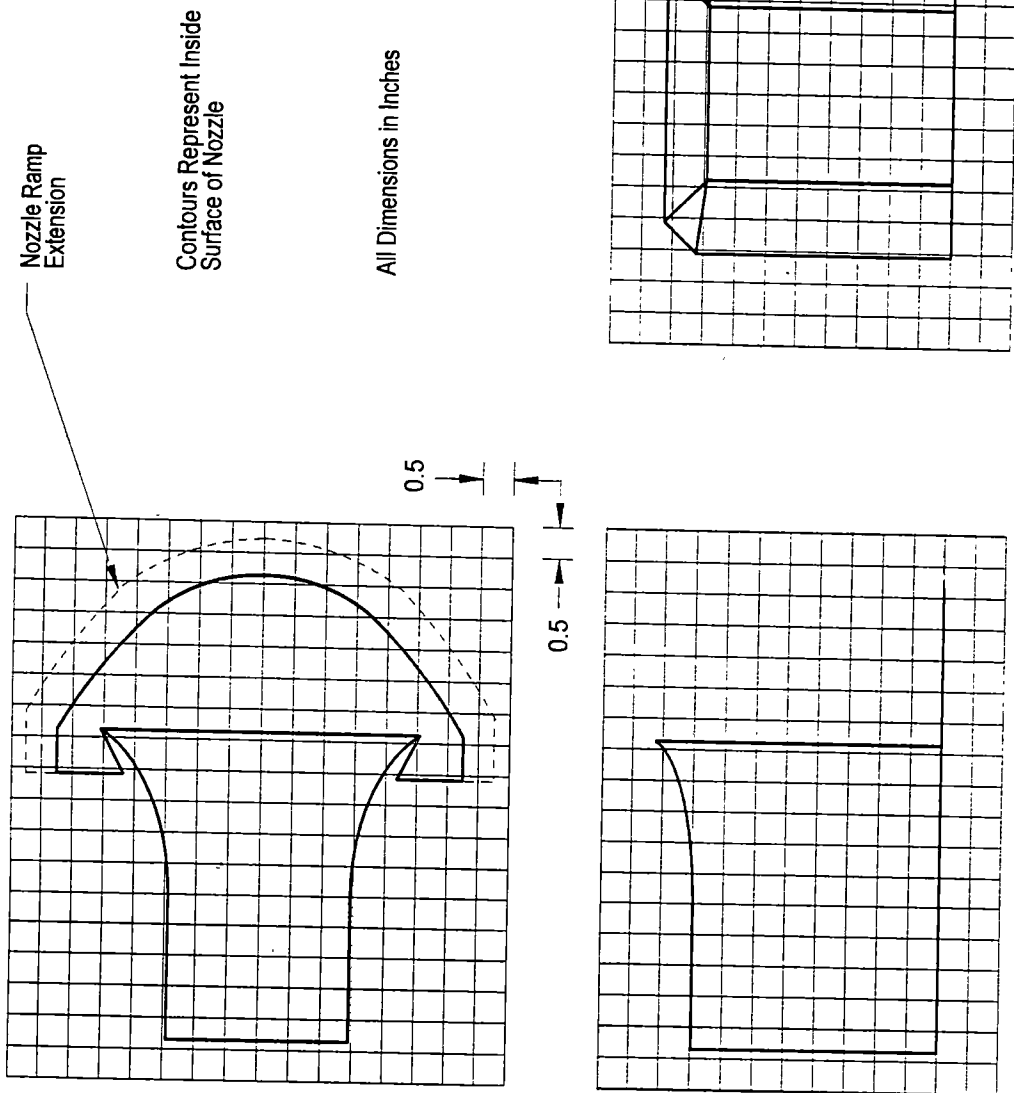
f. Position E

Figure 33. Concluded.



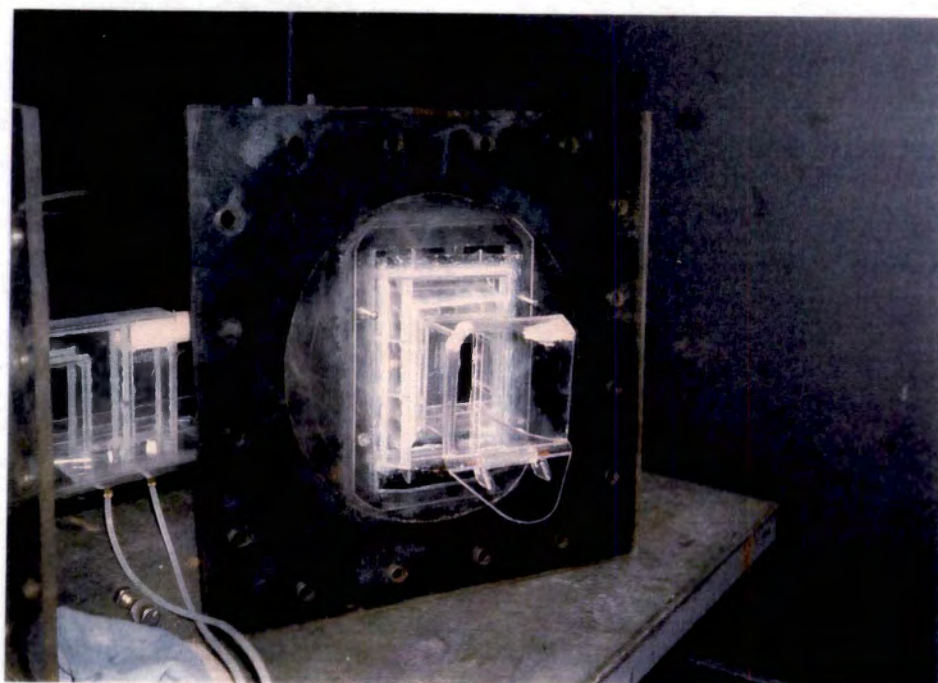
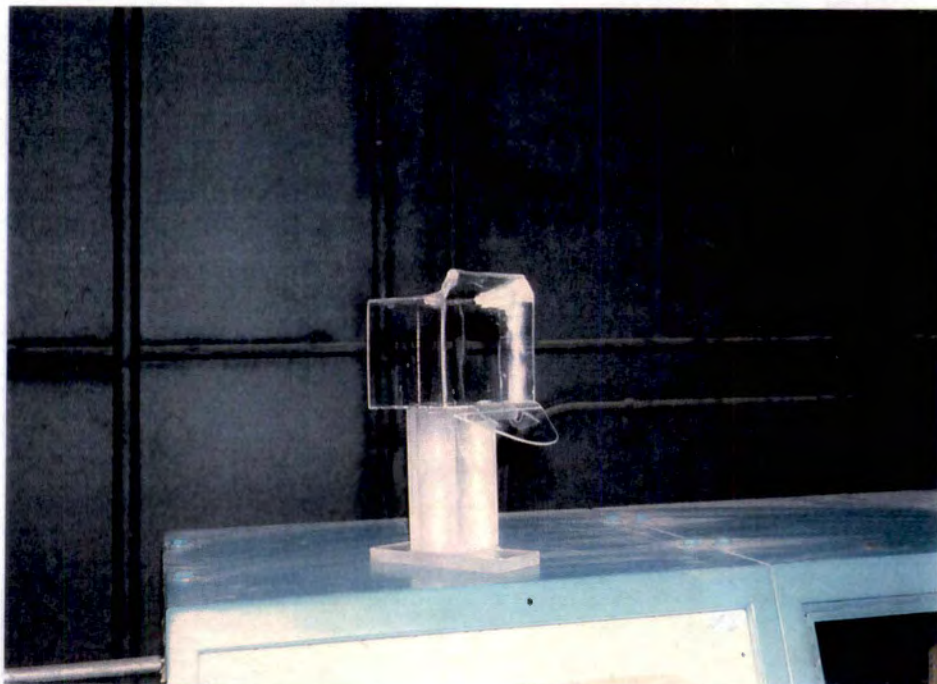
a. Isometric View

Figure 34. ASTF Nozzle Water Flow Model.



b. 3-View Showing Contours

Figure 34. Continued.



c. Photographs

Figure 34. Concluded.

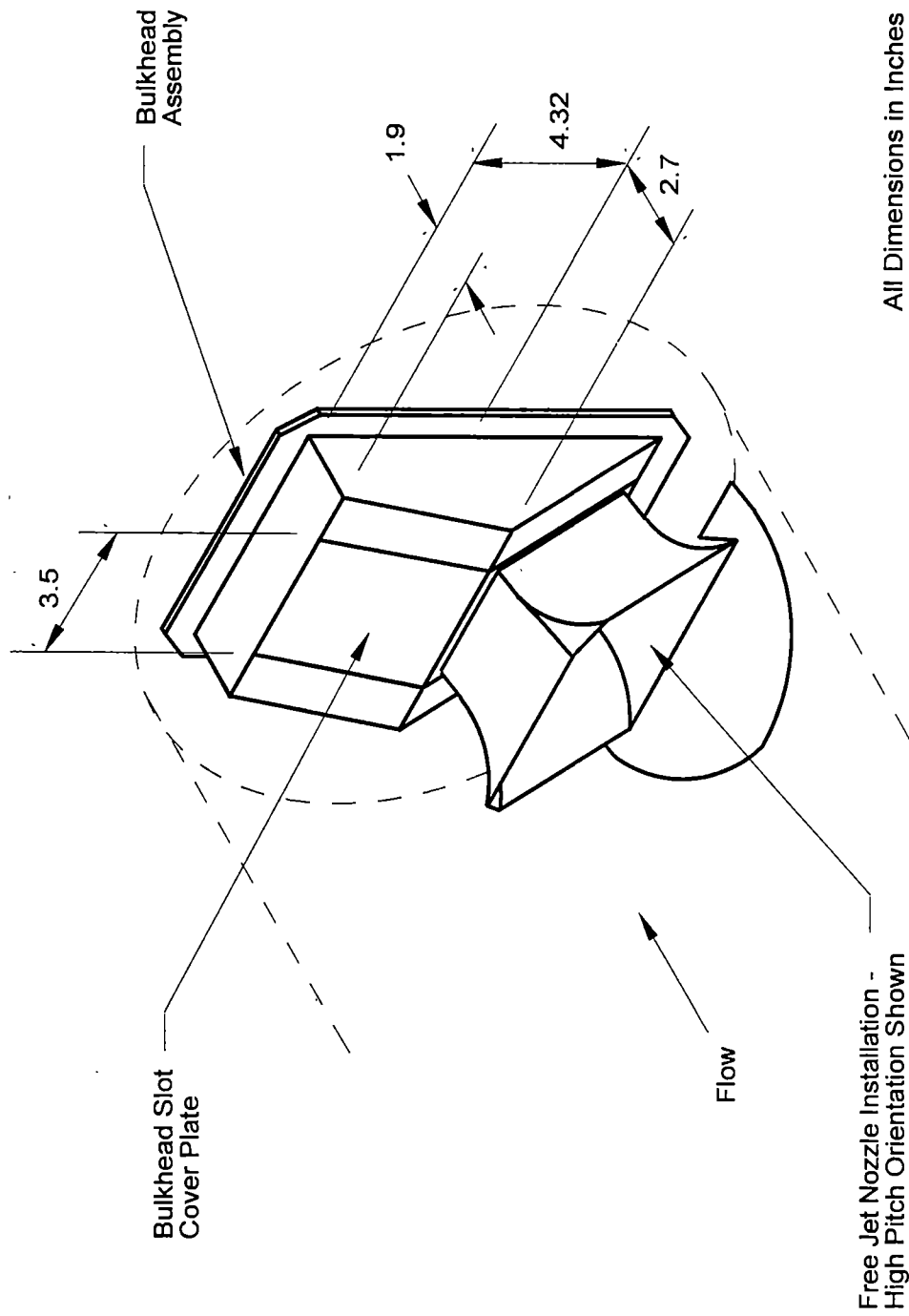
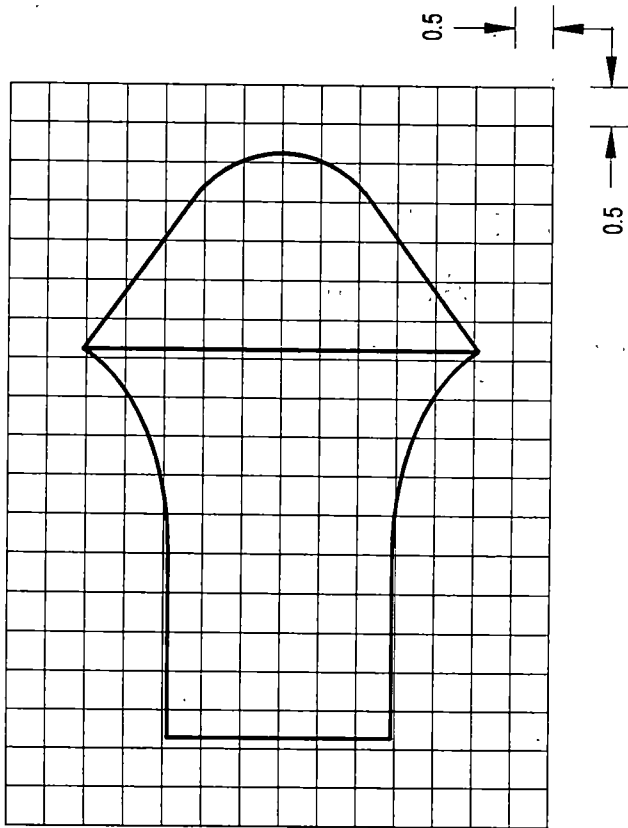


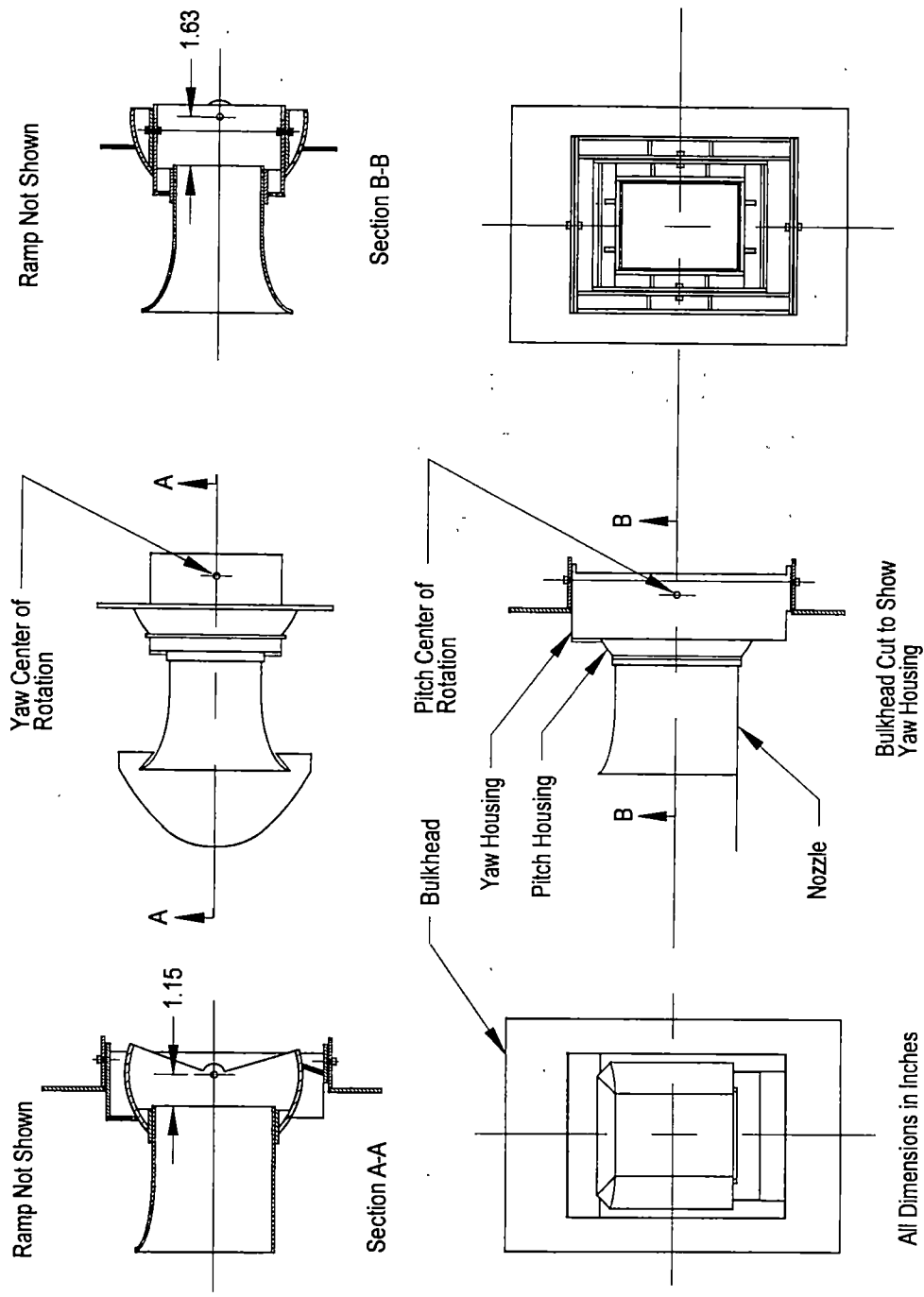
Figure 35. Mounting Fixture for ASTF Nozzle Water Flow Model.



Contours Represent Inside  
Surface of Nozzle

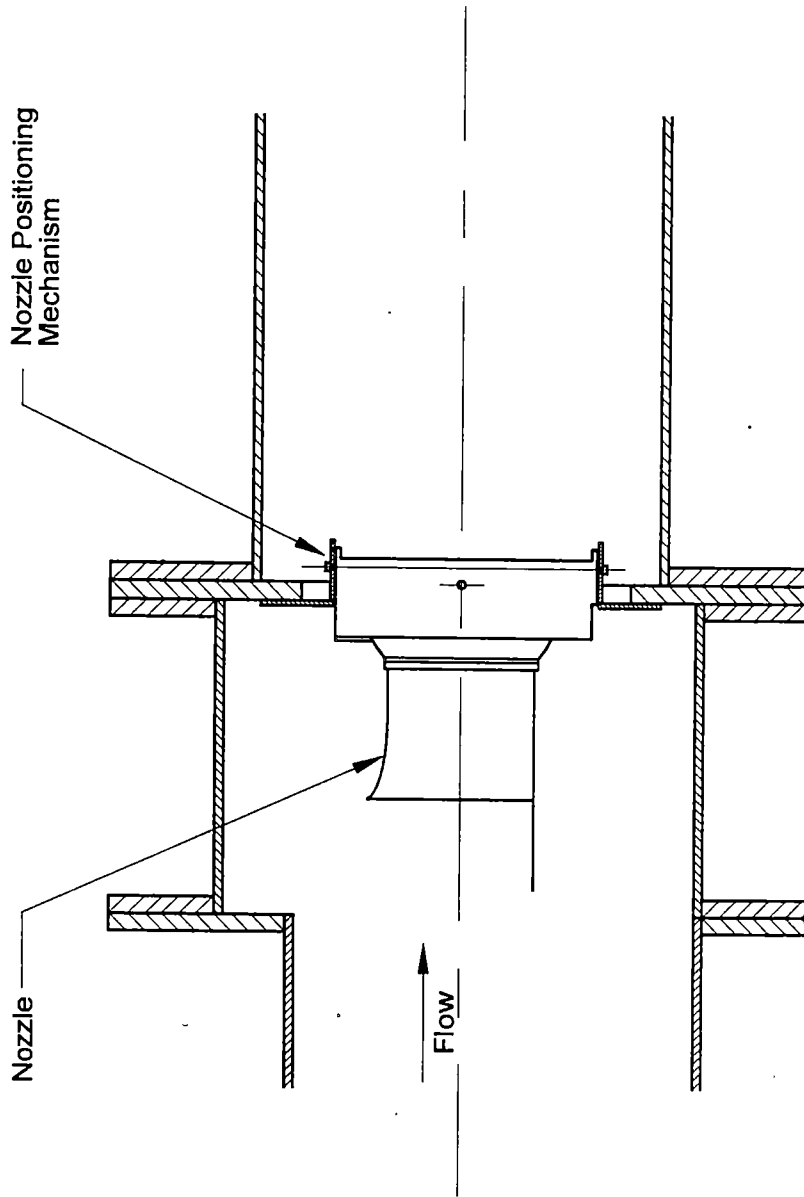
All Dimensions in Inches

Figure 36. ASTF Nozzle Water Flow Model Ramp B Planform.



a. 3-View

Figure 37. Water Flow Model of ATF Free-Jet Nozzle Attitude Positioning Mechanism.

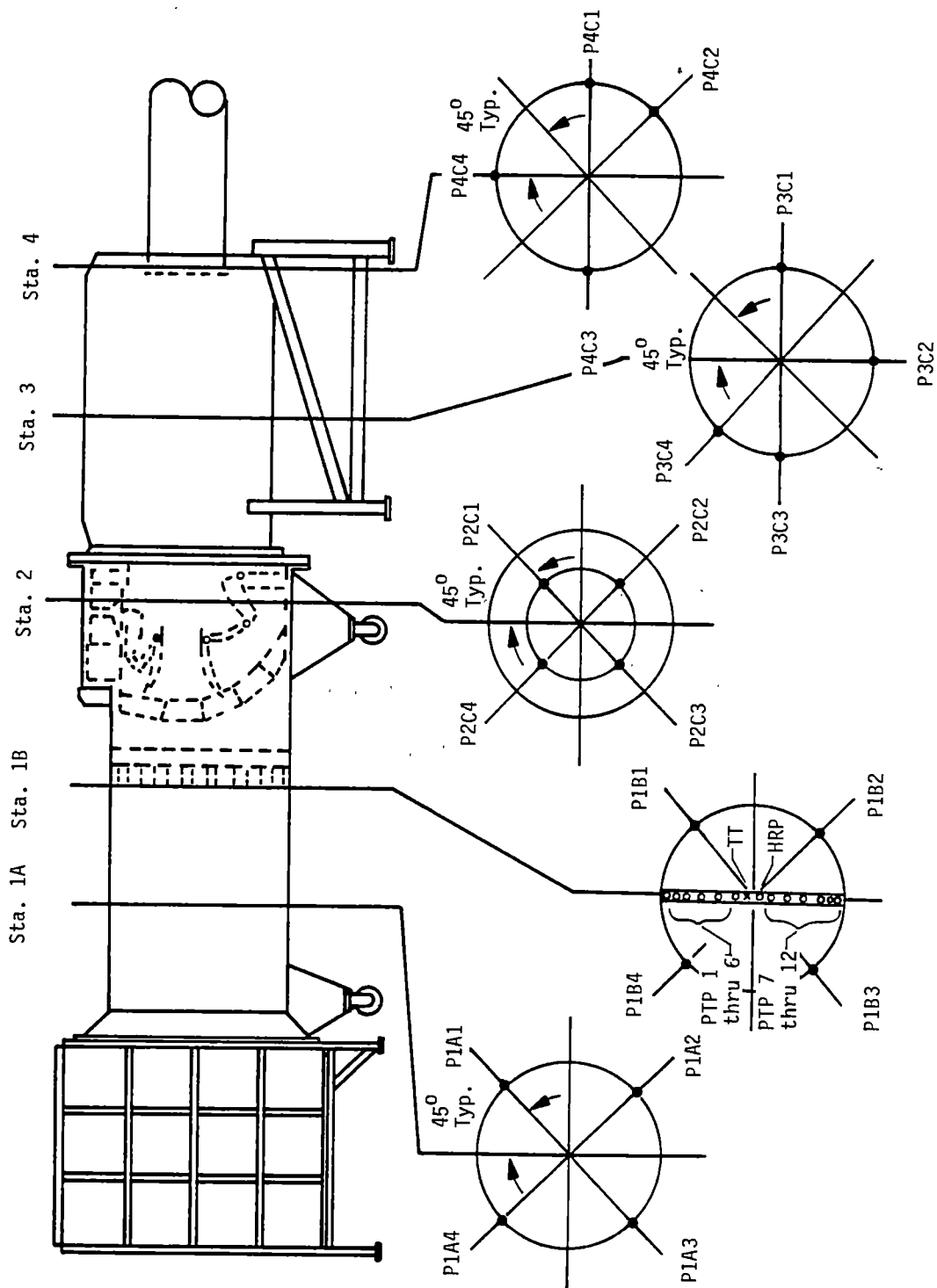


Plenum, Test Section, and Bulkhead Cut to Show Installation

b. Installation

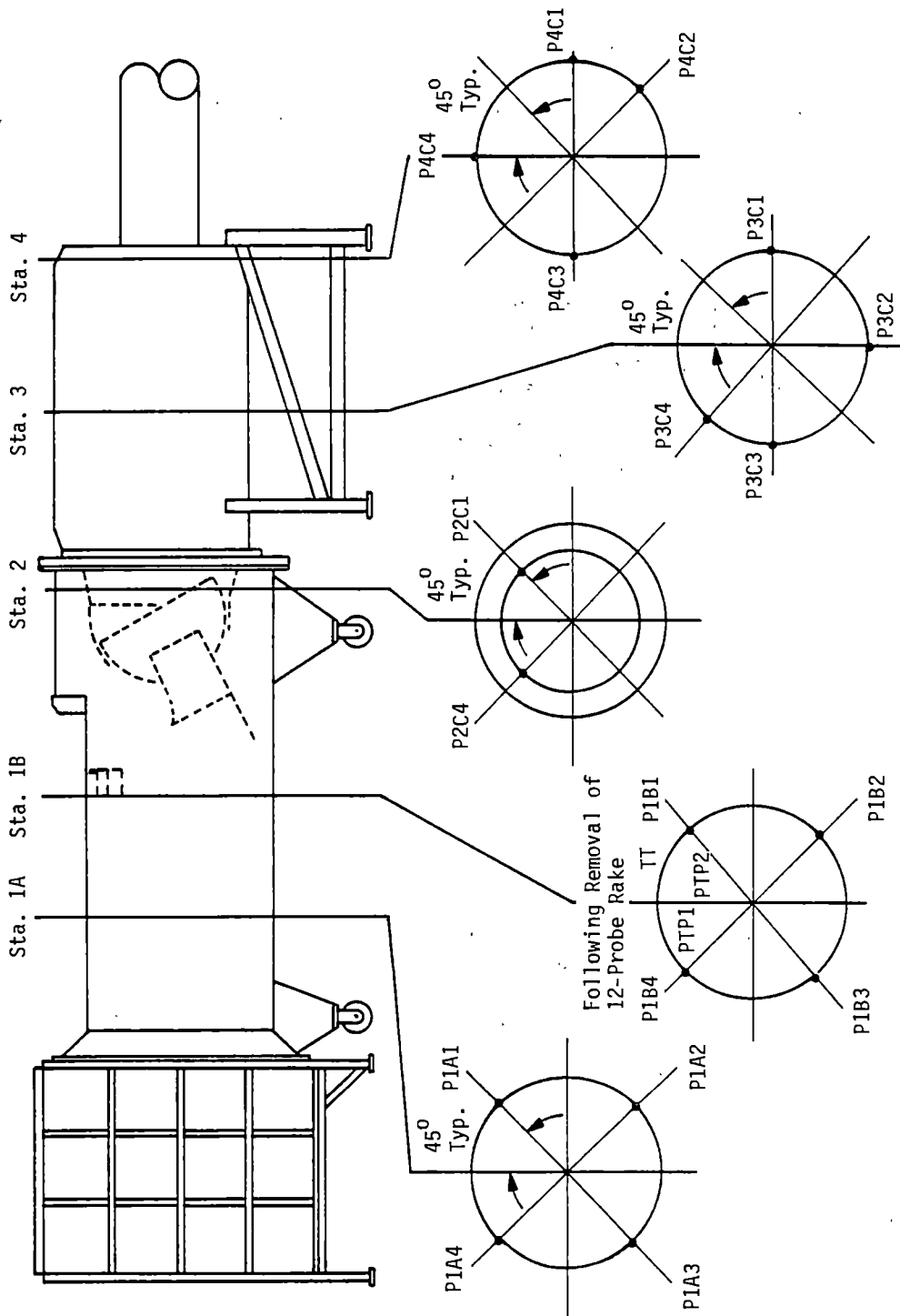
Figure 37. Concluded.





a. Variable-Area Nozzle Tests

Figure 38. R2A2 Test Cell Parameter Measurement Locations.



b. ASTF Nozzle Model Tests

Figure 38. Concluded.

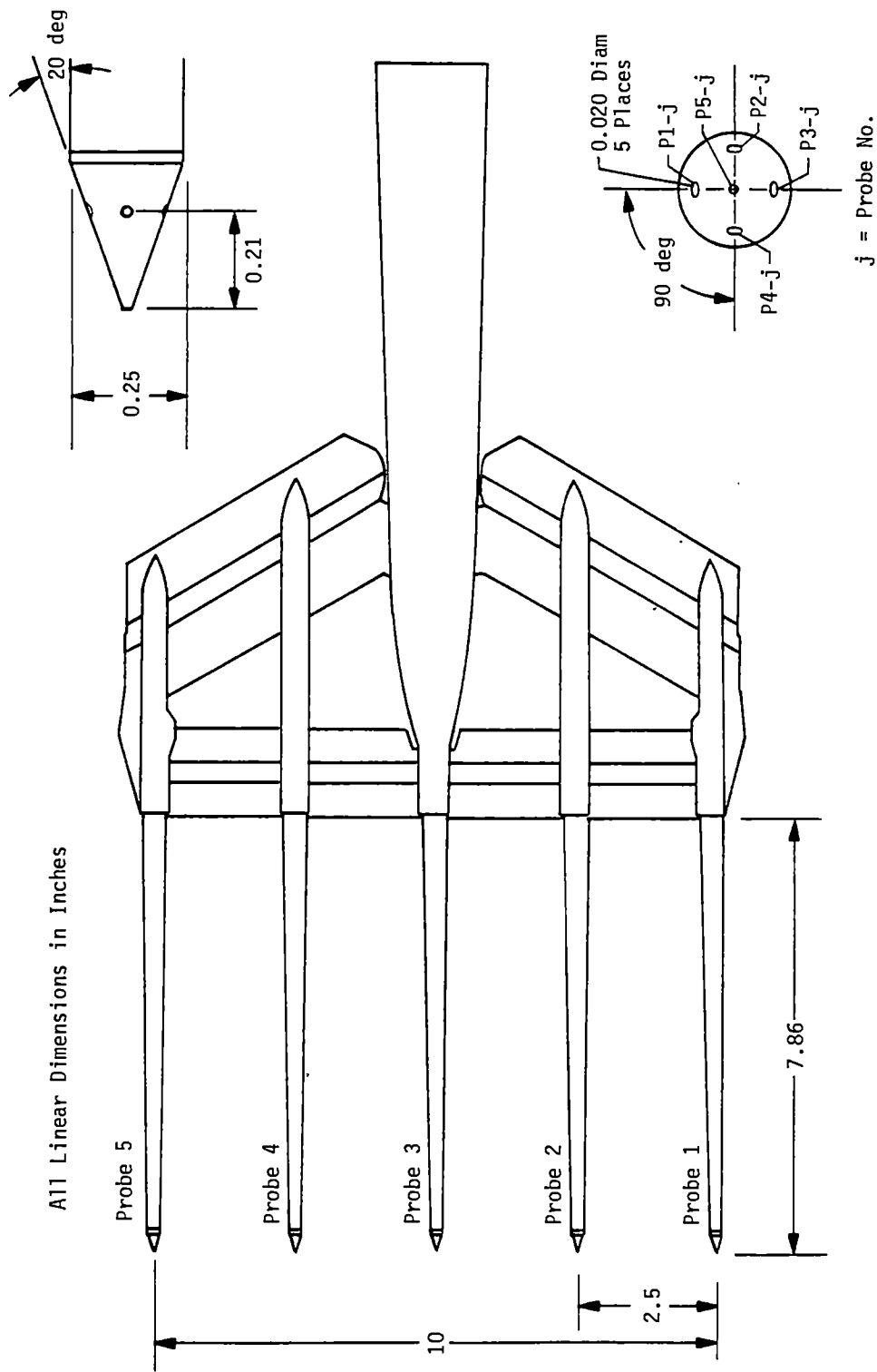
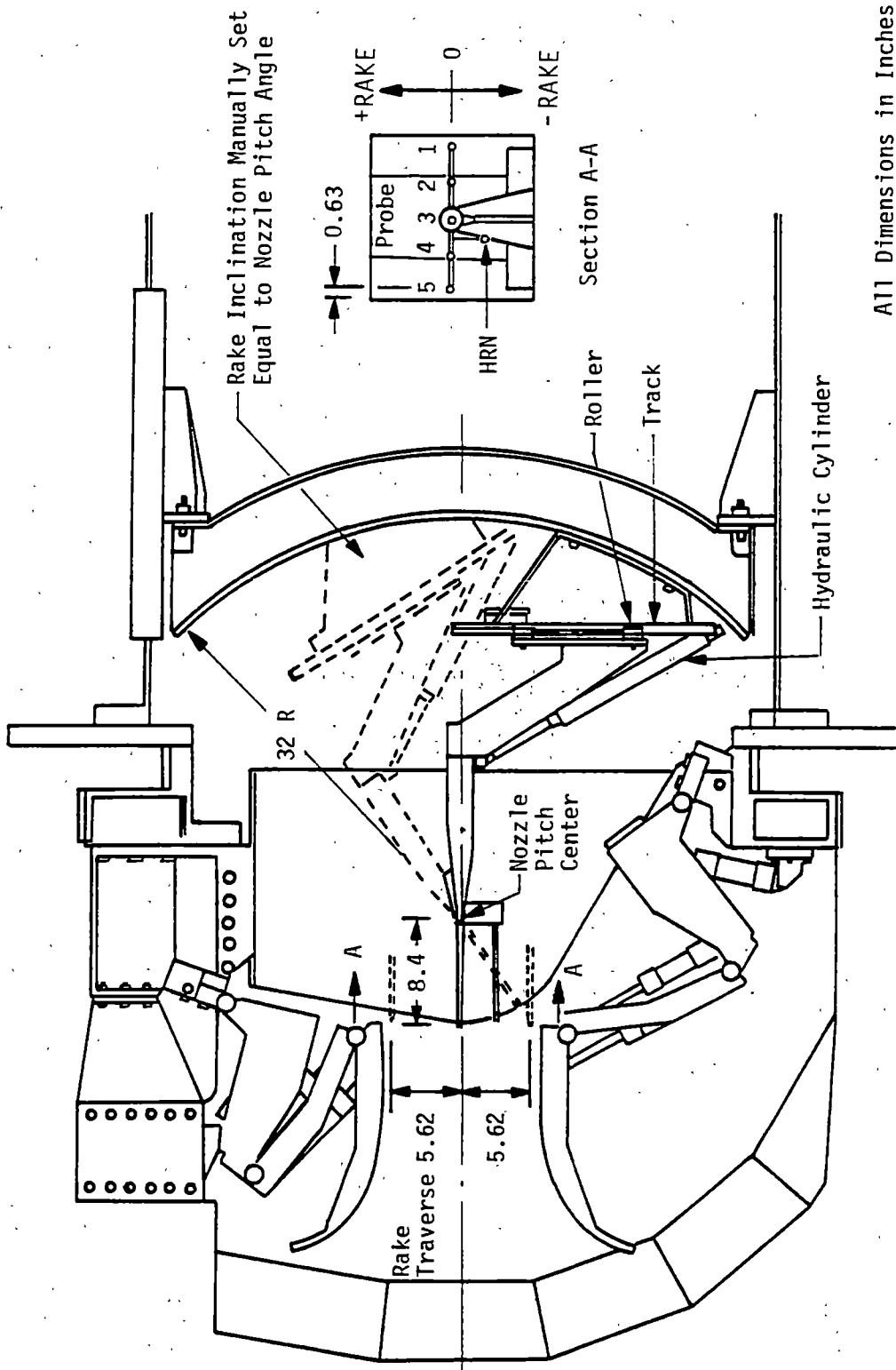


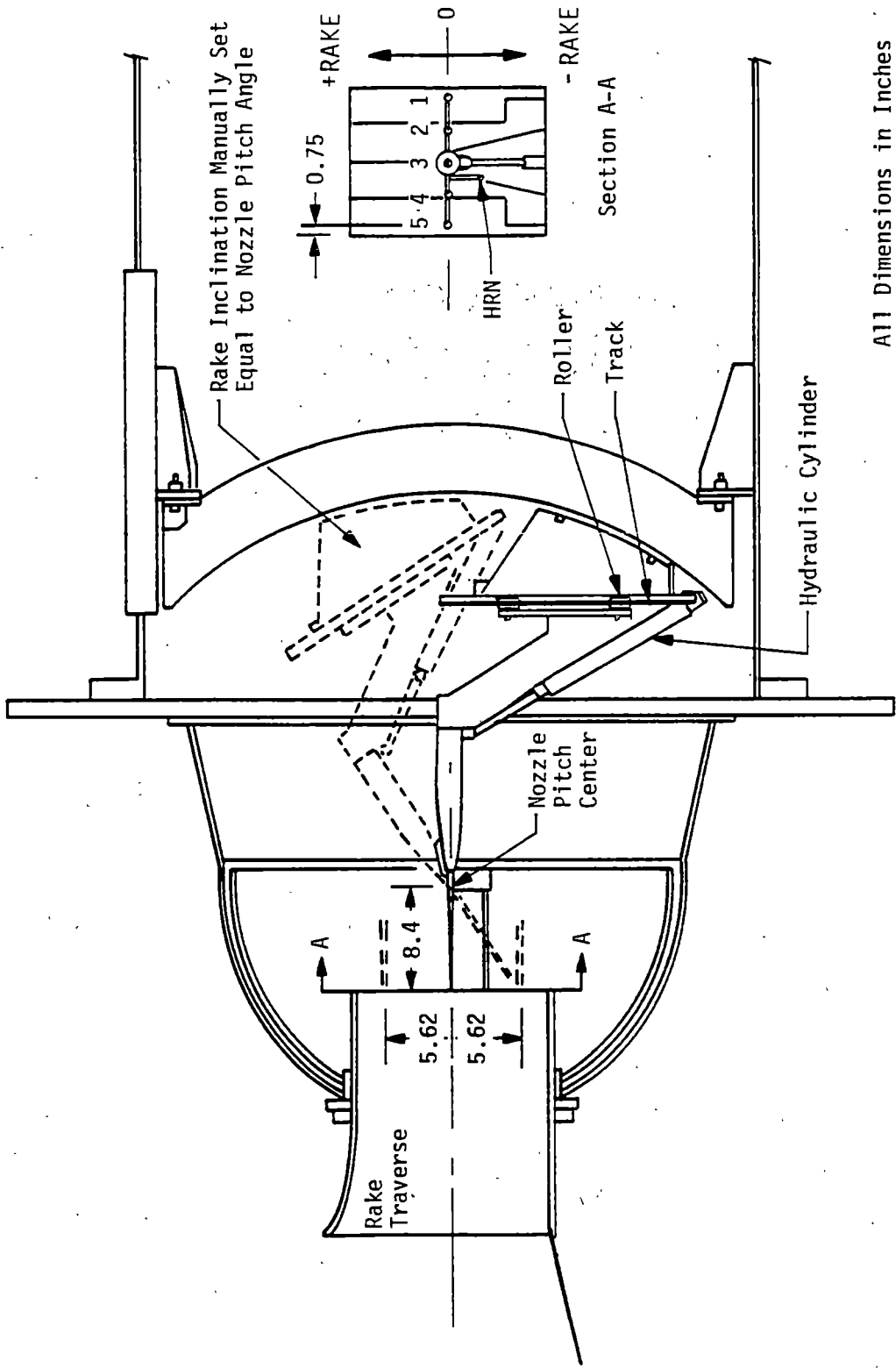
Figure 39. Mach/Flow Angularity Rake for Flow-Field Surveys in R2A2.



All Dimensions in Inches

a. Variable-Area Nozzle Tests

Figure 40. Mach/Flow Angularity Rake Installation in R2A2.



All Dimensions in Inches

b. ASTF Nozzle Model Tests

Figure 40. Concluded.

All Dimensions in Inches

Total Pressure ○  
 Static Pressure ●

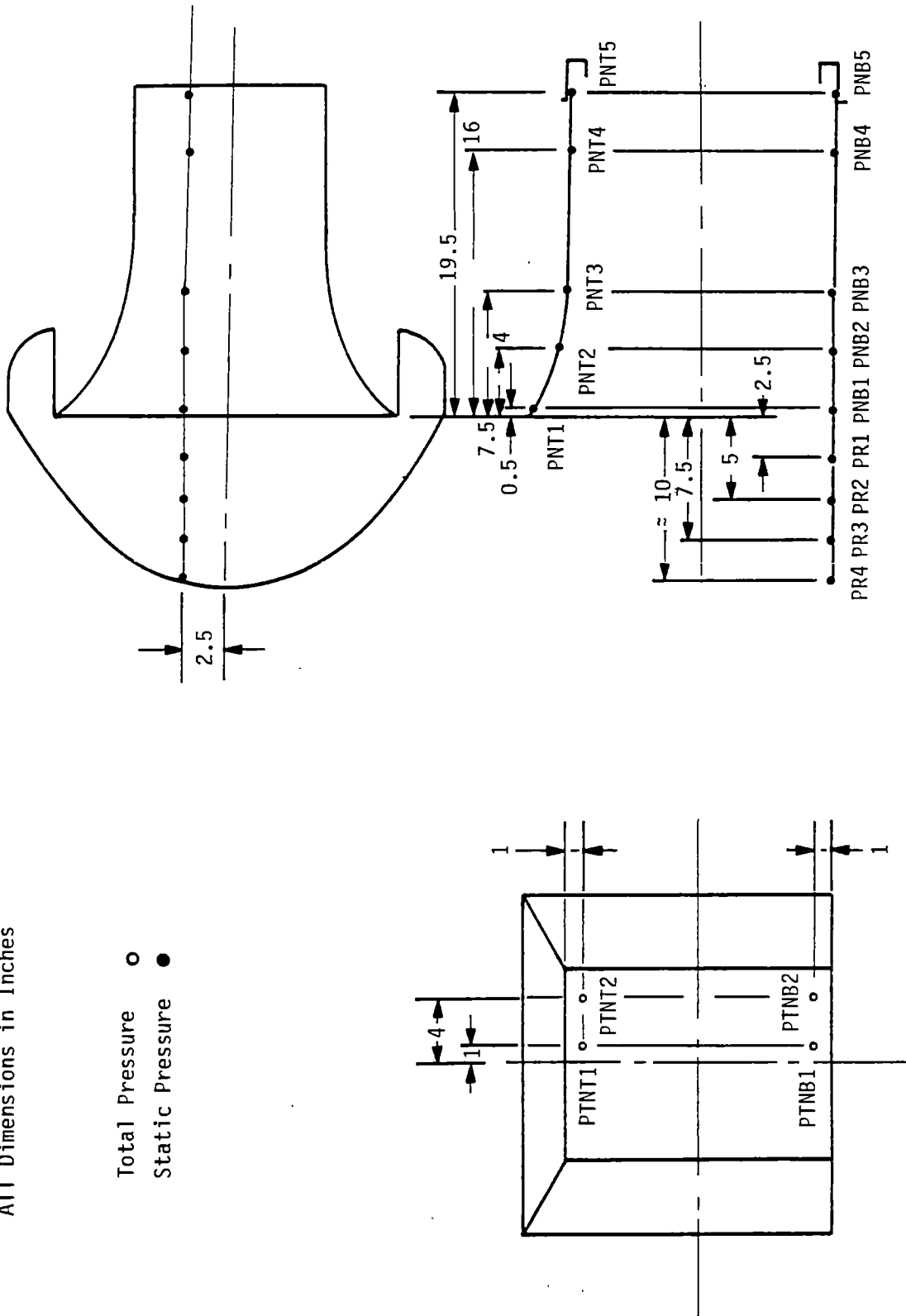


Figure 41. ASTF Nozzle Airflow Model Pressure Measurement Locations.

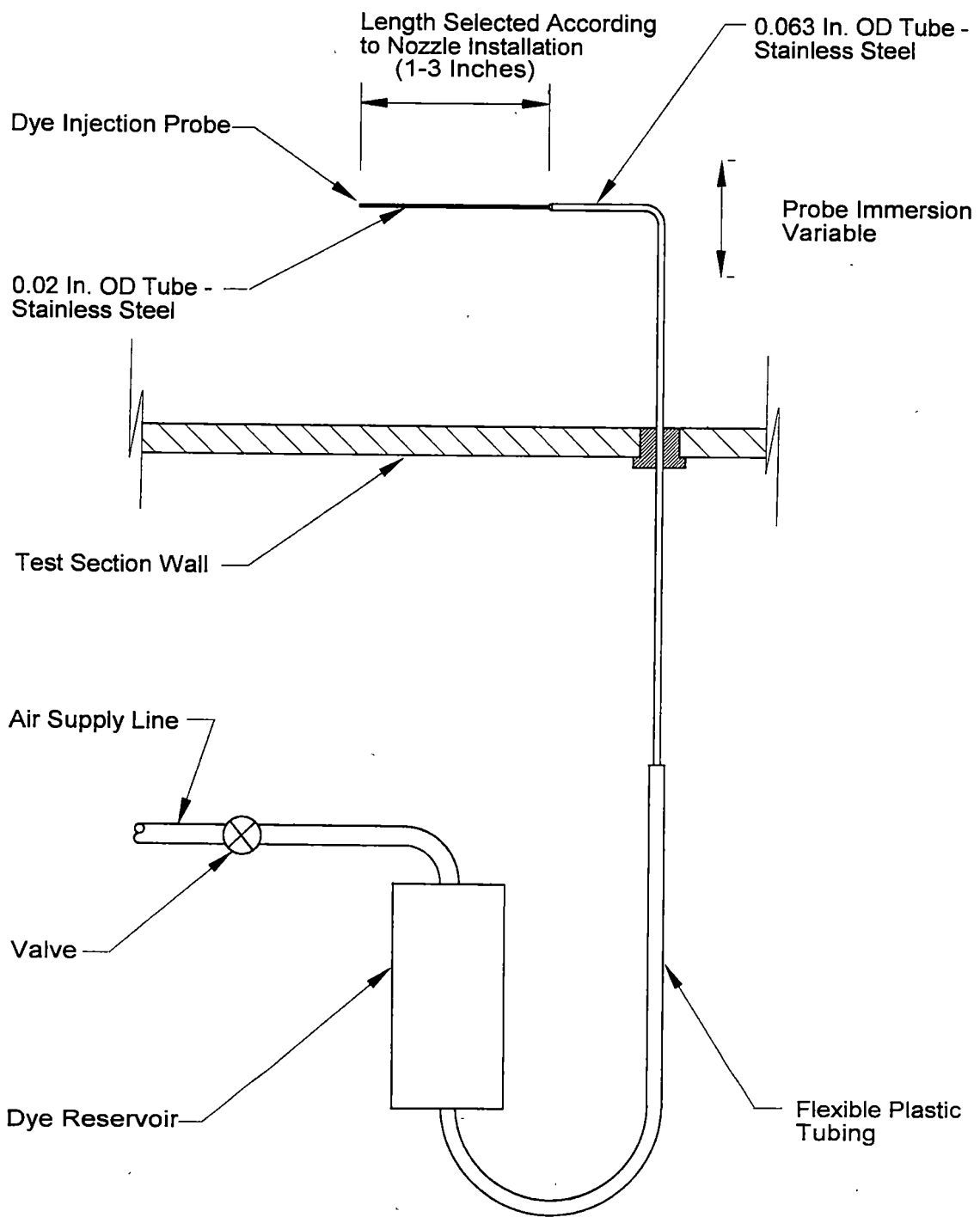


Figure 42. Water Flow Test Dye Injection Probe System.

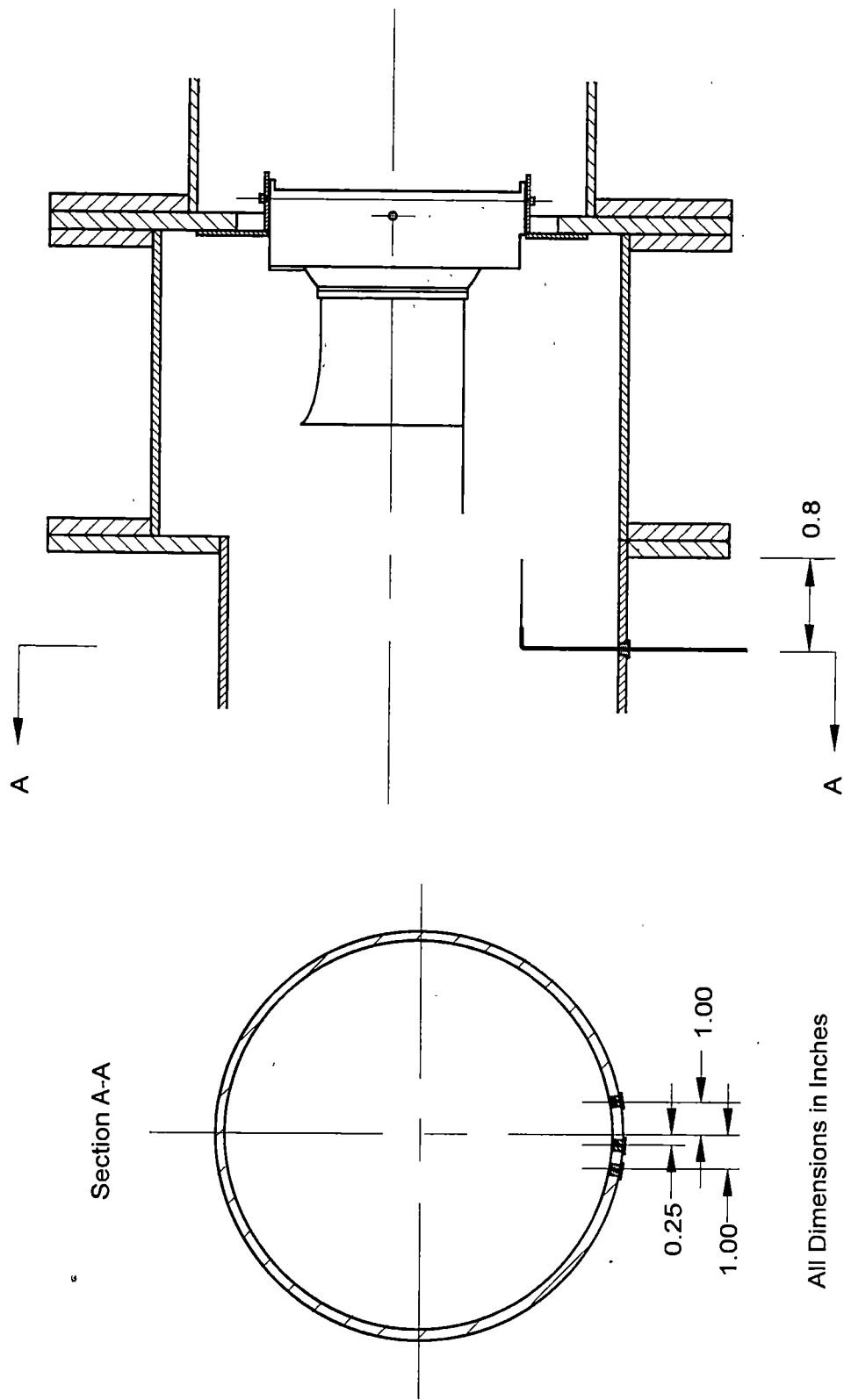


Figure 43. Water Flow Test Dye Injection Locations.



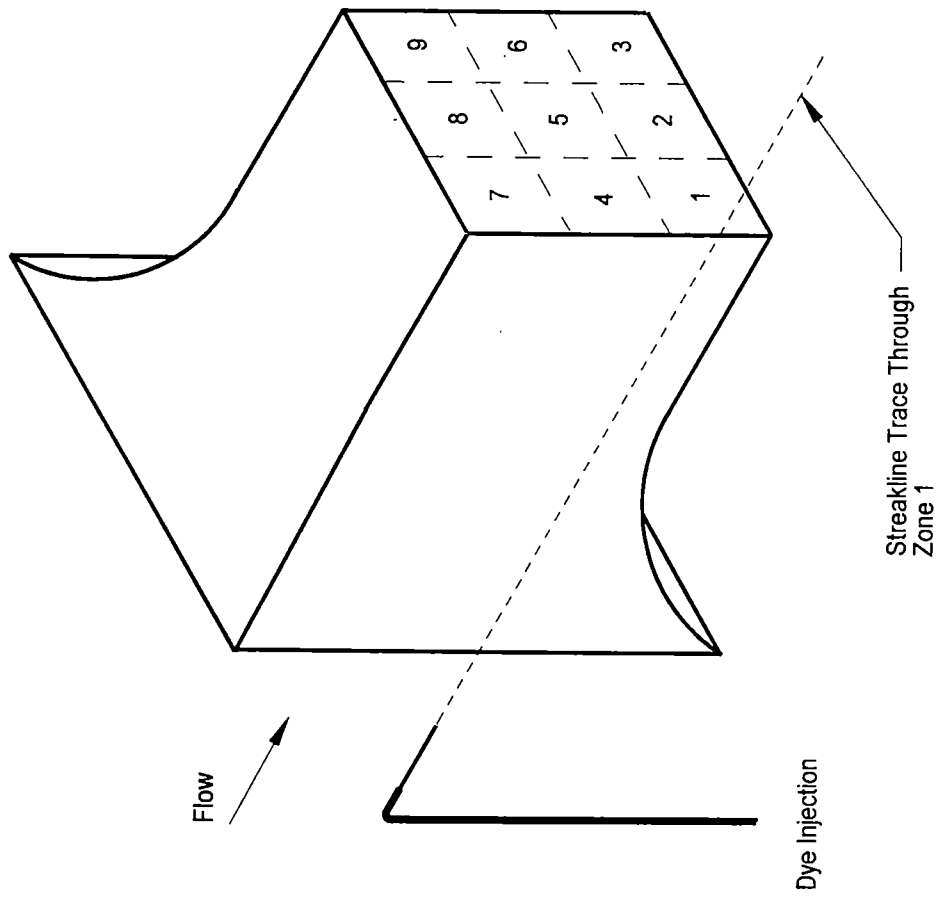
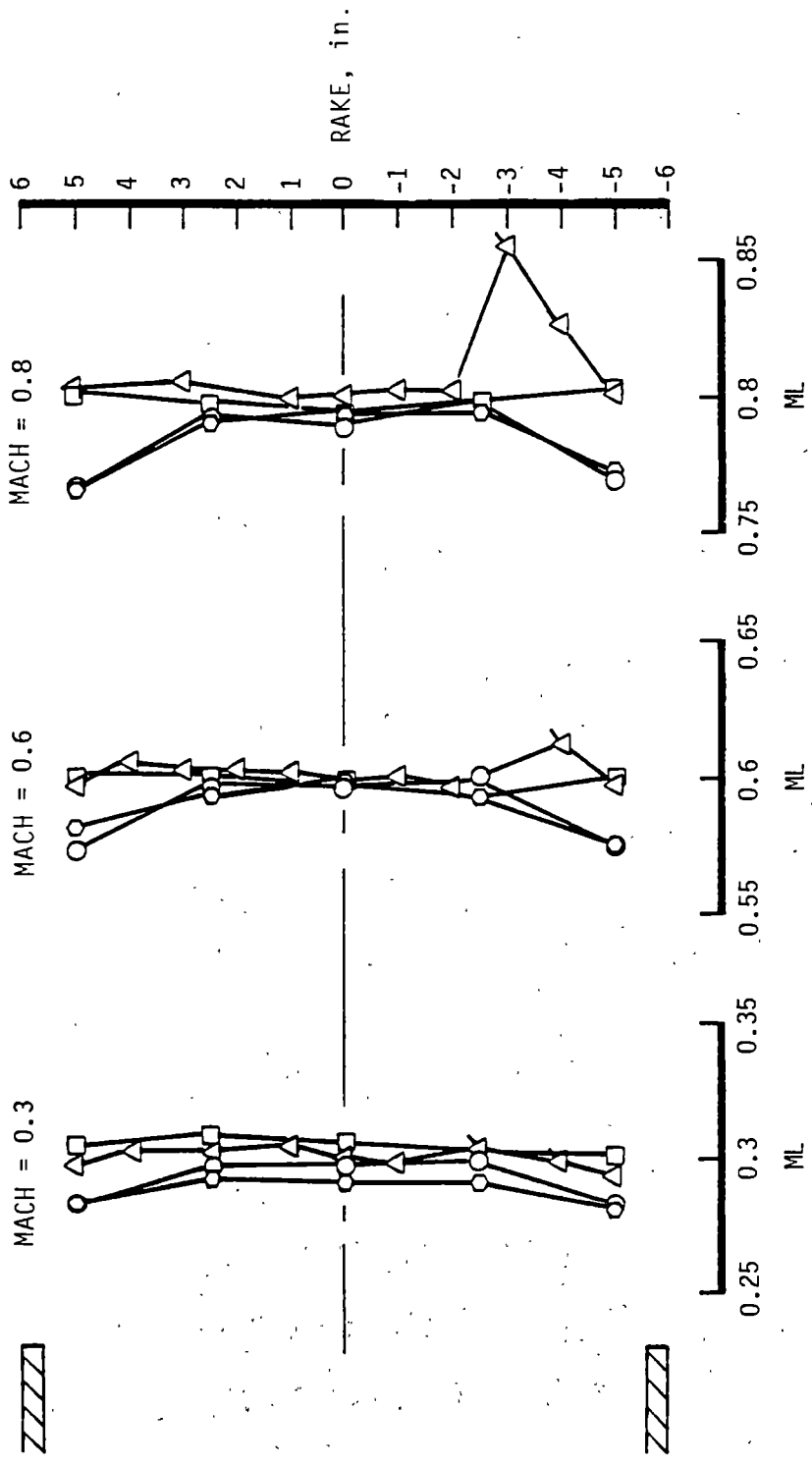


Figure 44. Water Flow Model Exit Dye Injection Zone Designations.

Sym PITCH, deg

- 0
- 20
- △ 30
- 40

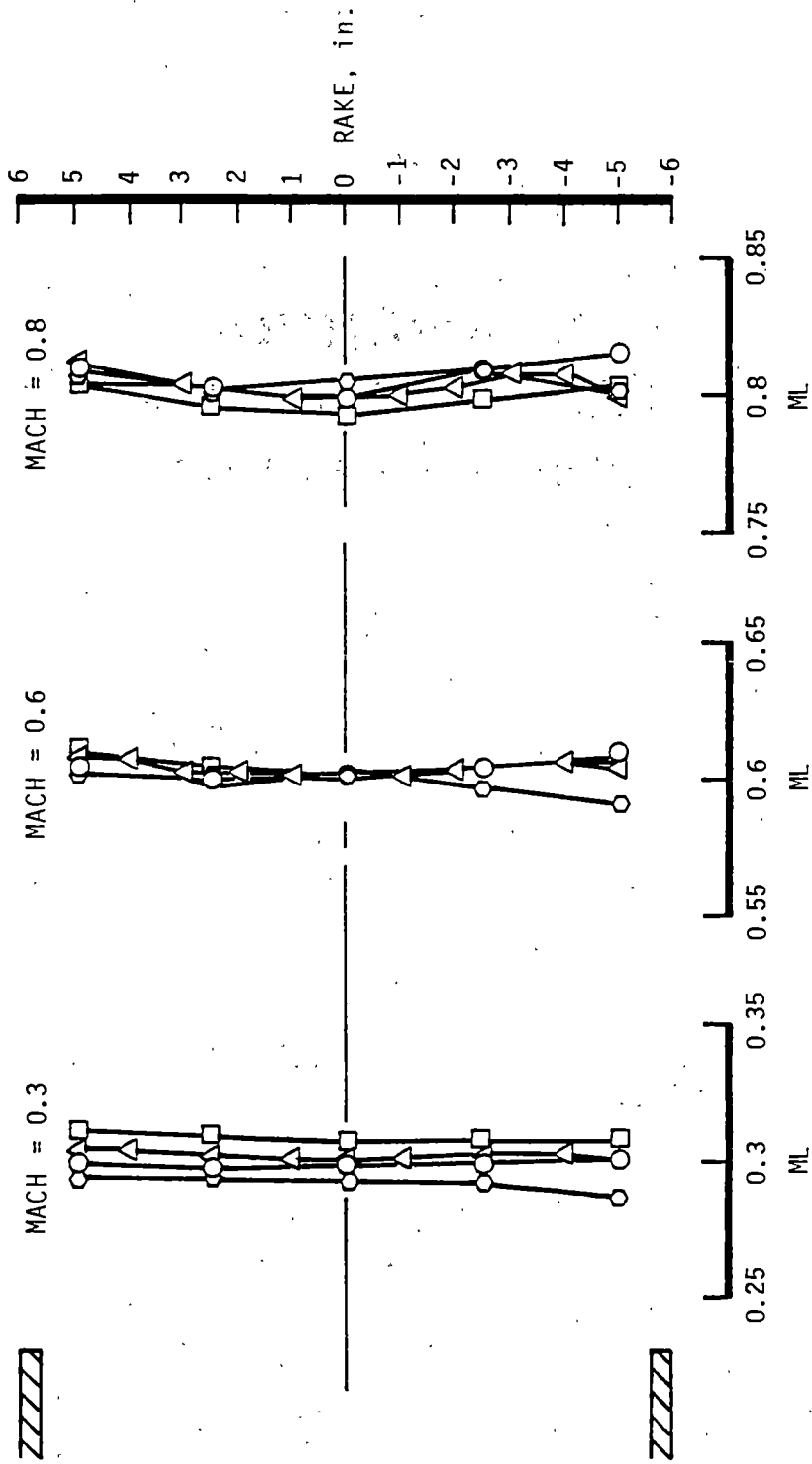
△ Probe Flow Angle Calibration Range Exceeded



a. Probe 1 Traverse

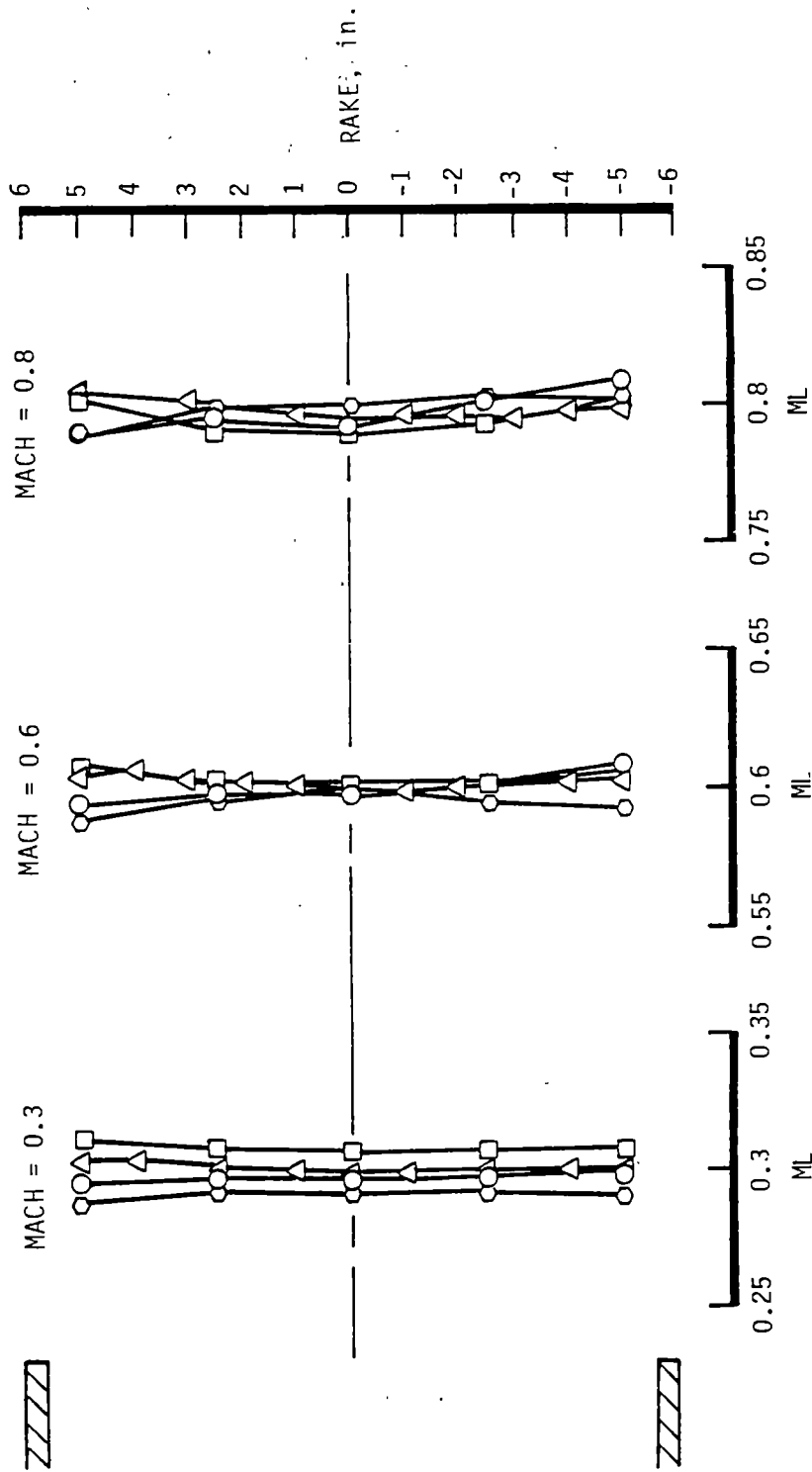
Figure 45. Variable-Area Nozzle Exit Mach Number Measurements with HN = 11.25 in. and DIV = 0 deg.

Sym    PIICH, deg  
 O        0  
 □        20  
 △        30  
 ○        40



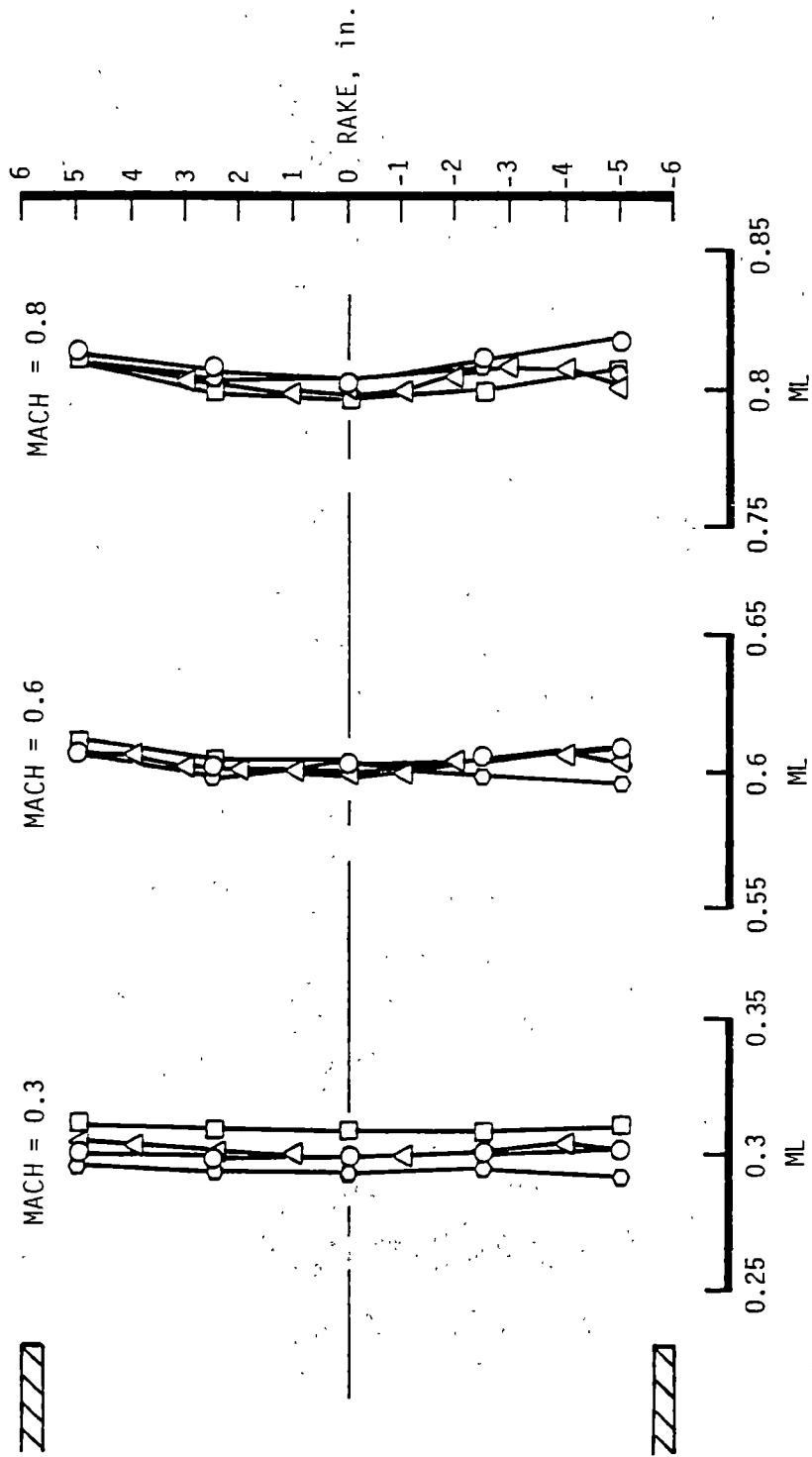
b. Probe 2 Traverse  
 Figure 45. Continued.

Sym	PITCH, deg
○	0
□	20
△	30
○	40



c. Probe 3 Traverse  
Figure 45. Continued.

Sym	PITCH, deg
○	0
□	20
△	30
◇	40

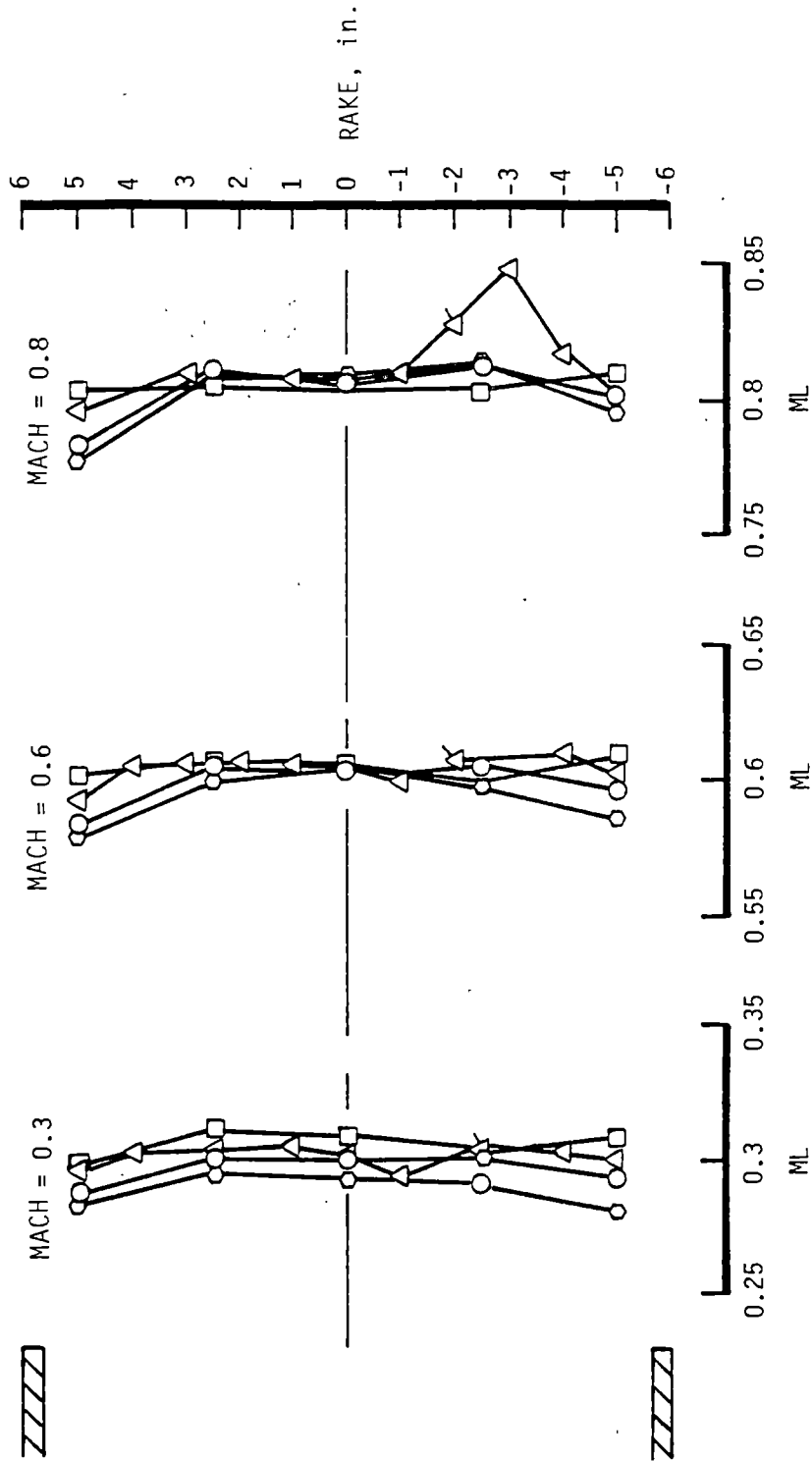


d. Probe 4 Traverse  
Figure 45. Continued.

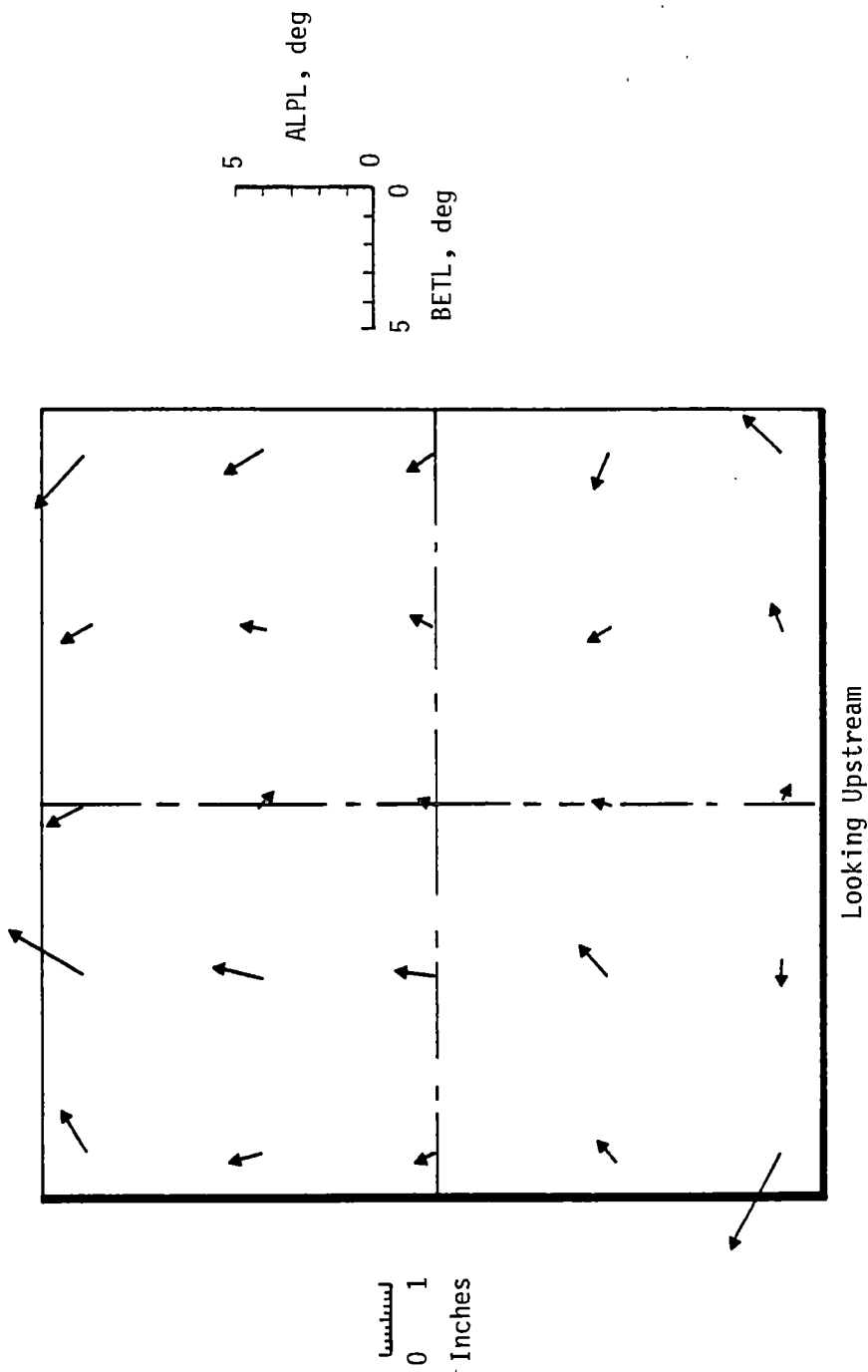
Sym | PITCH, deg

- 0
- 20
- △ 30
- ◊ 40

△ Probe Flow Angle Calibration Range Exceeded

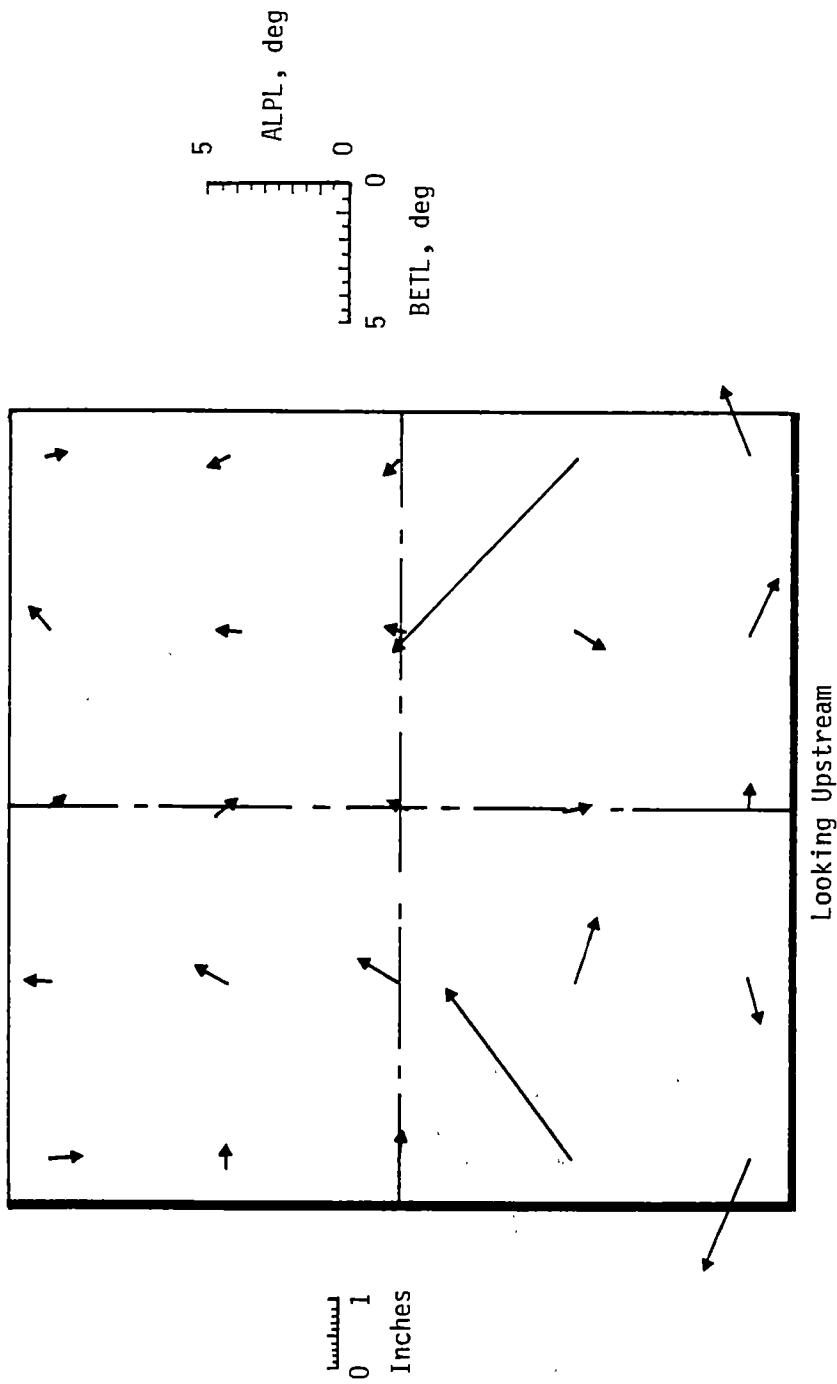


e. Probe 5 Traverse  
Figure 45. Concluded.



a. PITCH = 0 deg.

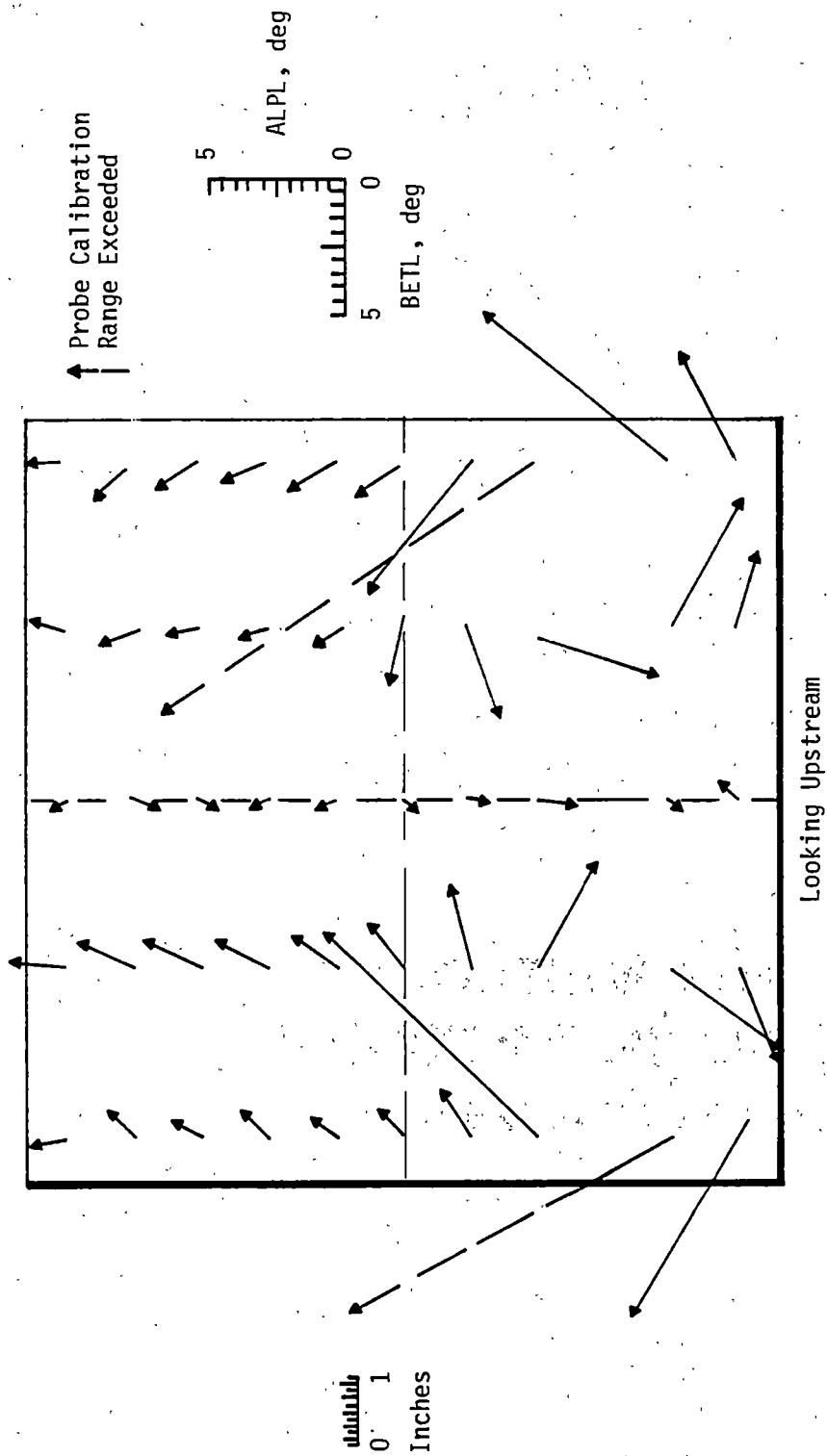
Figure 46. Variable-Area Nozzle Exit Flow Angularity Measurements with MACH = 0.6, HN = 11.25 in., and DIV = 0 deg.



b. PITCH = 20 deg

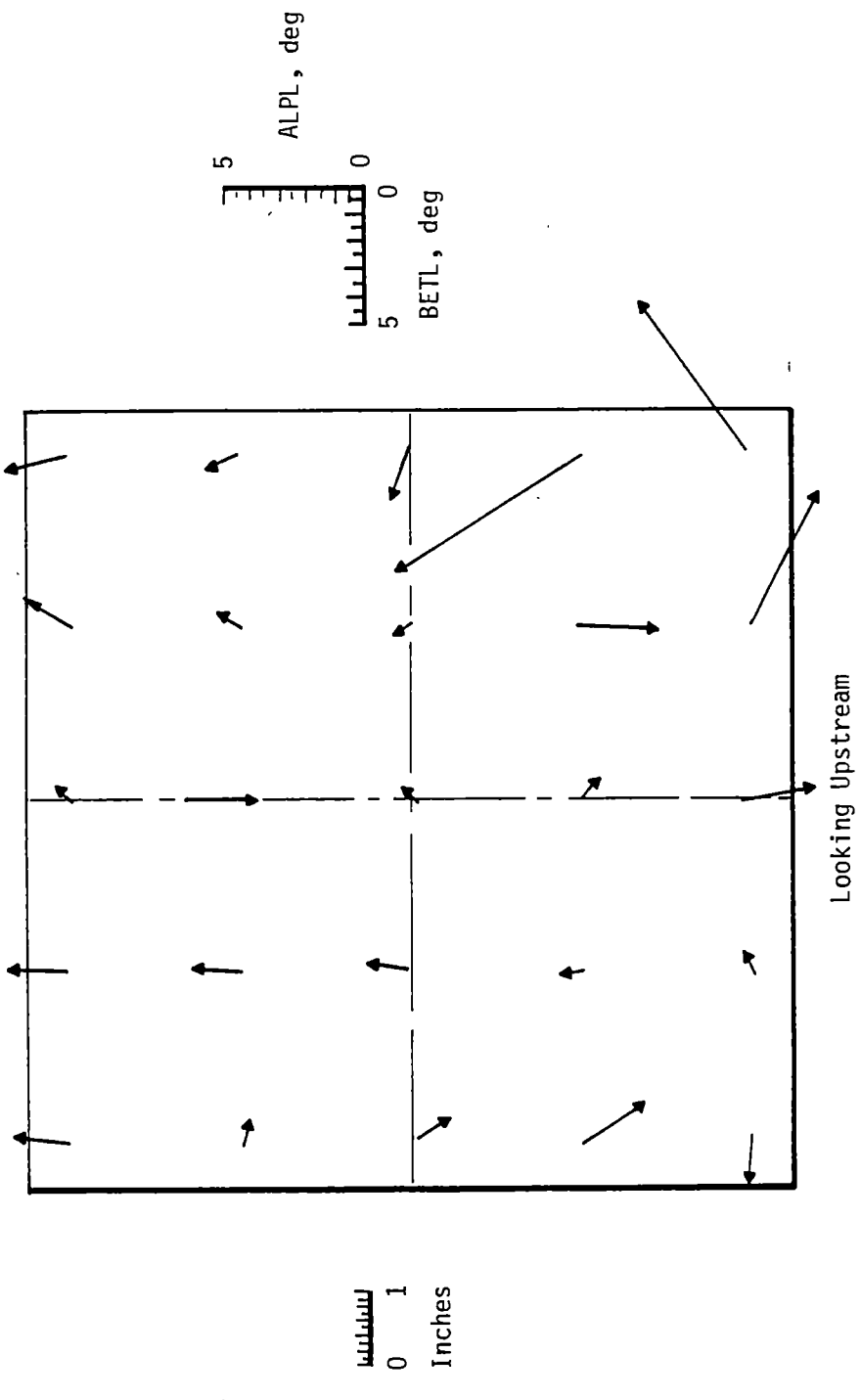
Figure 46. Continued.





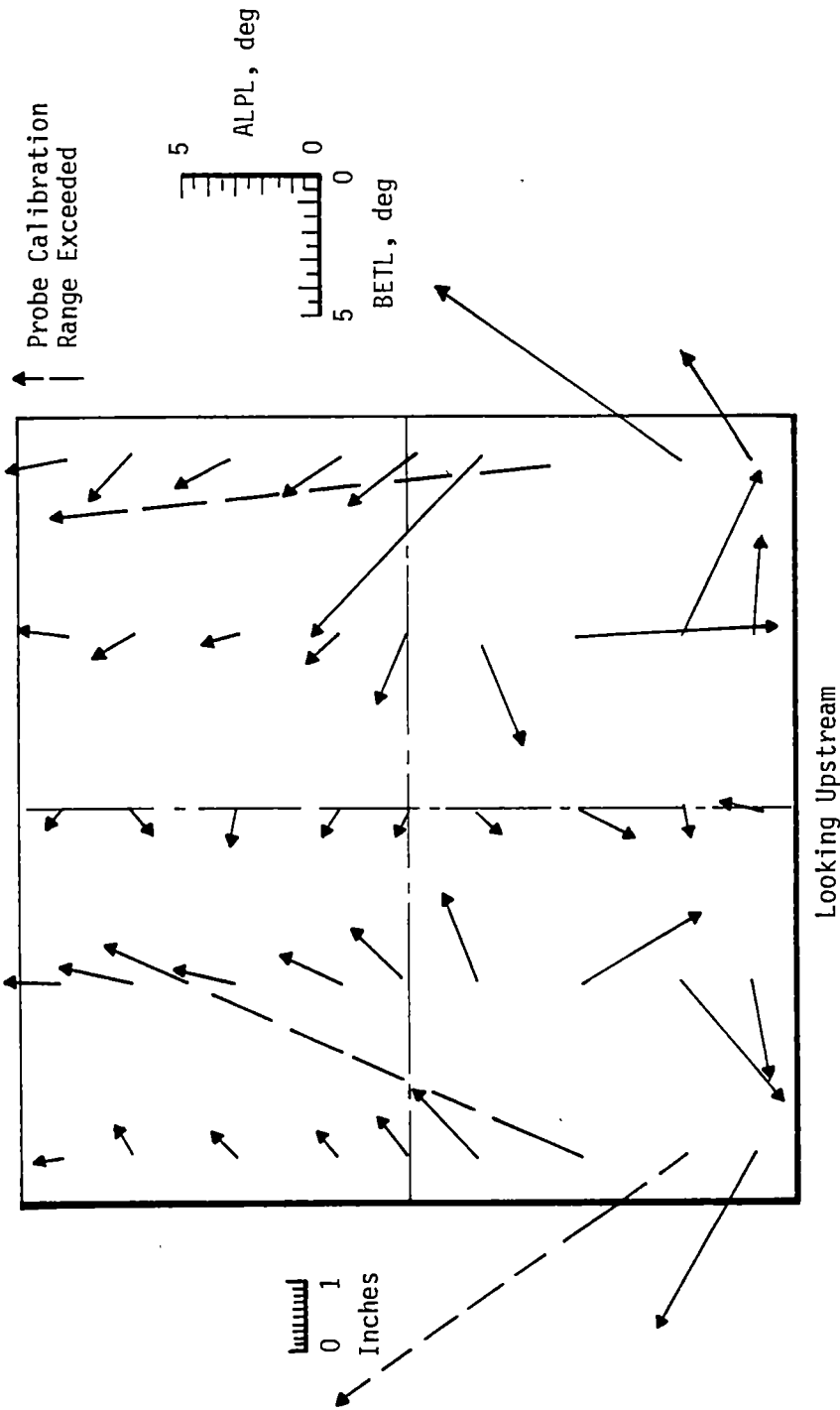
c. PITCH = 30 deg

Figure 46. Continued.



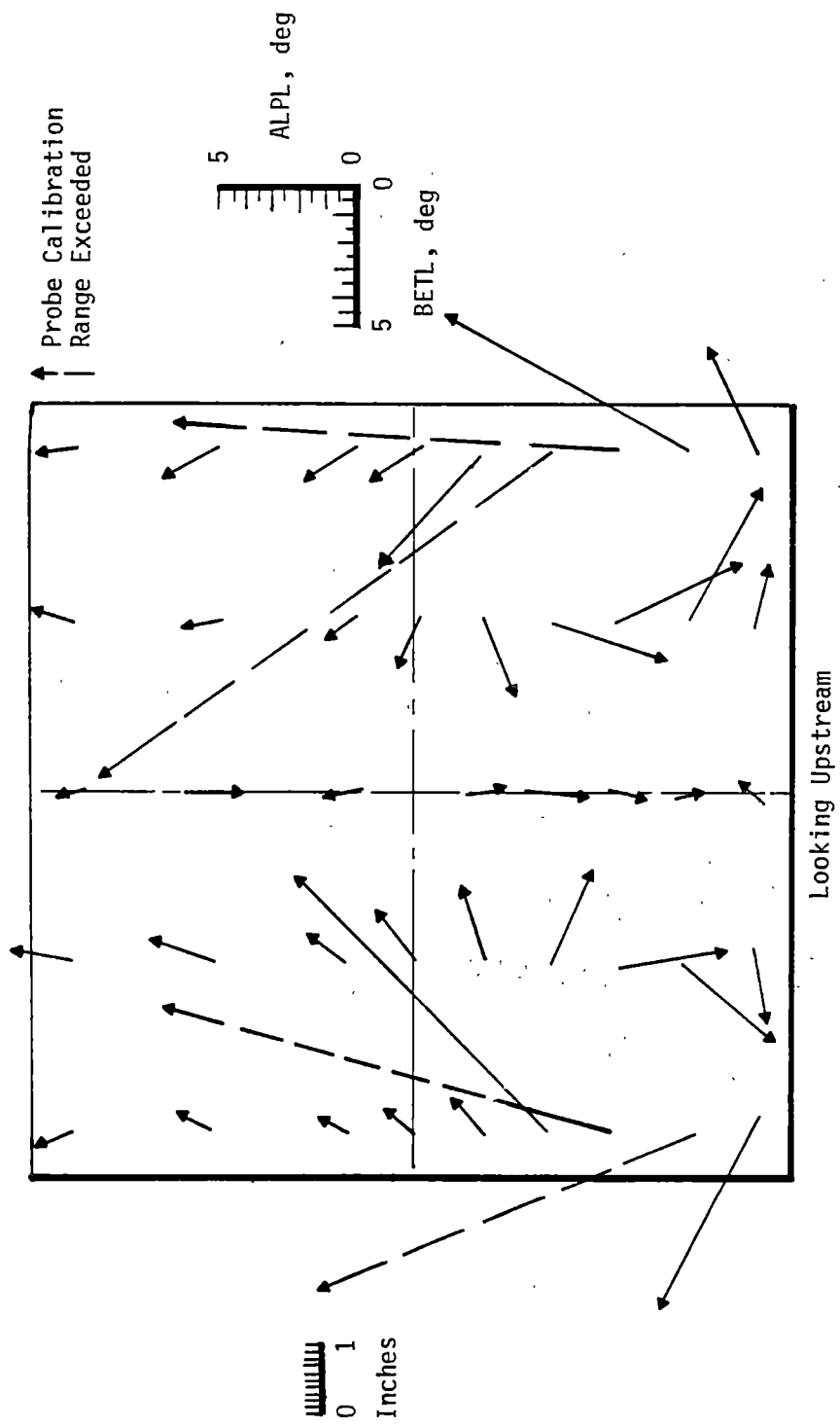
d. PITCH = 40 deg

Figure 46. Concluded.



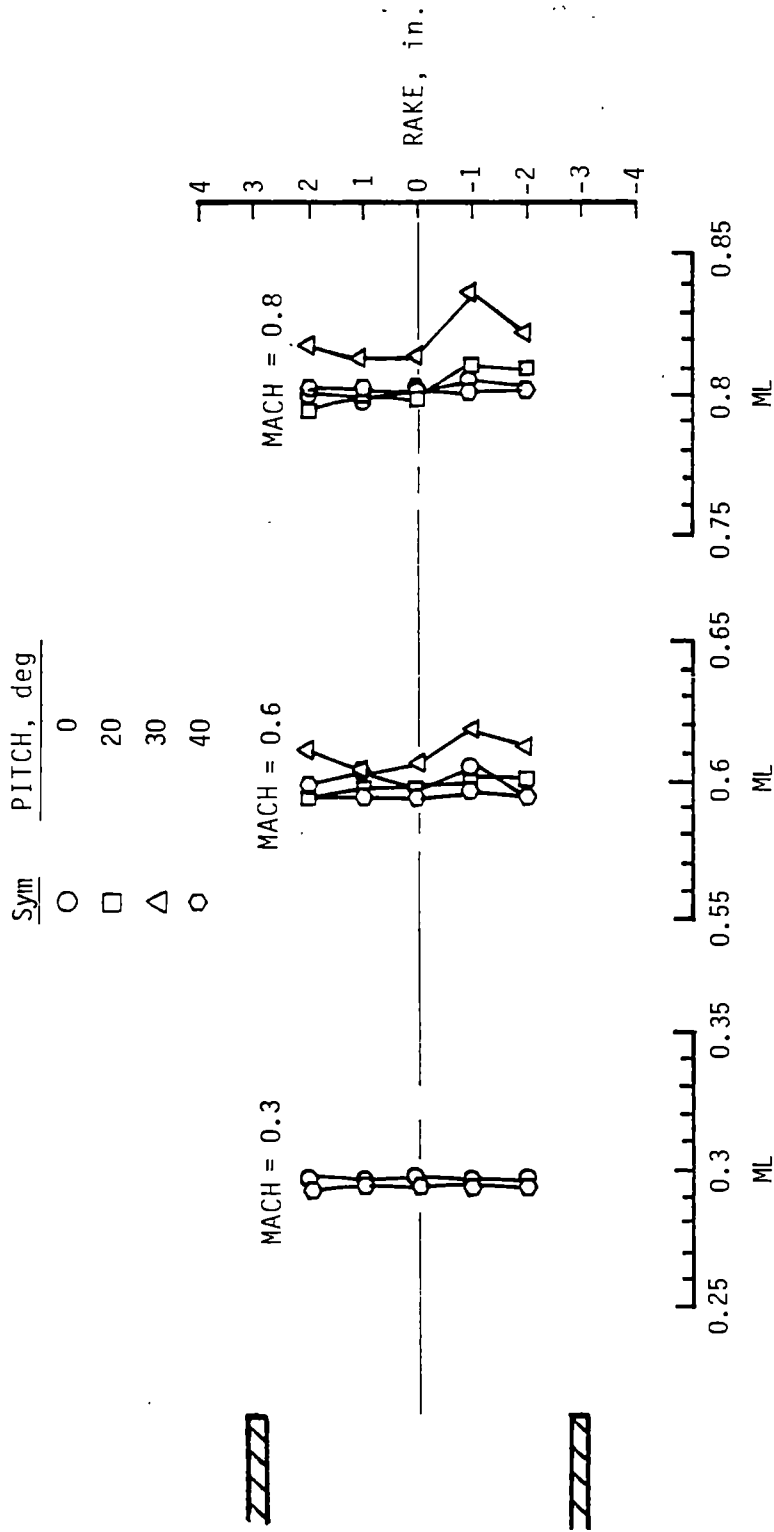
a. MACH = 0.3

Figure 47. Variable-Area Nozzle Exit Flow Angularity Measurements with  $\theta = 30$  Deg, HN = 11.25 in., and DIV = 0 deg.



b. MACH = 0.8

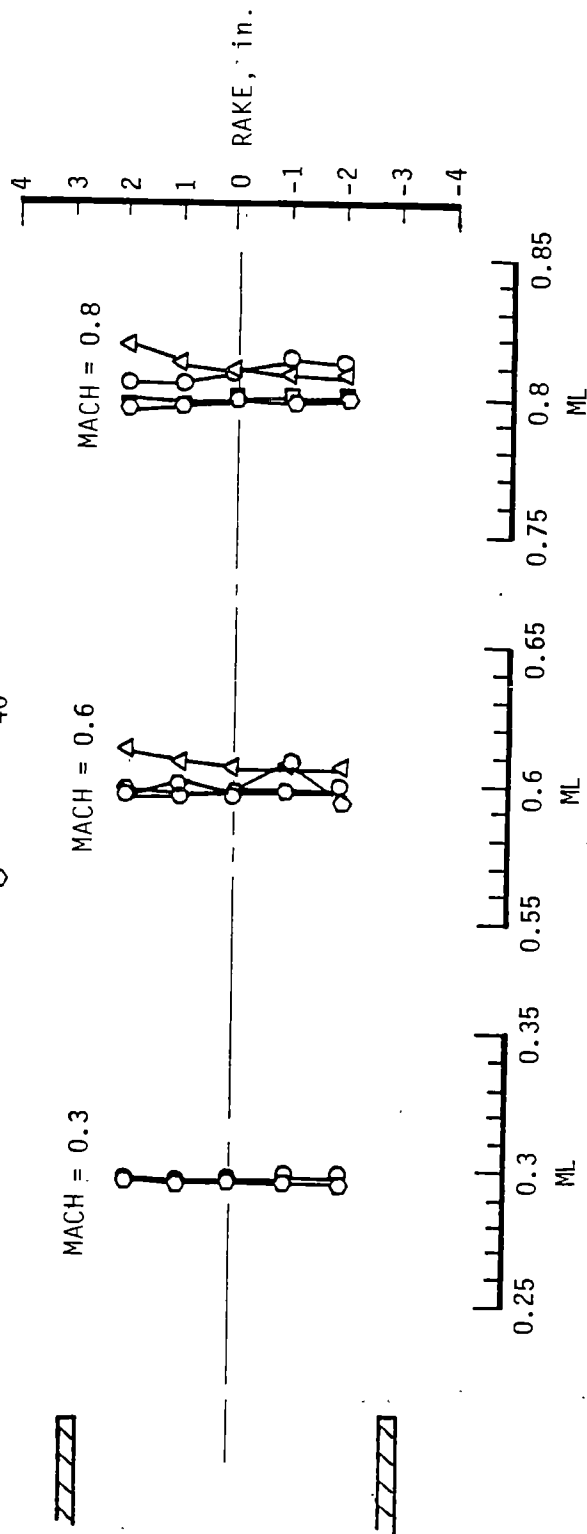
Figure 47. Concluded.



a. Probe 1 Traverse

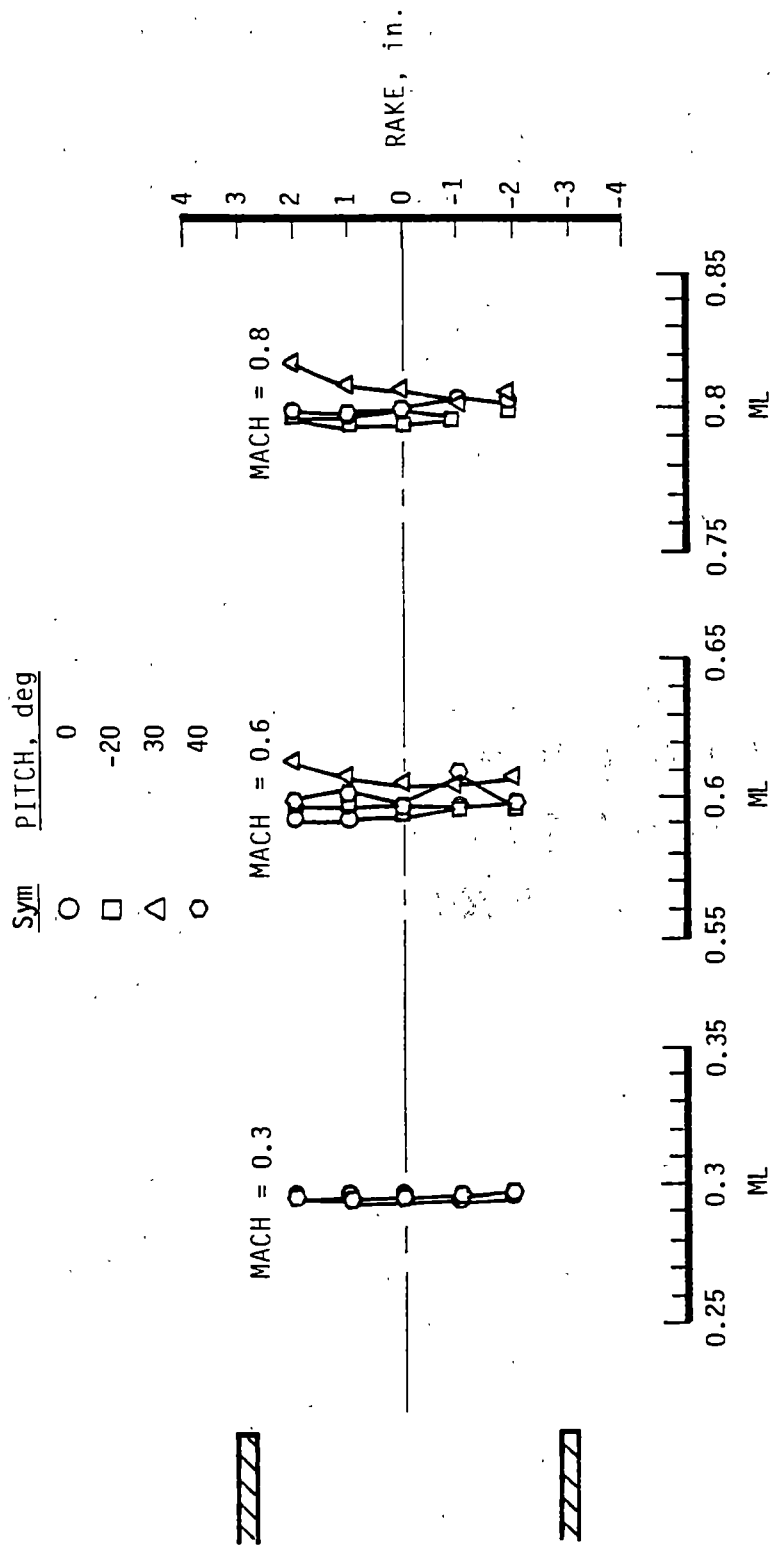
Figure 48. Variable-Area Nozzle Exit Mach Number Measurements with HN = 5.63 in. and DIV = 0 deg.

Sym	PITCH, deg
○	0
□	20
△	30
◊	40



b. Probe 2 Traverse

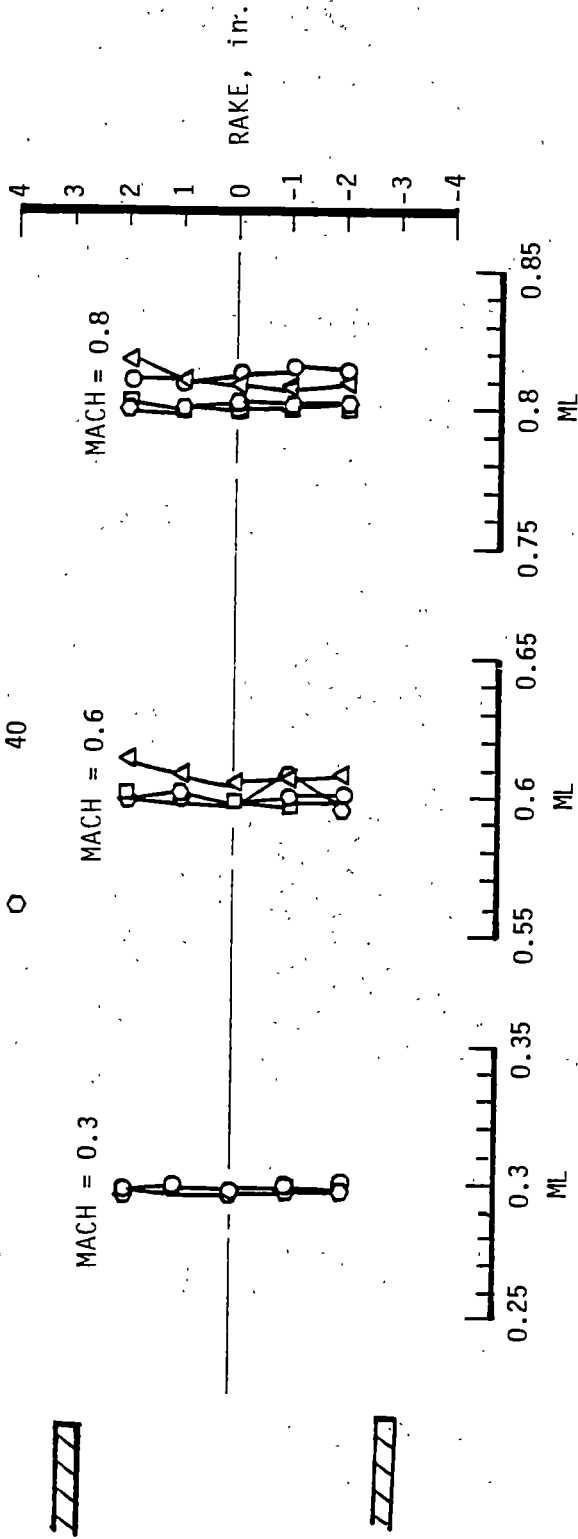
Figure 48. Continued.



c. Probe 3 Traverse

Figure 48. Continued.

Sym	PITCH, deg
○	0
□	20
△	30
○	40

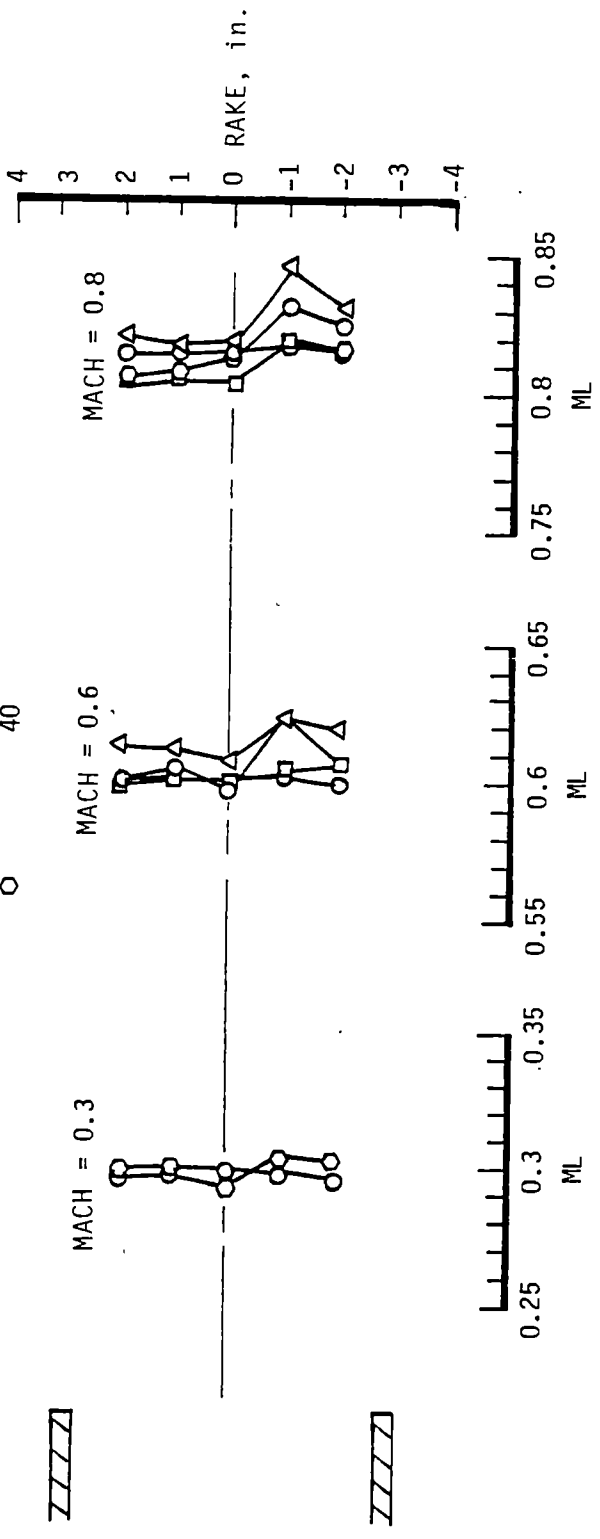


d. Probe 4 Traverse.

Figure 48. Continued.

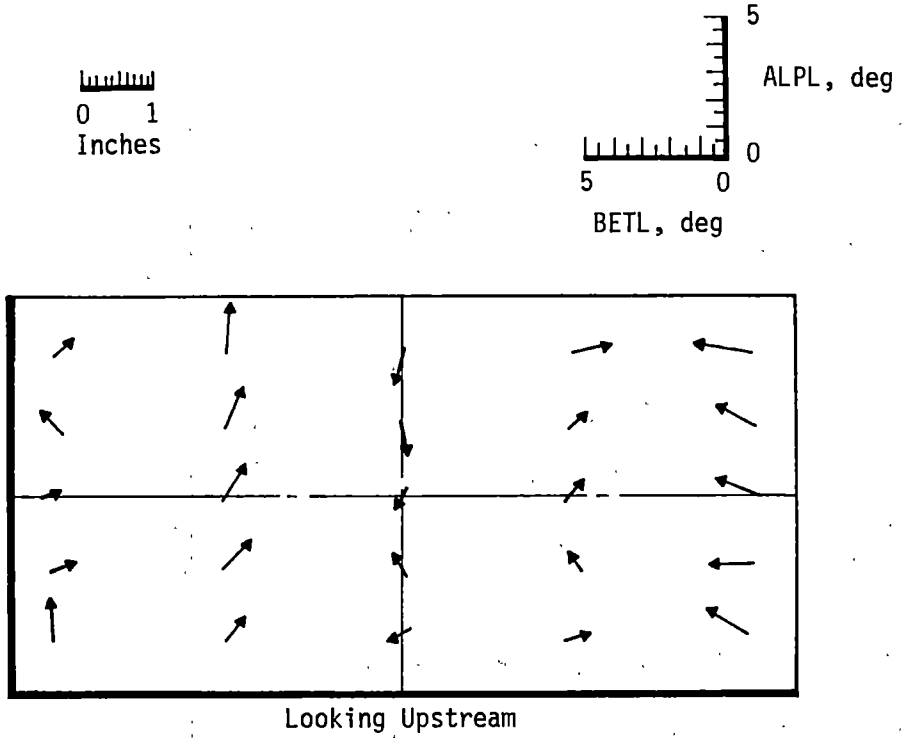


Sym	PITCH, deg
○	0
□	20
△	30
○	40

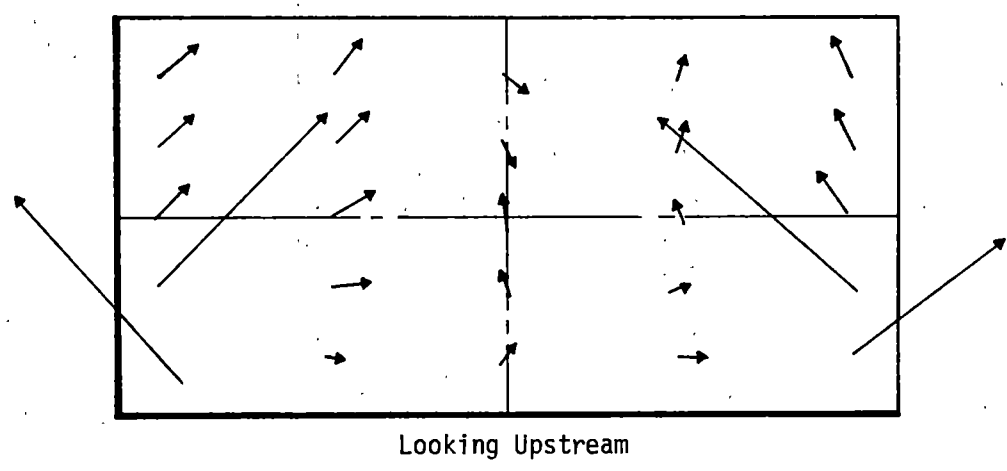


e. Probe 5 Traverse

Figure 48. Concluded.

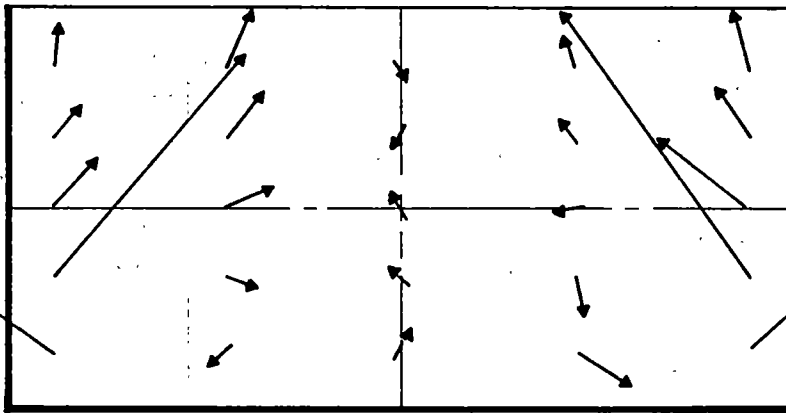
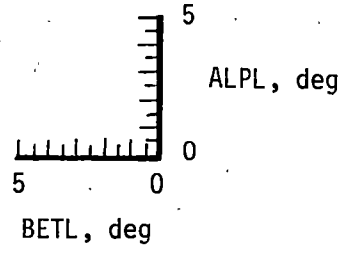
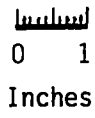


a. PITCH = 0 deg



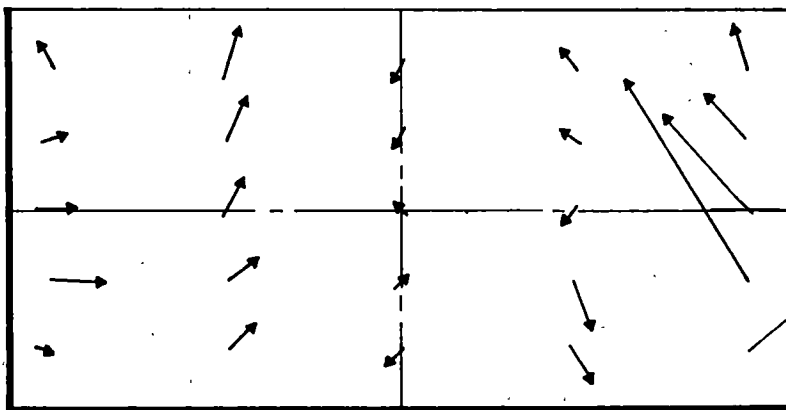
b. PITCH = 20 deg

Figure 49. Variable-Area Nozzle Exit Flow Angularity Measurements with MACH = 0.6, HN = 5.63 in., and DIV = 0 deg.



Looking Upstream

c. PITCH = 30 deg



Looking Upstream

d. PITCH = 40 deg

Figure 49. Concluded.

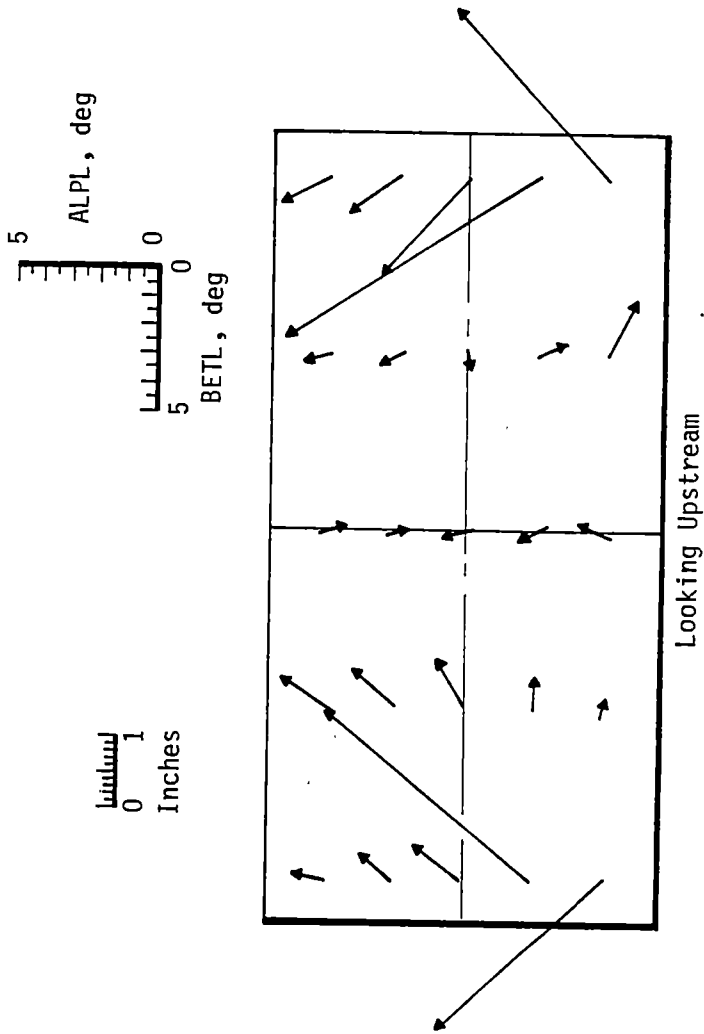


Figure 50. Variable-Area Nozzle Exit Flow Angularity Measurements with MACH = 0.8,  $\theta = 30$  deg, HN = 5.63 in. and DIV = 0 deg.

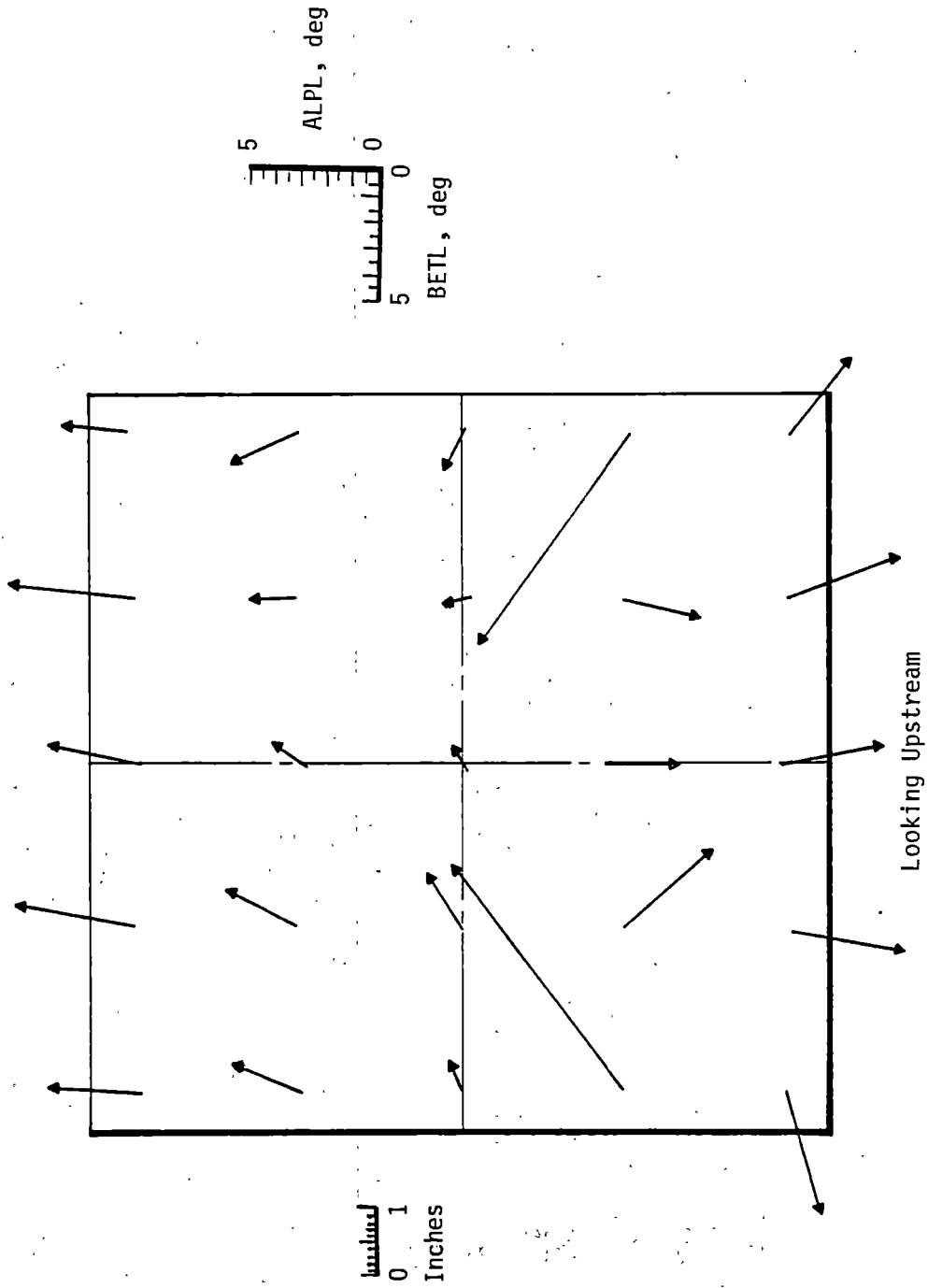
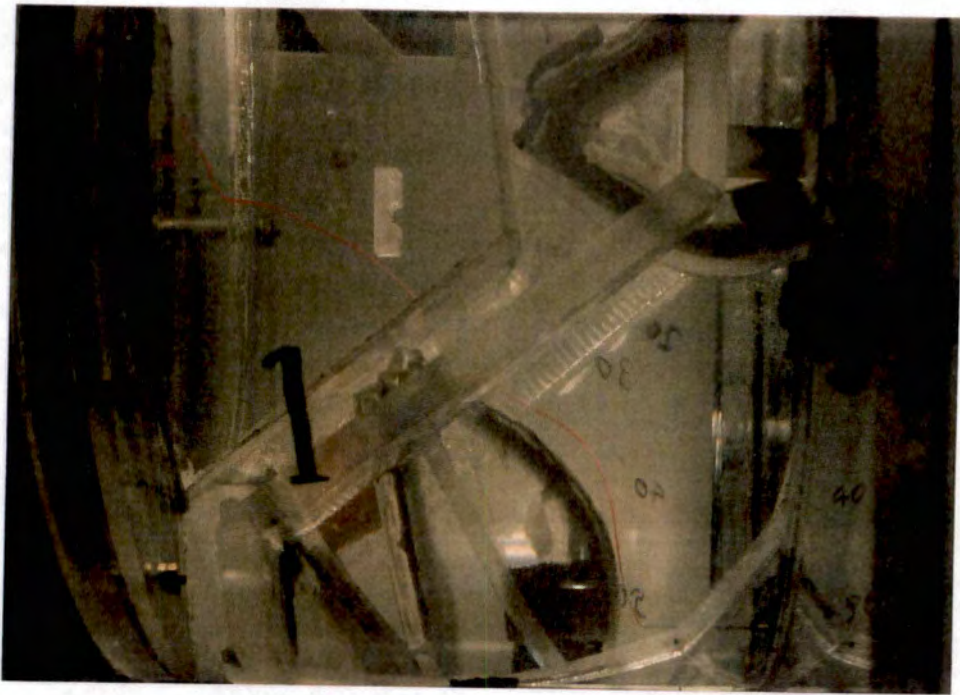
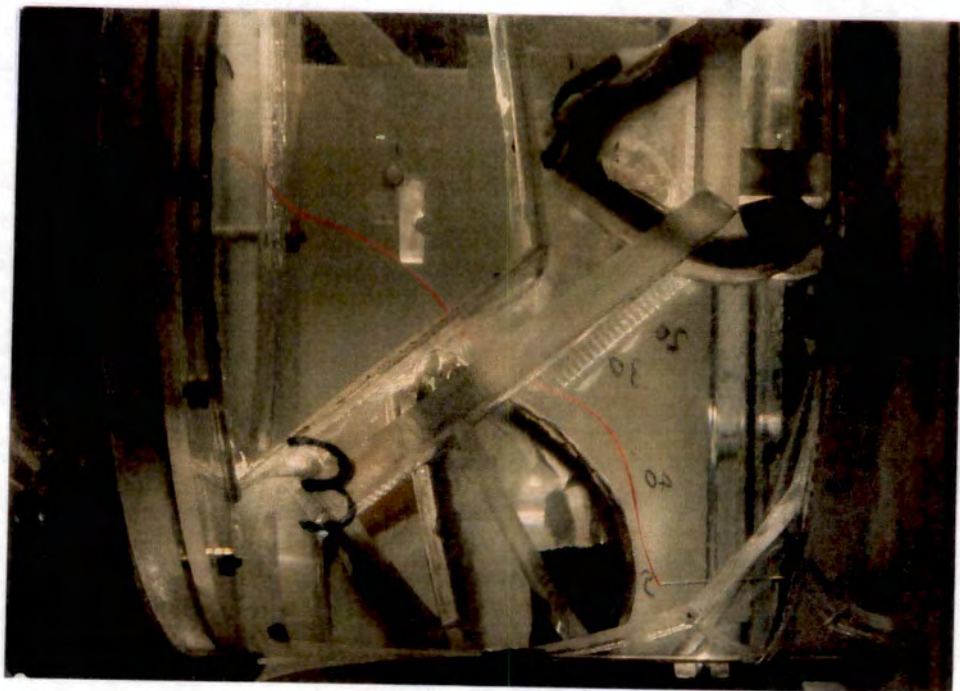


Figure 51. Variable-Area Nozzle Exit Flow Angularity Measurements with  
MACH = 0.6,  $\theta = 20$  deg, HN = 11.25 in., and DIV = 4 deg.



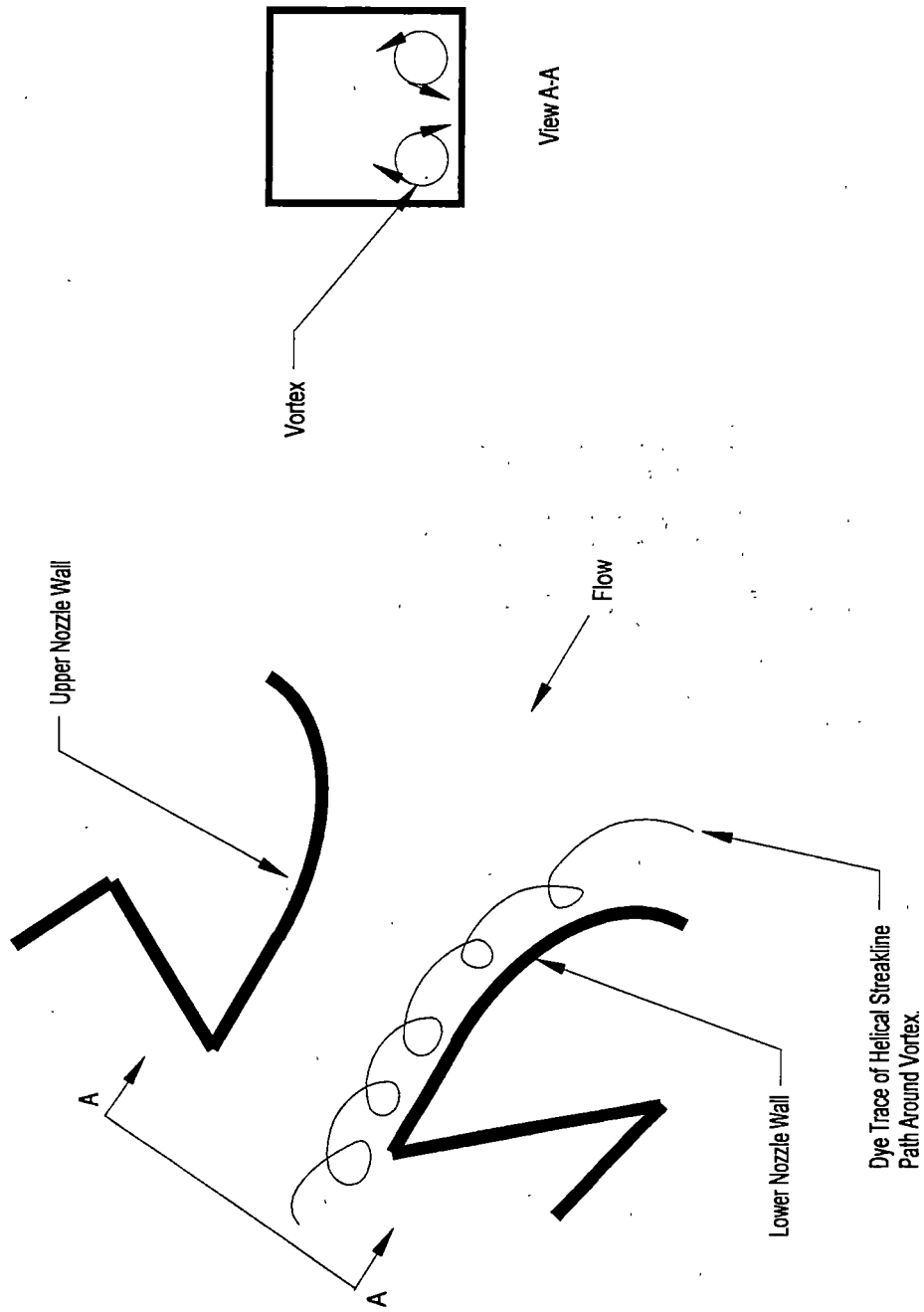
Zone 1



Zone 3

a. Photographs of Zone 1 and Zone 3 streaklines

Figure 52. Water Flow Visualization of Variable-Area Nozzle Vortices.



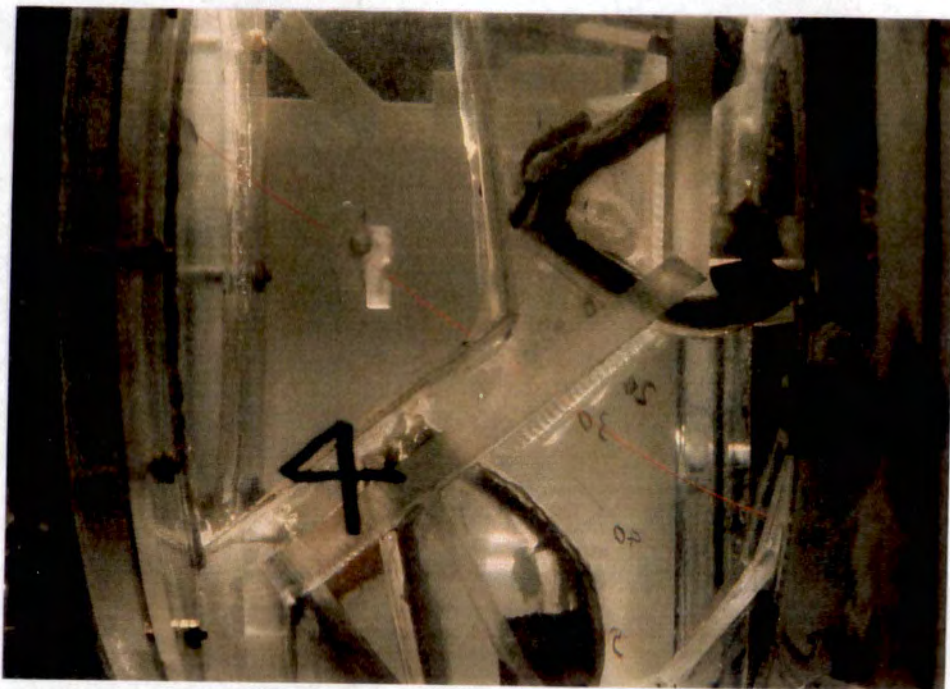
b. Sketch of Vortex

Figure 52. Concluded.





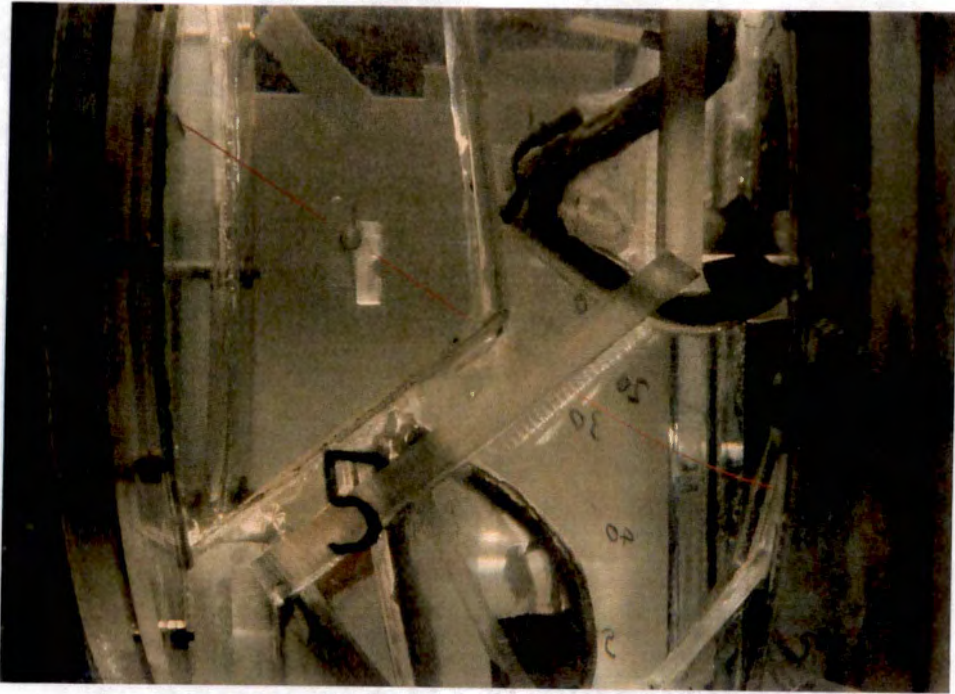
a. Zone 2



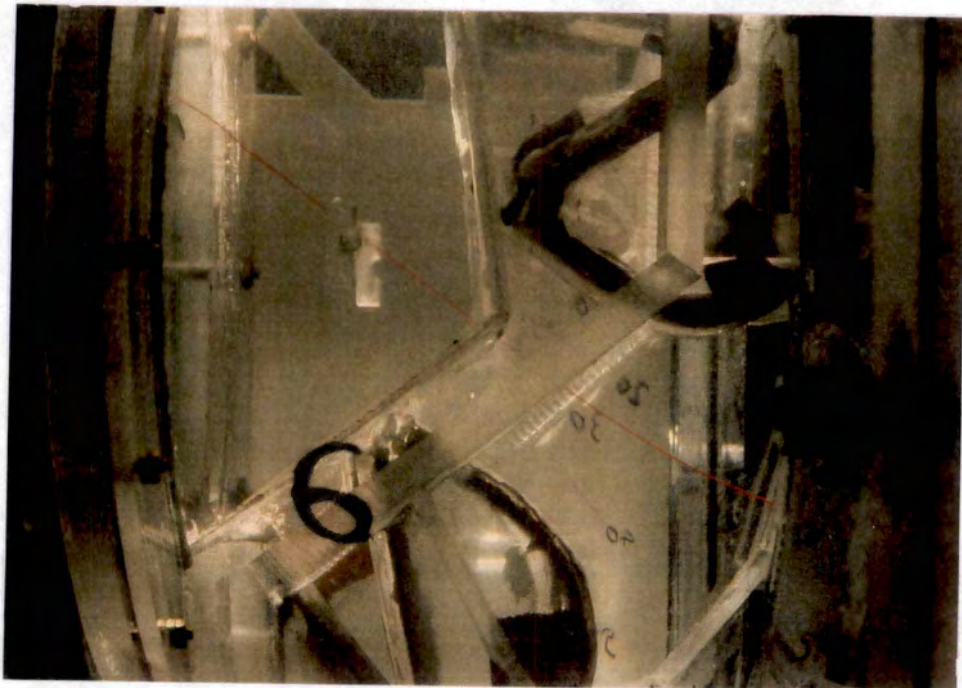
b. Zone 4

Figure 53. Water Flow Visualization of Variable-Area Nozzle Streaklines in Zones without Vortices.



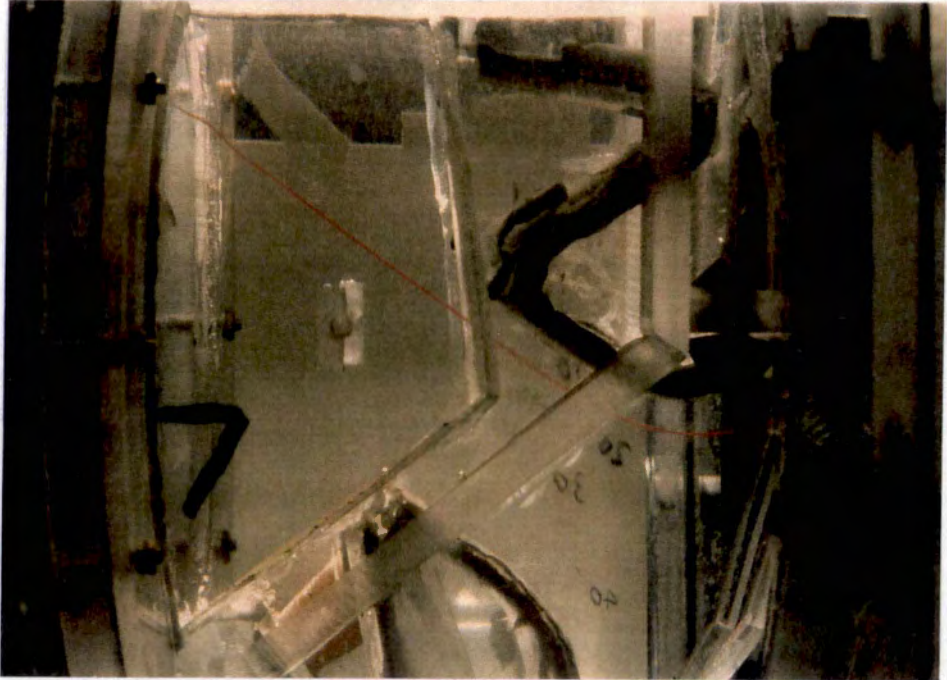


c. Zone 5

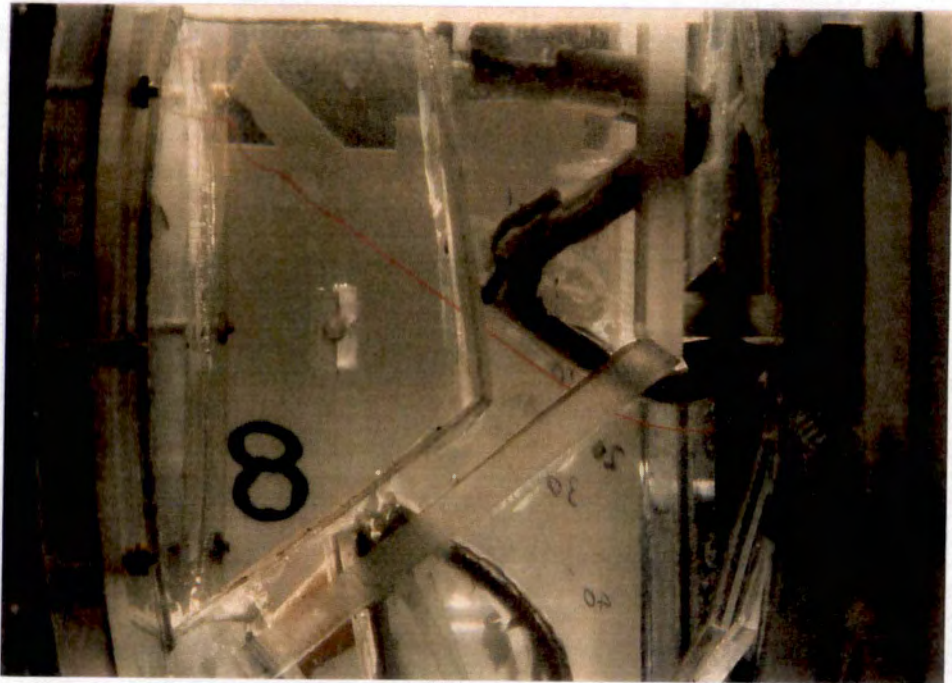


d. Zone 6

Figure 53. Continued.



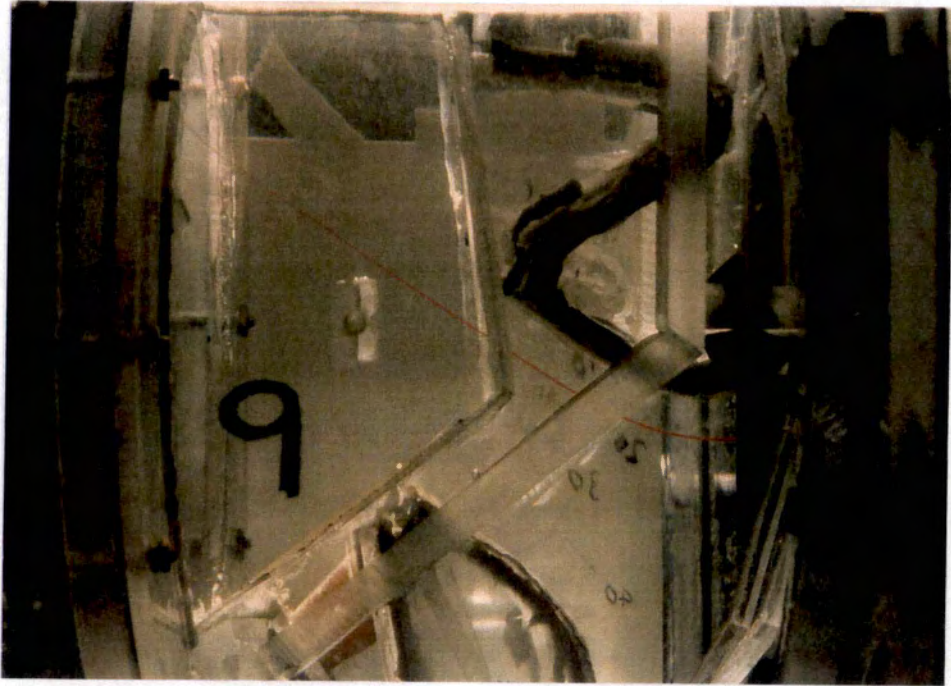
e. Zone 7



f. Zone 8

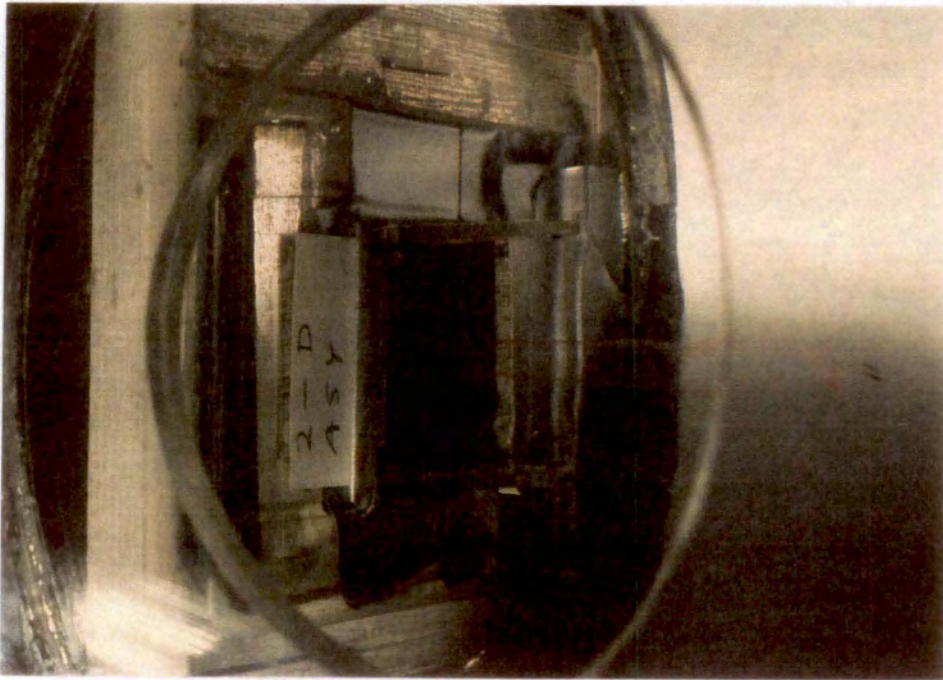
Figure 53. Continued.



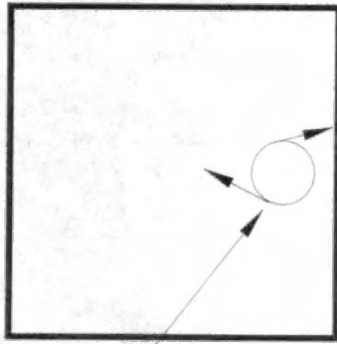


g. Zone 9

Figure 53. Concluded.



a. View Looking into Nozzle Exit,  $ZI = 1.4$  in.



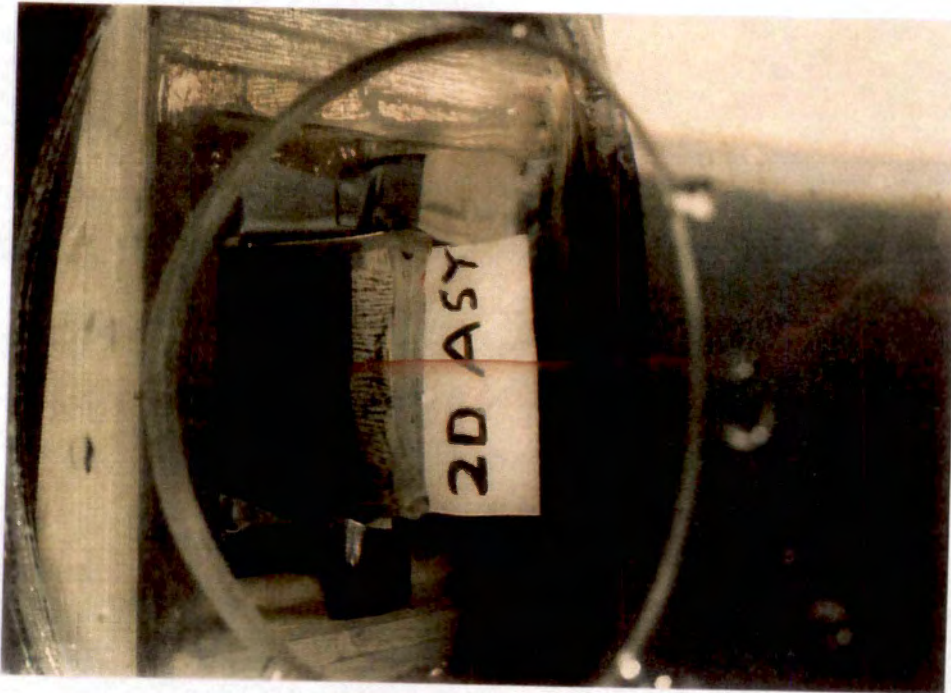
Vortex

View Upstream into Nozzle Exit

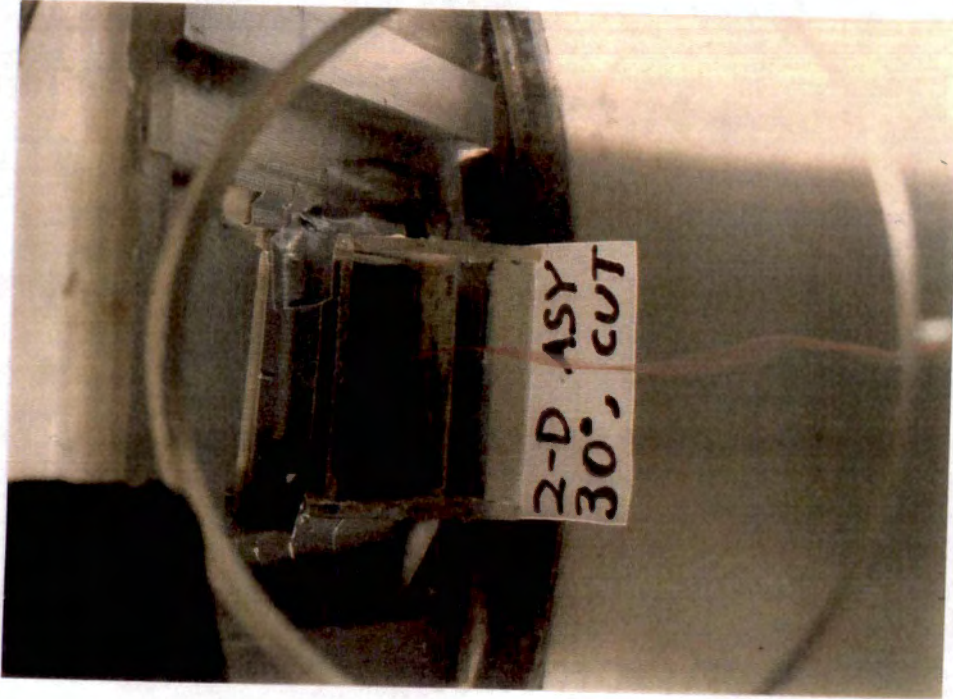
b. Sketch,  $ZI = 1.4$  in.

Figure 54. Water Flow Streaklines for 2-D ASY Nozzle Set at  $\theta = 30$  deg.



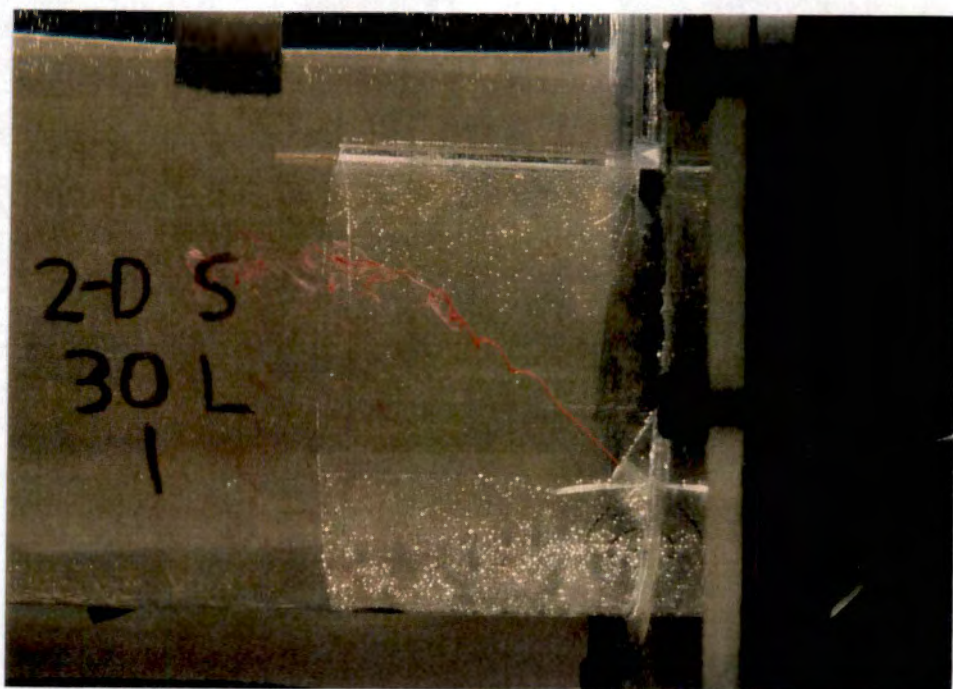


c.  $ZI = 3.1$  in.

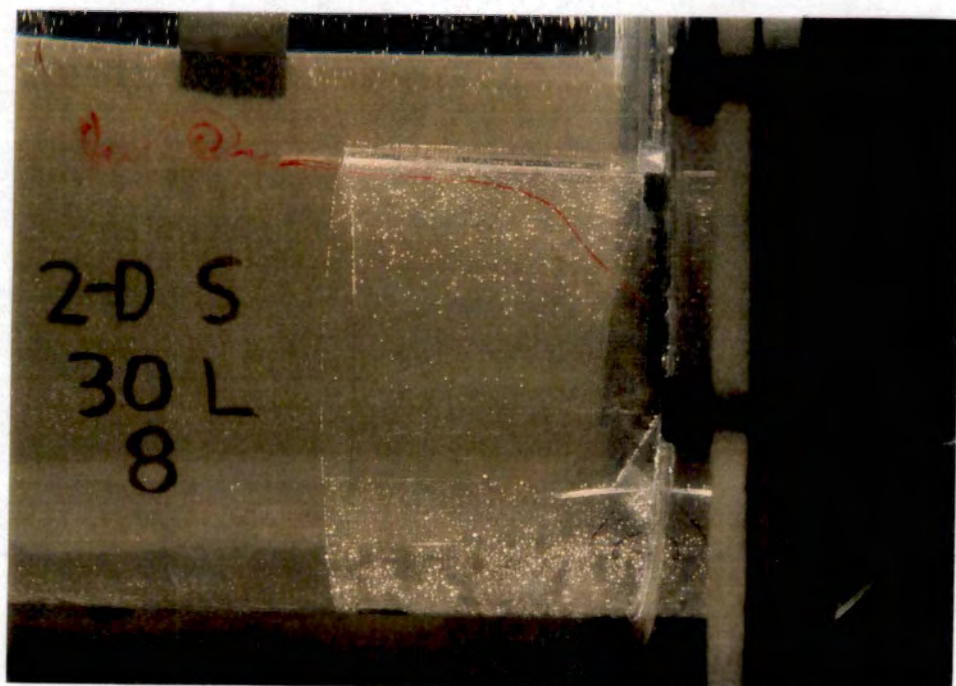


d.  $ZI = 0.6$  in.

Figure 54. Concluded.



a. Zone 1



b. Zone 8

Figure 55. Water Flow Streaklines Inside Nozzle Exit Cavity with 2-D SYM Nozzle Set at  $\theta = 30$  deg and ZI = 0.6 in.



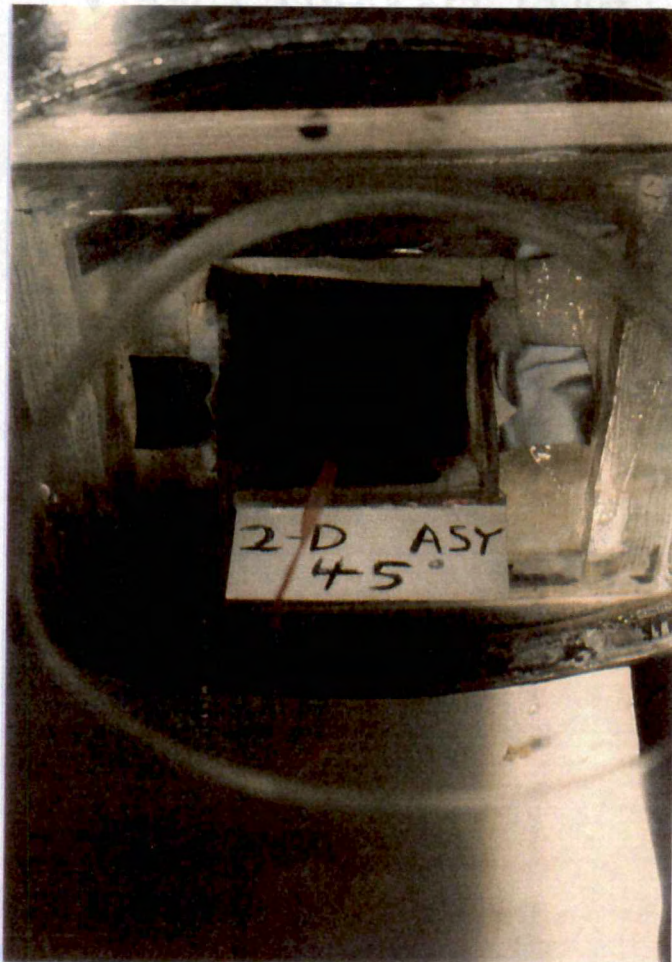


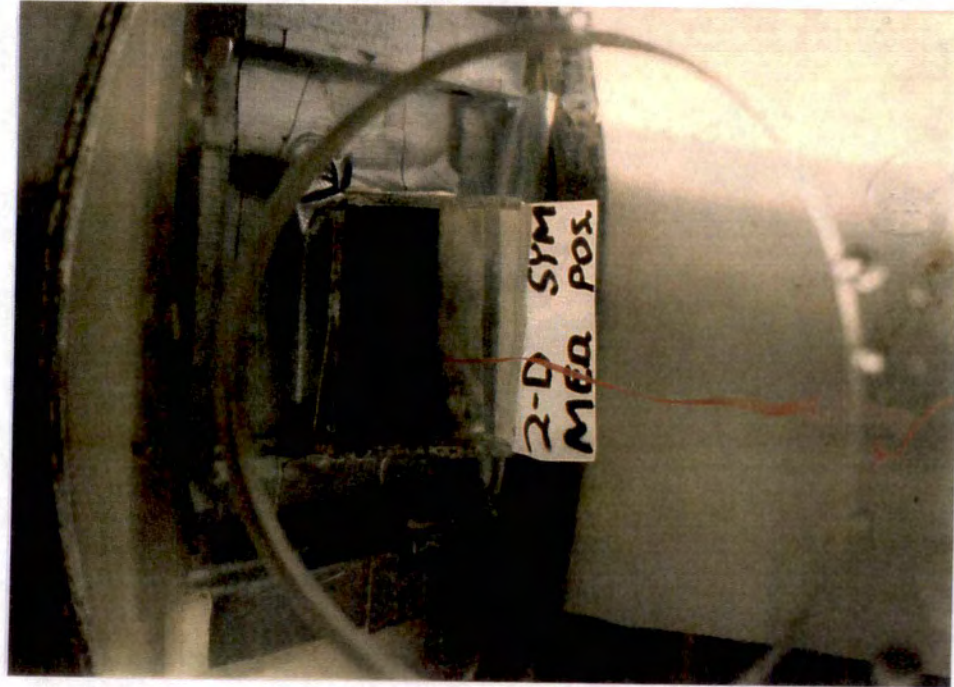
Figure 56. Water Flow Streaklines for 2-D ASY Nozzle  
Set at  $\theta = 45$  deg and ZI = 2 in.



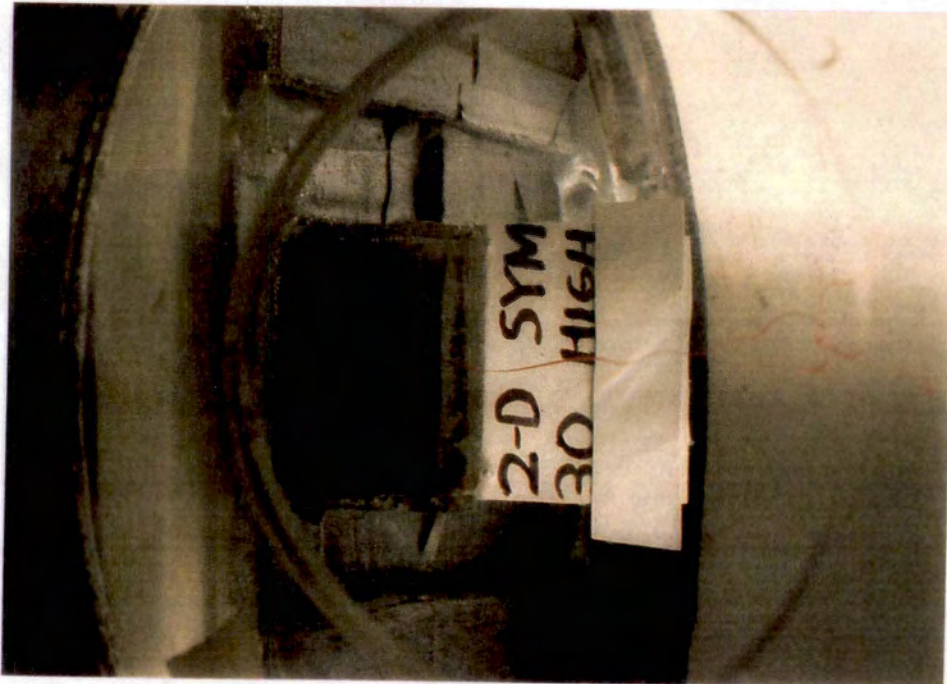
a.  $ZI = 0.6$  in.

Figure 57. Water Flow Streaklines for 2-D SYM Nozzle Set at  $\theta = 30$  deg.





c. ZI = 1.4 in.

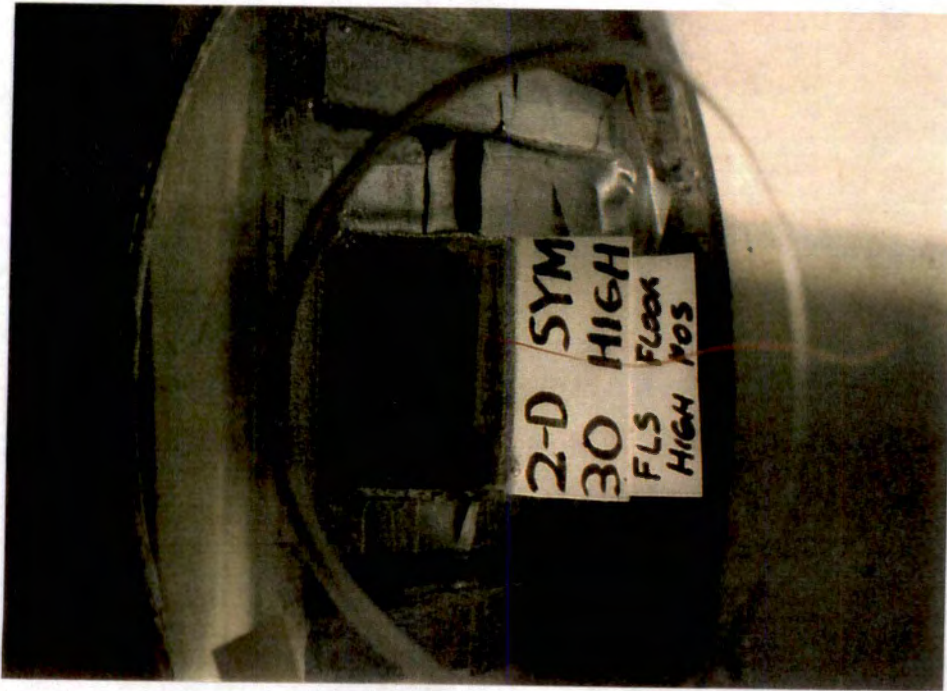


b. ZI = 3.4 in.

Figure 57. Concluded.



a.  $ZI = 0.6$  in.



b.  $ZI = 0.0$  in.

Figure 58. Water Flow Streaklines for 2-D SYM Nozzle Set at  $\theta = 30$  deg with Artificial Floor Installed.



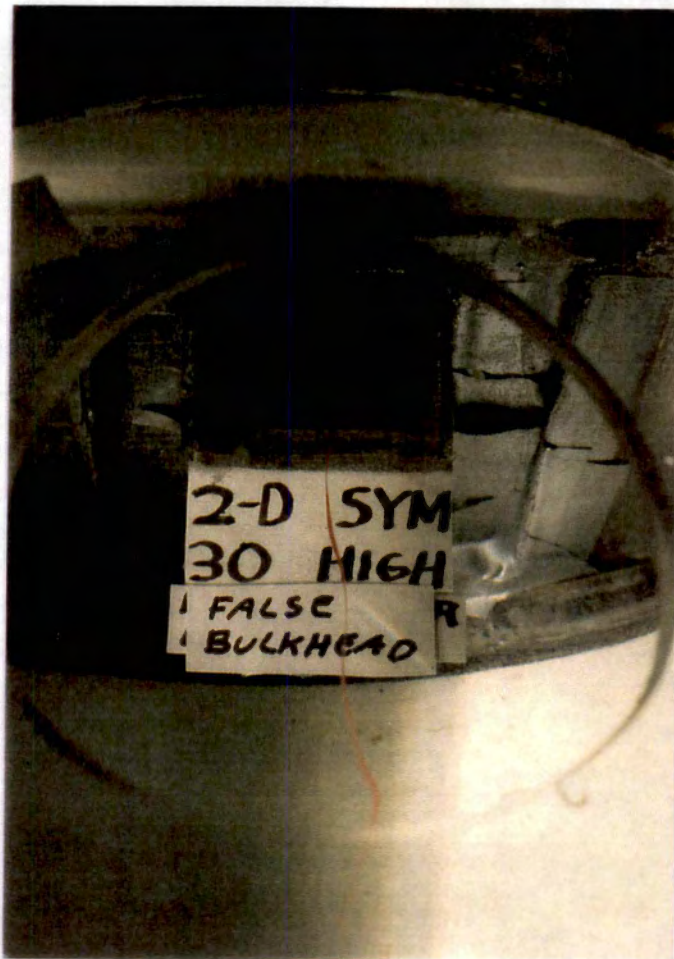
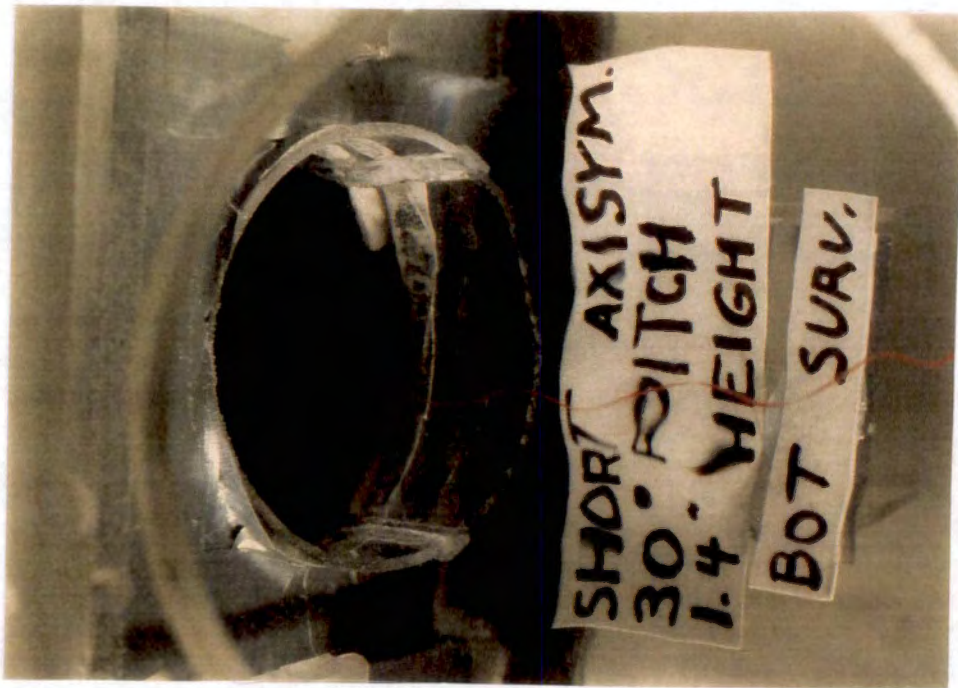
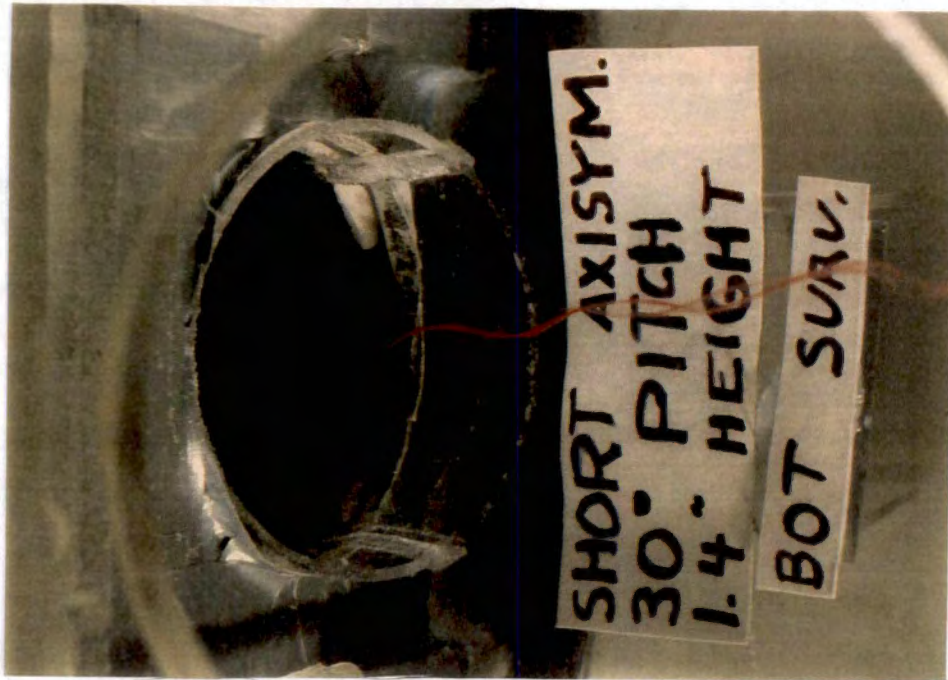


Figure 59. Water Flow Streaklines for 2-D SYM Nozzle Set at  $\theta = 30$  deg and  $ZI = 3.3$  in. with Artificial Bulkhead Installed.



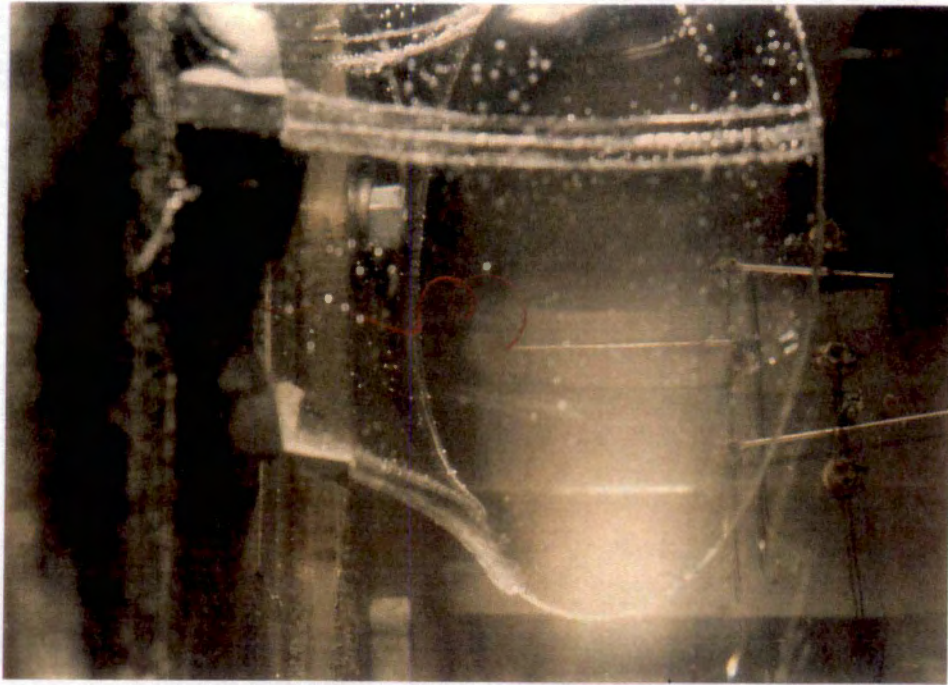
a.  $ZI = 1.4$  in., Vortex in First Position



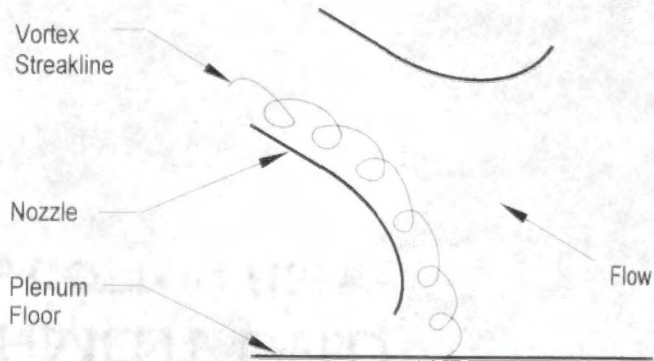
b.  $ZI = 1.4$  in., Vortex in Second Position

Figure 60. Water Flow Streaklines in Short Axisymmetric Nozzle Set at  $\theta = 30$  deg.



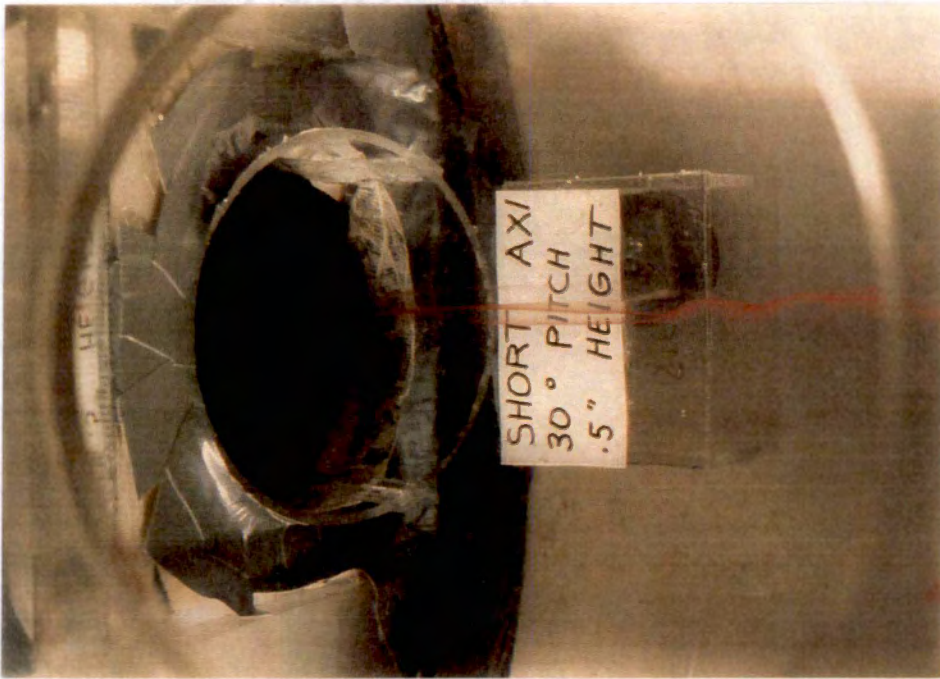


Camera View



c.  $ZI = 1.4$  in., Top View of Vortex Attachment Point on Plenum Wall

Figure 60. Continued.



d.  $ZI = 0.5$  in.



e.  $ZI = 0.5$  in., Top View of Vortex Attachment Point on Plenum Wall

Figure 60. Concluded.



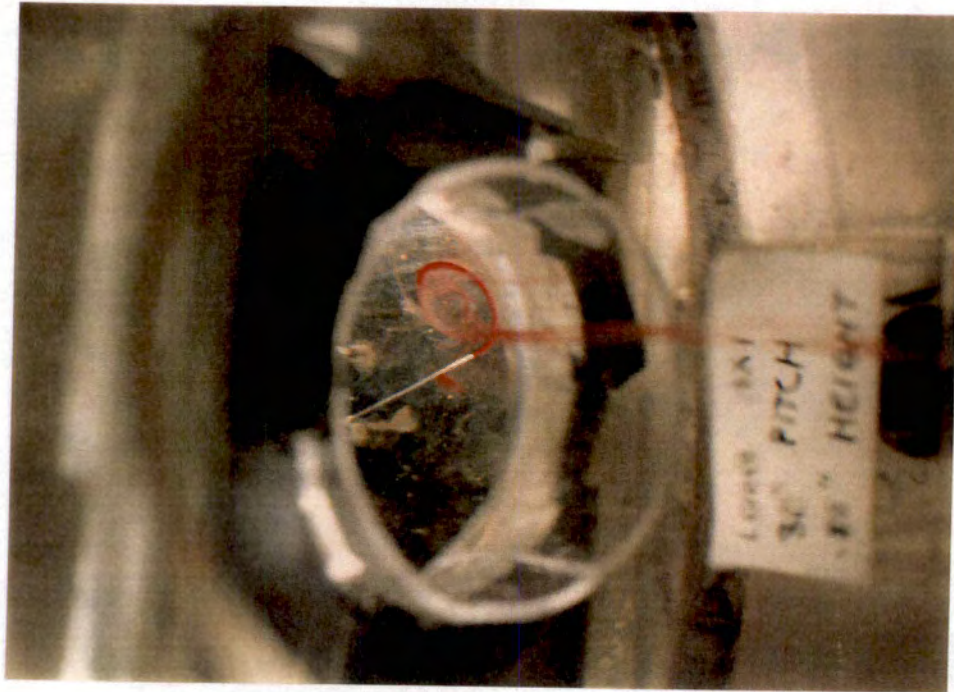
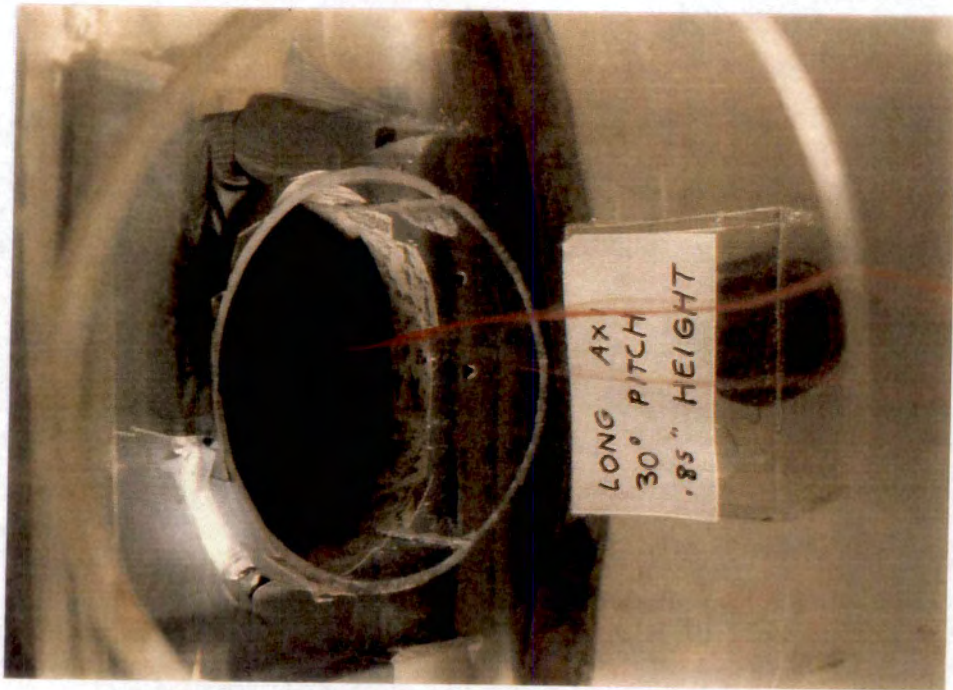
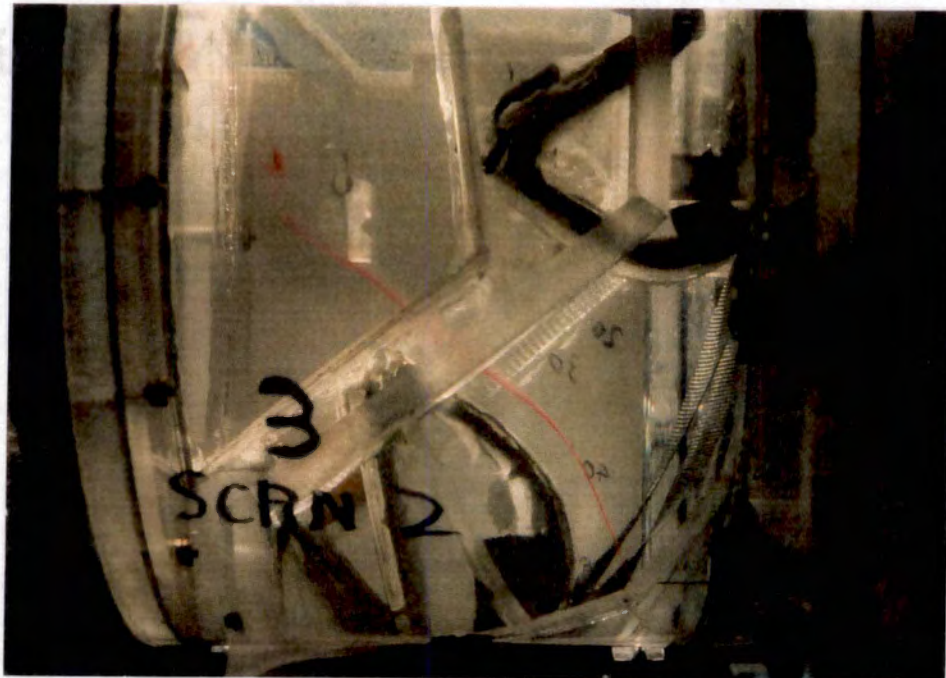


Figure 61. Water Flow Streaklines in Long Axisymmetric Nozzle Set at  $\theta = 30$  deg. and  $ZI = 0.85$  in.



a. Single Layer Screen



b. Two Layer Screen

Figure 62: Water Flow Streaklines in Zone 3 of Variable-Area Nozzle Set at  $\theta = 30$  deg with Inlet Screen Installed.





Figure 63. Water Flow Streaklines in Zone 3 of Variable-Area Nozzle Set at  $\theta = 30$  deg with Vertical Vanes Installed.



a. 0-deg Inclination with Respect to Nozzle Inlet Plane



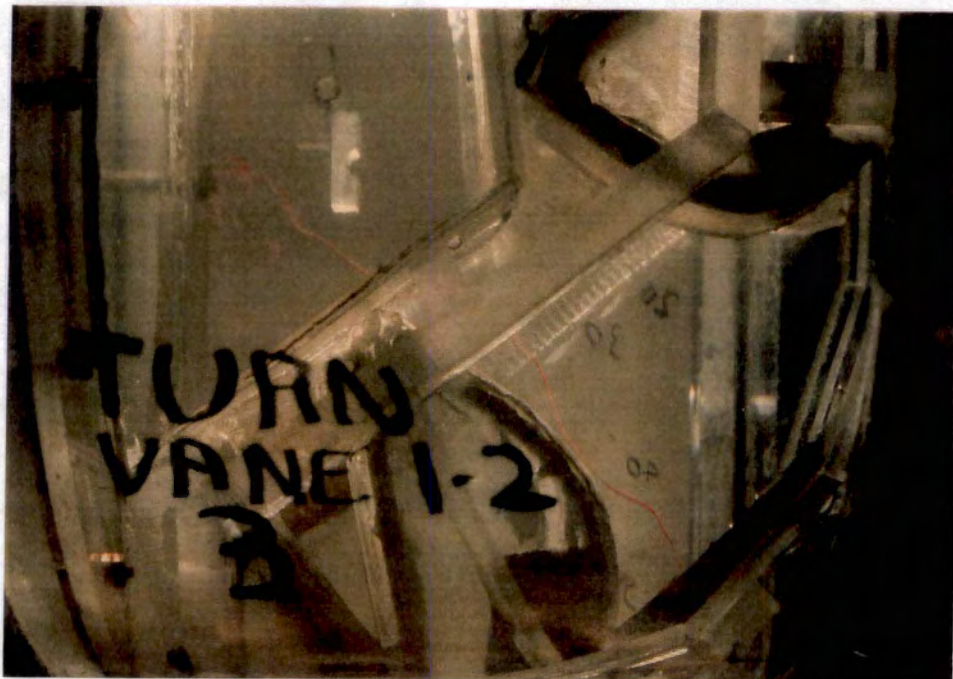
b. 20-deg Inclination with Respect to Nozzle Inlet Plane

Figure 64. Water Flow Streaklines in Zone 3 of Variable-Area Nozzle Set at  $\theta = 30$  deg with Honeycomb Installed.





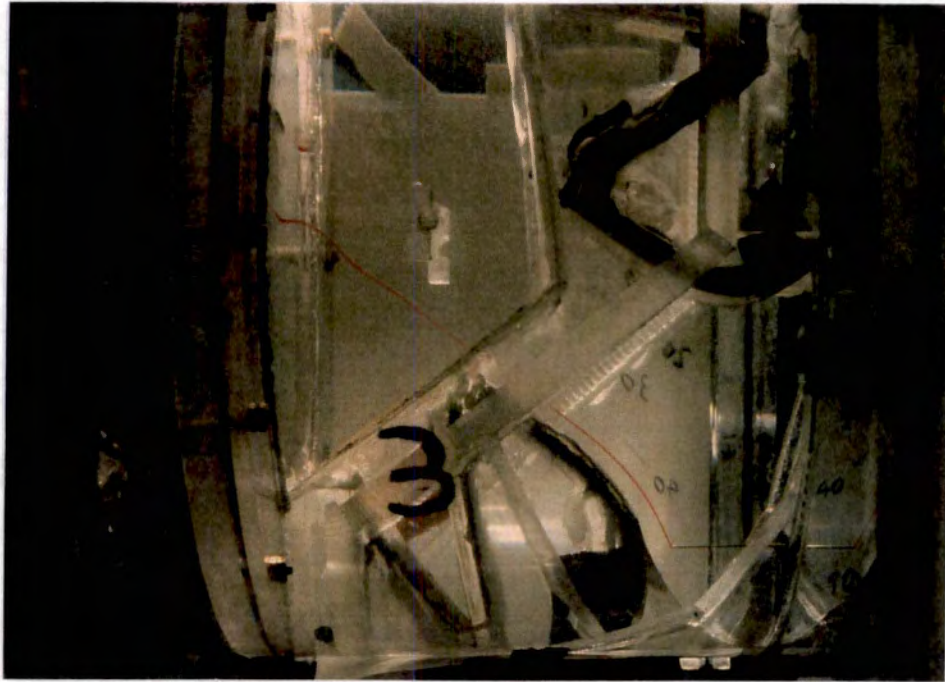
a. 0-deg Inclination with Respect to Nozzle Inlet Plane



b. 20-deg Inclination with Respect to Nozzle Inlet Plane

Figure 65. Water Flow Streaklines in Zone 3 of Variable-Area Nozzle Set at  $\theta = 30$  deg with Horizontal Turning Vanes Installed.





a. Ramp 1



b. Ramp 2

Figure 66. Water Flow Streaklines in Zone 3 of Variable-Area Nozzle Set at  $\theta = 30$  deg with Inlet Ramps Installed.



c. Ramp 3



d. Ramp 4

Figure 66. Continued.



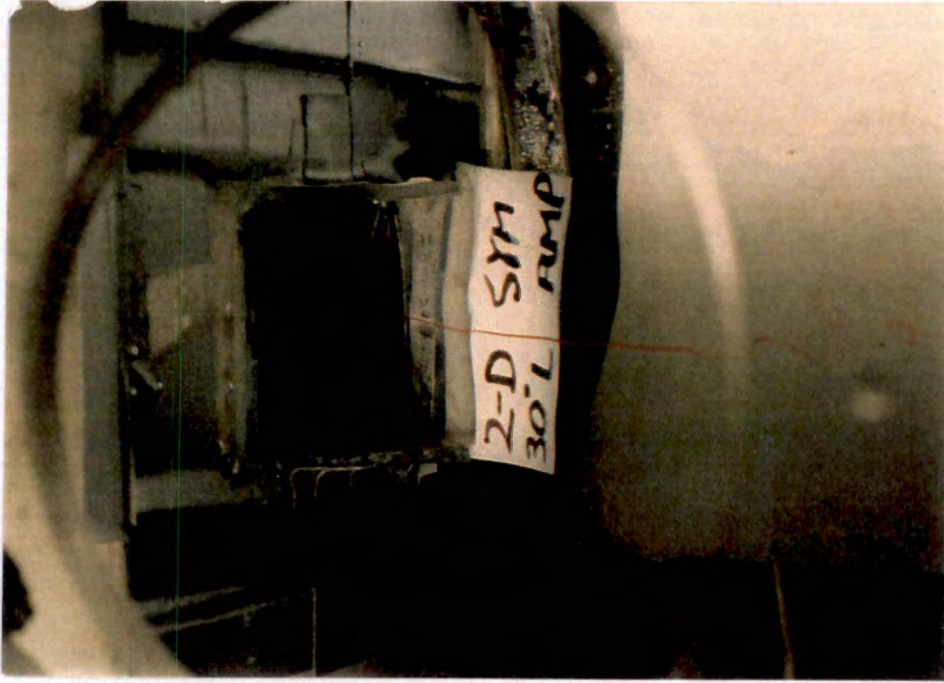


e. Ramp 5

Figure 66. Concluded.



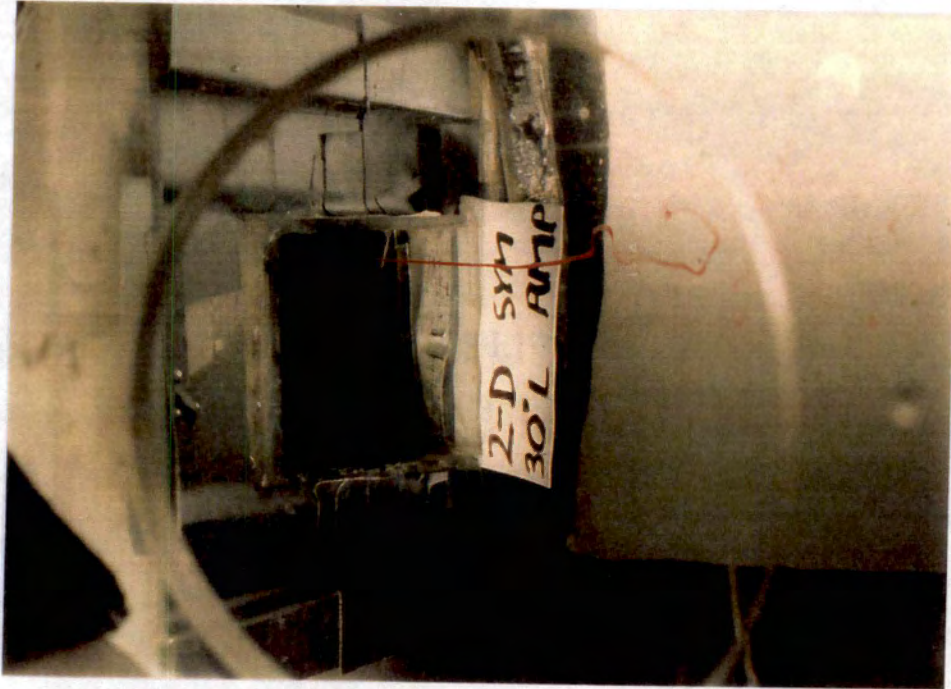
a. Zone 1



b. Zone 2

Figure 67. Water Flow Streaklines in 2-D SYM nozzle at  $\theta = 30$  deg and  $ZI = 1.4$  in. with Ramps Installed.





c. Zone 3

Figure 67. Concluded.





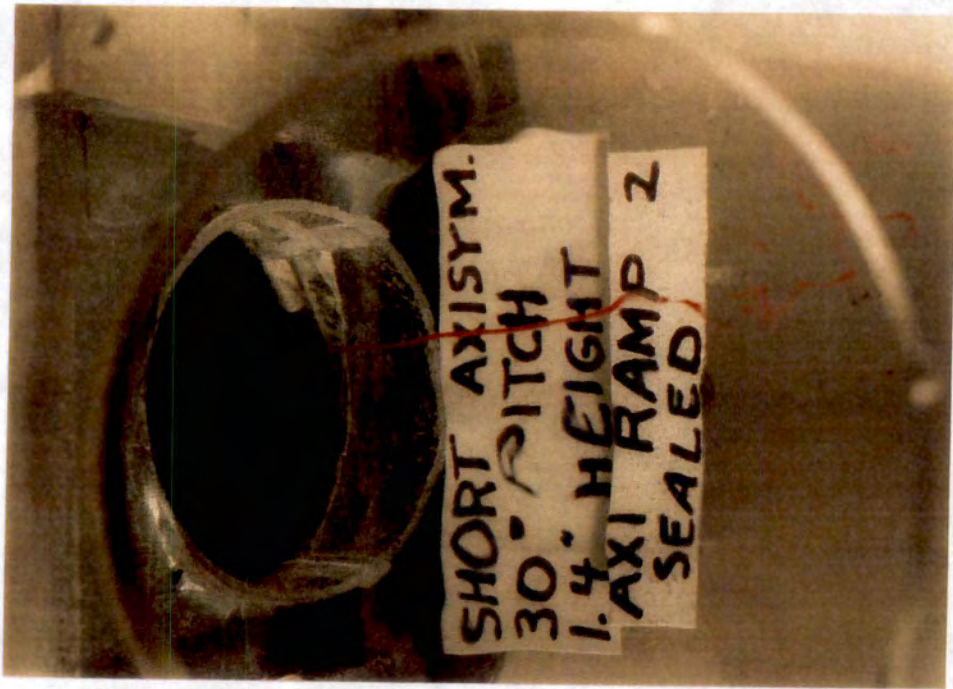
Figure 68. Water Flow Streaklines in Short Axisymmetric Nozzle at  $\theta = 30$  deg and  $ZI = 1.4$  in. with AXI Ramp 1 installed.



a. Position A

Figure 69. Water Flow Streaklines in Short Axisymmetric Nozzle at  $\theta = 30$  deg and  $ZI = 1.4$  in. with AXI Ramp 2 Installed.





a. Concluded



b. Position B

Figure 69. Continued.





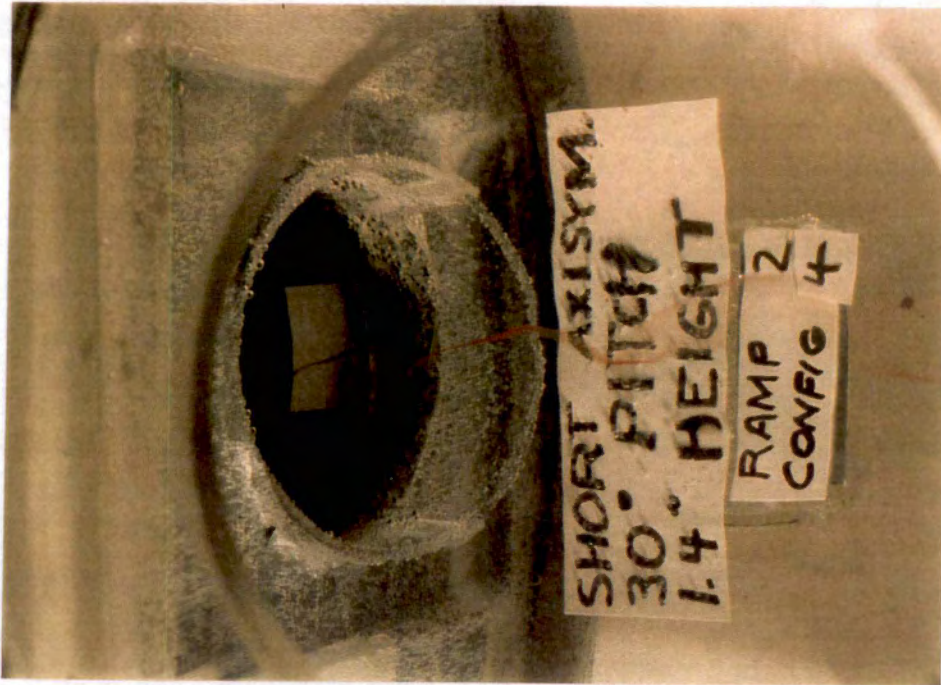
b. Concluded

Figure 69. Continued.





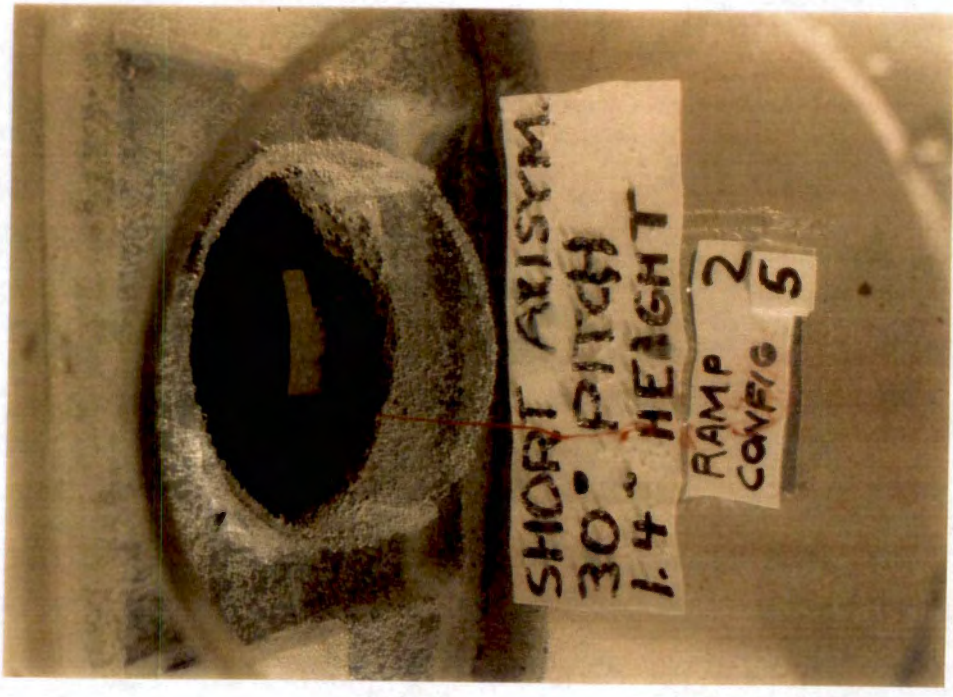
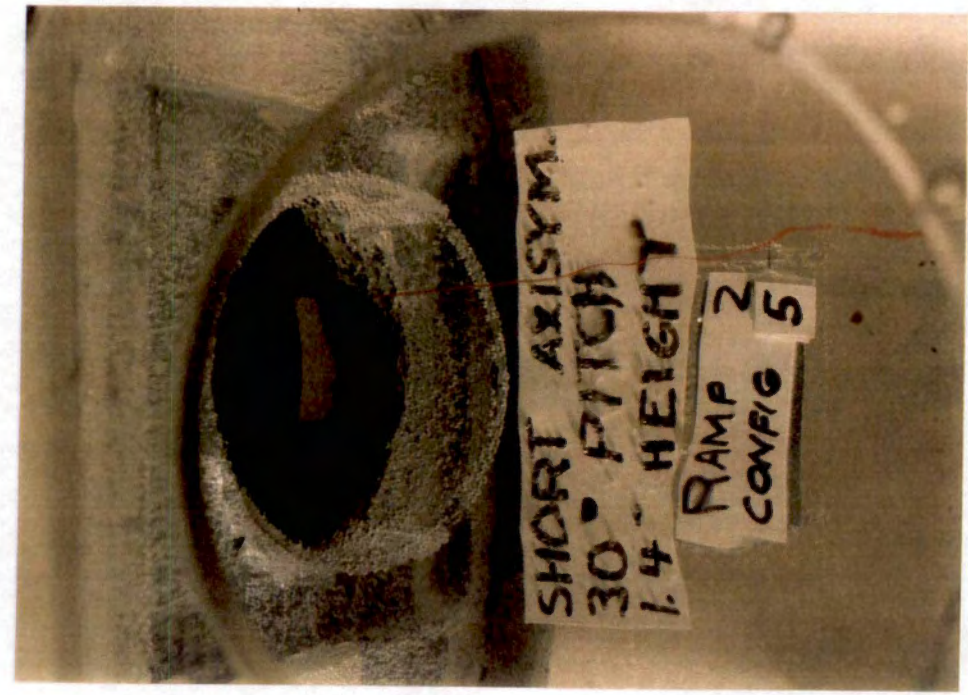
c. Position C



d. Position D

Figure 69. Continued.

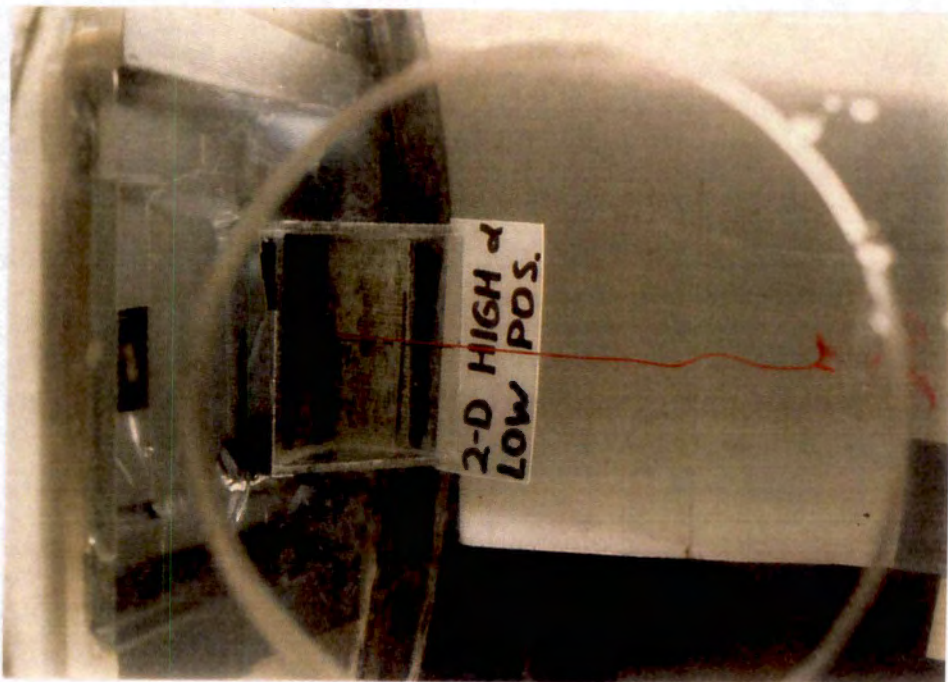




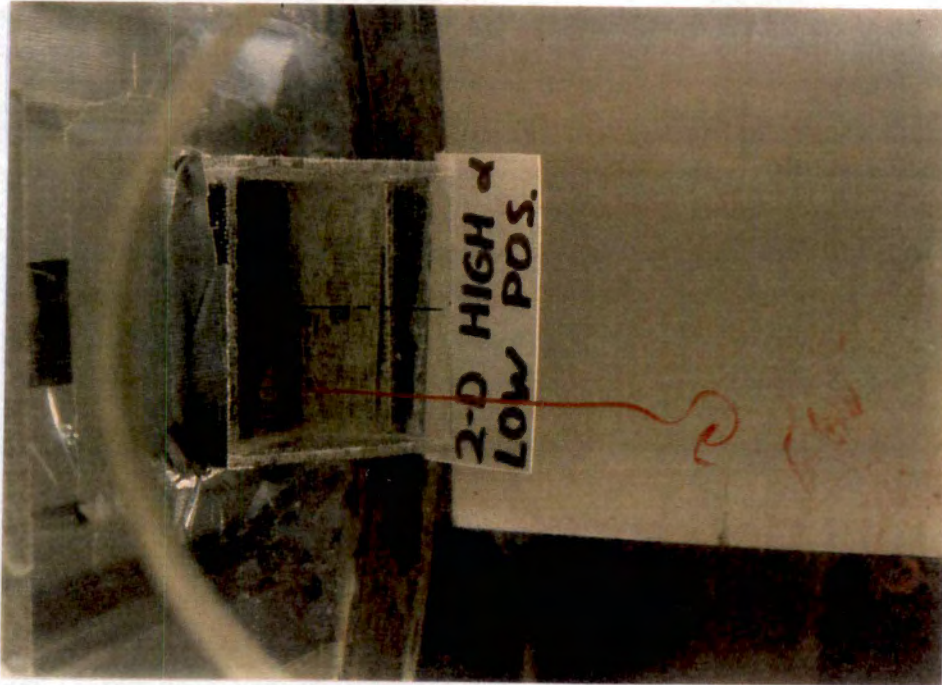
e. Position E

Figure 69. Concluded.



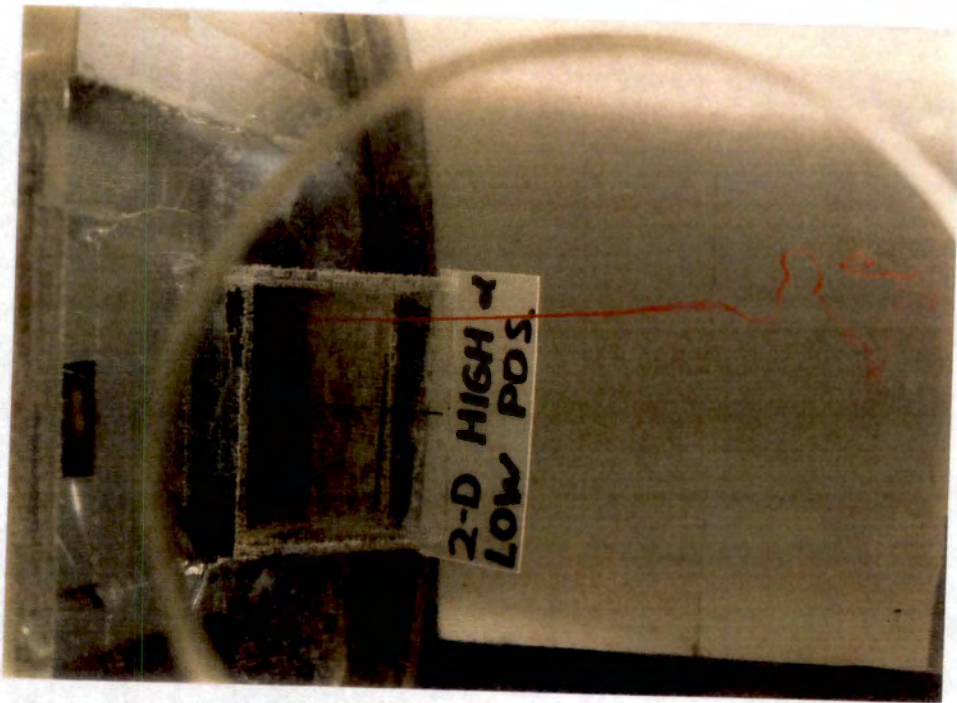


a. Zone 2, Without Extension

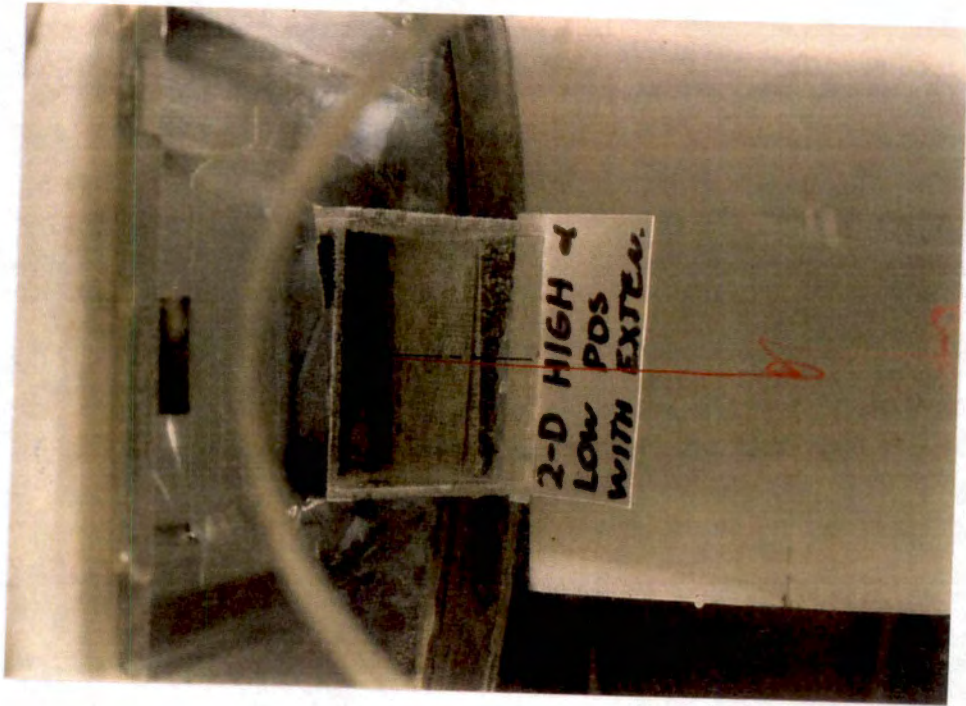


b. Zone 1, Without Extension

Figure 70. Water Flow Streaklines in 2-D High- $\alpha$  Nozzle Set at  $\theta = 30$  deg and  $ZI = 0.6$  in.



c. Zone 3, Without Extension



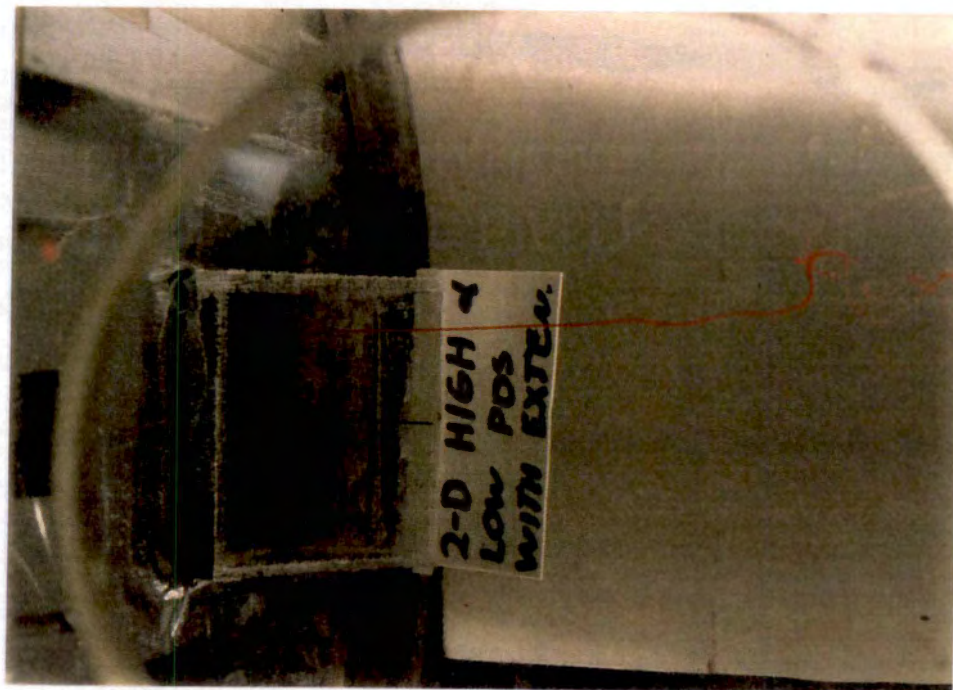
d. Zone 2, With Extension

Figure 70. Continued.



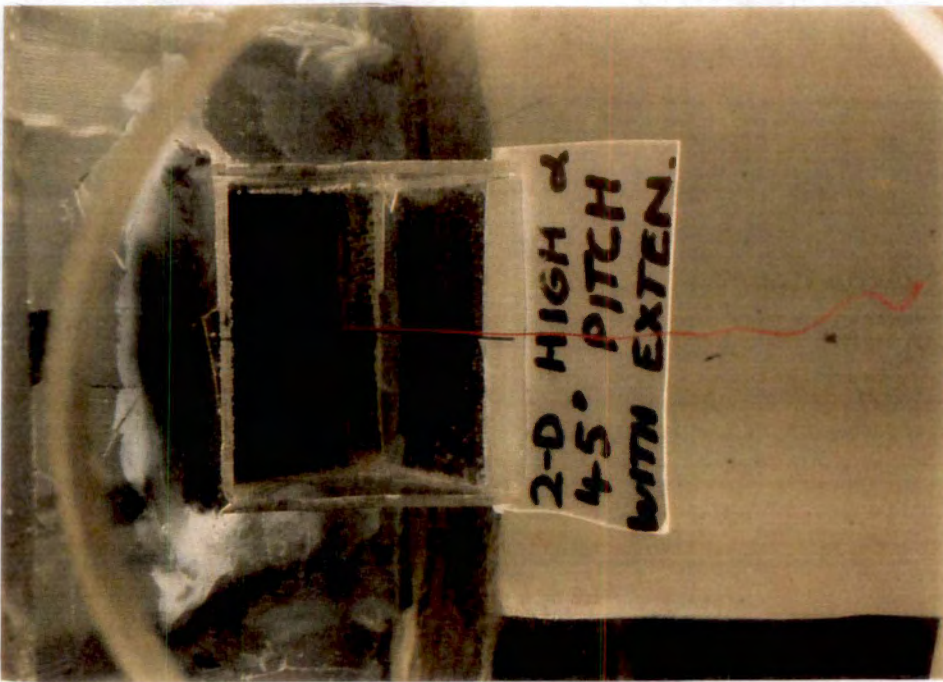


e. Zone 1, With Extension

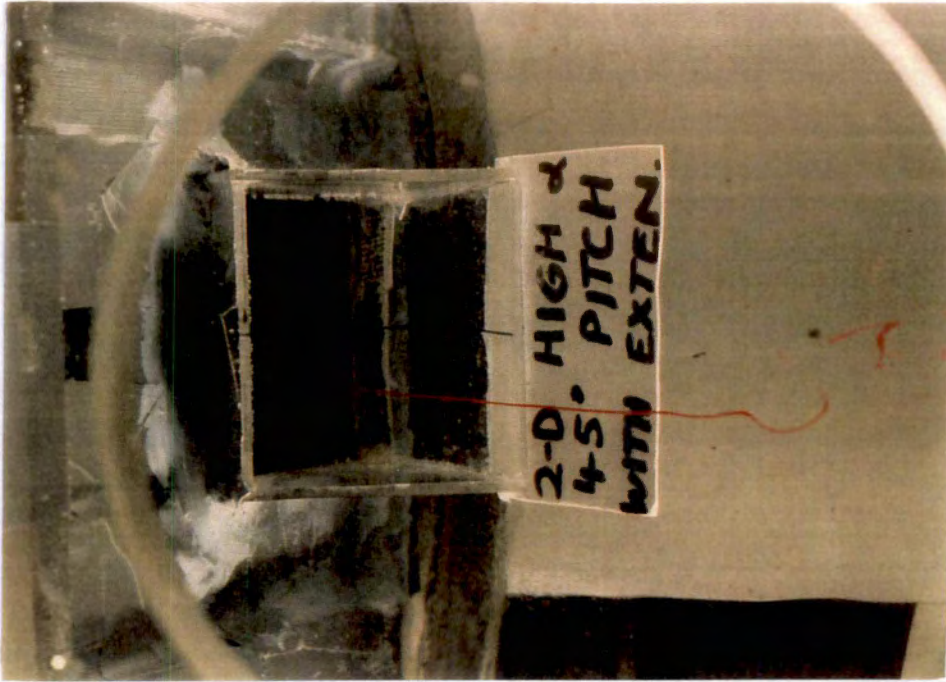


f. Zone 3, With Extension

Figure 70. Concluded.



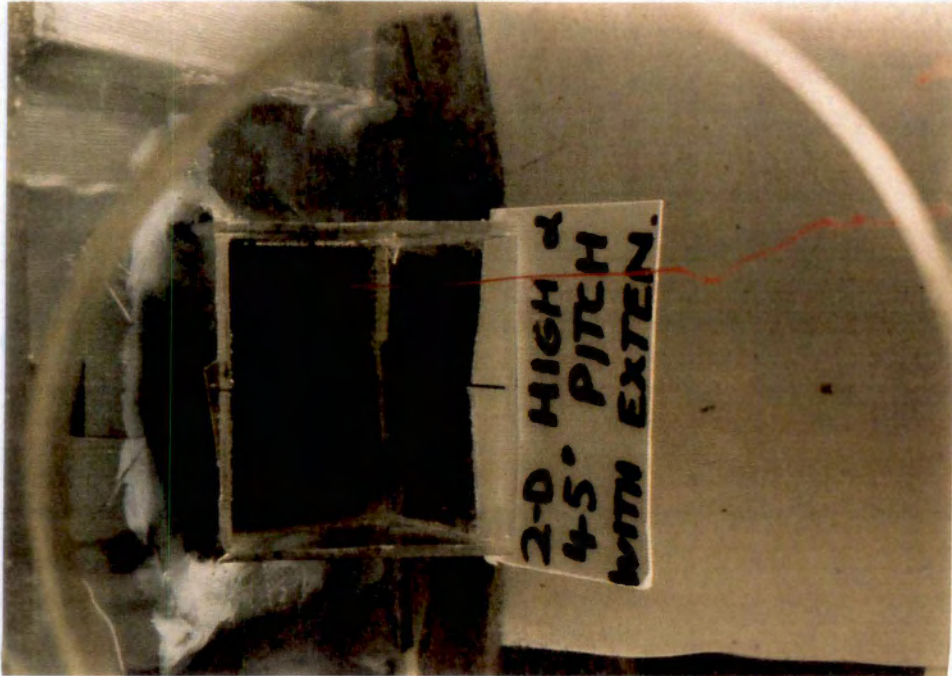
a. Zone 2



b. Zone 1

Figure 71. Water Flow Streaklines in 2-D High- $\alpha$  Nozzle Set at  $\theta = 45$  deg and  $ZI = 0.6$  in.





c. Zone 3

Figure 71. Concluded.

Sym	PITCH, deg	Ramp Config.
○	30	30-deg Contoured
□	30	30-deg Straight
△	50	50-deg Contoured
○	50	50-deg Straight

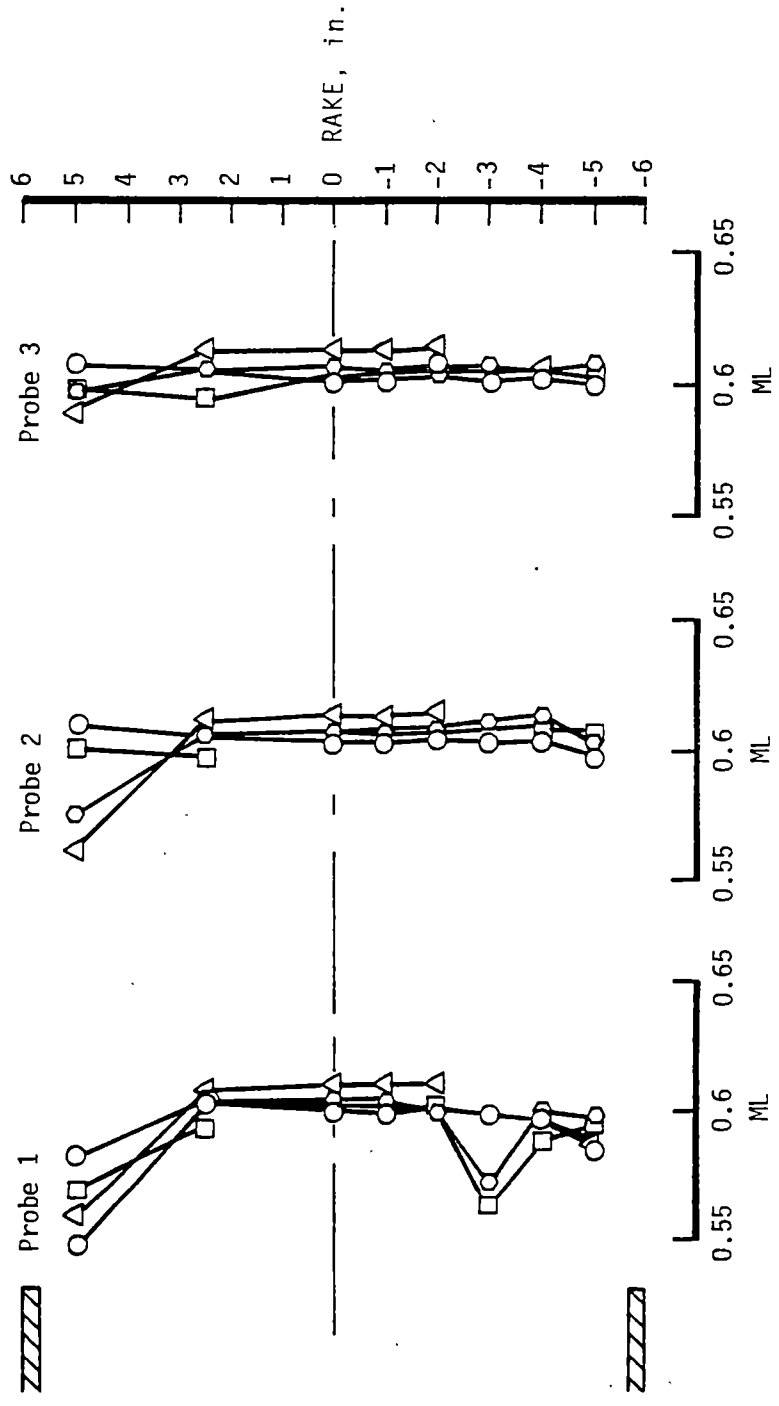


Figure 72. Variable-Area Nozzle Exit Mach Number Measurements at MACH = 0.6 with Ramp Installed.

Sym	PIITCH, deg	Ramp Config.
○	30	30-deg Contoured
□	30	30-deg Straight
△	50	50-deg Contoured
○	50	50-deg Straight

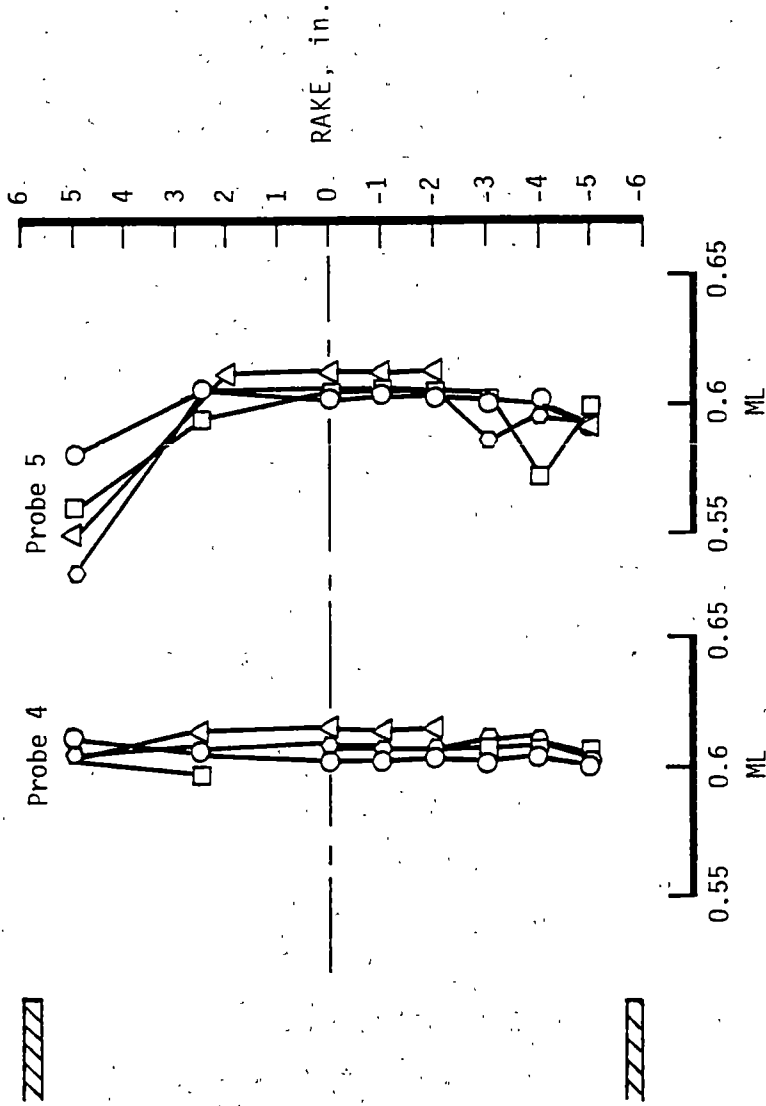
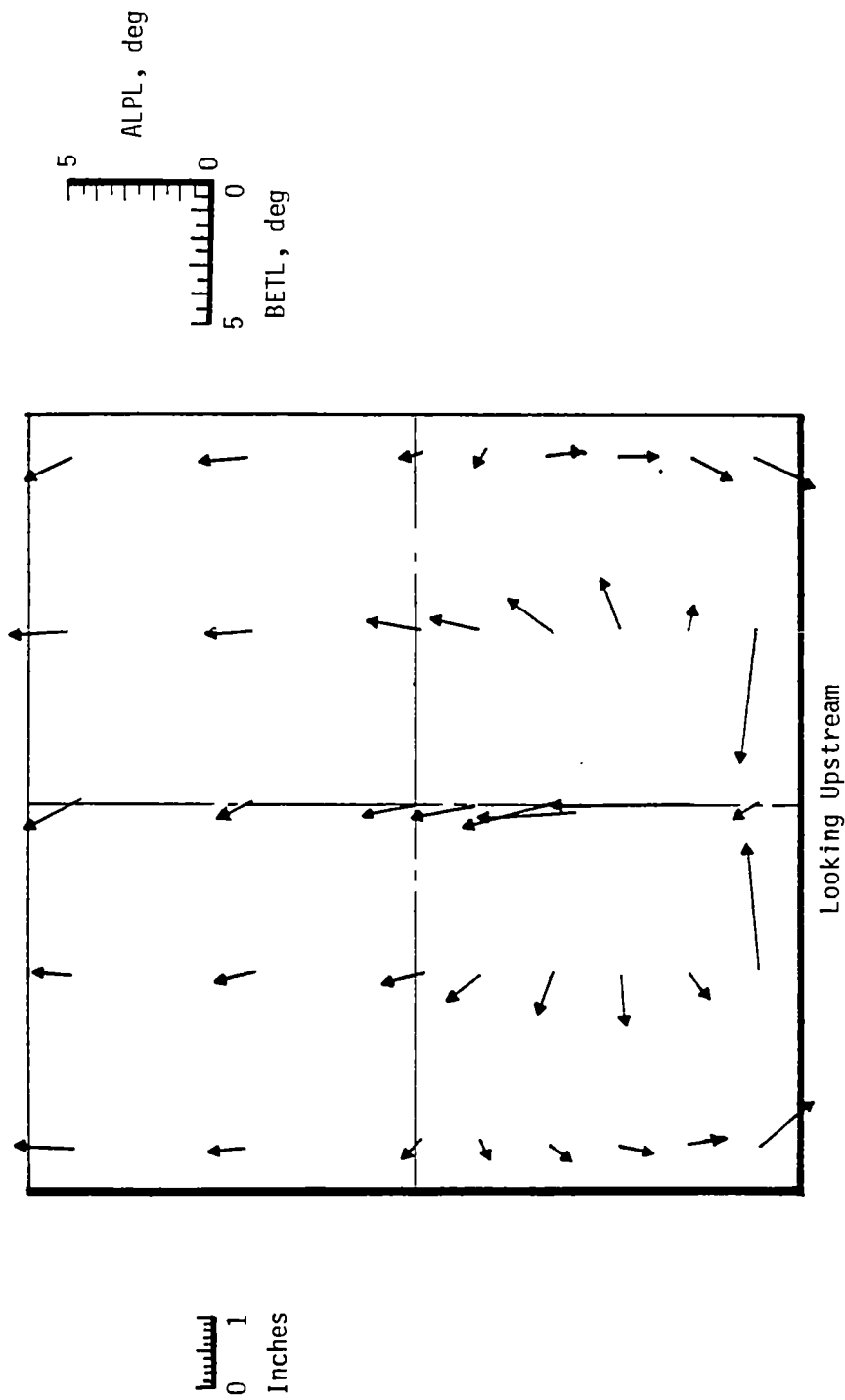
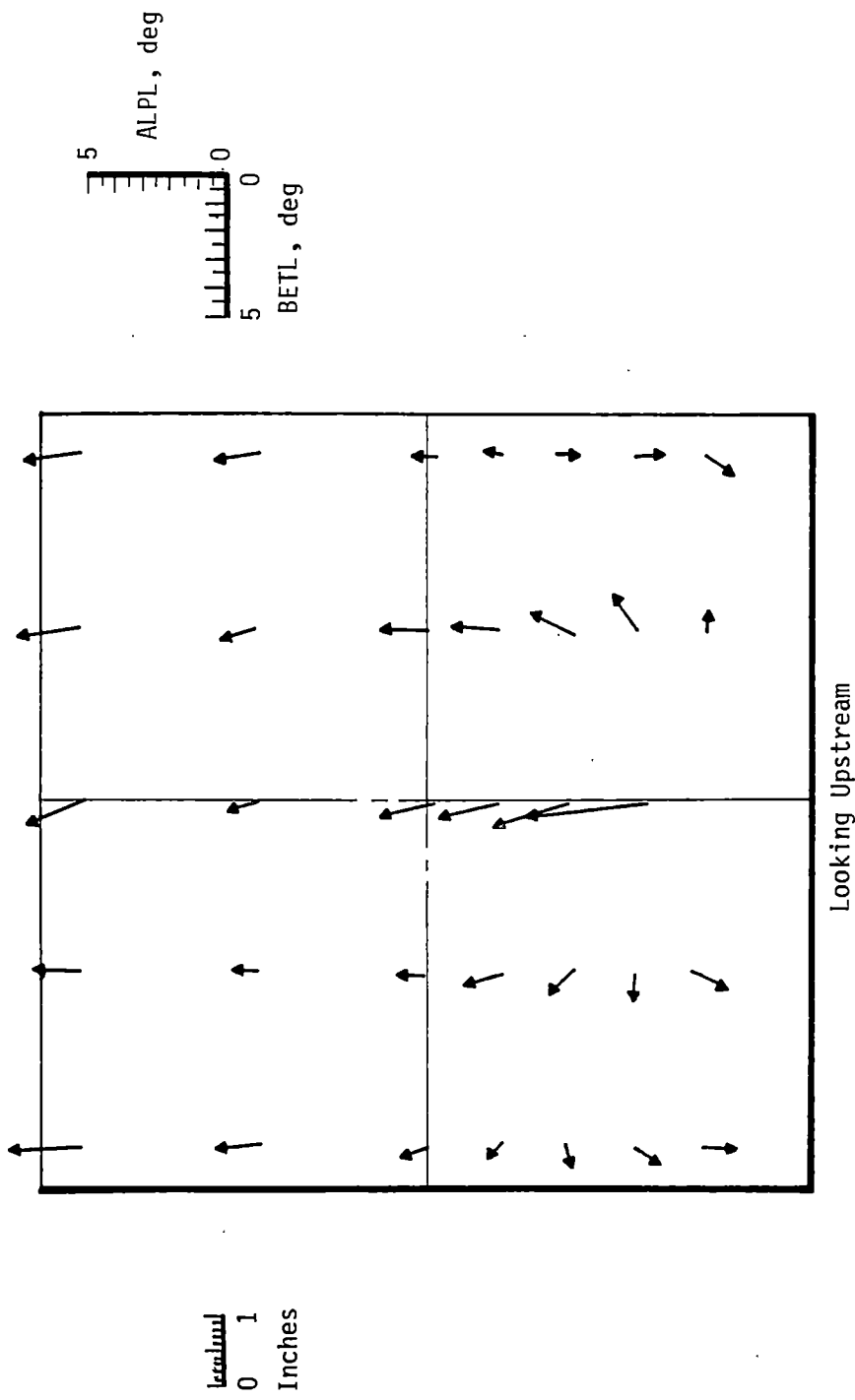


Figure 72. Concluded.



a. MACH = 0.6

Figure 73. Variable-Area Nozzle Exit Flow Angularity Measurements at  $\theta = 30$  deg with 30-deg Contoured Ramp Installed.



b. MACH = 0.9

Figure 73. Concluded.

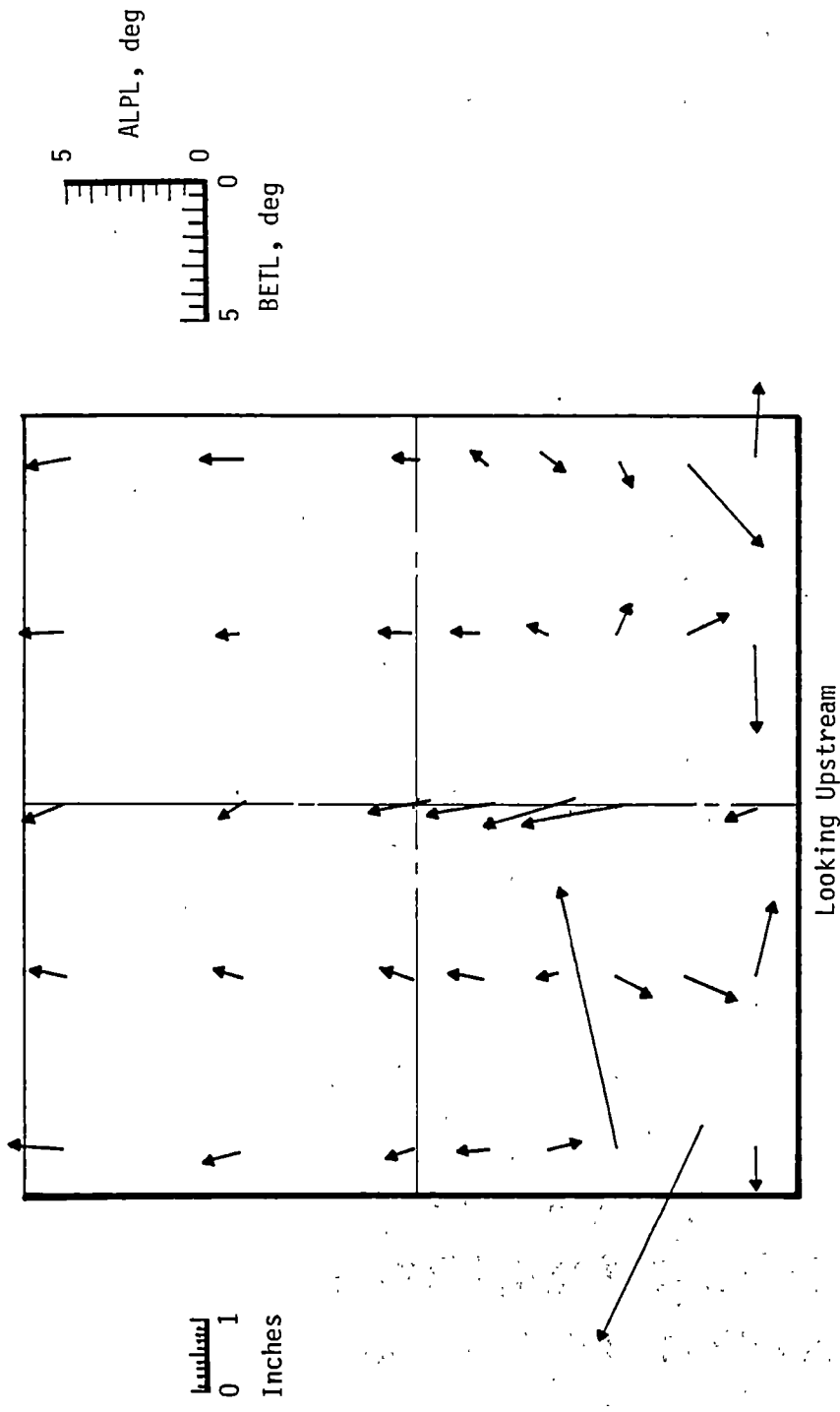
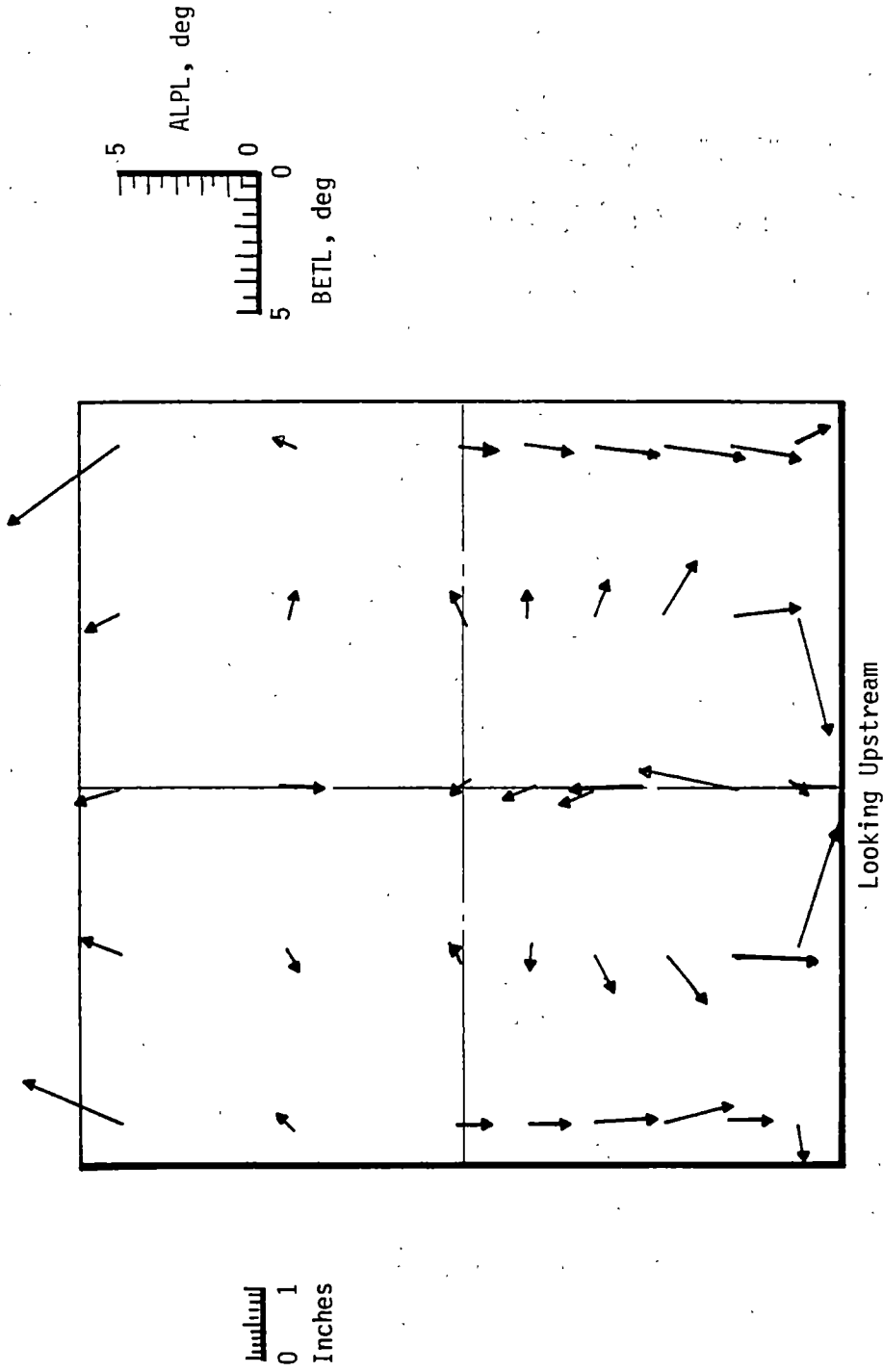


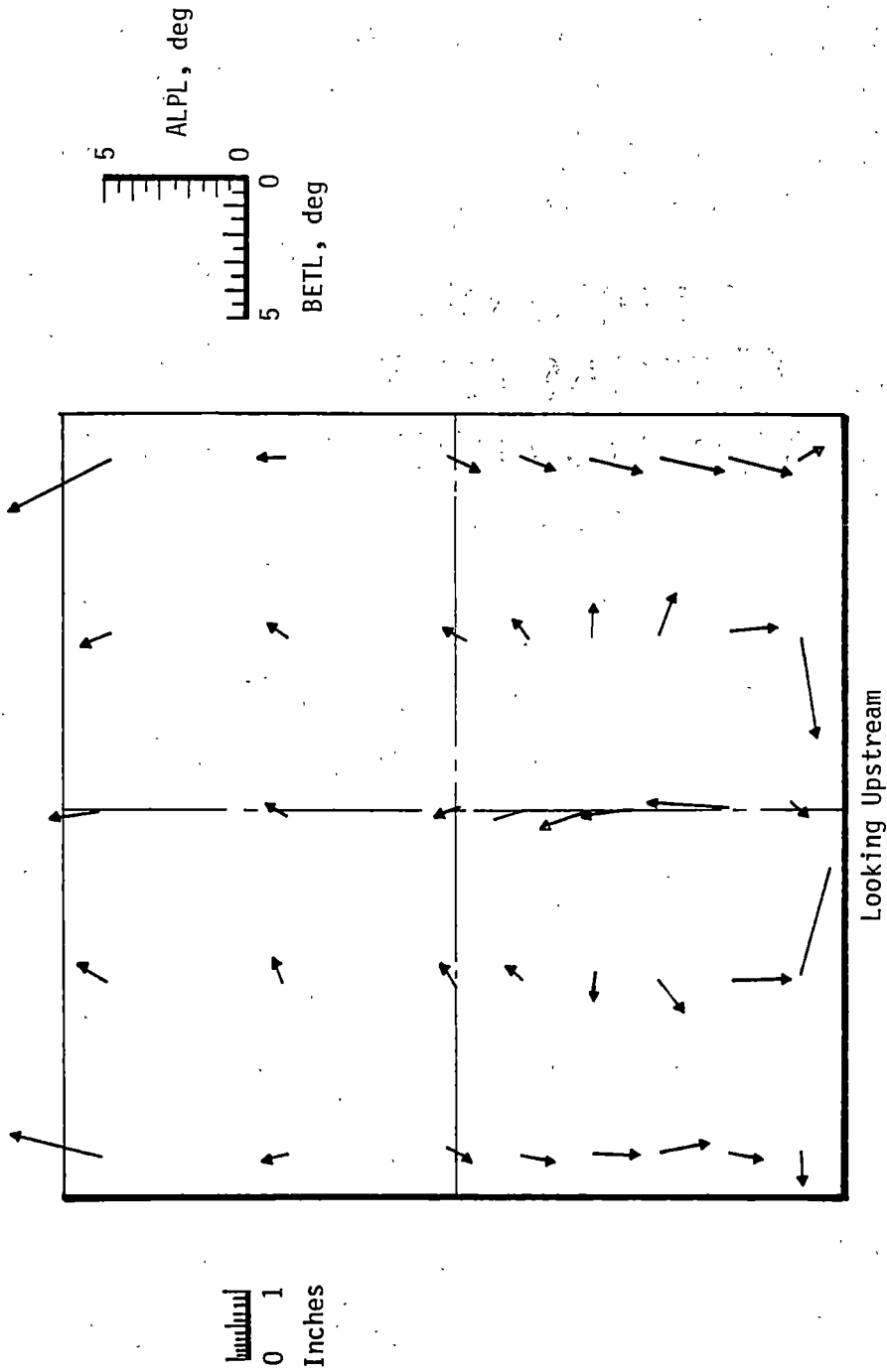
Figure 74. Variable-Area Nozzle Exit Flow Angularity Measurements at MACH = 0.6 and  $\theta = 30$  deg with 30-deg Straight Ramp Installed.





a. MACH = 0.6

Figure 75. Variable-Area Nozzle Exit Flow Angularity Measurements at  $\theta = 50$  Deg with 50-Deg Contoured Ramp Installed.



b. MACH = 0.9

Figure 75. Concluded.

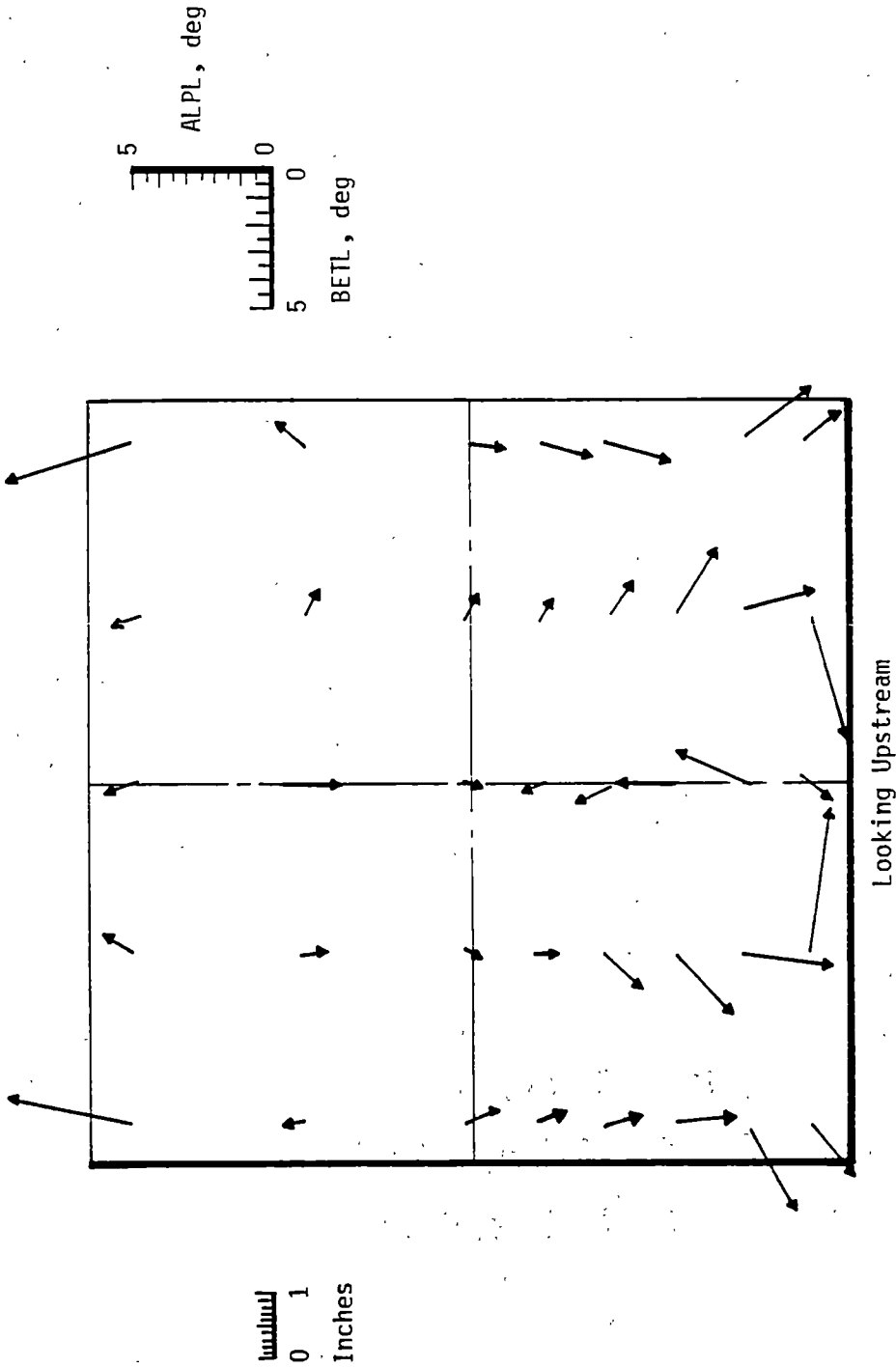
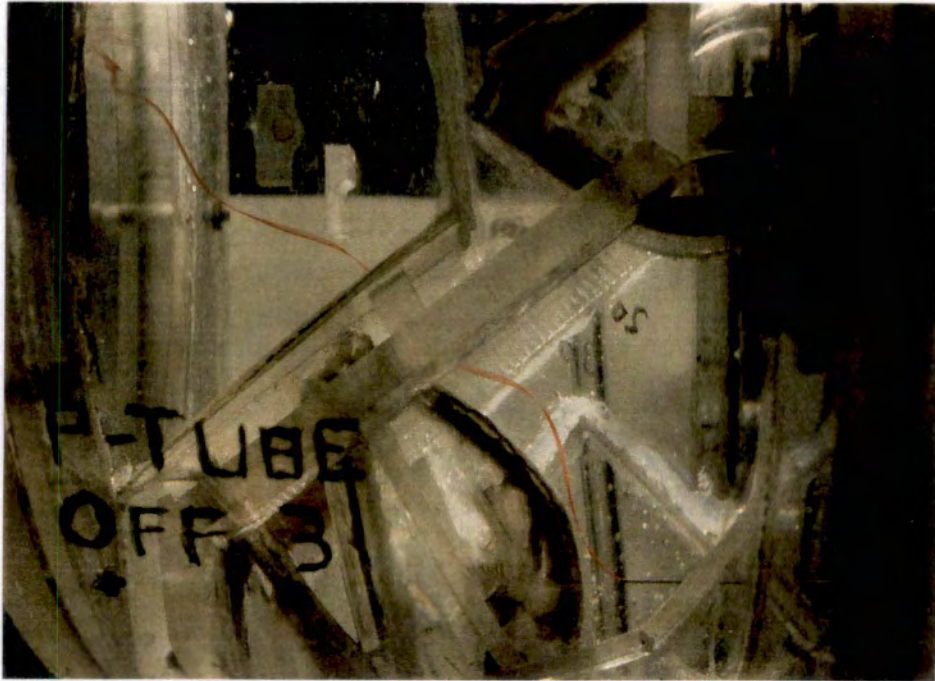
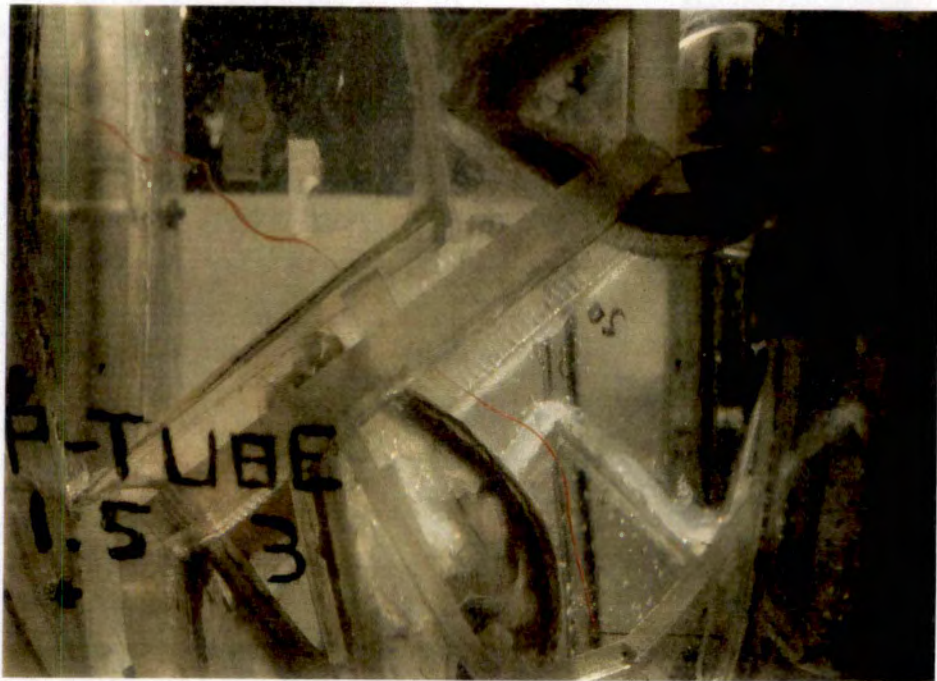


Figure 76. Variable-Area Nozzle Exit Flow Angularity Measurements at MACH = 0.6 and  $\theta = 50$  deg with 50-deg Straight Ramp Installed.



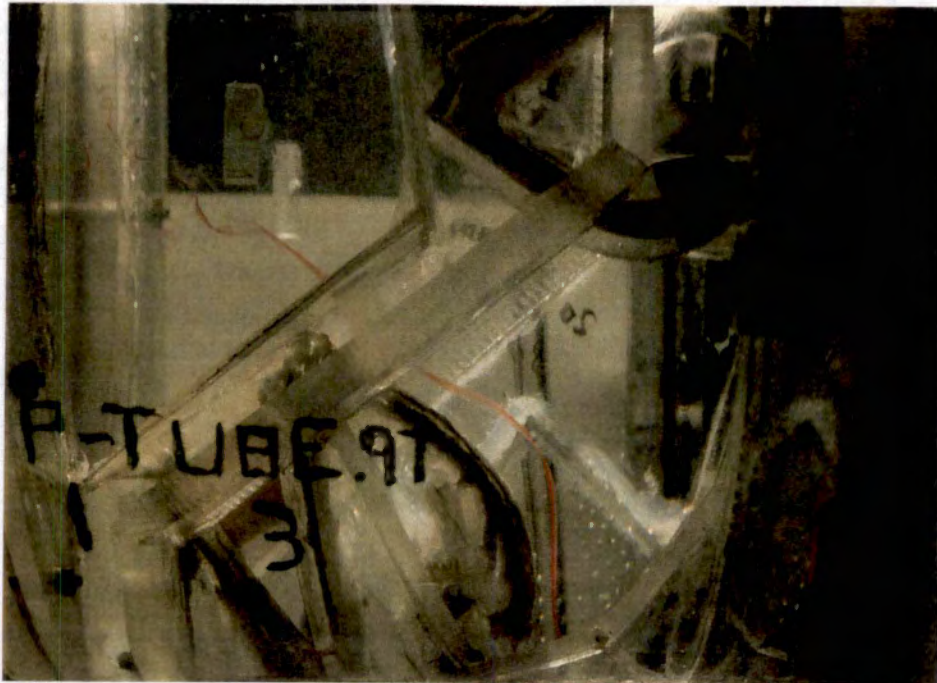
a. Zone 3,  $W = 0$  gph



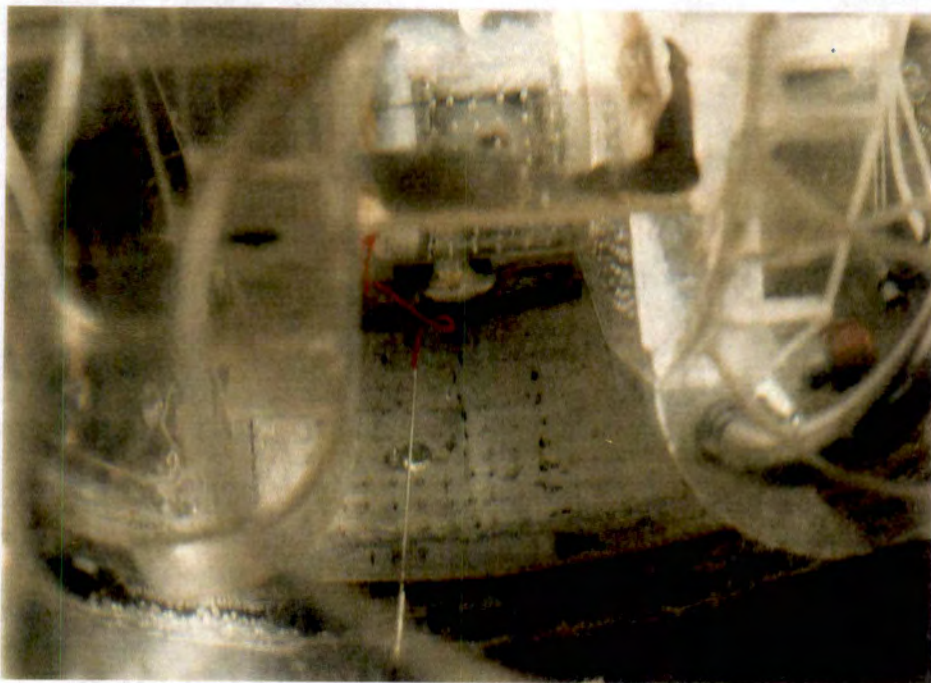
b. Zone 3,  $W = 1.5$  gph

Figure 77. Water Flow Streaklines in Variable-Area Nozzle at  $\theta = 30$  deg with Piccolo Tube Set at  $ZT = 0.75$  in. and  $YBL = 2.375$  in.



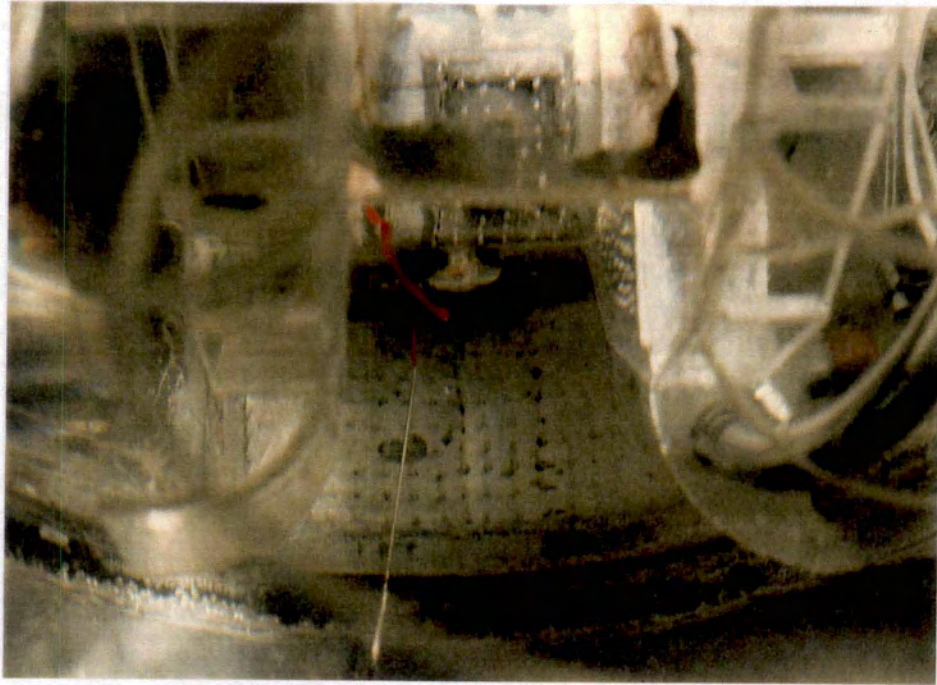


a. Side View of Zone 3 Streakline



b. View Downstream into Nozzle Contraction Section

Figure 78. Water Flow Streaklines in Variable-Area Nozzle at  $\theta = 30$  deg with Piccolo Tube Set at  $ZT = 0.75$  in. and  $YBL = 0.9$  in.



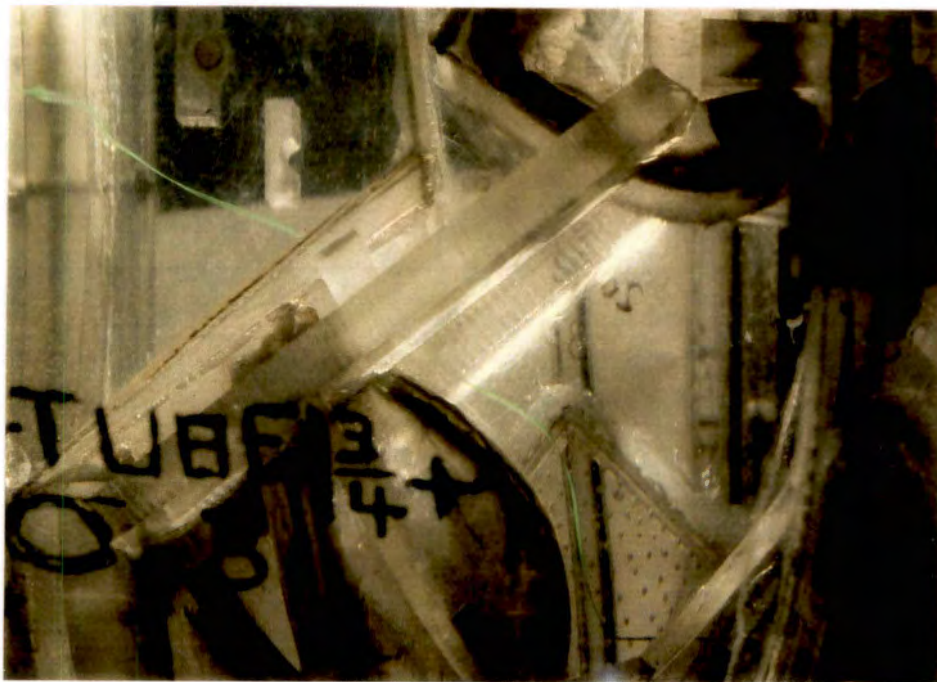
b. Concluded

Figure 78. Concluded.



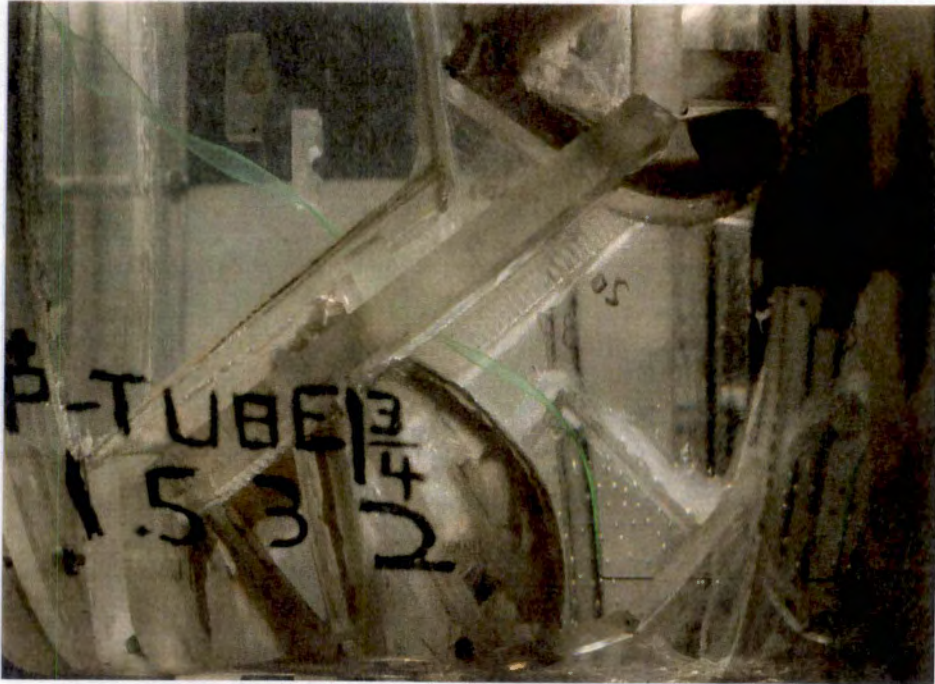


a. Zone 3, WT = 1.75 in.



b. Zone 3, WT = 1.875 in.

Figure 79. Water Flow Streaklines in Variable-Area Nozzle at  $\theta = 30$  deg with Piccolo Tube Set at ZT = 0.75 in. and Variable YBL.



a. Zone 3, WT = 1.75 in.



b. Zone 3, WT = 1.875 in.

Figure 80. Water Flow Streaklines in Variable-Area Nozzle at  $\theta = 30$  deg with Piccolo Tube Set at ZT = 1.19 in. and Variable YBL.





a. Zone 1,  $W = 20$  gph



b. Zone 1,  $W = 33$  gph

Figure 81. Water Flow Streaklines in Variable-Area Nozzle at  $\theta = 30$  deg with Region 1 Suction.



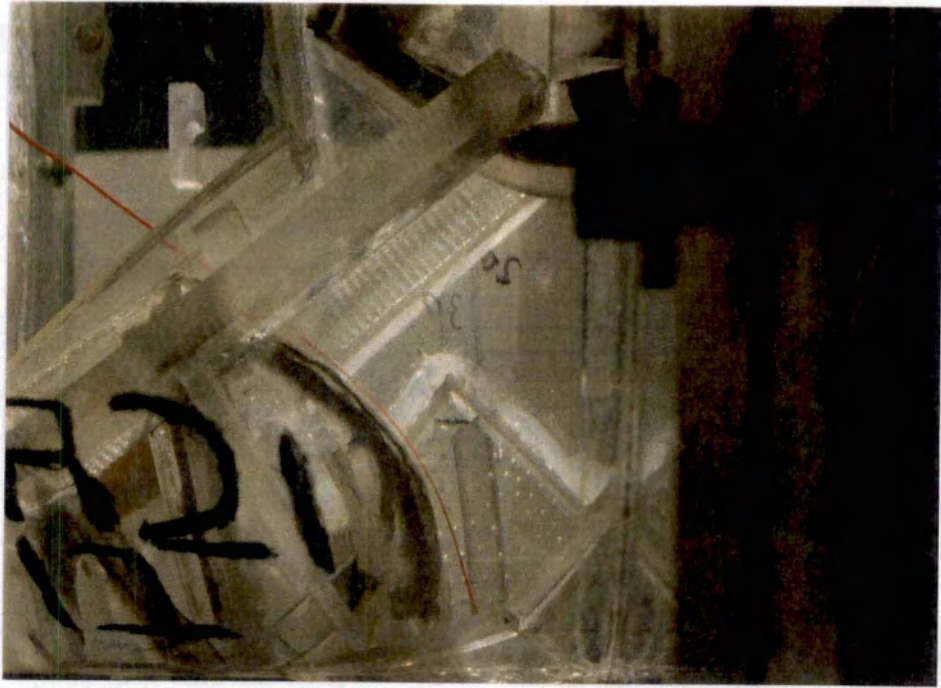
a. Zone 1,  $W = 8$  gph, Original Probe Position



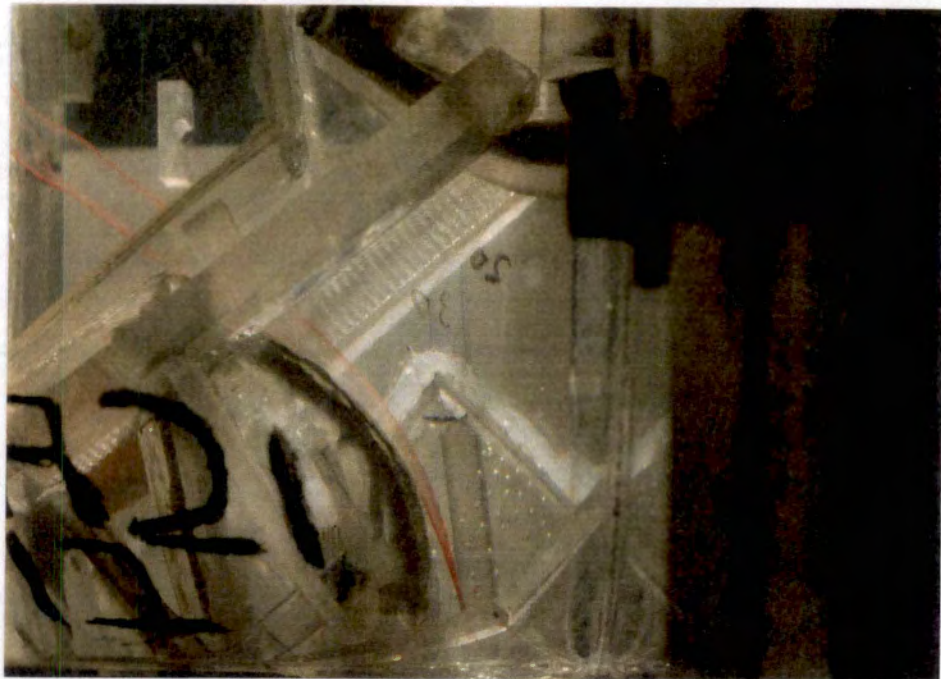
b. Zone 1,  $W = 8$  gph, Probe Displaced Toward Sidewall

Figure 82. Water Flow Streaklines in Variable-Area Nozzle at  $\theta = 30$  deg with Region 2 Suction.





c. Zone 1,  $W = 12$  gph, Original Probe Position



d. Zone 1,  $W = 12$  gph, Probe Displaced Toward Sidewall

Figure 82. Continued.



e. Zone 1,  $W = 16$  gph, Original Probe Position



f. Zone 1,  $W = 16$  gph, Probe Displaced Toward Sidewall

Figure 82. Concluded.





a. Zone 1,  $W = 14$  gph



b. Zone 1,  $W = 39$  gph

Figure 83. Water Flow Streaklines in Variable-Area Nozzle at  $\theta = 30$  deg with Region 3 Suction.





a. Zone 1, W = 20 gph

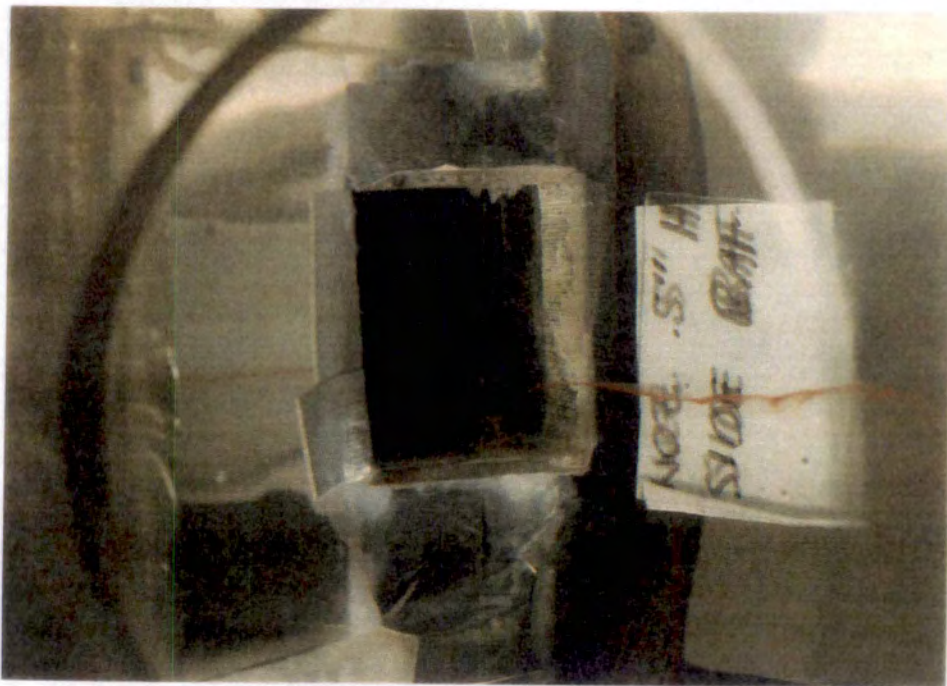


b. Zone 1, W = 35 gph

Figure 84. Water Flow Streaklines in Variable-Area Nozzle at  $\theta = 30$  deg with Region 4 Suction.



2011 NOV 24  
PARCHEM NT DFD



a. Vertical Baffles



b. Horizontal Baffles

Figure 85. Water Flow Streaklines in 2-D SYM Nozzle at  $\theta = 30$  deg and  $ZI = 0.6$  in. with Baffles Installed.





a. Zone 3, Ramp Position 1, Probe in Original Location



b. Zone 3, Ramp Displaced Toward Sidewall

Figure 86. Water Flow Streaklines in Variable-Area Nozzle at  $\theta = 30$  deg with Ramp 21 Installed.





c. Zone 3, Ramp Position 2

Figure 86. Concluded.



Zone 3

Figure 87. Water Flow Streaklines in Variable-Area Nozzle at  $\theta = 30$  deg with Ramp 22 Installed.



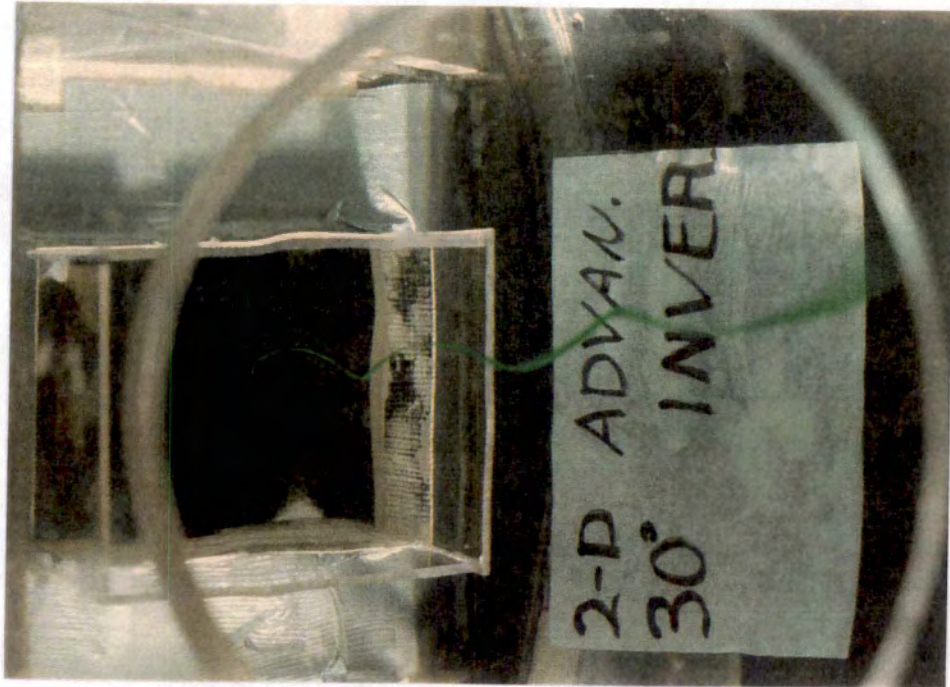
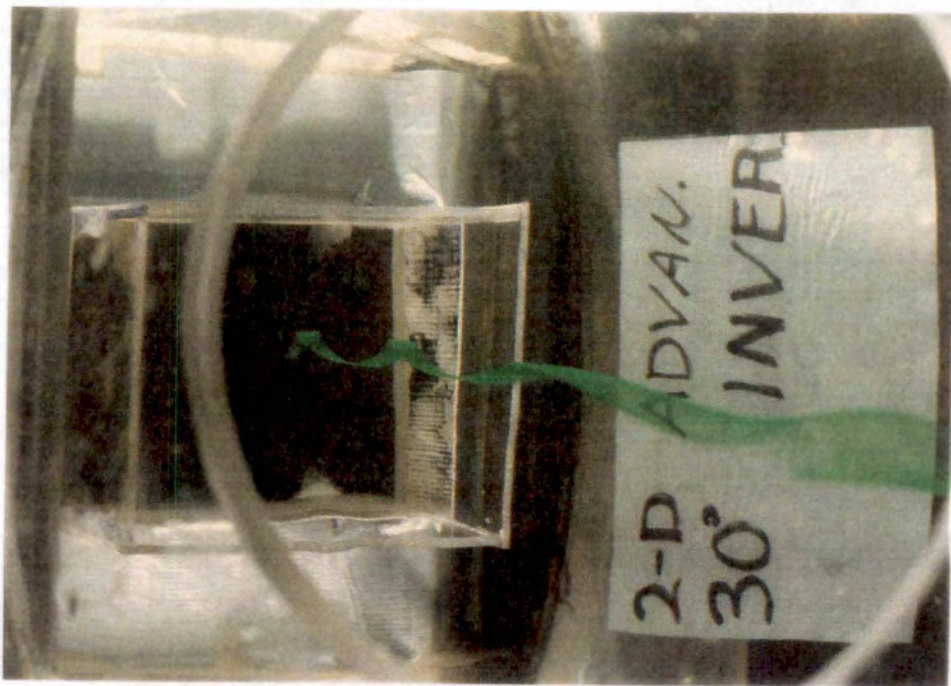
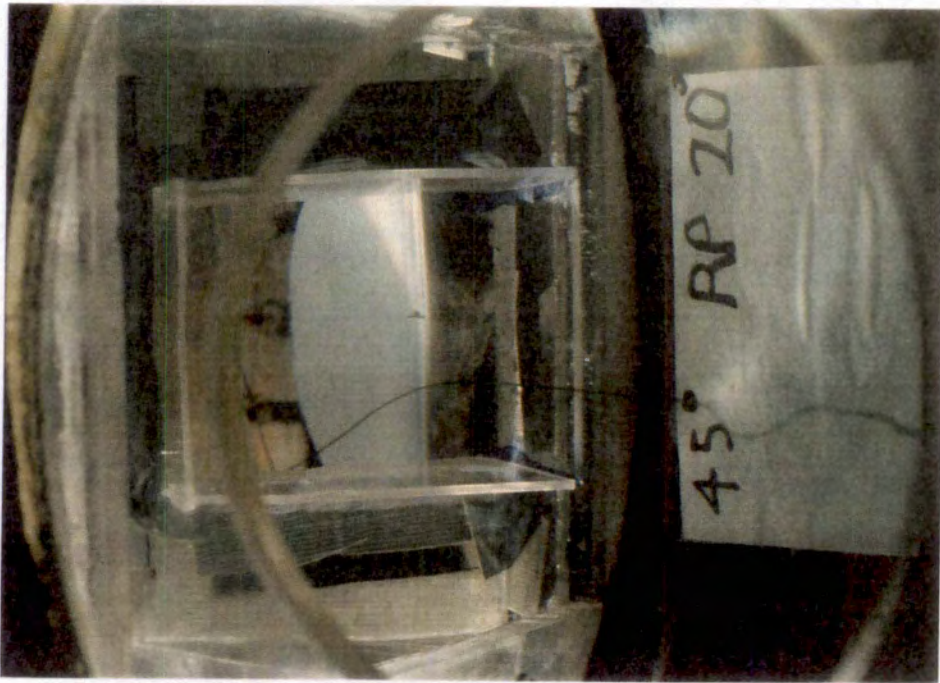
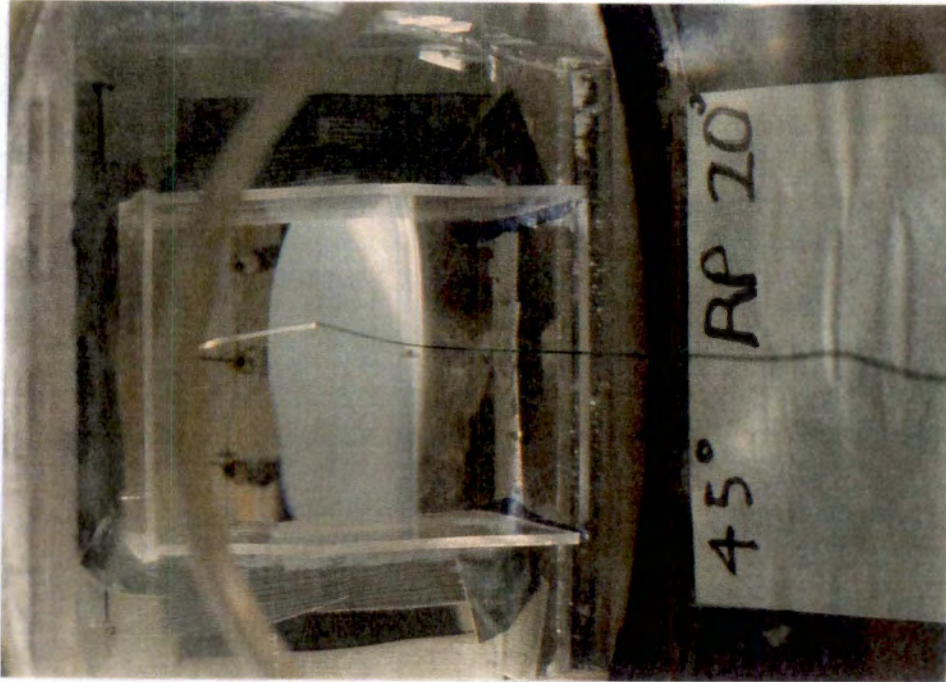


Figure 88. Water Flow Streaklines in ASTF Nozzle Model Installed Inverted and Set to  $\theta = 30$  deg and  $ZI = 1.6$  in.





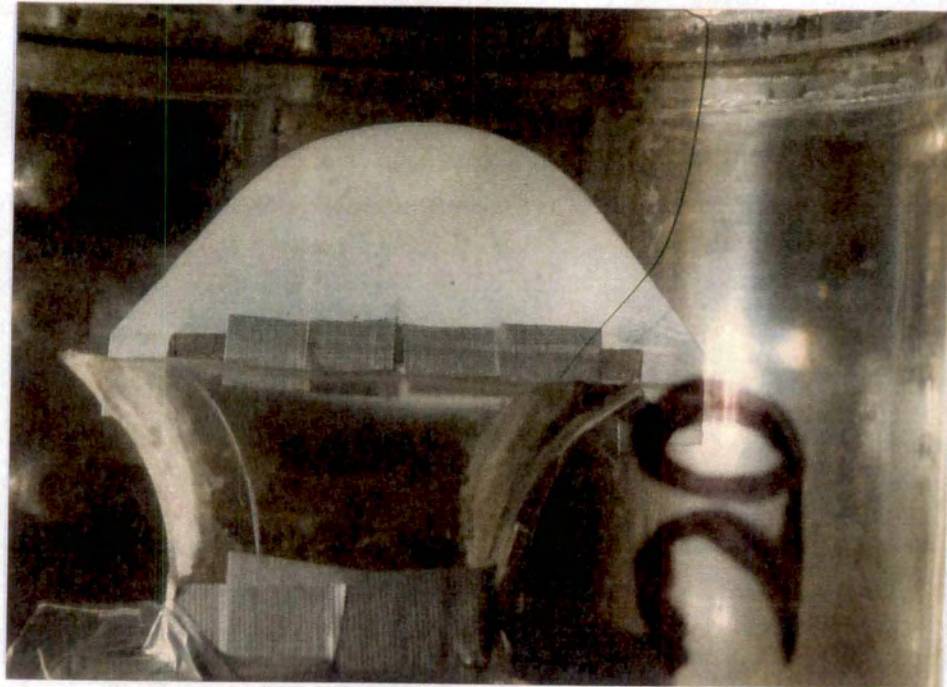
a. Zone 1



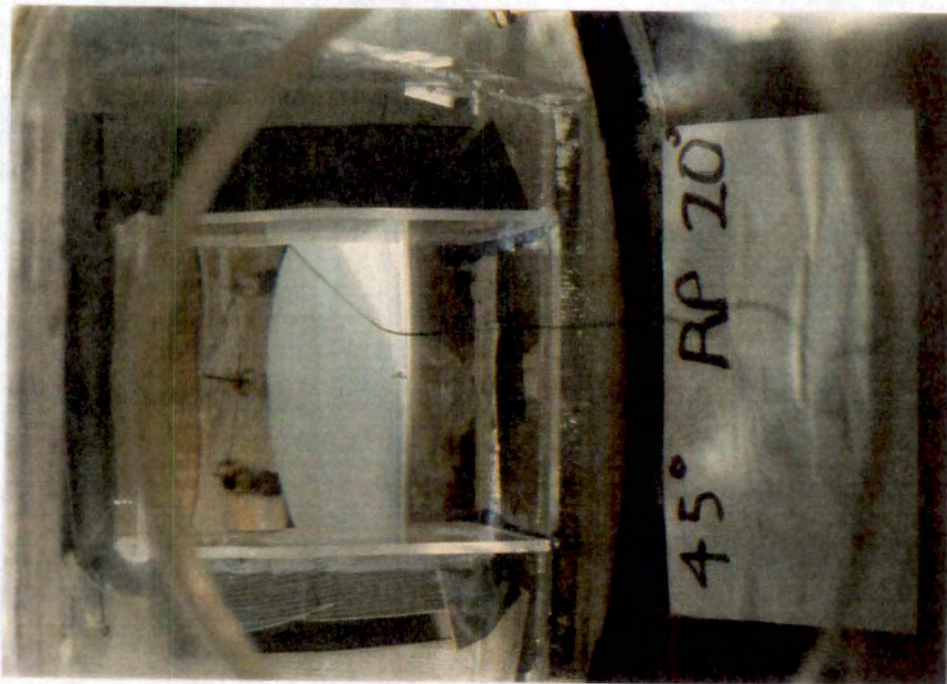
b. Zone 2

Figure 89. Water Flow Streaklines in ASTF Nozzle Model Set at  $\theta = 45$  deg and  $ZI = 1.2$  in. with  $RMP = 20$  deg.





d. Top View of Nozzle Inlet



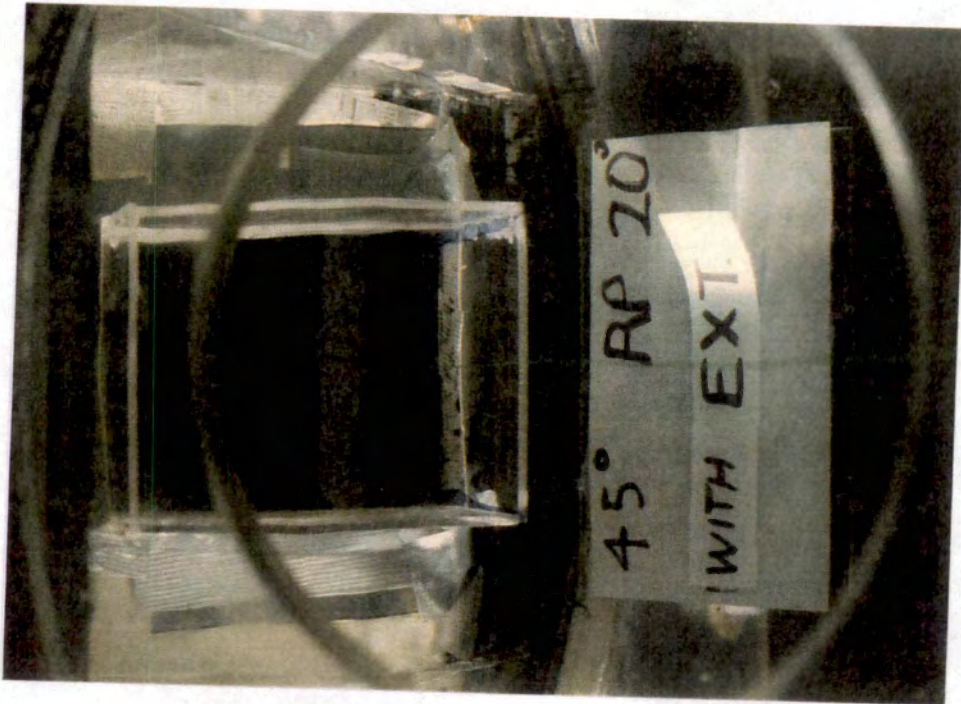
c. Zone 3

Figure 89. Concluded.



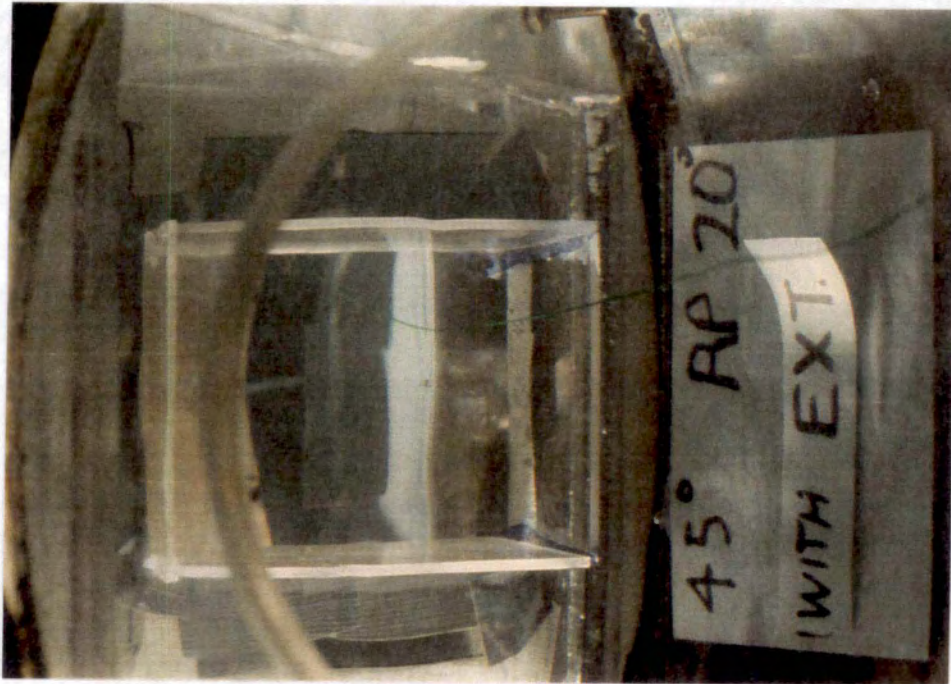


a. Zone 1



b. Zone 2

Figure 90. Water Flow Streaklines in ASTF Nozzle Model Set at  $\theta = 45$  deg and  $ZI = 1.2$  in. with Ramp Extension Installed.



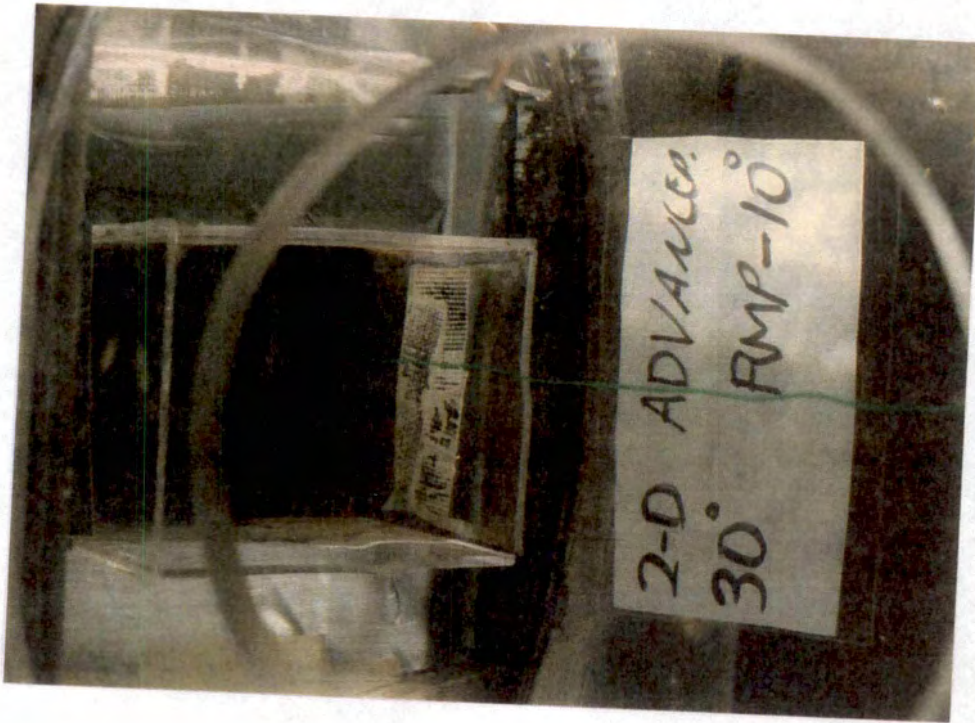
c. Zone 3

Figure 90. Concluded.





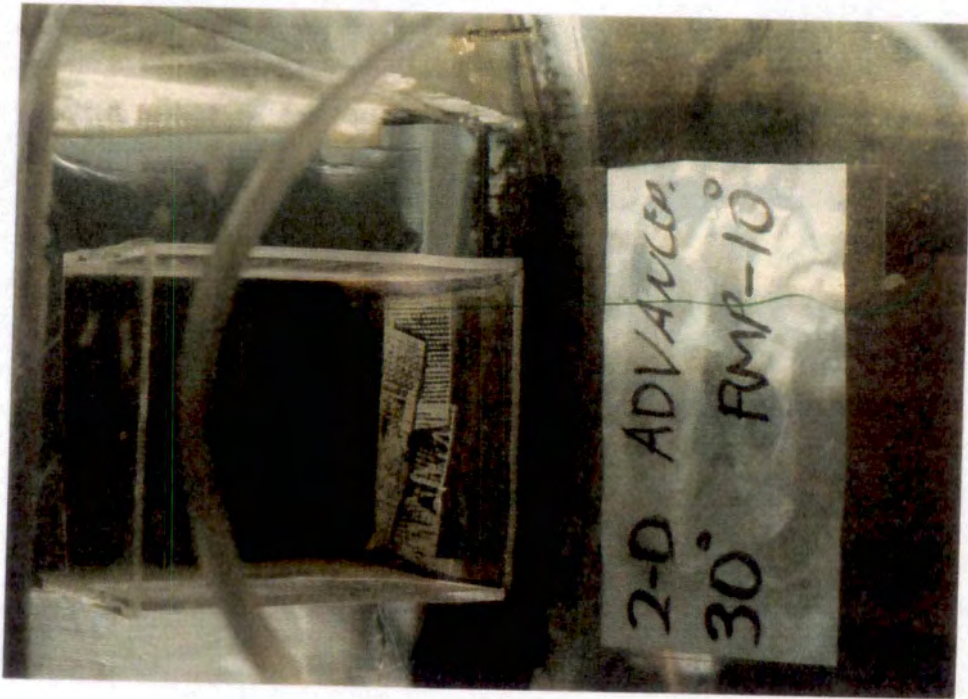
a. Zone 1, RMP = -10 deg



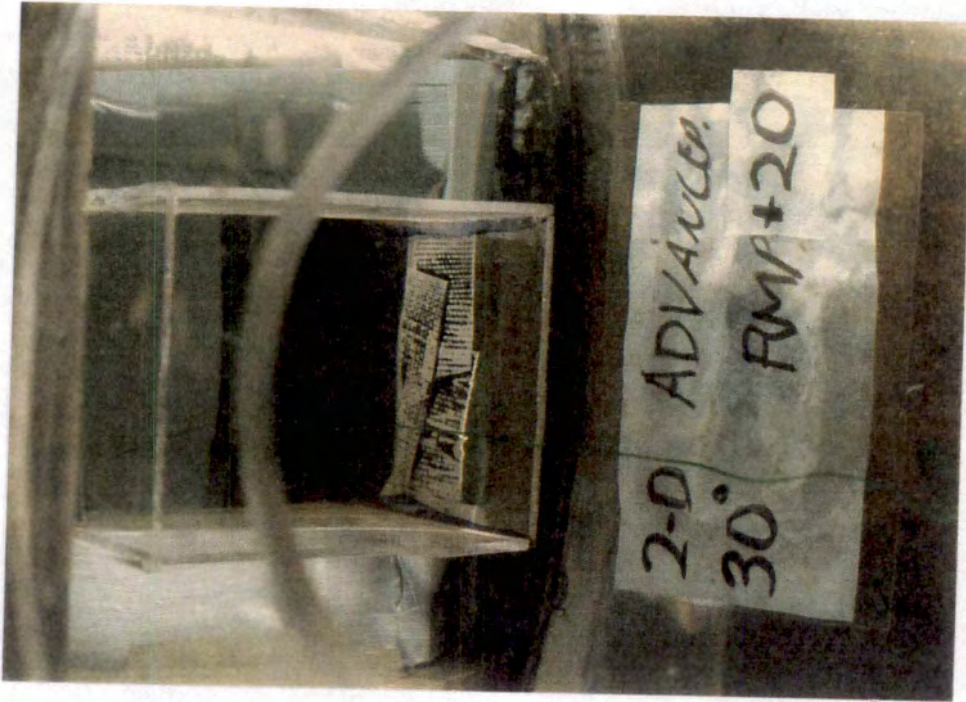
b. Zone 2, RMP = -10 deg

Figure 91. Water Flow Streaklines in ASTF Nozzle Model Set at  $\theta = 30$  deg and  $ZI = 2.25$  in.



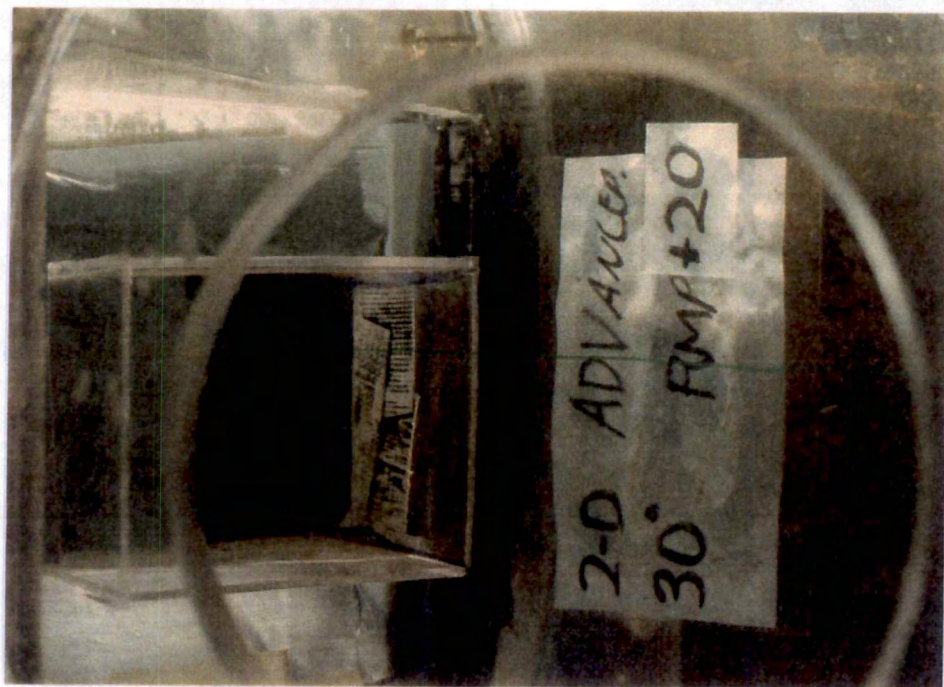


c. Zone 3, RMP = -10 deg



d. Zone 1, RMP = +20 deg

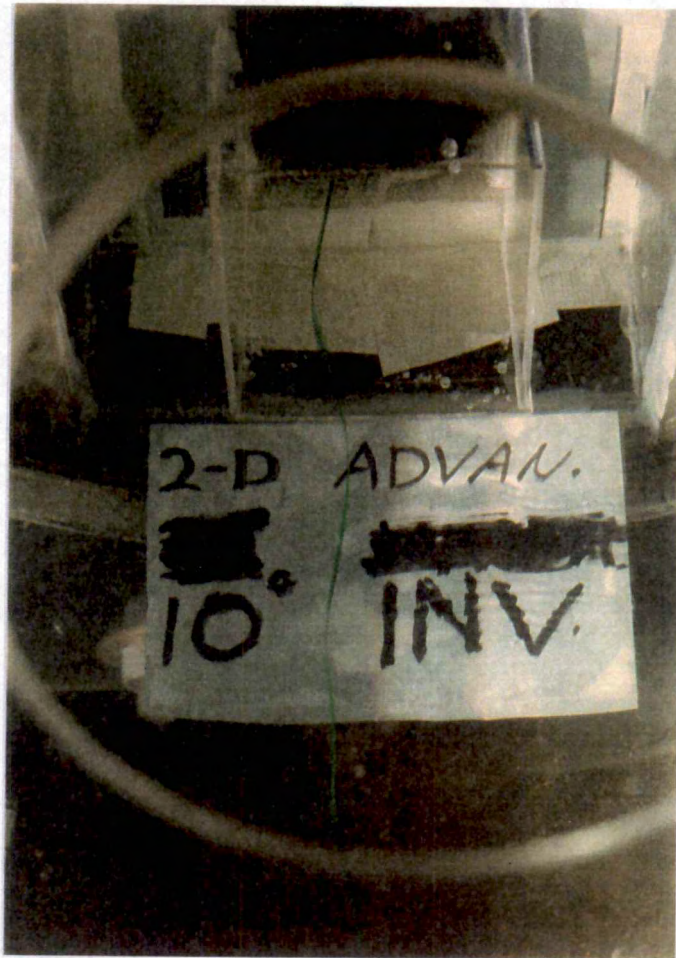
Figure 91. Continued.



e. Zone 3, RMP = +20 deg

Figure 91. Concluded.

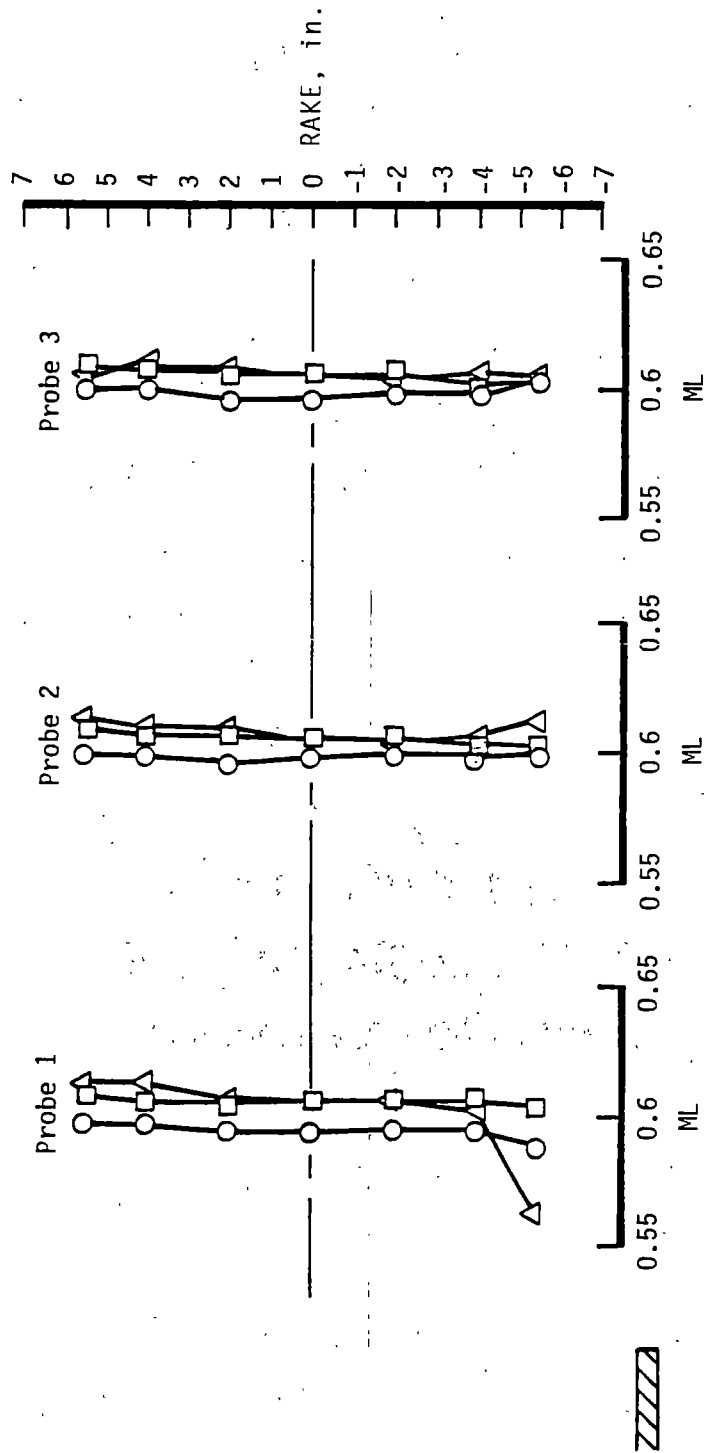




Zone 1

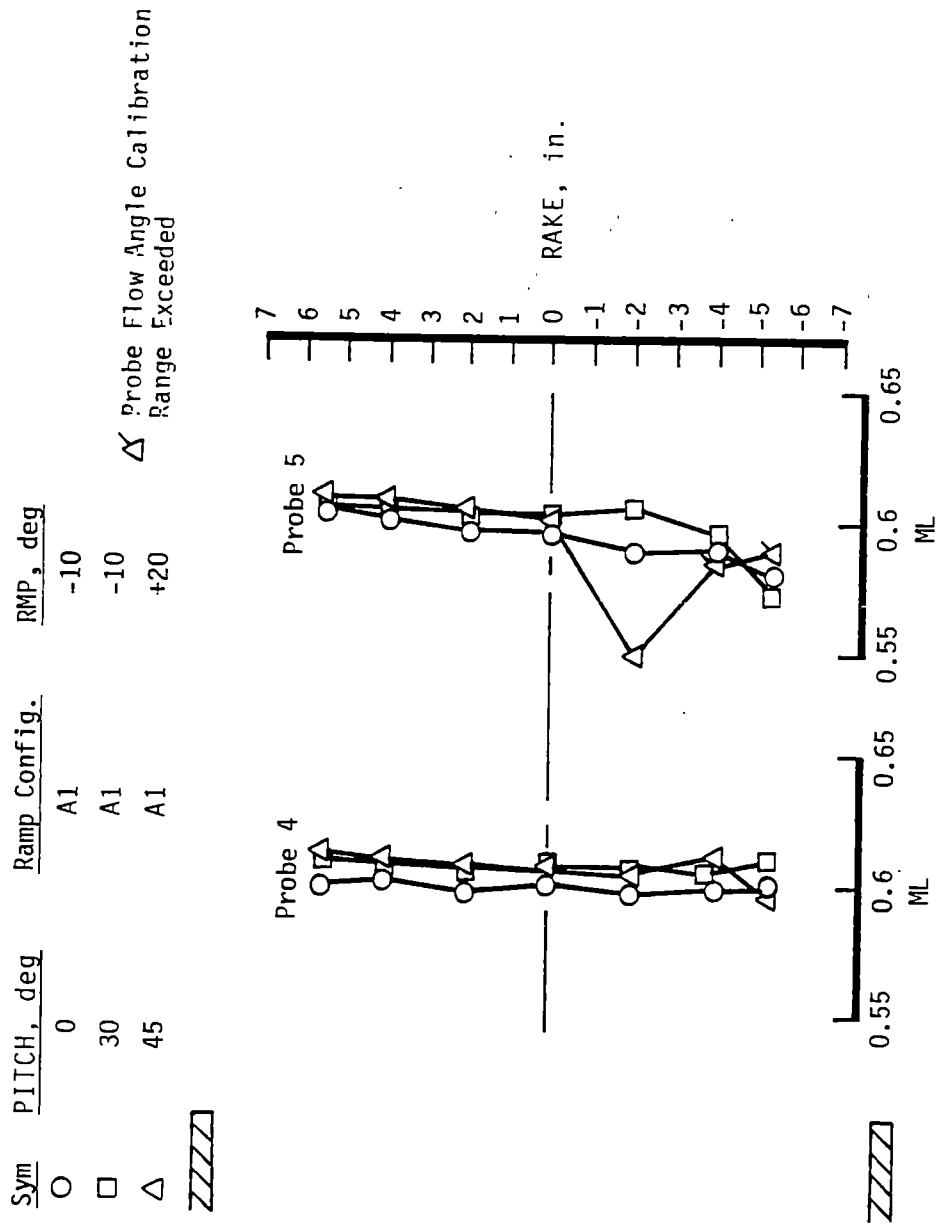
Figure 92. Water Flow Streaklines in ASTF Nozzle Model Set at  $\theta = -10$  deg and  $ZI = 1.05$  in.

Sym	PITCH, deg	Ramp Config.	RMP, deg
○	0	A1	-10
□	30	A1	-10
△	45	+20	



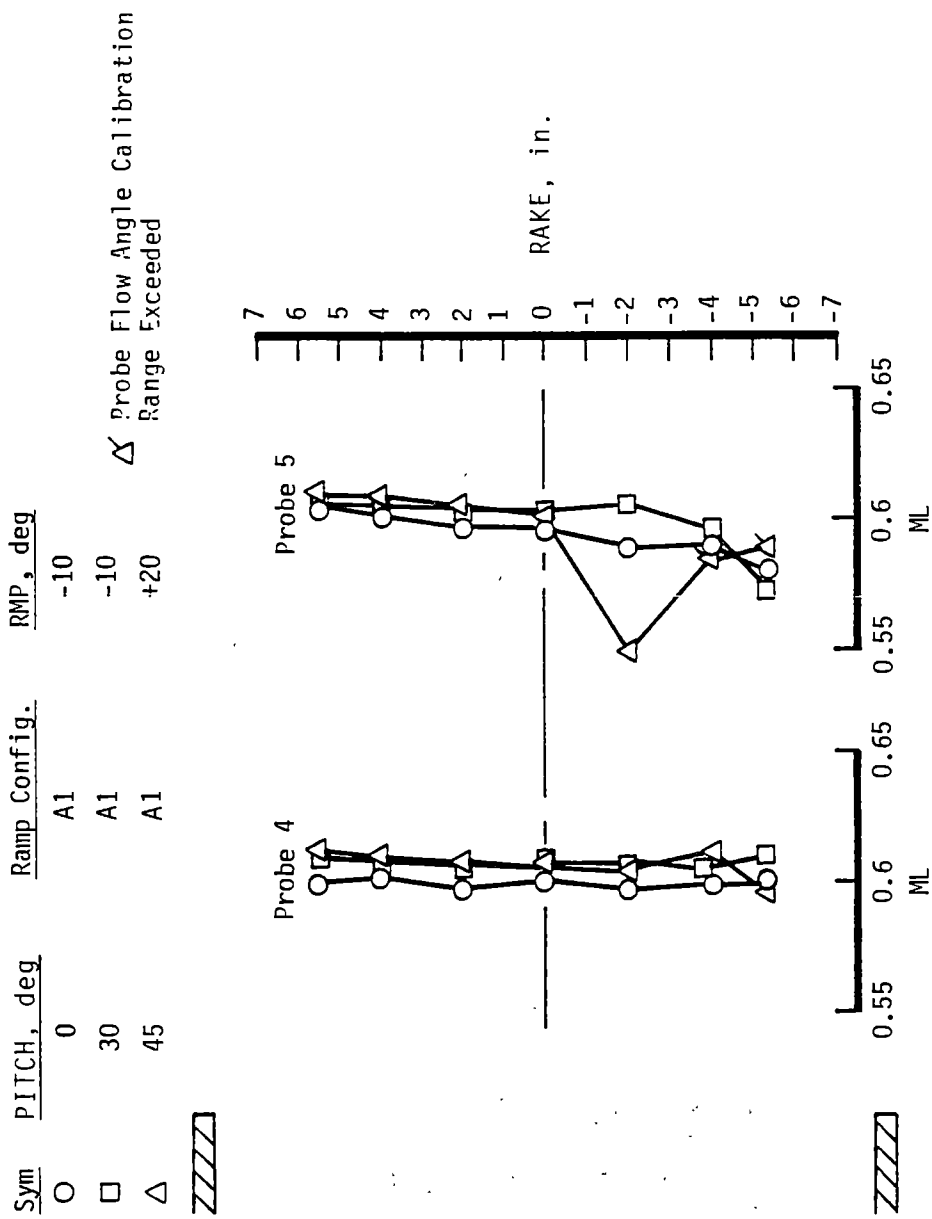
a. Absolute Mach Number

Figure 93. ASTF Nozzle Model Exit Mach Number Measurements with MACH = 0.6 and R2A2 Configuration A.



a. Concluded

Figure 93. Continued.

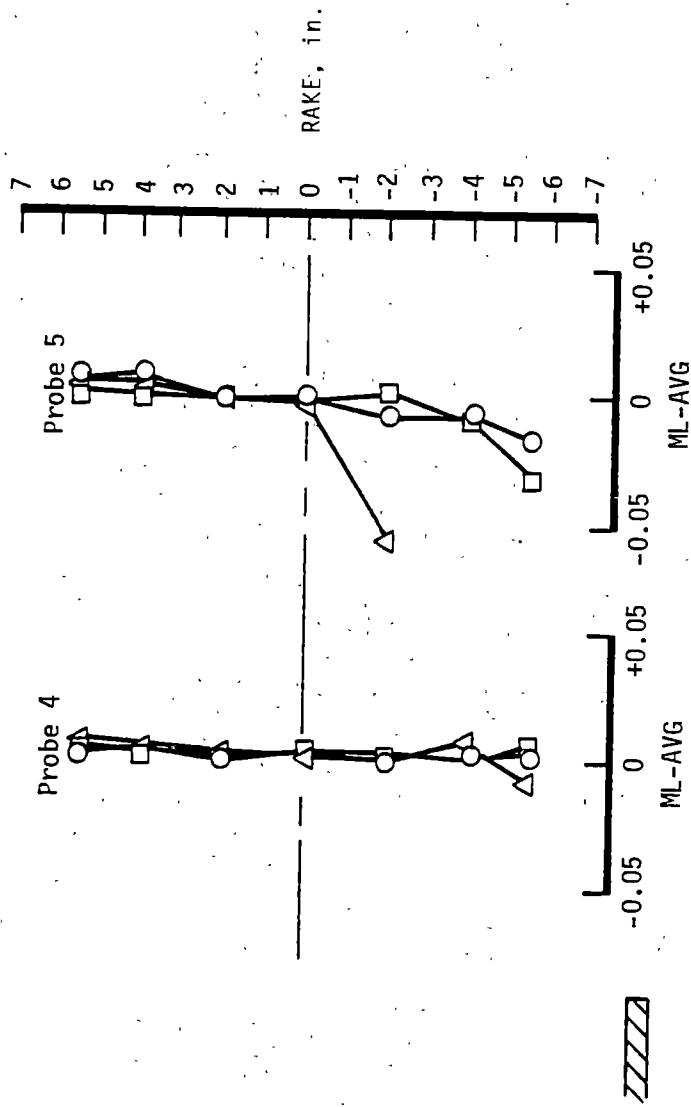


a. Concluded

Figure 93. Continued.



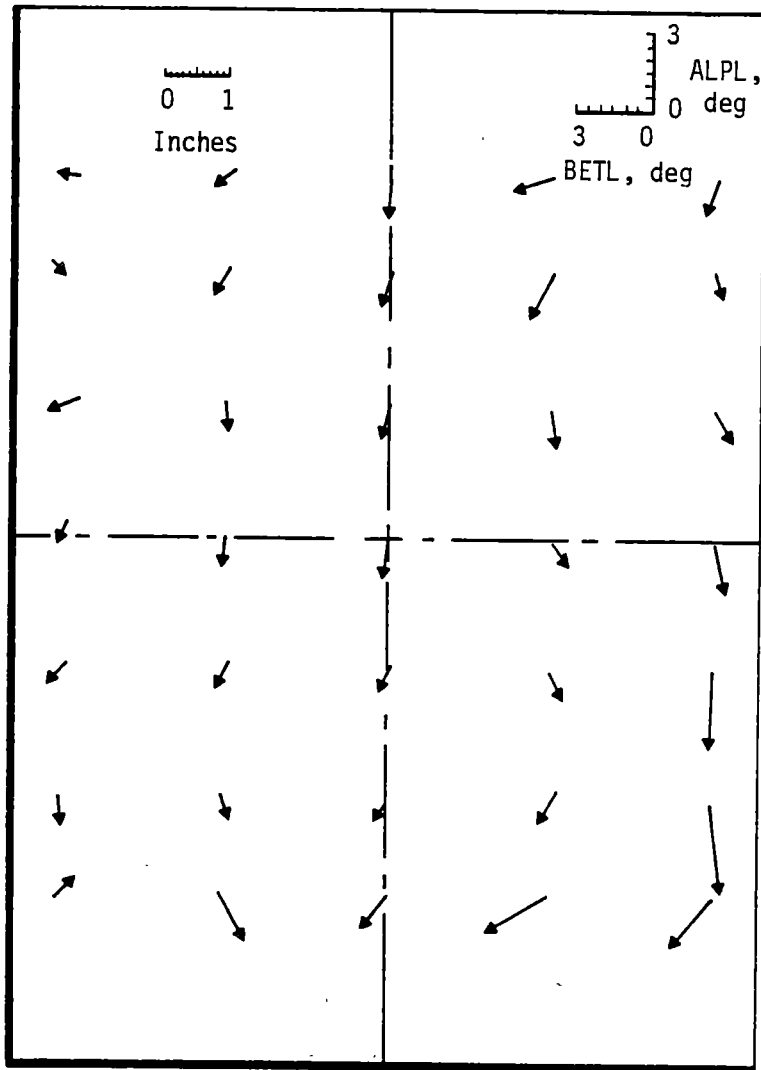
Sym	PIITCH, deg	Ramp Config.	RMP, deg	Avg. ML	Max. Dev.	Std. Dev.
○	0	A1	-10	0.5965	0.0085	0.0047
□	30	A1	-10	0.6043	-0.0307	0.0059
△	45	A1	+20	0.6036	-0.0550	0.0131



b. Concluded

Figure 93. Concluded.



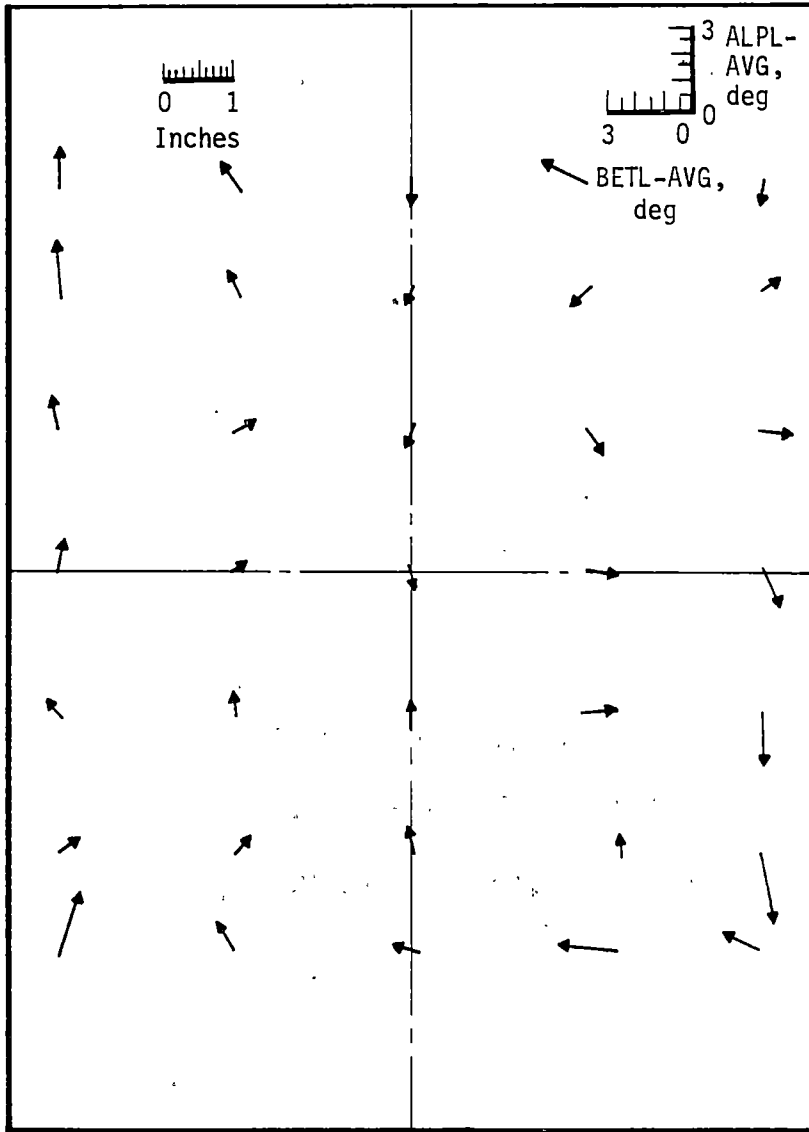


Looking Upstream

a. Absolute Flow Angle

Figure 94. ASTF Nozzle Model Exit Flow Angularity Measurements with MACH = 0.6,  $\theta = 0$  deg, Ramp Configuration A1, RMP = -10 deg, and R2A2 Configuration A.

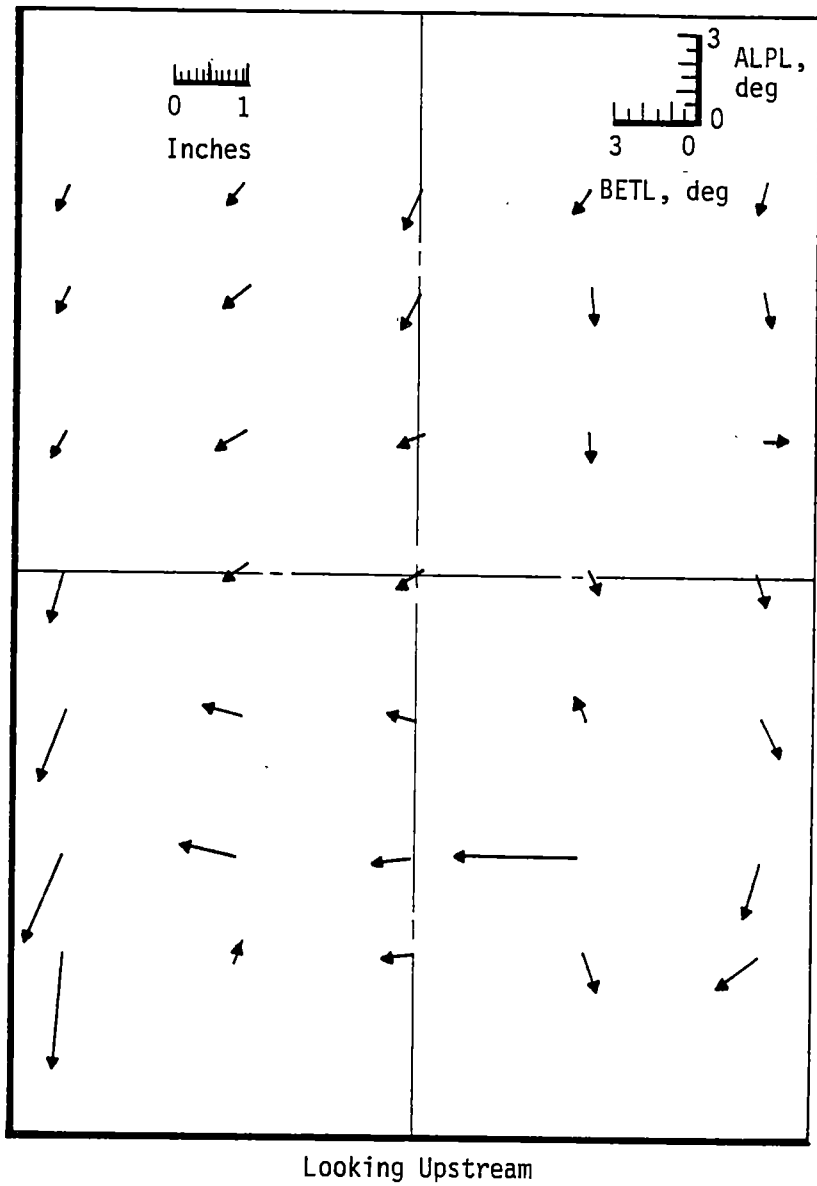
<u>Component</u>	<u>Average, deg</u>	<u>Max. Dev., deg</u>	<u>Std. Dev., deg</u>
ALPL	-1.040	2.646	0.841
BETL	0.256	2.124	0.662



Looking Upstream

b. Flow Angle Deviations from Average

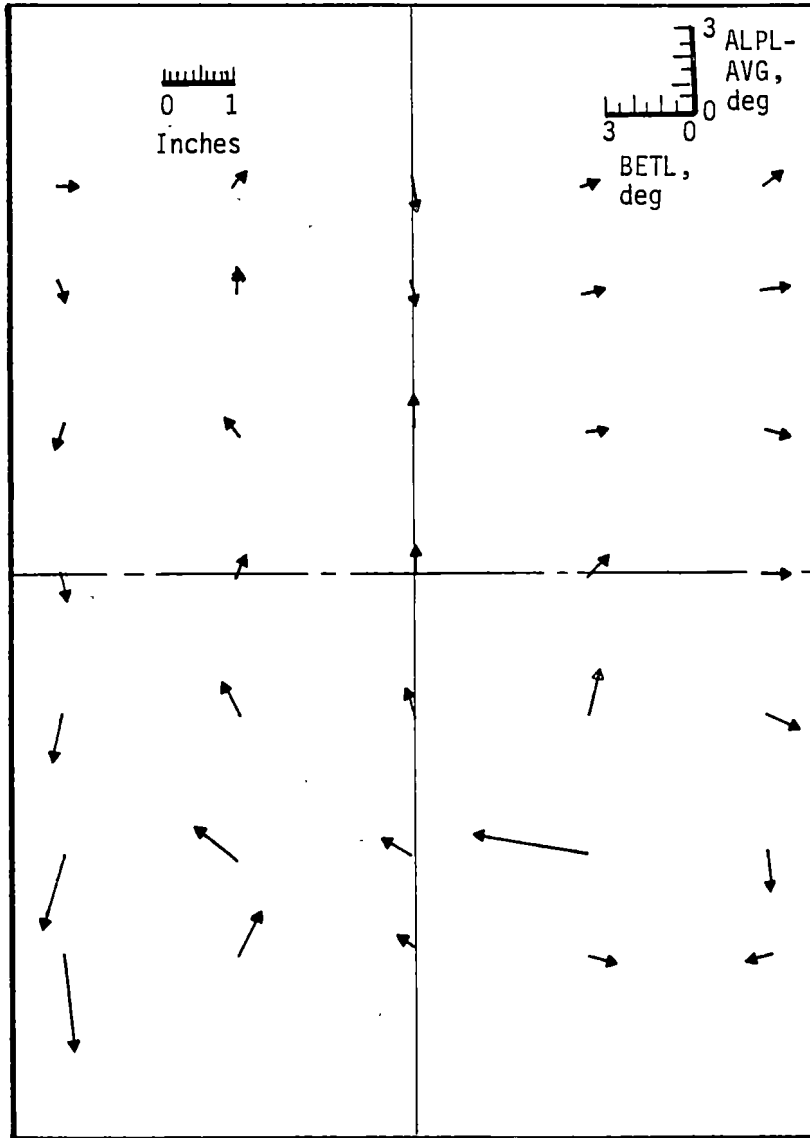
Figure 94. Concluded.



a. Absolute Flow Angle

Figure 95. ASTF Nozzle Model Exit Flow Angularity Measurements with MACH = 0.6,  $\theta = 30$  deg, Ramp Configuration A1, RMP = -10 deg, and R2A2 Configuration A.

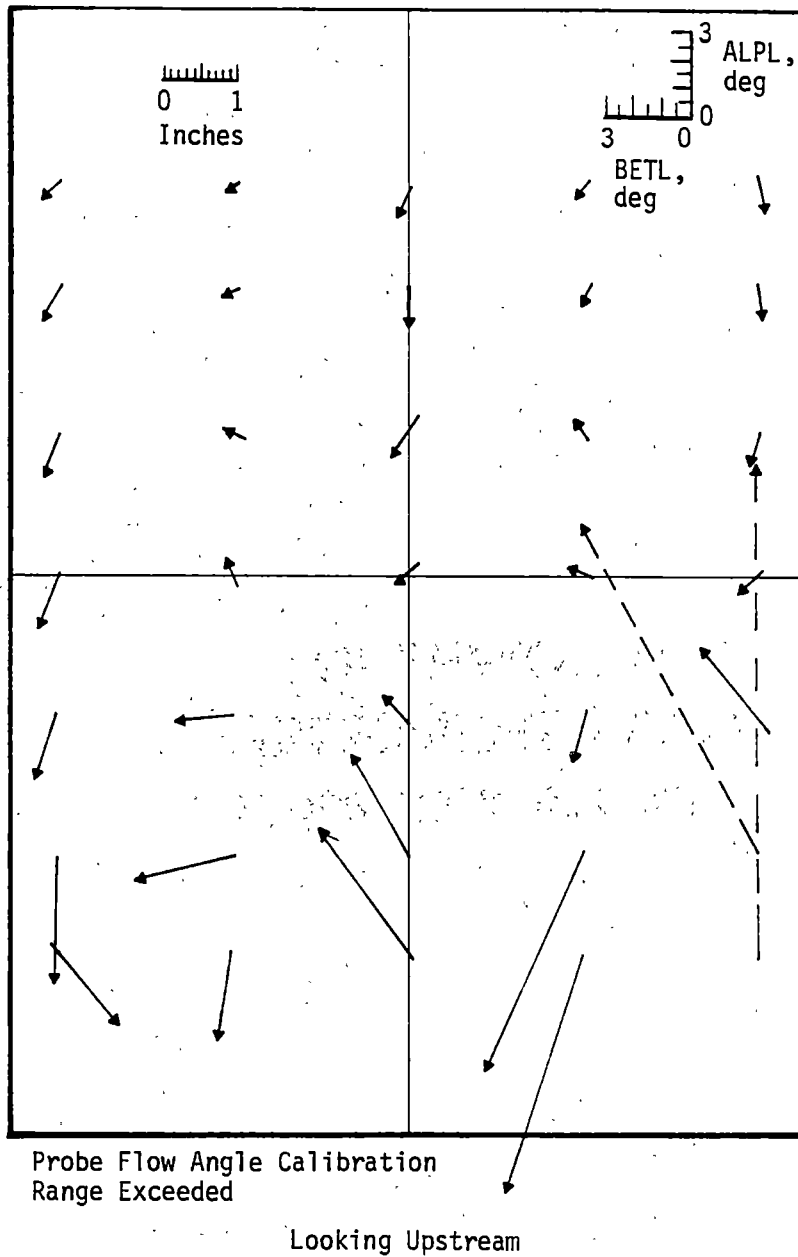
<u>Component</u>	<u>Average, deg</u>	<u>Max. Dev., deg</u>	<u>Std. Dev., deg</u>
ALPL	-0.739	-3.299	0.984
BETL	0.629	4.160	0.924



Looking Upstream

b. Flow Angle Deviations from Average

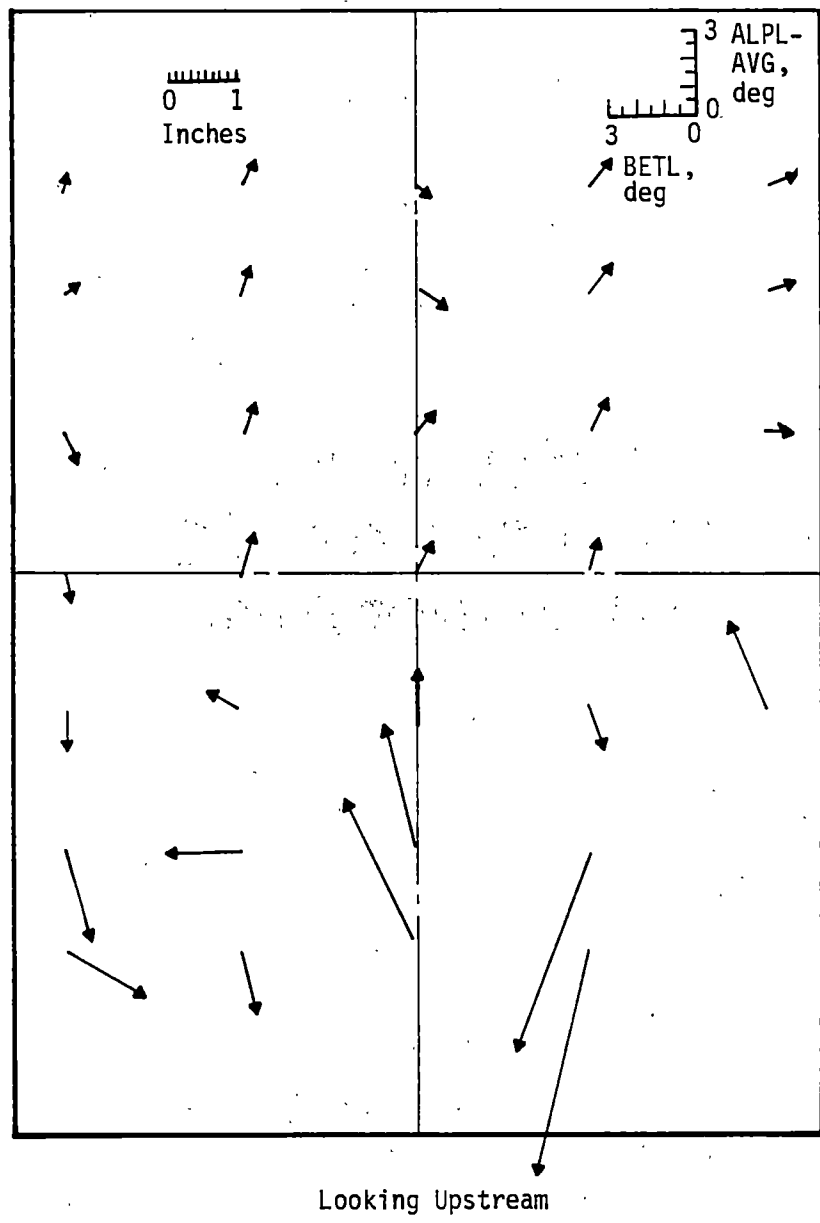
Figure 95. Concluded.



a. Absolute Mach Number

Figure 96. ASTF Nozzle Model Exit Flow Angularity Measurements with MACH = 0.6,  $\theta = 45$  deg, Ramp Configuration A1, RMP = -10 deg, and R2A2 Configuration A.

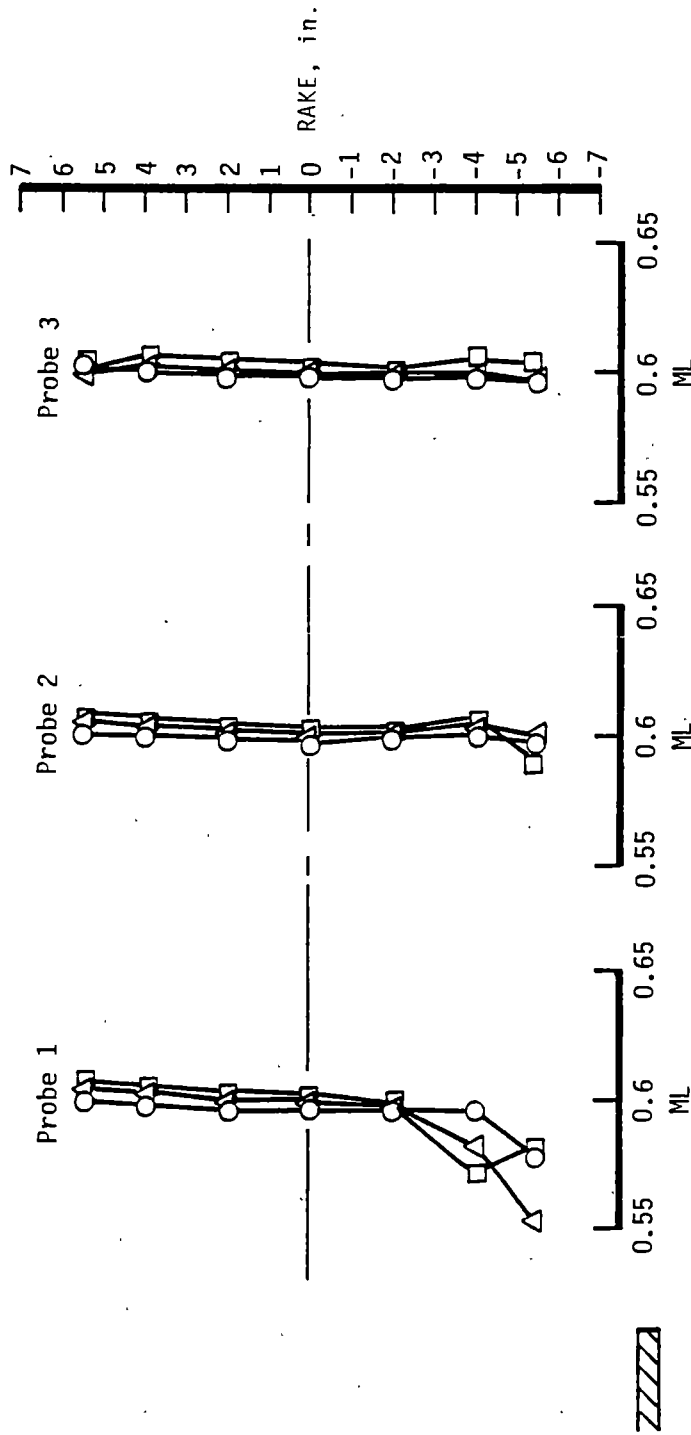
<u>Component</u>	<u>Average, deg</u>	<u>Max. Dev., deg</u>	<u>Std. Dev., deg</u>
ALPL	-0.849	-7.460	2.453
BETL	0.813	2.665	1.150



b. Flow Angle Deviations from Average

Figure 96. Concluded.

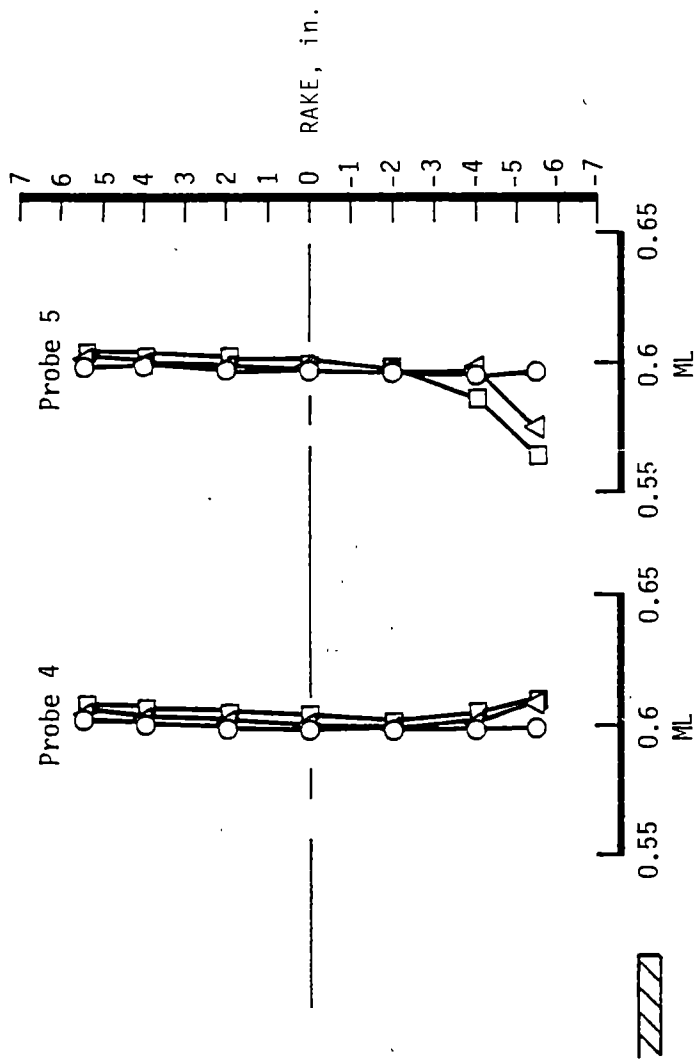
Sym	PITCH, deg	Ramp Config.	RMP, deg
○	30	A2	-10
□	45	A1	+20
△	45	A2	+20



a. Absolute Mach Number

Figure 97. ASTF Nozzle Model Exit Mach Number Measurements with MACH = 0.6 and R2A2 Configuration B.

Sym	PIITCH, deg	Ramp Config.	RMP, deg
○	30	A2	-10
□	45	A1	+20
△	45	A2	+20

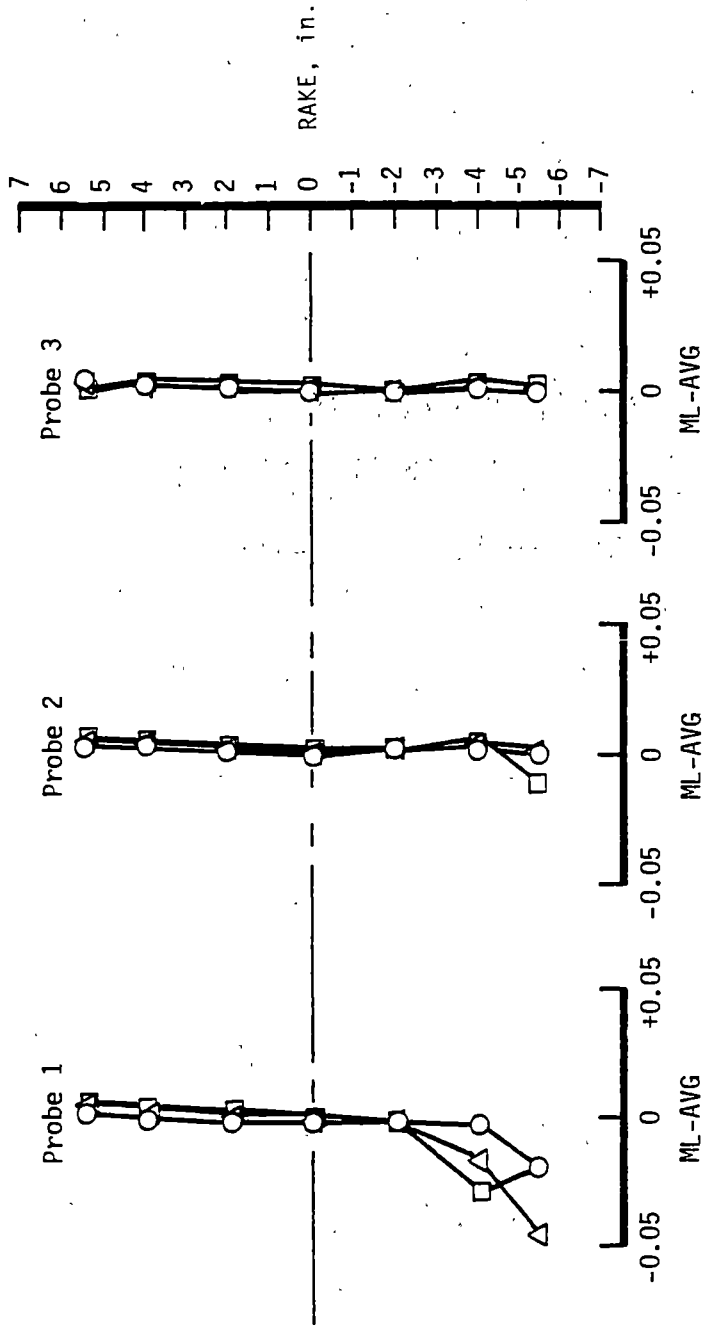


a. Concluded

Figure 97. Continued.



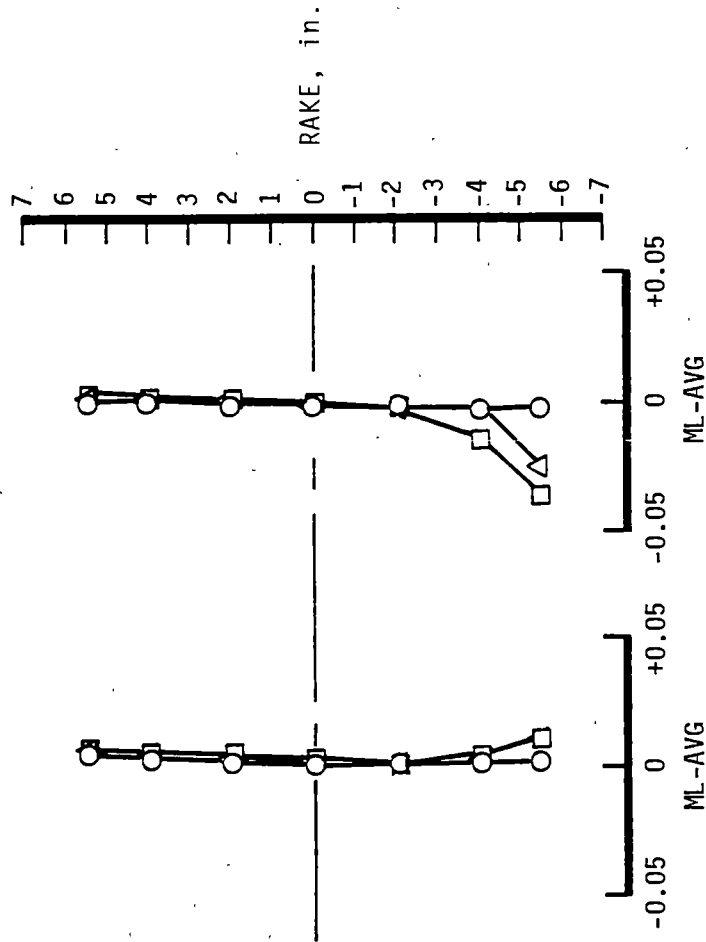
Sym	PIIICH, deg	Ramp Config.	RMP, deg
○	30	A2	-10
□	45	A1	+20
△	45	A2	+20



b. Mach Number Deviations from Average

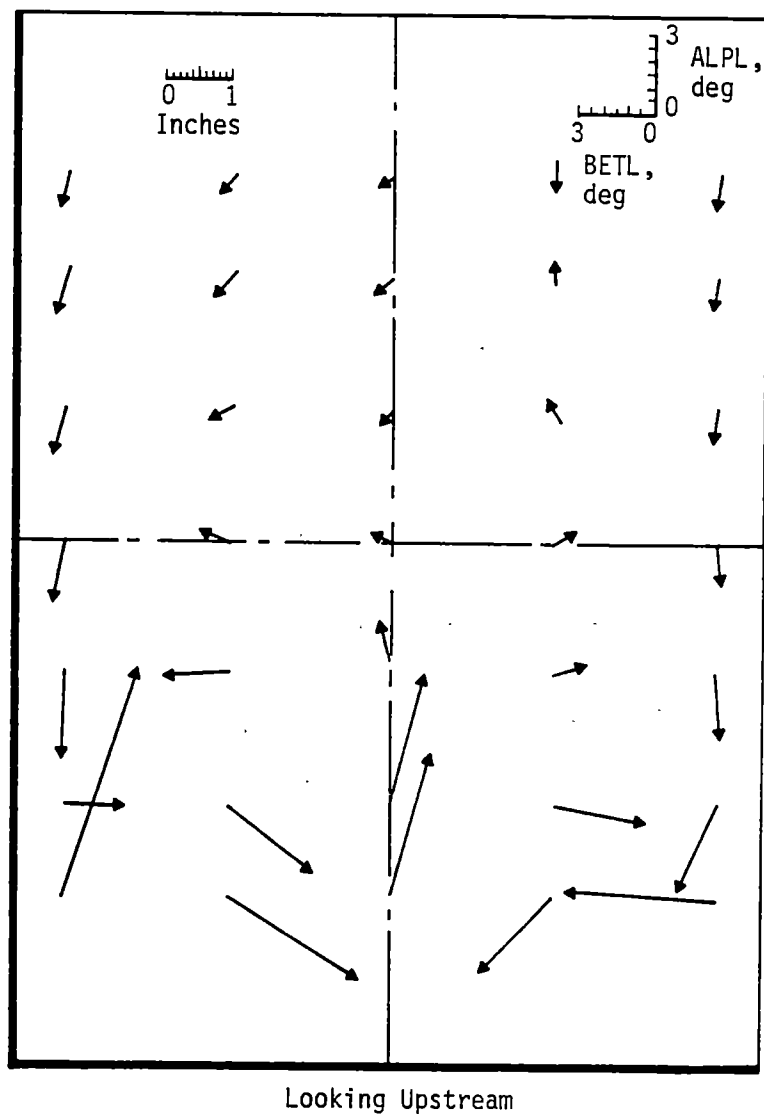
Figure 97. Continued.

Sym	PIITCH, deg	Ramp Config.	RMP, deg	Avg. ML	Max. Dev.	Std. Dev.
○	30	A2	-10	0.5976	-0.019	0.0038
□	45	A1	+20	0.6006	-0.0356	0.0100
△	45	A2	+20	0.5985	-0.0448	0.0099



b. Concluded.

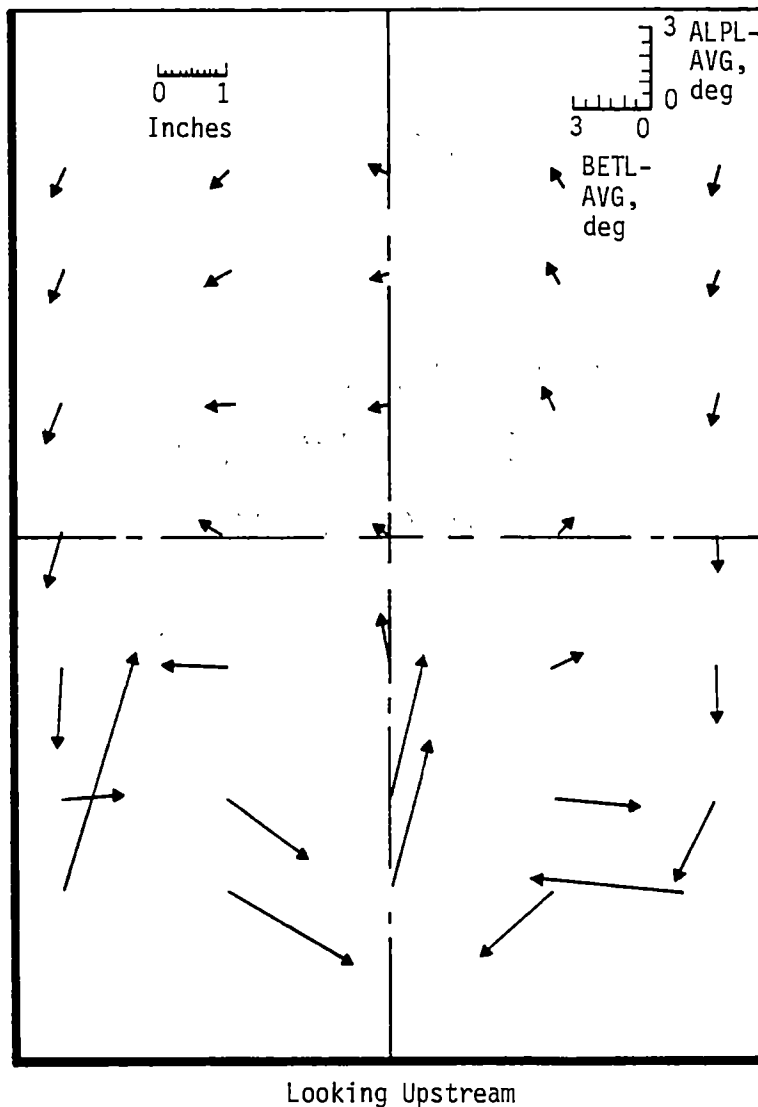
Figure 97. Concluded.



a. Absolute Flow Angle

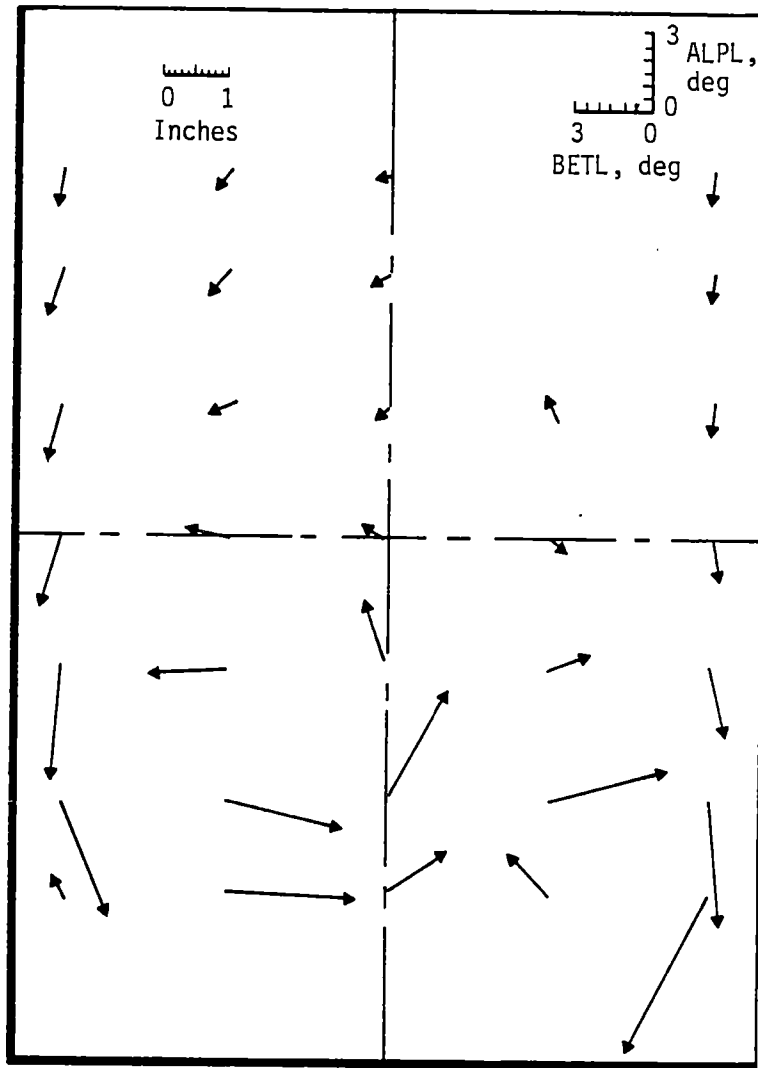
Figure 98. ASTF Nozzle Model Exit Flow Angularity Measurements with MACH = 0.6,  $\theta = 45$  deg, Ramp Configuration A1, RMP = +20 deg, and R2A2 Configuration B.

<u>Component</u>	<u>Average, deg</u>	<u>Max. Dev., deg</u>	<u>Std. Dev., deg</u>
ALPL	-0.286	9.168	2.480
BETL	-0.037	5.864	1.898



b. Flow Angle Deviations from Average

Figure 98. Concluded.

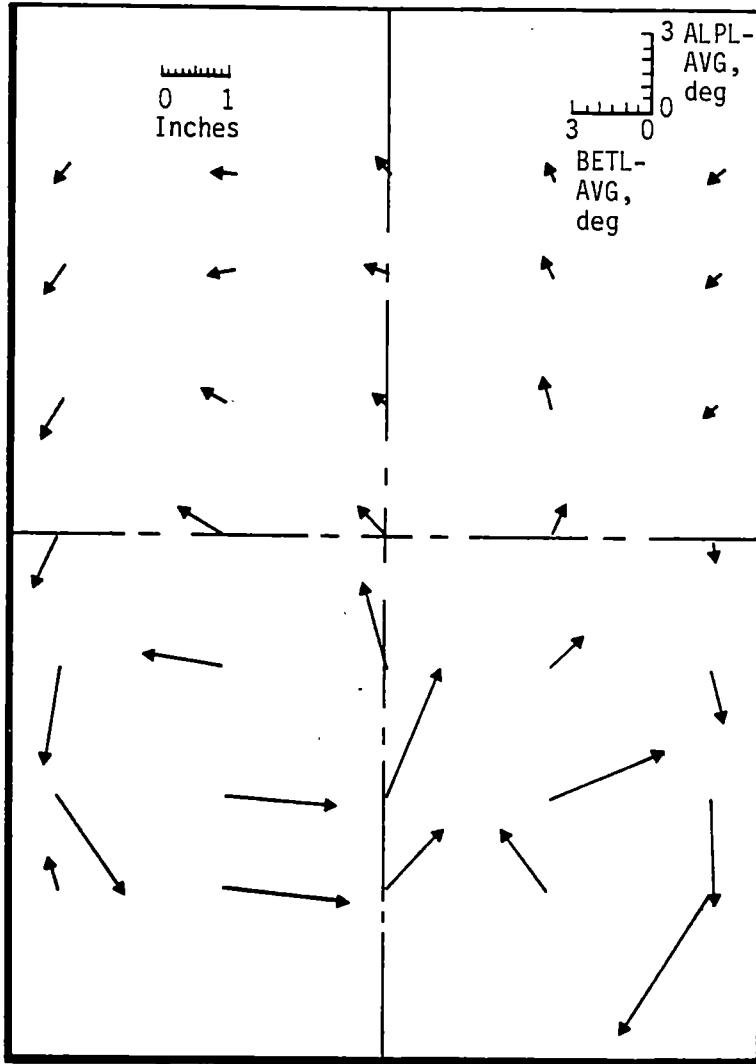


Looking Upstream

a. Absolute Flow Angle

Figure 99. ASTF Nozzle Model Exit Flow Angularity Measurements with MACH = 0.6,  $\theta = 45$  deg, Ramp Configuration A2, RMP = +20 deg, and R2A2 Configuration B.

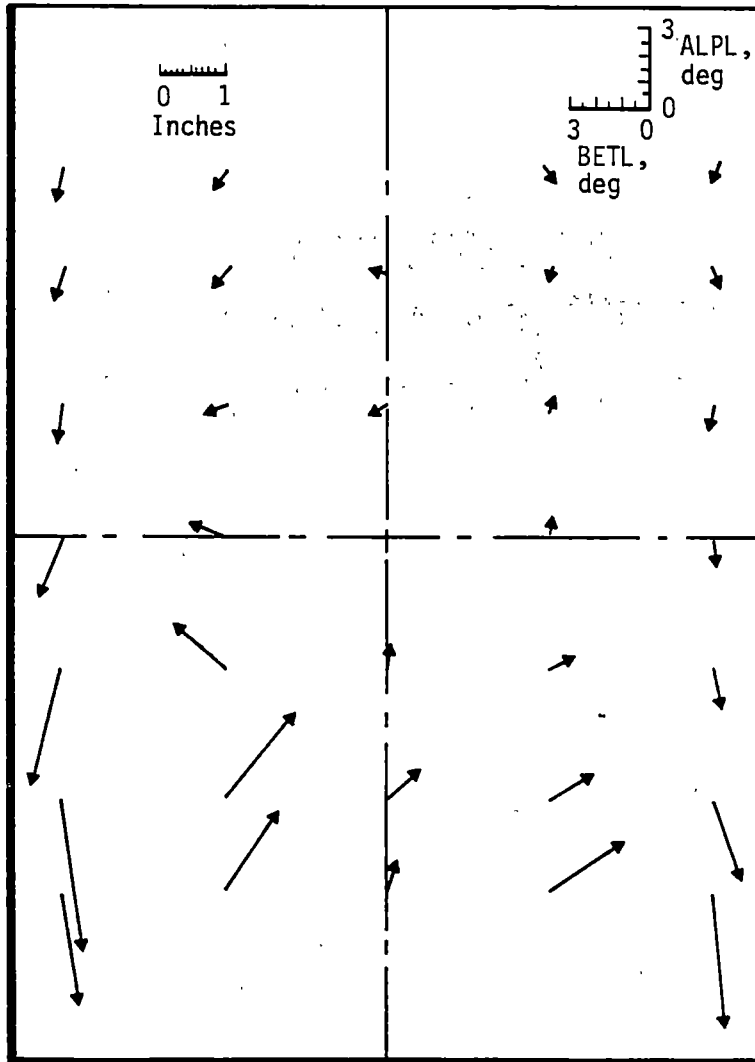
<u>Component</u>	<u>Average, deg</u>	<u>Max. Dev., deg</u>	<u>Std. Dev., deg</u>
ALPL	-0.739	-5.571	2.109
BETL	-0.153	-4.952	1.854



Looking Upstream

b. Flow Angle Deviations from Average

Figure 99. Concluded.

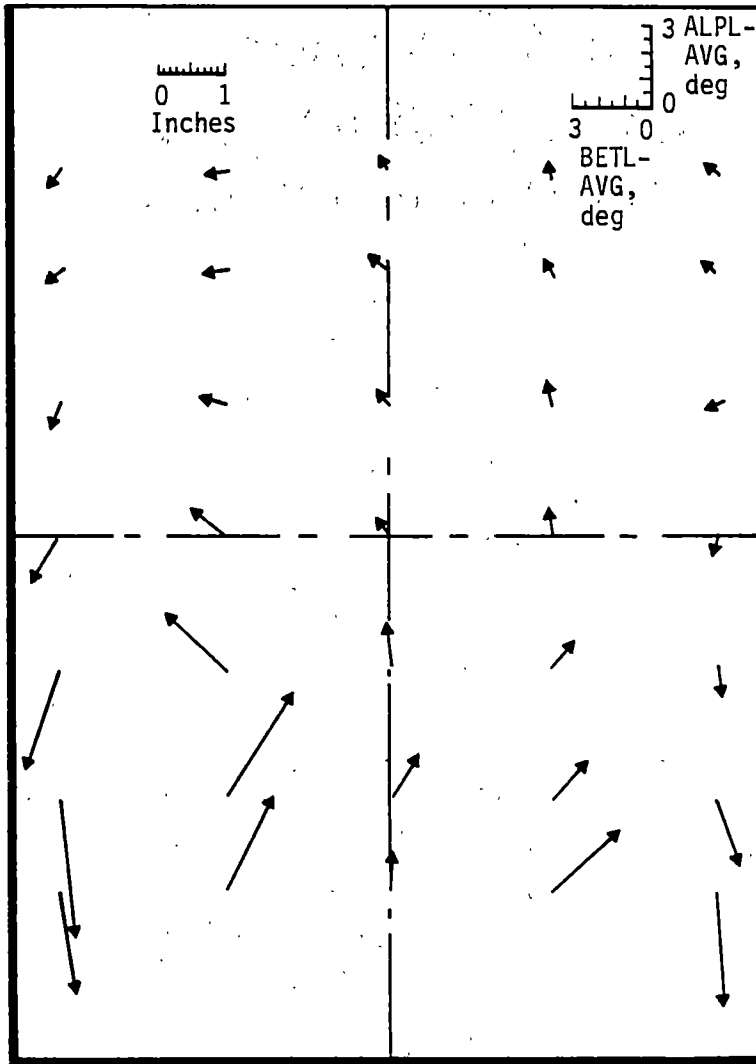


Looking Upstream

a. Absolute Flow Angle

Figure 100. ASTF Nozzle Model Exit Flow Angularity Measurements with MACH = 0.6,  $\theta = 30$  deg, Ramp Configuration A2, RMP = -10 deg, and R2A2 Configuration B.

<u>Component</u>	<u>Average, deg</u>	<u>Max. Dev., deg</u>	<u>Std. Dev., deg</u>
ALPL	-0.555	-5.285	2.113
BETL	-0.179	-2.639	1.040



Looking Upstream

b. Flow Angle Deviation from Average

Figure 100. Concluded.





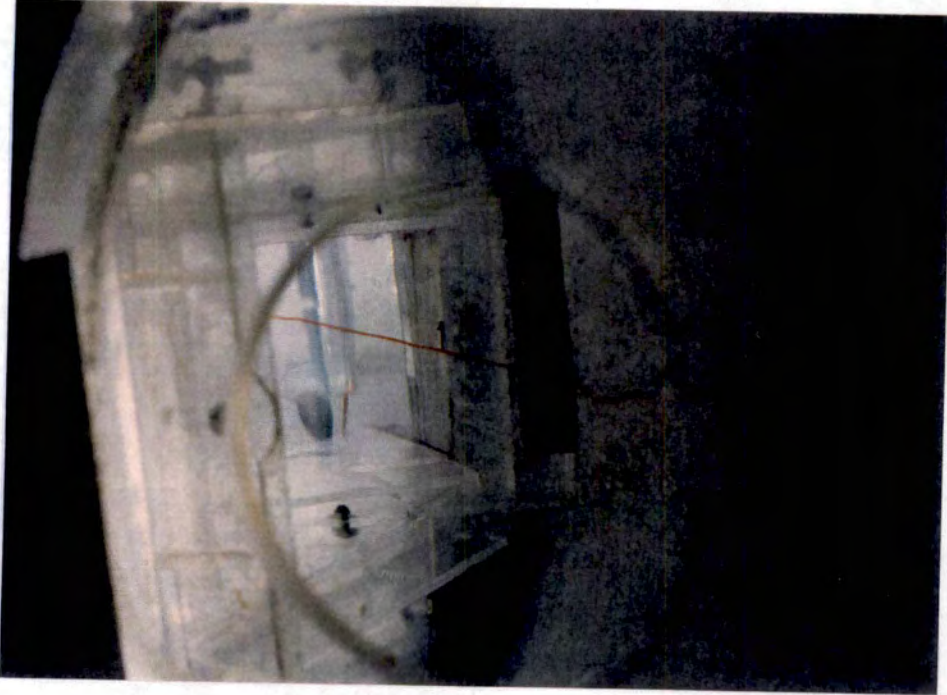
View Upstream into Nozzle Exit



Side View

a. Zone 1

Figure 101. Water Flow Streaklines in ASTF Nozzle Model with Ramp Configuration B at RMP = 20 deg,  $\theta = 45$  deg and  $\psi = 0$  deg.



View Upstream into Nozzle Exit

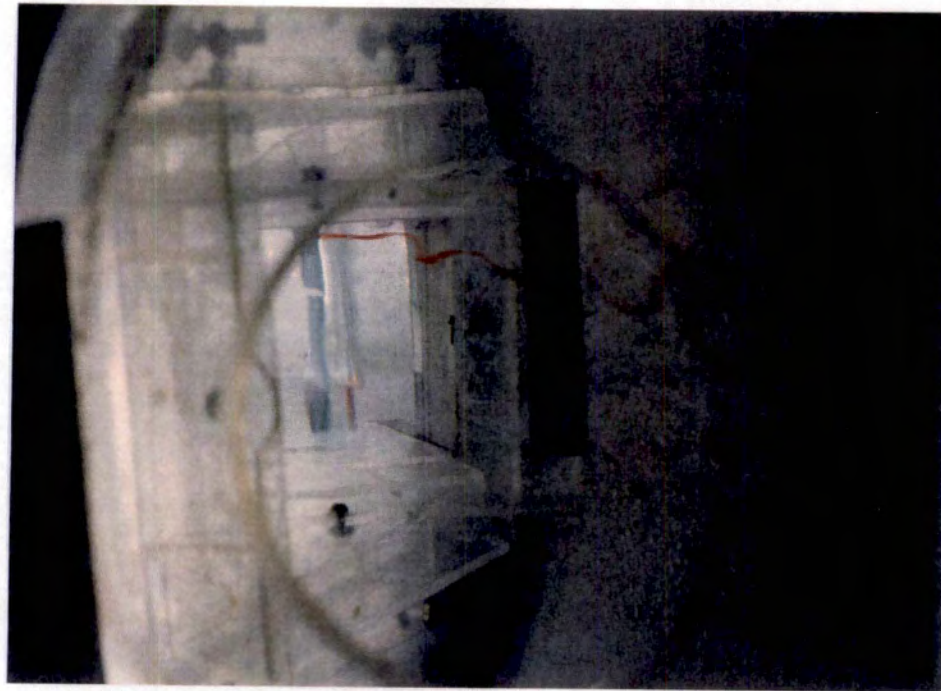


Side View

b. Zone 2

Figure 101. Continued.





View Upstream into Nozzle Exit



Side View

c. Zone 3

Figure 101. Continued.

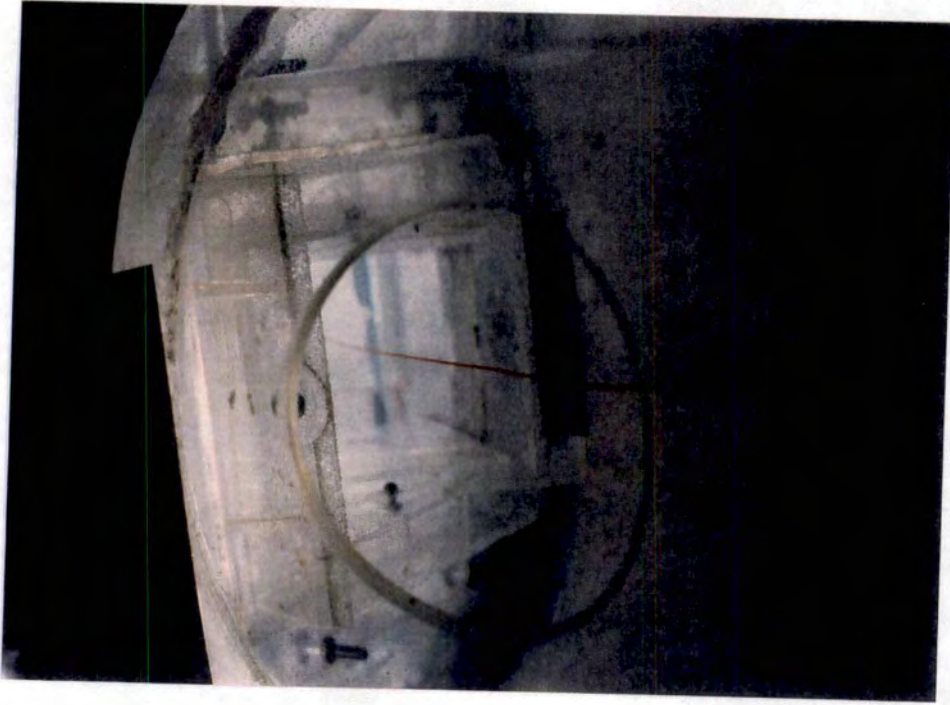


Side View

d. Zone 4

Figure 101. Continued.





View Upstream into Nozzle Exit



Side View

e. Zone 5

Figure 101. Continued.



View Upstream into Nozzle Exit

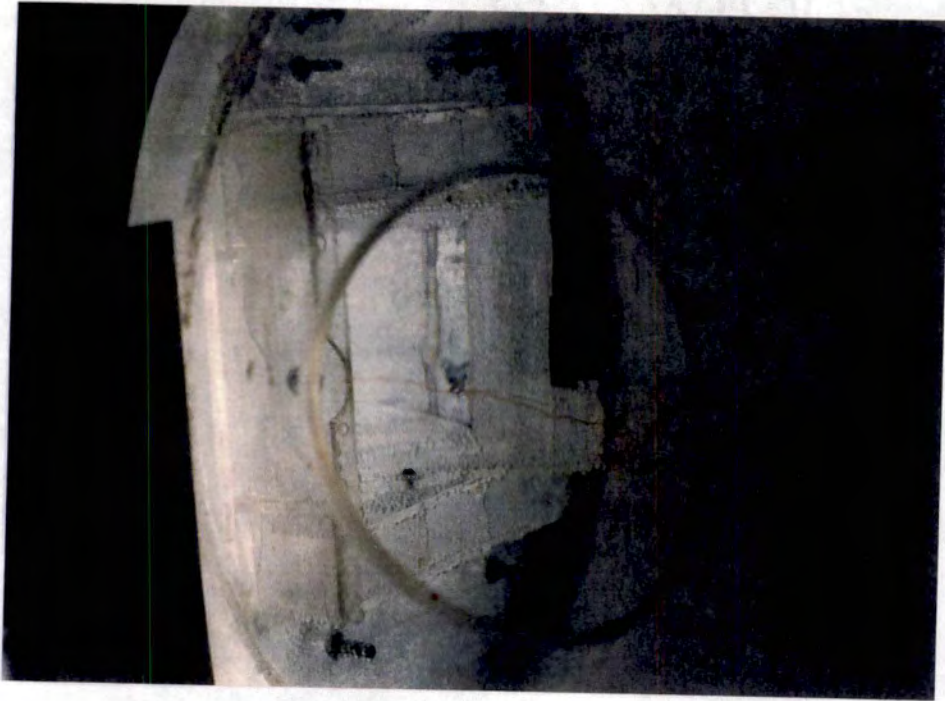


Side View

f. Zone 6

Figure 101. Concluded.





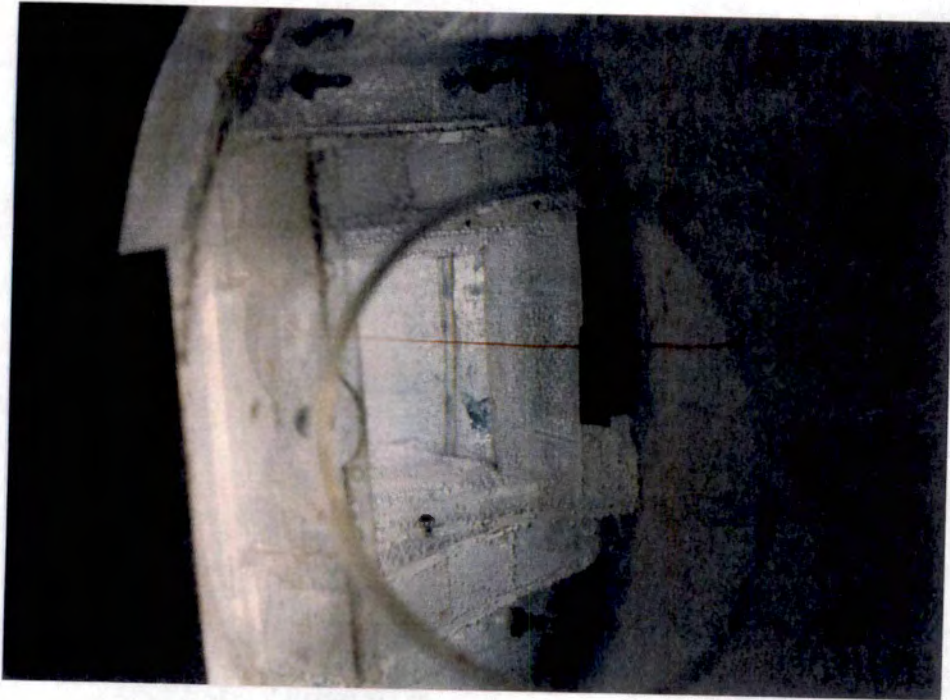
View Upstream into Nozzle Exit



Side View

a. Zone 1

Figure 102. Water Flow Streaklines in ASTF Nozzle Model with Ramp Configuration B at RMP = -10 deg,  $\theta = 30$  deg and  $\psi = 0$  deg.



View Upstream into Nozzle Exit



Side View

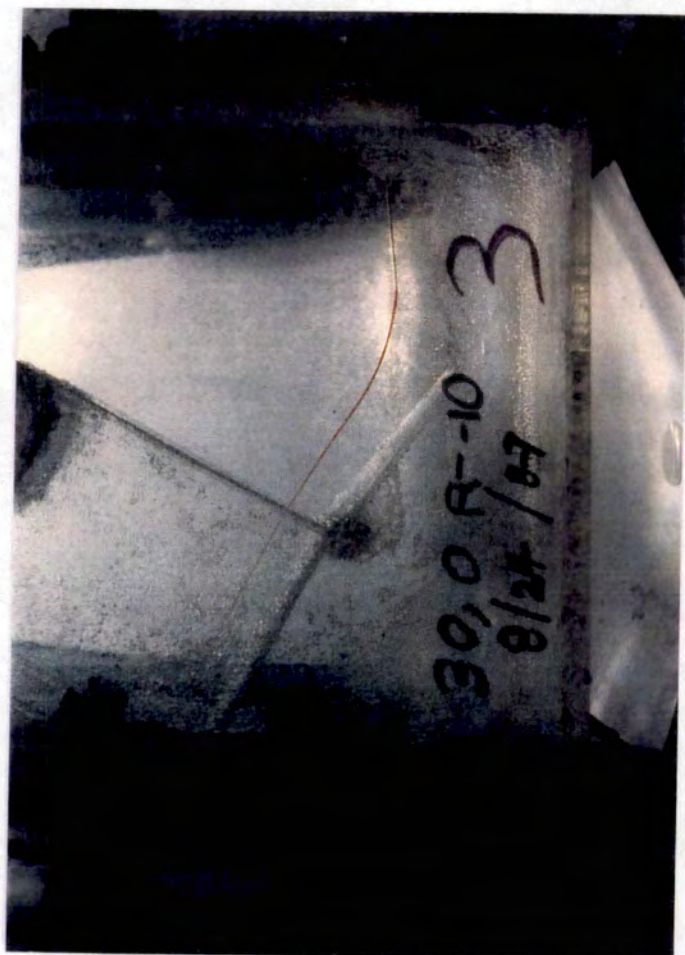
b. Zone 2

Figure 102. Continued.





View Upstream into Nozzle Exit



Side View

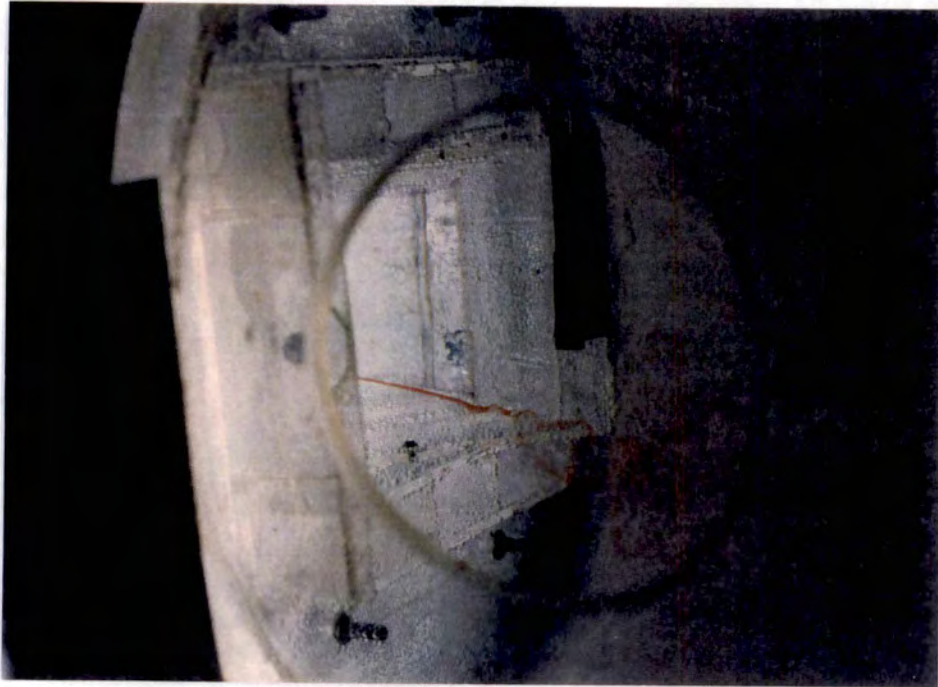
c. Zone 3

Figure 102. Continued.



Side View

d. Zone 4



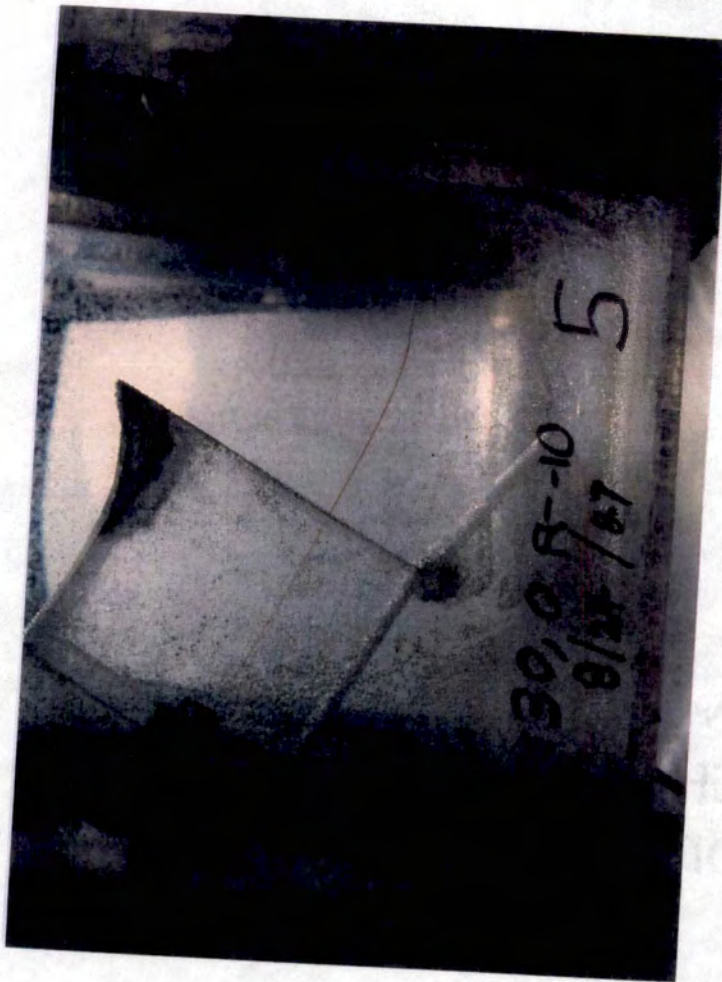
View Upstream into Nozzle Exit

Figure 102. Continued.





View Upstream into Nozzle Exit



Side View

e. Zone 5

Figure 102. Continued.



View Upstream into Nozzle Exit



Side View

f. Zone 6

Figure 102. Concluded.





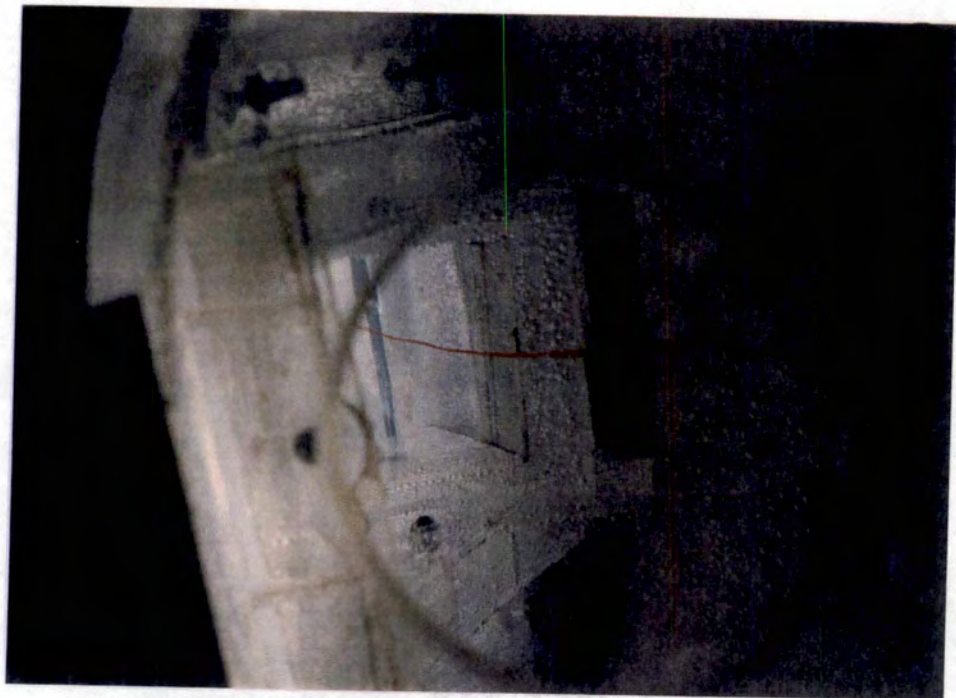
Zone 1, Side View

a.  $\Psi = -5$  deg



Zone 1, View Upstream into Nozzle Exit

Figure 103. Water Flow Streaklines in ASTF Nozzle Model with Ramp Configuration B at RMP = 20 deg,  $\theta = 45$  deg, and Variations in Yaw Angle.



Zone 2, View Upstream into Nozzle Exit

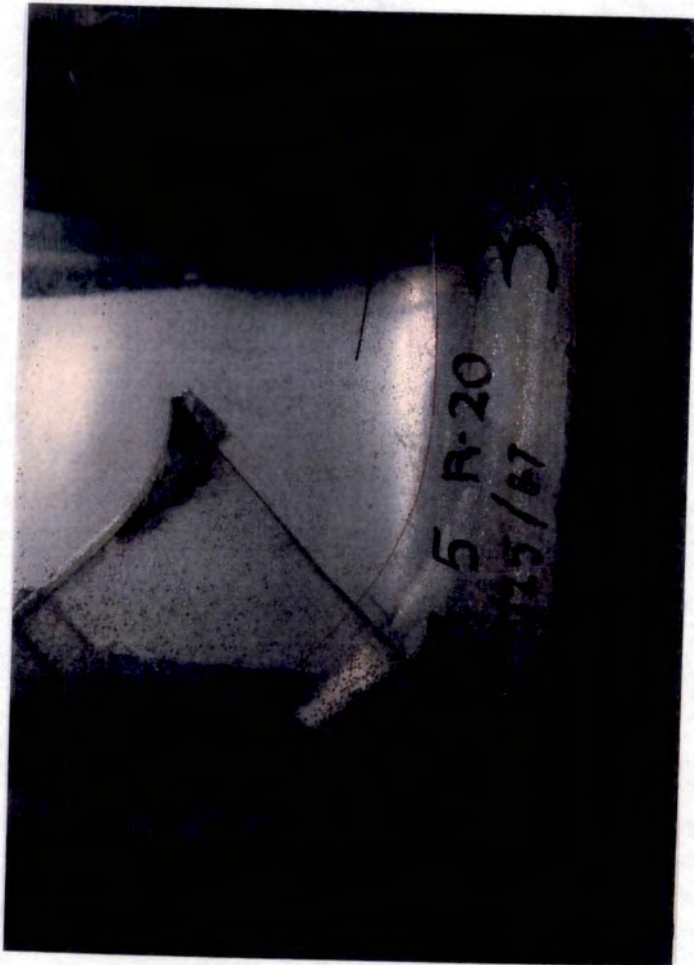


Zone 2, Side View

a. Continued

Figure 103. Continued.





Zone 3, Side View

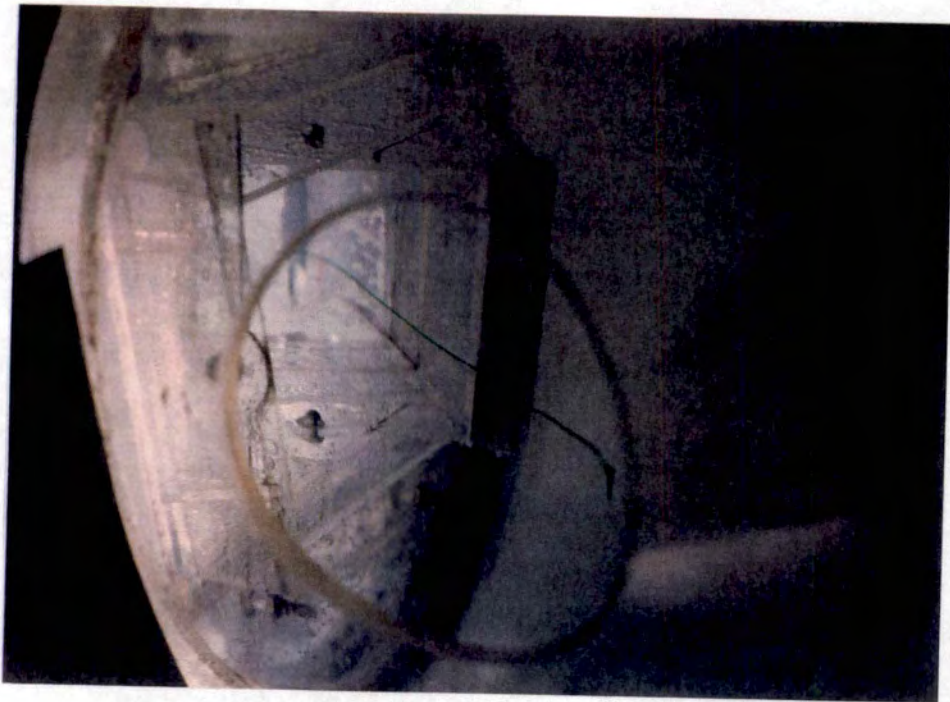
a. Concluded



Zone 3, View Upstream into Nozzle Exit

Figure 103. Continued.





Zone 1, View Upstream into Nozzle Exit



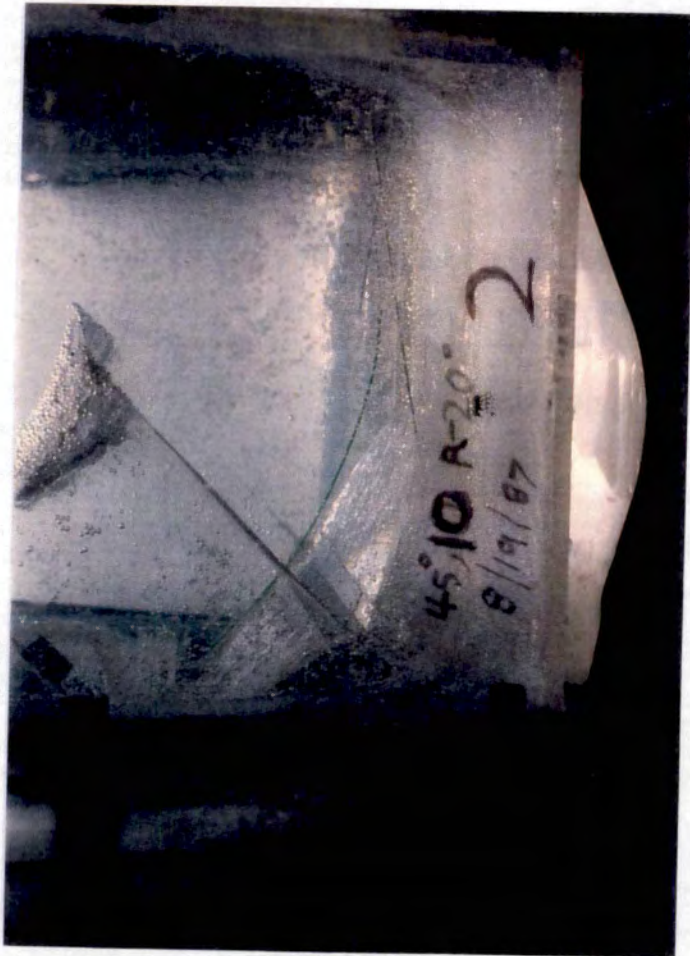
Zone 1, Side View

b.  $\Psi = -10$  deg

Figure 103. Continued.



Zone 2, View Upstream into Nozzle Exit



Zone 2, Side View

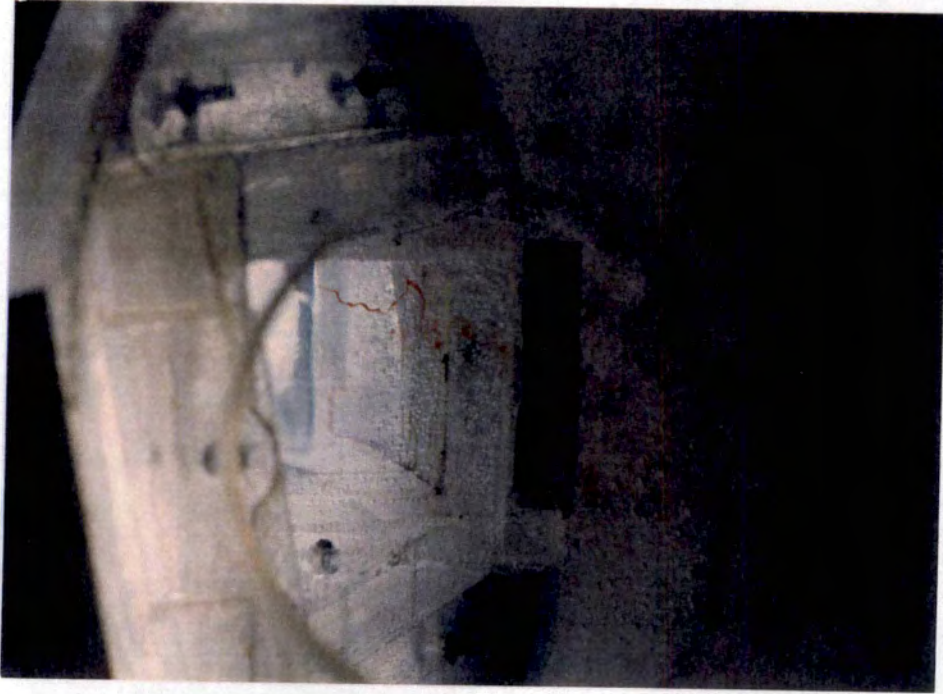
b. Continued

Figure 103. Continued.





Zone 3, Side View



Zone 3, View Upstream into Nozzle Exit

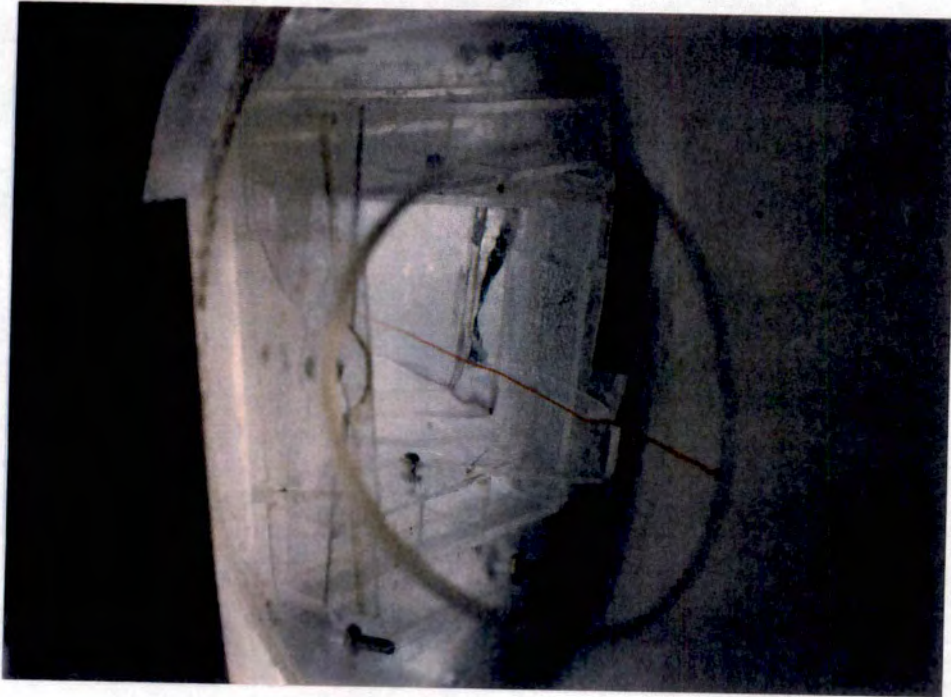
b. Concluded

Figure 103. Concluded.



Zone 1, Side View

a.  $\theta = 30$  deg, RMP = -10 deg



Zone 1, View Upstream into Nozzle Exit

Figure 104. Water Flow Streaklines in ASTF Nozzle Model with Ramp Configuration B,  $\psi = -10$  deg, and Variations in Pitch Angle.





Zone 3, View Upstream into Nozzle Exit



Zone 3, Side View

a. Concluded

Figure 104. Continued.



Zone 1, Side View

Zone 1, View Upstream into Nozzle Exit

b.  $\theta = 10$  deg, RMP = -20 deg

Figure 104. Continued.





Zone 3, Side View

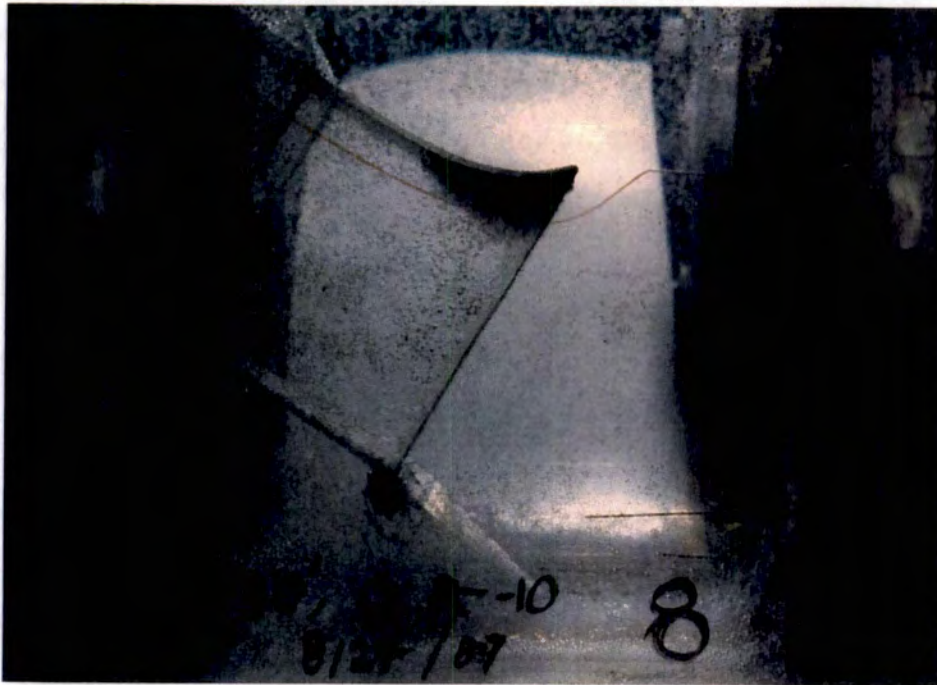


Zone 3, View Upstream into Nozzle Exit

b. Concluded

Figure 104. Concluded.



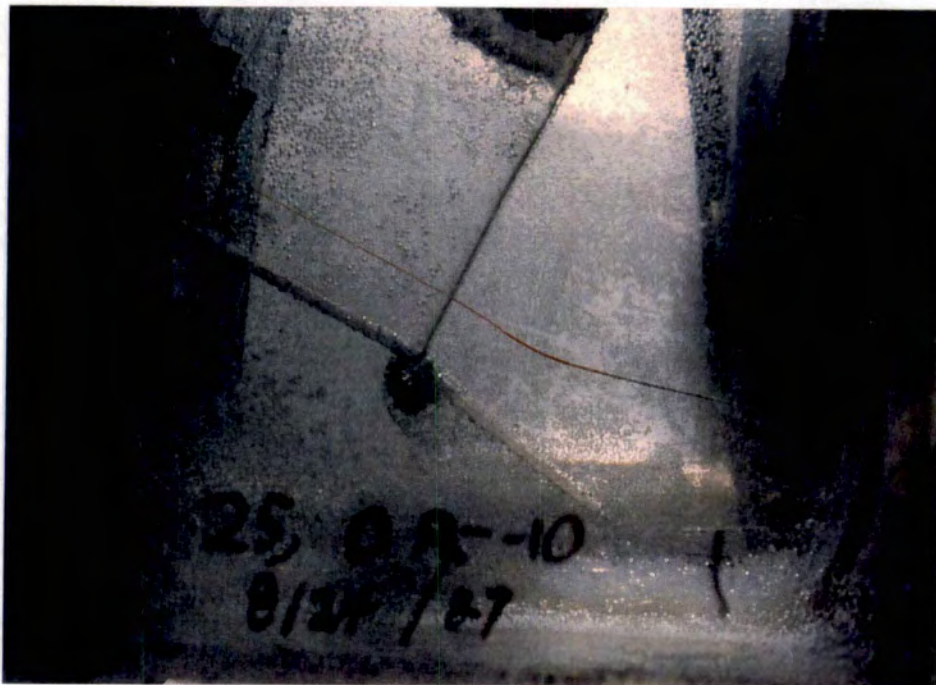


a.  $\theta = 30$  deg, RMP = -10 deg

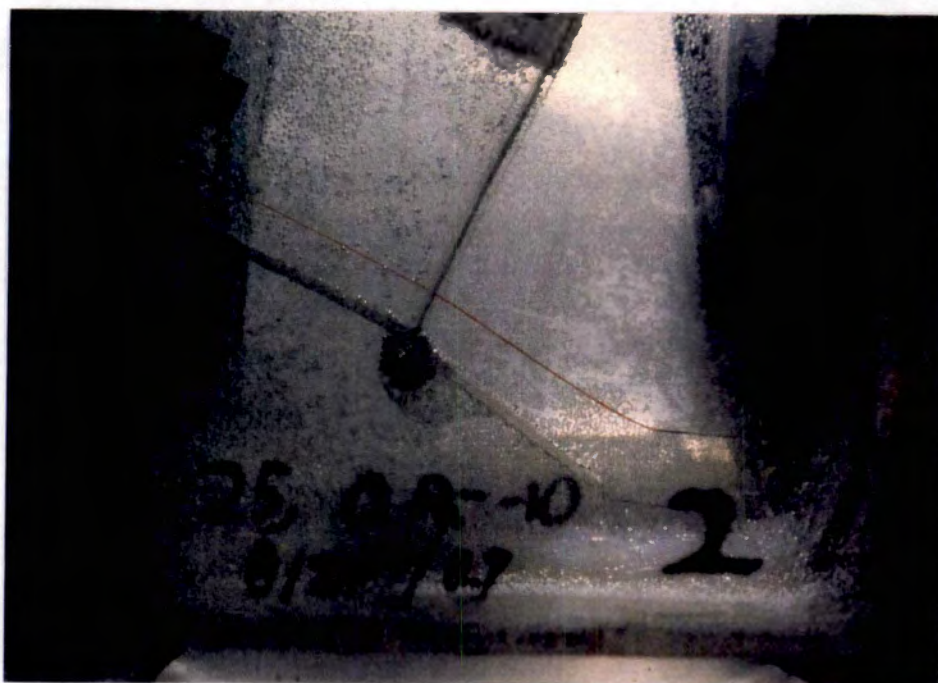


b.  $\theta = 45$  deg, RMP = 20 deg

Figure 105. Water Flow Streaklines in Zone 8 of ASTF Nozzle Model with Ramp Configuration B, Zero Yaw Angle, and Variations in Pitch Angle.



Zone 1

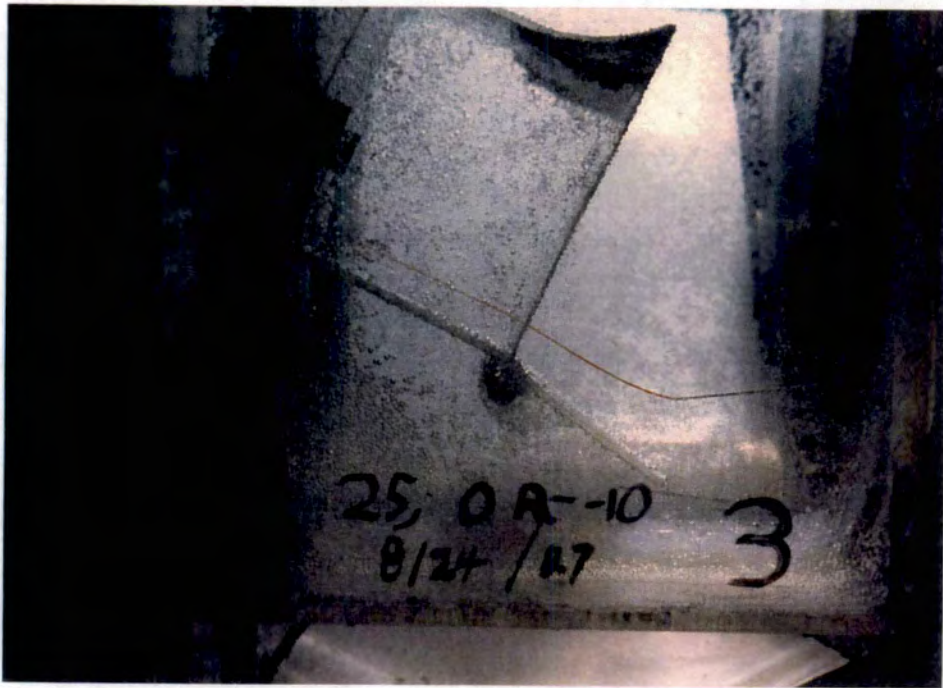


Zone 2

a. RMP = -10 deg

Figure 106. Water Flow Streaklines in ASTF Nozzle Model with Ramp Configuration B,  $\theta = 25$  deg,  $\psi = 0$  deg, and Variations in RMP.



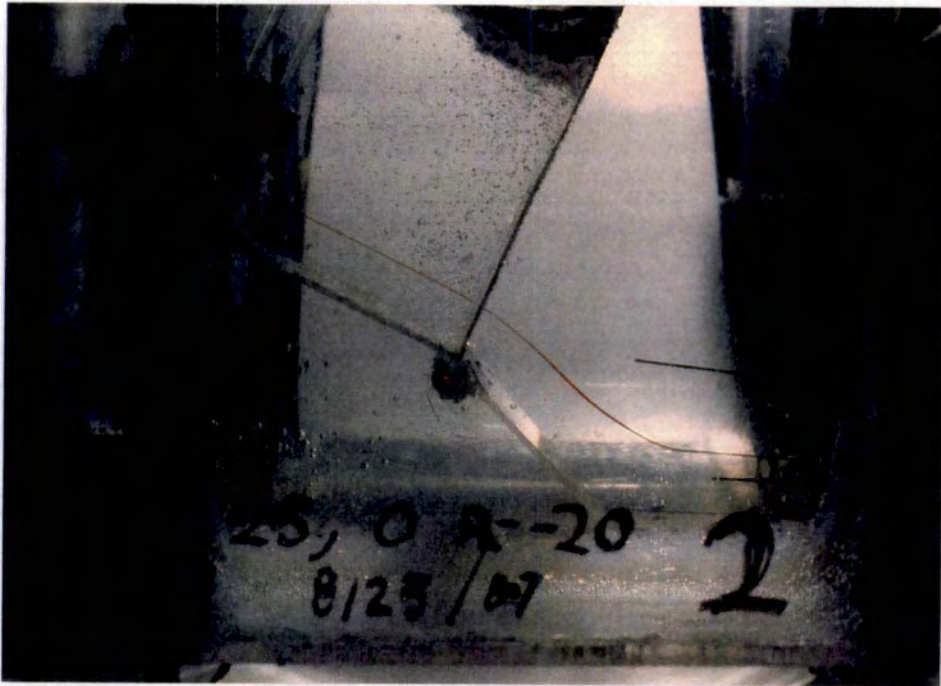


Zone 3  
a. Concluded

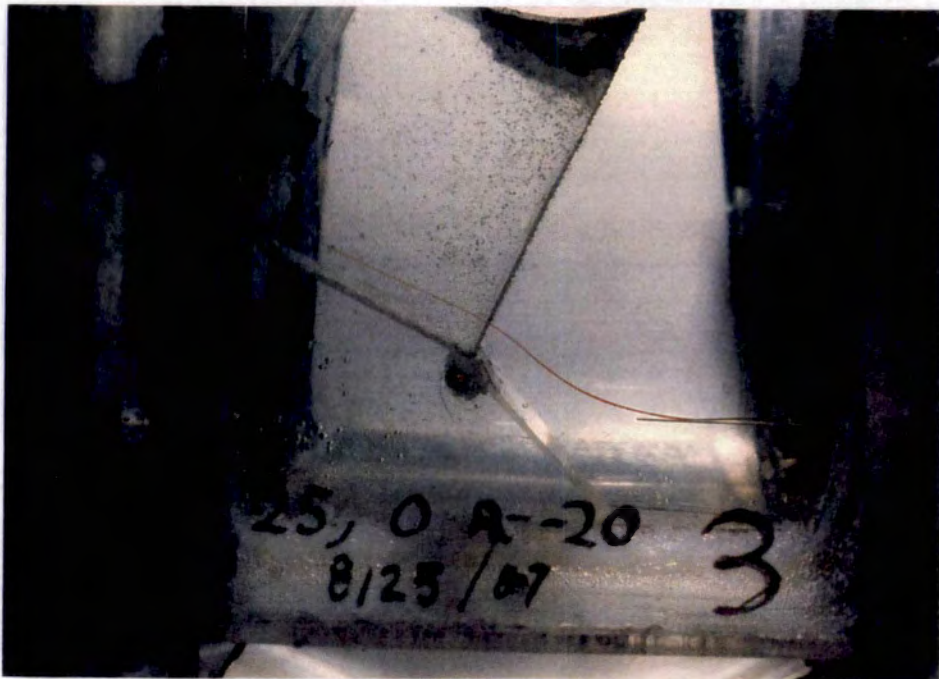


Zone 1  
b. RMP = -20 deg

Figure 106. Continued.



Zone 2



Zone 3  
b. Concluded

Figure 106. Concluded.

**APPENDIX B**

**TABLES**

Table 1. Airflow Test Phase I Matrix

		MACH													
		0.3						0.6						0.8	
PITCH, deg		DIV, deg													
		0	2	4	4/0*	6	0	2	4	4/0*	6	0	2	4	4/0*
0	9	10	10	11	11	9	10	---	---	11	11	9	10	11	---
	10	11	---	---	10	10	---	---	---	10	10	10	---	---	---
20	13	13	14	---	---	13	13	14	---	14	14	14	13	---	---
30	15	---	---	---	---	15	---	---	---	---	---	15	---	---	---
40	12	12	12	---	---	12	12	12	12	12	12	12	12	12	---
	16	---	---	---	---	16	16	16	16	16	16	16	16	16	---

HN = 11.25 in.

0	11	---	---	---	---	11	---	---	---	---	---	11	---	---	---
20	---	---	---	---	---	14	---	---	---	---	---	14	---	---	---
30	---	---	---	---	---	15	---	---	---	---	---	15	---	---	---
40	12	---	---	---	---	12	---	---	---	---	---	12	---	---	---
	16	---	---	---	---	16	---	---	---	---	---	16	---	---	---

HN = 5.625 in.

xx = Run Number  
 \* = 4/0, Top Wall Angle = 4 deg, Bottom Wall Angle = 0 deg

Table 2. Airflow Test Phase II Matrix.

		MACH					
		0.3		0.6		0.9	
		Ramp Configuration					
		Straight Contoured		Straight Contoured		Straight Contoured	
PITCH, deg	30	29	29	29	29	29	29
	50	30	30	30	30	30	30

xx = Run Number

Table 3. Airflow Test Phase III Matrix.

		Ramp Configuration													
		A1							A2						
		RMP, deg													
		-20	-15	-10	5	15	20	23.5	-20	-15	-10	5	15	20	23.5
PITCH, deg	0	31	31	31	---	---	---	---	---	---	---	---	---	---	---
	30	---	---	32	---	32	---	---	34	---	---	---	---	---	---
	45	---	---	---	---	33	33	34	---	---	---	---	---	34	34

xx = Run Number

Run 31 and Run 32 – R2A2 Config. A  
 Run 33 and Run 34 – R2A2 Config. B



Table 4. Water Tunnel Test Phase I Matrix

Nozzle	$\theta$ (deg)	ZI (in)	XI (in.)	Vortex Suppression Method
Variable Area	30	1.55	N/A	N/A, Exit Blockage Test Screen – 1 Layer Screen – 2 Layer Vertical Vane Honeycomb, 0 deg Inclination Honeycomb, 20 deg Inclination Horizontal Vane, 0 deg Inclination Horizontal Vane, 20 deg Inclination Ramp 1 Ramp 2 Ramp 3 Ramp 4 Ramp 5
▼	▼	▼	▼	▼
2-D ASY	30	1.4	0.9	N/A N/A, Exit Cavity in Position A N/A, Exit Cavity in Position B N/A
▼	▼	▼	▼	▼
2-D SYM	45	3.4	0.9	
▼	▼	▼	▼	▼
2-D SYM	30	2.0	0.9	
▼	▼	▼	▼	▼
2-D SYM	30	0.6	0.5	Exit Cavity Centered on Noz. Exit Nozzle Inlet Ramp
▼	▼	▼	▼	▼
2-D SYM	30	3.3	1.0	
▼	▼	▼	▼	▼
2-D SYM	30	0.0	0.0	N/A, Artificial Floor
▼	▼	▼	▼	▼
2-D SYM	30	0.6	0.1	N/A, Artificial Floor
▼	▼	▼	▼	▼
2-D SYM	30	3.3	0.1	N/A, Artificial Bulkhead
▼	▼	▼	▼	▼
2-D ASY	45	1.4	0.9	N/A
▼	▼	▼	▼	▼
2-D ASY	30	2.0	0.0	
▼	▼	▼	▼	▼
2-D High $\alpha$	30	0.6	0.5	
▼	▼	▼	▼	▼
2-D High $\alpha$	45	0.6	2.3	
▼	▼	▼	▼	▼
2-D High $\alpha$	45	1.8	1.8	

Table 4. Concluded.

Nozzle	$\theta$ (deg)	ZI (in)	XI (in.)	Vortex Suppression Method
SHORT AXI ↓	30 ↓	1.4 ↓	1.1 ↓	N/A Axi Ramp 1 Axi Ramp 2, Position A Axi Ramp 2, Position B Axi Ramp 2, Position C Axi Ramp 2, Position D Axi Ramp 2, Position E N/A
LONG AXI ↓	↓	0.5 0.85 1.4	↓ 0.8 ↓	↓

Table 5. Water Tunnel Test Phase II Matrix

Nozzle	$\theta$ (deg)	ZI (in.)	Vortex Suppression Method			
VAR AREA	30	1.55	Piccolo Tube:	<u>ZP (in.)</u>	<u>W (gph)</u>	<u>BL (in.)</u>
↓	↓	↓		1.13	1.5 - 4	2.38
				0.75	↓	↓
				↓		0.90
				1.19		1.75
				↓		1.88
				0.75		↓
				↓		1.75
						2.38
						0.90
						1.75
			Boundary Layer Suction:	<u>Region</u>		<u>W (gph)</u>
				1		6 - 33
				2		6 - 36
				3		6 - 33
				4		6 - 34
				1 & 3		6 - 33
				2 & 3		↓
				4 & 3		
			Ramp:	<u>Designation</u>	<u>Position</u>	
				21	A	
				↓	B	
				22		
2-D SYM	30	0.6	Vertical Baffle			
↓	↓	↓	Horizontal Baffle			
ASTF NOZ			Ramp: <u>RMP (deg)</u>			
↓	45	1.2		20		
	0	4.8		-10		
	↓	↓		-20		
	30	2.25		-10		
	↓	↓		20		
		1.60	N/A, Nozzle Inverted			
	↓	↓	Honeycomb on Plenum Floor, Nozzle Inverted			
	10	1.05	N/A, Nozzle Inverted (Yields, $\theta = -10$ deg)			

Table 6. Water Tunnel Test Phase III Matrix

$\theta$ (deg)	$\Psi$ (deg)	Ramp	RMP (deg)	Plenum
45	0	B	20	R2A2 Configuration
▼	-5	↓	▼	↓
40	-10		10	
35	0		0	
▼	-10		▼	
45	0	▼	20	ASTF C-2 Configuration
↓	▼	No Ramp	N/A	
40	-10	B	20	
▼	0	↓	10	
40	-10		▼	
40	0		20	
40	-10		20	
35	0		0	
↓	-10		↓	
30	-5		▼	
↓	0		-10	
30	-10		↓	
↓	-5		↓	
25	0		↓	
30	▼		↓	
↓	-10		↓	
25	-5		↓	
↓	0		↓	
20	-10		▼	
↓	-5		↓	
10	0		▼	
↓	▼		-20	
25	0		↓	
▼	-10		↓	
20	0		↓	
↓	-10		↓	
10	0		↓	
↓	-10		↓	
↓	-5		↓	

Table 6. Concluded

$\theta$ (deg)	$\Psi$ (deg)	Ramp	RMP (deg)	Plenum
45	0	B	20	ASTF C-2 Configuration ↓
35	-10	↓	0	
↓	-5		↓	
45	-10		20	
↓	-5		↓	
35	0		0	
35	-10		0	
40	0		10	
↓	-10		↓	
↓	-5		↓	

Table 7. Measured Parameter Uncertainties.

Parameter	Precision Index		Degree of Freedom	Bias		Uncertainty		Range
	Unit of Measurement			Unit of Measurement		Unit of Measurement		
PTP1-PTP12 Pi-j P1A1-P1A4 P1B1-P1B4 P2C1-P2C4 P3C1-P3C4 P4C1-P4C4 PNT1-PNT5 PNB1-PNB5 PR1-PR4 PTNT1-PTNT2 PTNB1-PTNB2	+/-0.10		>30	+/-0.722		+/-0.922		3-15 psia
P	+/-0.071		>30	+/-0.511		+/-0.653		3-15 psia
DP13-J DP24-J	+/-1.0		>30	+/-2.0		+/- 4.0		1-100 mm Hg
TT	+/-0.1		>30			+/- 2°F + 0.25%		-130 to +360 deg F
PITCH, RAKE	+/-0.1		>30	+/-0.5		+/-0.7		-5° to 45°, 0-5.5 in.

Table 8. Calculated Parameter Uncertainties.

a. Test Conditions

Parameter	Precision Index	Degree of Freedom	Bias	Uncertainty	Range
	Unit of Measurement		Unit of Measurement	Unit of Measurement	
MACH	+/-0.00298	>30	+/-0.02148	+/-0.0275	MACH = 0.3
	+/-0.00156		+/-0.01128	+/-0.0144	MACH = 0.6
	+/-0.00113		+/-0.00816	+/-0.0104	+/-0.0104
T		>30		+/-2.719 °R	MACH = 0.3
			+/-2.580 °R	+/-2.580 °R	MACH = 0.6
			+/-2.380 °R	+/-2.380 °R	MACH = 0.9
RE		>30		+/-1.75 x 10 <sup>5</sup>	MACH = 0.3
			+/-8.72 x 10 <sup>4</sup>	+/-8.72 x 10 <sup>4</sup>	MACH = 0.6
			+/-6.24 x 10 <sup>4</sup>	+/-6.24 x 10 <sup>4</sup>	MACH = 0.9



Table 8. Concluded.

b. Flow-Field Measurements

Parameter	Precision Index		Degree of Freedom	Bias		Uncertainty		Range
	Unit of Measurement			Unit of Measurement		Unit of Measurement		
Total Uncertainty								
ALPL BETL			>30			+/-1.4 +/-0.7 +/-0.6		0-10 deg at ML = 0.3 ML = 0.6 ML = 0.9
ML			>30			+/-0.03 +/-0.02 +/-0.02		ML = 0.3 ML = 0.6 ML = 0.9
Relative Uncertainty								
ALPL BETL			>30			+/- 0.25 +/- 0.15 +/- 0.15		0-10 deg at ML = 0.3 ML = 0.6 ML = 0.9
ML			>30			+/-0.003 +/-0.002 +/-0.002		ML = 0.3 ML = 0.6 ML = 0.9

Table 9. Summary of Water Tunnel Test Phase III Results

<u>Nozzle Orientation</u>		<u>Zone</u>					
$\theta$ (deg)	$\Psi$ (deg)	1	2	3	4	5	6
10	0						
10	-5						
10	-10			√			
20	0	√					
20	-10			√			
25	0	√		√			
25	-10			√			
30	0	√		√			
30	-5			√			
30	-10			√			
35	0	√		√			
35	-5			√			
35	-10			√			
40	0	√		√			
40	-5			√			
40	-10			√			
45	0	√		√			
45	-5			√			
45	-10			√			

√ = Unsteady Vortices Observed

**APPENDIX C**

**FLOW ANGLE DEFINITIONS**

## FLOW ANGLE DEFINITIONS

### 1.0 FREE-JET ORIENTATION AND AERODYNAMIC ANGLES

Simulation of flight conditions in a free-jet test cell requires correlating the free-jet flow angles to the flight aerodynamic angles. To accomplish this, it is useful to adopt conventions consistent with standard wind tunnel and flight aerodynamic angle definitions. The aerodynamic community generally defines the angle between the wind vector and the aircraft using two angles:

**ALPHA**      The angle between the projection of the wind x-axis ( $x_w$ ) on the body x-z plane and the body x-axis ( $x$ ). Positive rotates the +z-axis into the +y-axis,  $\text{ALPHA} = \arctan(w/u)$ .

**BETA**        The angle between the wind x-axis ( $x_w$ ) and the projection of the wind x-axis on the body x-z plane. Positive rotates the +y-axis into the +x-axis.  $\text{BETA} = \arcsin(v/V)$ .

Figure C-1 illustrates the wind axis system, body axis system, ALPHA, and BETA with the associated sign conventions. Corresponding free-jet aerodynamic angles, ALPFJ and BETFJ can be defined with the wind axis taken to be parallel to the nozzle axes.

In the wind tunnel (or in flight), combinations of the aerodynamic angles ALPHA and BETA are achieved by properly orienting the aircraft with respect to the wind vector. The relative orientation of the aircraft body axis may be defined through a series of angular rotations that start with the body axes aligned with the wind axes. The rotation

angles or orientation angles must follow a specified sequence consistent with the functions relating the orientation and aerodynamic angles.

Unlike the wind tunnel or flight cases, the free-jet test facility achieves combined ALPFJ and BETFJ by rotating the wind vector with respect to the test article. With the wind vector defined to be parallel to the nozzle x-axis, sequential rotations through a set of free-jet nozzle orientation angles may be used to provide a desired combination of ALPFJ and BETFJ. Any wind vector deviations from the nozzle axis will be detected by the inlet reference plane instrumentation and included in ALPFJ and BETFJ offsets. The free-jet nozzle orientation angle definitions include the following:

- PITCH      Angle of nozzle rotation around the nozzle y-axis ( $y_n$ ). Positive rotates the nozzle +x-axis ( $x_n$ ) into the nozzle +z-axis ( $z_n$ ).
- YAW        Angle of nozzle rotation around the nozzle z-axis ( $z_n$ ). Positive rotates the nozzle +y-axis ( $y_n$ ) into the nozzle +x-axis ( $x_n$ ).
- ROLL        Angle of nozzle rotation around the nozzle x-axis ( $x_n$ ). Positive when the nozzle +z-axis ( $z_n$ ) is rotated into the nozzle +y-axis ( $y_n$ ).

Figure C-2 illustrates the free-jet nozzle orientation angles. With the angles defined in this way, the standard relations between orientation and aerodynamic angles used in wind tunnel and flight testing may be applied in conjunction with a reversal in rotation sequence.

Combined ALPFJ/BETFJ conditions can be achieved using only two of the three orientation angles. PITCH and YAW will be used in some R2A2 tests and the ASTF

free-jet system. However, the R2A2 flow quality studies and early inlet model tests used PITCH and ROLL.

## 2.0 FLOW-FIELD MEASUREMENTS

The cone probes used for the nozzle exit flow-field measurements used calibrations based on the following definitions:

ALPL            The angle between the projection of the wind x-axis ( $x_w$ ) on the probe x-z plane and the probe x-axis ( $x_p$ ). Positive rotates the probe +z-axis ( $z_p$ ) into the probe +y-axis ( $y_p$ ).

$$ALPL = \arctan(w_p/v_p).$$

BETL            The angle between the projection of the wind x-axis ( $x_w$ ) on the probe x-y plane and the probe x-axis ( $x_p$ ). Positive rotates the probe +y-axis ( $y_p$ ) into the probe +x-axis ( $x_p$ ).

$$BETL = \arcsin(v_p/V_p).$$

Figure C-3 shows the angles. The ALPL definition is equivalent to ALPHA or ALPFJ defined relative to the probe. However, unlike a BETA or BETFJ definition for a probe, BETL is defined in the probe x-y plane. The definition follows a convention often used with probes as a convenience for displaying and interpreting the flow-field measurements. ALPL and BETL may be combined to provide a total flow angle, THETA, as shown.



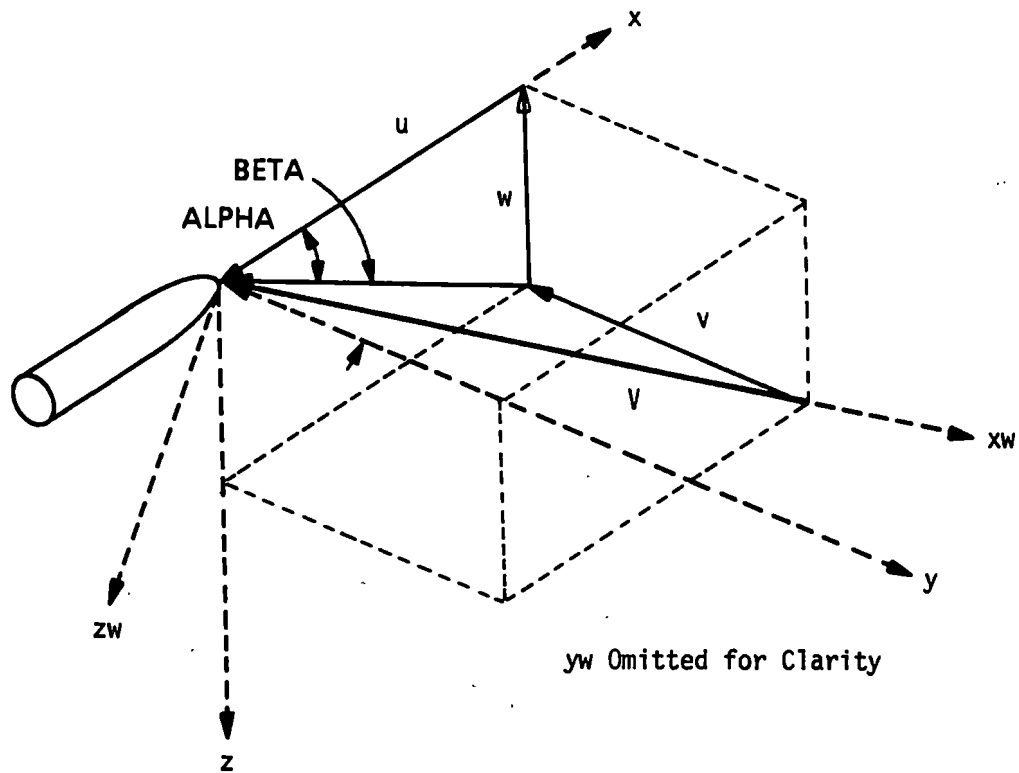


Figure C-1. Definition of ALPHA and BETA.

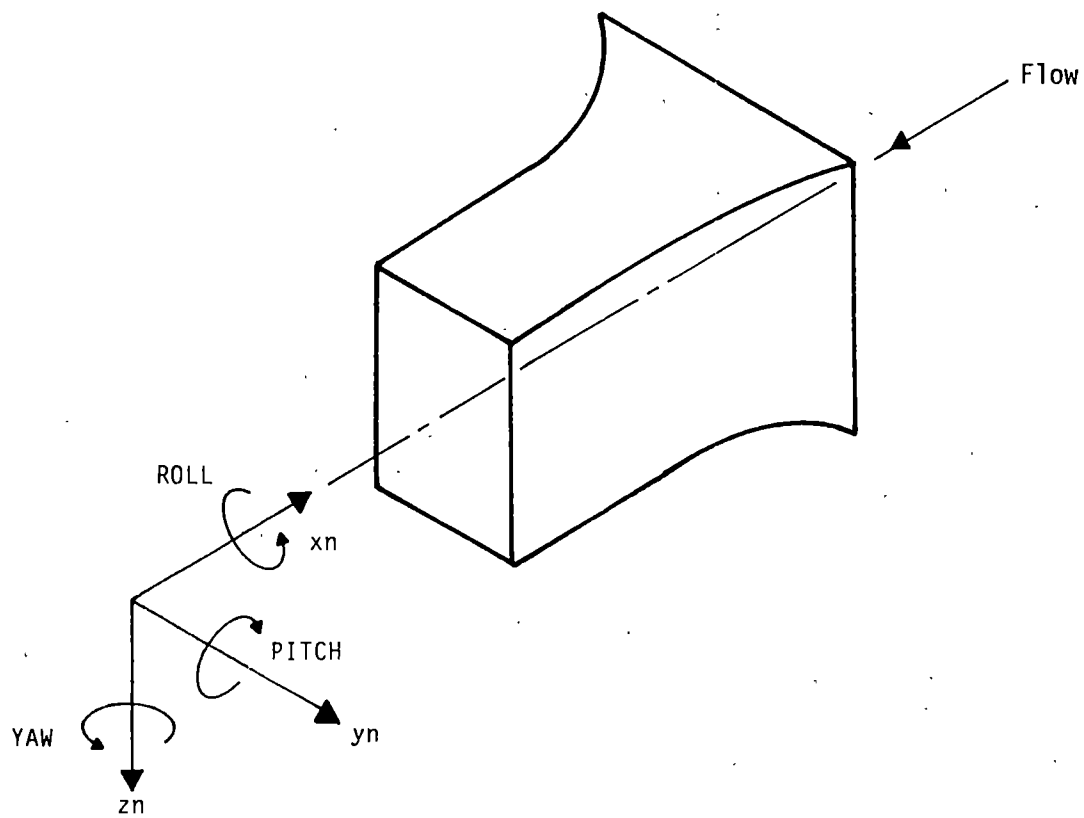


Figure C-2. Free-Jet Nozzle Orientation Angle Definitions.

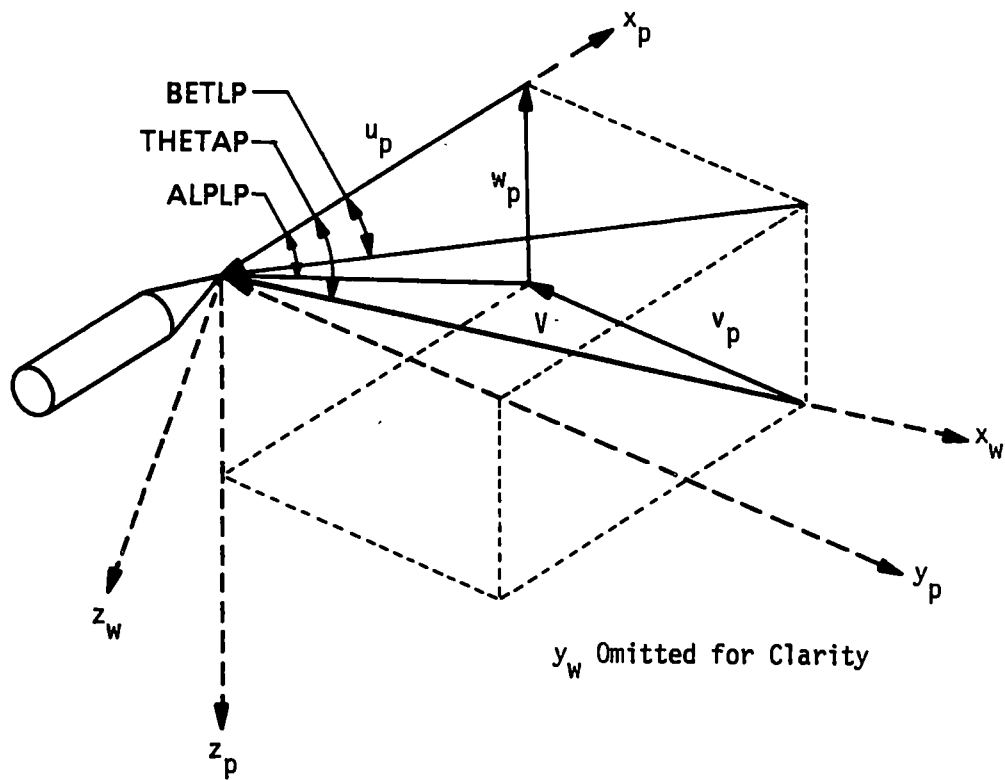


Figure C-3. Flow-Field Probe Aerodynamic Angle Definitions.

**APPENDIX D**

**ASTF SUBSONIC FREE-JET NOZZLE CONCEPT DEVELOPMENT**

# ASTF SUBSONIC FREE-JET NOZZLE CONCEPT DEVELOPMENT

## 1.0 INTRODUCTION

The criteria in place in 1984 served as the basis for the basic ASTF subsonic free-jet nozzle. The concept was formally submitted for preliminary full-scale design and tested in Research Test Cell R2A2. This appendix presents the nozzle concept as originally submitted.

Two overriding requirements dominated the subsonic free-jet nozzle concept formulation: (1) nozzle size requirements and nozzle flow-quality requirements. Nozzle sizing required consideration of the test article, ASTF C-2 test cell dimensions, required PITCH-YAW envelope, and the required altitude-Mach number envelope. Test article size and shape dictated a large nozzle to provide adequate coverage with the nozzle test rhombus. The PITCH-YAW envelope and test facility plenum dimensions drove the design toward a smaller nozzle to avoid mechanical interference. The altitude-Mach number envelope also forced the design toward a small nozzle due to the finite capability of the ASTF plant. To meet the conflicting constraints imposed by these considerations, it became necessary to tailor the nozzle geometry to match the test article geometry and the required test envelope. Evidently, different test articles or test envelopes might require design and fabrication of additional free-jet nozzles.

Early consideration of the free-jet test concept included the estimation of the flow quality that would be needed for applying the method to inlet-engine compatibility evaluations. The estimates became the basis for the establishment of flow quality criteria

that served the entire free-jet nozzle development process. Subsequent to the initial nozzle development, sub-scale validation tests, using aircraft inlet models, would verify the flow quality criteria. Thus, the allowable non-uniformity criteria reflected the objective of the first ASTF nozzle design, the achievement of flow free from major anomalies. Accordingly, the nozzle concept incorporated features designed to prevent the formation of large vortices and the associated non-uniform flow. As wind tunnel flow quality standards were not required, the design permitted a level of vorticity commensurate with the flow quality goals.

The following sections summarize the main assumptions adopted during the nozzle development, describe of the nozzle concept, and furnish details of the nozzle aerodynamic shape.

## 2.0 ASSUMPTIONS

The dependence of the nozzle configuration on test article geometry and test envelope necessitated the selection of appropriate criteria for nozzle specification.

Internal AEDC documents list the basic criteria. The main criteria specified include the following:

- A. Test article – F-15 inlet and engine simulator.
- B. Two subsonic nozzles corresponding to a low-pitch range, of  $-10$  to  $+25$  deg, and a high-pitch range of  $+25$  to  $+45$  deg.
- C. Yaw angle capability of  $\pm 10$  deg.
- D. Nozzles with exit areas of nominally 48 sq ft.

E. Test conditions:	<u>Mach No.</u>	<u>Altitude x <math>10^{-3}</math>, ft</u>
	0.3	5 to 40
	0.6	15 to 60
	0.9	25 to 65

- F. F-15 inlet may be mounted at 0- and 10-deg inclination angles to achieve a total pitch angle range of  $-10$  to  $+55$  deg.

Completion of the nozzle specification necessitated deviations from the above criteria. Analysis indicated that the 48-sq-ft nozzle would not adequately cover the F-15 inlet over the specified PITCH-YAW envelope. Therefore, the system needed a much larger nozzle. To minimize the impact of the nozzle exit area increase on the altitude-Mach number envelope, the design adopted a nozzle with a rectangular exit cross section.



Tailoring the nozzle exit dimensions to the F-15 inlet shape resulted in a nozzle exit area 30 percent lower than that of an axisymmetric nozzle providing the same test article coverage. A further deviation followed an ASTF free-jet system development program decision to cover the entire pitch angle range with a single nozzle.

The necessary deviations resulted in the need to revise the criteria. Furthermore, relief of the mechanical interference problems produced by the enlarged nozzle necessitated additional criteria. The main assumptions included the following:

- A. Test article – F-15 inlet and engine simulator.
- B. Forebody simulator configuration used in a full-scale subsonic F-15 inlet test in AEDC Propulsion Wind Tunnel 16T.
- C. Total pitch angle range of  $-10$  to  $+55$  deg.
- D. Yaw angle range of  $\pm 10$  deg.
- E. Inlet-forebody simulator assembly centered on test cell centerline in horizontal plane.
- F. Two-dimensional nozzle with exit area tailored to the shape of the F-15 inlet-forebody simulator assembly.
- G. Nozzle pitch mechanism consisting of a pitch frame rotating inside a yaw frame.
- H. Nozzle pitch rotation center and yaw rotation center located on the test cell centerline.
- I. Pitch and yaw rotation center axial stations independently selected to minimize nozzle size.

J. Single nozzle operated in two positions:

1. Low-pitch range:

- a. Nozzle in upstream position.
- b. F-15 inlet set at 0-deg inclination and centered on test cell centerline in vertical plane.
- c. Nozzle pitch range of -10 to +25 deg.
- d. Total pitch range of -10 to +25 deg.

2. High-pitch range:

- a. Inlet inclined 10 deg in vertical plane.
- b. Inlet face center point 20 in. above test cell centerline.
- c. Nozzle in downstream position.
- d. Nozzle pitch range of +15 to +45 deg.
- e. Total pitch range of +25 to +55 deg.

K. Test Conditions:

<u>Mach no.</u>	<u>Altitude x 10<sup>-3</sup>, ft</u>
0.3	9 to 40
0.4	28 to 60
0.9	37 to 65

The inclusion of item J prevents interference between the nozzle and the stilling chamber floor at high pitch angles. The approach takes advantage of the 10-deg inclination of the inlet to translate the nozzle further from the plenum floor. A 20-in. upward translation of the inlet that accompanies the rotation permits remounting the nozzle downstream in the mount providing additional clearance with respect to the plenum floor. Furthermore, at

high pitch the nozzle can be moved closer to the inlet without the test article entering the nozzle exit plane. Figure D-1 illustrates the two positions. Note that the nozzle rotation center location in the test cell does not change; only the location of the inlet face and the nozzle exit with respect to the rotation point. Therefore, the shifts in nozzle and test article positions do not affect the nozzle positioning mechanism design. Also note that inclining the inlet to the 10-deg position involves a change in inlet axial position for proper alignment of the inlet face. The consideration of nozzle blockage effects attributable to the proximity of the test article remains beyond the scope of the present work.

### 3.0 NOZZLE CONCEPT

The conflicting nozzle size constraints and the vortex suppression features resulted in a highly unconventional nozzle concept. The selection of a very large nozzle for test article coverage resulted in deviations from normal nozzle design practices to permit achievement of the required PITCH-YAW envelope within the confines of the stilling chamber walls and bulkhead. Planning for operation in two mounting positions provided a measure of relief; however, mechanical interference remained a primary driver in selecting nozzle length and contraction ratio. As implied, the process yielded a configuration characterized by very low values of length-to-height ratio and contraction ratio.

Enclosure of the F-15 inlet and wind tunnel subsonic forebody simulator within the nozzle test rhombus served as the basis for determining the nozzle exit dimensions. The assumption of a 6-deg shear layer half-angle and an empty nozzle delineated the nozzle test rhombus. The assumption resulted in a proportionality between the nozzle exit dimensions and the distance from the test article. The design minimized this distance without permitting the test article to extend upstream of the nozzle exit plane. The design process included the selection of the pitch and yaw rotation points as the nozzle attitude positioning mechanism had yet to be designed. The selections minimized the nozzle size under the constraints that both rotation centers remained on the test section centerline, and the nozzle symmetry planes intersected the respective rotation center. The addition of a boundary-layer thickness adjustment yielded a nozzle with exit dimensions of  $HN =$

124 in. and  $WN = 89$  in. The selections resulted in an exit area of 76.6 sq ft. Figure D-2 provides a sketch of the nozzle exit area layout including the rotation distances used.

The high-pitch condition, Fig. D-2a, fixed the nozzle exit height dimension.

The vortex suppression apparatus consists of a leading edge flap or ramp attached to the bottom wall of the nozzle. To accommodate the ramp and minimize interference with the stilling chamber floor, the design uses a flat nozzle bottom wall.

Figure D-3 shows the nozzle concept with the ramp installed. The relatively large size of the nozzle necessitated minimizing the length and contraction ratio. Using 0.3 as the maximum permissible inlet Mach number, the design adopted a nozzle contraction ratio of 2.075 (1-D inlet Mach number of 0.29). The nozzle used a length-to-height ratio of 1.25 as a minimum. At this length, it still became necessary to truncate the upper inlet corners to prevent contacting the plenum walls at  $PITCH = -10$  deg and  $YAW = +/- 10$  deg.

Figure D-4 illustrates the ASTF C-2 free-jet nozzle installation concept. At high pitch angle settings, the flap functions as a ramp preventing the formation of vortices. The ramp inclines upward with respect to the nozzle wall. Experiments conducted with ramps in test cell R2A2 have shown that the sharp discontinuity between the ramp and the nozzle wall may be tolerated for moderate ramp angles. At lower pitch angles, the flap pivots downward and functions as a flare on the lower wall. The use of moderate ramp angles in the downward deflections helps to prevent separation as the flow leaves the ramp and enters the nozzle. In addition, the ramp hinge concept further aids in preventing separation by preventing a sharp discontinuity between the ramp and the

nozzle wall. Figure D-5a shows the hinge concept used for the sub-scale R2A2 experiments. To simplify the work, the sub-scale configuration used a circular hinge section. Figure D-5b shows how the concept could be modified to provide an even more gentle transition. For a  $-10$ -deg ramp deflection angle, the ramp should slide approximately 10-in. upstream along the curve. The concept does not require a perfect seal between the curved surface and ramp leading edge.

## 4.0 NOZZLE GEOMETRY

The nozzle inlet side walls and top wall use elliptical contours. As a result of the large nozzle height, the design concentrates most of the nozzle contraction in the sidewalls. This provides the added advantage of reducing the mechanical interference problem encountered at the negative pitch angles. Lines tangent to the side and top walls, at the leading edges, form 60-deg angles with respect to the nozzle axis. The nozzle wall contours appear in Fig. D-6. The figures include tabulations of the contour coordinates and the defining equations. Figure D-7 shows the ramp planform. The line of intersection between the ramp plane and the stilling chamber wall, when the nozzle is positioned at 45-deg pitch and 10-deg yaw, defined the ramp planform. The shape of the intersection curve also depended on the ramp angle. The ramp definition used a ramp angle of 20 deg with respect to the lower nozzle wall. Note that the ramp x coordinates use the nozzle inlet plane as the reference. Therefore, the coordinates must account for any translation of the ramp trailing edge position with respect to the nozzle inlet plane that might accompany inclination angle changes. The hinge concept shown in Fig. D-5 locates the ramp leading edge close to the inlet plane for positive ramp inclinations. At negative inclinations, the ramp leading edge moves upstream of the nozzle inlet; however, this presents no difficulty as the effect occurs only at low pitch.



## 5.0 RAMP POSITION SCHEDULE

The ramp inclination angle with respect to the nozzle wall varies with nozzle pitch angle. The inclination angle ranges from  $-10$  deg to  $+20$  deg. A  $20$ -deg ramp inclination angle corresponds to a nozzle pitch angle of  $45$  deg. As the nozzle pitch angle drops, the ramp inclination also drops to maintain a constant ramp leading edge height above the stilling chamber floor. As the nozzle reaches  $30$ -deg pitch, the ramp inclination becomes  $-10$  deg. The ramp inclination then remains constant for the remainder of the pitch angles. Figure D-8 provides the ramp inclination schedule. The recommended schedule is actually a linear approximation of the calculated schedule. The approximation attempts to simplify ramp actuation by rendering ramp position directly proportional to pitch angle. A direct mechanical link would provide a valid ramp positioning approach. The schedule makes no allowances for ramp translation during inclination angle changes. The design included adequate clearance between the ramp and the chamber floor to accommodate the relatively small translations involved. If full-scale implementation were to adopt a hinge design yielding enough translation to cause mechanical interference, the slope of the ramp position curve could be changed accordingly. Any required slope alterations should be accomplished by adjusting the  $-10$ -deg inclination point rather than the  $+20$ -deg inclination point.

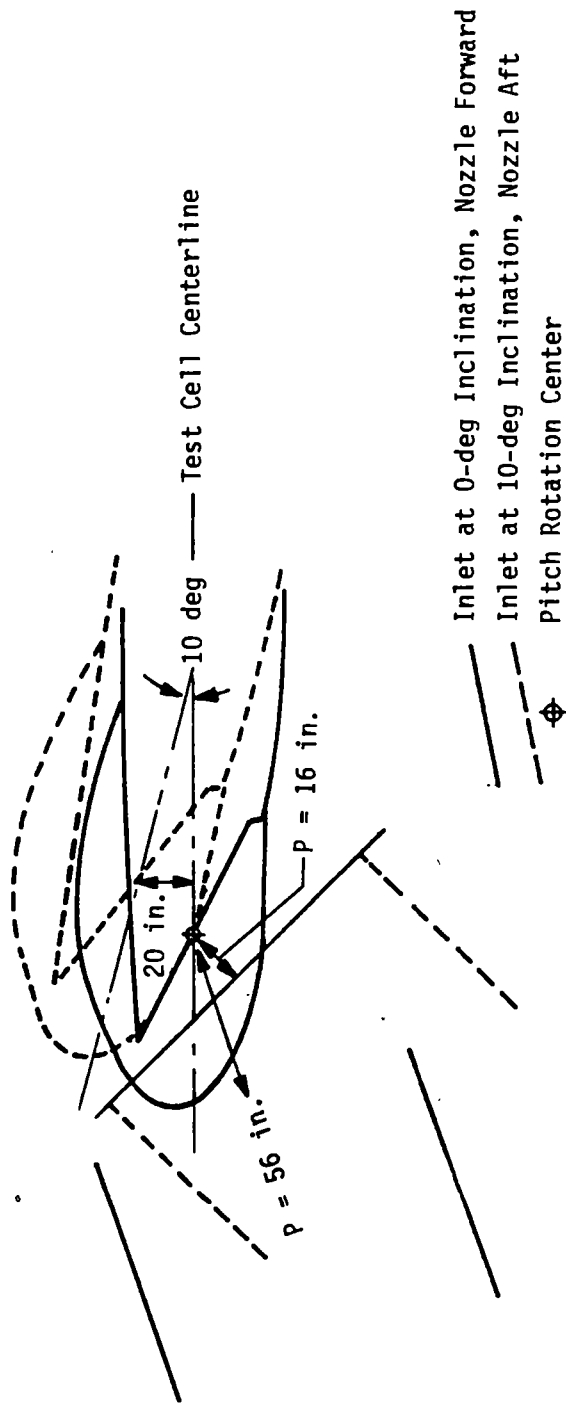
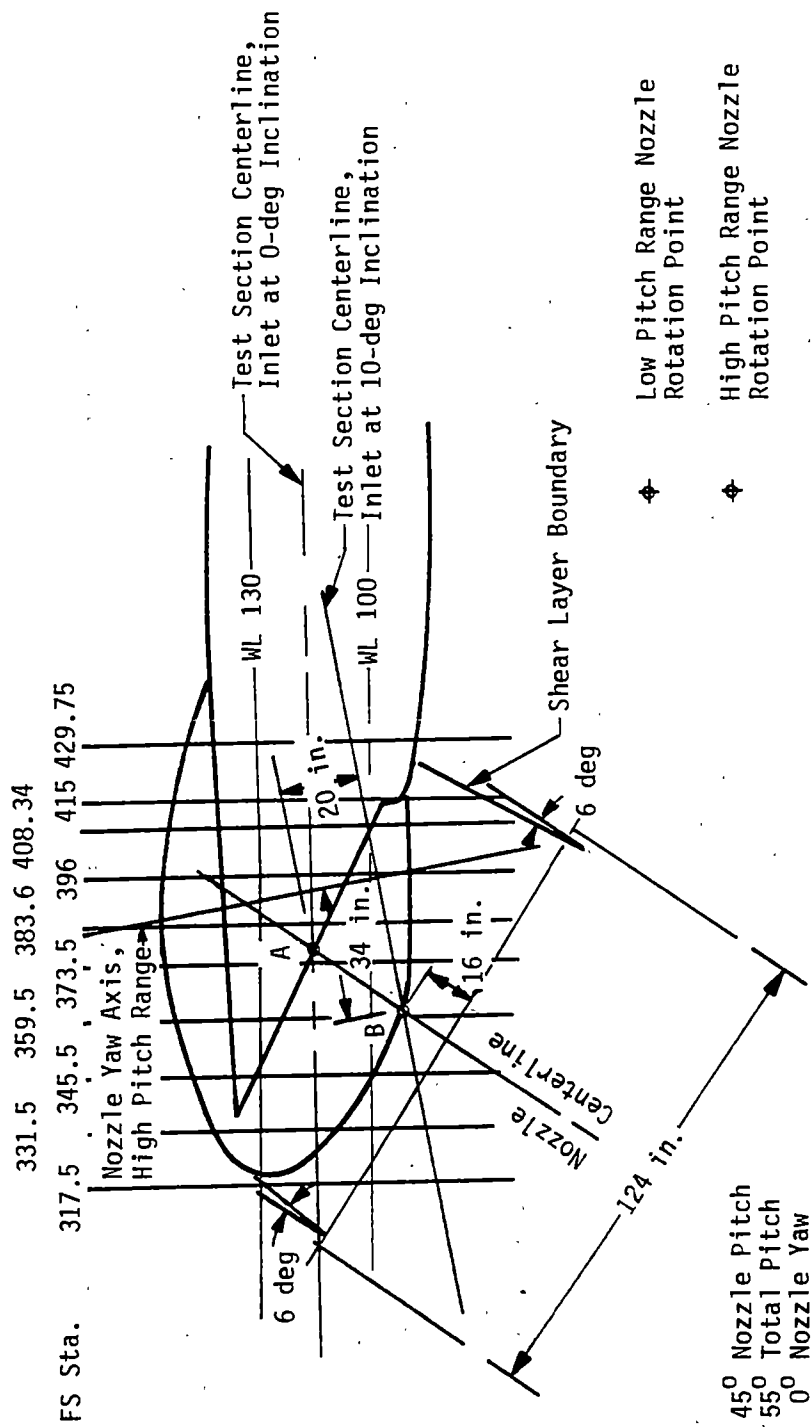
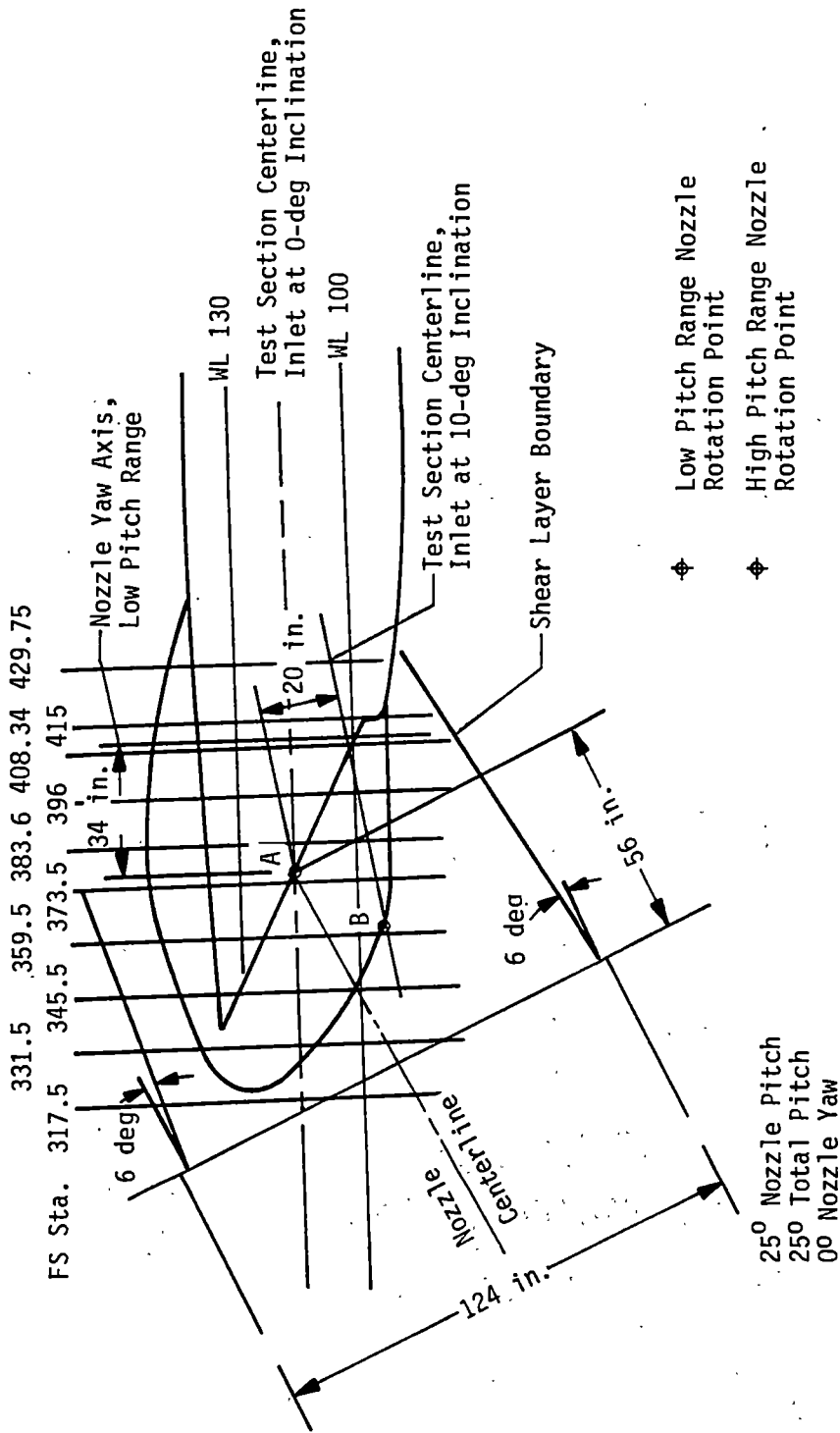


Figure D-1. Two-Position Nozzle Operation.



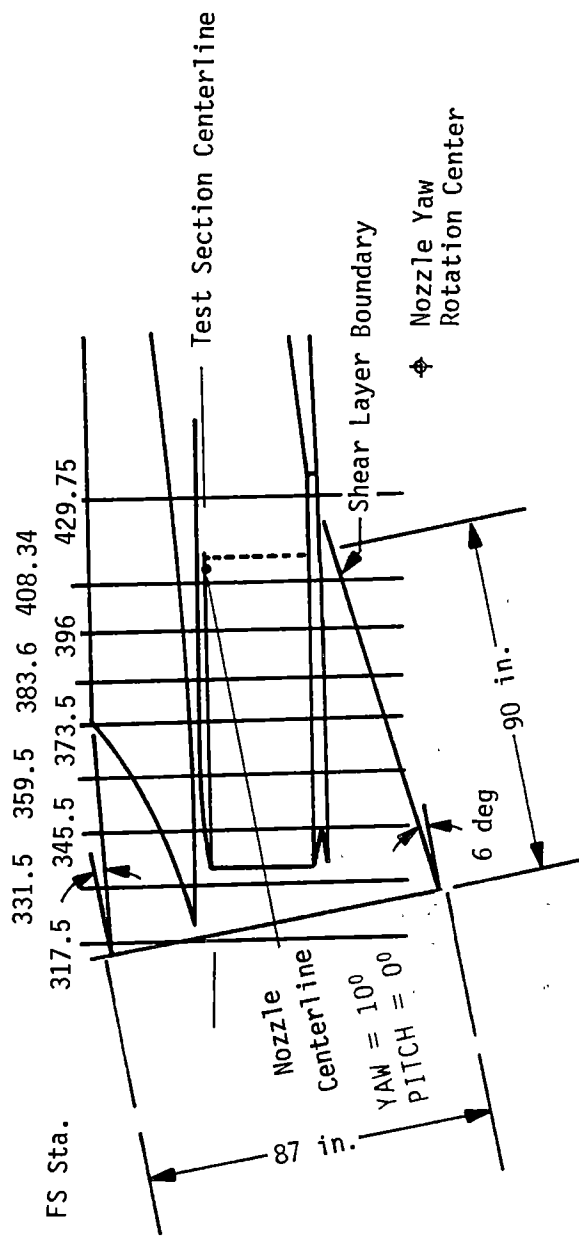
a. High Pitch Angle Range, Side View

Figure D-2. Nozzle Exit Area Layout.



b. Low Pitch Angle Range, Side View

Figure D-2. Continued.



c. Low Pitch Angle Range, Top View

Figure D-2. Concluded.

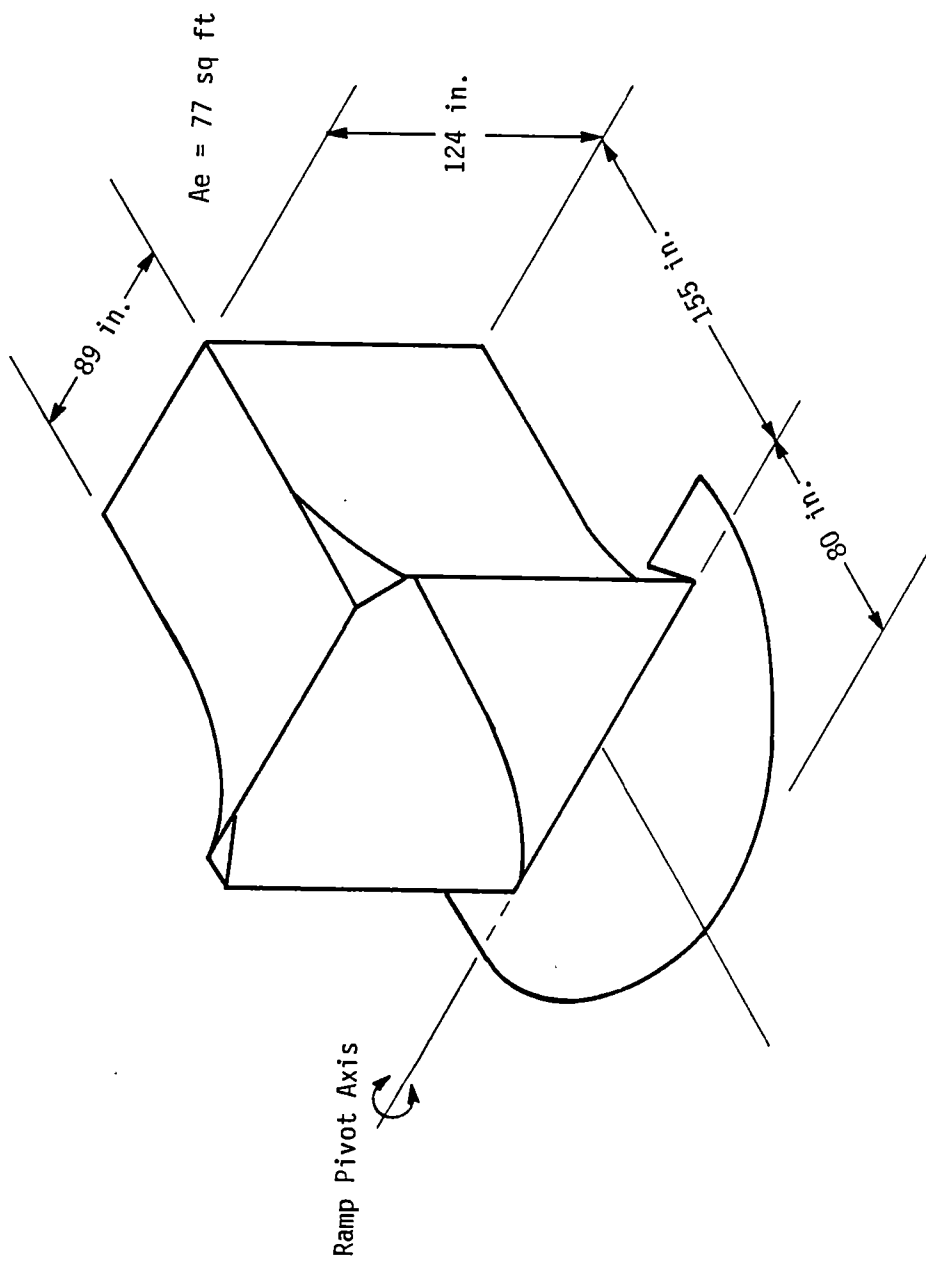


Figure D-3. Nozzle/Ramp Concept.

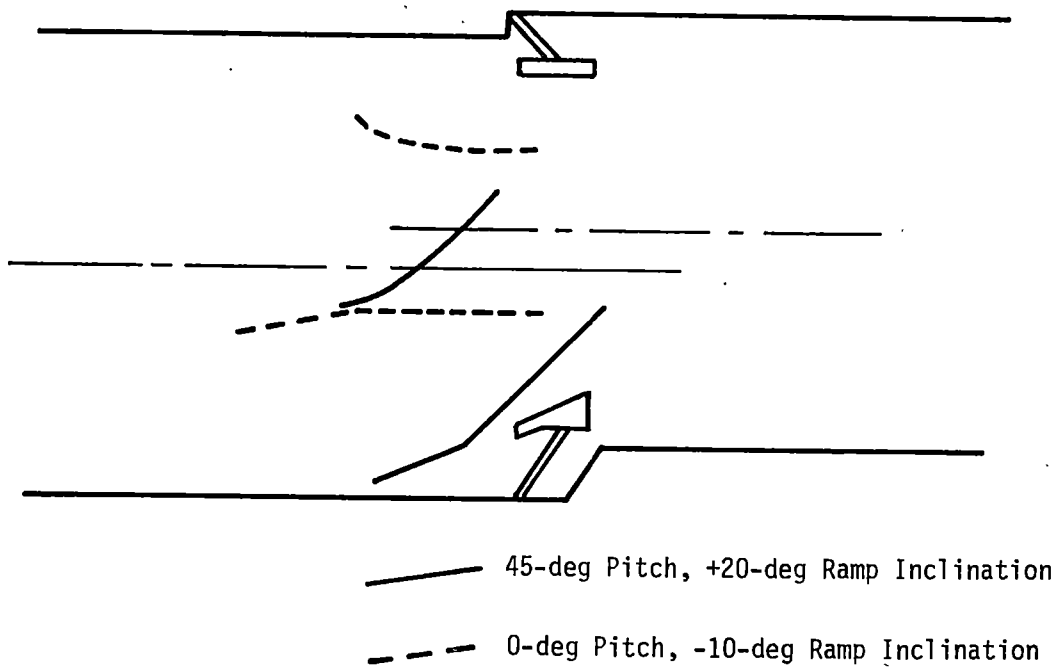
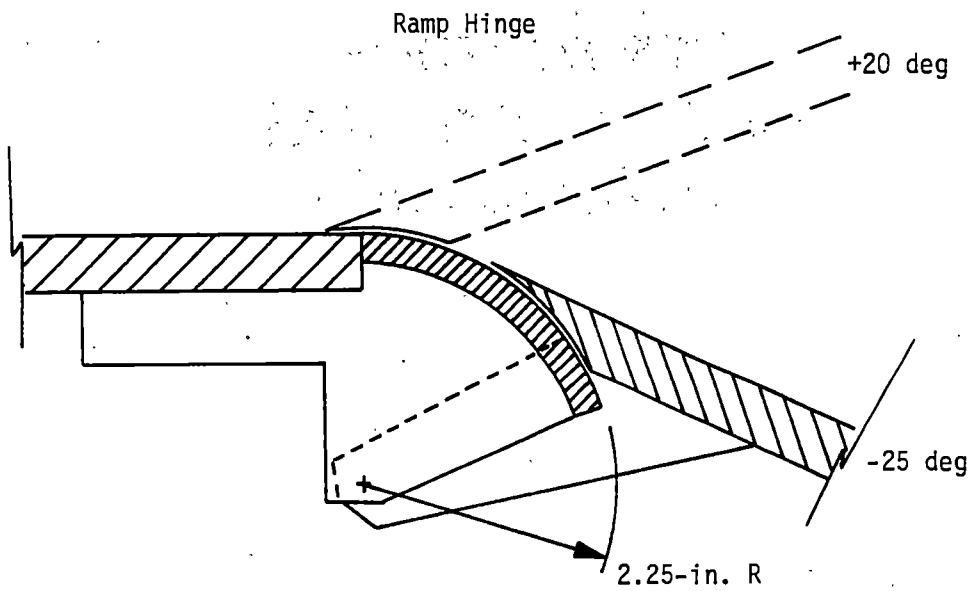
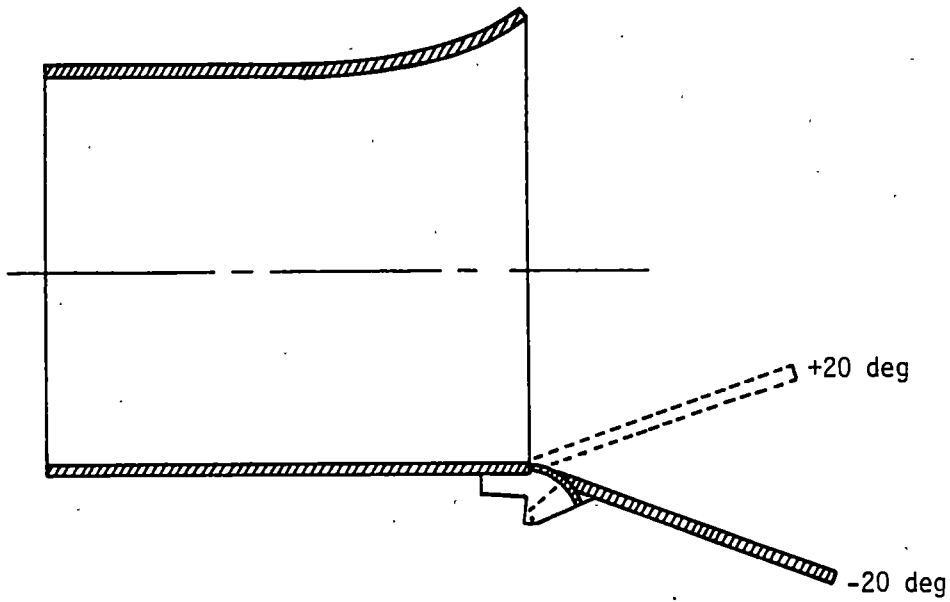


Figure D-4. Free-Jet Nozzle Installed in ASTF.

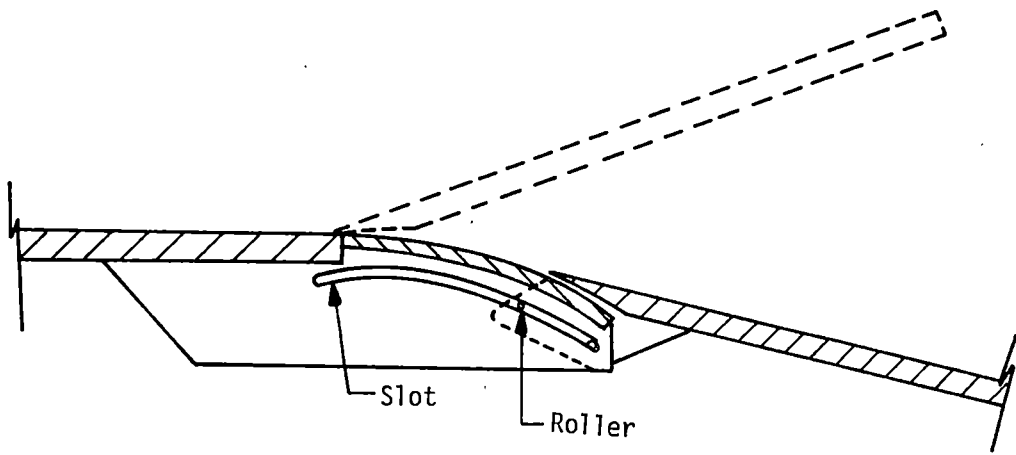


Side View



a. R2A2 Nozzle Model

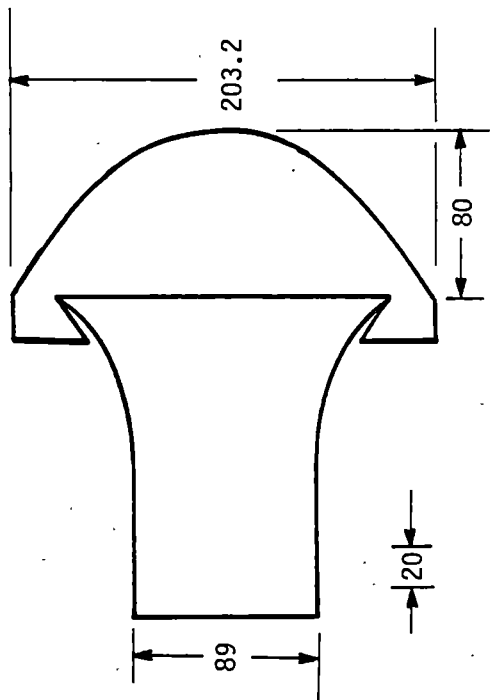
Figure D-5. Ramp Hinge.



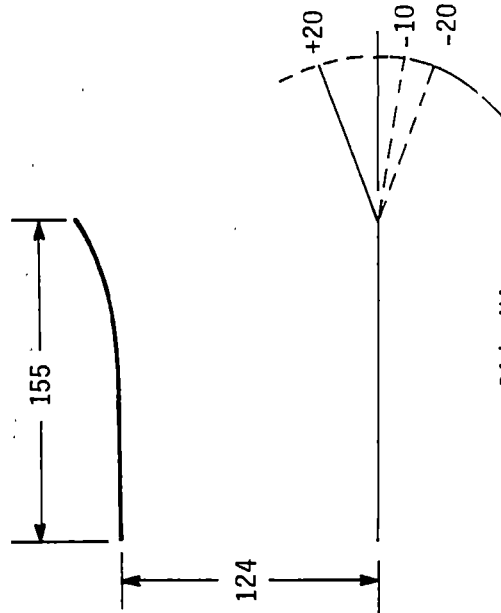
b. Modified Hinge Concept

Figure D-5. Concluded.

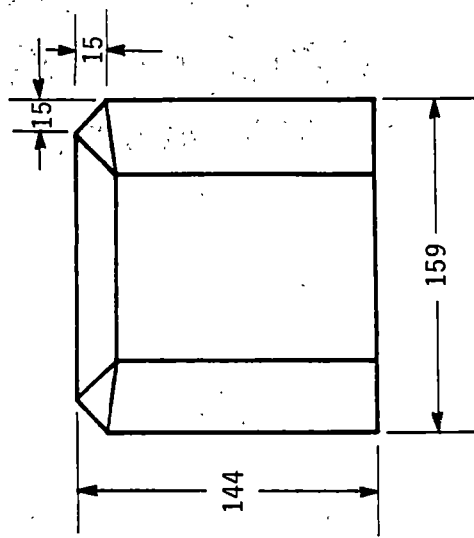
Inside Dimensions Shown  
 All Linear Dimensions in Inches  
 All Angular Dimensions in Degrees



Top View (RMP = 0 deg)



Side View

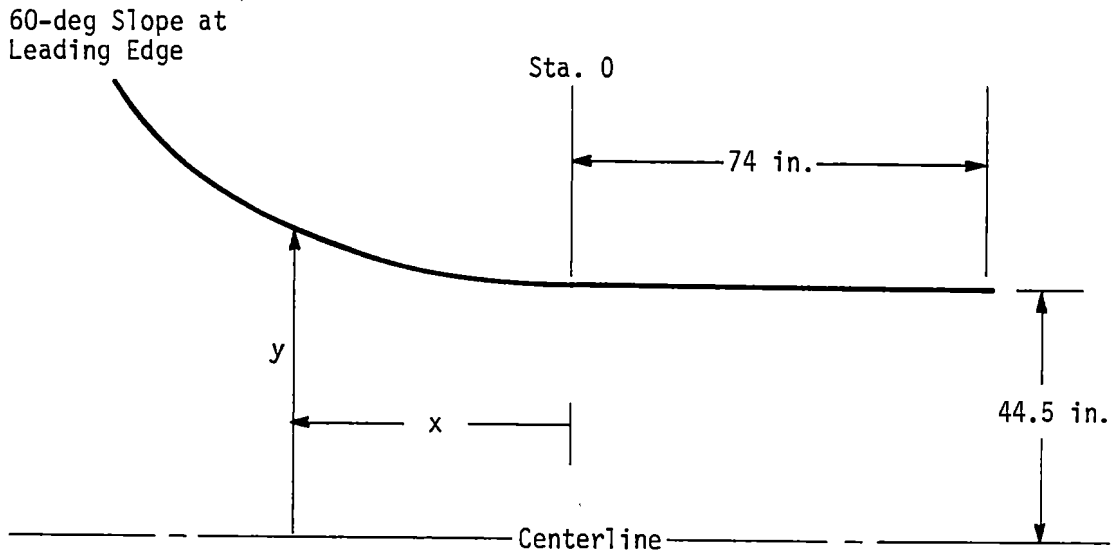


End View

a. Nozzle 3-View

Figure D-6. Nozzle Contours.

Sidewall Contour

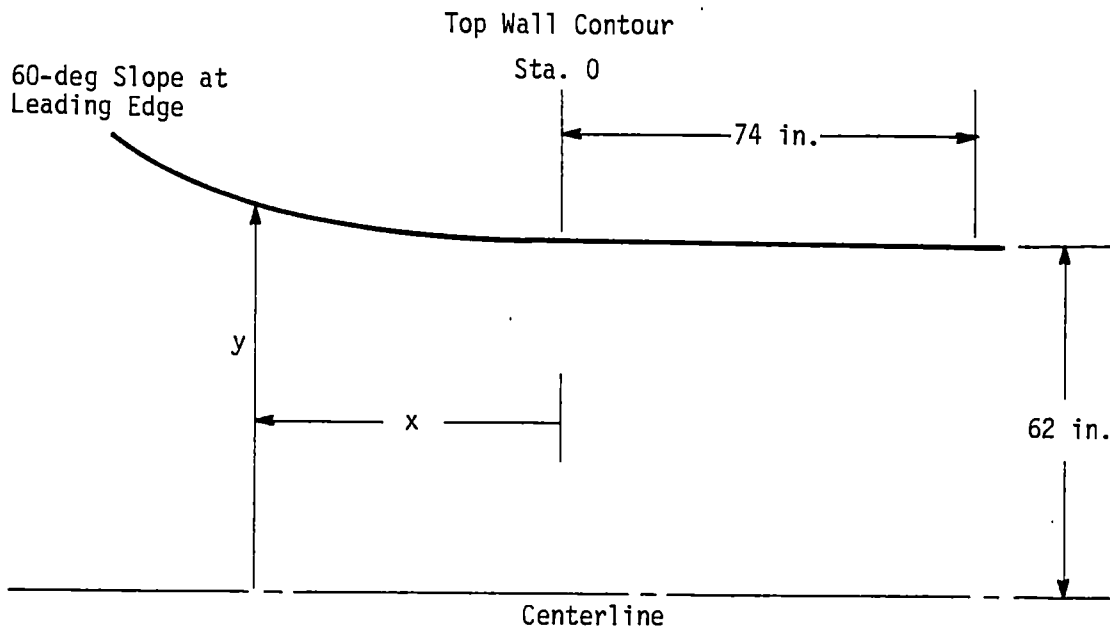


x, in.	y, in.
0.000	44.500
5.000	44.589
10.000	44.857
15.000	45.306
20.000	45.941
25.000	46.770
30.000	47.803
35.000	49.051
40.000	50.533
45.000	52.273
50.000	54.301
55.000	56.661
60.000	59.416
65.000	62.661
70.000	66.552
75.000	71.383
81.000	79.500

where  $y = 96.9263 - (2748.52 - 0.372632x^2)^{1/2}$

b. Nozzle Sidewall Contour

Figure D-6. Continued.

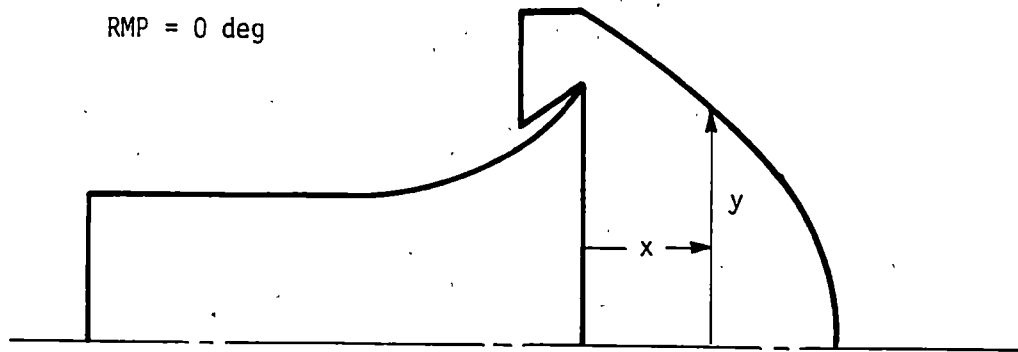


x, in.	y, in.
0.000	62.000
5.000	62.045
10.000	62.178
15.000	62.403
20.000	62.722
25.000	63.138
30.000	63.657
35.000	64.287
40.000	65.036
45.000	65.920
50.000	66.956
55.000	68.171
60.000	69.605
65.000	71.321
70.000	73.436
75.000	76.204
81.000	82.000

where  $y = 85.9882 - (575.434 - 0.0852809x^2)^{1/2}$

c. Nozzle Top Wall Contour

Figure D-6. Concluded.



x, in.	y, in.	x, in.	y, in.
0.000	101.591	60.000	54.337
5.000	98.324	62.000	52.233
10.000	94.966	64.000	49.883
15.000	91.510	66.000	47.250
20.000	87.948	68.000	44.283
25.000	84.273	70.000	40.910
30.000	80.476	72.000	37.019
35.000	76.544	74.000	32.427
40.000	72.467	76.000	26.773
45.000	68.228	78.000	19.139
50.000	63.809	79.000	13.606
55.000	59.188	80.000	0.000

where  $y = (33407.4 - (136.835 + 0.429138x)^2)^{1/2} - (19.5855 + 0.159807x)$

for  $0 \text{ in.} \leq x \leq 60 \text{ in.}$

and  $y = (4435.00 - 1.97307(x - 32.5894)^2)^{1/2}$

for  $60 \text{ in.} < x \leq 80 \text{ in.}$

Figure D-7. Ramp A1 Contour.

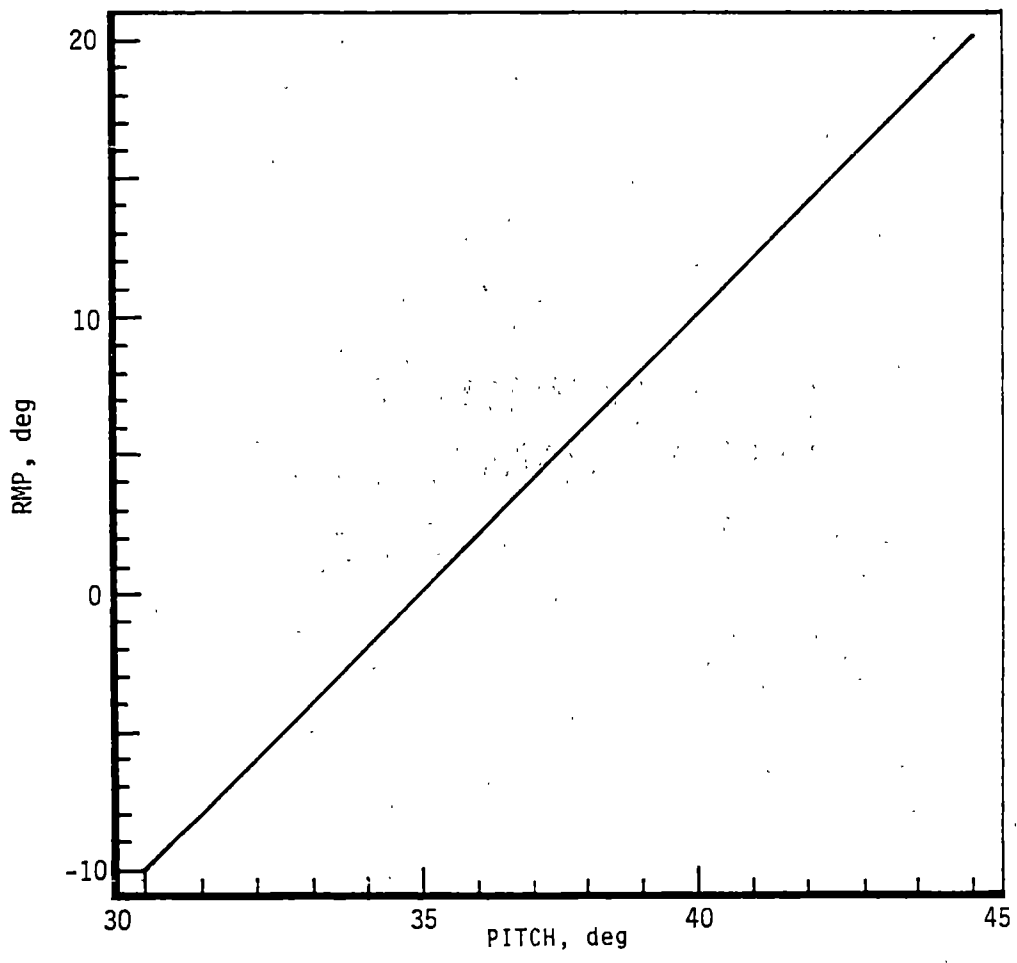
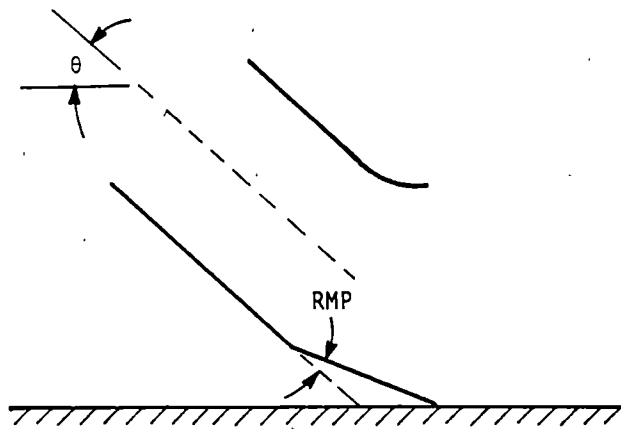


Figure D-8. Ramp Inclination Schedule.



## VITA

Dave Beale was born in Camden, New Jersey on May 21, 1955. He attended public schools and in 1973 graduated from Eastern Regional High School in Voorhees, New Jersey. In the Fall of 1973, he entered the engineering program at the Virginia Polytechnic Institute and State University. He graduated in 1977 with a Bachelor of Science degree in Aerospace and Ocean Engineering. Upon graduation, he moved to Tennessee and joined the Arnold Research Organization, the operating contractor for the Arnold Engineering Development Center (AEDC). From 1977 to 1981 he worked at the AEDC von Karman Facility in the supersonic and hypersonic wind tunnels with emphasis on flow-field measurement and wind tunnel flow quality. In 1981, he moved to the AEDC Engine Test Facility, with Sverdrup Technology, Inc., to work on the development and validation of a free-jet method for evaluating aircraft inlet-engine compatibility. The work included the investigation of secondary flows in free-jet nozzles and the development of flow quality improvement methods, the subjects of this thesis. The development concluded with a validation of the free-jet method using wind tunnel and pilot free-jet facility experiments.

Currently, he continues to focus on the development of improved turbine engine ground test methods with the development of improved airflow measurement techniques and methods for simulating the flow distortion experienced by turbine engines installed in high-performance maneuvering aircraft.